Development and testing of a coupled vegetation / sediment-transport model for dryland environments

Jerome R. Mayaud

Supervisors: Dr R. Bailey & Professor G. Wiggs

A thesis submitted for the degree of

Doctor of Philosophy

at the University of Oxford









Abstract

Drylands are characterised by patchy vegetation, erodible surfaces and erosive aeolian processes. The extreme nature of dryland environments means that semi-arid vegetation cover is often dynamic through time and space, due to complex relationships among plants, soil and transport processes. Understanding how ecogeomorphic processes interact and shape landscape evolution is critical for managing potential environmental and anthropogenic impacts in drylands, since these vulnerable regions are often used for pastoralism, agriculture and habitation.

Despite a wealth of vegetation distribution models that simulate distinctive patterning that is often observed in drylands, relatively little is known about the effects of vegetation patch distribution, geometry and scale on the entrainment and transport of aeolian sediment. Empirical and modelling studies have shown that vegetation elements provide drag on the overlying airflow, thus affecting wind velocity profiles and altering erosive dynamics on desert surfaces. However, these dynamics are significantly complicated by turbulence, porosity and pliability effects in canopies. This thesis therefore presents new high-resolution field data for parameterising wind flow around individual plants and vegetation patches.

Wind transport models have played a key role in simplifying aeolian processes in partly vegetated landscapes, but they remain challenging in some respects. Most models do not recognise the heterogeneous nature of desert surfaces, and those that do are often computationally expensive to run. Cellular automaton (CA) modelling has been successfully used to simulate dryland ecogeomorphic processes over large spatial and temporal scales. However, no existing CA model explicitly links vegetation growth, wind flow dynamics and sediment flux over a surface.

This thesis presents a new CA approach that couples a sophisticated vegetation distribution model with a sediment transport model. The Vegetation and Sediment TrAnsport model (ViSTA) is verified and validated against existing dunefield theory and field datasets. ViSTA is then forced with potential 21st century climate and land use change scenarios, to characterise possible transition scenarios between environmental states in the Kalahari Desert. ViSTA is shown to be a robust geomorphological tool for predicting landscape responses to a variety of human and environmental stresses.

Acknowledgements

This research would not have been possible without the help of a great many people. First, I would like to thank my supervisors, Dr Richard Bailey and Professor Giles Wiggs. They have both been inspirational, encouraging and, above all, fun. Great memories of their guidance and friendship will stay with me forever. Giles's expertise in the field, his unrivalled eye for detail and love of corned beef hash, matched with Richard's passion for modelling and enviable ability to think like a computer, have helped me to produce research that I can be proud of.

I am very grateful to all my funders throughout this DPhil: the Natural Environment Research Council for its generous Doctoral Training Grant (NE/L501530/1), St Catherine's College for a Graduate Scholarship and Hertford College for a Mann Senior Scholarship. NERC also provided me with an invaluable opportunity to undertake a policy internship at the Parliamentary Office for Science and Technology. My thanks go to the British Society for Geomorphology and the European Geosciences Union for funding my attendance to conferences, which have been crucial for disseminating my work and developing my academic network. I am thankful to several Colleges and the School of Geography and the Environment for employing me to teach undergraduate and Masters students.

Spending many months in Namibia's breath-taking deserts has undoubtedly been the most enjoyable part of my research. I thank the Ministry of Environment and Tourism in Namibia for a Skeleton Coast permit (1913/2014), and am indebted to Piet Swiegers at Klein Aus Vista and Pieter and Hannelie Möller at Terra Rouge Farm for their kind permission to conduct field experiments on their land. The Möllers, including Carla and Hano and their dogs Coco and Bussman, have become a second family to me. I regularly dream of being with them again, surrounded by the glowing red dunes of the Kalahari.

I have received superb academic help throughout this DPhil. I thank Dr Mona Edwards and Hong Zhang for their helpful assistance with equipment and in the laboratory, and Dr Matt Baddock for insightful methodological discussions whilst in the field. Other contributions, ranging from advice and comments to feedback on status reports and application references, were gratefully received from Professor Heather Viles, Professor David Thomas, Dr Lorraine Wild, Dr Simon Dadson, Professor Richard Washington, Professor Andreas Baas, Dr Troy Sternberg and Dr Katrin Wilhelm.

There are too many friends and colleagues to thank them all individually, but their contributions, big or small, have been very important to me. I would specifically like to recognise Pippa McClure for her patience and understanding throughout this process. Pippa, you will never know how many lifelines you threw me.

Finally, an unending 'merci' to my family. I would not have got here without you.

I dedicate this thesis with all my love to my parents, Isabelle and Philippe, and to the irreplaceable Chris Greenwood and Claudia Comberti.

Table of Contents

Abstract i
Acknowledgements ii
Table of Contents iii
Glossary of Terms vii
List of Figures xi
List of Tables xviii

SECTION ONE: RESEARCH CONTEXT 1

1. Introduction 2
1.1. Thesis rationale 3
1.2. Research aims and objectives 5
1.3. Thesis structure 6

2. Literature review 11
2.1. The drylands context 12
2.2. Vegetation patterning in drylands 15
2.2.1. Vegetation patterning mechanisms and feedbacks 16
2.2.2. Vegetation shifts in drylands 18
2.3. The impact of vegetation on wind flow 23
2.3.1. Plant wake dynamics 23
2.3.2. Vegetation as a form of surface roughness 27
2.3.3. Trapping of windborne sediment 28
2.3.4. Impacts of plant porosity, pliability and configuration 29
2.4. Sediment transport on vegetated surfaces 33
2.4.1. Evidence from wind tunnel, windbreak and field studies 33
2.4.2. Modelling sediment transport on vegetated surfaces 36
2.4.2.1. Shear stress partitioning 36
2.4.2.2. Okin (2008) model 39
2.4.2.3. Computational Fluid Dynamics modelling 41
2.5. Towards a coupled vegetation/sediment transport approach 43

SECTION TWO: FIELD EXPERIMENTS 46

3. Field Methods 47
3.1. Field site requirements 49
3.1.1. Short-term experiments 49
3.1.2. Longer-term experiments 51
3.2. Field site descriptions 52
3.2.1. Southwestern Kalahari Desert 54
3.2.2. Southern Namib Desert 57
3.2.3. Skeleton Coast National Park 59
3.2.4. Timing of field experiments 62
3.3 Field techniques 62
3.3.1 Measuring flow characteristics 62
3.3.1.1. Wind velocity 62
3.3.1.2. Flow turbulence 64
3.3.2. Calibration of cup anemometers 68
3.3.3. Measuring sediment transport 70

3.3.4. Grain size analysis 72
3.3.5. Vegetation porosity 75
3.3.6. Vegetation transects 79
3.4 Experimental setup 79
3.4.1 Short-term experiments 79
3.4.2 Longer-term wind flow experiments 83

4. Data preparation 87
4.1. Introduction 88
4.2. Sampling periods 89
4.3. Wind data corrections 91
4.3.1. Wind direction 91
4.3.2. Frame of reference rotation 92
4.4. Reynolds stress calculations 94
4.5. Testing data reduction methods 96
4.5.1. Measures of central tendency 96
4.5.2. Wind approach angle thresholds 98
4.5.3. Averaging periods 108

5. Characterizing turbulent wind flow around dryland vegetation (PAPER 1) 115
Abstract 116
5.1. Introduction 117
5.2. Methods 118
5.2.1. Field sites 118
5.2.2. Experimental setup 120
5.2.3. Data analysis 124
5.3. Results and Discussion 126
5.3.1. Mean wind velocity around single vegetation elements 126
5.3.2. Turbulence around single vegetation elements 132
5.3.3. Coherent flow structures 141
5.3.4. Shelter effect 146
5.4. Conclusions 149
Paper summary 152

6. Dynamics of skimming flow in the wake of a vegetation patch (PAPER 2) 153
Abstract 154
6.1. Introduction 155
6.2. Methods 157
6.2.1. Field site 157
6.2.2. Experimental setup 157
6.2.3. Data analysis 159
6.3. Results 164
6.3.1. Mean wind velocity 164
6.3.2. Turbulent stresses 168
6.3.3. Coherent flow structures 171
6.4. Discussion 172
6.5. Conclusion 176
Paper summary 178

7. A field-based parameterisation of wind flow recovery in the lee of dryland plants (PAPER 3) 179
Abstract 180
7.1. Introduction 181

7.2. Methods 183
7.2.1. Field site 183
7.2.2. Experimental setup 185
7.2.3. Data analysis 187
7.3. Results and Discussion 188
7.3.1. Wind velocity data 188
7.3.2. Parameterisation of wind velocity recovery 192
7.3.3. Comparisons to existing models 193
7.4. Conclusions 196
Paper summary 197

SECTION THREE: MODELLING EXPERIMENTS 198

8. A coupled vegetation/sediment-transport model for dryland environments: Model description (PAPER 4, part 1) 199
Abstract 200
8.1. Introduction 201
8.2. Model setup 202
8.3. Vegetation growth (Module 1) 204
8.3.1. Biomass dependencies 205
8.3.2. Neighbourhood interactions and precipitation stress 206
8.3.3. Plant growth 211
8.3.4. Probability of death from stress 215
8.3.5. Probability of recolonisation 219
8.3.6. Update frequencies for Module 1 221
8.4. Wind dynamics (Module 2a) 222
8.4.1. Wind velocity 222
8.4.2. Airflow compression 227
8.4.3. Wind (transport) direction 229
8.5. Sediment movement (Module 2b) 233
8.5.1. Erosion, transport and deposition 233
8.5.2. Surface moisture 236
8.5.3. Additional rules 238

9. A coupled vegetation/sediment-transport model for dryland environments: Model verification and validation (PAPER 4, part 2) 241
Abstract 242
9.1. Introduction 243
9.2. Stable solutions 243
9.3. Impact of stresses 245
9.4. Wake flow dynamics 252
9.5. Temporal and spatial scaling 253
9.6. Dune simulation 256
9.7. Coupled model behaviour 259
9.8. Summary of model verification 262
9.9. Simulating the evolution of a nebkha dunefield 263
9.9.1. Field experimental setup 263
9.9.2. Model setup 266
9.9.3. Simulation results 267
9.10. Conclusions 269
Paper summary 271

10. Modelled responses of the Kalahari Desert to 21st century climate and land use change (PAPER 5) 272

Abstract 273
10.1 Drylands as non-equilibrium environments 274
10.2. Methods 275
10.2.1. Study location 275
10.2.2. ViSTA model 276
10.2.3. Climate projections 279
10.2.4. Model experiments 280
10.3. Kalahari futures 282
10.4. The impact of fire and grazing 290
10.5. Conclusions 294
Paper summary 297

SECTION FOUR: CONCLUSIONS 298

11. Conclusions 298
11.1. Summary of findings 299
11.1.1. Key Question 1 299
11.1.2. Key Question 2 302
11.1.3. Key Question 3 308
11.1.4. Overall conclusions 311
11.2. Future research 312

References 317

Appendices 351
Appendix 1. Supplementary Information (Paper 4) 352
Appendix 2. Supplementary Information (Paper 5) 377

The full ViSTA model code is available on GitHub, an open-source repository, at:
https://github.com/jeromemayaud/ViSTA

Glossary of Terms

Parameter / Coefficient	Description	Unit	Value(s) in this study
a	Coefficient for wind recovery behind a tree	-	0.4
a_D	Empirically fitted constant for Dong et al. (2003) flux model	-	0.0035
age_0	Initial uniform plant age	months	-
α_G	Multiplicative factor for grass recolonization	-	-
α_{Gi}	Initial multiplicative factor for grass recolonization	-	-
α_S	Multiplicative factor for shrub recolonization	-	-
α_{Si}	Initial multiplicative factor for shrub recolonization	-	-
α_T	Multiplicative factor for tree recolonization	-	-
α_{Ti}	Initial multiplicative factor for tree recolonization	-	-
B	Plant biomass	-	-
B_{max}	Maximum plant biomass at full maturity	-	60–480
b	Coefficient for wind recovery behind a grass/shrub	-	-
b_l	Roughness element width (for roughness density)	m	-
b_s	Saturation rate parameter for D_S	-	-
β	Random value for mortality decision	-	0–1
c	Coefficient for wind recovery behind a tree	-	-4.2
c_i	Shell coefficient (vegetation neighbourhood)	-	-1.5–3
c_p	Column number of polled cell	-	-
c_t	Column number of target cell in determining wind path	-	-
C	Speed of sound	m s^{-1}	330
d	Zero-plane displacement height	m	-
d_p	Path distance of sonic transducer	m	-
D	Gaussian distribution constant for coefficient a	-	0.75
D_{con}	Consecutive number of droughts	-	-
D_S	Stress due to accumulated drought	-	-
ΔT_N	Time spent in the primary wind	hours	-
ΔT_1	Time spent in the secondary wind	hours	-
EX_{FL}	Flow exuberance	-	-
EX_{MAG}	Horizontal magnitude of flow exuberance	-	-
ε	Height limit for plant impact on p_{dV}	m	0.1
F_S	Stress due to fire	-	-
g	Acceleration due to gravity	m s^{-2}	9.81
G_{cum}	Cumulative growth of a plant	-	-
G_{mid}	Sigmoid midpoint of B	mm yr^{-1}	25–210
G_S	Stress due to grazing	-	-
G_{unit}	Growth gain unit	-	-0.05–1
h	Height of plant	m	0–6
h_d	Downwind distance normalised to plant height	-	-
h_L	Lateral distance normalised to plant height	-	-
h_{max}	Maximum height of plant	m	0–6
h_t	Trunk height of tree	m	0–5
H	Threshold criterion for quadrant analysis	-	-

θ	Wind angle	degrees	0–360
θ_i	Optical porosity of plant	%	0–100
θ_{cum}	Cumulative optical porosity of several plants	%	0–100
θ_D	Divergence angle between two winds	degrees	0–165
i	Intercept of wind path with domain edge	-	-
k_1	Steepness parameter for G_{unit}	-	15
k_2	Steepness parameter for B	-	0.015–0.14
k_c	Competition strength of a plant	-	-
k_f	Facilitation strength of a plant	-	-
κ	von Karman constant	-	0.4
l	Saturation rate parameter for F_S	-	-
λ	Roughness density	-	-
m	Scaling parameter for precipitation stress	-	0.8–1
m_{eff}	Effective surface moisture	-	0–1
M	Age-dependent stress	-	-
μ_T	Trunk height at which maximum airflow compression occurs	m	1.50
n	Slope factor for G_S	-	15
n	Number of roughness elements (for roughness density)	-	-
N	Transport ratio	-	1–5
Ω	Stocking rate	LSU ha^{-1}	0.015–0.06
p_d	Probability of deposition	-	0–1
p_{dV}	Probability of deposition in the presence of vegetation	-	0–1
p_e	Probability of erosion	-	0–1
p	Plant population density	-	0–1
p_0	Initial plant population density	-	0–1
p_{eq}	Stable plant population density	-	-
p_i	Peak position parameter for B	-	60–480
p_{RG}	Probability of recolonization by grass	-	-
p_{RS}	Probability of recolonization by shrub	-	-
p_{RT}	Probability of recolonization by tree	-	-
P_G	Current proportion of grass	%	-
P_S	Current proportion of shrub	%	-
P_T	Current proportion of tree	%	-
ρ	Precipitation stress	mm yr^{-1}	0–1000
ρ_{air}	Air density	kg m^{-3}	1.25
ρ_{equal}	Precipitation level where neither grass nor tree recolonization dominates	mm yr^{-1}	600
ρ_{mid}	Precipitation level that has neither a beneficial nor detrimental effect on a plant	mm yr^{-1}	180–500
Q	Mass flux (sediment transport rate)	kg m^{-1} s^{-1}	-
Q1	First quadrant event (outward interaction)	-	-
Q2	Second quadrant event (ejection)	-	-
Q3	Third quadrant event (inward interaction)	-	-
Q4	Fourth quadrant event (sweep)	-	-
r_p	Row number of polled cell	-	-
r_t	Row number of target cell in determining wind path	-	-

S	Surface area (for roughness density)	m^2	-
s_c	Sensitivity of a plant to competition	-	-
Sed_S	Stress due to sedimentation balance	-	-
s_f	Sensitivity of a plant to facilitation	-	-
s_h	Surface height	m	-
σ_{norm}	Normalised standard deviation of wind velocity	$m\ s^{-1}$	-
ζ	Volumetric porosity	%	-
t_r	Time since rain	hours	-
t_1	Signal propagation time from transmitter to receiver	seconds	-
t_2	Signal propagation time from receiver to transmitter	seconds	-
T	Total neighbourhood score	-	-
T_S	Total stress experienced by plant	-	-
$\tilde{T}$	Normalised total neighbourhood score	-	-
$\tilde{T}_{mid}$	Sigmoid midpoint of $\tilde{T}$	-	0.4
TI_{norm}	Normalised turbulence intensity	$m\ s^{-1}$	-
t	Time (of measurement/model iteration)	seconds	-
τ	Total drag	$N\ m^{-2}$	-
τ_r	Resultant horizontal shear stress	$N\ m^{-2}$	-
$\tau_{r_{CI}}$	Confidence interval – resultant horizontal shear stress	$N\ m^{-2}$	-
$\tau_{r\,norm}$	Normalised resultant horizontal shear stress	-	-
τ_R	Drag on individual roughness elements	$N\ m^{-2}$	-
τ_S	Drag on intervening surface	$N\ m^{-2}$	-
ϕ	Normalised mean wind velocity	$m\ s^{-1}$	-
u, U	Horizontal wind velocity	$m\ s^{-1}$	0–15
u_*	Wind shear velocity	$m\ s^{-1}$	-
u_0	Minimum wind velocity in lee of upwind plant	$m\ s^{-1}$	-
u_{ref}	Unobstructed wind velocity	$m\ s^{-1}$	-
u_{slope}	Slope-corrected wind velocity	$m\ s^{-1}$	-
u_{surf}	Wind velocity in plant wake	$m\ s^{-1}$	-
u_z	Wind velocity at height z above surface	$m\ s^{-1}$	-
u_t	Wind velocity threshold for sediment entrainment	$m\ s^{-1}$	5.1
u_0	Minimum wind velocity in lee of a plant	$m\ s^{-1}$	-
u_1	Measured horizontal wind velocity	$m\ s^{-1}$	-
u_2	Horizontal wind velocity after rotation	$m\ s^{-1}$	-
u'	Instantaneous horizontal wind velocity	$m\ s^{-1}$	-
$\overline{u'^2}$	Horizontal normal Reynolds stress	$m\ s^{-1}$	-
$\overline{u'^2}_{CI}$	Confidence interval – horizontal normal Reynolds stress	$m\ s^{-1}$	-
$\overline{u'^2}_{norm}$	Normalised horizontal normal Reynolds stress	-	-
$-\overline{u'w'}$	Reynolds shear stress	$N\ m^{-2}$	-
$-\overline{u'w'}_{norm}$	Normalised Reynolds shear stress	-	-
$\overline{U}$	Mean wind velocity	$m\ s^{-1}$	-
v	Lateral/spanwise wind velocity	$m\ s^{-1}$	-
v_1	Measured spanwise wind velocity	$m\ s^{-1}$	-
v_2	Spanwise wind velocity after rotation	$m\ s^{-1}$	-
v'	Instantaneous spanwise wind velocity	$m\ s^{-1}$	-
$\overline{v'^2}$	Spanwise normal Reynolds stress	$m\ s^{-1}$	-
$\overline{V}$	Average spanwise wind velocity	$m\ s^{-1}$	-
w	Vertical wind velocity	$m\ s^{-1}$	-

w_1	Measured vertical wind velocity	m s^{-1}	-
w_2	Vertical wind velocity after rotation	m s^{-1}	-
w'	Instantaneous vertical wind velocity	m s^{-1}	-
w_i	Width parameter for B	-	24–152
$\overline{w'^2}$	Vertical normal Reynolds stress	m s^{-1}	-
$\bar{W}$	Average vertical wind velocity	m s^{-1}	-
ω	Change coefficient for u_{slope}	-	0.1
x	Downwind distance from plant	m	-
γ	Additive factor for u_{slope}	-	-
ψ	Shelter parameter	-	-
z	Plant age	months	-
z_i	Height above surface	m	-
Z_S	Stress due to age	-	-
z_0	Aerodynamic roughness	m	-

List of Figures

Main body

Figure 1.1. Linkages between papers presented in this thesis.

Figure 2.1. The global distribution of drylands.

Figure 2.2. The multi-scaled interplay of biophysical and anthropogenic factors characterising many of the world's drylands.

Figure 2.3. Aerial imagery of dryland vegetation patterning.

Figure 2.4. Schematic representation of the competitive and facilitative interactions typical of trees or shrubs in drylands.

Figure 2.5. Flow visualisation around a single vegetation element, showing the development of six different flow regimes.

Figure 2.6. Flow visualisation downwind of a single tree.

Figure 2.7. Flow regimes and associated theoretical wake development.

Figure 2.8. Main zones of possible speedup/slowdown around a roughness element.

Figure 2.9. Image sequences of sediment deposition patterns.

Figure 2.10. Illustration of the parameters used to calculate roughness density (λ) in roughness studies.

Figure 2.11. The Telephone Pole Problem.

Figure 2.12. The distribution of reduced shear stress on the surface during wind erosion in the Raupach (1992) model.

Figure 2.13. Contours of shear stress around isolated cylindrical elements.

Figure 3.1. Definitions and example photographs of study vegetation elements.

Figure 3.2. Locations of the three field sites in Namibia.

Figure 3.3. Location map of the southwestern Kalahari field site.

Figure 3.4. Location map of the southern Namib field site.

Figure 3.5. Location map of the Skeleton Coast field site.

Figure 3.6. Example of an A-100 R cup anemometer and W200P wind vane used in the field study.

Figure 3.7. CSAT-3 sonic anemometers deployed in the field.

Figure 3.8. Linear regression between mean wind velocity measured using cup anemometers and corresponding wind velocity measured using a sonic anemometer.

Figure 3.9. Sediment traps and grain impact sensors.

Figure 3.10. Grain size distributions for samples taken at long-term and short-term experimental sites.

Figure 3.11. Transformation of a digital photograph of shrub $Sh_{cup}1$ from full colour to grayscale to black/white pixel count.

Figure 3.12. Workflow for calculation of volumetric porosity.

Figure 3.13. Comparison between volumetric porosity and optical porosity.

Figure 3.14. Schematic diagram of an example experiment setup.

Figure 3.15. Schematic representation of the experimental setup at L1 and L2.

Figure 3.16. Long-term instrument arrays at sites L1 and L2.

Figure 4.1. Wind velocity for the three experimental setups.

Figure 4.2. Required sampling period for velocity measurements as a function of wind velocity for different observation heights.

Figure 4.3. Schematic diagram of the three rotations most commonly applied for orienting the frame of reference of sonic anemometers.

Figure 4.4. Quadrant plot of four discrete momentum exchange structures.

Figure 4.5. Normal probability plot and frequency histogram for 10-second averaged wind velocity data from the reference anemometer in $Gr_{cup}2$.

Figure 4.6. Schematic plan-view diagram demonstrating the zones of potential measurement relative to the centreline of the prevailing wind, at different directional thresholds.

Figure 4.7. The effect of downwind distance on the maximum wind approach angle for detected wind to be interacting directly with the study element.

Figure 4.8. Total number of minutes in the usable datasets for each setup in experiment $Gr_{cup}2$.

Figure 4.9. The effect of different wind direction thresholds on wind flow parameters.

Figure 4.10. Percent difference in statistics of wind flow downwind of $Gr_{cup}2$ for different wind angle threshods.

Figure 4.11. The effect of changing the wind angle threshold on the relative standard error (RSE) of normalised 10 s wind velocities.

Figure 4.12. Total number of minutes in the usable datasets for each setup in experiment $Gr_{cup}2$.

Figure 4.13. The effect of averaging period on wind flow parameters.

Figure 4.14. Percent difference in statistics of wind flow downwind of $Gr_{cup}2$ for different averaging periods.

Figure 4.15. The effect of changing the averaging period on the relative standard error (RSE) of normalised wind velocity datasets.

Figure 5.1. Field locations and example experimental setup.

Figure 5.2. Spatial patterns of normalised mean wind velocity (Φ) at 0.30 m and element height.

Figure 5.3. Best fit regression lines for normalised mean wind velocity (Φ) downwind of the study elements at 0.30 m height.

Figure 5.4. Horizontal wind velocity distributions for instantaneous 10 Hz sonic anemometry data at 0.30 m height.

Figure 5.5. Horizontal spatial patterns of average normalised horizontal normal Reynolds stress ($\overline{u'^2}_{norm}$) at 0.30 m and element height.

Figure 5.6. Horizontal spatial patterns of average normalised Reynolds shear stress ($-\overline{u'w'}_{norm}$) at 0.30 m and element height.

Figure 5.7. Variations in normalised Reynolds shear stress ($-\overline{u'w'}_{norm}$), vertical streamline angle and normalised mean wind velocity (Φ) at 0.30 m and height of elements.

Figure 5.8. Horizontal magnitude of flow exuberance and flow positivity.

Figure 5.9. Variations in the shelter parameter (ψ) along the centreline of the three element wakes at 0.30 m height.

Figure 6.1. Location map of field site and photographs of experimental setup.

Figure 6.2. Contour plot of normalised mean wind velocity (Φ).

Figure 6.3. Best fit regression lines for normalised mean wind velocity (Φ) at all measurement heights downwind of the patch.

Figure 6.4. Variations in turbulence parameters downwind of the patch.

Figure 6.5. Frequency of occurrence (%) of coherent structures along patch wake.

Figure 7.1. Locations of field sites and example experimental setup.

Figure 7.2. Spatial patterns of normalised mean wind velocity (Φ) at 0.30 m height for the eight study elements.

Figure 7.3. Normalised mean wind velocity (Φ) along the centreline of the study element wakes at 0.30 m height.

Figure 7.4. Relationship between element optical porosity (θ_i) and b coefficient (i.e. recovery rate) and mean normalised wind velocity (Φ) in the immediate lee.

Figure 7.5. Parameterised wind velocity recovery along the wake centreline of an element with an optical porosity (θ_i) of 50%.

Figure 8.1. Flow diagram summarising the main module interactions within the ViSTA model.

Figure 8.2. Coefficient values for strength of competitive/facilitative effects depending on plant biomass.

Figure 8.3. Schematic representations of model functions.

Figure 8.4. Functions for stress due to plant age (Z_S) and stress due to sedimentation balance (Sed_S).

Figure 8.5. The distribution of reduced wind shear stress on the surface during wind erosion in the Raupach (1992) model, compared to the distribution of reduced wind velocity in the ViSTA model.

Figure 8.6. Example of wind speedup and slowdown as wind flow passes over a modelled barchanoid dune.

Figure 8.7. Schematic diagram showing how wind path is calculated.

Figure 8.8. Transport and feedback functions for surface moisture.

Figure 8.9. Shadow zones and avalanching.

Figure 9.1. Emergence of spatial vegetation patterning at different precipitation stress levels (ρ) for all three vegetation types.

Figure 9.2. Change in vegetation type proportions under low, medium and high precipitation regimes.

Figure 9.3. Change in vegetation type proportions and population density under different fire regimes, for different precipitation regimes.

Figure 9.4. Change in vegetation type proportions and population density under different grazing regimes, for different stocking rates.

Figure 9.5. Recovery of wind flow downwind of individual plants at differing distances apart.

Figure 9.6. Simulated morphology under varying iteration resolutions.

Figure 9.7. Simulated morphology evolving from different spatial grid resolutions.

Figure 9.8. Simulated dune morphologies in different wind direction variability and sediment availability regimes.

Figure 9.9. Simulated morphology, vegetation height and vegetation type in the fully coupled model, in a v-shaped precipitation regime and for different wind scenarios.

Figure 9.10. Photographs and TLS scans of the study nebkhas in the Skeleton Coast National Park.

Figure 9.11. Simulated morphology and vegetation cover in conditions similar to those observed in the Skeleton Coast National Park, Namibia.

Figure 9.12. Three-dimensional representations of combined vegetation and surface morphology for the Skeleton Coast simulation.

Figure 10.1. Location maps, observed and modelled vegetation states, and predicted future precipitation trends.

Figure 10.2. Projected changes in precipitation, separated by season, over the period 2017–2100.

Figure 10.3. Equilibrium landscape characteristics at the three study sites for the three chosen years.

Figure 10.4. Landscape characteristics during the transient model runs, from 2017 to 2100, at the three study sites.

Figure 10.5. Matrices of population density and grass:shrub ratios at Maun and Tsabong, with different fire frequencies and grazing intensities.

Figure 10.6. Cumulative frequency curves of absolute population density of grasses and shrubs at Maun and Tsabong, for different fire/grazing scenarios.

Appendices

Figure 9.S1. Emergence of spatial vegetation patterning at different precipitation stress levels (ρ).

Figure 9.S2. Comparison of selected modelled vegetation patterning states and satellite imagery of semi-arid vegetation in Niger.

Figure 9.S3. Normalised frequency distributions of patch perimeter lengths for all patches identified using FRAGSTATS from modelled and observed landscapes.

Figure 9.S4. Neighbourhood interactions for isolated spots and gaps of differing sizes.

Figure 9.S5. Influence of plant biomass on neighbourhood interactions, at different precipitation levels.

Figure 9.S6. Impact of initial uniform vegetation age (age_0) on population decline trajectories, when dead cells are not permitted to regrow in the model.

Figure 9.S7. Effect of sediment balance stress (Sed_S) on vegetation growth.

Figure 9.S8. Simulated morphology developing from different maximum angles at which shadowing occurs.

Figure 9.S9. Examples of wind direction variation across the model domain.

Figure 9.S10. The effect of vegetation porosity on the recovery of wind velocity downwind of a vegetation patch.

Figure 9.S11. Wake interactions between vegetation patches.

Figure 9.S12. Wind recovery downwind of three trees with different characteristics.

Figure 9.S13. The impact on surface evolution of changing the maximum number of cells a sand slab can travel downwind of its source cell.

Figure 9.S14. Simulated surface height 24 hours after a rain event, with different moisture feedback update frequencies and update resolutions.

Figure 9.S15. Simulated morphology evolving from varying the sediment depth and vegetation cover.

Figure 9.S16. Simulated patterning for different spatial grid resolutions of the vegetation module.

Figure 9.S17. Simulated dune morphologies in the parameter space $\{\theta_D, N\}$ of bidirectional wind regimes for two conditions of sediment availability.

Figure 9.S18. Wind flow data from a 10-day period in September recorded in the Huab Valley, Skeleton Coast, Namibia.

Figure 10.S1. Projected changes in average maximum daily temperature over the period 2017–2100.

Figure 10.S2. Modelled and observed total monthly precipitation for Maun, Tshane and Tsabong.

Figure 10.S3. Weibull distributions of wind velocities recorded at Twee Rivieren.

Figure 10.S4. The replacement of woody shrubs by perennial grasses following herbicide application ('de-bushing').

Figure 10.S5. Effect of rainfall variability on population density and proportions of vegetation types, for two rainfall scenarios (no trend, and v-shaped).

Figure 10.S6. Effect of rainfall variability on population density and proportions of vegetation types, for a scenario of decreasing rainfall.

Figure 10.S7. Effect of rainfall variability on population density and proportions of vegetation types, for a scenario of increasing rainfall.

Figure 10.S8. Equilibrium normalised annual average plant age for grasses, shrubs and trees at the three chosen years.

Figure 10.S9. Effect of varying the sediment importance factor on landscape characteristics.

Figure 10.S10. Effect of varying summer (DJF) rainfall (on grass:shrub ratios and population density) and effect of varying fixed shrub porosity (on total sediment transport).

List of Tables

Main body

Table 3.1. Field techniques and parameters measured during fieldwork.

Table 3.2. Sediment samples for grain size analysis, and their corresponding field experiments.

Table 3.3. Summary table of anemometer configurations and heights for short-term experiments.

Table 3.4. Vegetation density distributions at longer-term sites L1 and L2.

Table 4.1. Results of the Shapiro-Wilk Expanded Test for normality in all wind velocity datasets for experiment $Gr_{cup}2$.

Table 4.2. p-values derived from paired Student's t-tests between the wind velocity datasets for each wind approach angle threshold (10–30^{o}) and that for the 5^{o} threshold.

Table 4.3. p-values derived from paired Student's t-tests between the wind velocity datasets derived using averaging period from 20–60 s, and the dataset using the 10 s averaging period.

Table 5.1. Descriptive experimental statistics for the three sonic anemometry experiments around single vegetation elements.

Table 5.2. Average plant characteristics for grasses, shrubs and trees in relevant dryland regions, as reported in previous studies and unpublished data from authors.

Table 6.1. Quadrant frequencies in unperturbed flow over bare, flat surfaces, as reported in previous studies.

Table 8.1. Calculations of wind path through each polled cell, depending on the gradient of the wind trajectory and the local intercept conditions.

Table 9.1. Characteristics of the study nebkhas that were analysed using the TLS for the purposes of model validation.

Table 10.1. Summary of model state parameters and coefficients used in Paper 4.

Appendices

Table 9.S1. Initial conditions and parameters of the bidirectional wind regime in the numerical simulations on modes of dune formation.

Table 10.S1. Number of usable data points (over the period 1994–2013), and maximum likelihood estimates of the 2-parameter Weibull distribution.

SECTION ONE

RESEARCH CONTEXT

CHAPTER ONE

Introduction

1. INTRODUCTION

1.1. Thesis rationale

Aeolian landscapes in dryland regions are dominated by the interactions between ecological processes and sediment transport processes (Baas & Nield, 2007). Wind regime and sediment supply are known to largely control the formation of bare-sand dunes (e.g. Wasson & Hyde, 1983; Werner, 1995; Momiji et al., 2000; Bishop et al., 2002), but the dynamic interactions between vegetation and sediment movement, which form part of a wider, multi-scaled interplay of biophysical and anthropogenic factors, are less well understood (Hesp, 2002; Nield & Baas, 2008a).

The extreme nature of drylands means that semi-arid vegetation is often patchy and dynamic through time and space, due to complex relationships between plants, soil and transport processes (Meron et al., 2004; Borgogno et al., 2009; Wainwright, 2009; Bailey, 2011; Stewart et al., 2013; Getzin et al., 2014). Vegetation elements provide drag on the overlying airflow, thus affecting wind velocity profiles and aeolian dynamics on desert surfaces (Ash & Wasson, 1983; Wasson & Naninga, 1986; Gillette & Stockton, 1989; Wolfe & Nickling, 1993; Wiggs et al., 1994, 1995; Tegen et al., 2002; MacKinnon et al., 2004; King et al, 2005). These dynamics are complicated by turbulence, porosity and pliability in plant canopies. Although self-organised patchiness and catastrophic shifts in these environments have been investigated (e.g. Bailey, 2011), relatively little is known about the effects of vegetation distribution, geometry and scale on the entrainment, transport and redistribution of wind-blown material at the meso- and macro-scales. Significant uncertainty therefore remains about how these landscapes will react to increasing climate forcing and land-use pressure over the 21st century and beyond.

Previous attempts to quantify the impact of vegetation on erosivity and erodibility have been challenging in some respects. Dune mobility potential over long

timescales has been successfully modelled using simple wind-based indices (e.g. Thomas et al., 2005; Wang et al., 2009), but such an approach does not resolve sediment transport dynamics at the same scale as plant-flow interactions. Traditional shear stress partitioning methods (e.g. Raupach et al., 1993; Marticorena & Bergametti, 1995) rely heavily on the dimensionless roughness density (λ) and therefore suffer from its inherent requirement for a given surface to be treated homogenously. An alternative model by Okin (2008) emphasises gaps in vegetation structure and allows entrainment thresholds to vary across a surface. While this approach has several advantages, it still aggregates the total sediment flux produced over a given area, which does not allow bedforms or aeolian transport processes to be modelled at anything finer than landscape scale. CFD modelling can be used to resolve turbulent wind flow around individual vegetation elements (e.g. Dupont et al., 2014), but computational expense limits its ability to simulate long-term erosion at anything larger than the field scale.

A new modelling approach is therefore needed that recognises the heterogeneous nature of semi-arid surfaces, whilst allowing for landscapes to be simulated over large areas and long timescales. Predictive modelling of ecogeomorphic dynamics is crucial for improving our understanding and management of potential dryland landscape responses to both environmental and anthropogenic influences. Applications include mitigation of land degradation (Barbier et al., 2006), climate change impact assessments (Thomas et al., 2005; Seager et al., 2007; Wang et al., 2009) and investigating the effects of changes in land use (Levin & Ben-Dor, 2004) in drylands.

1.2. Research aims and objectives

The overall aim of this project is to measure, model and evaluate the interactions between wind flow, spatial vegetation patterning and sediment flux in dryland landscapes. This main aim will be addressed by three key questions, which are answered using research objectives based on fieldwork and modelling:

Key Question 1. *How does turbulent airflow vary around single vegetation elements in a dryland, and how is this affected by the type, size and porosity of plants?*

> **Objective 1.** Quantify extremes in erosivity by measuring wind structures (velocity and turbulence statistics) upwind and downwind of various plant types (shrubs, grasses and trees) of different sizes and porosities. [fieldwork]

Key Question 2. *How do different vegetation patterns affect wind flow, and therefore sediment movement, across a semi-arid landscape?*

> **Objective 2.** Measure wind flow at the patch scale in the wake of a vegetation patch experiencing skimming flow. [fieldwork]
>
> **Objective 3.** Couple a spatial vegetation patterning model to a wind erosion model, and simulate potential levels of aeolian transport in locations with different distributions, scales and geometries of vegetated patches. [modelling]
>
> **Objective 4.** Test model performance using: (i) theoretical relationships between sediment supply and wind direction variability to explore dune formation; (ii) high-resolution topography data of erosion/deposition zones in the wakes of plants. [fieldwork & modelling]

Key Question 3. *What is the likely response of a dryland landscape to future climate and land use change, and can we predict threshold-related transitions from stability to accelerating aeolian activity?*

> **Objective 5.** Force the coupled model with potential scenarios of future climate and land-use change. [modelling]

* *

The fieldwork undertaken during this project provides empirical data that can be used to better constrain the impact of plant type, configuration and porosity on wind flow in deserts. Such effects are not yet fully explored in the literature, so it is a valuable addition to our understanding of wind flow on semi-vegetated surfaces. The empirically-derived dynamics of wind around individual vegetation elements and small vegetation patches are integrated into a wind flow/sediment transport model, which is coupled with an adapted version of Bailey's (2011) vegetation distribution model to form the Vegetation and Sediment TrAnsport (ViSTA) model.

The ViSTA model allows potential levels of aeolian transport to be simulated in locations with different distributions, scales and geometries of vegetated patches. Its performance is tested using longer-term wind and vegetation patterning data collected in the field. The ViSTA model is then forced with potential scenarios of future climate and land-use change, to understand the likely response of a dryland landscape to such pressures. Ultimately, the model allows us to predict threshold-related transitions in vulnerable dryland environments around the world.

1.3. Thesis structure

This thesis follows the format of a thesis by papers, and is organised into four sections. Section One sets the research into a broader context, Section Two presents the methods and results from field experiments, Section Three provides a description of the model and results from modelling experiments, and Section Four discusses the implications of the results and conclusions. The papers are presented in standardised chapter formats, but the content is the same as is published by, or submitted to, the respective journal. A detailed structure of the thesis is outlined below, with linkages between the papers illustrated in Figure 1.1.

Section One: Research context

Chapter 1 has provided an overview of the thesis, including a summary of the background literature and the aims and objectives of the project. **Chapter 2** consists of an in-depth literature review of the current understanding of aeolian processes in deserts, focusing particularly on the effect that vegetation has on wind flow and sediment transport. Vegetation patterning in semi-arid areas is also examined, and concepts from complexity theory, specifically self-organisation, are introduced.

Section Two: Field experiments

Chapter 3 describes and explains the methods used in the field experiments. This includes site selection requirements, study site descriptions, discussion of measurement techniques used for monitoring wind flow and sediment transport over a variety of spatial and temporal scales, and the experimental setups for collecting data. **Chapter 4** follows on from this to outline the procedures used to clean and standardise the various short-term cup and sonic anemometry datasets in this study. Appropriate sampling period lengths are determined, and protocols for dealing with wind directional changes and frame of reference rotations of sonic anemometer are discussed. A preliminary investigation is then presented that explores: (i) the appropriate time-period over which to average wind flow parameters; (ii) the appropriate wind approach angle threshold with which to filter the datasets.

Chapter 5 (Paper 1) presents results from short-term sonic anemometry experiments conducted in Namibian drylands. Three-dimensional wind velocity is measured at high frequency (10 Hz) at two heights around a grass, a shrub and a tree. The recovery of mean wind velocity in the wakes of the three elements is initially explored, and the results compared to recovery patterns reported in previous

studies. The classical approach of Reynolds' rule of decomposition is then employed to derive various turbulence statistics, in order to provide an insight into how the turbulent characteristics of the flow change around the vegetation elements. Finally, the variation in frequency and magnitude of structured events within the flow around the elements are examined.

Chapter 6 (Paper 2) provides similar analysis of wind flow recovery in the wake of a vegetation patch above which skimming flow has developed. Three-dimensional wind velocity is measured at 10 Hz at four heights along a transect in the lee of an extensive patch of shrubs. The recovery of mean wind velocity, Reynolds stresses and structured events within the flow are measured, allowing aerodynamic behaviour changes to be characterised at high horizontal and vertical resolutions. The results are compared to the recoveries derived in Chapter 5.

In **Chapter 7 (Paper 3)**, a generic parameterisation of flow recovery based on plant height and porosity is presented. Best-fit parameters for the equation are derived using a field dataset of wind flow in the lee of eight individual plants. Together, Chapters 5, 6 and 7 provide empirical data of wind flow dynamics on partly vegetated surfaces, which can be usefully integrated into the main model later.

Section Three: Modelling experiments

Chapter 8 (Paper 4, part 1) presents a new, coupled vegetation/sediment transport model (the ViSTA model), which is designed to address issues with current wind erosion models raised earlier in the thesis. The technical aspects of the modules that constitute ViSTA are described, including a new method for implementing oblique winds and new empirically derived parameterisations for wind flow recovery in plant wakes. Various aspects of the model are then explored and tested in **Chapter 9**

(Paper 4, part 2), to ensure the model reproduces aeolian and ecological processes in a realistic manner. Verification tests include conservation of mass, wind dynamics on vegetated surfaces, depositional processes, the effects of surface moisture, and the impact of temporal and spatial scaling on model results. Several validation tests are then undertaken to verify the ability of the ViSTA to replicate realistic sediment transport dynamics. First, the sediment movement module is tested separately to investigate equilibrium recovery in the model, the impact of sediment supply and transport rate on resultant bedforms (tested against existing theory) and the model's ability to simulate sand deposits in the wake of porous plants (validated against field data). **Appendix 1** provides additional verification tests.

In **Chapter 10 (Paper 5)**, the ViSTA model is forced with a variety of scenarios representing potential future environmental and anthropogenic stresses on drylands. A range of human disturbances is a common feature of many drylands, and these can force a fragile ecosystem to rapidly shift to an alternative state. The model is used to understand the transitions leading from vegetated to low-productivity (bare-soil) states, in response to 21st century climate change and different fire/grazing regimes. Identifying observable indicators of fragility and threshold proximity in populated dryland systems has direct relevance to land management policies. **Appendix 2** provides more detail on the methods used in this paper, and additional analysis.

Section Four: Conclusions

Chapter 11 brings the substantive sections of the thesis together, to identify how the aim and objectives were addressed. The contributions of the findings of the individual

papers to the broader literature are discussed, and potential agendas for future research in this field outlined.

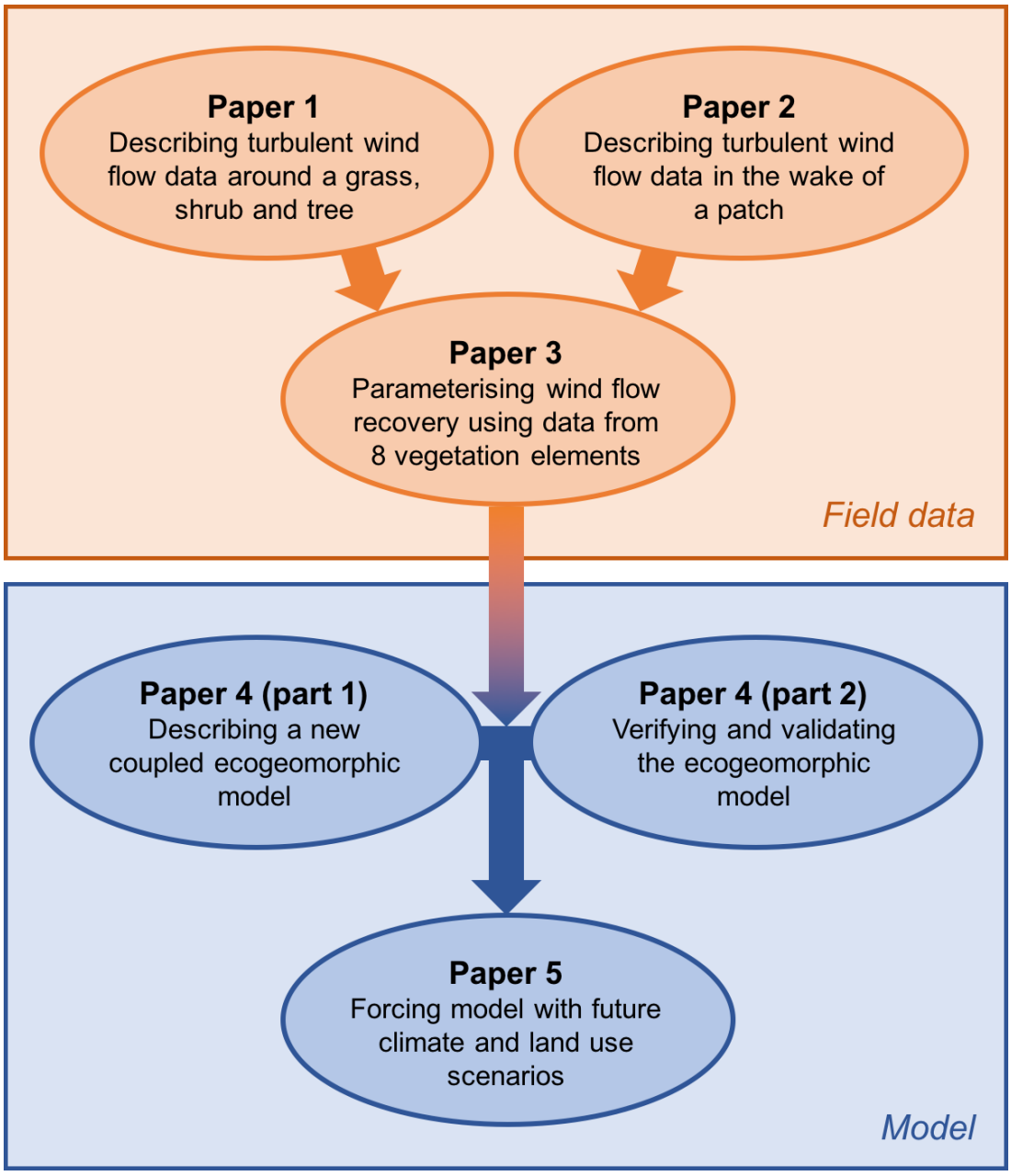


Figure 1.1 Linkages between papers presented in this thesis.

CHAPTER TWO

Literature Review

2. LITERATURE REVIEW

2.1. The drylands context

The terms ‘dryland’, ‘arid zone’ and ‘desert’ are used somewhat interchangeably in both popular and scientific literature, an inconsistency which often causes confusion in the delimitation of moisture-deficit regions (Thomas, 2011). UNEP’s (1998) four-fold classification of dryland environments – based on aridity indices that are defined by net surface water deficits – is perhaps the most comprehensive to date. According to UNEP’s scheme, drylands constitute about 47% of the global land area (Figure 2.1). Dryland environments are extreme in their nature, typified by non-equilibrium conditions in climate, vegetation and geomorphology (Viles, 2011).

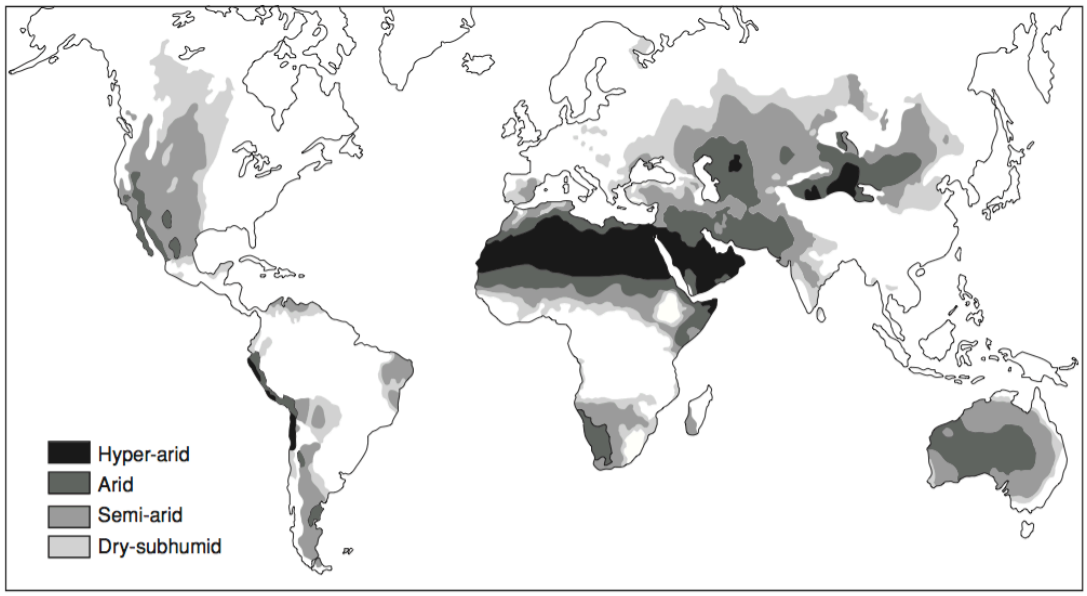


Figure 2.1 The global distribution of drylands (from Thomas, 2011, p.8).

Aeolian landscapes in dryland regions are dominated by the interactions between ecological processes and sediment transport processes (Baas & Nield, 2007). The strong interannual variability in precipitation characteristic of drylands (Thomas & Shaw, 1991; Goudie, 2002) often results in ephemeral vegetative cover (Ravi et al., 2010) or distinctive spatial patterning (Kéfi et al., 2007a). In turn, the limited nature of

vegetation cover makes it an important variable in dictating the rate and extent to which geomorphological – and notably aeolian – processes operate. However, the dynamic interactions between vegetation and sediment movement, which form part of a wider, multi-scaled interplay of biophysical and anthropogenic factors (Figure 2.2), are less well understood (Schlesinger et al., 1990; Hesp, 2002; Breshears et al., 2003; D'Odorico et al., 2007; Nield & Baas, 2008a; Ravi et al., 2010; Yan & Baas, 2015; Li et al., 2017).

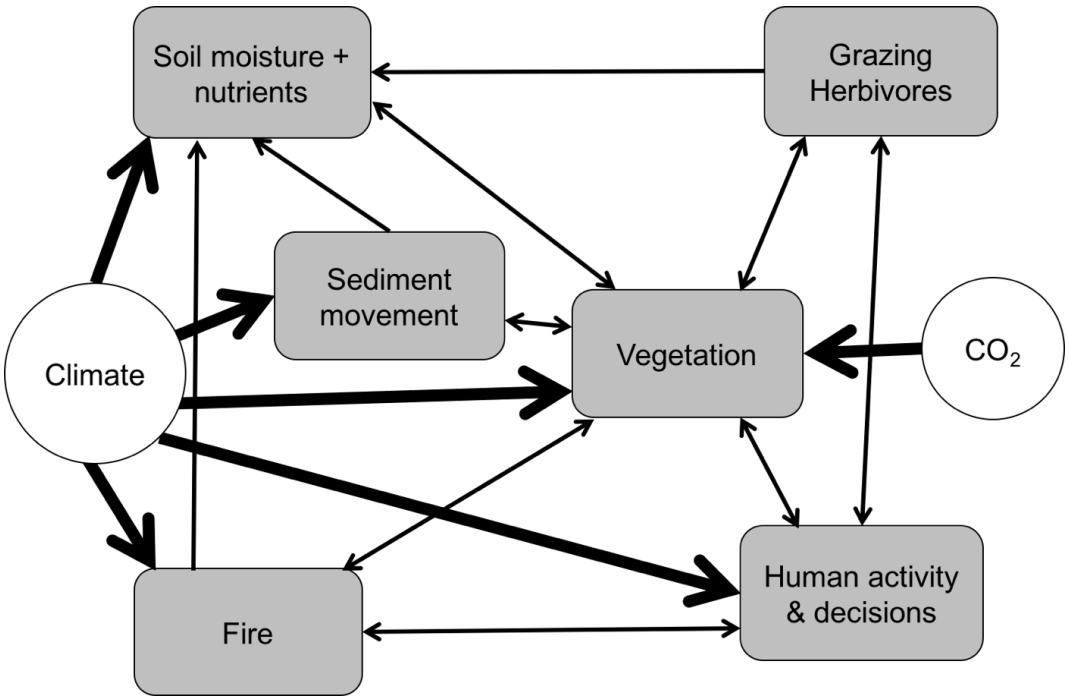


Figure 2.2 The multi-scaled interplay of biophysical and anthropogenic factors characterising many of the world's drylands. External inputs to the system are shown as white circles.

Wind erosion can be a dominant mechanism of sediment transport in arid and semi-arid environments, and aeolian processes are now viewed as major abiotic drivers that can have important consequences for landscape evolution (Thomas et al., 2005; Wang et al., 2009), biogeochemical cycling (Reynolds et al., 2001; Ravi et al., 2011), regional climate (Goudie & Middleton, 2006; Seager et al., 2007; Bogle et al., 2015), land degradation (Barbier et al., 2006; D'Odorico et al., 2013; Middleton & Sternberg,

2013) and public health (Griffin et al., 2001; Wiggs et al., 2003). The human population of the global arid zone has increased significantly over the 20th century to over 2 billion people, mostly in the developing world (UNDP, 2011). Land degradation is considered one of the major human-environmental issues in these regions, due to its impact on food security and environmental quality (Ravi et al., 2010). Although serious debate surrounds the causes and consequences of dryland degradation (Thomas, 1997; Veron et al., 2006), it is generally believed to result from a multi-scaled interplay of biophysical and anthropogenic factors (Geist & Lambin, 2004), making it a complex, nonlinear and often hysteretic[1] process (Meron et al., 2004).

Understanding these complex dynamics is increasingly important in the context of 21st century climate and land use change, since many of the subsequent impacts will be mediated through aeolian activity in dryland landscapes (Okin et al., 2006; Li et al., 2013). In these regions, growing population pressure for resources (MEA, 2005a; Huang et al., 2010) and increasingly arid conditions due to global climate change (Held et al., 2005; Burke et al., 2006; Seager et al., 2007; IPCC, 2013) are driving rapid, large-scale vegetation shifts that alter rates and patterns of soil erosion and modify ecosystem functioning and structure (Ravi et al., 2010; Kinast et al., 2013). An increase in aridity in drylands could strengthen the relative importance of abiotic factors that may, in combination with others such as increased grazing pressure and lack of adequate soil conservation practices, lead to large-scale reactivation of dune fields and desert encroachment in many of the world's most vulnerable regions (Thomas et al., 2005; Wang et al., 2009).

[1] i.e. depending on past as well as current environments

2.2. Vegetation patterning in drylands

The extreme nature of drylands means that semi-arid vegetation is often patchy and dynamic through time and space. Complex relationships between plants, soil and transport processes lead to the emergence of multi-scale vegetation patterns (Wainwright, 2009; Stewart et al., 2013), ranging from random distributions of bare soil and vegetation canopies (Caylor et al., 2004) to highly organised spatial formations such as bands, stripes, spots and rings, all with characteristic length-scales and orientations (Meron et al., 2004; Ravi et al., 2008; Borgogno et al., 2009; Tschinkel et al., 2012; Getzin et al., 2014).

Recent advances in numerical modelling have enabled an interpretation of such patterning in the context of complexity theory. Under this framework, the observable complexity in a system can be understood to emerge from numerous, relatively simple, local interactions (Baas, 2007). Key characteristics of complex systems include dissipative structures (i.e. structures that persist in the face of increasing entropy, due to the flow of matter and energy through a system when 'useful' energy is converted into a less useful form), manifested in spatial and temporal patterns that evolve through self-organisation (Baas, 2002). Such systems are typically non-linear in their responses, whereby outputs are not proportional to the inputs across the entire input range (Phillips, 1999), and these lead to unpredictable responses to forcing. The possibility of this type of behaviour must be included in analysis and modelling if realistic predictions and full understanding of ecogeomorphic systems is to be achieved (McMenamin et al., 2002; Naylor et al., 2002; Baas, 2007).

2.2.1. Vegetation patterning mechanisms and feedbacks

At the synoptic scale, a standard sequence of patterned states in vegetation structure ("gap → labyrinth → spot", see Figure 2.3) has been observed and modelled in semi-arid ecosystems (e.g. HilleRisLambers et al., 2001; Rietkerk et al., 2002; Gilad et al., 2007; Bailey, 2011; Gowda et al., 2014). This patterning sequence is thought to represent an adaptation to resource limitation, specifically of water. It is a resource concentration mechanism that leads to greater biomass than could be maintained where the vegetation is more evenly distributed (D'Odorico et al., 2006a; van der Stelt et al., 2012; Stewart et al., 2013; Gowda et al., 2014). Bailey (2011) showed that removing the interactions between neighbouring plants from a patterning model results in a significantly lower survival rate for vegetation across the domain; vegetative patches therefore provide self-sustaining environments that allow much higher levels of environmental stress to be tolerated than is the case for isolated plants.

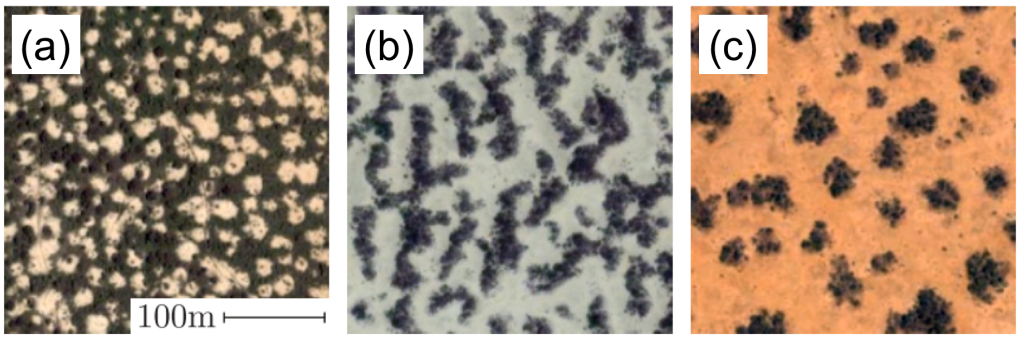


Figure 2.3 Aerial imagery of dryland vegetation patterning: (a) gap patterns, Senegal; (b) tiger bush labyrinth patterns, Niger; (c) spot patterns, Sudan (adapted from Gowda et al., 2014,, p.1).

Since vegetation patterns are often observed when topography and soils do not exhibit any heterogeneity, their formation has been thought to result from self-organisation (Lefever & Lejeune, 1997; Lejeune et al., 1999; HilleRisLambers et al., 2001; von Hardenberg et al., 2001; Rietkerk et al., 2002, 2004; D'Odorico et al.,

2007; Gilad et al., 2007; Getzin et al., 2014). The essence of self-organisation is the emergence of order in a system through its internal dynamics and feedback mechanisms, as opposed to the generation of regularity resulting from external forcing (Rohani et al., 1997; Baas, 2002). Self-organisation arises in vegetated contexts due to competitive and/or facilitative effects of individual plants on their neighbours, often in tandem and at differing ranges (Lefever & Lejeune, 1997; Kéfi et al., 2007b; Barbier et al., 2006, 2008; Brooker et al., 2008; Bailey, 2011; Ariza & Tielbörger, 2012).

As shown in Figure 2.4, plant-plant facilitation occurs at shorter ranges. Shading ameliorates the microenvironments under plants by reducing soil evapotranspiration and thermal amplitudes (Aguiar & Sala, 1999; Armas & Pugnaire, 2005; Kéfi et al., 2007b; Brooker et al., 2008), seeds are dispersed over short distances (Thompson et al., 2008), and water and nutrients accumulate under canopies, leading to 'islands of fertility' feeding back positively on plant growth (Schlesinger et al., 1990; von Hardenberg et al., 2001; Rietkerk et al., 2002, 2004; Gilad et al., 2007; Ridolfi et al., 2008). At slightly larger radial distances, plants compete for soil moisture and limited nutrients using their shallow root networks (Martens et al., 1997; Kéfi et al., 2007a; Barbier et al., 2008; Ariza & Tielbörger, 2012).

Although most vegetation patterning models focus on these self-organising facilitation and competition processes, there is some evidence that 'exogenous effects' imposed on a vegetation system by the landscape (e.g. changes in soil structure, local topography and random noisy fluctuations in external forcing) may also affect pattern formation (Thiéry et al., 1995; Dunkerely, 1997; D'Odorico et al., 2006a, 2007; von Hardenberg et al., 2010; Sheffer et al., 2012; Penny et al., 2013; Sherratt, 2015). For instance, the formation of grass rings may be partly linked to sediment movement processes (Sheffer et al., 2007, 2011; Ravi et al., 2008),

suggesting that vegetation patterns are biological indicators of abiotic processes and of source-sink areas for sediments in dryland landscapes (Ludwig et al., 2005). Vegetation patterning should therefore be interpreted both as a manifestation of plant response to environmental conditions, and a driver of local conditions for subsequent growth potential.

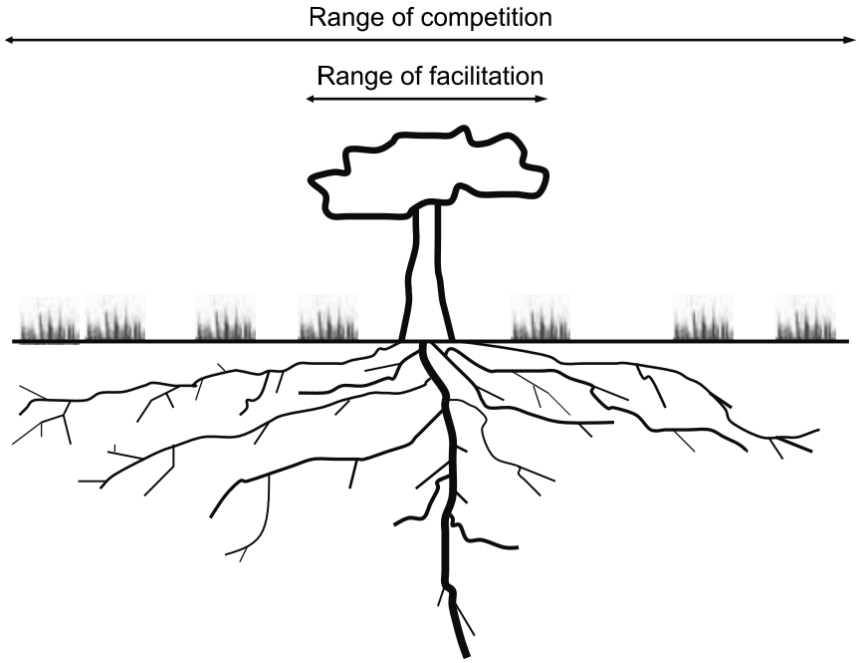


Figure 2.4 Schematic representation of the competitive and facilitative interactions typical of trees or shrubs in drylands (from Borgogno et al., 2009, p.9).

2.2.2. Vegetation shifts in drylands

The dynamic interactions between abiotic processes, vegetation and, increasingly, humans in drylands, often result in shifts in the composition and patterning of dryland ecosystems. Ecosystem regime shifts involve the transition from one stable state to an alternative stable state (Holling, 1973; Beisner et al., 2003; Lawrence et al., 2007; Bel et al., 2012), and can broadly be divided into two categories: (i) small, slow and reversible; and (ii) large, abrupt and irreversible. Large, abrupt shifts can be detrimental to dryland ecosystems because they cause rapid and widespread loss of

bioproductivity and biodiversity, affecting ecosystem function and stability (Loreau et al., 2001; MEA, 2005b) as well as economic resources (Rietkerk et al., 2004; Scheffer et al., 2009). Abrupt shifts have been attributed to bistability, where a stable state either loses stability due to strong amplifying (positive) feedbacks (Scheffer et al., 2001; van Nes & Scheffer, 2007; Suding & Hobbs, 2009; Turnbull et al., 2012), or ceases to exist following a change in exogenous forcing (i.e. environmental drivers and disturbances), so that the system bifurcates to alternative stable or unstable states (Scheffer & Carpenter, 2003).

Strong internal feedbacks within dryland ecosystems exert a great influence on their resilience (Turnbull et al. 2012), where ecological resilience is defined as the maximal disturbance that a system can absorb without shifting to another state (Holling, 1973; Walker et al., 2004; van Nes & Scheffer, 2007). Amplifying feedbacks, which serve to reduce ecosystem resilience, are generally associated with a strong predominance of abiotic processes (wind and water in the dryland context) at larger scales (Turnbull et al., 2012). For instance, the broad-scale redistribution and sorting of sediments (Hennessy et al., 1986; Leys & McTainsh, 1994) and nutrients (Schlesinger et al., 2000; Okin et al., 2006; Li et al., 2008) by aeolian processes has important effects on soil resources, and consequently on vegetation composition and structure (Schlesinger et al., 1990, 1996; Okin et al., 2001; Raupach et al., 2001). Conversely stabilising feedbacks, which act to increase ecosystem resilience, are associated with enhanced infiltration and trapping of sediment and nutrients that enable plant growth and the provision of plant-essential resources at smaller scales (Turnbull et al., 2012). For example, the local redistribution of nutrient-rich soil from inter-canopy areas to beneath shrub patches (Hennessy et al., 1985; Okin & Gillette, 2001; Ravi et al., 2009a) results in self-reinforcing ‘islands of fertility’ (IOF) (Schlesinger et al., 1990; Li et al., 2007; Field et al., 2012).

A range of human disturbances – namely agriculture, grazing and fire – is a common feature of many drylands, and these can force a fragile ecosystem to rapidly shift to an alternative state. Agricultural activities and grazing often enhance aeolian erosion by reducing vegetation cover, disturbing soil structure and crusting, and creating large patches of bare ground (Hagen, 1991; Belnap, 1995; Nash et al., 2004; Barbier et al., 2006; Middleton, 2011; Miller et al., 2012). The replacement of perennial plants by annual plants, a phenomenon commonly associated with dryland farming practices, becomes problematic as subsequent drought conditions can lead to high levels of degradation (van Auken, 2000; Belnap et al., 2009). Excessive trampling by animals promotes the onset of islands of fertility (Schlesinger et al., 1990) via feedbacks resulting from heterogeneities in water and soil resources, which can result in distinctive, dynamic vegetative pattern formation and possibly irreversible vegetation collapse (Rietkerk et al., 1997; HilleRisLambers et al., 2001). Even though periodic natural fires can increase the availability of some nutrients and controlled burning is often used as a management tool in grasslands (Havstad & James, 2010), fires commonly destroy vegetation and biocrusts (D'Odorico et al., 2006b; Levin et al., 2012) and induce differential soil-water repellence (Doerr et al., 2000; Ravi et al., 2009b), which act to increase surface erodibility (Breshears et al., 2009).

Dramatic shifts in vegetation cover can affect surface roughness, cover and patch size distribution, and therefore have important implications for the rates and patterns of soil erosion in dryland systems (Okin & Gillette, 2001; Gillette & Pitchford, 2004; Bergametti & Gillette, 2010; von Hardenberg et al., 2010; Sankey et al., 2012; Stewart et al., 2013). One particularly serious form of degradation arising from abrupt transitions in community structure is the encroachment of shrubs into grasslands (van Auken, 2000; Puigdefabregas, 2005; Gilad et al., 2004, 2007; Ravi et al., 2010). Although shrub encroachment cannot always be considered a form of land degradation (Thomas & Twyman, 2004; Reed et al., 2007; Reed & Dougill, 2010), it

is often cited as having negative impacts on socio-economic factors concerning pastoral activities (e.g. van Rooyen, 1998; UNDP, 2011). Amplifying feedbacks linked to rainfall variability (Gherardi & Sala, 2015), nutrient availability (Okin et al., 2009a), fire regime (Anderies et al., 2002; Li et al., 2008; Sankey et al., 2012) and intensive grazing (Eldridge et al., 2011) enhance the stability of the shrub-dominated state. This can result in a substantial increase in bare soil fractions and a subsequent enhancement of soil erosion rates in barren soil patches (Schlesinger et al., 1990; Huenneke et al., 2002; Ravi et al., 2012). The aeolian dynamics of vegetated systems are explored further in section 2.3.

Modelling approaches are increasingly used to understand the transitions leading from vegetated to low-productivity (bare-soil) states in drylands. Whilst relatively small perturbations (e.g. low grazing pressures, mild droughts) may result in a gradual shift to a low-productivity state that exhibits a subtle external expression (Bel et al., 2012), high-stress environments (e.g. intensive agriculture and grazing, severe drought, fire) can induce discontinuous transitions leading to hysteresis (Scheffer et al., 2001; Suding & Hobbs, 2009). Bailey (2011) demonstrated that quasi-stable (vegetated and bare-soil) population states can appear within a bistable region of a highly stressed system, and that the vegetation pattern response to environmental stress in semi-arid systems differs depending on whether the starting point is full vegetation cover or bare ground. Bailey's (2011) model implies that hysteretic movement of a semi-arid system along different degradation and recovery curves manifests itself in different pattern sequences (see Figure 2 in Bailey, 2011).

Heightened concern about the deterioration of drylands has prompted research efforts to devise early-warning indicators of impending shifts and associated degradation processes (Scheffer et al., 2009). Close to the critical threshold for catastrophic transitions, the resilience of an ecosystem decreases to a point that only

a small perturbation is needed to tip it into an alternative state. A basic, quantifiable property of bistable dynamical systems is 'critical slowdown', which describes the increase in relaxation time of a system following a small perturbation (Bailey, 2011). This can be understood as the shrinking of the basin of attraction around an ecosystem equilibrium state (Dakos et al., 2011; Lenton et al., 2013). Critical slowdown usually manifests itself by an increase of temporal autocorrelation and variance (Carpenter & Brock, 2006; Dakos et al., 2008; Bailey, 2011), skewness (Guttal & Jayaprakash, 2008) and kurtosis (Biggs et al., 2009) in time-series data.

Spatial statistics can also be reliable indicators for imminent regime shifts (Guttal & Jayaprakash, 2009; Dakos et al., 2010, 2011), especially in situations where simulated self-organised vegetation patterns are highly regular (e.g. HilleRisLambers et al., 2001; Rietkerk et al., 2002). Deviations from power-laws in patch-size distribution (Kéfi et al., 2007a, 2011), as well as visual changes in the nature of the patterns (Rietkerk et al., 2004; Bailey, 2011; Dakos et al., 2011), may act as indicators of an upcoming transition. However, random (stochastic) shocks play an important role in triggering transition far from bifurcations points, so care should be taken when interpreting indicators as signalling particular fragility levels (Scheffer et al., 2012).

Summary: Vegetation patterning in drylands

Vegetation in many drylands is patchy and dynamic through time and space due to complex relationships between plants, soil and transport processes. Distinct multi-scale vegetation patterning has been observed and modelled in semi-arid contexts, resulting primarily from self-organisation as a response to water limitation and competition-facilitation interactions with neighbours. The dynamic interactions between abiotic processes, vegetation and, increasingly, humans in drylands, often result in shifts in the composition and patterning of dryland ecosystems. The proximity of an ecosystem to a shift can be predicted using a 'critical slowdown' in time-series data, or spatial statistical indicators.

2.3. The impact of vegetation on wind flow

The presence of non-erodible roughness elements such as plants significantly complicates wind flow in deserts. By providing drag on the overlying airflow, non-erodible elements affect the velocity profile and thus alter erosion dynamics on desert surfaces (Ash & Wasson, 1983; Gillette & Stockton, 1989; Wolfe & Nickling, 1993; Wiggs et al., 1994, 1995; King et al., 2005; Gillies et al., 2017). In turn, the redistribution of sediment feeds back to the growth and survival rate of plants (Okin & Gillette, 2001; Sankey et al., 2012).

In dryland contexts, sparse vegetation modulates the erodibility of the surface and the erosivity of the wind through three primary mechanisms (Wolfe & Nickling, 1993). First, vegetation can directly shelter the soil from the wind by covering a fraction of the surface and providing a lee-side wake (Judd et al., 1996; Al-Awadhi & Willetts, 1999; Leenders et al., 2007). Second, vegetation directly affects wind velocity profiles by acting as a form of roughness that results in the growth of a boundary layer downwind (e.g. Wasson & Naninga, 1986; Gillette & Stockton, 1989; Gillies et al., 2002; Crawley & Nickling, 2003; Gillette et al., 2006; Dupont et al., 2014). Finally, vegetation acts to trap windborne particles, thus reducing flux and providing loci for sediment deposition (e.g. Gillies et al., 2000, 2014; Okin et al., 2006; Davidson-Arnott et al., 2012). These mechanisms are explored in further detail below.

2.3.1. Plant wake dynamics

Single roughness elements such as plants shed turbulent eddies in a way that causes the flow in the wake to be separated from the surrounding flow (Wolfe & Nickling, 1993). For smooth, solid objects the interaction with the flow is relatively predictable (van Gardingen & Grace, 1991), but characterising flow around live

plants that are porous, pliable and of diverse geometry, is significantly more complex. Using wind tunnel data, Judd et al. (1996) built on the work of Wolfe & Nickling (1993) to classify zones of flow around single porous roughness elements (see Figure 2.5). As wind approaches an obstacle (A), the air in the layer below the top of the element slows down and diverges upwind, with some air continuing through the porous obstacle to create a region of slower bleed flow in its immediate lee (C). As air is forced around the element and the flow lines are compressed, a region of accelerated wind develops above it and to its side (B). A low-velocity zone forms in the sheltered area of the obstacle (D), where wind velocity drastically decreases or even reverses in direction to form a recirculating eddy. This zone has variously been conceptualised as triangular in shape (e.g. Raupach, 1992) or as a 'corridor' of asymptotic recovery (Okin, 2008). Above and downwind of the low-velocity zone, a turbulent mixing zone grows downward from a thin layer at the top of the obstacle, and intersects the ground surface downwind (E). Eventually the mixing zone merges into an equilibration zone (F) as the airflow recovers to equate to the upwind profile.

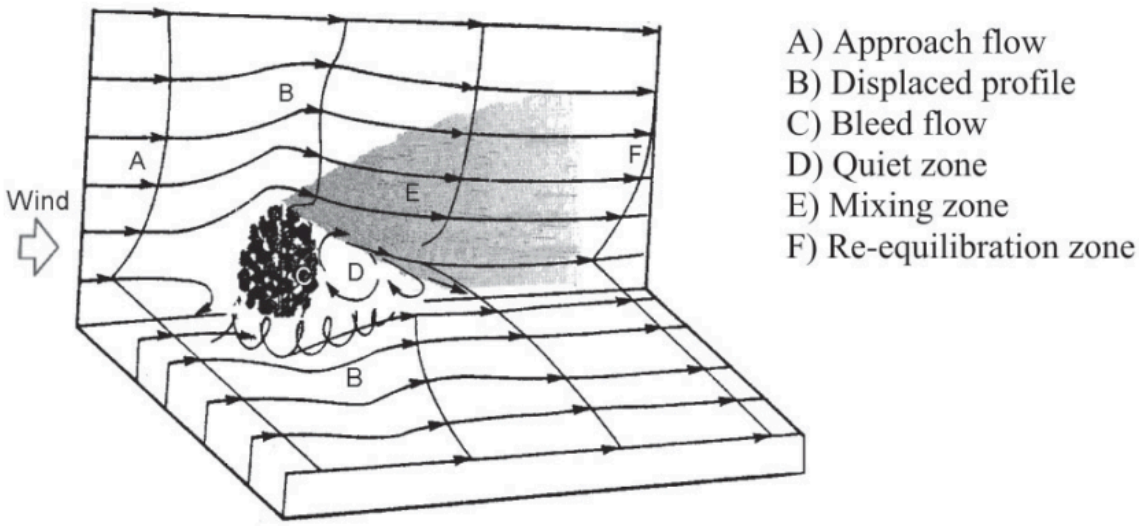


Figure 2.5 Flow visualisation around a single vegetation element, showing the development of six different flow regimes (from Leenders et al., 2007, p.1457, adapted from Wolfe & Nickling, 1993 and Judd et al., 1996).

The model of Judd et al. (1996) for individual plants has subsequently been supported by wind tunnel data (e.g. Sutton & McKenna-Neuman, 2008; Suter-Burri et al., 2013; Lee et al., 2014; Wu et al., 2015) and modelling experiments (e.g. Hesp & Smyth, 2017). However, few studies have sought to examine the turbulent wake structures generated by dryland plants in the field. The exception is Leenders et al. (2007), who observed distinct zones of flow acceleration and deceleration around single desert shrubs in the Sahel. Leenders et al. (2007) showed that time-averaged turbulence intensity was higher in low-velocity zones than at other locations, and concluded that the net effect of a shrub is to reduce wind velocity and trap sand particles near the soil surface.

Trees affect wind flow differently to shrubs, owing to the presence of a trunk and canopy in the tree case (Gross, 1987; Leenders et al., 2007; Dupont et al., 2014). Gross (1987) and Dupont et al. (2014) demonstrated using numerical models that wind flow accelerates over and around a single tree (Figure 2.6), and Leenders et al. (2007) observed in the field that wind speed increases locally around the base of the trunk. In the lee of a tree, trees produce a wake region similar to that of a shrub, although the greater size of a tree means it reduces wind speed more efficiently than a shrub (Leenders et al., 2007; Dupont et al., 2014). The length and strength of the reverse flow in the wake of a tree appears to increase with wind speed, and the location of the minimum wind speed to shift to higher levels as trunk height increases (Gross, 1987). Tree leaves may also be important for altering local airflow patterns (Endalew et al., 2009), by inducing updrafts and downdrafts in the upstream region that cause turbulent, upwelling recirculation zones to form (Lee et al., 2014).

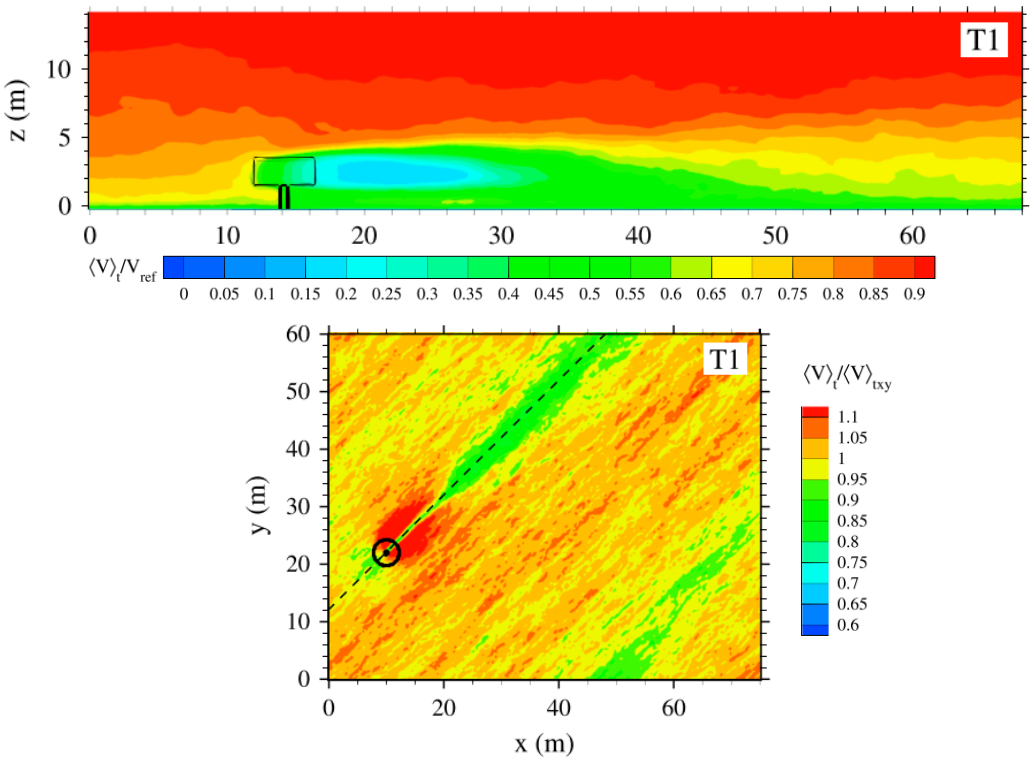


Figure 2.6 Flow visualisation downwind of a single tree, shown as: (top panel) the normalised time-averaged wind velocity (V_t/V_{ref}) simulated by Dupont et al.'s (2014) model, shown in vertical cross-section. Solid black lines delimit the tree; (bottom panel) the normalised time-averaged wind velocity (V_t/V_{txy}) simulated by the model at 0.1 m height, shown in horizontal cross-section. The solid black circles represent the tree crowns (adapted from Dupont et al., 2014, p.176).

Whilst single plants are present in drylands, vegetation often grows in patchy patterns (see section 2.2), which can have varying effects on wind flow. The interactions of individual plant wakes with their neighbours can be broadly described by three different flow regimes (Wolfe & Nickling, 1993; Figure 2.7). As roughness element density increases, the flow regime changes from one where the elements act individually on the flow (isolated roughness flow) to a regime where the airflow skims across the top of the elements (skimming flow). In dryland environments, vegetation is often spaced far enough apart that the wake shed by an individual plant can fully develop or is only slightly obscured by a downwind plant (wake-interference flow). Lee & Soliman (1977) classified these regimes by a ratio of inter-row spacing length to element height. However, this relationship often breaks down in dryland

systems because natural vegetative surface roughness changes are often irregular, thus affecting wind velocity profiles in differing ways (King et al., 2005).

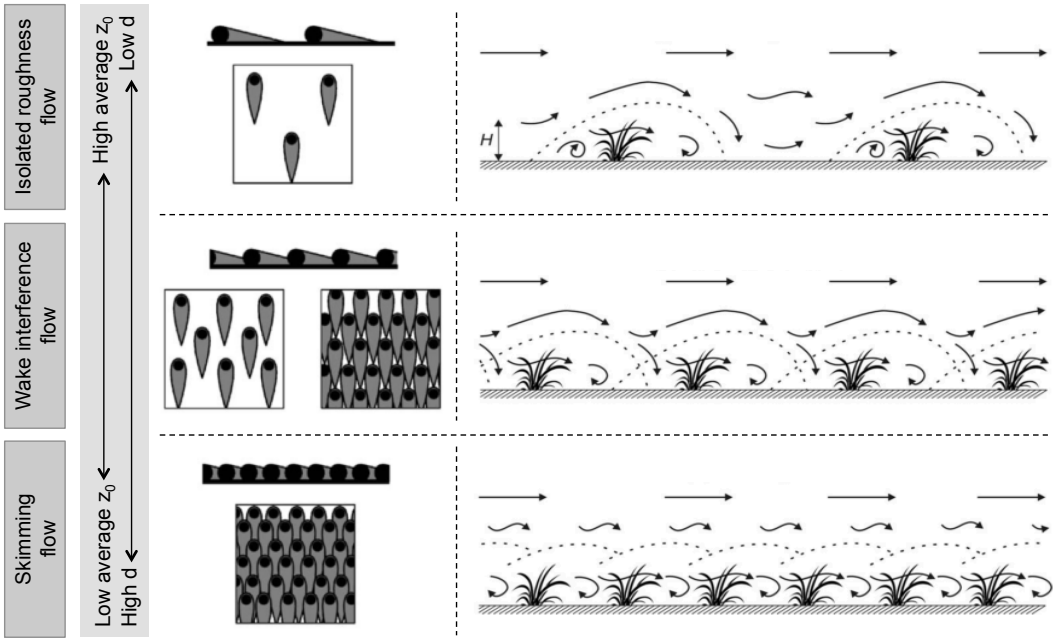


Figure 2.7 Flow regimes and associated theoretical wake development, shown in schematic plan and side view. Shaded areas are wake regions. The effect of different flow regimes on average z_0 (aerodynamic roughness) and *d* (displacement height) per plant unit is shown (adapted from Wolfe & Nickling, 1993, p.57, and Suter-Burri et al., 2013, p.66).

2.3.2. Vegetation as a form of surface roughness

Vegetation can directly affect wind velocity profiles on desert surfaces by acting as a form of roughness, thus extracting momentum from near-surface wind, which results in the growth of a boundary layer downwind (Wasson & Naninga, 1986; Gillette & Stockton, 1989; Liu et al., 1990). The impact of boundary layer growth on meso-scale erosion patterns depends strongly on the type of flow regime (Figure 2.7). When isolated roughness elements populate the surface (< 16% cover; Wolfe & Nickling, 1993), each plant sheds turbulent eddies by diverting wind flow around and above each plant (see section 2.3.1). This increases drag, thus raising shear stress and the

aerodynamic roughness (z_0), and potentially enhancing erosion locally (Ash & Wasson, 1983). An arch vortex with a reverse surface flow direction can develop directly downwind of individual elements, upwind of a flow stagnation region where the outer flow reattaches to the ground (Sutton & McKenna-Neuman, 2008; Walter et al., 2012b).

In wake-interference flow (c. 16–40% cover; Wolfe & Nickling, 1993), the increased drag and thus shear stress resulting from the presence of multiple elements may only be partly absorbed by the plants themselves. This results in stress being transferred to the inter-canopy surface, and potentially greater sediment transport (Breshears et al., 2009; Dupont et al., 2014). In the case of skimming flow (> ~40% cover; Wolfe & Nickling, 1993), the increased drag from the vegetation acts to displace z_0 upwards (establishing a zero-plane displacement height, d), which simultaneously extracts momentum from the surface wind and increases wind shear stress above the canopy (e.g. Wasson & Naninga, 1986; Gillette & Stockton, 1989; Wiggs et al., 1994; Gillies et al., 2002; Crawley & Nickling, 2003; Gillette et al., 2006; Dupont et al., 2014). The absorption of additional stresses by the plants therefore decreases the erosion potential at the surface, despite the additional above-canopy shear stress induced by the increased surface roughness.

2.3.3. Trapping of windborne sediment

Finally, vegetation acts to trap windborne particles, thus reducing the total horizontal and vertical flux and providing loci for sediment deposition (Okin et al., 2006; Gillies et al., 2017). The prevalence of this effect can differ depending on vegetation height (Davidson-Arnott et al., 2012): in the case of tall vegetation (e.g. trees and shrubs), saltation transport takes place primarily below canopy level in the open space between individual plants. In contrast, for short vegetation (e.g. grasses), sand

transport takes place primarily within and above the plant canopy, so that grasses may trap aeolian sediment more readily than shrubs. Trees affect sediment trapping differently to grasses and shrubs, owing to their trunk and elevated crown (Gross, 1987; Leenders et al., 2007; Dupont et al., 2014; Lee et al., 2014), but this has rarely been investigated in the field.

2.3.4. Impacts of plant porosity, pliability and configuration

Theoretical calculations (e.g. Raupach, 1992; Okin, 2008) and experimental measurements (Minvielle et al., 2003; Leenders et al., 2007; Youssef et al., 2012; Gillies et al., 2014; Wu et al., 2015; Hesp & Smyth, 2017) suggest that protective wakes downwind of individual vegetation elements extend to approximately 7–10 h (where h is the height of the element). However, this can vary significantly depending on plant porosity, pliability and configuration.

Much of the research on the effects of plant porosity and pliability on wind flow has been conducted on sand fences and windbreaks, and findings from these are of some relevance to plants (Grant & Nickling, 1998; Leenders et al., 2007). Taylor (1988) found that drag coefficients decreased exponentially as the porosity of a two-dimensional barrier increased, but Grant & Nickling (1998) demonstrated that a peak in drag coefficient occurred at an intermediate optical porosity (~20%) for three-dimensional trees. It has been shown that elements with a porosity less than 20% act to enhance wind speed recovery in their lee (Wang & Takle, 1996; Kim & Lee, 2002; Vigiak et al., 2003; Cornelis & Gabriels, 2005), so elements with intermediate porosity strike a compromise between shear stress reduction and the downwind distance for which it is effective (Musick et al., 1996; Lee et al., 2002). However, even porosity values of 50% can cause wake effects to extend to at least 50 h downwind of a windbreak (Bradley & Mulhearn, 1983). The sediment trapping

mechanism of plants (see section 2.3.3) also depends on plant porosity (Musick et al., 1996; Gillies et al., 2000, 2014), with wind tunnel (e.g. Lee et al., 2002) and field (e.g. Grant & Nickling, 1998) experiments showing that the trapping effect of vegetation is maximised at intermediate values of porosity (20–40%). Using wire mesh structures, Gillies et al. (2017) showed that porous elements have a greater potential for modulating sediment flux than solid elements in large spatial arrays.

The pliability of plants affects their aerodynamic behaviour. Some pliable plant stems alter their form to become more streamlined in higher winds, thus extracting momentum less effectively as wind speed increases (Gillies et al., 2000). This results in a decreased sheltering effect at increasing wind speeds, due to a narrowing of the lee-side wake and suppression of horseshoe vortices (Burri et al., 2011; Walter et al., 2012b). Therefore, the rigid, non-porous roughness elements commonly employed in many wind tunnel studies to simulate vegetation arrays may provide inadequate approximations to live plants (Walter et al., 2012b). Indeed, Gillies et al. (2014) showed that flow field responses between solid bluff body forms and elements of the same form and size that are covered with a porous outer layer surrounding a solid inner core are not equivalent. Moreover, scaling issues linked to boundary layer depths mean that full-scale elements are rarely used in wind tunnel experiments. This limits the applicability of findings from wind tunnels. A few studies (e.g. Burri et al., 2011; Walter et al., 2012a, 2012b) have recently used live canopies in wind tunnels, but live plants are far more complicated to control in terms of appearance and behaviour than artificial imitations (Burri et al., 2011).

The configuration, or geometric arrangement, of windbreaks has also been shown to affect their aerodynamic behaviour. Using a numerical model, Liu et al. (1990) showed that alternate and regular arrays of tree windbreaks provided the most protection, whereas a patchy arrangement, where trees were clumped together in

space, resulted in the highest erosive forces. Liu et al. (1990) hypothesised that this resulted from reduced diameter influences, whereby vegetation clumping decreases the total wake spread, thus reducing the protective effects of wake interference and allowing wind to flow through unimpeded. Wind tunnel studies (Cornelis & Gabriels, 2005; Wu et al., 2015) suggest that multiple-row barriers reduce wind velocities more efficiently than single-row barriers, at least in the immediate lee. This effect is likely due to the additional turbulence generated by a sequence of fences compared to an isolated barrier (Wilson & Yee, 2003). Wu et al. (2015) also showed that using multiple vegetation species can provide optimal sheltering effects. There is little research on the impact of vegetation patch configuration at the meso scale, excepting some scaled-down wind tunnel experiments (Burri et al., 2011; Youssef et al., 2012; Suter-Burri et al., 2013) and modelling studies of forest edges (Liu et al., 1996; Belcher et al., 2003; Frank & Ruck, 2008). Wind tunnel and modelling experiments have also been used to understand flow behaviour around backward-facing steps (e.g. Le et al., 1997; Wengle et al., 2001), although these configurations often have more extensive low-velocity zones and delayed reattachment points compared to vegetated cases, due to their almost parallel-to-wall streamlines.

Collating information from windbreak and vegetation studies allows the main zones of flow change to be identified and partially quantified (see Figure 2.8). However, whilst windbreak studies can be useful proxies for vegetation elements, the three-dimensional nature of live plants (as opposed to the two-dimensional problem represented by a fence) means that findings may not be completely transferable (Leenders et al., 2007; Gillies et al., 2014). For instance, the width of an element is known to affect the recovery of wind flow in its lee to a certain extent (McKenna-Neuman & Bédard, 2015; Hesp & Smyth, 2017; Gilles et al., 2017), but in windbreak experiments, the obstacle width is assumed to be infinite. Furthermore, it is unclear whether windbreaks affect flow turbulence in the same way as live vegetation. This is

particularly problematic in the field, where the dynamic complexity of the flow structures cannot be controlled in the same way as in modelled or wind tunnel environments (Clifford & French, 1993). This issue is pertinent given the increasing evidence that turbulence is an important driving force behind sediment entrainment and transport in aeolian environments (Butterfield, 1991; Sterk et al., 1998; Namikas et al., 2003; Schönfeldt & von Löwis, 2003; Baas & Sherman, 2005a,b; Leenders et al., 2005; Baddock et al., 2011; Weaver & Wiggs, 2011; Wiggs & Weaver, 2012).

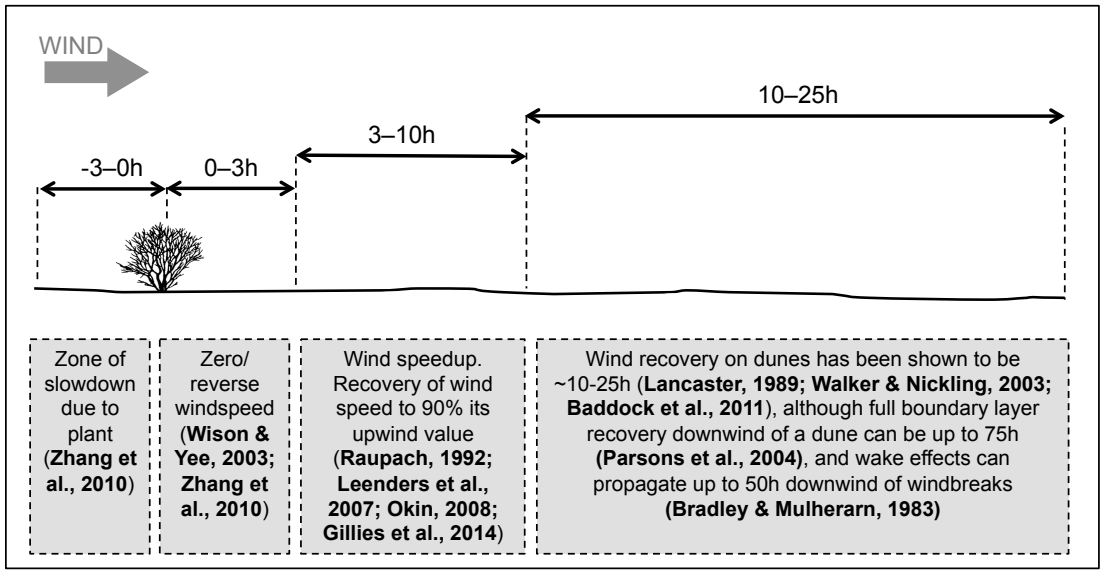


Figure 2.8 Main zones of possible speedup/slowdown around a roughness element, as collated from various vegetation and windbreak studies.

Summary: The impact of vegetation on wind flow

The presence of vegetation complicates wind flow in deserts. Vegetation elements shed protective wakes in their lee, but also act as a form of roughness that results in the growth of a boundary layer downwind. Grasses and shrubs have different aerodynamic behaviour compared to trees, due to the elevated crown of the latter. Wind flow dynamics depend on plant porosity, pliability and configuration. Windbreak studies provide useful information in this context, but two-dimensional fences represent a far simpler aerodynamic problem than three-dimensional live plants.

2.4. Sediment transport on vegetated surfaces

The relationship between wind stress (erosivity) and the susceptibility of a surface to erosion (erodibility) broadly determines the potential for sediment transport in deserts (Lancaster, 1988). Wind regime and sediment supply are known to largely control the formation of bare-sand dunes (e.g. Wasson & Hyde, 1983; Werner, 1995; Momiji et al., 2000; Bishop et al., 2002), but the dynamic interactions between vegetation and sediment movement, which form part of a wider, multi-scaled interplay of biophysical and anthropogenic factors, are less well understood (Hesp, 2002; Nield & Baas, 2008a). Most of the evidence for the interactions between dryland vegetation and wind erosion comes from wind tunnel, windbreak and field experiments. However, an increasing number of modelling studies are exploring these relationships further, and introducing important predictive capabilities.

2.4.1. Evidence from wind tunnel, windbreak and field studies

Wind tunnel studies have proved useful for studying the relationship between vegetation and wind-blown sediment transport under controlled conditions. Experiments have been conducted using dead vegetation (Molina-Aiz et al., 2006), live vegetation (Burri et al., 2011; Suter-Burri et al., 2013), or artificial vegetation (Cornelis & Gabriels, 2005; Udo & Takewaka, 2007; Wuyts et al., 2008; Youssef et al., 2012). Suter-Burri et al. (2013) used coloured sand to visualize spatial patterns of sediment redistribution within grass tussocks, allowing them to relate different canopy densities to their theoretical flow regimes (Figure 2.9). Wedge-shaped wake deposits developed fully in the low-density case (representing isolated roughness flow), overlapped with adjacent downstream tussocks in the medium-density case (wake-interference flow), and deposited grains were evenly distributed around the tussocks in the high-density case (skimming flow). Suter-Burri et al. (2013) observed

that the fraction of the surface that was exposed to erosion was substantially smaller (44–78%) than the area not covered by vegetation, owing to the turbulent wake structures around the tussocks.

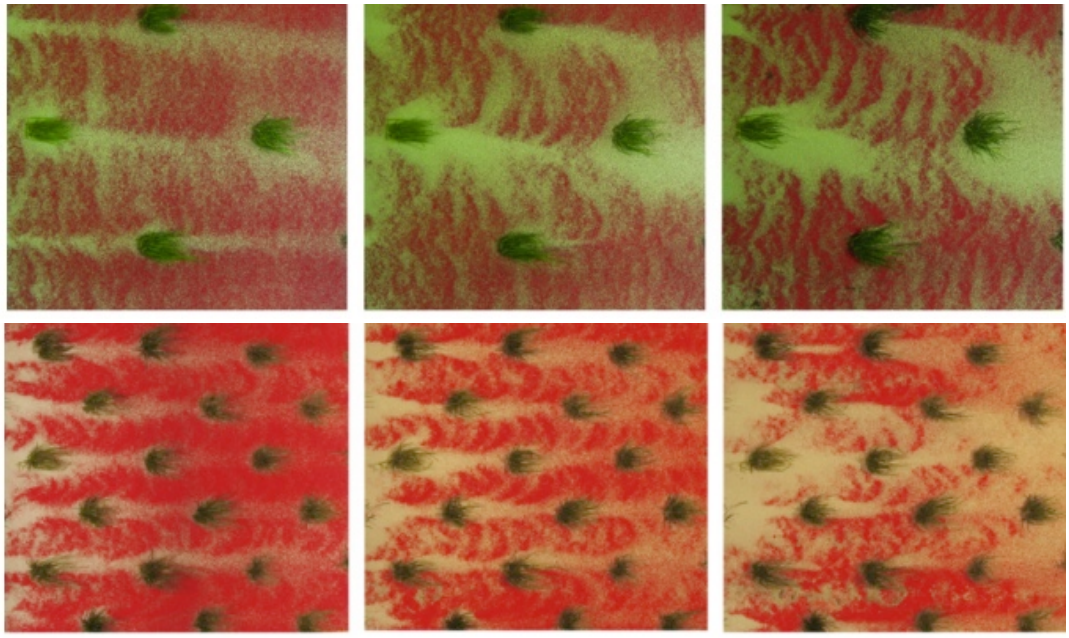


Figure 2.9 Image sequences of sediment deposition patterns in Suter-Burri et al.'s (2013) wind tunnel experiments, on surfaces populated by low-density (top row) and medium-density (bottom row) canopies. White sand was blowing in from upstream, with wind direction from left to right (adapted from Suter-Burri et al., 2013, p.69).

Wind tunnel studies have also shown that vegetation can act to increase erosion in some circumstances. The experiments of Burri et al. (2011) demonstrated that whilst sediment and dust flux was significantly reduced on high canopy-density surfaces compared to an unplanted configuration, low-density canopies (~3% cover) led to elevated shear stress on the bed resulting from flow acceleration, and thus higher sediment and dust fluxes. This region of elevated surface shear stress in the wake could result from counter-rotating vortices created by the roughness element (Sutton & McKenna-Neuman, 2008), or from oscillating movements of grass blades on the sand surface (Burri et al., 2011). In a 'regional' scale study (i.e. between

neighbouring land units), Youssef et al. (2012) used artificial 1:50 sized shrubs, laid out in different configurations in a wind tunnel, to measure the spatial distribution of sediment height after wind events. They found that shrubs bunched into patches resulted in far greater sediment fluxes than in the case of regular grids of single shrubs, likely because of a significant increase in turbulence between the patches.

Windbreak experiments (e.g. Raupach et al., 2001; Raupach & Lu, 2004; Zhang et al., 2010) also provide some insight about the impact of vegetation on sediment transport. When oncoming particle-laden airflow approaches a windbreak, particles are filtered from the flow passing through the windbreak and deposited on the element, whereas in the air flowing over the obstacle, particle concentrations remain similar to upwind values (Raupach et al., 2001). Raupach & Lu (2004) showed that wind speed reduction in the lee of a windbreak leads to lower particle concentrations, and that with increasing downwind distance, particles from the air flowing over the windbreak are progressively mixed downwards into the sheltered region. Using a high-speed camera system, Zhang et al. (2010) observed that sand transport rates were reduced by 37% directly in front of a fence due to momentum loss of particles colliding with the fence surface, and by 80% up to the downstream location of 3h. Similarly, the kinetic energy of saltating particles was reduced by more than 60% in the windward region, and up to 90% at 3h.

In the field, decoupling the influences of plants on sediment transport from those induced by variations in the wind or surface conditions is very difficult at the plant or patch scale (Walter et al., 2012b; Youssef et al., 2012). Several field-based studies have nonetheless attempted to demonstrate a gradient of surface activity in response to varying vegetation cover. There is evidence that vegetation cover of 12–15% provides a threshold for sand transport (Wiggs et al., 1995; Lancaster & Baas, 1998; Munson et al., 2011; Davidson-Arnott et al., 2012), but the use of percentage cover is

limiting because it provides no information about vegetation's spatially heterogeneous impact on erosion thresholds. It also does not account for the fact that erosion can still occur at relatively high (up to 45%) vegetation covers if the wind velocity is high enough (Ash & Wasson, 1983; Wasson & Nanninga, 1986). A more nuanced consideration of vegetation's impact on the balance between erosivity and erodibility factors is therefore needed.

2.4.2. Modelling sediment transport on vegetated surfaces

Wind erosion models form a key part of our understanding of sediment transport dynamics on partly vegetated surfaces, and are crucial for assessing the potential vulnerability of dryland regions to soil degradation (Okin et al., 2006; Ravi et al., 2011). The mobility potential of vegetated dunes over long timescales has been successfully modelled using wind-based indices that combine precipitation, temperature and wind data (e.g. Thomas et al., 2005; Wang et al., 2009). Whilst this approach is useful for simulating large dunefield dynamics, it does not resolve sediment transport dynamics at the same scale as plant-flow interactions. A variety of finer-scale models are examined here, from earlier theoretical models based on shear stress partitioning theory (Schlichting, 1936; Raupach et al., 1993; Marticorena & Bergametti 1995), to more recent approaches emphasising vegetation gaps (Okin, 2008; Li et al., 2013) and numerical models simulating patch-scale sediment movement (Turpin et al., 2010; Dupont et al., 2014).

2.4.2.1. Shear stress partitioning

Early methods for modelling the impact of roughness elements on wind and associated flux focused on quantifying the proportion of the wind shear stress or

shear velocity (u_*) that is acting on a surface compared to the proportion acting on vegetation elements (e.g. Gillette & Stockton, 1989; Musick & Gillette, 1990; Musick et al., 1996). The theoretical basis for such 'shear stress partitioning' came from the work of Schlichting (1936), who proposed that the total drag on a roughened surface (τ) is the sum of the drag on the intervening surface (τ_S) and the drag on all the individual roughness elements (τ_R). Marshall (1971) proposed that partition should be mostly dependent on the dimensionless roughness density (λ):

$$\lambda = \frac{nb_l h}{S} \tag{2.1}$$

where n is the number of roughness elements of width b_l and height h per unit surface area S (Figure 2.10). Although the relationship between partition and λ was not fully supported by later field observations (e.g. Ash & Wasson, 1983) and wind-tunnel experiments (Lyles et al., 1974; Gillette & Stockton, 1989; Musick & Gillette, 1990), the parameter was widely employed, particularly in the context of two principal partitioning models by Marticorena & Bergametti (1995) and Raupach (1992; Raupach et al. 1993). Both models have distinct approaches but are based on the 'shear stress ratio' (SSR) of shear stress required for erosion on a bare surface to the total shear stress threshold of the surface including roughness, relying on λ as a fundamental descriptor of surface roughness. The Marticorena and the Raupach approaches are summarised in King et al. (2005).

Although both the Marticorena and Raupach models provide good agreement with wind tunnel experiments using solid objects on non-complex surfaces (e.g. King et al., 2005, 2006; Gillette et al., 2006; Gillies et al., 2006, 2007, 2010), they are limited in several respects. The Marticorena model requires sediment sources to be continuous and unchanging (i.e. never supply-limited), whilst the Raupach model

performs badly in cases where tall elements interact with the saltation cloud (Gillies et al., 2006). Above all, by relying on the λ parameter, both models suffer from the inherent requirement for a given surface to be treated homogenously. In reality the spatial distribution of vegetation strongly affects horizontal sediment flux, even at low roughness densities (Okin & Gillette, 2001; Gillette et al., 2006; Lancaster et al., 2010; Li et al., 2013). The so-called 'Telephone Pole Problem' (Figure 2.11), where two roughness scenarios have the same effective 'amount' of roughness density but distribute it in very different ways, illustrates the limitations of using average vegetation density information to describe transport dynamics (Okin, 2008).

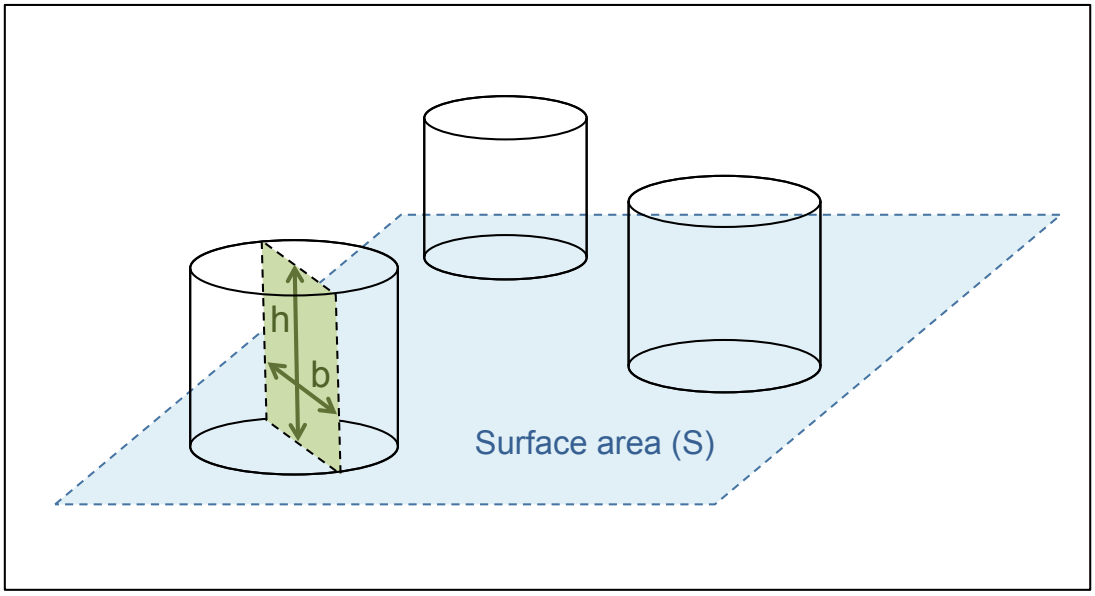


Figure 2.10 Illustration of the parameters used to calculate roughness density (λ) in roughness studies: h is element height, b is element base/width, n is the number of elements, and S is the surface area over which the calculation is made.

Other disadvantages of the λ parameter include scaling issues, whereby tall (> 0.10 m) elements appear to influence sand transport in a way that cannot be accounted for based solely on knowledge of roughness density (Gillies et al., 2006, 2007). This deficiency is minimised in large homogeneous areas of randomly or regularly spaced vegetation of the same height, but becomes problematic in natural environments

displaying structural anisotropy (Okin et al., 2006; Okin, 2008). λ has also been shown to inadequately describe three-dimensional objects, due an intrinsic bias in using the frontal silhouette area (Musick et al., 1996; Minvielle et al., 2003). Finally, λ is a very difficult parameter to measure in the field, especially at large scales. These issues have prompted others to devise alternatives to the stress partitioning method, which are explored below.

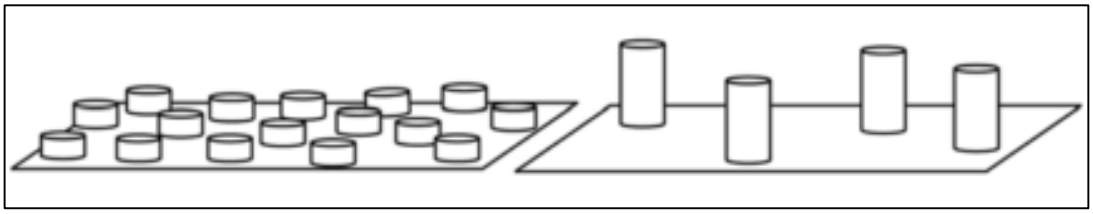


Figure 2.11 The Telephone Pole Problem. Both of these surfaces have the same roughness density, but on the left roughness density is partitioned into sixteen elements, whereas on the right, it is partitioned into four objects four times the height. Under the shear stress partitioning model of Raupach et al. (1993), both surfaces experience the same horizontal flux, although intuitively this is not an accurate representation of physical reality (from Okin, 2008, p.3).

2.4.2.2. Okin (2008) model

An alternative wind erosion model presented by Okin (2008) recognises the inherent irregularity of vegetation patterning in drylands, and emphasises the controlling influence of the size of 'gaps' or 'corridors' in the vegetation structure. By moving away from a single homogenous mean value for vegetation cover, Okin's (2008) approach allows aeolian erosion thresholds to vary across a surface. This notion is supported by field observations that flux is not ubiquitous across an entire landscape during a transport event (e.g. Gillette et al., 2006).

The Okin model assumes that plants are porous objects (Gillies et al., 2002; Minvielle et al., 2003), meaning that reverse flow in the lee of plants can be negligible and the surface shear velocities in the wake of the plant can be greater than zero

(Figure 2.12). Asymptotic recovery of shear stress has been observed downwind of porous fences (e.g. Bradley & Mulhearn, 1983) and nebkha vegetation (Gillies et al., 2014; Hesp & Smyth, 2017), so the model is formulated probabilistically to simulate the distribution of surface shear stress as a function of the distance to the nearest upwind plant.

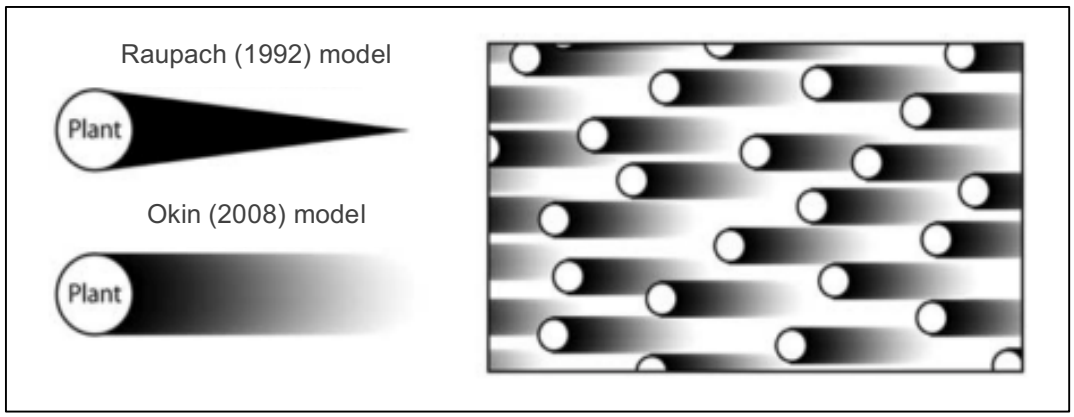


Figure 2.12 The distribution of reduced shear stress on the surface during wind erosion in the Raupach (1992) model, which envisions a triangular wake that experiences no shear stress at the surface (black area), compared to the Okin model, where shear stress increases from the downwind edge of the plant and eventually approaches the shear stress for an equivalent unvegetated surface (dark areas have lower shear stress). The landscape is seen as a series of 'corridors' of plants with their reduced shear stress areas sometimes interfering with one another (from Okin, 2008, p.5).

Okin's (2008) model shows good agreement with aeolian sand flux data at the plant/patch scale (e.g. Li et al., 2013; Sankey et al., 2013). It simulates transport around solid objects well when the model-calculated shear stress ratio is compared with the experimental data of King et al. (2005), which is noteworthy considering that the model negates return flow. Since the Okin model uses relatively simple spatial inputs, as opposed to the structural parameters of roughness elements needed for traditional shear stress partitioning models, data can be gathered over large scales using remote sensing techniques (e.g. Jupp et al., 2008; Karl et al., 2011; Sankey et al., 2013). Another notable advantage of the Okin (2008) model over partitioning methods is its scale explicitness, which allows individual unvegetated gaps as well as entire landscapes to be simulated.

Disadvantages of the Okin model include its aggregation of total sediment flux produced over a given area, which coarsens the model output, and its use of the time-averaged wind shear velocity (u_*) for formulating flux, despite u_* being an inappropriate measure of erosivity on complex, vegetated surfaces (Walker & Nickling, 2002; Raupach et al., 2006; King et al., 2008). Moreover, the Okin model does not directly account for the significant impact of roughness scale (especially roughness height) on transport efficiency (Gillies et al., 2006, 2007). Consequently, some studies have sought to first model wind and sediment transport at the finer plant scale, with a view to eventually predicting transport at the field scale.

2.4.2.3. Computational Fluid Dynamics (CFD) modelling

Computational fluid dynamics (CFD) modelling has been used to explicitly resolve turbulent wind flow and sediment flux around individual roughness elements to a high temporal and spatial resolution (e.g. Turpin et al., 2010; Dupont et al., 2013; 2014; Hesp & Smyth, 2017). CFD allows a more complete representation of flow structure than that obtained by field and wind tunnel experiments, so represents a promising approach for incorporating wind flow turbulence in vegetated contexts. Using CFD simulations, Turpin et al. (2010) identified a peak in shear stress in the low-shear zone behind individual elements and showed that the “inversion point” at which an element switched from reducing shear stress to increasing it varied with coverage density and roughness height (Figure 2.13). Turpin et al. (2010) could also test the effect of increasing the number and height of roughness elements on erosion patterns. Hesp & Smyth (2017) used a CFD model to investigate the impact of nebkha width on wind flow recovery in the lee. By accurately quantifying turbulent wind structures around each simulated nebkha, Hesp & Smyth (2017) could begin to link flow behaviour with resultant shadow dune formation.

Despite the high resolution and realistic flow structure representation that can be achieved using CFD, it is a computationally expensive method. To combat this, flow properties can be calculated using much coarser meshes, through large eddy simulations (LES) (Maruyama, 2008; Schröttle & Dörnback, 2012; Dupont et al., 2013, 2014). Dupont et al. (2014) coupled a LES model with a physically based saltation model to resolve turbulent wind flow over heterogeneous vegetated landscapes composed of trees and shrubs. The erosion patterns simulated by Dupont et al.'s (2014) model were qualitatively consistent with previous wind tunnel (Sutton & McKenna-Neuman, 2008; Burri et al., 2011) and field (King et al., 2006; Leenders et al., 2007) observations. Minimal dune models (e.g. Schwämmle & Hermann, 2005; Hermann et al., 2008), which combine analytical descriptions of turbulent wind velocity with continuum saltation models, have also been used to successfully simulate transitions between barchan and parabolic dunes (Durán & Hermann, 2006; Hermann et al., 2008).

Nevertheless, the computational requirements of CFD and LES methods still limit their use for simulating long-term erosion at larger than the field scale. Most of these models cannot account for surface deformation as erosion proceeds, and often require a regular arrangement of plants and constant wind velocity during simulations. These conditions are not representative of reality. A modelling approach is therefore needed that recognises the heterogeneous nature of semi-vegetated dryland surfaces, whilst allowing for landscapes to be simulated over large areas and long timescales, and which incorporates the dynamic feedbacks between plant growth, wind flow, and sediment movement.

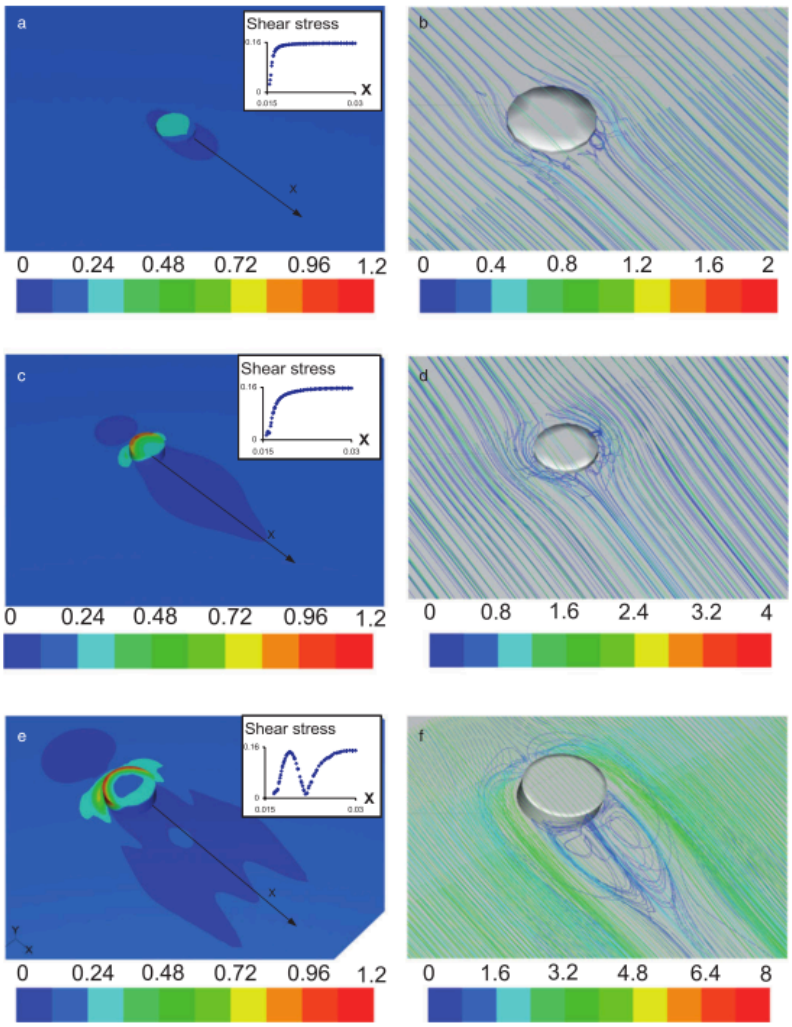


Figure 2.13 (a), (c) and (e): Contours of shear stress around isolated cylindrical elements; inset graphs represent the shear stress evolution downstream of the element. (b), (d) and (f): streamlines around isolated cylindrical elements (from Turpin et al., 2010, p.1424).

2.5. Towards a coupled vegetation/sediment transport approach

Ideally, holistic models of dryland landscape change should explicitly couple the interactions between major components of the system, such ecological processes and sediment transport processes (Baas & Nield, 2007). This is at the root of the emerging concept of 'landscape connectivity' (Peters et al., 2006; Okin et al., 2009b), which considers dryland landscapes as a series of conduits for processes (e.g. fire, wind and water propagation) that link vegetation growth, aeolian processes and

external forcing factors through various feedbacks (Turnbull et al., 2008, 2012; Stewart et al., 2014). The wind erosion models discussed in section 2.4.2, although useful in many respects, do not incorporate such feedbacks. Okin's (2008) model must be supplied with information on vegetation gap sizes and distributions, rather than allowing them to evolve independently in a vegetation distribution model. Dupont et al.'s (2014) CFD model does not account for surface change as wind erosion occurs.

A coupled approach to modelling dryland vegetation growth and sediment movement was presented by Baas & Nield (2007) and Nield & Baas (2008a,b). They used a cellular automaton (CA), a class of numerical models consisting of a regular, discrete grid of cells operated on by predefined rules, to capture full landscape-scale dynamics using only fundamental processes. The CA approach has been particularly productive in the context of dune-field patterning (e.g. Werner, 1995; Momiji et al., 2000; Bishop et al., 2002; Narteau et al., 2006), and the spatial nature of CAs lends itself well to analysing ecogeomorphic systems (Baas, 2007).

The Discrete ECogeomorphic Aeolian Landscape model (DECAL) (Baas & Nield, 2007; Nield & Baas, 2008a,b), later extended by Yan & Baas (2017), provides an approach for simulating the dynamics of vegetation-dependent dunes such as parabolic dunes and nebkhas, by incorporating feedbacks between sedimentation balance and vegetation growth. DECAL introduces a length scale to resultant landforms that remains otherwise dimensionless in bare-sand CAs. Usefully, the distributed dynamics of the model allow vegetation-dependent dunefields to be simulated over large spatial and temporal scales.

However, the biotic component in DECAL in its original form only incorporated as a generic, unitless 'vegetation effectiveness', which acts as a proxy for the aerodynamic effect of plants on sediment transport. Plant-plant interactions are

therefore not explicitly modelled, and the effects of vegetation form and porosity on local-scale wind flow are not considered. Yan & Baas (2017) extended DECAL to explicitly relate the vegetation effectiveness to the size and growth of individual plants. This allows seasonal sediment transport and vegetation growth to be simulated, but seasonality is imposed directly in the model, rather than emerging within the vegetation system in response to environmental or anthropogenic stress.

Therefore, a new, multi-scale cellular automaton model is needed, which captures the full range of feedbacks between vegetation growth, wind flow dynamics and sediment transport in dryland landscapes.

Summary: Sediment transport on vegetated surfaces

Previous attempts to evaluate the impact of vegetation on erosivity and erodibility in desert landscapes have been challenging in some respects. Traditional shear stress partitioning methods, which quantify the proportions of stress acting on the surface and on the vegetation, rely heavily on the dimensionless roughness density (λ) and therefore suffer from its inherent requirement for the surface to be treated homogenously. An alternative model proposed by Okin (2008) emphasises gaps in vegetation structure, and allows entrainment thresholds to vary across a surface. While this approach has several advantages, it still formulates sediment flux as a time-averaged function of u_*, which is an inappropriate measure of erosivity on complex, vegetated surfaces. CFD modelling has been used to resolve turbulent wind flow over heterogeneous vegetated landscapes, but computational expense limits its ability to simulate long-term erosion at the field scale or larger. Cellular automaton (CA) modelling can account for the heterogeneous ecogeomorphic processes occurring in drylands, whilst allowing simulations over large areas and long timescales. A new CA model is needed that captures the full range of interactions and feedbacks between vegetation growth, wind dynamics and sediment transport on desert surfaces. This will improve our understanding and management of potential dryland landscape responses to both environmental and human pressures.

SECTION TWO

FIELD EXPERIMENTS

CHAPTER THREE

Field Methods

3. FIELD METHODS

The objectives of the fieldwork were to quantify extremes in erosivity by measuring velocity and turbulence statistics around various plant types of different sizes and porosities (**Objective 1**), measuring wind flow recovery in the wake of a vegetation patch (**Objective 2**), and collecting topography data of erosion/deposition zones in the wakes of plants (**Objective 4**). Table 3.1 summarises the parameters measured and field techniques used, as well as their relevance to the objectives and their use in thesis chapters. The techniques are expanded upon in the next sections. Note that some methods were undertaken, but not used to in the thesis (e.g. sediment flux, some porosity data); a record of these methods is nonetheless provided.

Parameter	Technique	Reason	Research Objectives	Use in chapters
Wind turbulence	Sonic anemometer	Identify turbulence structures around and downwind of roughness elements	1, 2	5, 6, 7
Wind velocity	Anemometer	Characterise wind velocity recovery around and downwind of roughness elements	1	7
Wind velocity	Anemometer	Medium-term monitoring data for model input	4	5
Sediment flux	Impact sensor / sand trap	Quantify wind erosion at different sites, over different timescales	1, 2, 4	Not used
Grain size	Dry/wet grain size analysis	Quantify grain size distributions at field sites to infer transport potential	3, 4	3, 9
Surface height	Terrestrial laser scanner (TLS)	Identify regions of sediment erosion / deposition in wakes of plants at high resolution	4	9
Plant porosity	Camera + white card	Quantify plant porosity effects on turbulence generation (low-res)	1	5, 7
	Terrestrial laser scanner (TLS)	Quantify plant porosity effects on turbulence generation (high-res); Calibrate optical porosities	1, 4	9
Plant spacing / height	UAV	Characterise plant spacing and height at relevant field sites	2, 4	3, 9
	Manual transect measurements		2, 4	3, 5, 6

Table 3.1 Field techniques and parameters measured during fieldwork, with relevant Research Objectives and usage in thesis chapters.

3.1. Field site requirements

Short-term experiments were conducted to characterise spatial variations of wind velocity and turbulence around individual dryland plants, as well as downwind of more complex vegetation arrangements. Two longer-term stations were also set up to collect wind velocity and direction data in different vegetated contexts over periods of 3–4 weeks. These data were used to verify that conditions measured during the short-term experiments were representative of average conditions at the field sites.

3.1.1. Short-term experiments

The short-term experiments were carried out behind four broad vegetative 'types': grasses (denoted using the prefix '*Gr*'), shrubs (prefix '*Sh*'), trees (prefix 'T*r*') and patches (prefix '*Pa*'). Figure 3.1 shows how vegetation elements are classified and defined for the purposes of this study. In total, 3 grasses, 5 shrubs, 1 tree and 1 patch were examined here. 6 of the short-term experiments were carried out using cup anemometry, and 4 experiments were carried out using sonic anemometry (see section 3.3). The subscripts '*cup'* and '*sonic'* are employed to distinguish between the anemometer types used for each experiment.

Sites for the short-term experiments had to satisfy several criteria:

(a) topographically flat surfaces

To determine changes in windflow resulting solely from the presence of vegetation elements, complications arising from large-scale (e.g. low hills, sand dunes and incised valleys) and small-scale (e.g. gravel plain steps, large ripples) topographical obstacles were avoided where possible.

(b) a large fetch for boundary layer development

The upwind fetch had to be sufficiently large to allow for the development of a turbulent boundary layer in equilibrium with the surface, and unobstructed by other vegetation (apart from the experiments where inter-element interaction was required).

(c) reliable wind conditions

Winds had to be of a sufficient velocity and longevity to allow for airflow parameters to be identified. Importantly, wind direction for all the short-term experiments had to be as consistent as possible, to ensure accurate placement of equipment in the expected areas of change in flow.

(d) a range of vegetation types and configurations

In order to produce field data that would be relevant to model development, a range of vegetation types (i.e. grass, shrub or tree) and configurations (i.e. single shrub or patch) had to be investigated. In addition, it was necessary to choose vegetation elements with a range of heights and porosities.

Veg type	Example photograph	Description
Grass		Typically short plants consisting of long, narrow leaves, with a growing point that is mainly at ground level
Shrub		A vegetation element whose woody branches reach the ground (Leenders et al., 2007)
Tree		A vegetation element with a distinctive trunk below a canopy (Leenders et al., 2007)
Patch		A collection of shrubs and grasses that where skimming flow develops above the canopies

Figure 3.1 Definitions and example photographs of vegetation elements in this study.

3.1.2. Longer-term experiments

The requirements for the two longer-term sites were:

a) *distinctive vegetation patterning*

Both sites had to represent different vegetation patterning contexts, preferably with several different patterns and land covers distributed in discrete sectors

around the station. This would provide data of differing covers and patterning depending on wind direction.

b) *topographically flat surfaces*

Again, it was important to reduce complications imposed by large-scale topographical obstacles, to determine changes in windflow resulting solely from the spatial distribution of vegetation.

c) *variable wind direction*

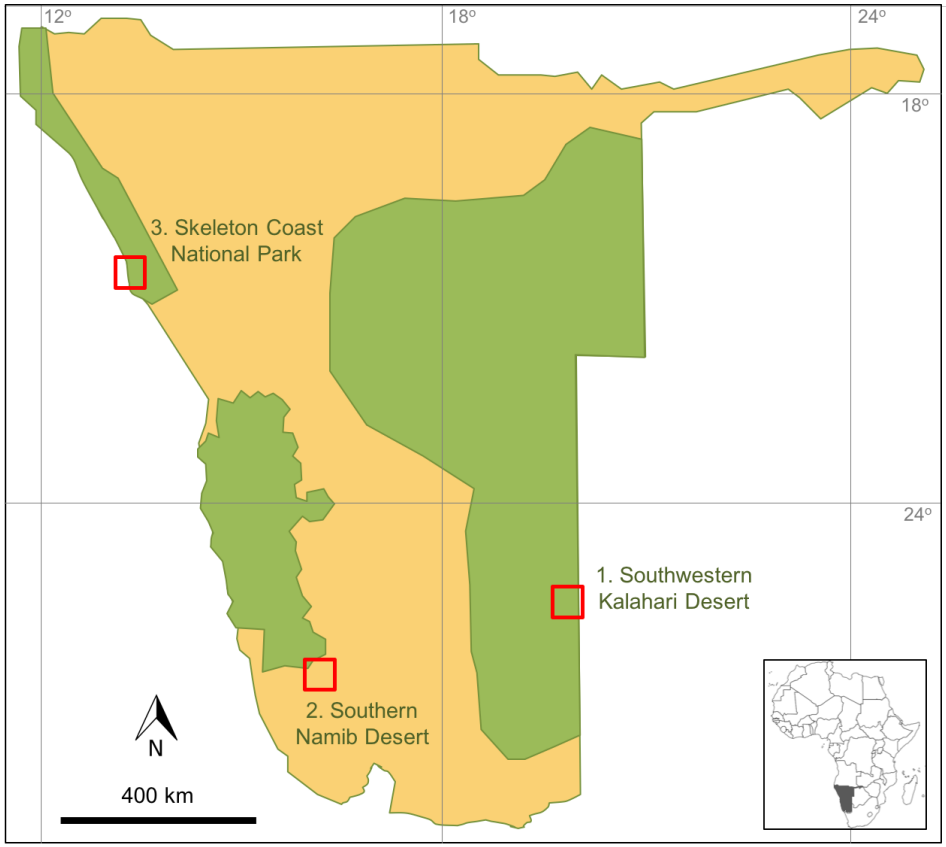
In order to capture full changes in wind flow over a variety of land covers, it was preferable to find a site where wind direction was variable.

d) *accessible and safe from human and animal interference*

Sites where data could be regularly and easily downloaded, and where the equipment was safe from interference, destruction or theft, were chosen.

3.2. Field site descriptions

Field experiments were carried out in three locations in Namibia, shown in Figure 3.2: the southwestern Kalahari Desert, the southern Namib Desert, and the southern half of the Skeleton Coast National Park. The tables in Figure 3.2 display the characteristics of the short-term experiments, as well as GPS and elevation information for all sites. Detailed descriptions of each field location are provided in the following three sections.



Exp.	Species	Date	Field site	Height (m)	Canopy width (m)		Optical porosity (%)
					E-W	N-S	
$Gr_{cup}1$	*Stipagrostis amabilis*	19/08/14	Kalahari	0.60	0.90	0.90	46
$Gr_{cup}2$	*Stipagrostis amabilis*	14/09/14	Kalahari	0.50	0.90	0.85	50
$Gr_{sonic}1$	*Stipagrostis amabilis*	27/09/14	Kalahari	0.75	1.30	1.10	53
$Sh_{cup}1$	*Rhigozum trichotomum*	19/08/14	Kalahari	0.60	0.95	0.75	69
$Sh_{cup}2$	*Zygophyllum stapfii*	05/09/14	Skel. Coast	0.65	1.90	1.50	63
$Sh_{cup}3$	*Zygophyllum stapfii*	05/09/14	Skel. Coast	0.55	1.50	1.40	71
$Sh_{cup}4$	*Zygophyllum stapfii*	06/09/14	Skel. Coast	0.65	1.10	1.20	38
$Sh_{sonic}1$	*Rhigozum trichotomum*	30/09/14	Kalahari	1.30	1.80	1.60	69
$Tr_{sonic}1$	*Acacia erioloba*	23/09/14	Namib	3.70	5.20	5.10	6
$Pa_{sonic}1$	Patch (various species)	04/10/14	Kalahari	1.10 (avg.)	-	-	-

Location	Field experiments	GPS coordinates (UTM, zone 33k)	Elevation (m)
Southwestern Kalahari	L1	0366811 E 7180540 N	1010
	$Gr_{cup}1$, $Gr_{cup}2$, $Gr_{sonic}1$, $Sh_{cup}1$, $Sh_{sonic}1$	0369913 E 7180634 N	983
	$Pa_{sonic}1$	0366872 E 7180590 N	1003
Skeleton Coast National Park	$Sh_{cup}2$	0343473 E 7691832 N	28
	$Sh_{cup}3$	0343451 E 7691829 N	31
	$Sh_{cup}4$	0343030 E 7691961 N	29
Southern Namib	L2	0619484 E 7047373 N	1223
	$Tr_{sonic}1$	0619715 E 7045842 N	1285

Figure 3.2 Locations of the three field sites in Namibia. The extents of the Namibian Kalahari Desert, Namib Desert and Skeleton Coast are shown in green. Upper table summarises experiment details for the ten short-term experiments. Lower table shows GPS coordinates and elevation information of the short-term and longer-term experimental sites.

3.2.1. Southwestern Kalahari Desert

The Kalahari (~900,000 km^2) consists of a semi-vegetated, intermittently active linear dune system (Thomas & Shaw, 1991), which responds to periods of human and environmental stress when vegetation cover is diminished (Wiggs et al., 1994; Bullard et al., 1997; Thomas et al., 2005). The desert experiences a strong South-North (from northern South Africa to continental Botswana) rainfall gradient of 150-500 mm (Thomas, 2011) that is highly seasonal, with 80% of annual precipitation occurring between October and March (Tyson, 1986).

The southwestern section of the Kalahari consists of natural grazing pressures as well as sporadic but intense cattle and sheep grazing. The region is defined as arid, with a high Budyko-Lettau dryness ratio (i.e. of mean annual net radiation to the product of mean annual rainfall and latent heat of evaporation) of 10 (Tyson, 1986). It is generally regarded as a low-energy (<15 m^3 m^{-1} yr^{-1}) environment (Thomas, 2011) and mean monthly wind speeds are thought to rarely reach the threshold for sand transport (Bullard, 1994, in Knight et al., 2004). Wind speed variability in the region is high during the austral spring, as winds may be absent on some days and blow strongly (> 6 m s^{-1}) on others.

Extensive areas of banded vegetation stripes, which are generally called tiger bush or brousse tigreé, are found in the southern Kalahari (Goudie & Viles, 2015). Tiger bush is formed of alternating bands of vegetation (grass, shrubs or trees) and interbands of bare soil (sometimes with termite mounds and/or grass clumps). The vegetated bands are usually curved, with the convex part facing upslope, and can be 'degraded' to different degrees, existing as banded, fuzzy, dashed and spotted states (Valentin et al. 1999). These arise when self-organising mechanisms develop on slopes rather than flat ground (in contrast to gaps, labyrinths and spots).

The experiments based in the southwestern Kalahari Desert (including the longer-term site L1) were conducted on farmland located ~4 k m north of the Auob River (Figure 3.3). The experimental sites were located in a field on raised, flat terrain, and a wide strip of grazed land allowed for short-term experiments to have a fetch of > 500 m. Various configurations of vegetation could be tested depending on the wind direction, with the site consisting mainly of *Stipagrostis amabilis* grasses, *Rhigozum trichotomum* shrubs and *Acacia erioloba* trees.

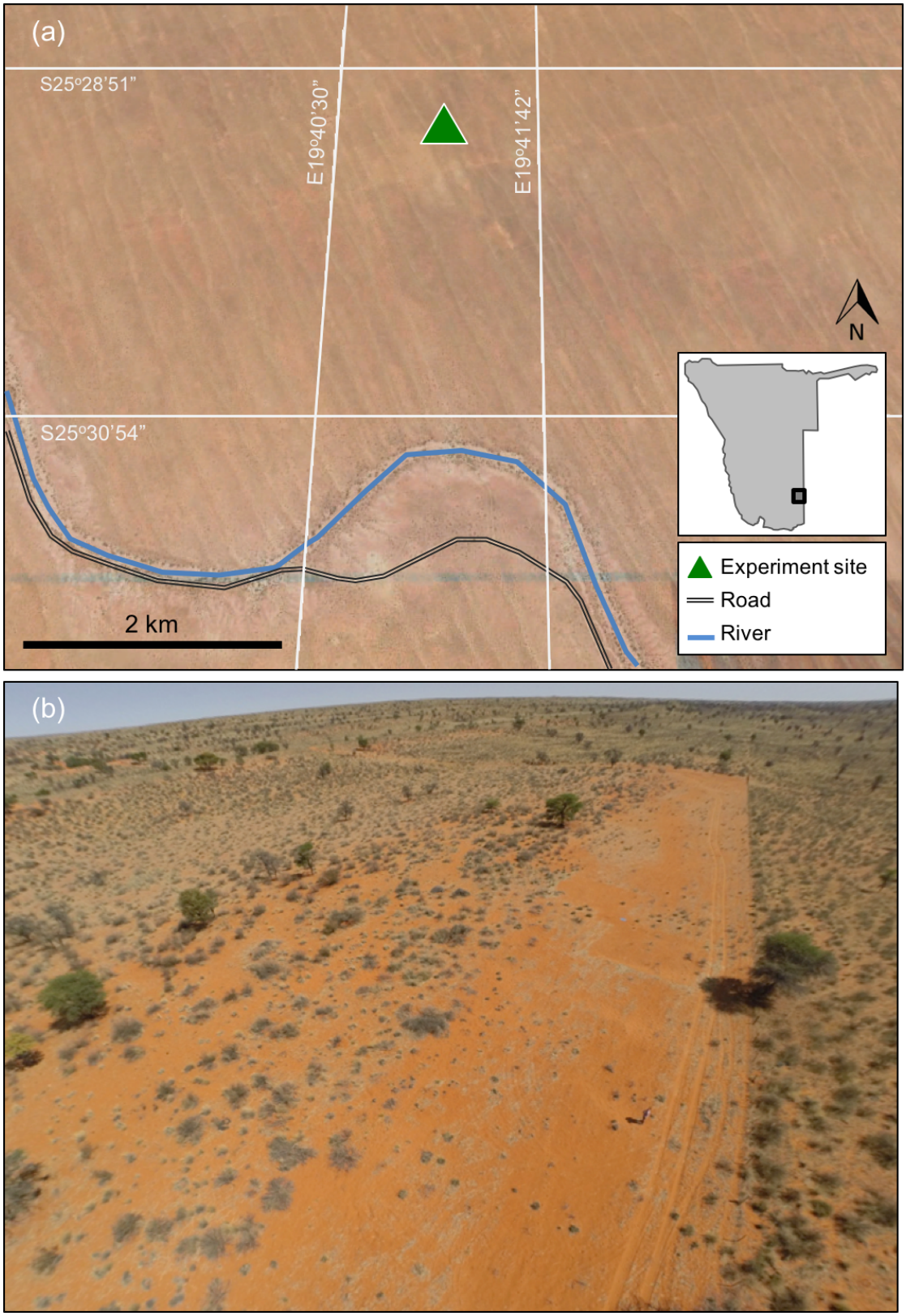


Figure 3.3 (a) Location map of the southwestern Kalahari field site. The area consists almost entirely of linear dunes orientated in a North-South direction; (b) aerial photograph (facing northeast) of the field where the experiments were undertaken.

3.2.2. Southern Namib Desert

The Namib Sand Sea covers an area of ~34,000 km^2 along the Namibian Atlantic Coast, extending inland to the western escarpment of the southern African plateau (Lancaster, 1985). The climate of the southern Namib is strongly influenced by the South Atlantic anticyclone, situated offshore at 30°S, which creates a pattern of stable outblowing S-SW winds that are overlain by local topographically and thermally induced circulations (Tyson & Seely, 1980). These winds are at their strongest and most frequent between late spring and summer (September to December), when the thermal contrast between sea and desert is greatest. The southern areas are characterised by high-energy wind regimes with a low directional variability, and thus high resultant potential sand flow (Lancaster, 1985). Topographically induced mountain-plain and down valley winds are common on the eastern margins of the desert (Tyson & Seely, 1980), and infrequent but high-velocity easterly 'berg' winds (occurring when pressure gradients are normal to the coast) are significant for sand movement in the southern Namib (Lancaster, 1989). Mean annual wind velocities are relatively high (6 m s^{-1}) in the southern part of the desert, but fall to around 3–4 m s^{-1} along its eastern margin (Lancaster, 1985).

The experiments conducted in the southern Namib Desert (including the longer-term site L2) were based in a 5 x 5 km area on the edge of the Sperrgebiet Reserve, near the small town of Aus (Figure 3.4). The site is typical of the southern half of the desert, comprising a large sandy gravel sheet set amidst rocky outcrops and sand ramps to the south and west. The area is characterised by zones of patterned (shrub and grass) vegetation, as well as some sparsely distributed *Acacia erioloba* trees.

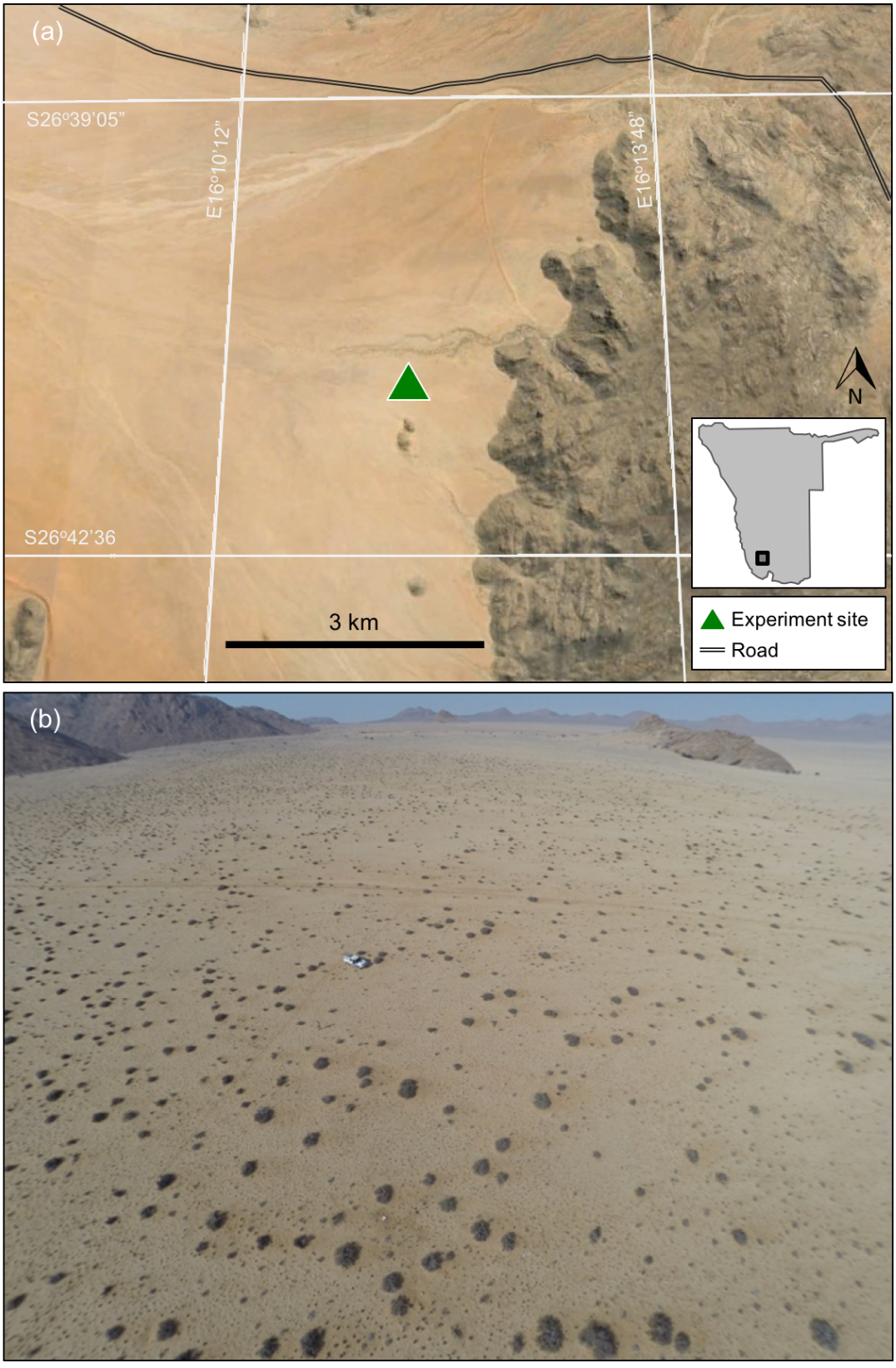


Figure 3.4 (a) Location map of the southern Namib field site; (b) aerial photograph (facing south) of the vegetation patterning at the site. Note off-road vehicle for scale.

3.2.3. Skeleton Coast National Park

In the arid northwest of Namibia, the Skeleton Coast erg stretches for 2000 km between Torra Bay and Hoarusib River (Krapf et al., 2003), and forms part of the northern Namib Sand Sea. Although the region is considered hyper-arid, seven major and several smaller ephemeral rivers flow W-SW towards the Atlantic Ocean across the erg, fed by catchment areas located 100–300 km inland (Krapf et al., 2003).

The climate of the northern Namib is considered arid to hyper-arid, and is strongly influenced by subtropical anticylonic cells at these latitudes. Air temperatures are relatively cool compared to other desert regions due to the proximity of the Benguela Current, although the influence of the current diminishes rapidly inland (Olivier, 1995). Mean annual daily maximum temperatures range from 17^{o}C at the coast up to 33^{o}C inland, and mean minima average 13–16^{o}C across the region (Buckle, 1996). The Benguela Current is also responsible for the presence of advective fog on ~150 days per year along the Skeleton Coast, as it cools moist oceanic air moving onshore (Olivier, 1995; Buckle, 1996). This can create fog precipitation (Viles, 2005). Rainfall in the area occurs mostly during the months of January to April, although it is highly variable both spatially and temporally (Lancaster, 1985).

Winds along the Skeleton Coast tend to blow from a SSE to SSW direction throughout the year (Lancaster, 1985), and are at their strongest and most frequent between late spring and summer (September to December), when the thermal contrast between sea and desert is at its greatest. During these months, the wind may be moving sediment for > 30–40% of the time. Like in the southern Namib, high-velocity easterly ‘berg’ winds sometimes occur when pressure gradients are normal to the coast (Lancaster, 1989).

The field site was situated in the southern half of the Skeleton Coast National Park, ~5 km inland from the coast along the Huab River valley (~20 km south of Torra Bay; Figure 3.5). In this area, relatively small nebkhas were distributed on a large, flat gravel plain, with a narrow band of barchan dunes emerging from an expanse of sandy substrate to the south. The few plants at the site were live and dead *Zygophyllum stapfii* shrubs. The site was chosen due to the relatively strong and reliable spring winds occurring in the region, and its accessibility via a ranger road.

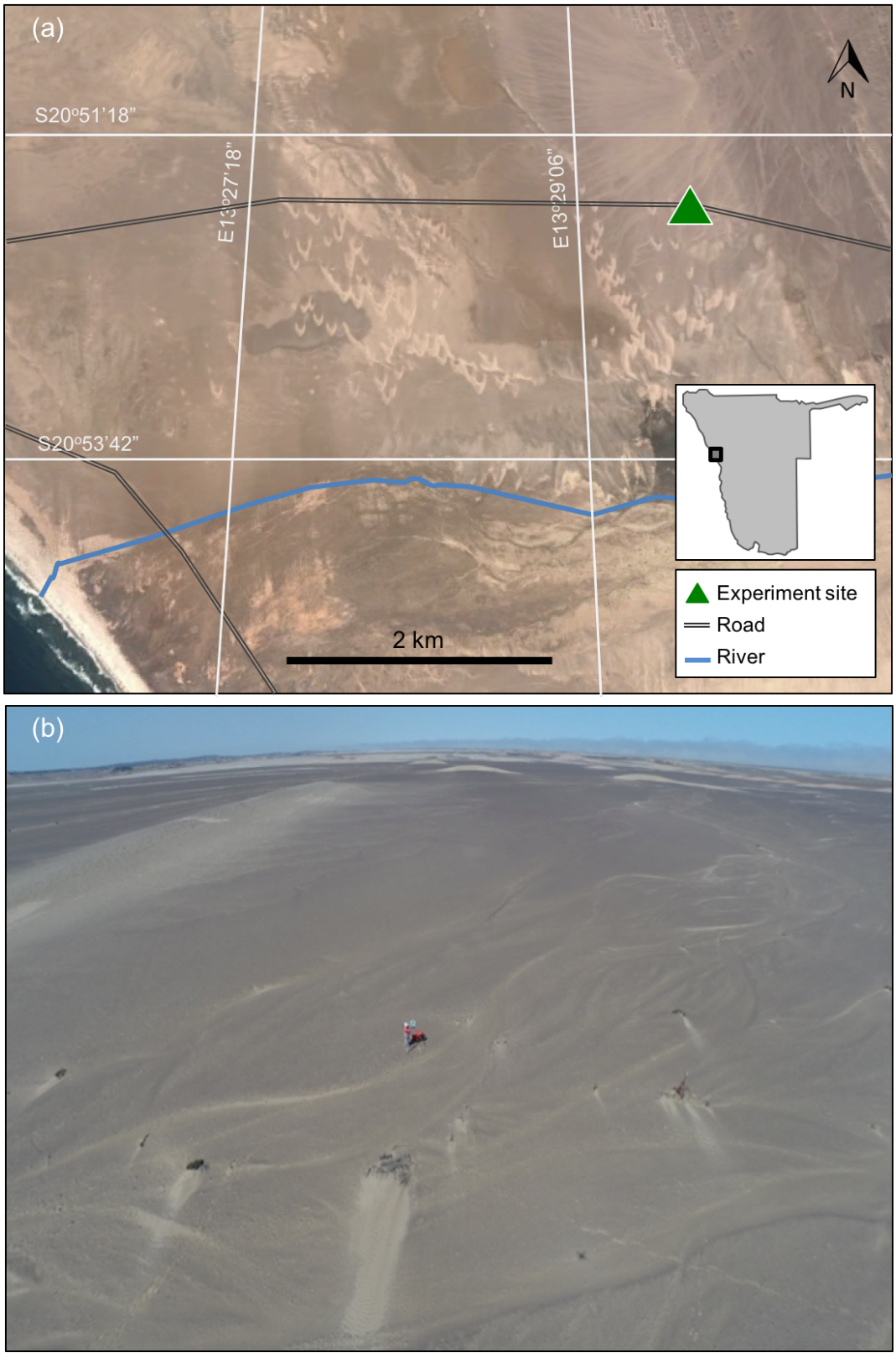


Figure 3.5 (a) Location map of the Skeleton Coast field site; (b) aerial photograph (facing south) of the individual nebkhas at the site. Note person for scale.

3.2.4. Timing of field experiments

The experiments for this field study were carried out over the months of August to October 2014, in order to coincide with the time when winds were at their maximum strength and frequency. In the southern Namib and the southwestern Kalahari, this 3-month window allowed for a wide range of wind directions and strengths to be tested for both longer- and short-term experiments. Mean wind speed in the southwestern Kalahari during the study period (17th August to 14th September) was 1.98 m s^{-1} and the maximum wind speed was 12.70 m s^{-1} (at 2.70 m height); in the southern Namib, mean wind speed was 4.60 m s^{-1} during the study period (16th September to 4th October) and maximum wind speed was 14.62 m s^{-1}. In the Skeleton Coast, short-term experiments were carried out over a few days in early September, when wind velocities were high in magnitude and consistently from a S-SW direction. Rainfall was observed only on two days during electrical thunderstorms in the southwestern Kalahari and southern Namib, and not at all during the experimental period in the Skeleton Coast.

3.3. Field techniques

3.3.1. Measuring flow characteristics

3.3.1.1. Wind velocity

Cup anemometers have been widely used in aeolian geomorphology (e.g. Wiggs et al., 1996a,b; Davidson-Arnott et al., 2009; Baddock et al., 2011; Nield et al., 2013; Gillies et al., 2014) due to their low cost, rugged nature, and ability to measure wind from any lateral direction. *A-100 R (Vector Instruments)* anemometers consisting of a vertical shaft with a 3-cup rotor were used for both short-term and longer-term experiments in this study, in order to measure mean wind velocity at various heights.

The threshold wind velocity for the cup anemometers is 0.15 m s^{-1}, they are capable of measuring velocities up to 75 m s^{-1}, and are accurate to 1% ± 0.1 m s^{-1} (Campbell Scientific User Guide, 2012). Each cup anemometer was attached to a metal pole (1 m for short-term experiments; 3 m for longer-term experiments) using a standard boss and clamp. The cup anemometers were calibrated in the field against one of the sonic anemometers (see section 3.3.2).



Figure 3.6 Example of an A-100 R cup anemometer and W200P wind vane used in the field study. The anemometers were secured to metal poles with a boss and clamp, and connected to a datalogger positioned downwind and offset, or buried underground.

A wind vane (*W200P Potentiometer, Vector Instruments*) was used at the longer-term sites L1 and L2, to measure wind direction at a height of 2.50 m (as close as possible to the highest cup anemometer without interfering with its airflow). The wind vane is composed of an attachable fin that rotates to align in a normal direction the wind flow. It is reliable for wind velocities above 0.6 m s^{-1} and accurate to ± 2° for wind velocities over 5 m s^{-1} (Campbell Scientific User Guide, 2012).

During sampling intervals, wind velocity was averaged over 10-second and 1-minute intervals, and recorded using a *Campbell CR1000* datalogger with data dumped to a storage module to prevent logger saturation. This rate of sampling corresponds to previous experimental findings that successful calculations of u_* and other wind parameters arise from averaging periods on the order of 10–40 seconds (Namikas et al., 2003; Wiggs et al., 2004a). The logger and data storage module were positioned downwind and offset from the anemometer arrays for the short-term experiments, or were buried in the case of the longer-term experiments, in order to avoid flow interference. Data were downloaded to a laptop computer using the *Campbell Scientific Loggernet* software at the end of each day of measurement.

3.3.1.2. Flow turbulence

Despite their prevalence in aeolian studies, cup anemometers are disadvantageous in some respects. The bulky nature of the anemometers and the effects of bombardment by sand grains preclude their use at heights close (< 30 cm) to the ground (Livingstone & Warren, 1996). Cup anemometers respond in a non-linear fashion to changes in wind velocity, responding more quickly to an increase in wind speed than to a decrease due to the angular momentum of the spinning cups (McKenna-Neuman et al., 2000). Moreover, the design of the cup anemometer means that only a temporally averaged estimate of wind velocity can be acquired,

over a minimum of tens of seconds. Such estimates cannot account for unsteady rapid fluctuations in airflow that have been identified as being potentially responsible for sediment entrainment and transport (e.g. Namikas et al., 2003; Schönfeldt & von Löwis, 2003; Baas & Sherman, 2005a; Baddock et al., 2011; Weaver & Wiggs, 2011; Wiggs & Weaver, 2012).

The recent development of ultrasonic anemometry has allowed airflow properties to be investigated at high frequencies in aeolian sediment transport research (e.g. Schönfeldt & von Löwis, 2003; van Boxel et al., 2004; Leenders et al., 2005; Walker, 2005; Baddock et al., 2007, 2011; Weaver & Wiggs, 2011; Chapman et al., 2012, 2013; Davidson-Arnott et al., 2012; Wiggs & Weaver, 2012; Barrineau & Ellis, 2013). A sonic anemometer is a wind sensor with no moving parts that measures high-frequency three-dimensional wind velocity by determining the time delay of an ultrasonic acoustic signal travelling over a set path distance between paired sonic transducer heads (Walker, 2005).

The principles of sonic anemometry are described in detail in Kaimal & Finnigan (1994), van Boxel et al. (2004) and Walker (2005). Essentially, the difference in time delay between both directions along the same path is proportional to the wind speed, such that if a sensor with path distance d_p (m) is placed in a fluid with a mean velocity along its path U (m s^{-1}), the time t_1 (s) for the signal to propagate from transmitter to receiver is given by:

$$t_1 = \frac{d_p}{C + U} \tag{3.1}$$

where C is the speed of sound (330 m s^{-1} in still, dry air at standard temperature and pressure). The second incoming signal is given by:

$$t_2 = \frac{d_p}{C - U}$$

(3.2)

By computing the difference between opposing travel times, the resultant flow vector U can be resolved by (Walker, 2005):

$$U = \left(\frac{d_p}{2}\right)\left({t_1}^{-1} - {t_2}^{-1}\right)$$

(3.3)

Sonic anemometers can thus provide simultaneous measurements of the three components of wind velocity: horizontal streamwise (u), lateral or spanwise (v) and vertical (w). These components provide the covariances (u', v' and w') to evaluate a variety of Reynolds shear stresses and coherent flow structures. Section 4.3 describes the post-processing procedures for sonic anemometer data.

Given their successful application in previous research requiring high-frequency wind data, three *Campbell CSAT-3* sonic anemometers (cf. Leenders et al., 2007) were used in this study to analyse turbulent wind flow around different vegetation elements. Each of the sonic anemometers was connected to one of two *Campbell CR1000* dataloggers, with data dumped to a storage module to prevent logger saturation. The logger and data storage module were positioned downwind and offset from the sonic anemometer arrays to avoid flow interference. Data were downloaded to a laptop computer using the *Campbell Scientific Loggernet* software at the end of each day of measurement. Offset errors of the *CSAT-3* sonic anemometers at wind speeds < 30 m s^{-1} are ± 8 cm s^{-1} in the u and v components and ± 4 cm s^{-1} in the w component; gain errors are < ± 2% for a wind vector within 5° of horizontal, < ± 3% for a wind vector within 10° of horizontal, and < ± 6% for a wind

vector within 20^{o} of horizontal (Campbell Scientific User Guide, 2012). The sonic anemometers were individually calibrated by the manufacturer shortly before their use in the field.

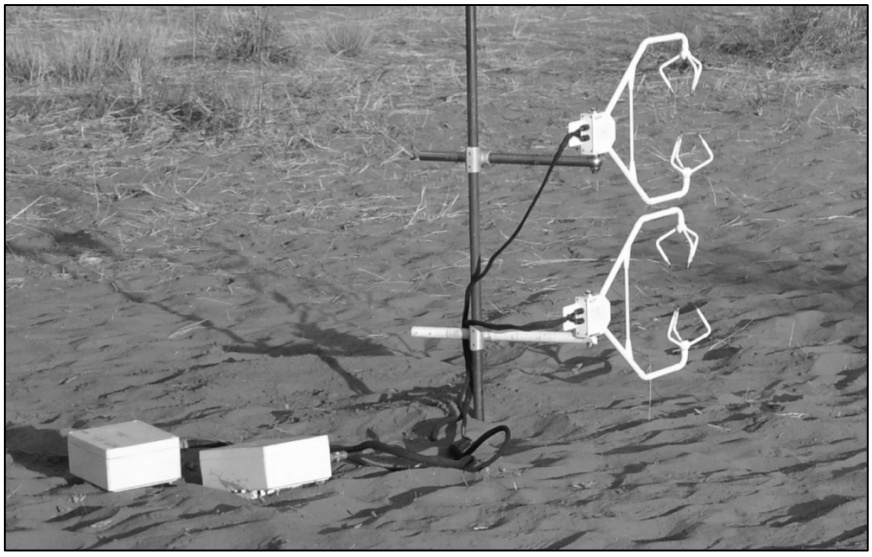


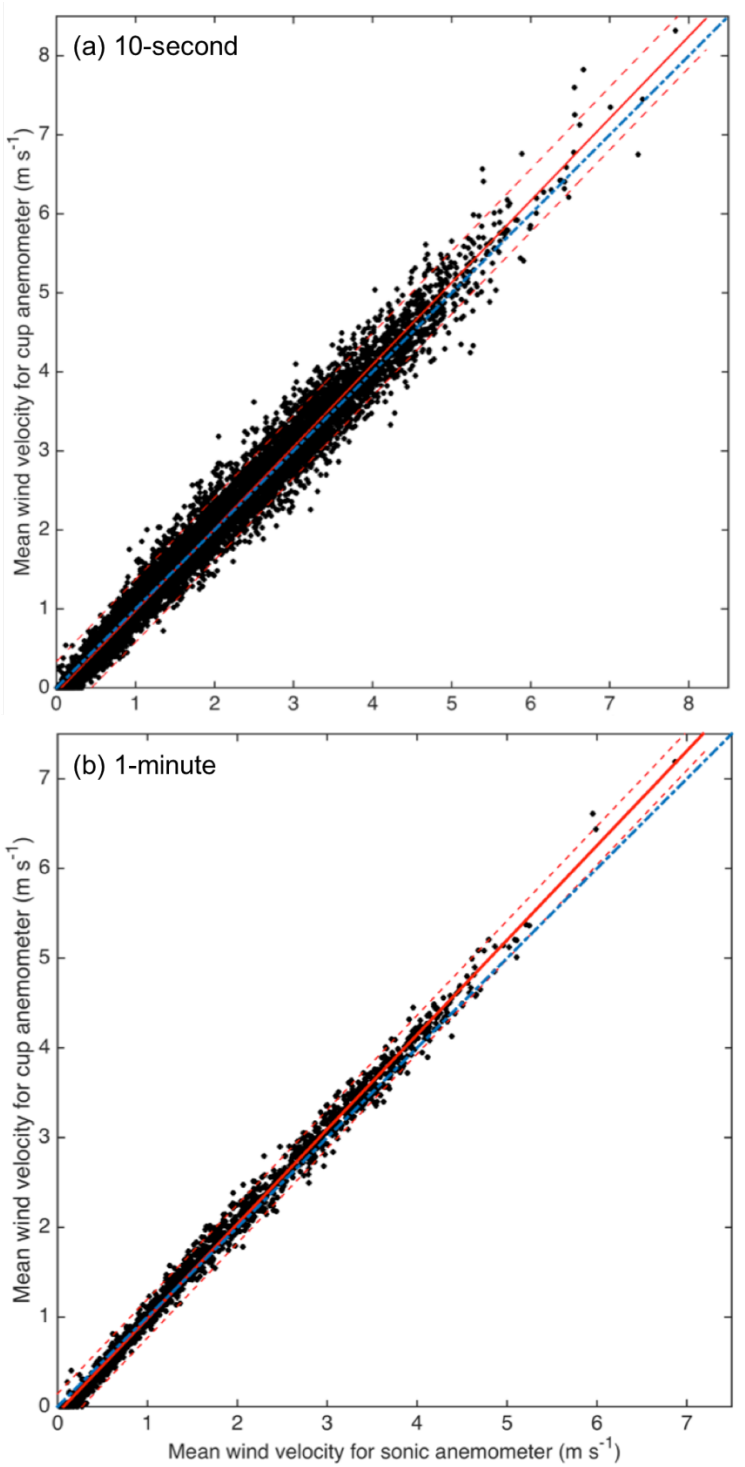
Figure 3.7 CSAT-3 sonic anemometers deployed in the field. Each sonic anemometer was connected to a Campbell CR1000 datalogger (not shown). Transducer heads were oriented to point directly into the wind (wind blowing from top right to bottom left in this image).

Three-dimensional wind velocity was sampled at a frequency of 10 Hz in all sonic anemometry experiments. Close to the surface, low-frequency structures in the airflow (large vortices) are suppressed by the bed, and there is an increased identification of higher frequency turbulence spectra (van Boxel et al., 2004). Therefore, valuable information on the turbulent structure of the airflow is lost from the signal if the sampling frequency is too low (Weaver, 2008). The sampling frequency of 10 Hz chosen for this study allows for the turbulent nature of wind flow to be measured even very close (~0.30 m) to the surface (cf. Leenders et al., 2005).

3.3.2. Calibration of cup anemometers

The calibration of cup anemometers can drift over time due to dust contamination and operator wearing (Weaver, 2008), so it is necessary to verify that they measure wind speed precisely. All three sonic anemometers used in this study were calibrated by the manufacturer immediately prior to the field season. The eight cup anemometers were calibrated in the field by comparing their velocity readings to those obtained from one of the sonic anemometers at the Kalahari site. The cup anemometers and the sonic anemometer were left to record wind velocity data simultaneously at 0.30 m height, at 10-second intervals, over a total period of 66 hours.

Figure 3.8 shows the mean wind velocity as measured by the cup anemometers compared to the mean wind velocity measured using the sonic anemometer, with data averaged over 10 seconds and one minute. Both the 10-second and 1-minute data showed a very strong correlation between the cup and sonic measurements (R^2 = 0.978 and R^2 = 0.993, respectively). If only low wind velocities (< 3 m s^{-1}, as measured by the sonic anemometer) are considered, the correlation is still very strong (R^2 = 0.96; RMSE = 0.25). This suggests a lack of a significant 'hysteresis effect' (e.g. Kaganov & Yaglom, 1976; Knott & Warren, 1981; Weaver, 2008), whereby cup anemometers exhibit a nonlinear response to changes in wind velocity due to the inertia of the instrument. The response delay of the cup anemometers in this study was relatively low, with cup anemometers overestimating wind speeds by < 3% at 6 m s^{-1}.



Time interval	Equation	R^2	RMSE
10-second	y = 1.039x – 0.06336	0.978	0.2026
1-minute	y = 1.054x – 0.07043	0.993	0.1095

Figure 3.8 Linear regression between mean wind velocity measured using cup anemometers and corresponding wind velocity measured using a sonic anemometer, for (a) 10-second averaged, and (b) 1-minute averaged data. The 95% confidence bounds for the lines of best fit are shown as dotted red lines. A 1:1 reference line is shown as a blue dot-dash line. Regression statistics are shown in the table.

3.3.3. Measuring sediment transport

Accurate estimations of aeolian sediment are necessary for quantifying wind erosion, for validating sediment transport models and for evaluating the mechanisms of wind erosion control (Zobeck et al., 2003). In this study, two *Big Spring Number Eight* (*BSNE*, Fryrear, 1986) samplers and one high-frequency piezoelectric *Sensit* (e.g. Baas, 2004; Wiggs et al., 2004a; Belnap et al., 2009) impact responder were deployed at each longer-term site (L1 and L2). This allowed for sediment transport to be monitored over a weekly to monthly timescale, and provided information on thresholds of entrainment that could be integrated into the development of the numerical model.

The *BSNE* sampler (Figure 3.9a) traps sediment by allowing air to pass through a vertical inlet and deposit its material into a collection pan. *BSNE* traps were chosen for this study because of their ease of use, portability, low cost, and relatively strong efficiencies (e.g. Shao et al., 1993; Nickling & McKenna Neuman, 1997; Zobeck et al., 2003; Okin et al., 2006; Field et al., 2012; Ravi et al., 2012; Gillies et al., 2014). The sampling efficiency of *BSNE* samplers varies depending on wind speed and particle size, but generally lies between 86% and 108% (Shao et al., 1993; Goossens et al., 2000; Mendez et al., 2011). By sampling material at different heights, *BSNE* measurements can be integrated to provide an estimation of horizontal mass transport (i.e. the amount of soil passing per horizontal unit area between two definite heights; e.g. Li et al., 2007, 2013). Further technical details of *BSNE*s can be found in Fryrear (1986).

While sediment traps provide measures of mean sediment transport rate, they do not account for extremes of flux resulting from instantaneous wind velocity maxima (Bauer & Namikas, 1998). Consequently, high-frequency impact responders that do not require the capture of measurable quantities of sand are increasingly prevalent in aeolian investigations. The *Sensit* (Figure 3.9b) is a commercially developed, cylinder-shaped impact sensor that has been used to detect periods of saltation in the field (Baas, 2004; Wiggs et al., 2004a; Ravi et al., 2012). The instrument consists of an omnidirectional sensing area of 325 mm^2 (Sherman et al., 2011) made from a piezoelectric crystal that produces a pulse signal proportional to the number of grain impacts (Stockton & Gillette, 1990). The responsiveness of the *Sensit* increases with particle size and wind speed, and its relative efficiency peaks at 75% (van Pelt et al., 2009; Sherman et al., 2011). With an impact measurement frequency of 1 Hz,

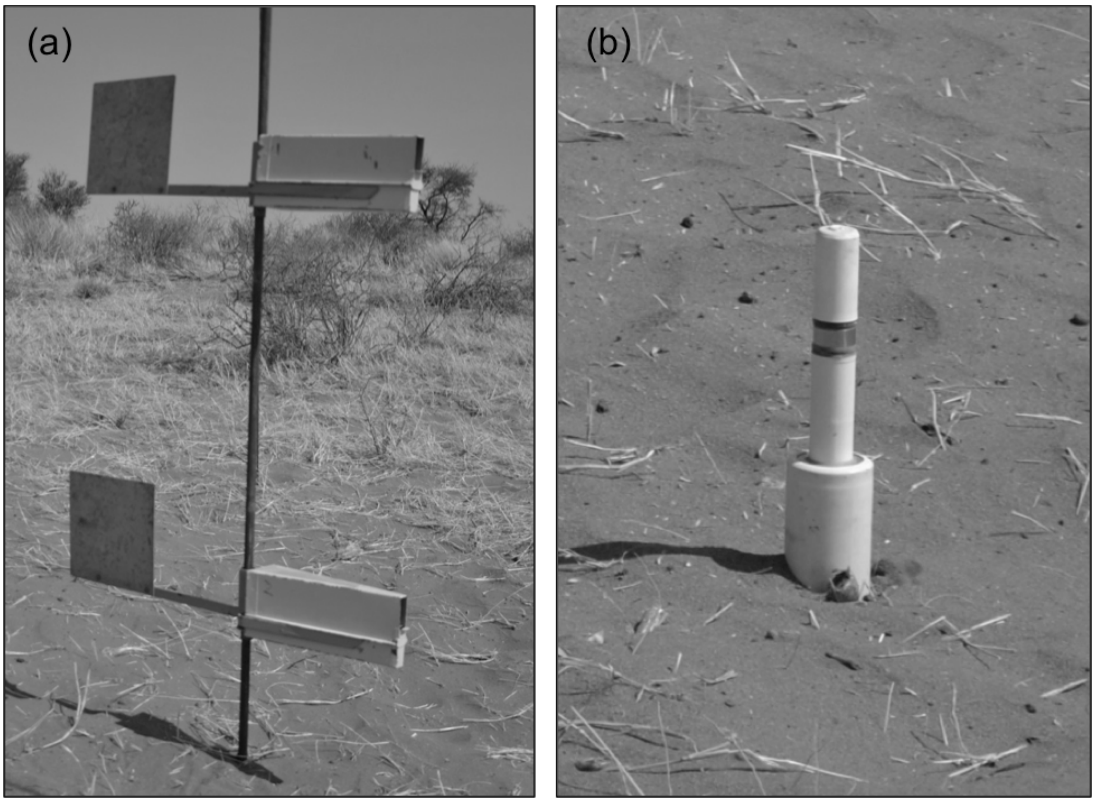


Figure 3.9 (a) *Big Spring Number Eight* (*BSNE*) sediment traps set up at longer-term site L1; (b) *Sensit* grain impact sensor used in this study (although not buried fully for the purposes of the photograph, the piezoelectric ring was at 0.05 m above the surface during the experiments).

Sensits can quantify the onset and intermittency of saltation, but traditional sand traps must still be deployed alongside to determine site-specific relationships between mass transport and signal response (Baas, 2004; Stout, 2004; Weaver, 2008; van Pelt et al., 2009).

Note that the sediment transport data were not used in this thesis, because of issues with the *Sensit* not being responsive during the entirety of the experimental period, and due to very little sediment being recorded in the *BSNE* sand traps.

3.3.4. Grain size analysis

Grain size was analysed using sediment samples collected at both longer-term stations (L1, L2), and one sample from each of the main short-term experiment sites (see Table 3.2 for the sites represented by each sediment sample). Two sediment samples were taken at the site of $Sh_{cup}4$, in order to characterise both the gravel surface and the underlying sediment. Sediment samples were acquired by scooping the top 5 cm of the surface in a single fluid motion, using a stainless-steel trowel. Both wet and dry grain size analysis was performed on each sample in a laboratory.

For dry grain size analysis, samples were sieved to retain sediment definable as 'sand' (<2 mm). Representative subsamples were run through a Malvern Mastersizer 2000 particle size analyser at 1 bar pressure, using the predefined Scirocco Statement of Procedure (SOP). If the obscuration rate did not fall between 1% and 3%, the test was repeated with an appropriate increase or decrease of sediment.

For wet grain size analysis, samples were also sieved to retain sand-size particles, and the moisture content inferred after repeated drying until sample mass loss was not greater than 5 % (m/m) per 24 hours. In order to remove soluble salts for the wet

grain size analysis, subsamples were desalinated by immersion in deionized water and centrifugation (with the addition of $MgCl_2$ solution to induce flocculation if necessary). Carbonate ions were removed from the samples by treatment with Ch_3COONa, adjusted to a pH of 5, followed by pH adjustment to pH 9–10 using 1 M NaOH. Organic material was removed by the addition of NaClO (adjusted to pH 9.5), centrifugation, and rinsing with 0.1 M NaCl to wash out the products of organic matter decomposition. Representative subsamples were run through a Malvern Mastersizer 2000 particle size analyser at 1 bar pressure, and the obscuration rates were verified to lie between 10% and 20%.

Sediment sample	Location	Corresponding field experiments
GS1	Kalahari	L1, $Sh_{cup}1$, $Sh_{sonic}1$, $Gr_{cup}1$, $Gr_{cup}2$, $Gr_{sonic}1$, $Pa_{sonic}1$
GS2	Namib	L2
GS3	Skeleton Coast	$Sh_{cup}2$, $Sh_{cup}3$
GS4	Skeleton Coast	$Sh_{cup}4$ (gravel surface)
GS5	Skeleton Coast	$Sh_{cup}4$ (underlying sand surface)
GS6	Namib	$Tr_{sonic}1$

Table 3.2 Sediment samples for grain size analysis, and their corresponding field experiments

Figure 3.10 displays the grain size distributions of sediment found at all experimental sites. The differences between wet and dry grain size analyses arise from the fact that dry analysis measures the size of grains (some of them amalgamated) as found in the field, whereas wet analysis breaks the amalgamations down into their constituent parts. It is therefore expected that dry analysis should produce larger proportional frequencies of coarser grains than the wet analysis, and that wet analysis should produce larger frequencies of finer grains than dry analysis.

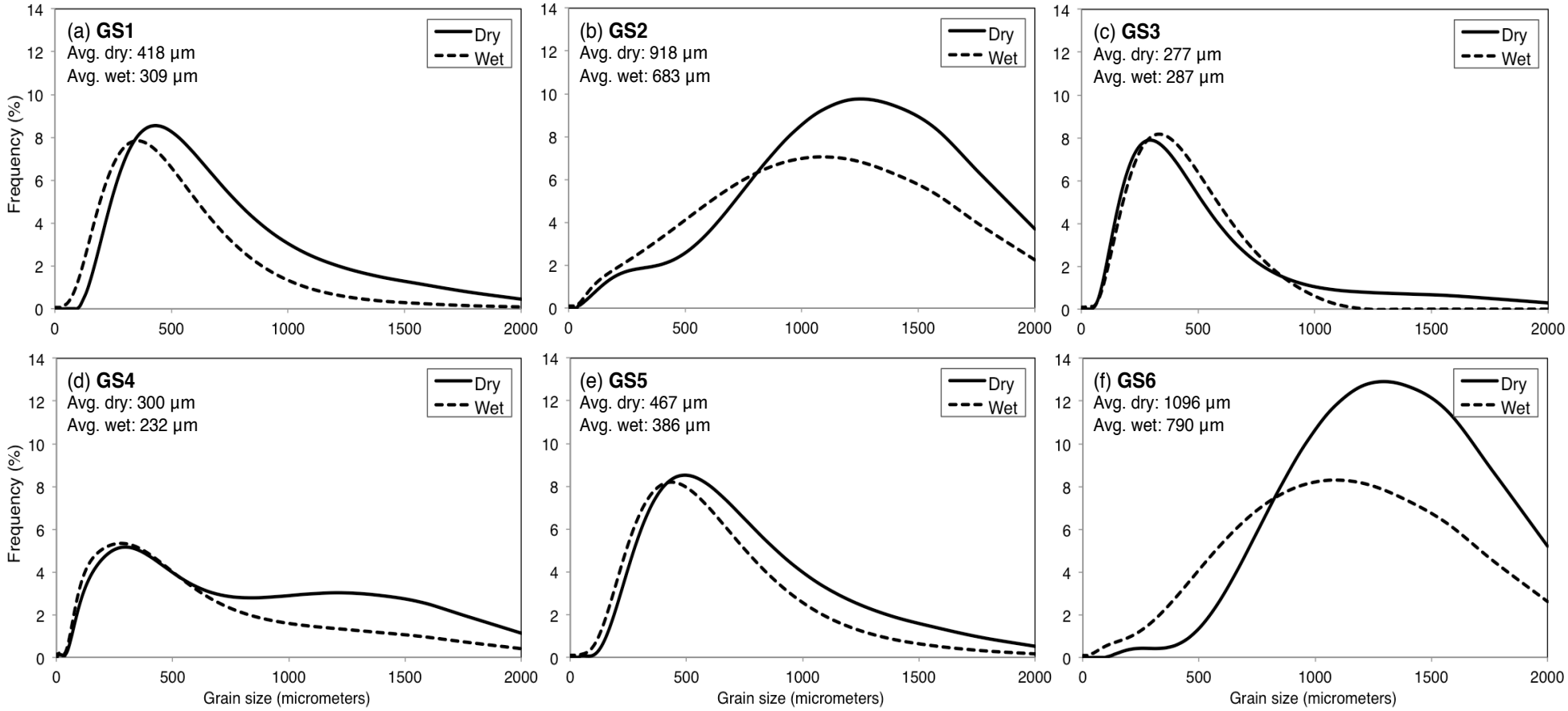


Figure 3.10 Grain size distributions for samples taken at long-term and short-term experimental sites. Results from dry and wet grain size analyses are shown. Median grain sizes, as determined from both methods, are also given. See Table 3.2 for the sites represented by each sediment sample.

3.3.5. Vegetation porosity

Optical porosity (as opposed to volumetric porosity) is defined as the ratio of the open surface to the total surface of an object (Lee et al., 2014). The optical porosity of the vegetation elements (θ_i) in this study was determined using a digital photogrammetry method adapted from Kenney (1987). Digital photographs of part of the canopy were taken at approximately 0.40 m from shrubs and grasses, and 3.0 m from tree canopies, using a Nikon D3100 DSLR camera with a resolution of 14.2 Megapixels, from the four principal cardinal directions. The photographs were enlarged to fill the image dimensions, turned into black and white images, and the perimeter of the plant was defined within a polygon. A variety of threshold values for black (plant branches) and white (open area) pixels were calculated, and the best fit to actual element shape was visually determined (cf. Gillies et al., 2000; Leenders et al., 2007). The percentage of white pixels, averaged across all directions, was taken as the mean porosity of the element canopy (Figure 3.11).



Figure 3.11 Transformation of a digital photograph of shrub $Sh_{cup}1$ from full colour (left) to grayscale (middle) to black/white pixel count (right), based on the original method of Kenney (1987).

Optical porosity is generally an underestimation of volumetric porosity because much of the small-scale porosity (i.e. between leaves and branches) is beyond the resolution of the analysis, and light transmission is obscured by the element (Grant &

Nickling, 1998). In a field experiment, Grant & Nickling (1998) estimated the porosity of a shrub using both an optical method and a simple volumetric water displacement technique, and found that optical porosity (θ_i) increased as a power function of volumetric porosity (ζ), such that:

$$\theta_i = \zeta^{2.782} \tag{3.4}$$

To calibrate the optical porosity method employed in this study, volumetric analysis was performed using laser-scanning datasets. Three shrubs ($Sh_{cup}2$, $Sh_{cup}3$ and $Sh_{cup}4$; see section 3.4.1) were scanned using a *Leica P20 Scanstation* terrestrial laser scanner (TLS) to produce high-resolution (mm-scale) point clouds of their structures (e.g. Nield et al., 2011; Nield & Wiggs, 2011). The TLS scans were post-processed in *Cyclone* software, and the vegetation structures isolated from data points for the surrounding sand and ground. Point-cloud data of small vegetation elements are difficult to stitch together into a coherent, realistic mass because of data 'noise' resulting from varying reflective properties of different parts of the shrub, as well as saltating sand in aeolian environments (Nield, J., *pers. comm.*). Noise was removed by dividing the point clouds into high-resolution 'slices' in the x-y plane (R), and 'shrub objects' in each slice were filtered according to a size threshold (ST) (see workflow in Figure 3.12). The volumetric porosity was taken to be the proportion of pixels covered by shrub objects compared with the total pixel coverage across all slices.

Figure 3.13 displays the relationships derived between volumetric and optical porosities for the three study shrubs, for a range of R and ST values. All the relationships display strong coefficients of determination (R^2 = 0.88–0.99), and several are very similar to the relationship derived by Grant & Nickling (1998). Note

that volumetric porosities were not employed to characterise element porosities in Chapters 5 and 7, as the porosity of most of the elements in these studies was calculated using the standard optical porosity technique, and it is unclear which of the relationships shown in Figure 3.13 best describes the conversion between the two porosity types. However, volumetric porosities were used in Chapter 9, to relate the study nebkhas to model output.

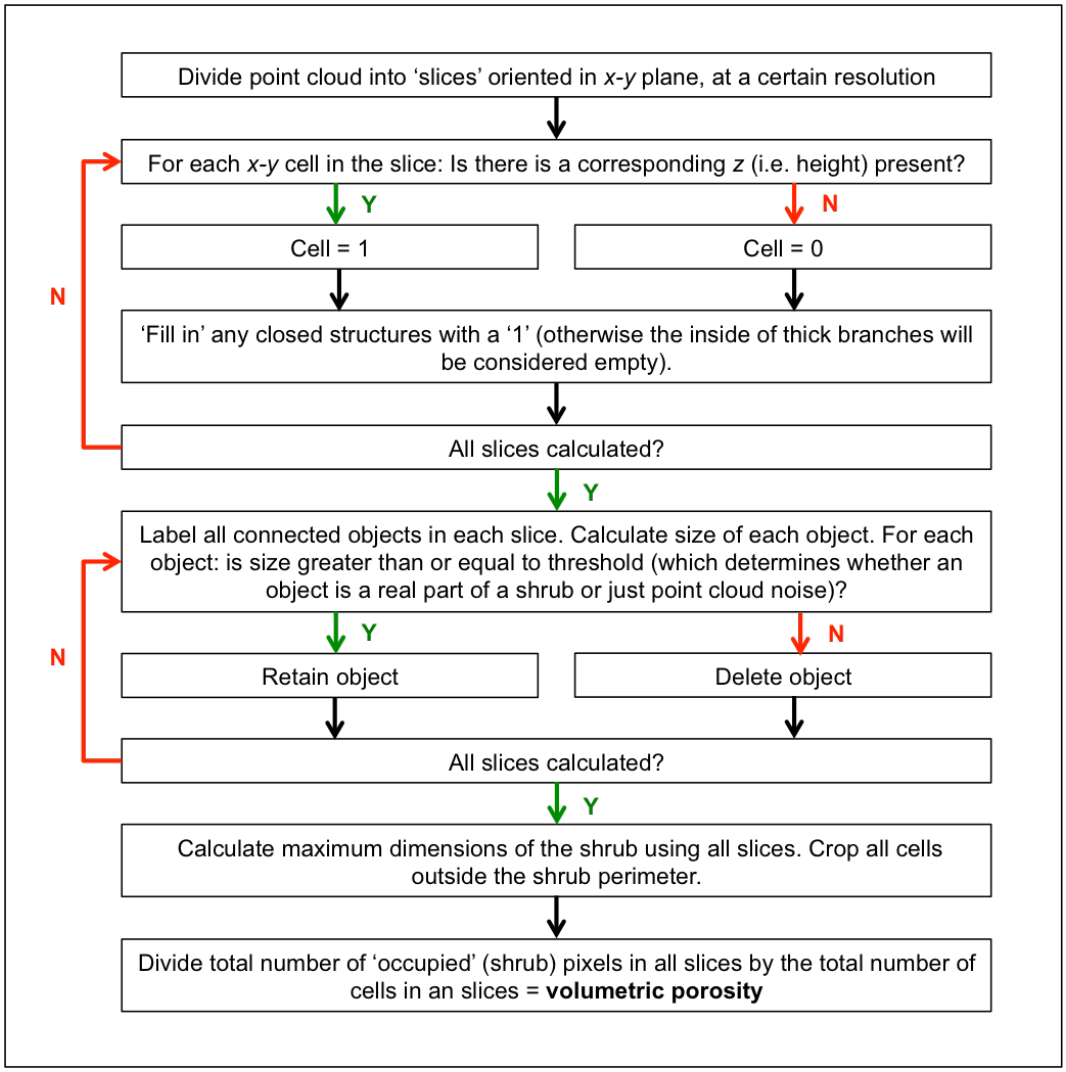


Figure 3.12 Workflow for calculation of volumetric porosity from TLS-derived xyz point clouds of shrub structures.

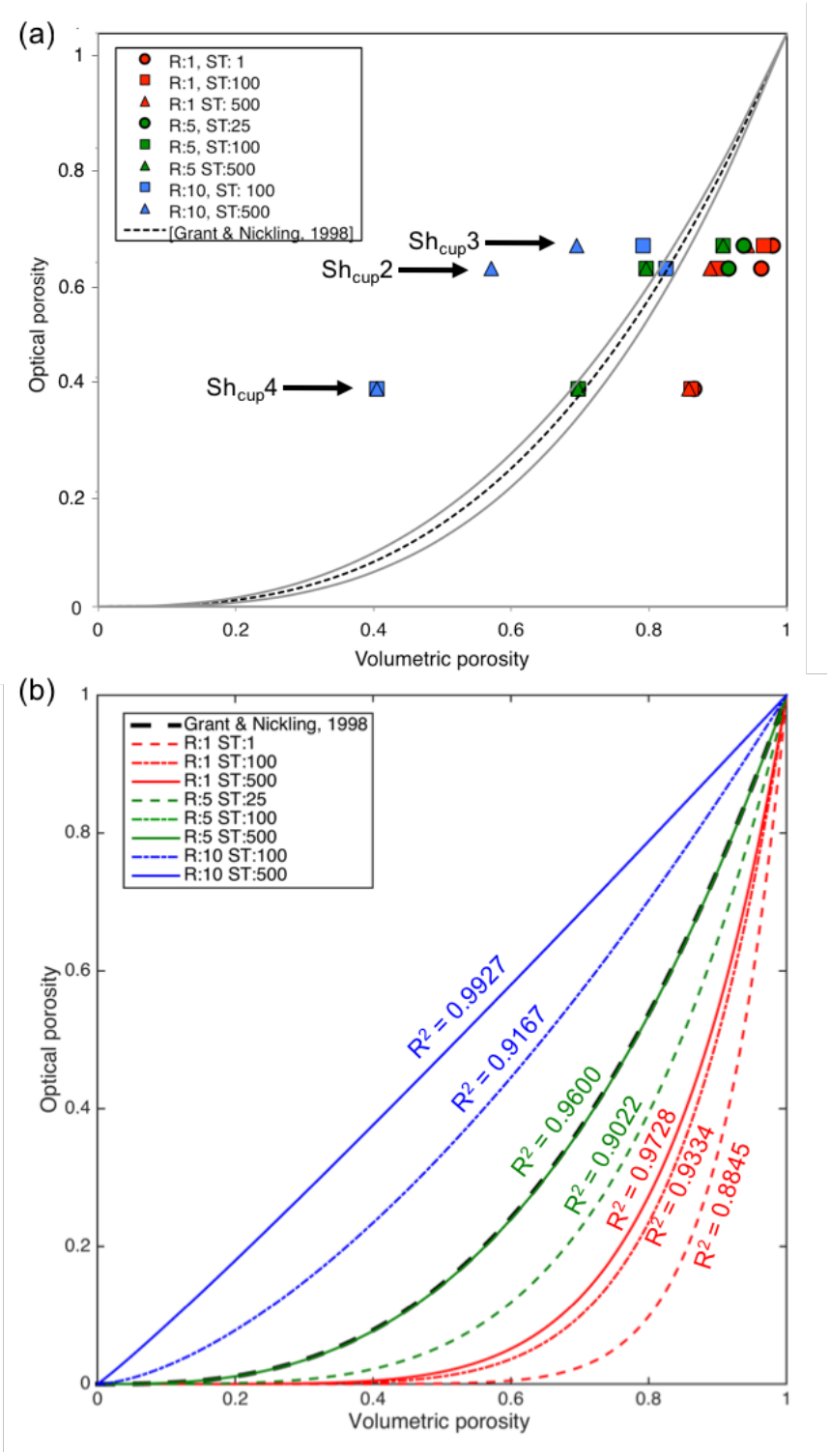


Figure 3.13 (a) Comparison between volumetric porosity (derived using technique shown in Figure 3.12) and optical porosity (derived using the method of Kenney, 1987), for the three study shrubs: Sh$_{cup}$2, Sh$_{cup}$3 and Sh$_{cup}$4. Volumetric porosities were calculated according to different rows/slices ('R') in the x-y plane (R = 1–10), and different size thresholds ('ST') for shrub objects in each slice (ST = 1–500). Relationship derived by Grant & Nickling (1998) is shown as a dotted black line (grey lines show 95% confidence bounds); (b) relationships between volumetric and optical porosity derived from data points shown in (a). Coefficients of determination (R^2) for each relationship are also shown.

3.3.6. Vegetation transects

Manual vegetation transects were conducted at the longer-term stations (L1 and L2) to quantify vegetation cover and patterning. Eight vegetation transects were carried out at both locations, radiating outwards for 25 m from a common central point at the anemometry mast, oriented along the eight main (inter-) cardinal axes. A tape measure was used to define the transect line, and for every change in vegetation type (bare ground included), the transect distance, the height and length of the vegetation element, and the porosity (estimated by eye in relative terms - i.e. low, medium, high) of the element were recorded.

To complement the manual transects, aerial imagery was captured using an unmanned aerial vehicle (UAV, *DJI Phantom 2* equipped with a 12.1 Megapixel GoPro camera), to provide meso-scale (> 100 m) analysis of the vegetated landscape at each field location (see section 3.2 and section 5.2.2). Plant densities were calculated by defining a 100 x 100 m area centred around each long-term station, flying the UAV to ~100 m height, taking several photographs and subsequently counting the number of individual plants within the defined area. This was cross-referenced to oblique photographs taken at ground level.

3.4. Experimental setup

3.4.1. Short-term experiments

Of the 9 short-term experiments carried out behind individual vegetation elements (i.e. excluding the patch experiment, $Pa_{sonic}1$ – see Methods in Chapter 6 for the experimental setup in this case), 6 used cup anemometry and 3 used sonic anemometry. Except for a difference in the type and number of anemometers deployed, the format for both experiment types was the same. In both cases, the cup

or sonic anemometers were deployed around each study element to collect wind velocity data in a number of different 'setups' (see Figure 3.14 and Table 3.3) designed to cover as many of the important zones of disturbed wind flow as possible (Judd et al., 1996). Each setup was named sequentially and in alphabetical terms (i.e. A, B, C, …). For the cup anemometer experiments, eight different 'mobile' anemometers fixed to thin steel masts were deployed simultaneously during each setup. For the sonic anemometer experiments, one mobile anemometer was deployed during each setup, with the anemometer arms aligned parallel with the prevailing wind direction and level in the horizontal plane.

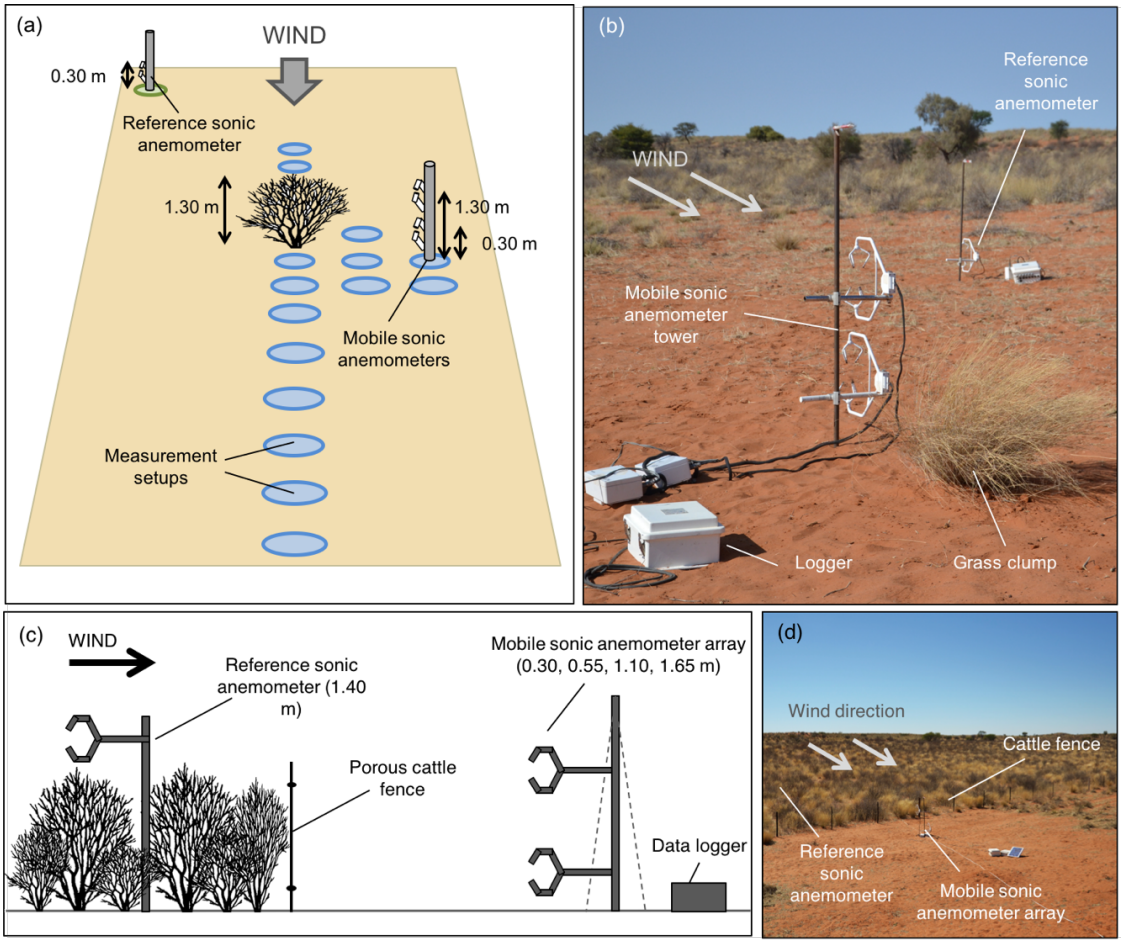


Figure 3.14 (a) Schematic diagram of an example experiment setup designed to cover zones of interest around individual vegetation elements; (b) annotated photograph of a setup in the field; (c) schematic diagram of the experiment setup for the patch of $Pa_{sonic}1$; (d) annotated photograph of the patch setup in the field.

In most cases, the mobile anemometers were mounted at 0.30 m height, which corresponds to a balance between capturing wind characteristics that occur close to the surface, whilst minimising the interference of saltating sand with the sonic measurement path (Weaver & Wiggs, 2011). For some experiments, wind flow was measured at additional heights, to provide a more detailed structure of the airflow (see Table 3.3). For both experiment types, an extra sonic anemometer was mounted at 0.30 m height and placed at a fixed location 20 h upwind and 15 h to the side of the experimental plots in a non-distorted environment (i.e. with a significant fetch over a flat, bare surface). This provided a mean upwind reference wind velocity ($\overline{U}$) for each setup against which mobile anemometry data could be normalised, as well as wind direction data. Normalisation is indicated using the '*norm*' subscript.

The mobile anemometer(s) were moved within a grid formation upwind, downwind and to the sides of each element (as represented by the blue discs in Figure 3.14a), oriented in the direction of the wind. Each grid was divided into several measurement setups (named A, B, C, …), during which the mobile anemometer(s) and reference anemometer simultaneously recorded wind velocity. To ensure sufficient data were acquired for subsequent analysis, each setup was run for a minimum of 20 minutes. The alignment of the experimental plot relative to the wind was altered after every instrumental setup to reflect any minor wind directional changes, and any misaligned data were removed in subsequent analysis (see section 4.3.2).

Throughout this study, annotation for measurement locations is given as h_d (downwind distance from the centre of the element) and h_L (lateral distance from the centre of the element) in terms of the height of the element. Wind flow was measured from -2 h_d (i.e. upwind) to 15–20 h_d depending on the element, and up to 3 h_L. Lateral wind flow was only measured on one side of each element, as wind dynamics are roughly symmetrical about the centreline of the wake (Leenders et al., 2007).

Veg. type	Exp. n°	Anem. type	N° of anems.	Mobile anem. height (m)	Ref. anem. height (m)	N° of setups
Grass	$Gr_{cup}1$	Cup	8	0.30	0.30	4
	$Gr_{cup}2$	Cup	8	0.30	0.30	3
	$Gr_{sonic}1$	Sonic	2	0.30, 0.75	0.30	13
Shrub	$Sh_{cup}1$	Cup	8	0.30	0.30	10
	$Sh_{cup}2$	Cup	6	0.30	0.30	5
	$Sh_{cup}3$	Cup	6	0.30	0.30	4
	$Sh_{cup}4$	Cup	6	0.30	0.30	4
	$Sh_{sonic}1$	Sonic	2	0.30, 1.30	0.30	15
Tree	$Tr_{sonic}1$	Sonic	2	0.30, 1.50	0.30	11
Patch	$Pa_{sonic}1$	Sonic	2	0.30, 0.55, 1.50, 1.65	1.40	6

Table 3.3 Summary table of anemometer configurations and heights for short-term experiments. Each experiment was composed of a various number of setups, ranging from 3 to 15. These were named in consecutive alphabetical order (i.e. A, B, C, …).

Whilst plant height and porosity could to some extent be constrained through the choice of elements, plant pliability and the range of observed wind velocities were difficult to control for in the field. Plant pliability can affect the aerodynamic behaviour of individual plants, by altering their form to become more streamlined in high winds (Gillies et al., 2000; Burri et al., 2011; Walter et al., 2012a). This phenomenon may therefore partly affect the experimental results, particularly in the case of pliable stems such as grasses. There is evidence from wind tunnel (Hagen & Skidmore, 1971; Wu et al., 2015) and modelling experiments (Hesp & Smyth, 2017) that wind velocity affects the sheltering effect of three-dimensional plants, and therefore the sediment transport dynamics in their lee. However, since the non-uniform turbulent flows measured in these experiments have high Reynolds numbers, it can be assumed that wind velocity has a negligible impact on wake structures (Lim et al., 2007).

It should be noted that no sediment transport data were collected during the short-term experiments, due to logistical issues of deploying equipment at various field

sites. It is therefore difficult to make direct conclusive statements about sediment transport from our wind velocity and turbulence data. Since wind flow in the immediate lee of individual plants or patches does not exist as a well-developed equilibrium boundary layer, it is theoretically impossible to infer sediment transport potential in this zone (Schlichting, 1955). It has been argued that only the shear stress measured directly at the surface (e.g. using Irwin sensors) can provide information on erosion potential in non-equilibrium conditions (Walter et al., 2012a). Nevertheless, statistics such as the shelter parameter (see Chapter 5), which is derived from a combination of wind velocity and turbulence parameters, can provide some indication of sediment transport potential around plants.

3.4.2. Longer-term experiments

Two longer-term measurement stations, L1 and L2, were deployed in order to obtain synchronised time series of wind velocity and sediment transport data over a period of several weeks. Station L1 was erected for 28 days (17th August to 14th September 2014) in the southwestern Kalahari, and station L2 was erected for 18 days (16th September to 4th October 2014) in the southern Namib.

Each site consisted of two instrument arrays, spaced roughly three metres apart (Figure 3.15). One array was an anemometry tower composed of three cup anemometers at 0.30 m, 1.00 m and 2.70 m height, and a wind vane at 2.50 m height. The second array was a sediment trap mast composed of two *Big Spring Number Eight (BSNE)* sand traps (section 3.3.3) at 0.30 m and 1.00 m height. In addition, a high-frequency *Sensit* grain impact sensor was deployed roughly 2 m away from the anemometry tower, and buried such that its piezoelectric sensor ring was 0.05 m above the sand surface. The distance between the towers and the *Sensit*

ensured that the wind speed and transport histories would be comparable across datasets while minimising flow disruption (cf. Wiggs et al., 2004a).

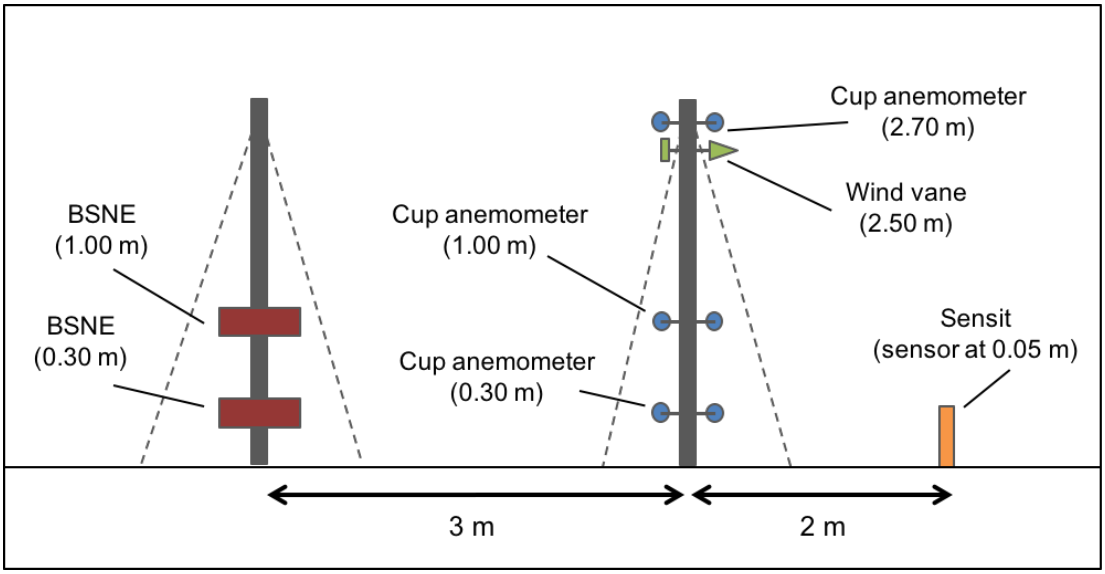


Figure 3.15 Schematic representation of the experimental setup at L1 and L2.

The cup anemometers and wind vane recorded 10-second averaged wind velocity for the entire duration of each longer-term study and dumped the data to a *CR1000* datalogger. Occasional short (< 1 hour) periods when data were being manually downloaded were removed from the datasets. The *Sensit* impact responder was programmed to switch on and remain on for three minutes once the wind speed detected by the highest cup anemometer exceeded 5.0 m s^{-1}. This value represents a realistic potential wind speed threshold for sediment entrainment (cf. 5.6–6.0 m s^{-1} measured in the Kalahari by Bullard, 1994, in Knight et al., 2004). Such a threshold allowed sand transport to be detected when it was likely to occur, yet minimised battery drainage in the field. The *BSNE* sand traps were checked regularly (approximately every three weeks) and their contents emptied and measured.

Site L1 was located on a farmer's field set amongst a series of wide linear dunes that were orientated North-South (Figure 3.16a). The instrument arrays were erected in the centre of an elevated, flat interdune section, which had been grazed heavily by sheep until two days prior to the experiment. The dominant wind direction for the plot was from N/NW, although there was significant directional variability over the study period. The central strip where the instruments were located had relatively low vegetation cover compared to the areas east and west of it (Table 3.4), where there was a dense coverage of shrubs and grasses (delimited by a fence, which had little to no aerodynamic impact, to the east). The main vegetation species present were Kalahari dune grass (*Stipagrostis amabilis*), Driedoring tree-thorned bushes (*Rhigozum trichotomum*) and Camel Thorn trees (*Acacia erioloba*).

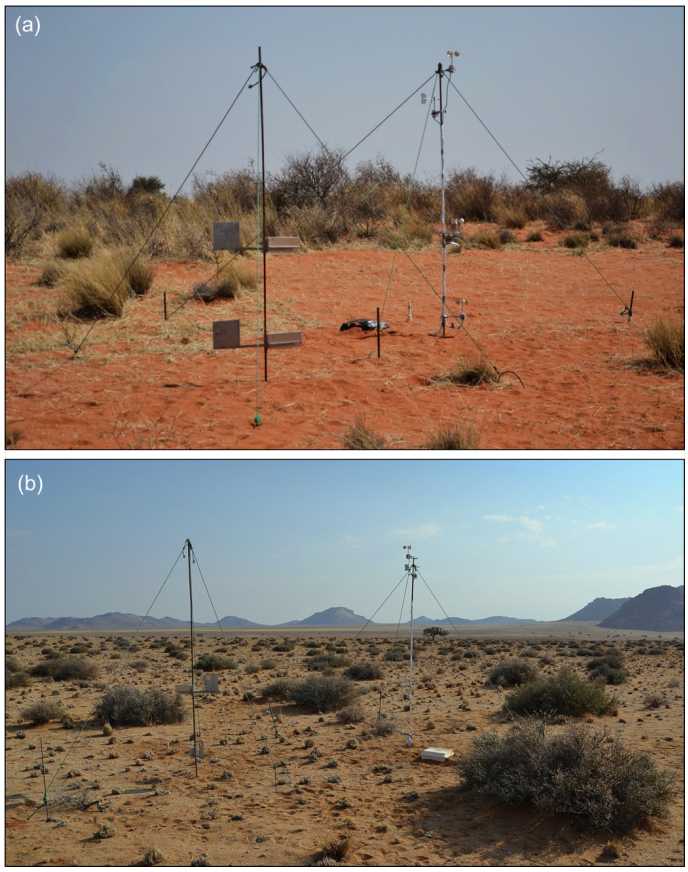


Figure 3.16 (a) The longer-term instrument array at L1, southwestern Kalahari, showing the BSNE sand traps on the left tower and the cup anemometer array on the right tower. Photograph is facing west; (b) the longer-term instrument array at L2, southern Namib, showing the BSNE sand traps on the left tower and the cup anemometer array on the right tower. Photograph is facing northeast.

The location of site L2 was chosen to provide a contrasting patterned environment to L1 (Figure 3.16b). Although some natural grazing did occur in the area around L2 and some animal tracks and dung were observed, it was generally in a zone of low human and animal interference. The anemometry and sand trap towers were set up in a large area of regularly distributed large shrubs and small grass clumps (Table 3.4) ~2 km to the west and north of a curved mountain ridge.

Site	Zones	Vegetation type	Element density
L1	Central strip (instrument location)	Grass	15 %
		Shrubs (< 0.3 m)	6000 km^{-2}
		Shrubs (> 0.3 m)	3000 km^{-2}
		Trees	1 km^{-2}
	East of instruments	Grass	45%
		Shrubs (< 0.3 m)	3500 km^{-2}
		Shrubs (> 0.3 m)	9000 km^{-2}
		Trees	100 km^{-2}
	West of instruments	Grass	40 %
		Shrubs (< 0.3 m)	7000 km^{-2}
		Shrubs (> 0.3 m)	8000 km^{-2}
		Trees	500 km^{-2}
L2	Around instruments	Grass	3 %
		Shrubs (< 0.5 m)	1500 km^{-2}
		Shrubs (> 0.5 m)	2000 km^{-2}
		Trees	60 km^{-2}

Table 3.4 Vegetation density distributions at longer-term sites L1 and L2, determined using UAV imagery. Element densities were estimated by extrapolating from the number of elements in a representative 100 m x 100 m area centred on the main anemometer mast.

Note that data from sites L1 and L2 were not used in much detail in the context of this thesis, except to confirm that the wind velocities measured during the short-term experiments were representative of the longer-term wind regime at those locations.

CHAPTER FOUR

Data Preparation

4. Data preparation

4.1. Introduction

The experimental methods described in Chapter 3 provided a variety of data, which are used in Chapters 5, 6 and 7 (Papers 1, 2 and 3, respectively). The raw short-term wind velocity datasets (cup and sonic anemometry) had to be cleaned, to remove data that were inappropriate for the papers (e.g. erroneous measurements, measurements that had not interacted with roughness elements correctly, etc.). This chapter outlines the procedures used to clean the various wind velocity datasets in this thesis. Appropriate sampling period lengths are determined, and protocols for dealing with wind directional changes and frame of reference rotations of sonic anemometer are discussed. A preliminary investigation is then presented that explores: (i) the appropriate time period over which to average wind flow parameters; (ii) the appropriate wind approach angle threshold with which to filter the datasets.

The data from experiment $Gr_{cup}2$ was chosen for the preliminary investigation because the wind was fairly constant in strength during its entirety but showed some directional variability. Wind flow was measured around a single *Stipagrostis amabilis* grass shrub (element height = 0.50 m) using three setups (A, B and C) of eight cup anemometers, all placed at 0.30 m from the ground surface, and set to record mean wind velocity every 10 s. The experiment was conducted in the Kalahari Desert on 14th September 2014, from 11.10 to 13.21. Figure 4.1 displays the reference mean wind velocity for the three individual experimental setups for $Gr_{cup}2$. Mean wind velocity decreased slightly and gradually across the experiment period, so that mean wind velocity was < 1 m s^{-1} lower on average at the end than at the beginning. This change is not deemed significant enough to have affected the levels of wind energy from one setup to the next.

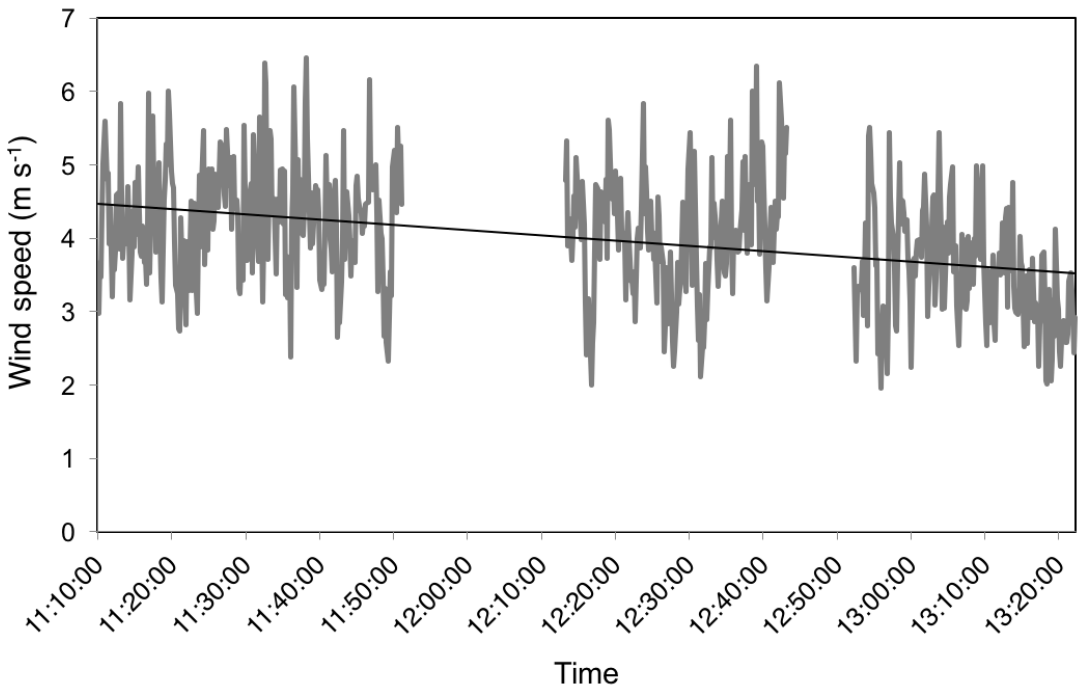


Figure 4.1 Wind velocity (10 s average) for the three experimental setups over the duration of $Gr_{cup}2$ as recorded by the reference sonic anemometer. Linear trend line shown.

4.2. Sampling periods

Previous work on turbulent wind flows has shown that sampling periods for velocity measurements must be long enough to contain most of the largest eddies, and thus be representative of the processes occurring in the boundary layer (e.g. van Boxel et al., 2004). Measurement periods that are too short risk excluding the low-frequency end of the spectrum that contributes to variations in wind velocity or uw covariance. The suitability of the sampling period depends on two factors, namely the height at which measurements are taken, and the wind velocity (see Figure 4.2; van Boxel et al., 2004; Walker, 2005). Low-frequency losses determine the required sampling period, whereas the high-frequency losses determine the sampling frequency (Chapman et al., 2012). The sediment bed suppresses large vortices that result from low-frequency variations in the wind spectrum, so the sampling period can be relatively short if the sensor is placed close to the surface. However, as the

instrument approaches the ground, high-frequency losses increase and the sampling frequency must be increased. At higher wind velocities, flow variations shift towards the high-frequency end of the spectrum, such that capturing the larger low-frequency vortices becomes less of a requirement (Wilczak et al., 2001; van Boxel et al., 2004).

Figure 4.2 shows that, for wind velocities of 2–6 m s^{-1} (realistic averages at all field sites in this study) and observation heights up to 1 m (the highest mobile anemometer in this study was at 0.40 m), a convenient minimum sampling or averaging period is on the order of 4–10 minutes. Accordingly, each setup was left to run for at least 20 minutes, which allowed for small periods within that to be removed in case the wind direction was not within the appropriate range (see sections 4.3 and 4.5.2).

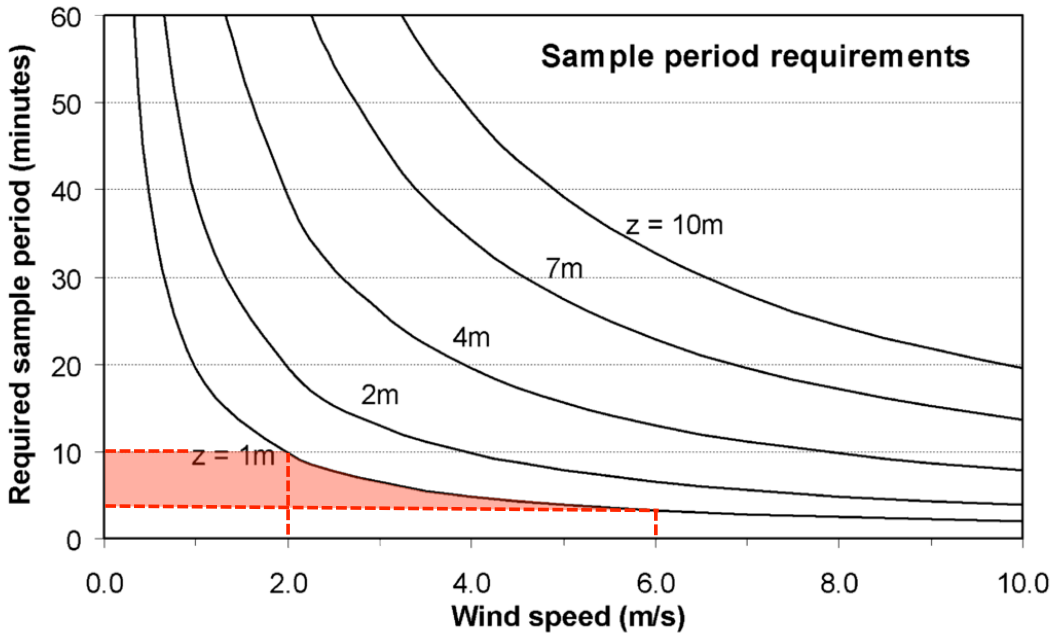


Figure 4.2 Required sampling period for velocity measurements as a function of wind velocity for different observation heights, for the 5% low-frequency cut-off point in the uw covariance. Red shaded area represents the range of required sampling periods given the range in mean wind velocities during all short-term experimental setups (adapted from van Boxel et al., 2004, p.136).

4.3. Wind data corrections

4.3.1. Wind direction

The signal between the heads of a sonic anemometer can be disrupted by saltating sand grains, which may affect the accuracy of some measurements. This is especially the case under constant saltation conditions or when the instruments are positioned close to the ground surface (van Boxel et al., 2004; Walker, 2005). The wind velocity data were checked before the analysis stage to highlight any saltation-induced errors, usually manifested as a 'no data' value of -6999 in the time series (Weaver, 2008). No such cells were identified. In a few cases, one of the loggers would skip a timestep due to a drifting in its time-keeping mechanism. This was solved by removing the missing time period from the associated dataset from the other logger, and all loggers were reset at the start of each experiment and day to minimise the occurrence of problems related to logger slowdown and saturation.

For all short-term experiments, a sonic anemometer was used to determine the reference wind velocity and direction upwind of the study element. As well as serving to normalise the data from the mobile anemometers, this allowed for the filtering out of periods when the instrument setup was misaligned with the main wind direction (and thus when the instruments were no longer measuring wind flow directly downwind, upwind or to the side of the element). Such 'invalid' periods could arise from a manual sensor misalignment or as a result of the complex nature of boundary layer flows (e.g. Walker & Nickling, 2003; Baddock et al., 2007; Weaver & Wiggs, 2011). Instead of maintaining the experimental plot fixed in a single direction (as performed by Leenders et al., 2007), in this study the alignment of the experimental plot relative to the wind was altered after every instrumental setup to reflect wind directional changes (if any). This meant moving the mobile anemometers rather than the plant, such that the central axis of the experimental plot was always aligned

parallel to the wind direction during the setup. Any minor misalignments of the data (which arise due to natural variability in wind gusts) were removed afterwards, using frame-of-reference rotation (see section 4.3.2).

4.3.2. Frame of reference rotation

For turbulent parameters to be correctly calculated from sonic anemometry data, the u, v and w components need to be oriented in the correct fashion. However, manual sensor misalignment and/or changing wind directions can sometimes result in sonic anemometers being tilted slightly away from the prevailing wind direction over a given timescale (Walker & Nickling, 2003; Baddock et al., 2007; Weaver & Wiggs, 2011). Without any correction for this effect, a particular fraction of a component would be interpreted as a fluctuation in the direction of another component, which can have important implications for the determination of turbulent flow parameters and Reynolds shear stress (Chapman et al., 2012). Following many other similar studies, specific rotation of the sonic anemometers' frames of reference was applied post-measurement, but prior to data analysis.

The most commonly applied technique for correction involves a series of three rotations applied at the end of each turbulent averaging period (Wilczak et al., 2001): yaw rotation, which removes misalignment in the u-v plane (such that streamwise velocity becomes the resultant vector in the horizontal plane); pitch rotation, which removes misalignment in the u - w plane; and roll rotation, which removes misalignment in the v-w plane (Figure 4.3).

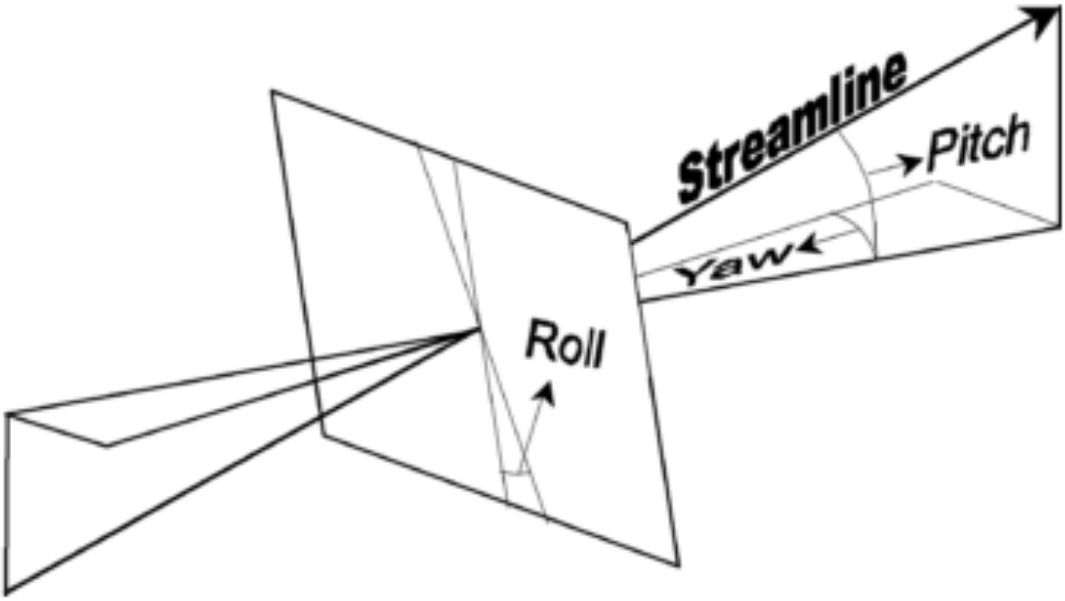


Figure 4.3 Schematic diagram of the three rotations most commonly applied for orienting the frame of reference of sonic anemometers (from van Boxel et al., 2004, p.139).

In all experiments presented in this study, the sonic anemometer arms were aligned parallel with the prevailing wind direction and level in the horizontal plane (as determined by a level bubble). The streamwise frame of reference was rotated in accordance with the local streamline angle using yaw rotation (see Walker, 2005; Weaver & Wiggs, 2011), described by:

$$u_2 = u_1 cos\theta + v_1 sin\theta \tag{4.1}$$

$$v_2 = -u_1 sin\theta + v_1 cos\theta \tag{4.2}$$

$$w_2 = w_1 \qquad \text{with} \qquad \theta = \arctan\left(\frac{\overline{v_1}}{\overline{u_1}}\right) \tag{4.3}$$

where u_1, v_1 and w_1 are the measured components of wind velocity and u_2, v_2 and w_2 are the components after rotation. The overlines denote time averages. This rotation effectively corrects the average spanwise velocity to zero ($\overline{V}$ = 0).

Whilst yaw correction is often performed to correct sonic anemometry data, the application of pitch and roll rotation in the field of geomorphology is more ambiguous (e.g. Kaimal & Finnigan, 1994; Roy et al., 1996; Wilczak et al., 2001; van Boxel et al., 2004; Walker, 2005; Weaver & Wiggs, 2011; Chapman et al., 2012; Lee & Baas, 2012). Uncertainties exist in the application of pitch rotation, because it removes implicit and potentially significant vertical velocity variations (Walker, 2005), which are important in identifying coherent turbulence events in the flow (Lu & Willmarth, 1973). If the vertical velocity component is unnecessarily altered using pitch rotation, values for instantaneous kinematic and time-averaged Reynolds stress estimates, as well as relevant quadrant analysis, may be adversely affected (Walker, 2005). Since the purpose of the short-term experiments was to characterise the behaviour of wind flow horizontal to the surface, rather than along the plane of the streamlines, pitch rotation (which forces the average vertical velocity to zero, $\overline{W}$ = 0) was omitted here.

The application of roll rotation remains disputed practice for three-dimensional flow over non-uniform terrain (Kaimal & Finnigan, 1994; Lee & Baas, 2012), but the need for such a rotation is obviated by accounting for the spanwise flow component when calculating the resultant horizontal shear stress (see Equation 4.4).

4.4. Reynolds stress calculations

Following frame-of-reference rotation, the remaining velocity data were decomposed into their average ($\overline{U}, \overline{V}$ and $\overline{W}$) and fluctuating (u', v' and w') components, from which the horizontal ($\overline{u'^2}$) and vertical ($\overline{w'^2}$) components of Reynolds stress were

derived. The Reynolds shear stress ($-\overline{u'w'}$) was calculated using the time-averaged covariance of the instantaneous horizontal and vertical turbulent components. The resultant horizontal shear stress (τ_r), which is a more robust estimate of the total shearing force acting on the surface than the traditionally-employed Reynolds shear stress, was also calculated in Chapter 6, using both the streamwise and spanwise shear (Lee & Baas, 2012):

$$\tau_r = (\overline{u'w'}^2 + \overline{v'w'}^2)^{1/2} \tag{4.4}$$

The local near-surface wind streamline angles (θ) along the wake transects were calculated as:

$$\theta = \arctan\left(\frac{\overline{W}}{\overline{U}}\right) \tag{4.5}$$

From these parameters, the incidence of coherent structures in the flow around the grass, shrub and tree elements was established using conditional-sampling quadrant analysis (Lu & Willmarth, 1973). This technique defines four discrete categories of momentum exchange based on the relative signs of u' and w' (Figure 4.4). Ejections (Q2 events; $u' < 0$, $w' > 0$) and sweeps (Q4; $u' > 0$, $w' < 0$) contribute positively to the production of Reynolds stress, while outward interactions (Q1; u'>0, $w' > 0$) and inward interactions (Q3; $u' < 0$, $w' < 0$) contribute negatively to Reynolds stress (Smith, 1996). In order to isolate significant bursts of turbulent stress from weaker background variability (Lapointe, 1992; Clifford & French, 1993), stress events of low magnitude were removed from quadrant analysis using a threshold criterion (*H*). Following previous studies (Bauer et al., 1998; Sterk et al., 1998; Leenders et al., 2005; Weaver, 2008; Wiggs & Weaver, 2012), the size of *H* was chosen to be

equivalent to one standard deviation (σ) of the Reynolds shear stress ($-\overline{u'w'}$), such that a flow structure was only classified if $-u'w' > \pm H.(-\overline{u'w'})$.

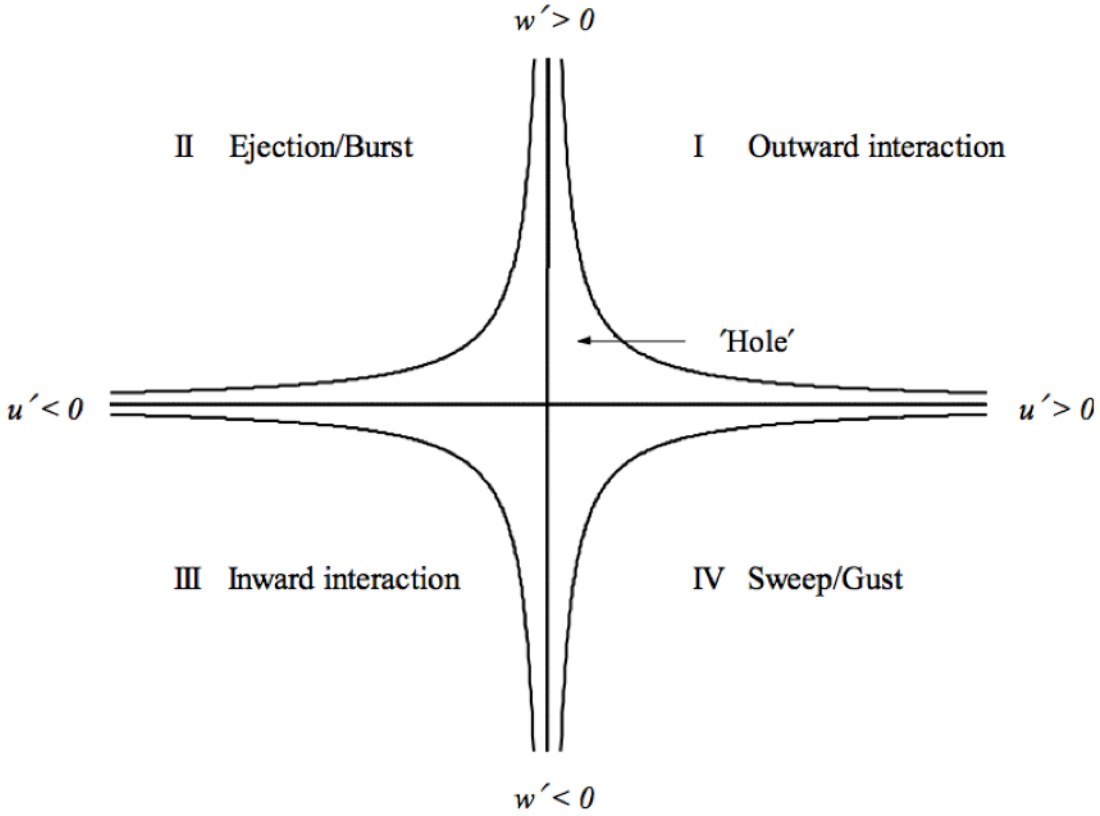


Figure 4.4 Quadrant plot of four discrete momentum exchange structures, based on the turbulent velocity fluctuations in the horizontal (u') and vertical (v') directions (from Leenders, 2006, p.38).

4.5. Testing data reduction methods

4.5.1. Measures of central tendency

Most aeolian studies concerned with average wind velocities use the mean as the measure of central tendency. The mean directly takes account of extremes in erosivity, but it assumes normality within the dataset. The Shapiro-Wilk Expanded Test was performed to test for normality in the dataset of each anemometer location in experiment $Gr_{cup}2$, filtered using a 5^{o} wind approach angle threshold (see section 4.5.2). The results of the normality test at the 95% level, as well as skewness values,

are presented in Table 4.1. In most cases, the wind velocity data were distributed in a close-to-normal fashion. Non-normal velocity distributions were observed in locations close to the shrub; the deviation from normality here may be a result of turbulent processes.

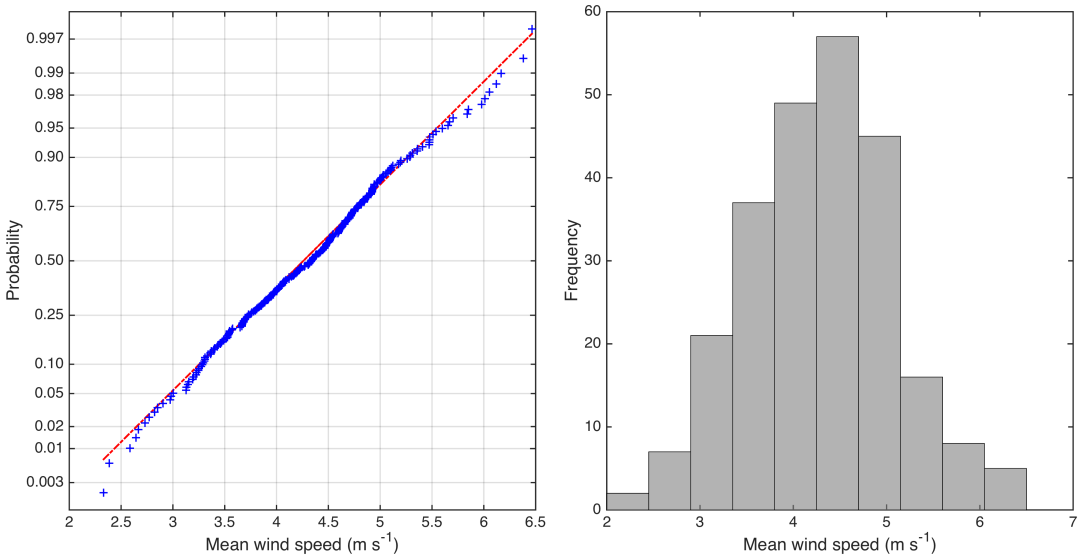


Figure 4.5 Normal probability plot and frequency histogram for 10-second averaged wind velocity data from the reference anemometer in $Gr_{cup}2$. Dotted red line shows the theoretical normal probability line.

Figure 4.5 shows the frequency histogram for 10-second averaged wind velocities measured by the reference anemometer in $Gr_{cup}2$. The plots indicate that the data also followed a normal distribution. Given the general normality identified here, the mean can be considered a valid measure of central tendency in this study, and is therefore used in subsequent analysis.

Downwind *h*	Lateral *h*	*W* statistic	*p* value	*W* test result	Skewness
-2	0	0.9927	0.8898	accept	-0.1010
-1	0	0.9932	0.9195	accept	-0.0369
1	0	0.9850	0.3600	accept	0.1537
2	0	0.9273	<0.0001	reject	1.1984
3	0	0.9687	0.0234	reject	0.7513
4	0	0.9743	0.0604	accept	0.3987
5	0	0.9841	0.5678	accept	0.2606
6	0	0.9907	0.7603	accept	0.1855
7	0	0.9753	0.2190	accept	0.2230
8	0	0.9869	0.4757	accept	0.2833
10	0	0.9879	0.7793	accept	0.0545
12	0	0.9862	0.6860	accept	0.0662
14	0	0.9876	0.7645	accept	-0.0081
16	0	0.9863	0.6904	accept	-0.1087
18	0	0.9861	0.6815	accept	-0.0389
0	2	0.9449	0.0212	reject	0.2930
0	1	0.9657	0.1547	accept	0.5237
1	0	0.9470	0.0257	reject	0.8422
1	2	0.9871	0.8556	accept	0.1511
1	1	0.9840	0.7283	accept	-0.0096
2	2	0.9907	0.9624	accept	0.1251
2	1	0.9865	0.8355	accept	0.1602
3	1	0.9728	0.2986	accept	0.3140

Table 4.1 Results of the Shapiro-WIlk Expanded Test (at the 95% level) for normality in all wind velocity datasets for $Gr_{cup}2$. Grey cells highlight cases where the null hypothesis (H_0) is rejected (i.e. where the data are not normally distributed).

4.5.2. Wind approach angle thresholds

Natural wind flows are characterised by directional variability. In this study, the anemometers were fixed in position during the entirety of each experimental setup, so it is necessary to define a threshold in wind direction deviation (as measured by the reference sonic anemometer), above which data are discounted from further analysis. This approach angle threshold must reach a balance between eliminating measurement intervals where the wind flow does not interact fully with the vegetation

element, and retaining enough measurement intervals such that the required sampling period (see Figure 4.2) is observed.

Figure 4.6 shows the zones from which measurements would be accepted under different directional threshold scenarios, when the experimental plot is oriented along the centreline of the prevailing wind direction. As downwind distance increases, the arc along which measurements may be accepted increases significantly with larger thresholds, to the extent that some distant anemometers may be measuring wind that is not interacting with the element in any way.

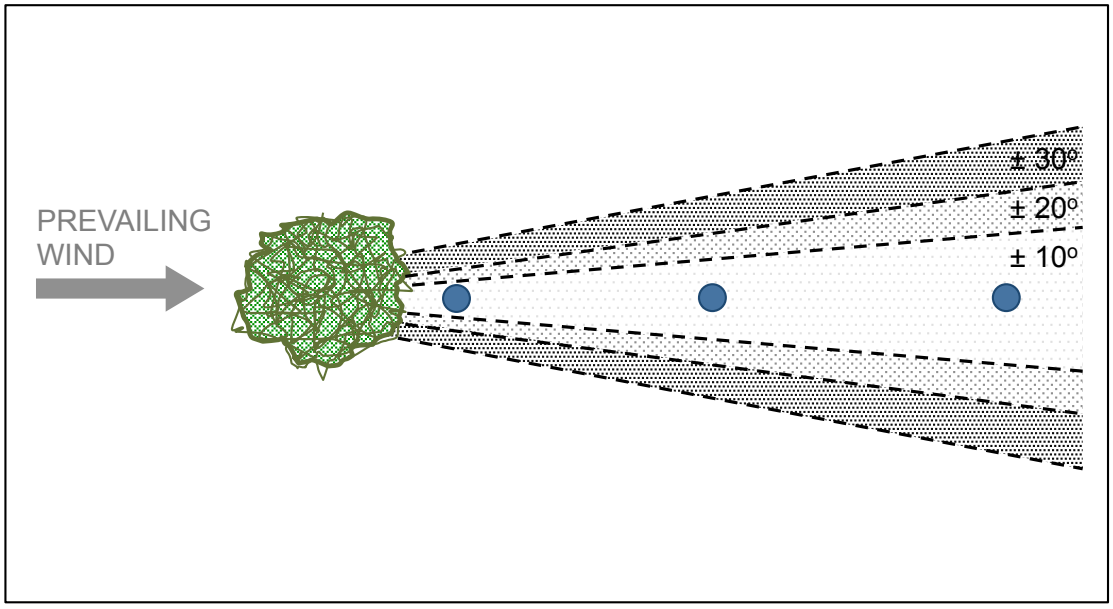


Figure 4.6 Schematic plan-view diagram demonstrating the zones of potential measurement relative to the centreline of the prevailing wind, at different directional thresholds. Anemometers oriented along the centreline of the prevailing wind direction are shown as blue circles. Diagram not to scale.

The $Gr_{cup}2$ dataset was filtered for five different thresholds relating to the upwind reference wind direction. Data were removed when wind approach angle was > ±30°, > ±20°, > ±15°, > ±10° and > ±5° from the central plot alignment. Wind velocities at each anemometer location were averaged over the remaining data for each threshold, and the standard deviation and coefficient of variation (commonly used as an indicator of turbulence intensity, e.g. Stull, 1988; Leenders et al., 2007) were also

calculated. These statistical measures were normalised with the average values of the corresponding time periods for the upwind reference anemometer, to produce normalised mean wind velocity (Φ), normalised standard deviation (σ_{norm}) and normalised turbulence intensity (TI_{norm}).

For any given wind approach angle, the likelihood of an anemometer measuring wind that has directly interacted with the element decreases with increasing distance downwind. Figure 4.7a shows this effect in schematic form, with the anemometer closest to the element 'seeing' a greater maximum angle of wind affected by the

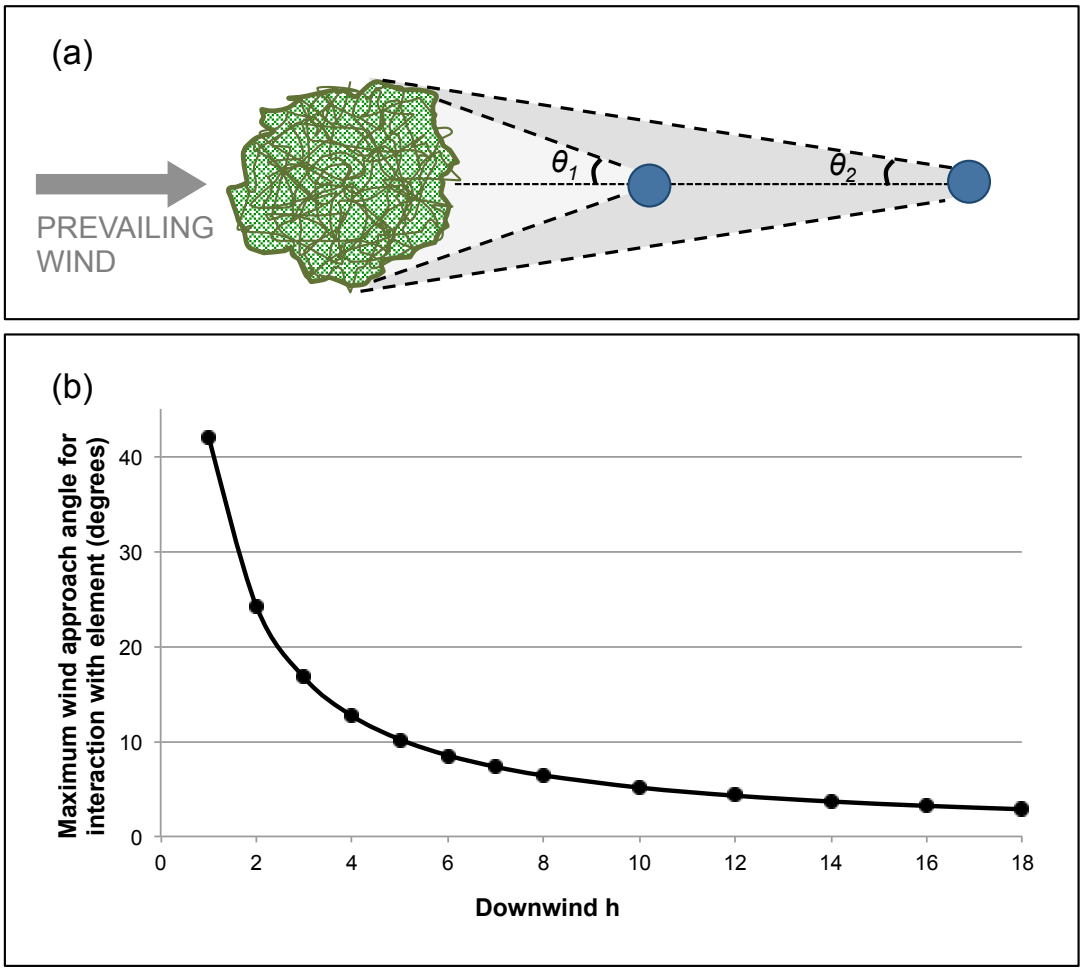


Figure 4.7 The effect of downwind distance on the maximum wind approach angle for detected wind to be interacting directly with the study element: (a) schematic plan-view representation of the maximum approach angle, *θ,* with shrub shown in green and anemometers shown in blue; (b) graph of maximum approach angle for the wind to still be interacting with the element, as a function of downwind distance (upwind points are not shown, as these are simply a mirror image of the curve shown here).

element (θ_1) than the anemometer located further downwind (θ_2). Figure 4.7b displays the maximum angle at each measurement location in experiment $Gr_{cup}2$. In theory, a wind approach angle threshold of 30° filters out non-affected wind up to ~2 h_d, a 20° threshold up to ~3 h_d, a 15° threshold up to ~4 h_d, a 10° threshold up to ~5 h_d, and a 5° threshold up to ~10 h_d. As wind approach angle increases for a given measurement location, it is also expected that the proportion of the measured wind flow going through a representative path length of the shrub should decrease.

Figure 4.8 displays the effect of decreasing the accepted wind approach angle threshold on the size of each dataset (in terms of total usable minutes), for all three setups in $Gr_{cup}2$. Disparities in usable minutes between setup A and setups B and C arose from the initially longer duration of setup A. For all setups, all wind angle thresholds from 5°–30° resulted in a long enough dataset for the largest turbulent eddies to be accounted for (see section 4.2). Although Setup C was composed of only eight usable minutes when filtered using the 5° approach threshold, this is

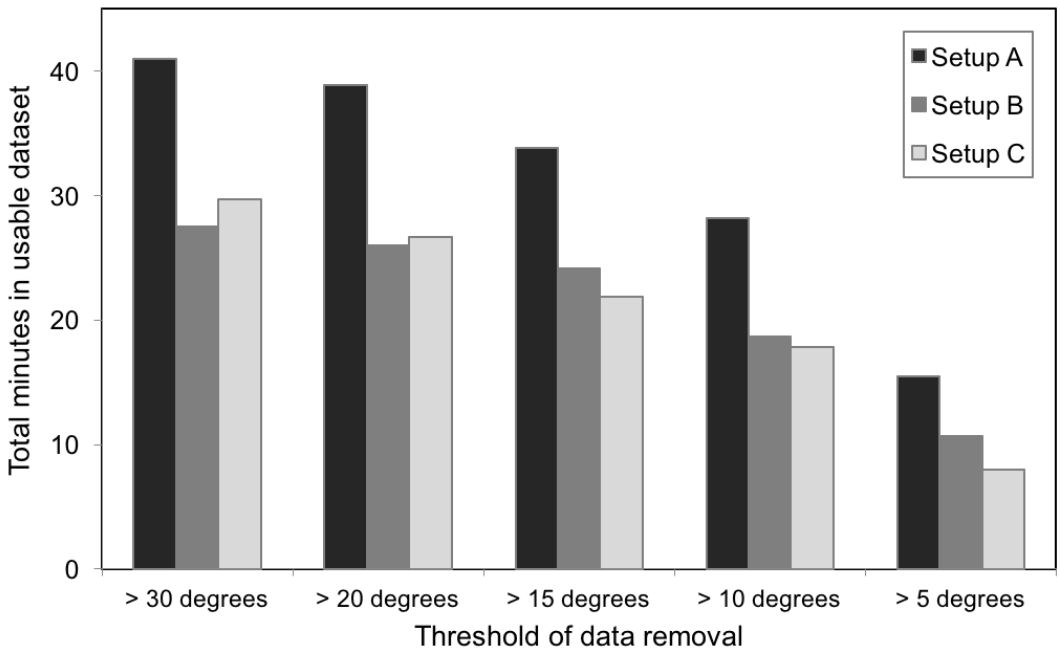


Figure 4.8 Total number of minutes in the usable datasets for each setup in experiment $Gr_{cup}2$, after the removal of data according to various wind angle thresholds.

greater than the minimum recommended by van Boxel et al. (2004), given the mean wind velocity (3.52 m s^{-1}) during this setup.

Figure 4.9 displays the changes in normalised mean wind velocity (Φ), normalised standard deviation (σ_{norm}) and normalised turbulence intensity (TI_{norm}) across the experimental profile, depending on threshold wind angle. Φ decreased from unity directly in front of the shrub to Φ ≈ 0.3 at 1 h_d, before exponentially increasing back to unity around 7–9 h_d (Figure 4.9a). Increasing the wind angle threshold tended to result in decreased normalised wind velocity at all measurement locations, because wider wind angles permit side winds that are not fully impacted by the entire body of the plant to be included in the calculation. The effect is particularly evident immediately downwind of the element, and tends to decrease further downwind.

σ_{norm} decreased from unity upwind to values of 0.5–0.8 immediately downwind of the shrub (Figure 4.9b). σ_{norm} then tended to exponentially increase to 1.1, excepting an increase at 2–4 h_d perhaps resulting from variable turbulent structures in this zone. Values of σ_{norm} above unity at 16–18 h_d may result from the shrub's 'wind shadow' becoming proportionally smaller compared to the arc of potential wind approaching the anemometer (see Figure 4.6). Lower wind angle thresholds resulted in lower σ_{norm} in the zone 0–8 h_d. Beyond 8 h_d, a smaller wind threshold led to greater σ_{norm}.

TI_{norm} peaked to a value of 2.0–2.5 around 2 h_d, before returning to unity by 5 h_d (Figure 4.9c). High turbulence is to be expected in the immediate lee of a plant (Leenders et al., 2007). Lower wind angle thresholds resulted in decreased TI_{norm} around 0–8 h_d, and increased TI_{norm} from 8 h_d to 18 h_d.

Figure 4.10 shows variations in the percent difference between the datasets filtered at 30°, 25°, 20° and 10°, and the dataset filtered at 5°. The largest discrepancies in Φ, σ_{norm} and TI_{norm} occurred in the immediate lee of the shrub (0–4 h_d). As wind angle

thresholds increased, the discrepancies also increased; the 30° and 20° thresholds produced Φ values > 15% greater than the 5° threshold in the zone 0–4 h_d (Figure 4.10a). From 4 h_d, all wind angle thresholds produced Φ within 5% of the 5° threshold values. The same general pattern was observed for standard deviations, with σ_{norm} being overestimated by 35–75% for wind thresholds of 20° and 30° in immediate lee (Figure 4.10b). From 5 h_d, σ_{norm} discrepancies were mostly reduced to ± 5% for all wind angle thresholds. TI_{norm} was overestimated in the immediate lee of the shrub by all wind thresholds compared to the 5° threshold, but further downwind TI_{norm} was underestimated by up to 10% using the 10° and 30° thresholds (Figure 4.10c).

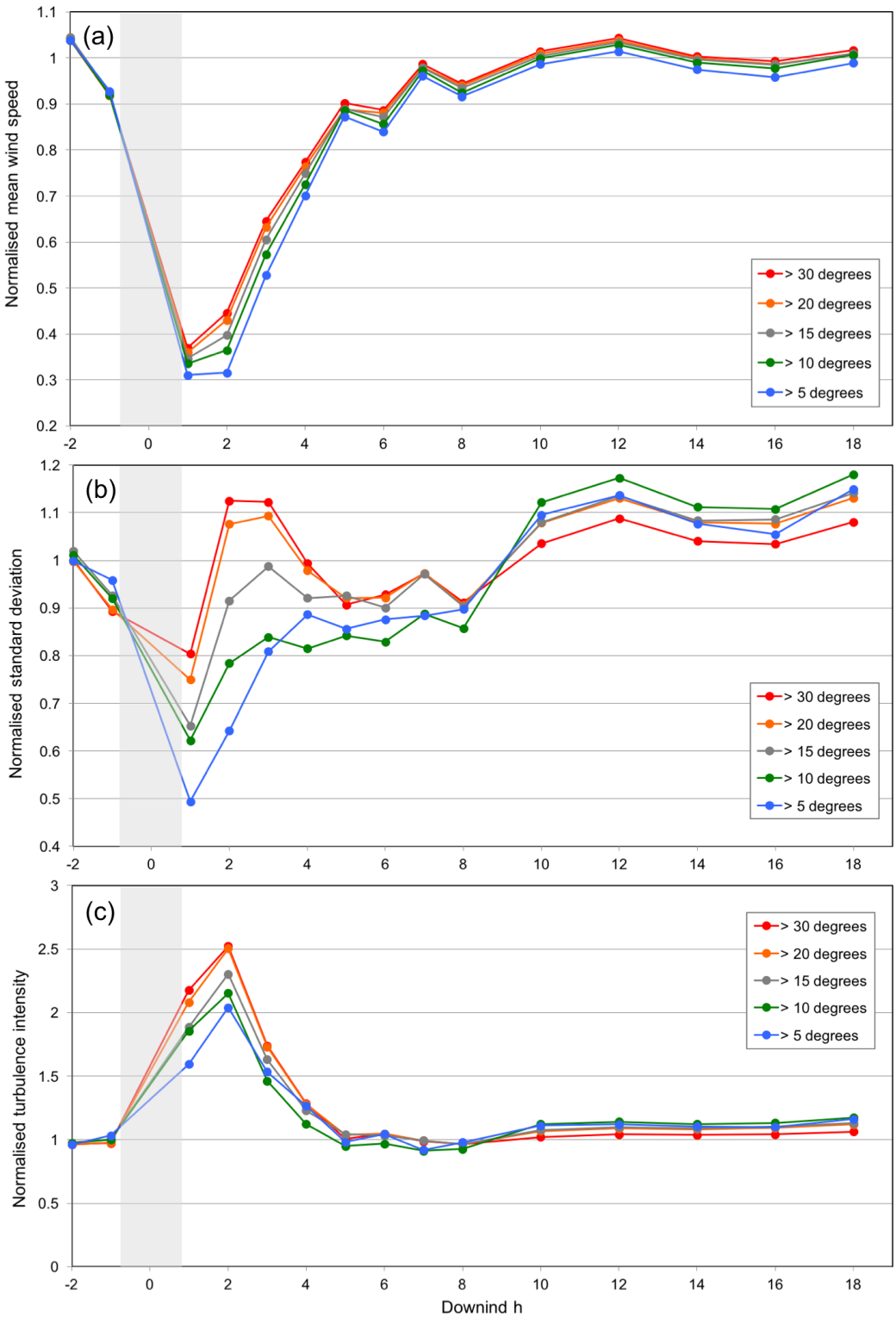


Figure 4.9 The effect of different wind direction thresholds on changes in: (a) normalised mean wind velocity; (b) normalised standard deviation; and (c) normalised turbulence intensity at 0.30 m height downwind of $Gr_{cup}2$. Lateral changes are not shown. Grey shading represents location of study element, where wind parameters are uncertain.

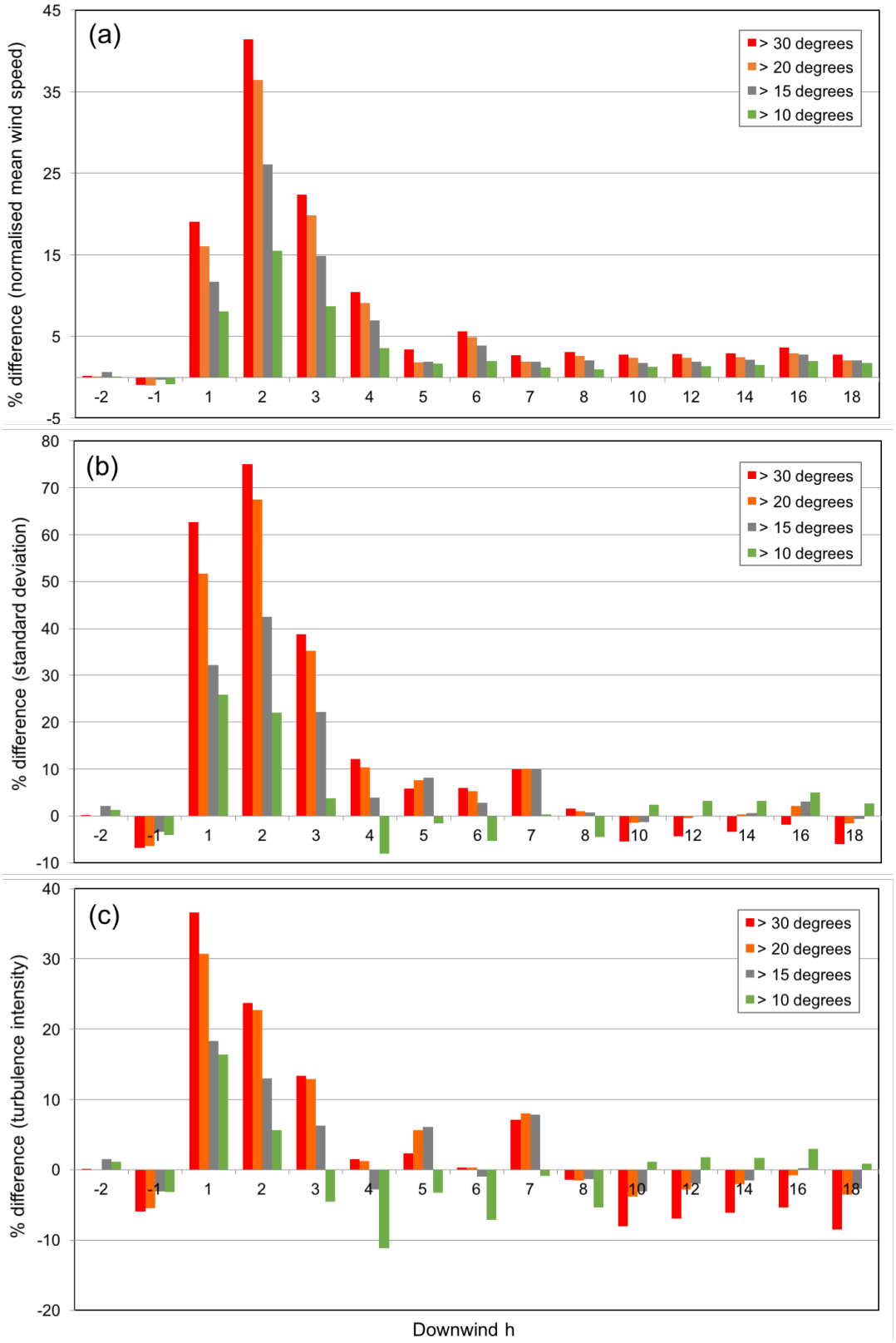


Figure 4.10 Percent difference in statistics of wind flow downwind of $Gr_{cup}2$ for different wind angle thresholds compared to the 5% wind angle threshold. Differences in (a) normalised mean wind velocity; (b) normalised standard deviation; and (c) normalised turbulence intensity.

Given that decreasing the wind angle threshold decreases the size of the usable dataset (Figure 4.8), Figure 4.11 displays the effect of decreased dataset sizes on the relative standard error (RSE) of the mean ($\left(\frac{(\frac{\sigma}{\sqrt{n}})}{\mu}\right)$ x 100). The RSE was calculated at four key locations upwind and downwind of the element, identified from preliminary analysis (-2 h_d, 2 h_d, 8 h_d and 18 h_d). The RSE increased as the approach angle threshold (and thus the sample size) decreased; at all locations, the 5° threshold produced the largest absolute standard error and RSE, at most by 1.44% compared to the 30° threshold (at 2 h_d). The largest RSEs were observed at 2 h_d (2.92–4.36%), and the smallest at -2 h_d (0.76–1.38%).

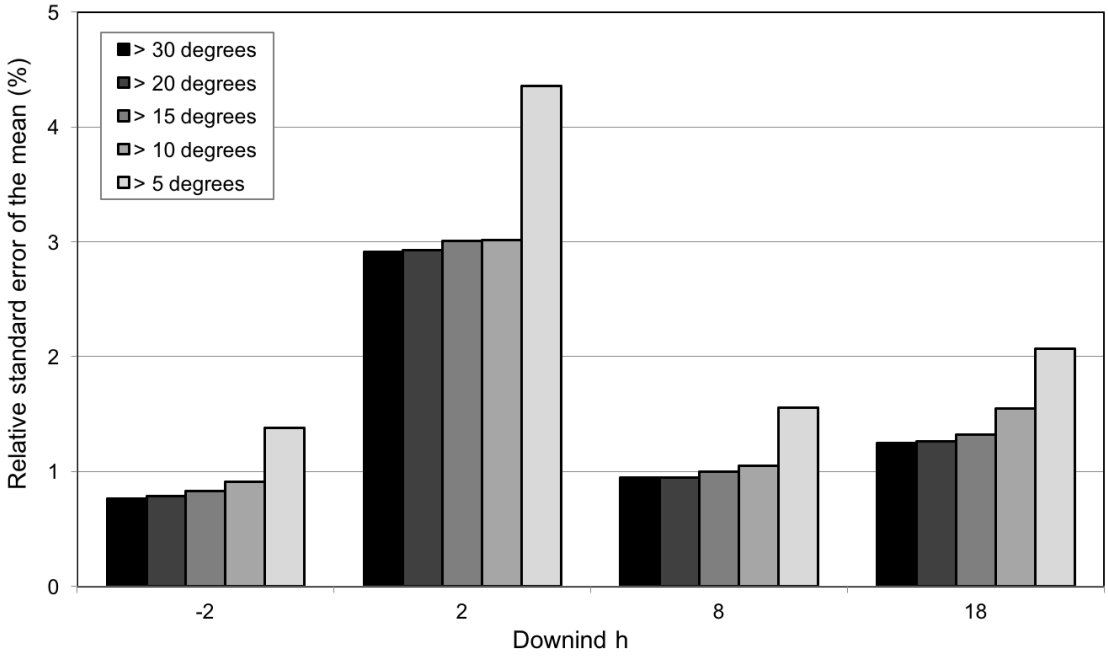


Figure 4.11 The effect of changing the wind angle threshold on the relative standard error (RSE) of normalised 10 s wind velocities at key locations upwind and downwind of $Gr_{cup}2$.

Table 4.2 displays the p-values for paired Student's t-tests of the mean wind velocity derived from each wind angle threshold compared to that derived from the 5° threshold, at the four key locations mentioned above. The null hypothesis (i.e. there is no difference between the means of datasets filtered using different angle

thresholds) was accepted in all cases for -2 h_d, 8 h_d and 18 h_d, at the 5% significance level. Generally, at these three locations, p-values increased with decreasing wind angle thresholds. At -2 h_d, $p > \sim 0.8$ (i.e. close similarity) for all thresholds. However, immediately downwind of the shrub at 2 h_d, $p < 0.05$ in all cases. The results of the t-tests are not affected when the potential instrument error of the anemometers (± 1%) is included in the calculations.

Wind angle threshold	Downwind distance (h_d) -2	2	8	18
> 30°	0.975	< 0.001	0.090	0.163
> 20°	0.957	< 0.001	0.155	0.362
> 15°	0.795	< 0.001	0.279	0.356
> 10°	0.942	0.012	0.633	0.488

Table 4.2 p-values derived from paired Student's t-tests between the wind velocity datasets for each wind approach angle threshold (10–30°) and that for the 5° threshold. Cells are coloured red if H_0 (i.e. no difference between the datasets) is rejected at the 5% significance level.

Ideally, each dataset in this study should comprise measurements taken when the approach angle of the wind was as close to the centreline of the experimental plot as possible. The 5° threshold represents the smallest deviation from the centreline, and in all situations examined here produced enough data to match the minimum requirements recommended by van Boxel et al. (2004) (Figure 4.8). Although the 5° threshold resulted in the smallest datasets, and thus the largest confidence intervals (Figure 4.11), the differences in RSE compared to the datasets derived from larger angle thresholds were relatively low in most cases. Moreover, whilst the association between the other thresholds and the 5° threshold was strong at some locations along the measurement transect (Table 4.2), mean normalised wind velocities in the immediate lee were somewhat dependent on the wind angle threshold. The 5°

threshold constitutes a good balance between including enough data to represent processes the turbulent boundary layer (i.e. minimum of 4 minutes of data, as determined in section 4.2), and producing wind flow parameters that closely resemble conditions at the correct positions around the study element. The 5^{o} threshold is therefore used to filter all subsequent short-term datasets.

4.5.3. Averaging periods

While high-frequency wind turbulence parameters have been shown to correlate well with sediment transport dynamics (e.g. Schönfeldt & von Löwis, 2003; van Boxel et al., 2004; Weaver & Wiggs, 2011; Wiggs & Weaver, 2012; Chapman et al., 2013), there is also evidence that increasing the averaging period of wind velocity measurements can suppress short-term system variability and thus offer a better correlation with sand transport (Namikas et al., 2003; Wiggs et al., 2004a). While sediment transport was not directly measured during the short-term experiments in this study, it is of interest to investigate the impact of different averaging periods on the normalised statistics for wind parameters. The original 10 s dataset for $Gr_{cup}2$ was averaged over different periods and re-filtered using a 5^{o} wind approach angle threshold. The averaging period was increased by increments of 10 s to a maximum of 60 s. Averaging beyond this limit for a 10–20 minute sample was deemed inappropriate, owing to the small sample size generated (Wiggs et al., 2004b).

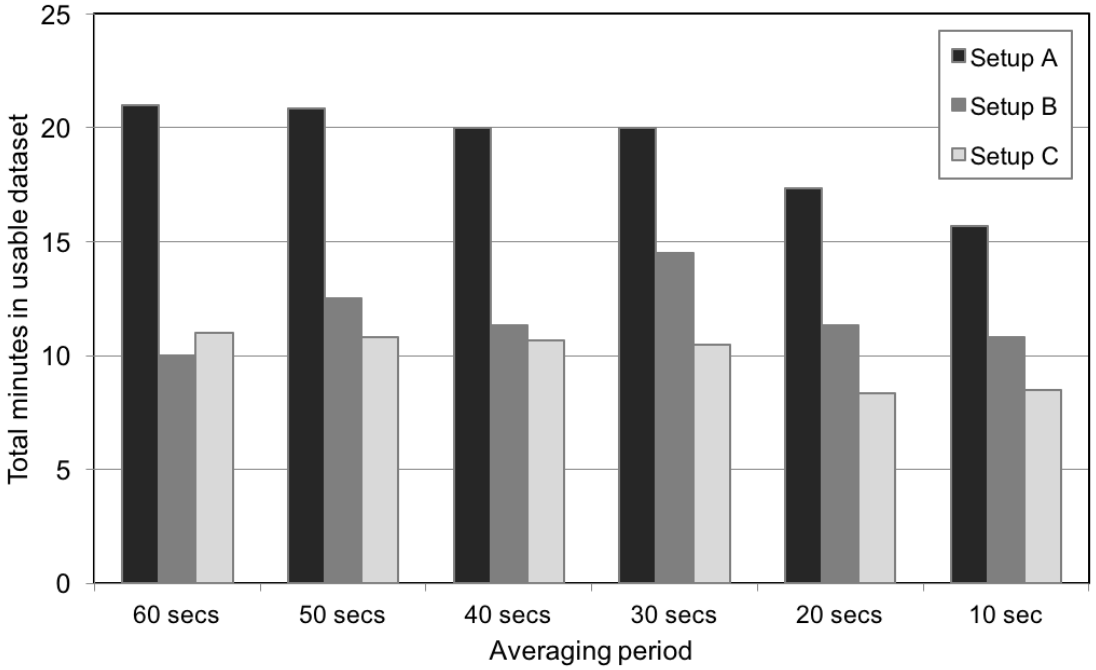


Figure 4.12 Total number of minutes in the usable datasets for each setup in experiment $Gr_{cup}2$, depending on the averaging period used to calculate the data.

Figure 4.12 displays the total number of minutes in the usable datasets when different averaging periods were used to calculate wind velocities and wind approach angles. As the averaging period decreased from 60 s to 10 s, the amount of usable data tended to decrease. This effect was particularly noticeable for Setups A and C, with a reduction of 25% and 23% respectively in usable minutes for the 10 s averaging period compared to the 60 s averaging period.

Figure 4.13 displays the changes in normalised mean wind velocity (Φ), normalised standard deviation (σ_{norm}) and normalised turbulence intensity (TI_{norm}) across the experimental profile, depending on the averaging period. Increasing the averaging period from 10 s to 60 s tends to result in greater Φ, especially in the immediate lee of the shrub (Figure 4.13a). Figure 4.14, which displays the percent difference between the statistics of the datasets averaged at 20–60 s and those of the dataset averaged at 10 s, supports this finding. The largest discrepancies were observed in

the immediate lee of the shrub, where differences reached +27% (Figure 4.14a). Downwind of this zone, differences decreased to < 10%.

Increasing the averaging period tended to result in a higher Φ in the immediate lee of the shrub, with decreases observed further downwind (Figure 4.13b). This was corroborated by discrepancies of up to ~70% between the datasets averaged at 10 s and those averaged over longer periods in the immediate lee, which decreased to < 10% after 7 h_d (Figure 4.14b). The differences in TI_{norm} were also greatest in the immediate lee (Figure 4.13c), and a 60 s averaging period underestimated TI_{norm} by ~30% compared to a 10 s averaging period around 5–7 h_d (Figure 4.14c).

It should be noted that the longer averaging windows presented in Figure 4.13 and Figure 4.14 may in some instances have included time periods where the approach wind angle was greater than 5^o (i.e. before the dataset was filtered). This could explain why the longest averaging windows produce recovery patterns in Figure 4.13 that are similar to those of the largest wind direction thresholds in Figure 4.9. It is therefore necessary to consider the impact of sampling windows on the 'acceptability' of data before a directional filtering is performed.

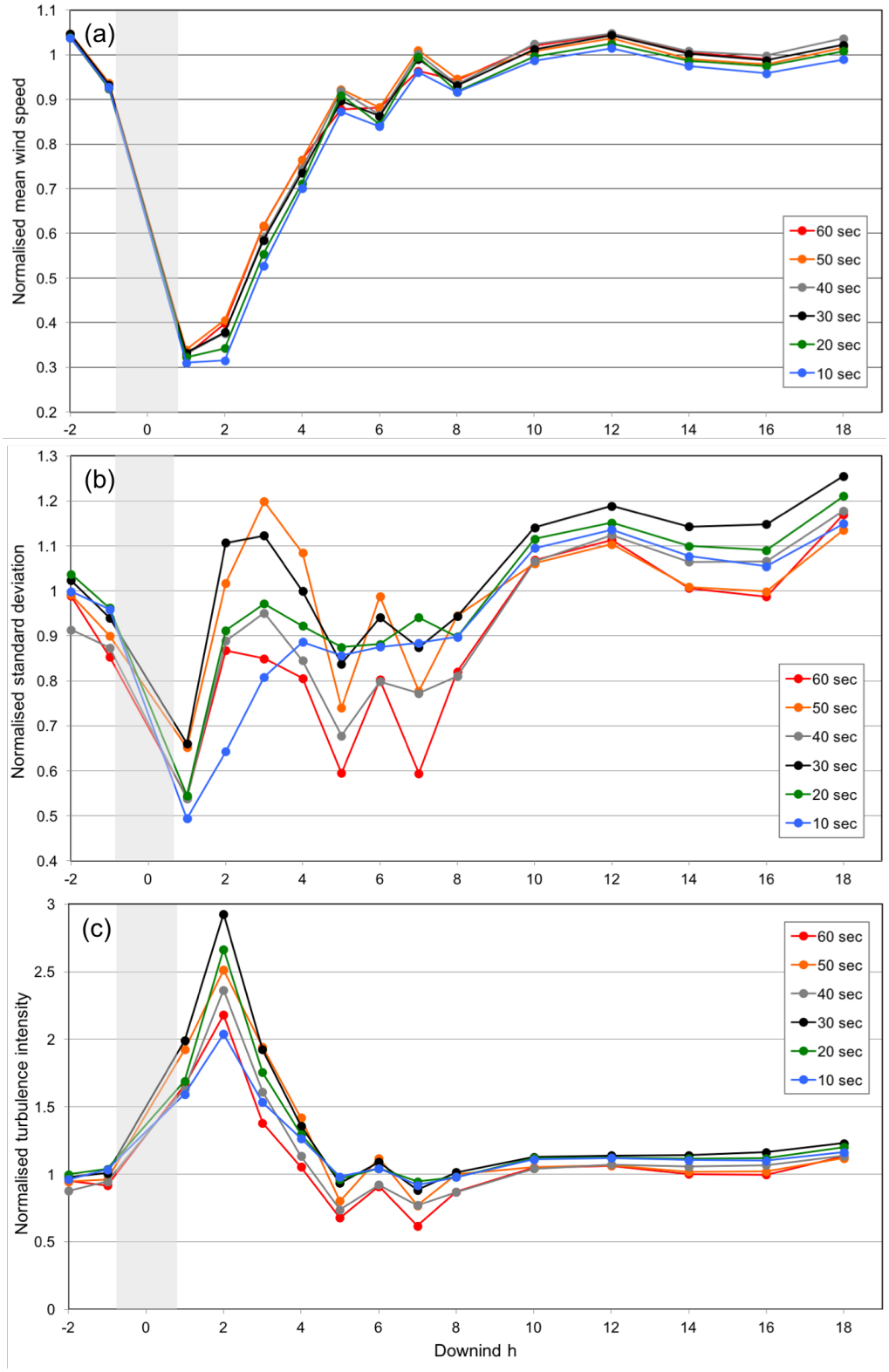


Figure 4.13 The effect of averaging period on changes in (a) normalised mean wind velocity; (b) normalised standard deviation; (c) normalised turbulence intensity, at 0.30 m height downwind of $Gr_{cup}2$. Lateral changes are not shown. Grey shading represents location of study element, where wind parameters are uncertain.

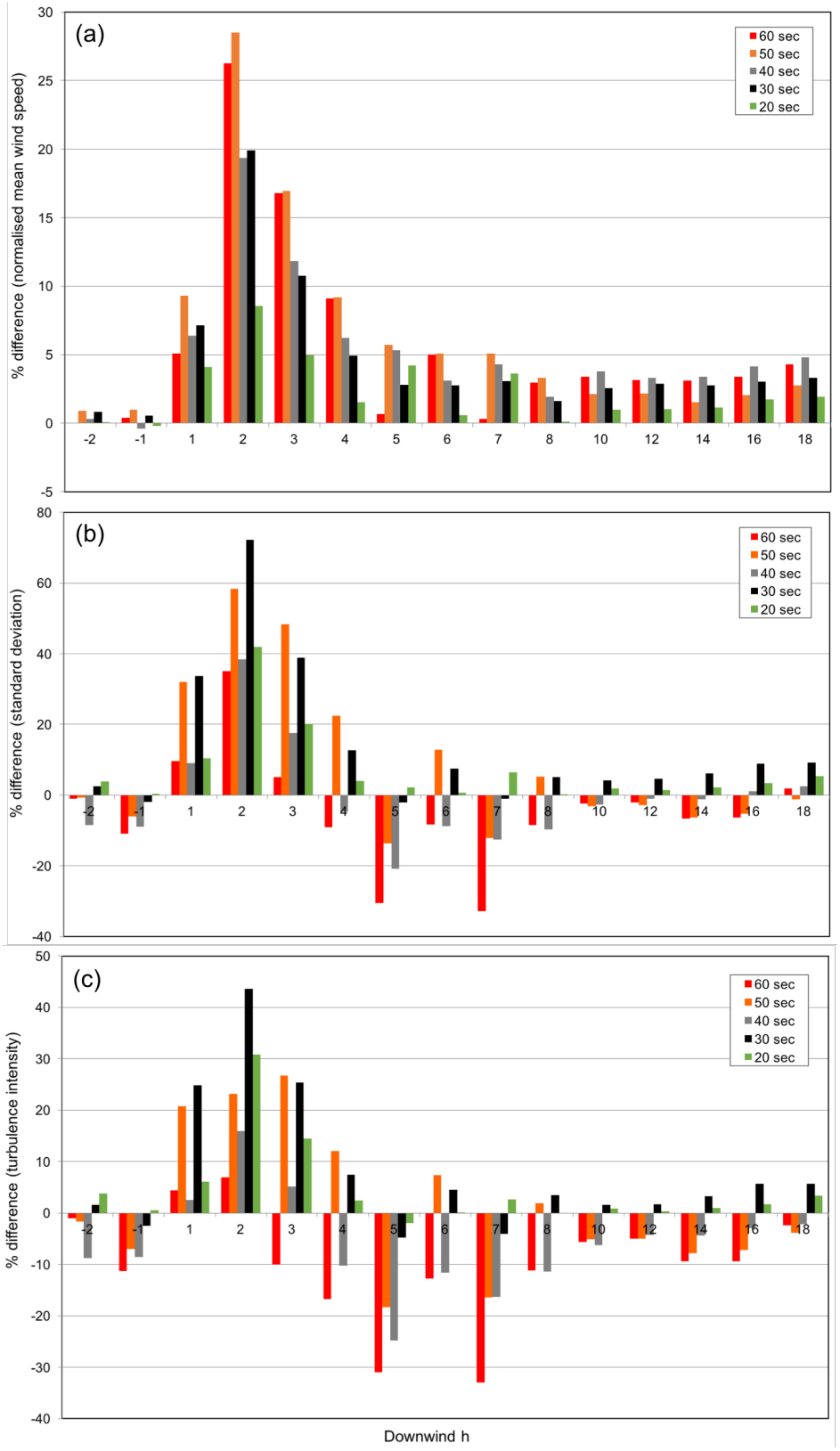


Figure 4.14 Percent difference in statistics of wind flow downwind of $Gr_{cup}2$ for different averaging periods compared to the 10 s averaging period. Differences in (a) normalised mean wind velocity; (b) normalised standard deviation; (c) normalised turbulence intensity.

Figure 4.15 displays the RSE of the wind velocity datasets normalised against corresponding reference velocities, averaged over periods from 10 s to 60 s. The RSE was calculated at the four key locations identified above. At -2 h_d, 8 h_d and 18 h_d, the RSE was relatively low (< 3%), and the 20 s and 30 s averaged datasets produced the lowest RSE. At 2 h_d, RSE decreased as the averaging period shortened.

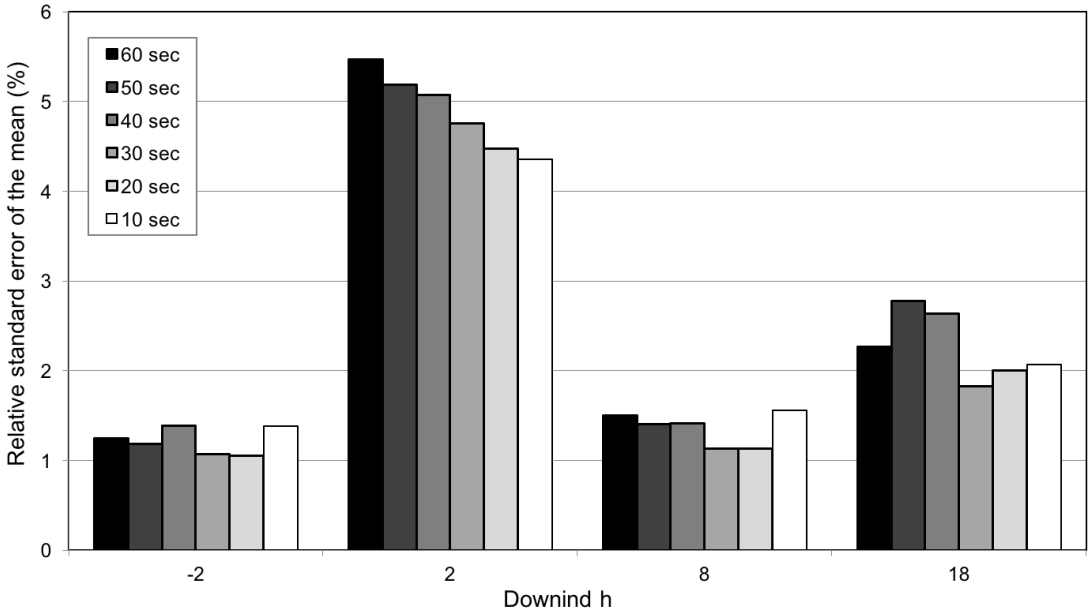


Figure 4.15 The effect of changing the averaging period on the relative standard error (RSE) of normalised wind velocity datasets at key locations upwind and downwind of $Gr_{cup}2$.

Table 4.3 displays the p-values for paired Student's t-tests between wind velocity datasets derived using averaging periods of 20–60 s, compared to the dataset derived using the 10 s averaging period, at the four key locations. There were no significant differences (at the 5% significance level) between the averaging periods in all cases at -2 h_d, 8 h_d and 18 h_d. Generally, at these three locations, p-values increased as the averaging period decreased. At 2 h_d, $p < 0.05$ for averaging periods of 30–60 s, suggesting a significant difference between datasets in this zone.

Generally, increasing the averaging period from 10 s to 60 s did not significantly affect wind velocity recovery statistics. This is supported by previous findings that the highest frequencies for successful u_* calculations can vary from 10-40 s (Namikas et al., 2003; Wiggs et al., 2004a), and that even longer 10-minute averaging periods can provide strong correlations between wind velocity and transport intensity (e.g. Davidson-Arnott et al., 2012). However, longer averaging periods inherently tend to include larger directional deviations from the experimental centreline, which are then hidden from the filtering process. To ensure comparability across datasets derived from both cup and sonic anemometers, analysis of wind statistics was performed at an averaging period of 10 s, unless noted otherwise in specific papers.

Averaging period	Downwind distance (h)			
	-2	2	8	18
60 secs	0.698	< 0.001	0.178	0.144
50 secs	0.881	< 0.001	0.106	0.387
40 secs	0.895	0.008	0.392	0.109
30 secs	0.895	0.005	0.530	0.188
20 secs	0.572	0.306	0.582	0.487

Table 4.3 p-values derived from paired Student's t-tests between the wind velocity datasets derived using averaging period from 20–60 s, and the dataset using the 10 s averaging period. Cells are coloured red if H_0 (i.e. no difference between the datasets) is rejected at the 5% significance level.

Following the cleaning and standardisation of the various wind velocity datasets, these were analysed in detail to meet Objectives 1 and 2. The experiments and relevant findings are presented in Chapters 5, 6 and 7, which were separately published in peer-reviewed journals.

CHAPTER FIVE



Characterizing turbulent wind flow around dryland vegetation

Paper 1: Mayaud, J. R., Wiggs, G. F. S. & Bailey, R. M.
Status: published in *Earth Surface Processes and Landforms, 41*(10), 1421–1436 (2016)

Abstract

Wind flow has been studied in situations where it encounters porous and solid windbreaks, but there has been a lack of research exploring turbulent wind dynamics around and in the lee of real vegetation elements. In dryland contexts, sparse vegetation plays an important role in modulating both the erosivity of the wind and the erodibility of surfaces. Therefore, understanding the interactions between wind and vegetation is key for improving aeolian transport modelling in desert landscapes. In this study, turbulent wind flow around three typical dryland vegetation elements (a grass clump, a shrub, and a tree) was examined in Namibia using high-frequency (10 Hz) sonic anemometry. Spatial variations in mean wind velocity, as well as Reynolds stresses and coherent turbulent structures in the flow, were compared and related to the porosities and configurations of the study elements. A shelter parameter, originally proposed by Gandemer (1979, *J. Ind. Aerodyn., 4*, 371–389), was derived to describe the combined impact of the different elements on the energy and variability of horizontal wind flow. Wind velocity was reduced by 70% in the immediate lee of the grass and 40% in the lee of the shrub, but velocity recovered exponentially to equilibrium over the same relative distance in both cases (~9 element heights downwind). Quadrant analysis of the high-frequency wind flow data revealed that the grass clump induced a small recirculation zone in its lee, whereas the shrub did not. Also, higher Reynolds shear stress ($-\overline{u'w'}$) and higher 'flow positivity magnitude' (ratio of Q1 (outward interaction) and Q4 (sweep) quadrants to Q2 (ejection) and Q3 (inward interaction) quadrants) was generally observed in the wake of the grass. These differences arose because the porosity of the grass clump (53%) was lower than the porosity of the shrub (69%), and thus bleed flow through the shrub was more significant. The bluff-body behaviour of the grass resulted in a more intense and more extensive sheltering effect than the shrub, which implies that overall sediment transport potential is lower in the wake of the grass. The tree displayed a different wake structure to the grass and shrub, owing to the elevation of its crown. A 'bottom gap' effect was observed, whereby wind velocities increased possibly due to streamline compression in the gap between the ground and the underside of the tree crown. Differences in flow momentum between the bottom gap and the low-pressure leeward region of the crown are a probable explanation for the formation of a large recirculation vortex. The bottom gap effect led to decreased sheltering up to 3 tree heights downwind, but the surface became increasingly protected by the frontal impact of the crown over a further 8 tree heights downwind (~30 m). The extraction of momentum from the air by the tree therefore resulted in a far more extensive sheltering effect compared to the grass and shrub. This study represents an important investigation of the impact of different vegetation types on turbulent wind flow, and results can be integrated as parameterisations into spatial sediment transport models that explore landscape-scale change on semi-vegetated desert surfaces.

This chapter addresses **Objective 1** (to quantify extremes I erosivity by measuring wind structures upwind and downwind of various plant types of different sizes and porosities). **Methods**: sonic anemometers, cup anemometers, optical porosity, vegetation transects.

This chapter is a modified version of the paper by Mayaud et al. (2016b). The Introduction section of the paper has been shortened, to avoid repetition of material provided in Chapter 2 of this thesis.

5. Characterizing turbulent wind flow around dryland vegetation

5.1. Introduction

The presence of non-erodible roughness elements such as plants significantly complicates wind flow in deserts. By providing drag on the overlying airflow, non-erodible elements affect the velocity profile and thus play a considerable, and sometimes conflicting, role in controlling the erodibility of desert surfaces (see section 2.3). Theoretical calculations (e.g. Raupach, 1992; Okin, 2008) and experimental measurements (Leenders et al., 2007; Youssef et al., 2012; Gillies et al., 2014; Wu et al., 2015) suggest that protective wakes downwind of vegetation elements extend to approximately 7–10 h (where h is the height of the element), but this can vary significantly depending on plant porosity and pliability.

Much of the research on the effects of porosity has been conducted on sand fences and windbreaks, and findings from these are of some relevance to plants (Grant & Nickling, 1998; Leenders et al., 2007). However, the three-dimensional nature of live plants (as opposed to the two-dimensional problem represented by a fence) complicates these interactions (Leenders et al., 2007). In particular, the impact of vegetation on flow turbulence remains a poorly understood phenomenon, which is pertinent given the increasing evidence that turbulence is an important driving force behind sediment entrainment and transport in aeolian environments (Butterfield, 1991; Weaver & Wiggs, 2011; Wiggs & Weaver, 2012).

Wind erosion models form a key part of our understanding of sediment transport dynamics on partly vegetated surfaces, and are crucial for assessing the potential vulnerability of dryland regions to soil degradation (Okin et al., 2006; Ravi et al., 2011). However, the current lack of field-based research on turbulence around desert

plants hinders the accuracy of wind flow parameterisations in these models. Therefore, the objectives of this study are:

(i) To characterise spatial variations of wind velocity and turbulence around three key dryland vegetation elements (a grass, a shrub, and a tree);

(ii) To relate any differences in flow properties to the characteristics of the vegetation elements;

(iii) To connect observations of turbulent wind patterns, vegetation form and potential zones of enhanced aeolian erosion/deposition in a more formalised way.

The overall aim is to provide empirical data on the impact of vegetation on wind flow, in order to provide appropriate parameterisations of sediment transport potential in large-scale models of dryland landscape evolution. This will help to improve current understanding of how environmental and anthropogenic changes can impact processes occurring on semi-vegetated desert surfaces.

5.2. Methods

5.2.1. Field sites

The field study was carried out in two locations in Namibia (see Figure 5.1a). A grass experiment ($Gr_{sonic}1$) and shrub experiment ($Sh_{sonic}1$) were conducted in the southwest Kalahari Desert, ~4km north of the Auob River (0369913 E, 7180634 N), and a tree experiment ($Tr_{sonic}1$) was conducted on the edge of the Sperrgebiet Reserve in the southern Namib Desert (0619715 E 7045842 N). The Kalahari Desert site was in a farmer's field on raised, flat terrain populated mainly by *Stipagrostis amabilis* grasses, *Rhigozum trichotomum* shrubs and *Acacia erioloba* trees. A wide strip of grazed land meant that the experiments had a fetch of > 500 m. The Namib

Desert site comprised a large sandy gravel sheet and was populated by patterned shrubby and grassy vegetation, with some sparsely distributed *Acacia erioloba* trees.

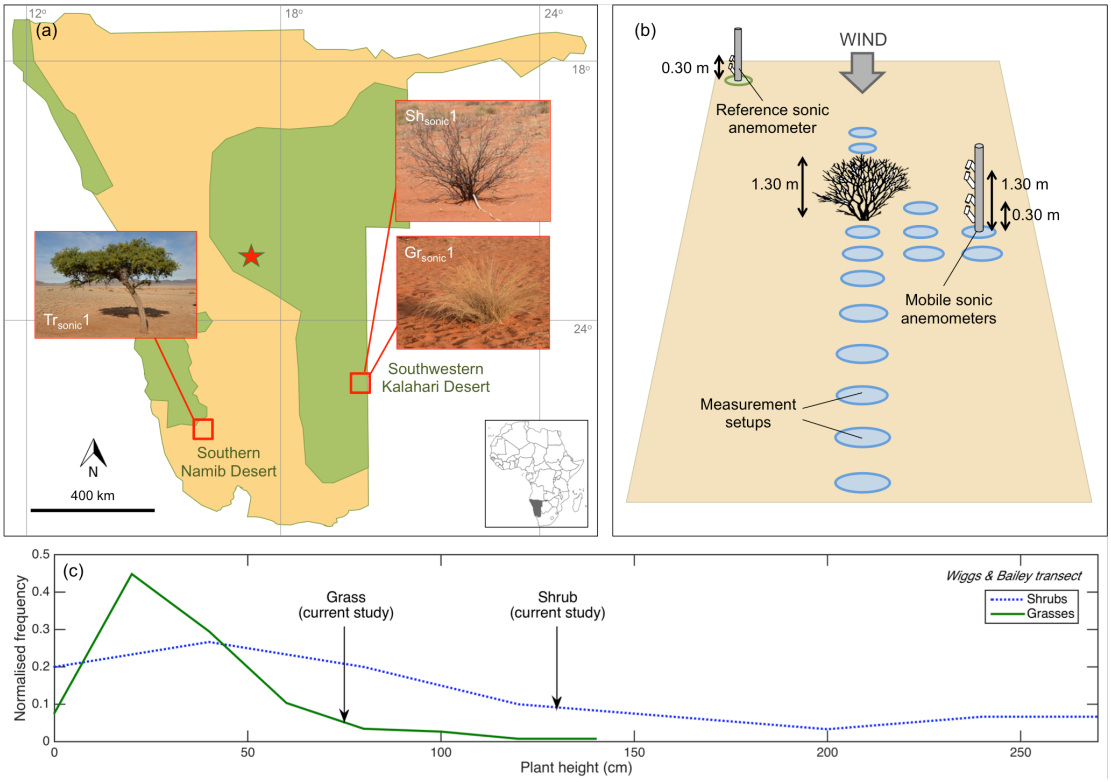


Figure 5.1 (a) Locations of the two field sites in Namibia, and general characteristics of the three study elements; (b) Example of experimental setup for Sh$_{sonic}$1.

Gr$_{sonic}$1 was conducted around a *Stipagrostis amabilis* grass of 0.75 m height, Sh$_{sonic}$1 around a *Rhigozum trichotomum* shrub of 1.30 m height, and Tr$_{sonic}$1 around an *Acacia erioloba* tree of 3.70 m height (see Table 5.1 for vegetation characteristics). The three vegetation elements were chosen to be representative of their surrounding populations in terms of height, width and porosity. Table 5.2 summarises plant height and width ranges reported in previous field studies, as well as average plant characteristics along vegetation transects conducted at each field site (A) and at five other sites located < 150 km away from the Kalahari site (B). The frequency distribution of grass and shrub heights along the latter transects are shown in Figure 5.1c. The three vegetation elements in this study fall within the majority of

reported height/width ranges, and the grass and shrub elements in this study had a standard (Z) score of 1.32 and 0.44 respectively, relative to the distributions in Figure 5.1c. The study elements are therefore considered to be generally representative of their surrounding environments.

The optical porosity of the study elements was determined using a digital photogrammetry method adapted from Kenney (1987). Digital photographs of part of the canopy were taken at approximately 0.40 m from shrubs and grasses, and 3.0 m from tree canopies, using a Nikon D3100 DSLR camera with a resolution of 14.2 Megapixels, from the principal wind direction (thus accounting for the plant structures that the wind interacts with directly). The photographs were enlarged to fill the image dimensions, converted to greyscale images, and the perimeter of the plant was defined using a polygon that was inputted into the code manually. A variety of threshold values for black (plant branches) and white (open area) pixels were calculated, and the best fit to actual element shape was visually determined (cf. Gillies et al., 2000; Leenders et al., 2007). The percentage of white pixels, averaged across all directions, was taken as the mean optical porosity of the element canopy.

5.2.2. Experimental setup

Three 3D sonic anemometers (*Campbell CSAT-3*) were deployed around each study element to collect wind velocity data (u, horizontal; v, spanwise; and w, vertical) at a sampling frequency of 10 Hz. A mobile anemometer array was erected with two sonic anemometers fixed onto a mobile steel mast: one at 0.30 m height, which is low enough to capture turbulence potentially responsible for surface entrainment whilst minimising the interference of saltating sand with the sonic measurement path (Weaver & Wiggs, 2011), and another at the height of the vegetation element. In the case of the tree experiment, this second sonic anemometer was restricted to 1.50 m

height due to a limited mast height. This is not problematic for this study, because it captures the main zone of interest between the ground surface and underside of the canopy, where a 'bottom gap' effect (flow compression) is hypothesised to occur. In all experiments, a third sonic anemometer was mounted at 0.30 m height and placed 20 h upwind and 15 h to the side of the experimental plot in a non-distorted environment (i.e. with a significant fetch over a flat, bare surface). This provided reference wind data against which mobile anemometry data could be normalised. Practicality constraints meant that data collected at the height of each vegetation element was normalised against reference data measured at 0.30 m height (the normalisation of wind velocities at multiple heights using a single reference height is common practice; e.g. Wiggs & Weaver, 2012). The anemometers were all aligned parallel with the prevailing wind direction and level in the horizontal plane. The experimental setup of $Gr_{sonic}1$ is shown in Figure 5.1b as an illustrative example.

The mobile mast was moved within a grid formation upwind, downwind and to the sides of each element, oriented in the direction of the wind. Each grid was divided into a number of measurement setups, during which both mobile anemometers simultaneously recorded wind velocity. To ensure sufficient data were acquired for subsequent analysis, each setup was run for a minimum of 20 minutes. The alignment of the experimental plot relative to the wind was altered after every instrumental setup to reflect any minor wind directional changes, and any misaligned data were removed in subsequent analysis (see section 2.3). Throughout this study, annotation for measurement locations is given as h_d (downwind distance) and h_L (lateral distance) in terms of the height of the element. Wind flow was measured from -2 h_d (i.e. upwind) to 11–18 h_d depending on the element, and up to 2 h_L. Lateral wind flow was only measured on one side of each element, as wind dynamics were considered to be effectively symmetrical about the centreline of the wake (Leenders et al., 2007). This is confirmed by symmetrical sand tails observed in the field.

Exp.	Date	Species	Height (m)	Width (m)	Optical porosity (%)	u (m s^{-1}) during experiment				u (m s^{-1}) during entire month			
						Min	Max	Mean	St. Dev.	Min	Max	Mean	St. Dev.
$Gr_{sonic}1$	27/09/14	*Stipagrostis amabilis* (Grass)	0.75	1.30	53	1.72	4.83	3.02	0.72	0.00	8.81	1.32	1.21
$Sh_{sonic}1$	30/09/14	*Rhigozum trichotomum* (Shrub)	1.30	1.80	69	0.89	4.22	2.64	0.73				
$Tr_{sonic}1$	23/09/14	*Acacia erioloba* (Tree)	3.70 (trunk: 2.30; crown: 1.40)	5.20	6	1.22	4.33	2.97	0.62	0.00	8.77	2.45	1.73

Table 5.1 Descriptive experimental statistics for the three sonic anemometry experiments around single vegetation elements, as measured at the reference anemometer at 0.30 m height. Width is given as the length of the element axis perpendicular to the axis of the experimental plot. Tree porosity refers to the porosity of the crown. Also shown are monthly wind velocity data measured at 0.30 m height at the same field sites (17/08/14–15/09/14 in the southwest Kalahari; 16/09/14–05/10/14 in the southern Namib).

Study	Location	Plant type	Height (m)	Width (m)	Porosity (%)
Wiggs et al. (1994)	Southwest Kalahari	Grass	0.8–1.0	-	-
Wiggs et al. (1995)	Southwest Kalahari	Grass/shrub	0.1–0.3	-	-
Wiggs et al. (1996a)	Southwest Kalahari	Grass/shrub	0.3–0.6	-	-
van Rooyen et al. (2001)	Southwest Kalahari	Grass	0.2–2.0	-	-
		Shrub	0.5–2.0	-	-
		Tree	2.0–6.0	-	-
Thomas & Leason (2005)	Southwest Kalahari	Grass	0.2–0.3	-	-
Vegetation transects A (current study)	Southwest Kalahari	Grass	0.1–1.1	0.1–1.9	31–43
		Shrub	0.3–1.7	0.5–3.2	38–71
	Southern Namib	Shrub	0.4–1.6	0.3–2.1	63–69
		Tree	3.0–5.5	4.0–7.5	4–10
Vegetation transects B (Wiggs & Bailey, unpublished)	Southwest Kalahari	Grass	0.05–1.5	0.05–1.3	-
		Shrub	0.05–2.9	0.1–3.4	-
		Tree	1.4–5.1	1.1–6.0	-

Table 5.2 Average plant characteristics for grasses, shrubs and trees in relevant dryland regions, as reported in previous studies and unpublished data from authors. The vegetation transects conducted for this study (A) consisted of eight individual transects of 25 m length and 1 m width at both sites; along each transect, the height, width and porosity of each plant was recorded. The vegetation transects of Wiggs & Bailey (B) were conducted in September 2010 at five separate sites in the southwest Kalahari, each located <150 km from the current study site.

5.2.3. Data analysis

The three experiments were carried out on separate windy days in September 2014 (Table 5.1). Mean approach (i.e. reference) wind velocities during the experiments ranged from 2.64 m s^{-1} to 3.02 m s^{-1}, which were representative of the average conditions measured at the same field sites over a period of approximately one month. Reynolds numbers (Re) for the experiments are high (7.9–8.8 x 10^5), so it can be assumed that small differences in wind velocity across the experiments have a negligible impact on wake structures.

In order to ensure that the airflow detected at each measurement location had interacted as much as possible with the study element, the datasets were filtered to exclude oncoming wind directions > 5^o from the centreline of the experimental plot. Previous work on turbulent wind flows has shown that sampling periods for velocity measurements must be long enough to capture the full range of turbulent eddies, and thus be representative of the processes occurring in the boundary layer. van Boxel et al. (2004) recommend that for an average wind velocity of 2.5 m s^{-1} and observation heights up to 1.50 m, a convenient sampling period is on the order of 4–7 minutes. The mean number of minutes per measurement setup (after being filtered using the 5^o threshold) ranged from 6.6 minutes to 8.6 minutes, thus conforming to van Boxel et al.'s (2004) recommendation. Across all measurement setups, the total number of data points at each measurement height was 56,160 ($Gr_{sonic}1$), 63,900 ($Sh_{sonic}1$) and 46,200 ($Tr_{sonic}1$). Unless otherwise stated, all wind flow parameters were normalised against the mean wind velocity ($\overline{U}$) recorded by the upwind reference anemometer at 0.30 m height. Normalisation is indicated using the '*norm*' subscript for each parameter.

The sonic anemometer data from all three experiments were post-processed to correct for misalignment errors. The streamwise frame of reference was rotated in

accordance with the local streamline angle using yaw rotation (cf. Frank, 1996; van Boxel et al., 2004; Walker, 2005; Weaver & Wiggs, 2011; Chapman et al., 2012). Roll and pitch rotation were omitted from the correction procedure because the streamlines were considered to be horizontal over the desert surface. Subsequent to yaw rotation correction the average spanwise velocity was zero ($\overline{V}$ = 0), and so no further analysis of this component was undertaken. The remaining velocity data were decomposed into their average ($\overline{U}, \overline{V}$ and $\overline{W}$) and fluctuating (u', v' and w') components, from which the horizontal ($\overline{u'^2}$) and vertical ($\overline{w'^2}$) components of Reynolds stress were derived. The Reynolds shear stress ($-\overline{u'w'}$) was calculated using the time-averaged covariance of the instantaneous horizontal and vertical turbulent components. The local, near-surface streamline angle (θ) was determined as:

$$\theta = \arctan\left(\frac{\overline{W}}{\overline{U}}\right) \tag{5.5}$$

From these parameters, the incidence of coherent structures in the flow around the grass, shrub and tree elements was established using conditional-sampling quadrant analysis (Lu & Willmarth, 1973). This technique defines four discrete categories of momentum exchange based on the relative signs of u' and w'. Ejections (Q2 events; $u' < 0$, $w' > 0$) and sweeps (Q4; $u' > 0$, $w' < 0$) contribute positively to the production of Reynolds stress, while outward interactions (Q1; u'>0, $w' > 0$) and inward interactions (Q3; $u' < 0$, -$w' < 0$) contribute negatively to Reynolds stress (Smith, 1996). In order to isolate significant bursts of turbulent stress from weaker background variability (Lapointe, 1992; Clifford & French, 1993), stress events of low magnitude were removed from quadrant analysis using a threshold criterion (*H*). Following previous studies (Bauer et al., 1998; Sterk et al., 1998; Leenders et al.,

2005; Weaver, 2008; Wiggs & Weaver, 2012), the size of *H* was chosen to be equivalent to one standard deviation (σ) of the Reynolds shear stress ($-\overline{u'w'}$), such that a flow structure was only classified if $-u'w' > \pm H.(-\overline{u'w'})$.

5.3. Results and discussion

5.3.1. Mean wind velocity around single vegetation elements

Figure 5.2 displays the spatial patterns of mean normalised wind velocity (Φ) around the three study elements. Normalised wind velocities at each measurement location were interpolated using a triangulation-based natural neighbour algorithm, with a grid spacing of 0.1 m. This resolution was chosen because the measurement locations around the elements were determined at a scale of 0.1-1.0 m. The algorithm was chosen because it produced robust spatial features that were present using several other commonly used interpolation algorithms. Since wind velocity was quantified only on one side of each element in the field, the measured velocities were plotted symmetrically over the centreline of the elements in order to provide better visualisation of recovery patterns.

The contour plots at 0.30 m height show clear regions of reduced wind velocity compared to upwind values (Φ < 1.0) in the wakes of the grass (Figure 5.2a) and the shrub (Figure 5.2c). These correspond with low-velocity zones previously identified in the lee of windbreaks and other flow obstructions (Judd et al., 1996; Musick et al., 1996; Lee et al., 2002). Wind slowdown was more intense in the lee of the grass compared to the shrub. There was a reduction in wind velocity directly upwind and a slight speedup to the sides of the two elements, although these were minor compared to the slowdown observed along the centreline of the wake.

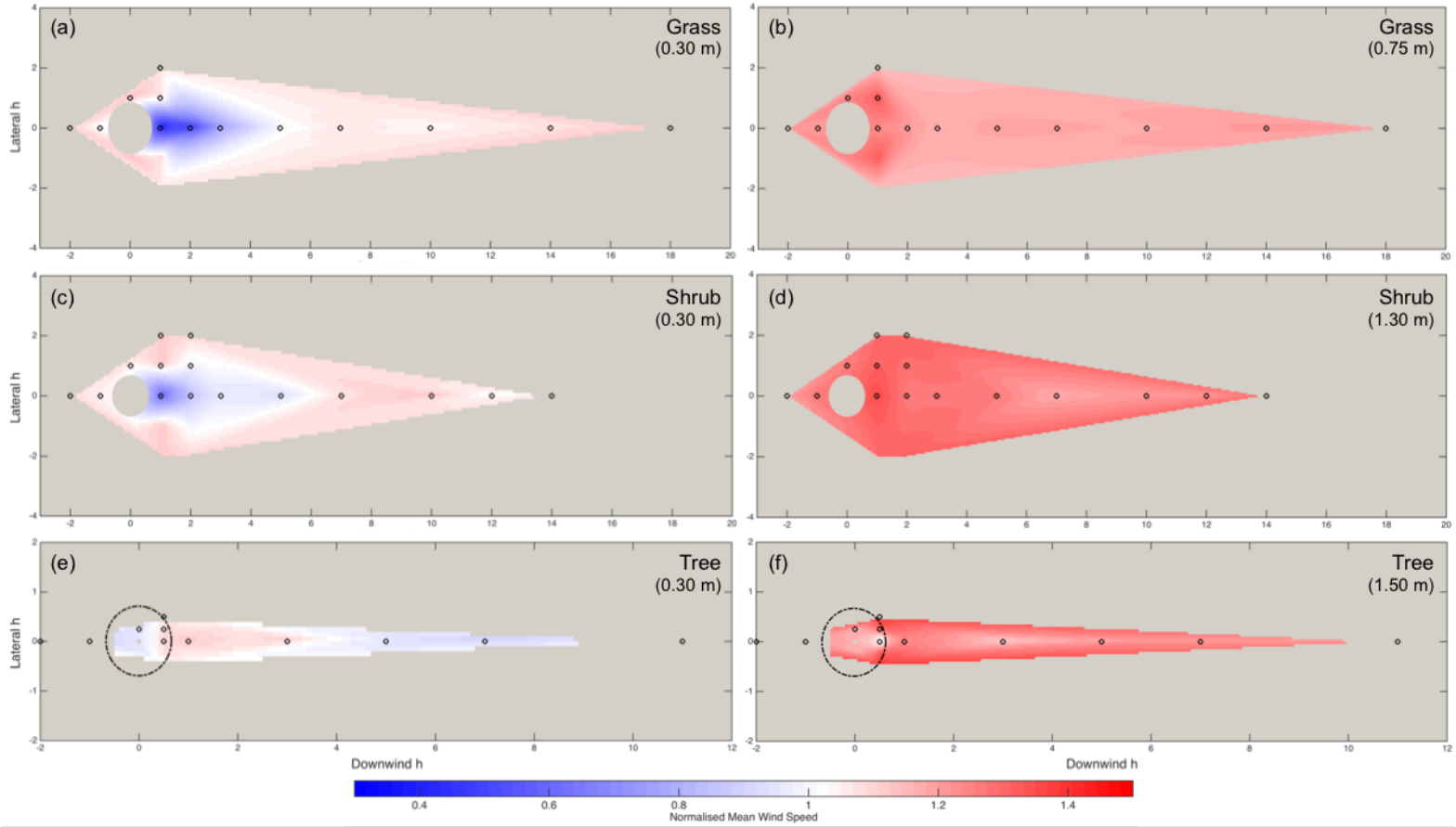


Figure 5.2 Spatial patterns of normalised mean wind velocity (Φ) at 0.30 m and element height (1.50 m for tree) for: (a), (b) a grass clump; (c), (d) a shrub; and (e), (f) a tree. Data were interpolated using a triangulation-based natural neighbour algorithm, with a grid spacing of 0.1 m. Location of grass and shrub elements are shown by white ellipses, and tree crown extent is shown as a dotted ellipse. Black circles represent anemometer locations. Downwind h for trees is calculated using total tree height (i.e. trunk + crown). Lateral wind velocity data are mirrored across the centrelines of the element wakes.

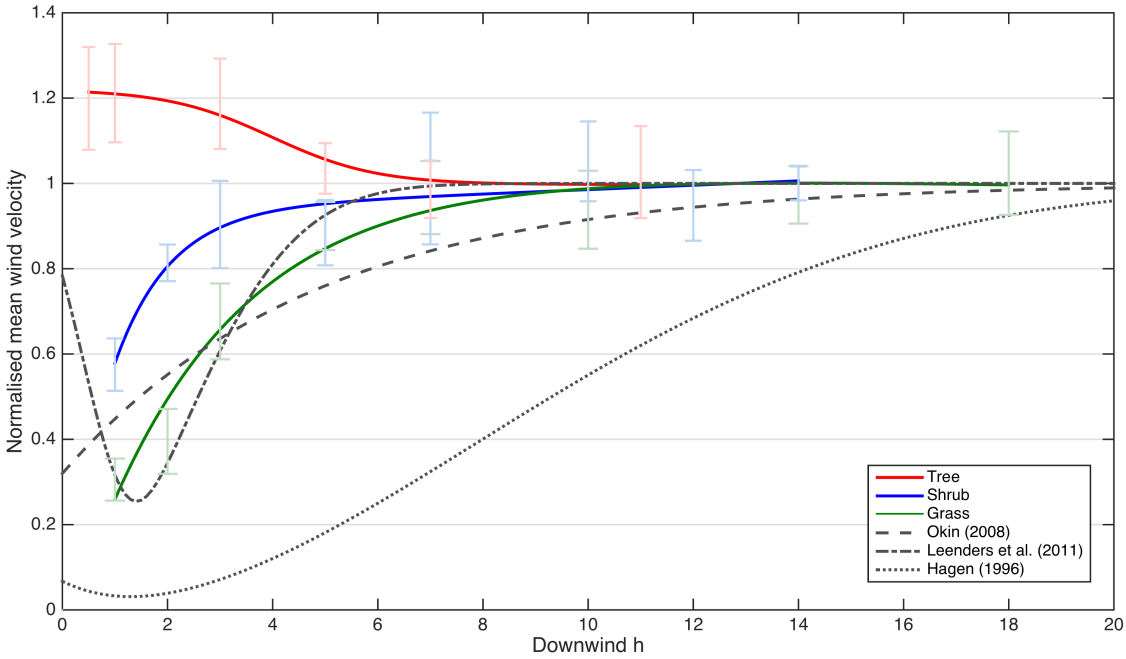
At the height of the grass and shrub elements, normalised wind velocity was higher in comparison to the surface, because the reference anemometer was placed lower than the mobile anemometer (0.30 m and element height, respectively). In the grass case (Figure 5.2b), there was some disturbance to the flow up to 2 h_d, with flow accelerating by 6–8% above the grass clump, but recovery to upwind values was almost immediate. In contrast, the wind was more significantly impacted in the case of the shrub (Figure 5.2d), with flow accelerating by 8–10% above and to the side of the element, and normalised wind velocity remaining high until 5 h_d. These changes are comparable to the wind tunnel results of Wu et al. (2015), who found that certain shrub species induce above-canopy flow acceleration of up to 13%. The comparatively limited impact of the grass on mean wind velocity at the element height is likely due to the pliable nature of the grass stems, which alter their form to become more streamlined as wind velocities increase and thus extract momentum less effectively at height (Gillies et al., 2000). Since the shrub was 0.55 m taller than the grass element, wind velocity at shrub height is likely to be higher in absolute terms than at grass height. Given that both datasets were normalised to reference wind flow measured at 0.30 m height, it should be expected that Φ values are greater at shrub height than at grass height.

The tree, on account of its elevated crown, caused visibly different wind velocity changes when compared with the grass and shrub. At 0.30 m height (Figure 5.2e), normalised wind velocity decreased upwind and up to 0.5 h_d of the tree trunk, and was above unity from the downwind edge of the crown until ~4 h_d. This sub-crown wind speedup has previously been termed the ‘bottom gap’ effect (Ruck & Schmitt, 1986). The effect arises because wind flowing near the top half of the tree moves over the tree crown (Gross, 1987; Lee et al., 2014), whereas in the lower region of the tree, a dominant downdraft speeds up the wind due to streamline compression in the gap between the ground and the underside of the crown (Kim & Lee, 2002;

Dupont et al., 2014). At 1.50 m height (Figure 5.2f) two zones of relative wind slowdown were observed: one directly beneath the crown, and one between 2–5 h_d. The sonic anemometer at this height was measuring wind flow just 0.80 m below the underside of the crown, so the observed slowdown likely resulted from the frontal impact of the crown being increasingly felt downwind. A localised speedup of wind around the sides of the tree trunk due to lateral streamline compression, as reported in previous studies (e.g. Gross, 1987; Leenders et al., 2007), was not observed in our wind data. This was probably because the closest anemometer to the trunk was too far away (0.90 m) to capture this aerodynamic effect. However, there was some evidence of sediment deflation in the immediate vicinity of the trunk (~0.20 m deflation, extending for ~0.40 m downwind), and this could probably be linked to local wind acceleration.

Figure 5.3 displays the recovery of normalised mean wind velocity (Φ) at 0.30 m height along the centreline of the three element wakes. The grass and shrub data were fitted using a saturating exponential function, as the recovery of wind flow downwind of an obstruction can generally be described as an exponential curve (Bradley & Mulhearn, 1983). The wind data around the tree was fitted using a logistic function, as this was visually and statistically determined to fit the data most appropriately. The derived functions showed very good fits with the observed values, with high R^2 and low SSE and RMSE values (see table in Figure 5.3). Also presented are recovery rates published in other studies, assuming an obstacle porosity of 53% (same as the grass element in this study): (i) Hagen's (1996) friction velocity reduction factor behind a windbreak; (ii) Leenders et al.'s (2011) adaptation of Hagen's (1996) function for a single shrub; (iii) Okin's (2008; corrected in Li et al., 2013) parameterisation of reduced shear stress downwind of a plant, fitted to Bradley & Mulhearn's (1983) empirical data downwind of a wind fence. Although the functions of Hagen (1996) and Okin (2008) were developed to describe friction velocity/shear

stress, these parameters are linearly related to wind velocity such that recovery rates should be comparable (Leenders et al., 2011).



Element	Function	Coefficient values				Goodness of fit		
		a	b	c	d	SSE	R^2	RMSE
Grass	$ae^{-bx} + c$	-1.099	0.3849	1.106	-	0.0202	0.964	0.0636
Shrub	$ae^{-bx} + c$	-0.8837	0.7162	1.054	-	0.0158	0.914	0.0561
Tree	$a + (b-c)/(1 + e^{x-d})$	0.9176	7.814	7.608	3.967	0.0023	0.948	0.0339

Figure 5.3 Best fit regression lines for normalised mean wind velocity (Φ) downwind of the study elements at 0.30 m height. Error bars represent the standard deviation of the mean. Also shown are the models of Okin (2008) and Leenders et al. (2011) for porous shrubs, and of Hagen (1996) for a porous windbreak. A porosity of 53% is assumed for the Leenders et al. (2011) and Hagen (1996) models. Table displays function form, coefficients and goodness of fit statistics for the general fitting models.

With reference to Figure 5.3, it is clear that wind velocity recovered to equilibrium flow at approximately the same distance (~9 h_d) downwind of the grass and the shrub, which is comparable to recovery lengths for solitary elements identified in other similar studies (Leenders et al., 2007; Gillies et al., 2014; Wu et al., 2015). However, the overall rate of recovery (i.e. gradient of the best fit line) was higher in the case of the grass, because initial wind slowdown at 1 h_d of the grass (70% reduction) was larger than that of the shrub (40% reduction). This suggests that the

grass acted as more of a bluff body, with the lower porosity of the grass (53%) compared to the shrub (69%) resulting in a higher drag coefficient and thus greater momentum loss in the lee. These data support previous findings (Skidmore & Hagen, 1970; Perera, 1981) that lower-porosity elements induce more intense wind slowdown in their lee but allow flow to recover to upstream conditions sooner than more porous elements. Starting from Φ = 1.2 (due to wind speedup caused by the 'bottom gap' effect as previously discussed), wind velocity downwind of the tree experienced an increasing decline until ~4 h_d, followed by a reduced rate of slowdown until equilibration at ~7 h_d (26 m). The initially rapid rate of slowdown can be attributed to the frontal impact of the elevated crown being increasingly felt at the surface. The height of the trunk likely dictates the downwind distance at which the effect of the crown is first detected at the surface, and the height of the crown determines the distance over which the wind velocity recovers back to Φ = 1.0.

The recovery curves derived from the grass and shrub data in this study compared relatively well to the Leenders et al. (2011) formulation for wind velocity recovery downwind of a shrub, although wind speedup occurs more rapidly and equilibrium reached sooner in the Leenders et al. (2011) model. This difference can be ascribed to the lower optical porosity (18%) of the test shrub in the Leenders study, which, as discussed above, is thought to induce a faster recovery of wind velocity over a given distance. The decrease in normalised wind velocity between 0–1 h_d simulated by the Leenders et al. (2011) model could not be verified, as wind was not measured closer than 1 h_d in this study, but the location of minimum wind velocity is likely also located in this zone in the case of our grass and shrub. The recovery rates simulated by the models of Hagen (1996) and Okin (2008) were much slower than the rates observed in this study, with normalised wind velocity reaching equilibrium at 21 h_d and 18 h_d respectively. This implies that two-dimensional wind fences may not be suitable analogues for three-dimensional, partially bluff forms such as grasses and shrubs, as

concluded by Gillies et al. (2014) for nebkha dunes and Lee et al. (2014) for single trees. The recovery curve of the tree in this study was not well simulated by any of the presented models, because none of them allows Φ to rise above 1.0 in an element's wake, such that wind speedup associated with the 'bottom gap' effect is not accounted for.

5.3.2. Turbulence around single vegetation elements

While mean wind velocity data provide some information about vegetative impacts on flow, turbulent variations must also be considered when characterising different zones of flow around individual elements, because there is increasing evidence that turbulence is an important driving force behind aeolian sediment entrainment and transport in complex flows (Butterfield, 1991; Sterk et al., 1998; Schönfeldt & von Löwis, 2003; Leenders et al., 2005, 2007; Wiggs & Weaver, 2012). Reynolds stresses provide a direct representation of turbulent fluctuations by accounting for instantaneous deviations from the mean flow, and these stresses have to some extent been related to sediment transport dynamics at the dune scale (Baddock et al., 2011; Weaver & Wiggs, 2011; Chapman et al., 2012). Investigating the spatial variability of turbulent stresses around plants is therefore useful for identifying specific zones of potential erosion/deposition on partially vegetated surfaces.

Figure 5.4 shows how the distribution of horizontal wind velocity (measured at 10 Hz) at 0.30 m height around the study elements changed relative to the approach flow. Student's T-test results suggest that the mean wind velocities measured downwind and to the sides of the elements were in most cases significantly different ($p < 0.001$) to the approach flow, although the clearest differences were observed in the immediate lee of the grass and shrub. Chi-squared tests comparing the entire wind

velocity distributions at each measurement location with the approach flow reveal that significant differences (at the 95% level) only occurred in the lee of the grass and shrub up to 2 h_d. In this region, the centres of the distributions were shifted to lower wind velocities, resulting in skewness values that were up to 63% higher (i.e. more positive) than the skewness of the approach flow. Increased positive skewness is caused by infrequent, intermittent events of accelerated fluid with respect to the ambient flow, and is an indicator of elevated turbulence within the flow (Sterk, 2000).

Figure 5.5 displays the spatial variations of normalised horizontal normal Reynolds stress ($\overline{u'^2}_{norm}$) around the study elements. Vertical velocity variations were roughly an order of magnitude smaller than the horizontal components of flow in this study (cf. Sterk et al., 1998; van Boxel et al., 2004; Leenders et al., 2005; Weaver & Wiggs, 2011), so vertical normal Reynolds stress ($\overline{w'^2}$) data are not presented. Downwind of the grass (Figure 5.5a,b), $\overline{u'^2}_{norm}$ peaked at 3 h_d at element height and at 7 h_d at the surface. In contrast, $\overline{u'^2}_{norm}$ was low in the lee of the shrub at both heights and peaked at 12 h_d (Figure 5.5c,d), five element heights further than the grass. Zones of elevated $\overline{u'^2}_{norm}$ occurred to the side of the shrub but not to the side of the grass. The observed regions of elevated stress probably result from counter-rotating vortices induced by the elements, which can act to increase sediment entrainment potential (Sutton & McKenna-Neuman, 2008; Burri et al., 2011). In the case of the tree (Figure 5.5e,f), $\overline{u'^2}_{norm}$ was relatively low beneath the crown at both heights, although a slight increase was observed to the sides of the crown at 1.50 m height, which could also result from small vortices induced by the underside of the canopy.

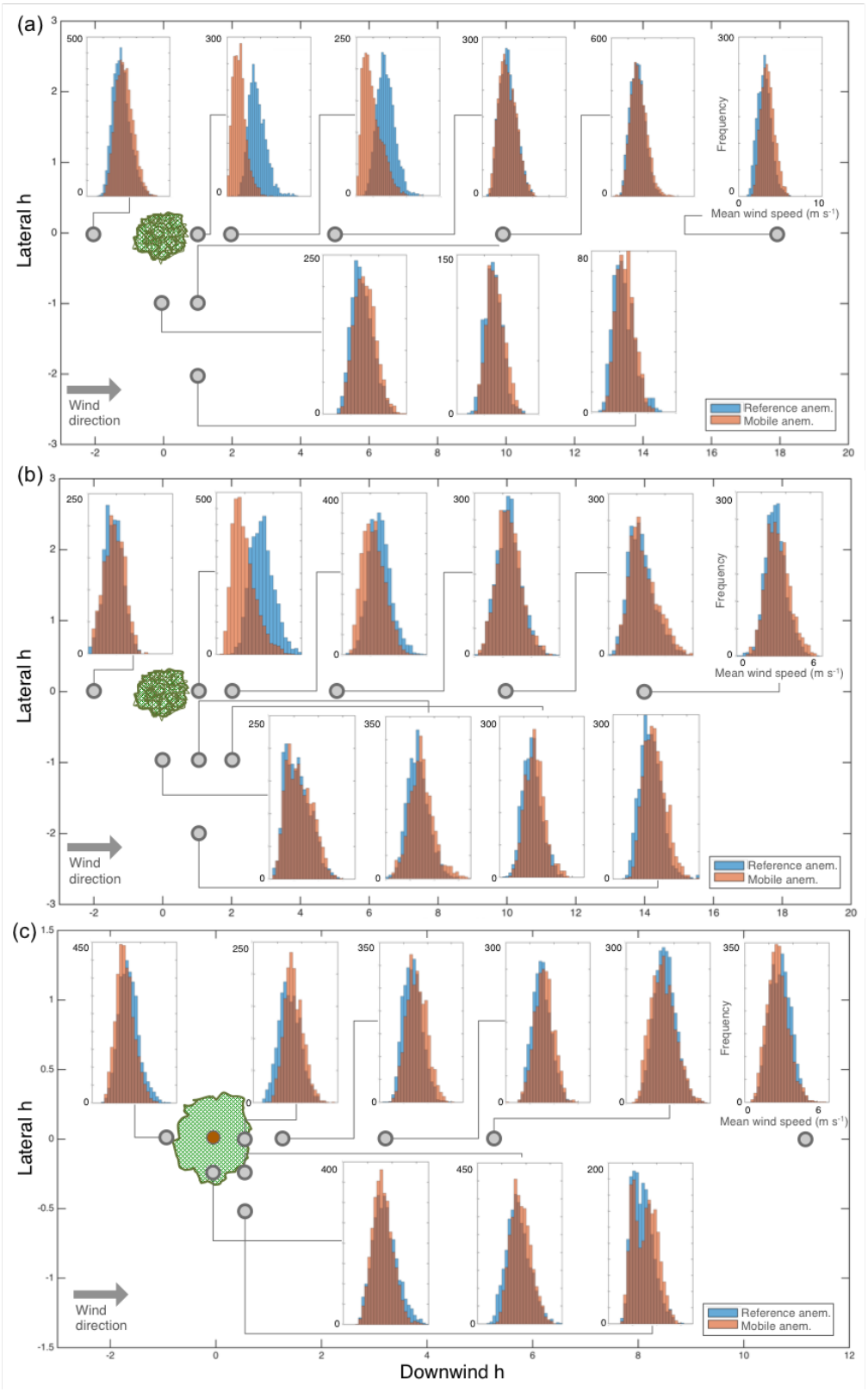


Figure 5.4 Horizontal wind velocity distributions for instantaneous 10 Hz sonic anemometry data at 0.30 m height, at different locations around: (a) a grass; (b) a shrub; (c) a tree. Anemometer locations are shown as grey circles. Vegetation element location is shown as green ellipse. Histograms for reference and mobile sonic anemometers are shown.

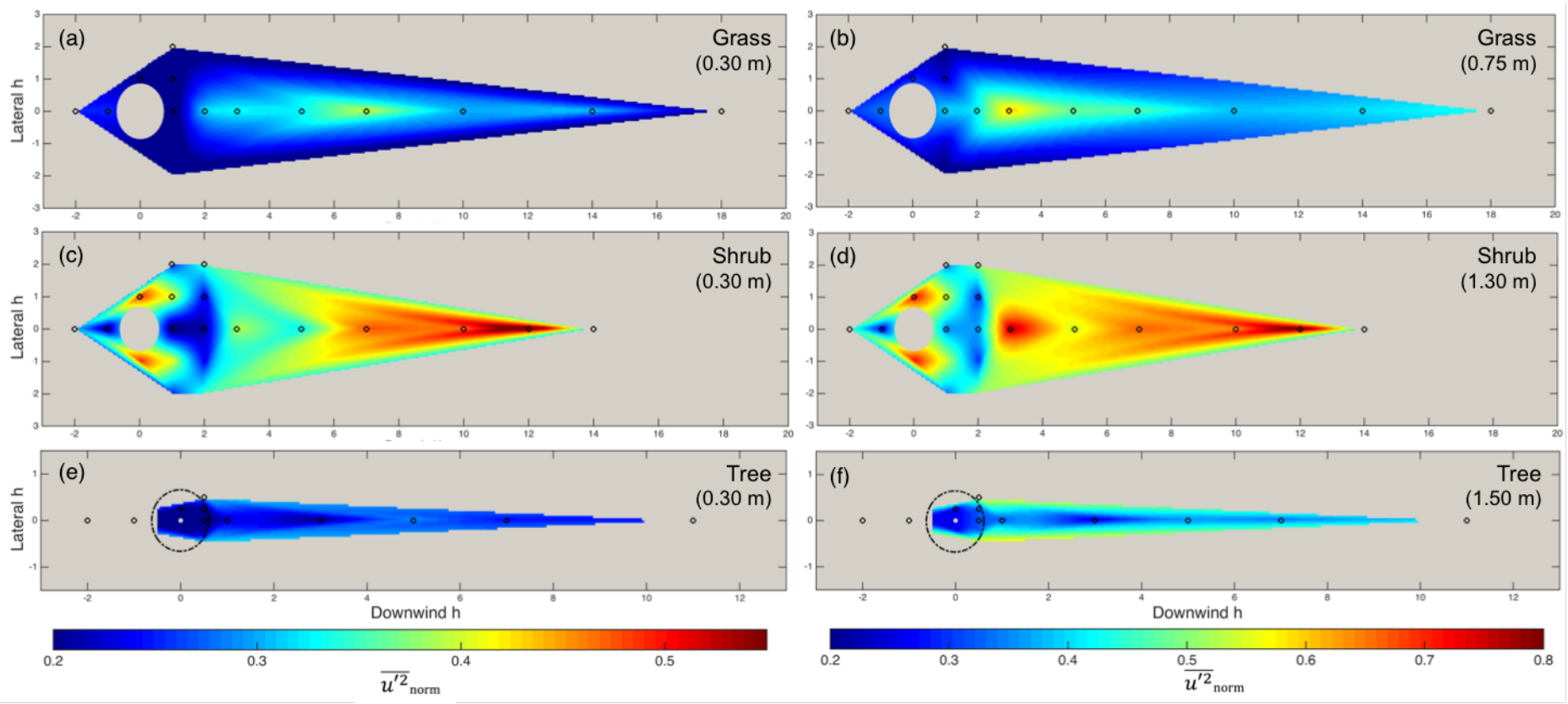


Figure 5.5 Horizontal spatial patterns of average normalised horizontal normal Reynolds stress ($\overline{u'^2}_{norm}$) at 0.30 m and element height (1.50 m for tree): (a), (b) a grass; (c), (d) a shrub; and (e), (f) a tree. Data were normalised to $\overline{U}$ of an upwind reference anemometer at 0.30 m height, and interpolated using a triangulation-based natural neighbour algorithm, with a grid spacing of 0.1 m. Locations of grass and shrub elements are shown by white ellipses. Tree crown is shown as a dotted ellipse. Black circles represent anemometer locations. Downwind *h* for the tree is calculated using total tree height (trunk + crown). Lateral turbulence data are mirrored across the centreline of each element wake.

The spatial variations of normalised Reynolds shear stress ($-\overline{u'w'}_{norm}$) around the three elements are shown in Figure 5.6. The grass clump induced an area of high $-\overline{u'w'}_{norm}$ in its lee that was much wider than around the shrub (Figure 5.6c,d), and Reynolds shear stress was generally much lower around the shrub compared to the grass. Results presented in Figure 5.5 and Figure 5.6 suggest that by allowing a larger proportion of wind flow to bleed through its canopy, the shrub induced less intense turbulence in its immediate lee than the grass. However, the more significant bleed flow acted to disrupt the airflow further downwind (particularly evident for the $\overline{u'^2}_{norm}$ parameter). Peaks in $-\overline{u'w'}_{norm}$ were observed around 10 h_d from the grass (Figure 5.6a, b), which are explored further in relation to Figure 5.7 (see below). The tree did not appear to induce large turbulent variations at the surface along most of the wake, but an increase in $-\overline{u'w'}_{norm}$ at 8–10 h_d suggests that the turbulence impacts of the crown may be felt at the surface much further downwind due to its elevation. The interaction between slower-moving wind in the lee of the crown and the faster-moving, unobstructed wind beneath the crown was likely responsible for strong increases in $-\overline{u'w'}_{norm}$ recorded up to 1 h_d, as well as the strongly negative $-\overline{u'w'}_{norm}$ values in the tree's wake at 1.50 m height.

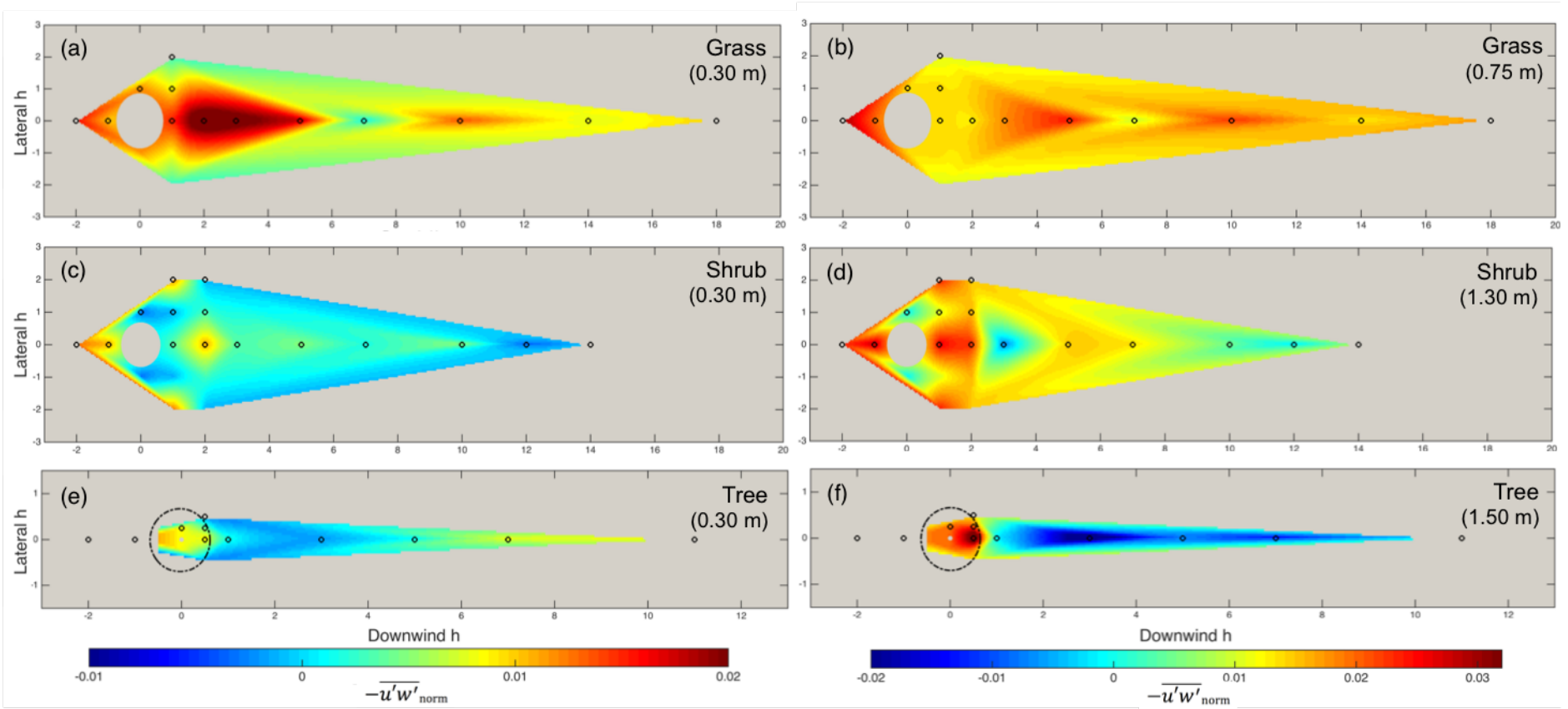


Figure 5.6 Horizontal spatial patterns of average normalised Reynolds shear stress ($-\overline{u'w'}_{norm}$) at 0.30 m and element height (1.50 m for tree) for: (a), (b) a grass; (c), (d) a shrub; and (e), (f) a tree. Data were normalised to $\overline{U}$ of an upwind reference anemometer at 0.30 m height, and interpolated using a triangulation-based natural neighbour algorithm, with a grid spacing of 0.1 m. Locations of grass and shrub elements are shown by white ellipses. Tree crown is shown as a dotted ellipse. Black circles represent anemometer locations. Downwind *h* for trees is calculated using total tree height (trunk + crown).

Elements protruding into a boundary layer topographically force the wind to move around them to greater or lesser extents, thus impacting wind streamline angles. Figure 5.7 displays streamline angle variations in the vertical (uw) plane along the centreline of the element wake, together with changes in Φ and $-\overline{u'w'}_{norm}$. Upwind of the grass and shrub, the streamlines became more positive as the wind was forced upwards above the elements, and decreased as the wind flowed over the top of the plants. The effect was more pronounced above the grass clump than the shrub, and the streamline angle became negative in the immediate lee of the grass. This is indicative of the formation of a small recirculation zone, which is expected to occur when low wind velocities in the immediate lee of a bluff element create a region of lower pressure that draws flow down and round towards its base (Hagen & Skidmore, 1971; Cornelis & Gabriels, 2005; Sutton & McKenna-Neuman, 2008; Lee et al., 2014). There was no evidence for a recirculation zone in the lee of the shrub.

At 0.30 m height in the case of the grass and the shrub (Figure 5.7a,c), $-\overline{u'w'}_{norm}$ tended to increase where flow acceleration was strongest (i.e. as Φ was recovering most rapidly in the leeside wakes). Thereafter, $-\overline{u'w'}_{norm}$ tended to decrease as acceleration to Φ = 1 was reduced. This pattern may be partly attributable to u' and w' peaks having a larger impact on shear stress calculations when average velocities are low. However, it is interesting to note that relatively large changes in turbulence occurred at the heights of both the grass and the shrub (Figure 5.7b,d), despite only minor corresponding changes in horizontal wind velocity. This suggests that peaks in turbulence at element height may result from different wind velocities at the surface and at element height driving a vertical exchange of small-scale turbulent eddies. In this way, surface turbulence in the lee of the elements is communicated upwards along the wake. Such a mechanism explains the simultaneous streamline angle increase at 0.30 m height and streamline angle decrease at the height of the elements in the flow recovery region (Figure 5.7). The smaller differences between

flow velocity at the height of the shrub and at the surface compared to the grass, resulted in less shear at the top of the shrub and thus a weaker streamwise momentum transfer within the mixing zone (Judd et al., 1996).

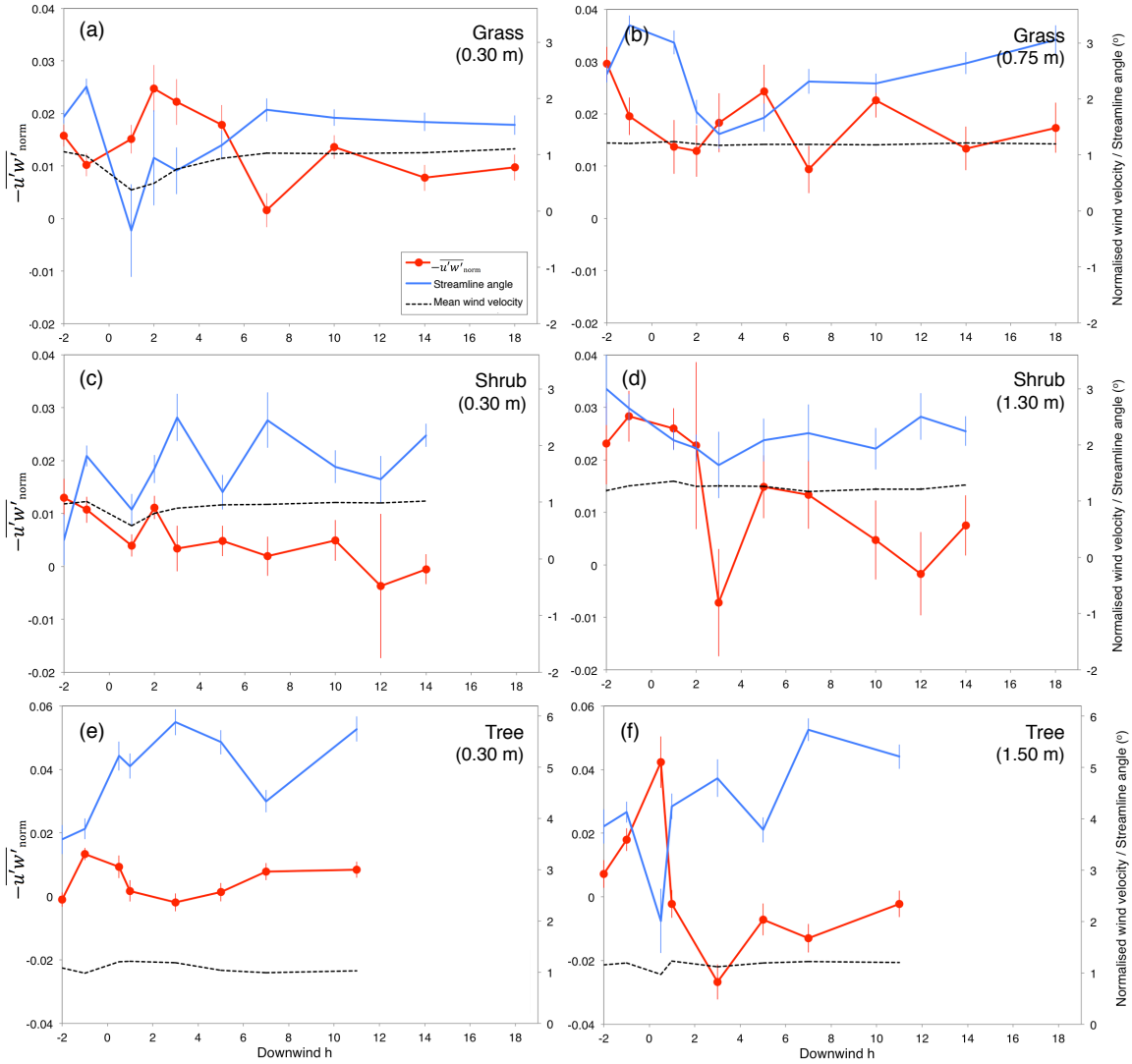


Figure 5.7 Variations in normalised Reynolds shear stress ($-\overline{u'w'}_{norm}$), vertical streamline angle and normalised mean wind velocity (Φ) at 0.30 m and height of elements (1.50 m for tree) along the centre-line of: (a), (b) a grass; (c), (d) a shrub; and (e), (f) a tree. Reynolds shear stress and wind velocity data were normalised to mean horizontal wind velocity measured upwind at 0.30 m height. Confidence intervals at the 95% level are shown as vertical bars. Downwind *h* for the tree is calculated using total tree height (trunk + crown).

In the case of the tree (Figure 5.7e,f), the streamline angle tended to increase with increasing downwind distance. However, there was a strong decrease in streamline

angle in the lee of the trunk at 1.50 m height, which indicates an incursion of downward moving air as wind flow was deflected by the underside of the crown. Such a deflection process could be responsible for the large Reynolds shear stress values recorded beneath the crown, as well as the decreased wind velocities observed at 1.50 m height (Figure 5.2f). The streamline angle also decreased around 5–7 h_d at both heights, which was likely due to the air displaced over the top of the tree moving downwards and reconnecting with the surface flow.

Clearly, the relationships between individual Reynolds stress components, flow de/acceleration and streamline angles around vegetation elements of differing porosities and configurations are complex. There is some evidence from Reynolds stress analysis that the bluff nature of the grass resulted in a more intense but less extensive impact on flow turbulence compared to the shrub. These differences may result from differential wind slowdown at the surface and at element height leading to varying intensities of vertical mixing and turbulent eddy exchange. However, it is difficult to separate the true covariance between u' and w' from the impact of flow velocity changes, as well as from topographically forced changes to the shape of the airflow. Future wind tunnel experimentation, using coloured smoke for instance, could clarify how airflow structure in and around plants of various porosities affect turbulent eddy exchange. This may help elucidate the complex relationships between the turbulence parameters analysed here. In order to segregate the stress budget between different structures in the flow around the elements in the context of this study, which in turn provides a way of assessing likely erosion and deposition zones, quadrant analysis (Lu & Wilmarth, 1973; see section 5.2.3) was conducted.

5.3.3. Coherent flow structures

Previous aeolian studies have highlighted the importance of the coherency, or structured nature, of turbulence in the context of plant canopies (e.g. Finnigan, 1979; Shaw et al., 1983; Yue et al., 2007) and dunes (e.g. van Boxel et al., 2004; Leenders et al., 2005; Chapman et al., 2012, 2013; Wiggs & Weaver, 2012). In the fluvial domain, a turbulent 'bursting process', whereby ejections (Q2) of low-velocity fluid from the wall region interact with sweeps (Q4) of high-velocity fluid towards the wall (Roy et al., 1999), has been shown to be a key determinant of sediment transport (Best & Kostaschuk, 2002). The bursting process can be identified using the flow exuberance (EX_{FL}), defined as the ratio of total occurrence of outward (Q1) and inward (Q3) interactions to Q2 and Q4 events (Shaw et al., 1983; Yue et al., 2007; Chapman et al., 2012). In effect, EX_{FL} expresses the ratio of negative to positive contributions to Reynolds stress generation. Whilst exuberance describes the skewness of quadrant plot distributions, it does not account for the magnitudes of u' and w' that constitute the individual quadrant events. In our study, the absolute value of the u' component for every occurrence of a given quadrant event ($\left|u'_{QX}\right|$) was averaged over the total measurement time at each location, and combined in the same ratio as flow exuberance. This provides a combined measure of the horizontal strength and occurrence of exuberance, EX_{MAG};

$$EX_{MAG} = \frac{\overline{\left|u'_{Q1}\right|} + \overline{\left|u'_{Q3}\right|}}{\overline{\left|u'_{Q2}\right|} + \overline{\left|u'_{Q4}\right|}} \tag{5.2}$$

Figure 5.8a,b shows the variation in EX_{MAG} along the centreline of the element wakes. EX_{MAG} values for the grass remained relatively steady (0.6–0.7) at both heights, signifying an overall dominance of the power of ejections (Q2) and sweeps

(Q4). At 0.30 m height in the case of the grass clump, EX_{MAG} was at its minimum at 1 h_d, supporting the notion that a small recirculation zone formed in the lee. A peak in EX_{MAG} at 7 h_d suggests that Q1 and Q3 events became more important around the region of flow equilibration. EX_{MAG} along the centreline of the shrub's wake was generally higher than for the grass at both heights, suggesting that the shrub acted to dampen the bursting process relative to the grass. In the case of the tree, EX_{MAG} declined at both heights around the trunk before peaking significantly at 3 h_d. The low exuberance observed around the trunk likely results from incursions of sweeps from within the tree crown, as previously reported in Large Eddy Simulation (LES) studies (e.g. Shen & Leclerc, 1997; Su et al., 1998; Yue et al., 2007). The EX_{MAG} peak at 3 h_d implies the presence of an upwelling region, which likely corresponds to the formation of a relatively large vortical structure. This arises in the wake of trees due to momentum differences between the flow funnelled beneath the crown (the bottom gap) and the flow in a low-pressure region in the lee of the crown (Lee et al., 2014). In this study, wind flow was not measured above 1.50 m and so the low-pressure region was not directly observed, but the existence of such a zone is likely given the low porosity (6%) of the tree crown. The occurrence of large EX_{MAG} peaks in zones of strongly negative $-\overline{u'w'}$ (Figure 5.6e,f, Figure 5.7e,f) confirms the presence of a counter-clockwise recirculation vortex in the wake of the tree (cf. Lee et al., 2014). Across all three elements, the $-\overline{u'w'}$ parameter was strongly negatively correlated with EX_{MAG} (R^2 = 0.943 at 0.30 m height and R^2 = 0.842 at 0.75 m height), because high Q1 and Q3 incidence is indicative of flow where u' and w' co-vary in the same relative direction.

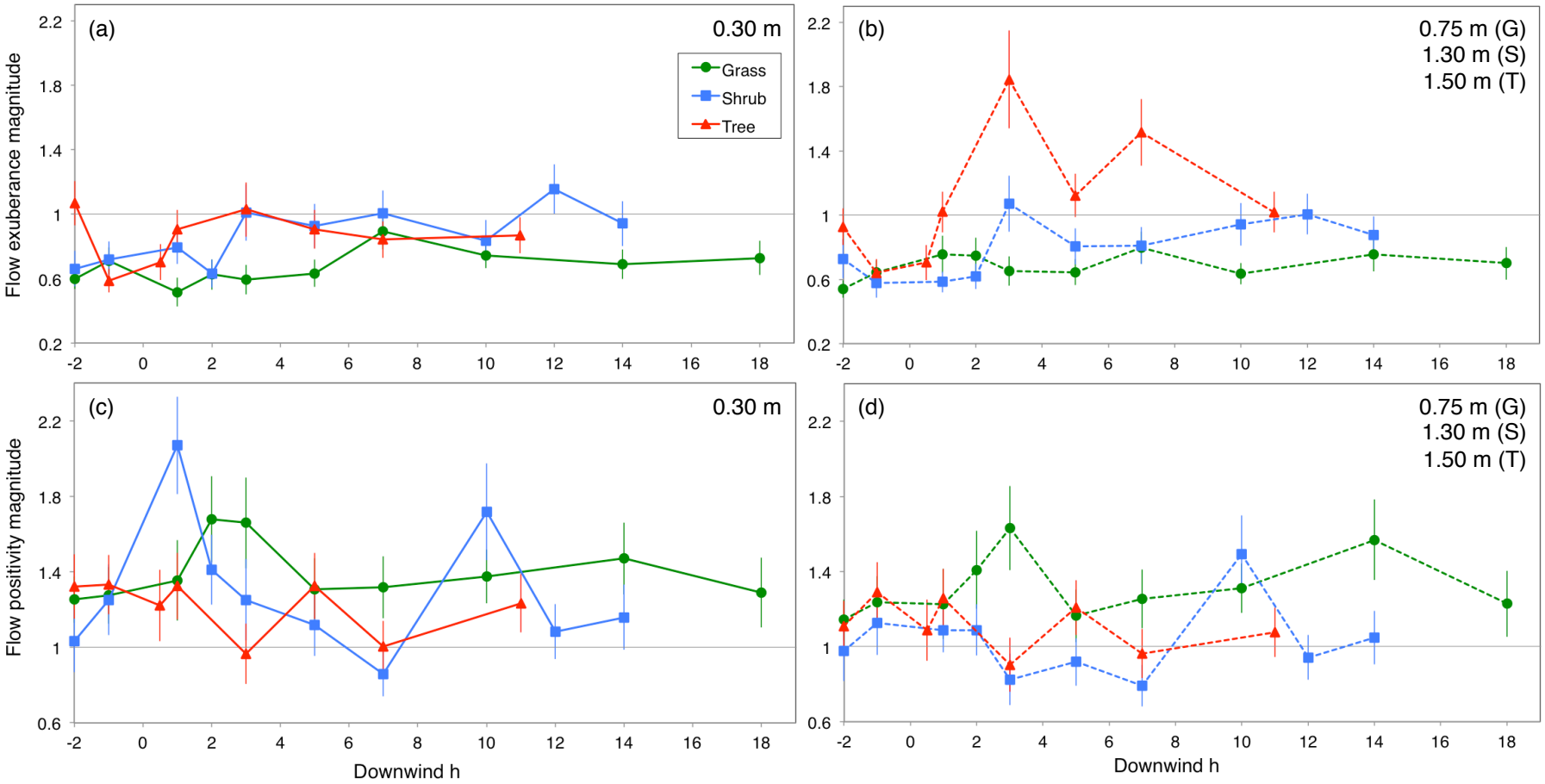


Figure 5.8 (a), (b) Horizontal magnitude of flow exuberance (EX_{MAG} = ($\overline{|u'_{Q1}|} + \overline{|u'_{Q3}|}$)/($\overline{|u'_{Q2}|} + \overline{|u'_{Q4}|}$)); and (c), (d) Horizontal magnitude of flow positivity (PO_{MAG} = ($\overline{|u'_{Q1}|} + \overline{|u'_{Q4}|}$)/($\overline{|u'_{Q2}|} + \overline{|u'_{3}|}$)), along the centreline of each element wake at 0.30 m and element height (1.50 m for tree). Confidence intervals at the 95% level are shown as vertical bars. Downwind *h* for the tree was calculated using total tree height (trunk + crown). Measurement heights are indicated in the top right corner of each panel.

Whilst the bursting process is well related to fluvial transport, there is increasing evidence (e.g. Sterk et al., 1998; Schönfeldt & von Löwis, 2003; van Boxel et al., 2004; Wiggs & Weaver, 2012; Chapman et al., 2013) that aeolian transport is better associated with turbulent structures characterised by a positive streamwise fluctuating velocity ($u' > 0$, Q1 and Q4). This may be due to the greater disparity in density ratio between particles and wind compared to water (Wiggs & Weaver, 2012). Similarly to EX_{MAG}, the horizontal magnitude of the overall 'positivity' of the flow, PO_{MAG}, can be defined as the ratio of the mean absolute u' for Q1 and Q4 events to Q2 and Q3 events:

$$PO_{MAG} = \frac{\overline{|u'_{Q1}|} + \overline{|u'_{Q4}|}}{\overline{|u'_{Q2}|} + \overline{|u'_{Q3}|}} \tag{5.3}$$

Flow positivity thus expresses the ratio of the strength of positive ($u' > 0$) to negative ($u' < 0$) contributions to streamwise velocity. Figure 5.8c,d shows the variation in PO_{MAG} along the centreline of the three element wakes. Flow positivity tended to be higher in the wake of the grass compared to the shrub, although at 1 h_d of the grass the small recirculation zone reduced the proportional incidence of Q1 and Q4 events. The peak in PO_{MAG} at 2–3 h_d of the grass (Figure 5.8c,d) is indicative of the strong positive component of the flow as it rapidly recovered behind the bluff element. In contrast, PO_{MAG} increased significantly in the immediate lee of the shrub at 0.30 m height, suggesting that Q2 and Q3 events were dampened as the flow bled through the plant body. Moreover, PO_{MAG} was significantly lower at the height of the shrub than at the surface. This difference in flow positivity across the two heights, which was absent in the case of the grass, resulted in momentum transfer being maintained much further downwind of the shrub than the grass. This explains the earlier peak in $\overline{u'^2}$ downwind of the grass (at 7 h_d; Figure 5a,b) compared to the shrub (at 10–12 h_d;

Figure 5c,d). Along the centreline of the tree's wake, PO_{MAG} values remained mainly above unity. The decrease in PO_{MAG} at 3 h_d from the tree likely corresponded to the reattachment of the counter-clockwise recirculation vortex in its wake, and the PO_{MAG} decline at 7 h_d probably resulted from airflow displaced over the tree crown moving downwards and reconnecting with the surface flow, thereby dissipating some of the wind's horizontal energy. Across all three elements, $-\overline{u'w'}$ was weakly correlated with PO_{MAG} (R^2 = 0.104 at 0.30 m height and R^2 = 0.162 at 1.30 m height), due to contributions of Q1 and Q4 events offsetting each other in Reynolds stress calculations (Weaver & Wiggs, 2011; Chapman et al., 2013)

This quadrant analysis shows that EX_{MAG} and PO_{MAG} patterns can be used to: (i) support the hypothesis that the bluff grass clump had a more intense but short-lived impact on flow turbulence than the shrub; (ii) confirm the existence of a recirculation zone in the lee of the grass; and (iii) identify the formation of a large vortical structure in the lee of the tree. The shrub generally dampened the bursting process (i.e. lower EX_{MAG}) and flow positivity (PO_{MAG}) to a greater extent than the grass, and induced lower $-\overline{u'w'}$, but it is not clear which of these turbulence parameters is appropriate for determining sediment transport potential. Whilst findings from dune-based studies imply that higher PO_{MAG} or $-\overline{u'w'}$ might act to increase transport (Wiggs et al., 1996b; Weaver & Wiggs, 2011; Chapman et al., 2012, 2013; Wiggs & Weaver, 2012), evidence from Leenders et al. (2007) suggests that areas of high turbulence intensity in plant wakes are not necessarily associated with greater erosion, because they tend to be located within low-velocity zones where the energy of the flow is simply not large enough to entrain sediment. It is therefore difficult to identify zones of potential sediment transport around vegetation elements based simply on one or more turbulence parameters. In all likelihood, the combined impact of an element on both the mean and turbulent properties of the wind should be considered to

adequately characterise the energy and variability of the flow at any point on a vegetated surface.

5.3.4. Shelter effect

Perera (1981) proposed Gandemer's (1979) 'shelter parameter' (ψ) to express the overall sheltering effect of a windbreak, taking into account both the speedup/slowdown of wind and its streamwise turbulence. The parameter was later modified by Kim & Lee (2002) and Lee et al. (2014) to include the w' component. However, vertical velocity variations in natural wind flow are roughly an order of magnitude smaller than the horizontal components (Sterk et al., 1998), and the w' component has been shown to be poorly correlated with aeolian sediment transport (Schönfeldt & von Löwis, 2003; Leenders et al., 2005; Wiggs & Weaver, 2012), so Gandemer's (1979) original formulation for ψ is used:

$$\psi = \frac{\left(|\overline{U}| + \sqrt{\overline{u'^2}}\right)}{\left(\overline{U}_{ref} + \sqrt{\overline{u'^2}_{ref}}\right)} \tag{5.4}$$

By combining the salient features of horizontal turbulent wind flow, the shelter parameter (ψ) provides a method of simultaneously accounting for the mean energy of the flow (i.e. $\overline{U}$) and the deviations away from it ($\overline{u'^2}$). $\overline{u'^2}$ is used to characterise turbulence instead of the Reynolds shear stress ($-\overline{u'w'}$) because it better accounts for the streamwise variability that is thought to drive sediment transport in aeolian environments (e.g. Weaver & Wiggs, 2011). In the formulation above, lower ψ values correspond to a greater sheltering effect, and vice versa.

The spatial variation of ψ at 0.30 m height is shown in Figure 9. The grass induced a more intense sheltering zone in its lee than the shrub, which extended further downwind and laterally. These observations are statistically significant at the 95% level, given the distinct lack of overlap between the confidence bars of the grass and shrub curves in the immediate lee (Figure 9a). This implies that sediment transport for a given approach wind velocity will tend to be lower in the wake of the grass compared to the wake of the shrub, even though full wind velocity recovery occurs at approximately the same distance downwind of both elements.

From 7 h_d of both the grass and shrub, a zone of increased ψ – and thus increased transport potential – was observed where the mixing layer intersected with the ground surface (cf. Judd et al., 1996). This region was more extensive in the case of the shrub than the grass. The apparent 'overshoot' above ψ = 1 may result from counter-rotating vortices induced by the elements creating a zone of elevated surface stress (Sutton & McKenna-Neuman, 2008; Burri et al., 2011), which corresponds to the wind speedup observed at the sides of the shrub (Figure 5.2c). Walter et al. (2012b) posited that the pliable nature of grassy plants results in grass clumps having a reduced sheltering effect at high wind speeds, due to a narrowing of the lee-side wake and suppression of horseshoe vortices. The results presented here suggest that the bluff nature of the grass clump offsets this potential narrowing at the observed wind velocities, inducing a greater sheltering effect than a less pliable woody shrub. However, the shelter parameter had not recovered to unity by 18 h_d in the grass case and 14 h_d in the shrub case, suggesting flow was still being affected by the elements at these distances downwind.

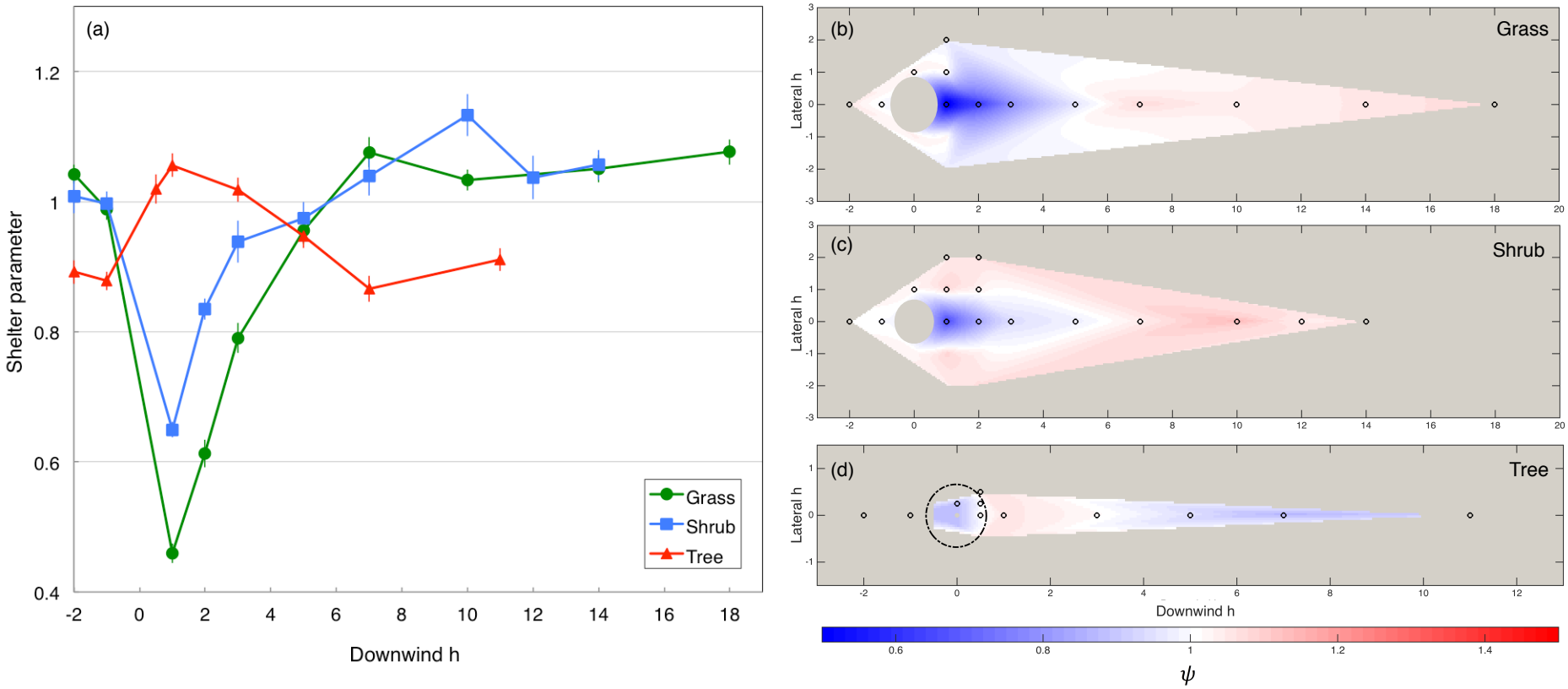


Figure 5.9 (a) Variations in the shelter parameter (ψ) along the centreline of the three element wakes at 0.30 m height. 1-sigma error bars are shown; (b), (c), (d) Horizontal spatial patterns of ψ around a grass, shrub and tree at 0.30 m height. Data were interpolated using a triangulation-based natural neighbour algorithm, with a grid spacing of 0.1 m. Locations of grass and shrub elements are shown by white ellipses. Tree crown is shown as a dotted ellipse. Black circles represent anemometer locations. Downwind *h* for trees is calculated using total tree height (trunk + crown). Lateral turbulence data are mirrored across the centreline of each element wake.

In the case of the tree, there was a slight sheltering effect upwind of the trunk, but the general impact of the trunk and crown between 0.5 h_d and 3 h_d was to drastically decrease sheltering at the surface, primarily because of wind speedup linked to the bottom gap effect. This zone is therefore characterised by the highest sediment transport potential. Localised wind speedup around the trunk, which was not observed in the wind data but was inferred from a small topographical depression around the base of the trunk, also leads to increased localised erosion (Leenders et al., 2007). From 3 h_d, where the frontal impact of the crown was increasingly felt at the surface, the tree sheltered the surface for at least eight tree heights.

While grasses and shrubs may trap sediment more readily than tall trees thanks to their low hanging branches and blades (Raupach et al., 2001; Davdison-Arnott et al., 2012), this study supports previous findings (Leenders et al., 2007; Dupont et al., 2014) that despite wind speedup resulting from a bottom gap, an elevated tree canopy extracts horizontal momentum from the air in such a way that a more extensive sheltering effect occurs downwind. Therefore, incorporating a parameter such as ψ that emphasises multiple salient features of horizontal turbulent flow, rather than relying entirely on wind velocity, may provide a better indicator of erosion potential around plants.

5.4. Conclusions

Results from this study show that dryland grass, shrub and tree elements impact turbulent wind flow in differing ways. Wind velocity was reduced by 70% in the immediate lee of the grass clump and 40% in the lee of the shrub, but velocity recovered exponentially to equilibrium by ~9 h_d in both cases. This is comparable to the recovery lengths reported in previous studies for single elements. However,

comparisons with existing models of wind recovery based on wind fence data (Hagen, 1996; Okin, 2008) suggest that wind flow downwind of three-dimensional, partially bluff elements cannot be suitably parameterised using two-dimensional analogues. Instead, a flow recovery curve of the form $ae^{-bx}+c$ produces a closer match with the field data in this study and with the empirically derived model of Leenders et al. (2011).

Despite the similar recovery distances of the grass and shrub, the bluff nature of the grass clump (53% porosity) induced more intense wind slowdown in its lee than the shrub (69% porosity). Bleed flow through the shrub was more significant than the grass, resulting in smaller differences between flow velocity at the surface and at the height of the shrub. This in turn led to lower shear stress and weaker vertical and streamwise exchange of small-scale turbulent eddies in the mixing zone of the shrub. The shrub therefore disrupted the airflow less intensely, but over a greater distance than the grass clump, as shown for the $\overline{u'^2}$ parameter. This supports previous findings (Skidmore & Hagen, 1970; Perera, 1981) that low-porosity elements induce turbulence in their lee but allow flow to recover to upstream conditions sooner than more porous elements. While the shrub generally dampened the bursting process (high ejection (Q2) and sweep (Q4) activity) and induced lower $-\overline{u'w'}$ than the grass, these turbulence parameters may not be wholly appropriate for determining sediment transport due to the contradictions inherent to their calculation (Weaver & Wiggs, 2011; Chapman et al., 2013). Instead, a parameter that emphasises the salient features of horizontal turbulent flow such as the shelter parameter (ψ) may provide a better indicator of erosion potential around plants. Spatial analysis of ψ in this study suggests that sediment transport potential is lower in the protective wake of the grass clump than in that of the shrub.

The tree produced a different wake structure to the grass clump and shrub, on account of its elevated canopy. The recovery of wind velocity downwind of the tree was best described using a logistic function ($a+((b-c)/(1-e^{x-d}))$) due to a 'bottom gap' effect (Ruck & Schmitt, 1986; Kim & Lee, 2002; Dupont et al., 2014), whereby wind speeds up due to streamline compression in the gap between the ground and the underside of the tree crown. Differences in momentum arising between the flow funnelled through the bottom gap and the flow in the low-pressure leeward region are a probable explanation for the formation of a large recirculation vortex in the wake of the tree at ~3 h_d. The bottom gap effect led to decreased sheltering beneath the crown and up to $3h_d$, but the surface became increasingly sheltered by the frontal impact of the crown over a further eight tree heights (~30 m) at least. Whilst trees are not capable of trapping saltating particles due to the height of their crowns, the extraction of momentum from the air by their elevated canopies could result in a far more extensive sheltering effect compared to grasses and shrubs.

This study provides important insights into the impacts of different vegetation types on turbulent wind flow. By characterising the effects of key dryland plant types on local wind patterns, we build on existing parameterisations to provide a better constraint on the sheltering effects of vegetation. Since shifts in vegetation structure relating from environmental and anthropogenic stresses such as grazing, fire and climatic change have the potential to significantly impact sediment mobility in semi-arid regions, it is vital improve our understanding of the aerodynamic behaviour of common dryland plant types. The new high-frequency data presented in this study can be integrated into robust, spatially explicit models of sediment transport and landscape change. This will contribute to answering key questions, at meaningfully large scales, about how semi-vegetated desert surfaces may respond to future environmental and anthropogenic stresses.

Summary: Paper 1

Paper 1 focused on evaluating turbulent wind flow at a high spatial and temporal scale around three individual plants. It showed that dryland grass, shrub and tree elements impact turbulent wind flow in differing ways. The bluff nature of the grass induced more intense wind slowdown in the lee than the shrub, although the bleed flow through the shrub resulted in a longer overall recovery distance. This supports previous findings that low-porosity elements allow flow to recover to upstream conditions sooner than more porous elements. The tree induced some speedup under its canopy due to a 'bottom gap' effect.

Coherent flow structures, which provide information on the stress budget of disrupted flow, were used to define instances of 'flow positivity' and a 'flow exuberance' in the flow around the elements. By combining information from flow positivity and exuberance, plant-scale turbulent structures could be identified. However, it was difficult to make conclusive statements about the impact of turbulent structures on likely erosion/deposition zones around the vegetation elements. Analysis of a shelter parameter (ψ), which emphasises the salient features of horizontal turbulent flow, suggested that sediment transport potential may be lower in the wake of the grass clump than in that of the shrub.

This study represents an important stepping stone for parameterising wind flow behaviour around individual plants, which is necessary for the spatially explicit modelling approach developed later in this thesis. However, detailed characterisation of wind flow in the lee of vegetation patches, which impact flow different to single elements, is still lacking in a field context. Paper 2 therefore seeks to fill this gap.

CHAPTER SIX


flow
wind
patch
height
sediment
velocity
stress
surface
shear
downwind
Research
Surface
Wiggs
recovery
wake
Lee
lee
erosion
Earth
Bowel
Baas
Sterk
Gillies
Bauer
Desert
Aeolian
Boundary
Fluid
Layer
Field
King
Von
York
Mean
Dunes
2012
REF
SEQ
Gaussian
anemometer
Research
Surface
elements
structures
turbulence
events
using
average
increasing
around
likely
plant
sand
tunnel
shown
lower
upwind
greater
desert
edge
region
vertical
model
setup
driving
impact
velocities
increased
transect
function
presence
normal
plants
fences
response
curves
Chapman
Usgsf
along
models
fence
drag
canopy
order
based
effect
Dreshaers
Wasson
Ohio
Hasan
Kim
Sherman
Bagnold
relative
measured
provides
mobility
cover
bare
sonic
change
porous
Flow
Bauer
Bradley
Hanna
Nickling
Namikas
Sherman
Walker
Wilson
Wiggs
Gillies
Baas
Sterk
Chapman
Boxel
Earth
Lee
Von
York
Mean
Dunes
2012
REF
SEQ
Gaussian
anemometer
Research
Surface
elements
structures
turbulence
events
using
average
increasing
around
likely
plant
sand
tunnel
shown
lower
upwind
greater
desert
edge
region
vertical
model
setup
driving
impact
velocities
increased
transect
function
presence
normal
plants
fences
response
curves
Chapman
Usgsf
along
models
fence
drag
canopy
order
based
effect
Dreshaers
Wasson
Ohio
Hasan
Kim
Sherman
Bagnold
relative
measured
provides
mobility
cover
bare
sonic
change
porous
Flow
Bauer
Bradley
Hanna
Nickling
Namikas
Sherman
Walker
Wilson

Dynamics of skimming flow in the wake of a vegetation patch

Paper 2: Mayaud, J. R., Wiggs, G. F. S. & Bailey, R. M.
Status: published in *Aeolian Research, 22*, 141–151 (2016)

Abstract
Dryland vegetation is often spatially patchy, and so affects wind flow in complex ways. Theoretical models and wind tunnel testing have shown that skimming flow develops above vegetation patches at high plant densities, resulting in little or no wind erosion in these zones. Understanding the dynamics of skimming flow is therefore important for predicting sediment transport and bedform development in dryland areas. However, no field-based data are available describing turbulent airflow dynamics in the wake of vegetation patches. In this study, turbulent wind flow was examined using high-frequency (10 Hz) sonic anemometry at four measurement heights (0.30 m, 0.55 m, 1.10 m and 1.65 m) along a transect in the lee of an extensive patch of shrubs (z = 1.10 m height) in Namibia. Spatial variations in mean wind velocity, horizontal Reynolds stresses and coherent turbulent structures were analysed. We found that wind velocity in the wake of the patch effectively recovered over ~12 patch heights (h) downwind, which is 2–5 h longer than previously reported recovery lengths for individual vegetation elements and two-dimensional wind fences. This longer recovery can be attributed to a lack of flow moving around the obstacle in the patch case. The step-change in roughness between the patch canopy and the bare surface in its wake resulted in an initial peak in resultant horizontal shear stress (τ_r) followed by significant decrease downwind. In contrast to τ_r, horizontal normal Reynolds stress ($\overline{u'^2}$) progressively increased along the patch wake. A separation of the upper shear layer at the leeside edge of the patch was observed, and a convergence of τ_r curves implies the formation of a constant stress layer by ~20 h downwind. The use of τ_r at multiple heights is found to be a useful tool for identifying flow equilibration in complex aerodynamic regimes. Quadrant analysis revealed elevated frequencies of Q2 (ejection) and Q4 (sweep) events in the immediate lee of the patch, which contributed to the observed high levels of shear stress. The increasing downwind contribution of Q1 (outward interaction) events, which coincides with greater $\overline{u'^2}$ and wind velocity, suggests that sediment transport potential increases with greater distance from the patch edge. Determining realistic, field-derived constraints on turbulent airflow dynamics in the wakes of vegetation patches is crucial for accurately parameterising sediment transport potential in larger-scale dryland landscape models. This will help to improve our understanding of how semi-vegetated desert surfaces might react to future environmental and anthropogenic stresses.

This chapter addresses **Objective 2** (to measure wind flow at the patch scale in the wake of a vegetation patch experiencing skimming flow). **Methods**: sonic anemometers, vegetation transects.

This chapter is a modified version of the paper by Mayaud et al. (2016c). The Introduction section of the paper has been shortened, to avoid repetition of material provided in Chapter 2 of this thesis.

6. Dynamics of skimming flow in the wake of a vegetation patch

6.1. Introduction

The extreme nature of drylands means that semi-arid vegetation is often patchy and dynamic through time and space, due to complex relationships between plants, soil and transport processes (see section 2.2). The impact of patchy dryland vegetation on the erosivity of the wind depends on the type of flow regime it induces (Wolfe & Nickling, 1993). When isolated roughness elements populate the surface (< 16% cover; Wolfe & Nickling, 1993), each plant sheds turbulent eddies by diverting windflow around and above each plant (Judd et al., 1996; Sutton & McKenna-Neuman, 2008; Suter-Burri et al., 2013; Lee et al., 2014). This increases drag, thus raising shear stress and the aerodynamic roughness (z_0), and potentially enhancing erosion locally (Ash & Wasson, 1983). In wake-interference flow (c. 16–40% cover; Wolfe & Nickling, 1993), the increased drag and thus shear stress resulting from the presence of multiple elements may only be partly absorbed by the plants themselves, resulting in stress transference to the inter-canopy surface and potentially greater sediment transport (Breshears et al., 2009; Dupont et al., 2014). In the case of skimming flow (> ~40% cover; Wolfe & Nickling, 1993), the increased drag from the vegetation acts to displace z_0 upwards (establishing a zero-plane displacement height, d), which simultaneously extracts momentum from the surface wind and increases wind shear stress above the canopy (e.g. Wasson & Naninga, 1986; Wiggs et al., 1994; Gillies et al., 2002; Gillette et al., 2006). The absorption of additional stresses by the plants therefore decreases the erosion potential at the surface.

The recovery of wind in the wakes of substantial vegetation patches, where skimming flow is in operation, are poorly studied, excepting some wind tunnel studies

(e.g. Burri et al., 2011; Youssef et al., 2012; Suter-Burri et al., 2013) and a few field and modelling studies of forest edges (e.g. Gash, 1986; Liu et al., 1996; Frank & Ruck, 2008). Belcher et al. (2003) provided a useful model for describing the adjustment of a turbulent boundary layer to the step-change in surface roughness represented by a forest patch, focusing mainly on the above-canopy zone. Wind tunnel and modelling experiments have also been conducted to understand flow behaviour around backward-facing steps (e.g. Le et al., 1997; Wengle et al., 2001), although these configurations often have more extensive low-velocity zones and delayed reattachment points compared to vegetated cases due to their almost parallel-to-wall streamlines. To our knowledge no field-based study has characterised turbulent flow recovery in the wake of a real dryland vegetation patch.

A wind erosion model presented by Okin (2008) recognises the inherent irregularity of vegetation patterning in drylands, and emphasises the controlling influence of the size of ‘gaps’ or ‘corridors’ in the vegetation structure. The Okin model assumes that plants are porous objects, such that surface shear velocities in the wake of plants can be greater than zero and recover asymptotically. Whilst the Okin model shows good agreement with aeolian sand flux data at the plant/patch scale (Li et al., 2013; Sankey et al., 2013), its parameterisation of shear stress recovery downwind of a vegetated patch is based on two-dimensional wind fence and drag plate data from Bradley & Mulhearn (1983). In reality, two-dimensional fences represent a far simpler aerodynamic problem than three-dimensional live plants (Leenders et al., 2007), yet robust field data on the aerodynamic impact of vegetation patches is still lacking.

This study therefore aims to collect field-based, empirical data on the recovery of turbulent wind flow in the lee of a live, three-dimensional vegetation patch. Improved parameterisations of flow turbulence and sediment transport potential in vegetation patches in large-scale dryland landscape models are key for enhancing current

understanding of how semi-vegetated desert surfaces might react to future environmental and anthropogenic changes.

6.2. Methods

6.2.1. Field site

The field study was carried out in the southwestern Kalahari Desert in Namibia (Figure 6.1), ~4 km north of the Auob River (25°29'15" S, 19°40'35" E). The experimental site was located in a farmer's field on raised, flat terrain populated mainly by *Stipagrostis amabilis* grasses and *Rhigozum trichotomum* shrubs. The patch of vegetation chosen for this study was made up of dense grass and shrub cover separated from a non-vegetated area by a short, highly permeable wire fence. The vegetation patch on the upwind side was approximately 70 m x 70 m, with a mean surface cover of ~80 %, a mean height of 1.10 m and a standard deviation of 0.11 m (large shrubs) and 0.08 m (grasses). Mean surface cover and height were assessed by recording the height and canopy width of each plant within nine 4 m^2 quadrats placed at random locations within the patch. Heavy grazing on the downwind side of the cattle fence had resulted in a distinct patch of reduced vegetation cover, which was raked to clear any remaining nonerodible elements for the purposes of the experiment (Figure 6.1b).

6.2.2. Experimental setup

Three 3D sonic anemometers (*Campbell CSAT-3*) were deployed at the study site to collect wind velocity data (u, horizontal; v, spanwise; and w, vertical) at a sampling frequency of 10 Hz. A mobile anemometer array (Figure 6.1c) was erected with two

sonic anemometers fixed onto a mobile steel mast to allow the array to be moved along a transect downwind of the patch edge, in two setups. In setup 1, the anemometers were mounted at heights of 0.30 m and 1.10 m. A height of 0.30 m corresponds to a balance between capturing turbulence that occurs close to the surface, whilst minimising the interference of saltating sand with the sonic measurement path (Weaver & Wiggs, 2011). A height of 1.10 m corresponds to the average element height (1 h) of the vegetation patch. In setup 2, the anemometers were erected at heights of 0.55 m and 1.65 m, representing 0.5 h and 1.5 h of the average patch height respectively. The downwind distance from the patch edge, in terms of average patch height, is referred to as 'h_d'. The mobile array was progressively moved downwind from the patch edge, such that wind velocity was recorded at all four heights at six locations: 1 h_d, 4 h_d, 7 h_d, 11 h_d, 15 h_d and 20 h_d.

A third anemometer was mounted at 1.40 m height (mean patch height + 0.30 m) and placed 8 h (8.80 m) upwind and 30 h (33.0 m) to the side of the measurement transect. By being located above the vegetation patch to capture the skimming flow at the same relative height as the near-surface measurements in the patch wake (i.e. 0.30 m height), this third anemometer provided reference wind data against which the mobile anemometry data could be normalised. Figure 6.1d demonstrates that this reference reflected an undisturbed measurement of uniform flow over the patch. The anemometers were all aligned parallel with the prevailing wind direction and level in the horizontal plane. To ensure sufficient data were acquired for subsequent analysis, each setup was run for a minimum of 20 minutes.

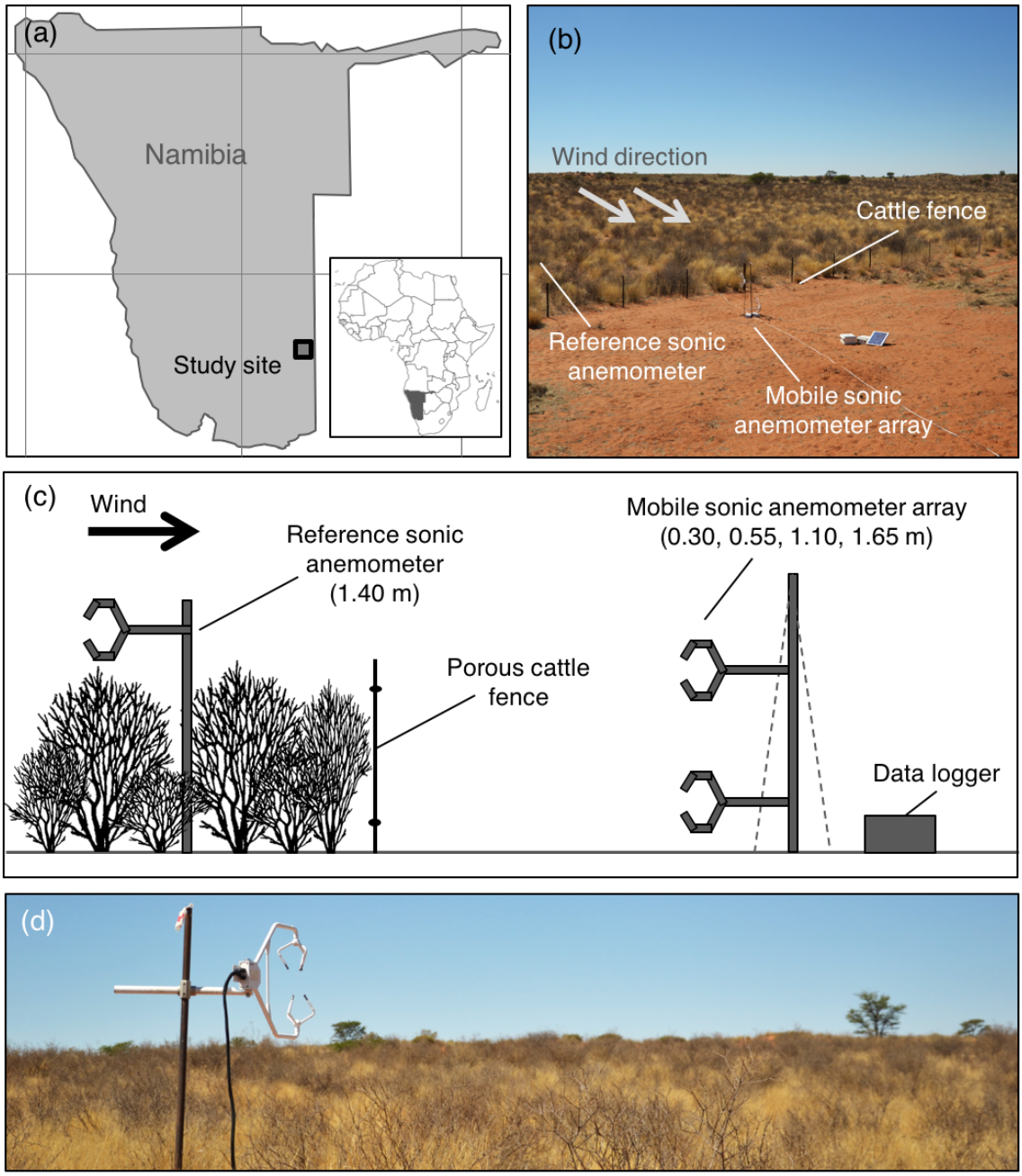


Figure 6.1 (a) Location map of the field site in the southwestern Kalahari Desert; (b) photograph of the experimental setup downwind of the vegetation patch; (c) schematic diagram of the experimental setup (not to scale); (d) close-up of the reference anemometer.

6.2.3. Data analysis

Mean approach wind velocities as measured by the reference anemometer during each measurement setup ranged from 2.57 m s^{-1} to 3.70 m s^{-1}. In order to ensure

that the airflow detected at each measurement location had interacted with roughly the same length of upwind patch (~70 m), the datasets were filtered to exclude approach wind directions > 5^{o} from the mean wind direction throughout the course of the experiment (cf. Mayaud et al., 2016b). Following the application of the 5^{o} threshold filter, the remaining datasets for each setup were 5.5–15.0 minutes long, which is in accordance with the recommendations of van Boxel et al. (2004) for capturing the full range of turbulent eddies to accurately represent boundary layer processes. Since Reynolds stress calculations are somewhat dependent on the interval length used, calculations from 5.5-minute subsets of longer measurement runs were compared to those derived from the full run periods. Results did not vary by more than ±1.3%. All wind flow parameters were normalised by the appropriate measurement recorded simultaneously by the upwind reference anemometer at 1.40 m height. Normalisation is indicated using the '*norm*' subscript for each parameter.

The sonic anemometer data were post-processed to correct for any minor errors in aligning the anemometer heads into the mean approach wind flow. The streamwise frame of reference was rotated in accordance with the local streamline angle using yaw rotation (cf. van Boxel et al., 2004; Walker, 2005; Weaver & Wiggs, 2011; Chapman et al., 2012). Subsequent to yaw rotation correction the average spanwise velocity was zero ($\overline{V}$ = 0), and so no further analysis of this component was undertaken. There is much discussion in the literature (e.g. Lee & Baas, 2012) about the necessity to correct for pitch in sonic anemometer datasets, which forces the average vertical velocity to zero ($\overline{W}$ = 0). The purpose of this study is to characterise the behaviour of wind flow horizontal to the surface, rather than along the plane of the streamlines, so pitch rotation was omitted here. The application of roll rotation remains disputed practice for three-dimensional flow over non-uniform terrain (Kaimal & Finnigan, 1994; Lee & Baas, 2012), but the need for such a rotation is

obviated by accounting for the spanwise flow component when calculating shear stress (see Equation 4.4).

The remaining velocity data were decomposed into their average ($\overline{U}, \overline{V}$ and $\overline{W}$) and fluctuating (u', v' and w') components, from which the horizontal ($\overline{u'^2}$) and vertical ($\overline{w'^2}$) components of Reynolds stress were derived. The resultant horizontal shear stress (τ_r), which is a more robust estimate of the total shearing force acting on the surface than the traditionally-employed Reynolds shear stress (τ , or $-\overline{u'w'}$), was calculated using both the streamwise and spanwise shear (Lee & Baas, 2012):

$$\tau_r = (\overline{u'w'}^2 + \overline{v'w'}^2)^{1/2} \tag{6.1}$$

The local near-surface wind streamline angles along the wake transect were calculated as:

$$\theta = \arctan\left(\frac{\overline{W}}{\overline{U}}\right) \tag{6.2}$$

From these parameters, the incidence of coherent structures in the flow was established using conditional-sampling quadrant analysis (Lu & Willmarth, 1973). This technique defines four discrete categories of momentum exchange based on the relative signs of u' and w'. Ejections (Q2 events; $u' < 0$, $w' > 0$) and sweeps (Q4; $u' > 0$, $w' < 0$) contribute positively to the production of Reynolds stress, while outward interactions (Q1; $u' > 0$, $w' > 0$) and inward interactions (Q3; $u' < 0$, $w' < 0$) contribute negatively to Reynolds stress (Smith, 1996). In order to isolate significant bursts of turbulent stress from weaker background variability (Lapointe, 1992; Clifford

& French, 1993), stress events of low magnitude were removed from quadrant analysis using a threshold criterion (*H*). Following previous studies (Bauer et al., 1998; Sterk et al., 1998; Leenders et al., 2005; Weaver, 2008; Wiggs & Weaver, 2012, Mayaud et al., 2016b), the size of *H* was chosen to be equivalent to one standard deviation (σ) of the resultant horizontal shear stress (τ_r), such that a flow structure was only classified if $\tau_r > \pm H.\ \tau_r$.

95% confidence intervals for the resultant horizontal shear stress ($\tau_{r_{CI}}$) and horizontal normal Reynolds stress ($\overline{u'^2}_{CI}$) were established using the standard error of the mean around the relevant parameters (adapted from Lee & Baas, 2016):

$$\tau_{r_{CI}} = 1.96\sqrt{\left(\frac{\sigma_{u'w'}}{\sqrt{N}}\right)^2 + \left(\frac{\sigma_{v'w'}}{\sqrt{N}}\right)^2} \tag{6.3}$$

$$\overline{u'^2}_{CI} = 1.96\sqrt{\left(\frac{\sigma_{u'^2}}{\sqrt{N}}\right)^2} \tag{6.4}$$

where N is the sample size. For normalised parameters, the total confidence interval for each data acquisition was calculated by summing the confidence intervals for both the local and reference shear stress parameters.

Shear velocity (u_*) can be related directly to the turbulent momentum flux (Walker, 2005; Lee & Baas, 2016):

$$u_* = (\overline{u'w'}^2 + \overline{v'w'}^2)^{1/4} \tag{6.5}$$

This relationship is important because it allows the aerodynamic roughness length (z_0) to be characterised using sonic anemometer datasets at single heights, without the need for a full velocity profile to be measured at multiple heights. The logarithmic profile for the inertial sublayer follows the 'Law of the Wall' (see King et al., 2005), which can be described by the Karman-Prandtl velocity distribution:

$$\frac{u_z}{u_*} = \frac{1}{\kappa} \ln \frac{z_i}{z_0} \tag{6.6}$$

where u_z is the mean wind speed at height z_i (m), and κ is the von Karman constant (dimensionless) equal to 0.4. By rearranging Equation 6.6 and substituting τ_r for u_* (Equation 6.5), z_0 can be estimated directly from the resultant horizontal shear stress at a single height:

$$z_0 = \frac{z_i}{e^{\kappa \frac{u}{\sqrt{\tau_r}}}} \tag{6.7}$$

The Law of the Wall is only valid in cases where the internal boundary layer is in equilibrium with the surface roughness (King et al., 2005). Therefore, the analysis based on Equation 6.6 and Equation 6.7 is only applied to data collected above the vegetation patch (where the skimming flow is considered in equilibrium with the patch roughness), and sufficiently far downwind of the reattachment point in the lee of the patch, where the internal boundary layer has grown in equilibrium with the desert surface.

In summary, our sonic anemometer data were employed to calculate variations in mean wind velocity, turbulent stresses, and coherent structures above and downwind

of the vegetation patch. Mean wind velocity changes allow simple interpretations of wind flow recovery to be made, whilst turbulence parameters and coherent structures provide a more detailed picture of how the airflow structure varies at different points along the flow trajectory. In conjunction with aerodynamic roughness calculations made in zones where flow has equilibrated, these turbulence data can be used to identify the growth of an internal boundary layer, which has previously been shown to develop downwind of a step-change in roughness.

6.3. Results

6.3.1. Mean wind velocity

Figure 6.2 displays the spatial patterns of mean normalised wind velocity (Φ) downwind of the patch. Normalised wind velocities at each measurement location were interpolated using a triangulation-based natural neighbour algorithm, with a grid spacing of 0.1 m. The algorithm was chosen because it produced realistic spatial features that were present using several other commonly used interpolation algorithms, and without obvious artefacts. Since the reference anemometer was placed at 1.40 m height, normalised velocities are expected to stabilise below Φ = 1.0 at the lowest measurement heights in the patch wake.

The contour plot (Figure 6.2a) shows a distinct region of lower wind velocity (Φ < 1.0) near the surface (< ~0.7 h) until ~6 h_d. At average patch height (i.e. 1 h) and above, there was a region of lower wind velocity from 0–12 h_d, followed by a marked zone of increased velocity (Φ > 1.0) from 14–20 h_d. These differences relative to the reference anemometer likely result from the expansion of the wind flow into the gap in the lee of the patch, and from the different roughness represented by the patch compared to the bare surface in its wake; these points are explored further in relation

to Figure 6.3. The semi-logarithmic vertical profiles of Φ at each measurement location (Figure 6.2b) were noticeably kinked up to a distance of 15 h_d, suggesting that airflow was disrupted, with a large amount of retardation near the surface, to at least this distance downwind of the patch edge.

Figure 6.3 displays the best-fit normalised mean wind velocity curves (Φ) in the patch wake. The data at the four measurement heights were fitted using a saturating exponential function because this generally describes the recovery of wind flow downwind of an obstruction (Bradley & Mulhearn, 1983). Also presented is the recovery rate published by Okin (2008, corrected in Li et al., 2013) for parameterising surface shear stress downwind of a plant, based on the wind fence and drag plate data of Bradley & Mulhearn (1983).

The curves at 0.30 m and 0.55 m height were similar in shape, recovering to ~90% of their exponential saturation values (deemed to represent effective flow recovery; Okin, 2008) at 12–13 h_d. In comparison, Okin's (2008) curve recovers more quickly at ~10 h_d, and reported windflow recovery distances downwind of solitary elements are between 7–9 h_d (Leenders et al., 2007; Gillies et al., 2014; Wu et al., 2015; Mayaud et al., 2016b). The recovery curves at 1.10 m and 1.65 m height were much shallower than at 0.30 m and 0.55 m height due to a smaller initial leeside reduction in wind velocity.

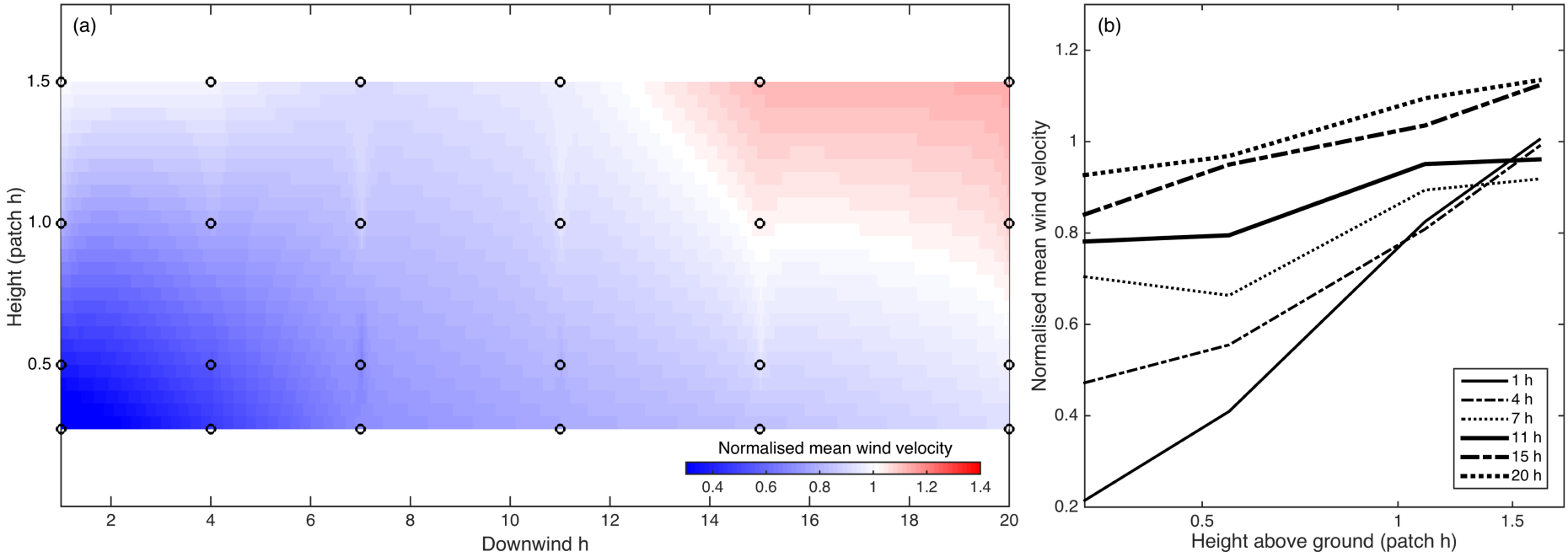


Figure 6.2 (a) Contour plot of normalised mean wind velocity (Φ) at all measurement locations (in terms of patch height, *h*) downwind of the patch. Black circles represent anemometer locations; (b) Vertical profile of Φ at the six measurement locations along the wake transect (note that x axis is logarithmic).

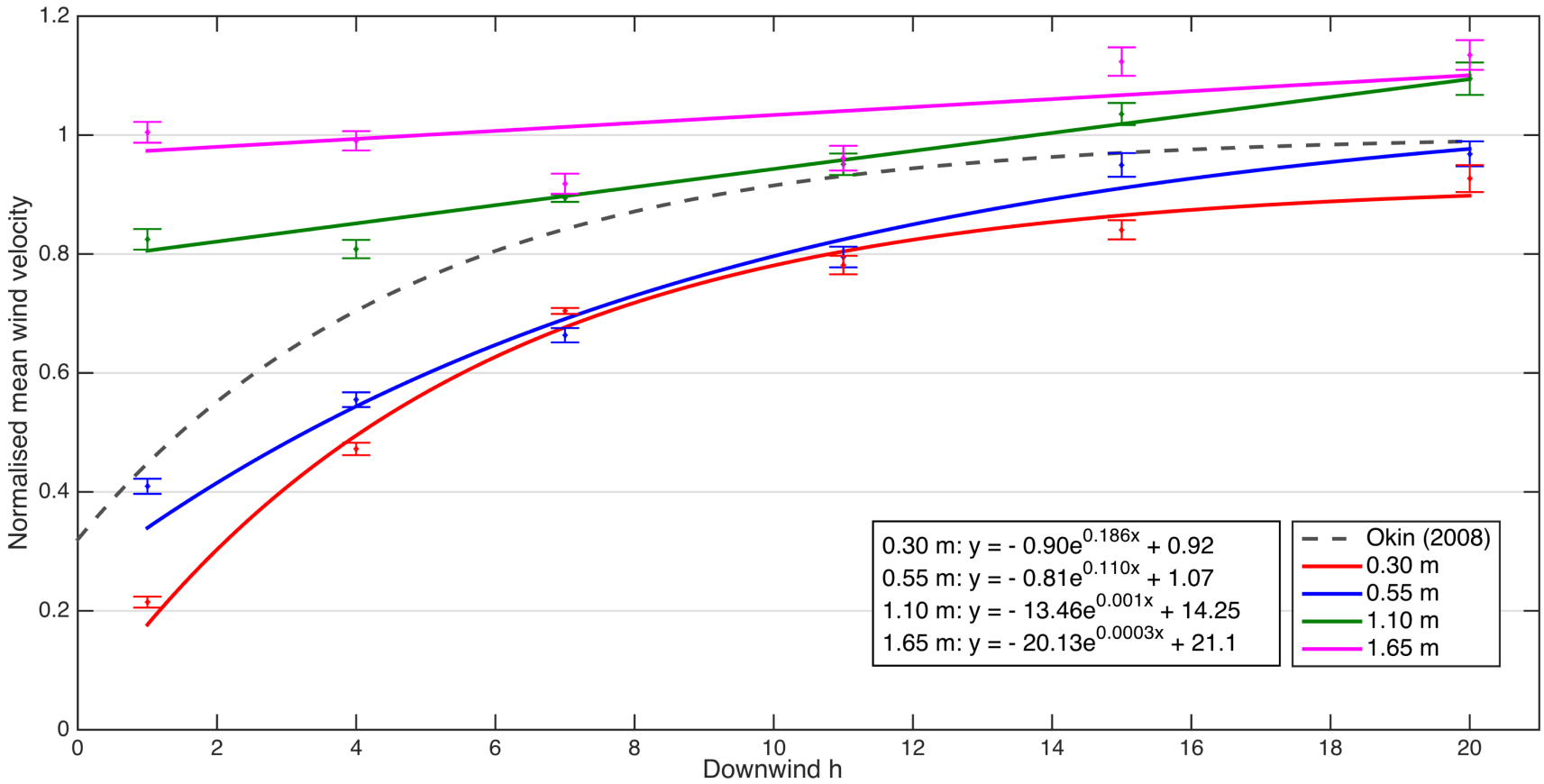


Figure 6.3 Best fit regression lines for normalised mean wind velocity (Φ) at all measurement heights (0.30 m, 0.55 m, 1.10 m and 1.65 m) downwind of the patch. Error bars represent the standard deviation of the mean. Also shown is Okin's (2008; corrected in Li et al., 2013) parameterisation of reduced shear stress downwind of a plant. Table displays function form for the general fitting models at each measurement height.

6.3.2. Turbulent stresses

Figure 6.4 displays variations in normalised resultant horizontal shear stress ($\tau_{r\,norm}$), normalised horizontal normal Reynolds stress ($\overline{u'^2}_{norm}$) and streamline angle variations from the horizontal plane, downwind of the patch edge. Vertical velocity variations were roughly an order of magnitude smaller than the horizontal components of flow in this study (cf. Sterk et al., 1998; van Boxel et al., 2004; Leenders et al., 2005; Weaver & Wiggs, 2011; Mayaud et al., 2016b), so play only a very minor role in flow dynamics. Vertical normal Reynolds stress ($\overline{w'^2}$) data are therefore not presented here.

Values of $\tau_{r\,norm}$ (Figure 6.4a) were generally highest in the immediate lee of the patch, particularly at greater measurement heights, and decreased with increasing downwind distance. Stress curves at all heights converged further downwind, starting with the curves at the two lowest heights around 15 h_d, and progressive convergence at greater heights. This indicates the progressive equilibration of the new internal boundary layer forming in response to the smoother desert surface (Belcher et al., 2003). A constant stress layer was observed at 20 h_d, corresponding to the equilibrating semi-logarithmic vertical profiles of Φ shown Figure 6.2b. This constant stress layer displayed lower shear stress values than the constant stress layer above the vegetation patch (i.e. $\tau_{r\,norm} < 1$) due to the lower surface roughness of the bare sand surface compared to the vegetation. The impact of the changing surface roughness on wind flow was also evident from shear velocity (u_*) calculations (Equation 6.5) with u_* = 0.46 m s^{-1} above the vegetation patch (corresponding to an aerodynamic roughness (z_0) of 0.022 m), and u_* = 0.24 m s^{-1} (z_0 = 0.001 m) at 20 h_d. In contrast to $-\overline{u'w'}_{norm}$, values of $\overline{u'^2}_{norm}$ (Figure 6.4b) were lowest in the immediate lee of the patch and increased at greater downwind distances, broadly following the pattern of normalised wind velocity.

The change in airflow structure resulting from the patch/bare surface transition can also be observed in the streamline angles of the flow (Figure 6.4c). Streamline angles were negative (i.e. the flow was angled towards the surface as the air expanded into the void in the lee of the patch) in the immediate lee of the patch until at least 4 h_d. At 1 h_d at 0.30 m height, horizontal wind flow was negative for 11.2% of the time, implying that the downward movement of air occasionally translated into bursts of flow moving back towards the patch, whereas at all other measurement locations (including the above-patch reference anemometer) horizontal wind flow was negative <0.01% of the time. Whilst this does not imply the formation of a full recirculation zone, the low wind velocities in the immediate lee of the patch likely create a zone of semi-recirculation near the base of the vegetation (e.g. Hagen & Skidmore, 1971; Cornelis & Gabriels, 2005; Sutton & McKenna-Neuman, 2008; Lee et al., 2014). From 7–15 h_d, streamline angles increased to ~3^o, likely resulting from the deflection of downward-moving wind as the flow reattached to the surface.

While shear stress and streamline angle variation in the airflow is useful to some extent in characterising wind flow (see Discussion section), previous aeolian studies have highlighted the significance of the coherency, or structured nature, of turbulence in the context of plant canopies (e.g. Shaw et al., 1983; Yue et al., 2007) and dunes (e.g. van Boxel et al., 2004; Leenders et al., 2005; Chapman et al., 2012, 2013; Wiggs & Weaver, 2012). In order to segregate the stress budget between different structures in the flow in the patch wake, quadrant analysis (Lu & Wilmarth, 1973; see section 2.3) was conducted.

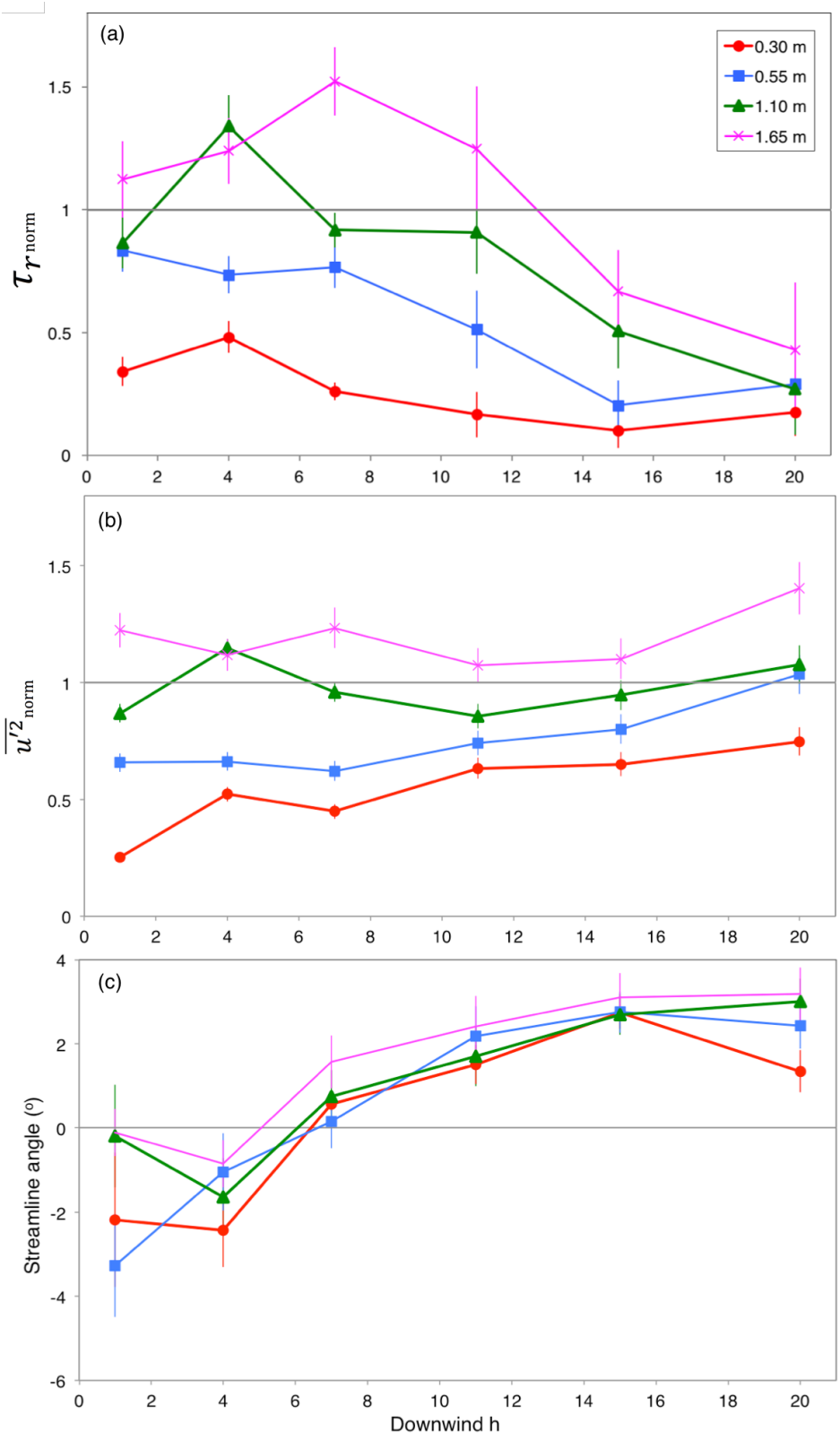


Figure 6.4 Variations in turbulence parameters downwind of the patch, at the four measurement heights: (a) normalised resultant horizontal shear stress ($\tau_{r\,\mathrm{norm}}$); (b) horizontal normal Reynolds stress ($\overline{u'^2}_{\mathrm{norm}}$); (c) streamline angle variation from the horizontal plane. Confidence intervals at the 95% level are shown as vertical bars.

6.3.3. Coherent flow structures

Figure 6.5 displays the frequency of occurrence of coherent structures (quadrant events) along the patch wake at the four measurement heights. There was a sharp increase in the frequency of Q4 (sweep) events in the immediate lee of the patch, particularly nearer the surface, where Q4 events constituted up to 61.8% of the flow. From 0.55 m to 1.65 m height, there was a high frequency of Q2 (ejection) events in the immediate lee. Q2 and Q4 events were also very prevalent above the patch canopy. The dominance of Q2 and Q4 events progressively decreased with greater downwind distance, and Q1 and Q3 event frequencies increased from <15% in the immediate lee to reach 15–30% at most heights around 15–20 h_d. The equilibration of flow was evident from the stabilisation of all quadrant curves by 20 h_d, supporting evidence from the measure variations in τ_r (Figure 6.4). The quadrant frequencies at

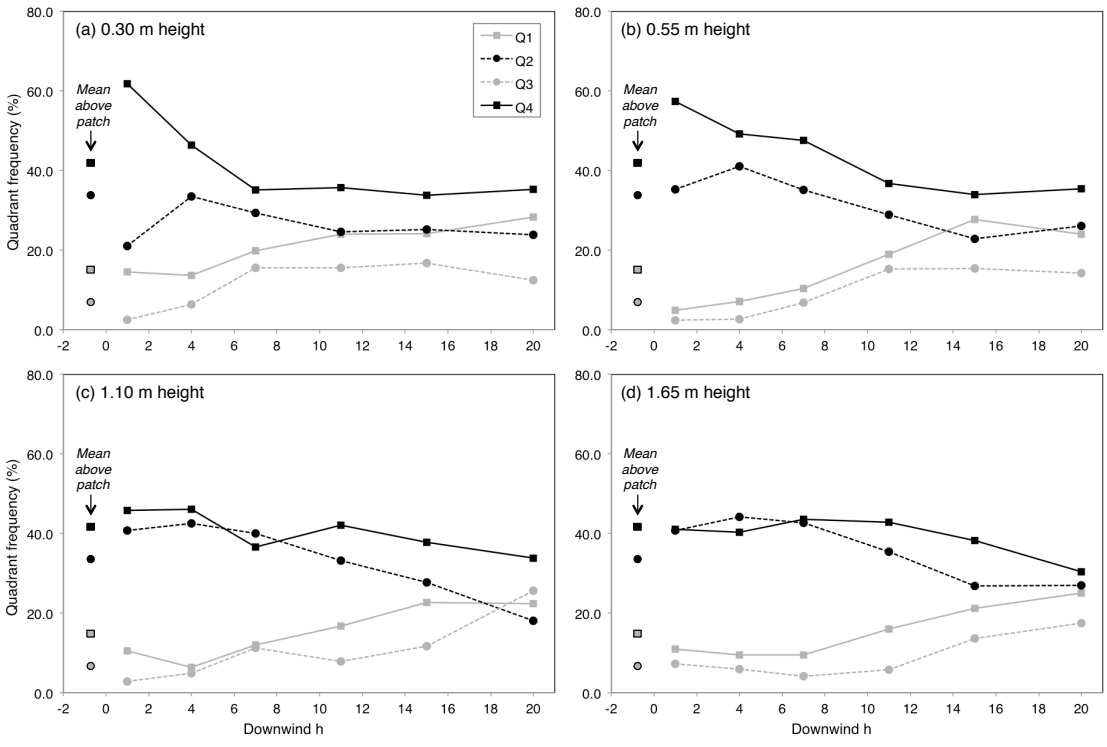


Figure 6.5 Frequency of occurrence (%) of coherent structures along the patch wake, at the four measurement heights: Q1= outward interaction (u'>0, $w' > 0$), Q2 = ejection ($u' < 0$, $w' > 0$), Q3 = inward interaction ($u' < 0$, $w' < 0$), Q4 = sweep ($u' > 0$, $w' < 0$). Mean quadrant values above the patch are also shown for reference.

20 h_d in this study are similar to previously reported quadrant frequencies in unperturbed flow over bare, flat surfaces (see Table 6.1).

Study	Measurement height (m)	Quadrant frequency range (%)			
		Q1	Q2	Q3	Q4
Mayaud et al. (2016b)	0.30	19–26	31–39	8–16	33–37
Weaver (2008)	0.30	19–22	31–33	16–19	29–32
	1.50	19–23	32–36	18–22	22–27
Leenders et al. (2005)	2.0	23–27	22–33	11–18	33–36

Table 6.1 Quadrant frequencies in unperturbed flow over bare, flat surfaces, as reported in previous studies.

6.4. Discussion

A distinct near-surface region of lower wind velocity ($\Phi < 1.0$) was detected at several heights in the wake of our study patch (Figures 3 and 4). The longer recovery length downwind of the patch (~12 h_d) compared with isolated elements of equivalent height reported in other studies (7–9 h_d; Leenders et al., 2007; Gillies et al., 2014; Wu et al., 2015; Mayaud et al., 2016b) can be attributed to a lack of flow moving around the patch. In contrast, isolated elements divert wind flow around their sides, leading to faster-moving airflow that mixes with slower-moving flow in their wakes via counter-rotating vortices and leads to more rapid recovery (Sutton & McKenna-Neuman, 2008). In a numerical modelling study designed to simulate airflow around forest edges, Liu et al. (1996) also found that the effect of a forest patch on mean wind velocity could be detected relatively far downwind, up to 22 h_d. Okin's (2008) recovery curve is based on data from a two-dimensional wind fence experiment where the change in roughness was not sufficient to engender skimming flow, so the more significant alteration to flow equilibrium in the patch case examined in this study

understandably results in a longer recovery than Okin's curve. This could imply that the potential for sediment transport downwind of a skimming flow regime is reduced compared to isolated roughness and wake interference flow regimes.

The recovery curves at greater heights (1.10 m and 1.65 m) were much shallower than at the surface due to a smaller initial leeside reduction in wind velocity. Flow above the patch was retarded relative to the bare surface due to the higher roughness value of the vegetation, which resulted in wind velocities at average vegetation height (z = 1.10 m) increasing in relative terms downwind of the patch. The observed slowdown in wind velocity at 1.65 m height likely resulted from the static pressure at the downwind edge of the patch increasing as a response to airflow expanding into the un-vegetated zone below, as well as from the difference in roughness (Belcher et al., 2003) represented by the patch (z_0 = 0.022 m) compared to the bare surface in its wake (z_0 = 0.001 m at 20 h_d).

It should be noted that the range of mean reference wind velocities recorded during this study was relatively narrow (2.57–3.70 m s^{-1}). Several windbreak studies (e.g. Hagen & Skidmore, 1971; Wu et al., 2015) have shown that free stream velocity affects windbreak performance. In wind tunnel experiments conducted over a range of wind velocities (5–12.5 m s^{-1} at an equivalent real-world height of 10 m), Wu et al. (2015) showed that the zone of reduced velocity in the immediate lee of a windbreak expands by up to 3 h_d (thus leading to a decreased recovery rate) as the free-stream velocity increases. Using wind data at 20 h_d of our study patch, where the airflow was broadly in equilibrium with the bare surface, the wind shear velocity (u_* = 0.24 m s^{-1}) and the aerodynamic roughness (z_0 = 0.001 m), Law of the Wall assumptions suggest that wind velocities at 10 m height (cf. Hagen & Skidmore, 1971; Wu et al., 2015) were ~5.5 m s^{-1} during our experiment. This value is at the lower end of Wu et al.'s (2015) experimental conditions, which could mean that airflow recovery

observed in the wake of our study patch may differ slightly at higher wind velocities. However, since the non-uniform turbulent flows measured in this study likely have high Reynolds numbers, an increase in wind velocity is unlikely to result in major changes to the wake structure.

Alongside characterising mean wind velocity, the impact of vegetation on driving flow turbulence must also be considered. High shear stresses observed at multiple heights in the immediate lee of the patch (Figure 6.4a) were likely a result of airflow at the surface accelerating in response to the lack of vegetation and skimming flow expanding into the leeside void, leading to a growth of an internal boundary layer (Greeley & Iversen, 1985; Wiggs et al., 1994, 1996). The change in wind structure was evident from the kinked profiles in Figure 6.2b, as the flow re-equilibrated to the new roughness. Flow above the mean patch height (> 1.10 m height) was still responding to the quasi-stable above-canopy drag induced by the vegetation (Belcher et al., 2003; Tischmacher et al., 2013), up until 4–7 h_d. Nearer the surface, the rapidly declining shear stress indicated a separation of the upper shear layer, as previously reported above porous wind fences (e.g. Kim & Lee, 2002). Further downwind, the convergence of stress curves at all heights and the decline in aerodynamic roughness length suggests that the new internal boundary layer forming in response to the smoother surface was progressively equilibrating. The z_0 measured at 20 h_d of our study patch (~0.001 m) was very similar to that measured by Wiggs et al. (1994) above a bare, burnt surface in the Kalahari (0.002–0.003 m). Above the study patch, our calculated z_0 (0.022 m) was roughly an order of magnitude lower than Wiggs et al.'s (1994) calculated z_0 (0.2 m) above a vegetated surface (z = 0.8–1.0 m), most likely because flow at their vegetated site had not developed into skimming flow.

The changing distributions of quadrant events (Figure 6.5) along the measurement transect provide context for the Reynolds stress patterns identified in Figure 6.4. The high prevalence of Q2 and Q4 events in the lee contributed positively to τ_r calculations, and thus account for the peak in τ_r in this region (Figure 6.4a). Meanwhile, the increasing occurrence of Q1 events downwind can be linked to the observed increase in $\overline{u'^2}$ along the wake (Figure 6.4b), since outward interactions are partly defined as positive deviations away from mean horizontal flow. The relative changes in turbulent structure proportions resulting from the presence of vegetation are important to quantify, because of the role they are understood to play in driving sediment transport. In the fluvial domain, a turbulent 'bursting process' (relatively greater occurrence of Q2 and Q4 events), has been shown to be a key determinant of transport (Best & Kostaschuk, 2002), but there is evidence that aeolian sediment transport is better associated with turbulent structures characterised by a positive streamwise fluctuating velocity (u'> 0, Q1 and Q4 events) (e.g. Sterk et al., 1998; Schönfeldt & von Löwis, 2003; van Boxel et al., 2004; Wiggs & Weaver, 2012; Chapman et al., 2013). This is why the $\overline{u'^2}$ parameter, which directly accounts for streamwise variability, is often better correlated with sediment transport than Reynolds shear stress (Wiggs & Weaver, 2011). The difference between aeolian and fluvial turbulent processes driving sediment transport is likely to be due to the greater disparity in density ratio between sand particles and wind compared with water (Wiggs & Weaver, 2012).

While no direct links can be made between horizontal turbulence and sediment transport in this study, there is increasing evidence that some turbulent stresses are important driving forces for aeolian sediment entrainment and transport in complex flows (Butterfield, 1991; Sterk et al., 1998; Schönfeldt & von Löwis, 2003; Leenders et al., 2005, 2007; Baddock et al., 2011; Weaver & Wiggs, 2011; Wiggs & Weaver, 2012; Chapman et al., 2012, 2013). Given that the wind flow in the immediate lee of

the patch did not exist as a well-developed equilibrium boundary layer, it is not possible to interpret the sediment transport potential in this zone (Schlichting, 1955). It has been argued that only the shear stress measured directly at the surface (e.g. using Irwin sensors) can provide information on erosion potential in non-equilibrium conditions (Walter et al., 2012b). However, as the flow equilibrated downwind of the reattachment point, the relative increases in Q1 events, wind velocities and $\overline{u'^2}$ suggest that sediment transport could develop downwind of the flow recovery zone.

6.5. Conclusion

Results from this study show that in the wake of a vegetation patch that is extensive and dense enough to produce skimming flow, wind velocity effectively recovers by ~12 h_d. This is 2–5 h longer than previously reported recovery distances for individual vegetation elements and two-dimensional wind fences (e.g. Raupach, 1992; Minvielle et al., 2003; Leenders et al., 2007; Okin, 2008; Gillies et al., 2014; Mayaud et al., 2016b), which can be attributed to a lack of faster flow moving around the obstacle in the patch case.

The use of τ_r measurements at multiple heights was shown to be a useful tool for characterising airflow structure across the patch/bare surface transition. The step-change in roughness between the patch canopy and the bare surface, evident from the difference in aerodynamic roughness (z_0) above the patch (z_0 = 0.022 m) compared to 20 h_d (z_0 = 0.001 m), caused an initial peak in resultant horizontal shear stress (τ_r) as the skimming flow expanded into the leeside void, followed by a large reduction in τ_r as a new internal boundary layer grew. The convergence of τ_r across all measurement heights implied the formation of a constant stress layer (i.e. equilibration) by 20 h_d.

Quadrant analysis identified elevated frequencies of Q2 (ejection) and Q4 (sweep) events in the immediate lee of the patch, which accounts for high τ_r in this region and a potential enhancement to the 'bursting process' in the lee. Whilst it is not possible to directly link the turbulent wind flow parameters reported in this study to sediment transport, the increasing contribution of Q1 (outward interaction) events along the patch wake, coinciding with increasing $\overline{u'^2}$ and wind velocity, suggests that sediment transport potential most likely increases with greater distance from the patch edge.

By providing the first field-based dataset of wind flow in the wake of a real vegetation patch, this research builds on existing parameterisations to better constrain the effects of vegetation on turbulent wind dynamics. Since shifts in vegetation structure relating from environmental and anthropogenic stresses such as grazing, fire and climatic change could significantly impact sediment mobility in semi-arid regions (Okin & Gillette, 2001; Sankey et al., 2012), it is vital to improve our understanding of the aerodynamic behaviour of patchy vegetation. The new data presented here can be integrated into wind erosion and landscape evolution models, in order to better understand the potential response of semi-vegetated surfaces to future environmental and anthropogenic stresses.

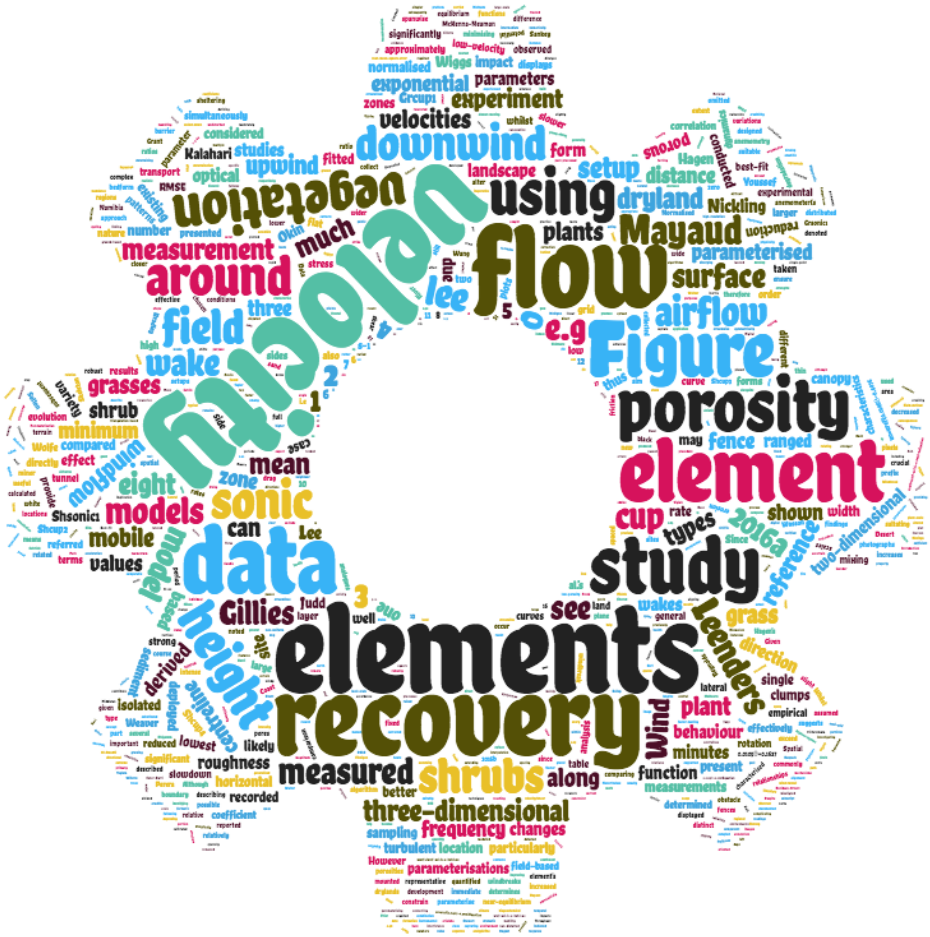
Summary: Paper 2

Paper 2 provided data on windflow in the lee of an extensive vegetation patch experiencing skimming flow. The recovery length downwind of the patch (~12 h_d) was longer compared with isolated elements of equivalent height reported in Paper 1 and other studies. The difference in recovery length is attributed to a lack of flow moving laterally around a patch, in contrast to isolated vegetation elements, where faster-moving airflow mixes with slower-moving airflow in the wake via counter-rotating vortices.

Turbulence statistics, specifically Reynolds shear stress (τ_r), were also used to identify flow recovery in the lee of the patch. Measuring shear stress at multiple heights usefully characterises the airflow structure across the patch/bare surface transition, and highlights the formation of a new internal boundary layer that progressively equilibrates.

The dataset presented in this paper represents the first field-based assessment of turbulent wind flow in the wake of a real vegetation patch. Together with findings from Paper 1, it provides a detailed evaluation of flow recovery in very different vegetated contexts. However, to reliably parameterise wind flow for the purposes of modelling, a larger dataset of flow recovery around multiple plants of various types and sizes is needed. Paper 3 therefore presents recovery data around eight different elements from two Namibian deserts.

CHAPTER SEVEN



A field-based parameterisation of wind flow recovery in the lee of dryland plants

Paper 3: Mayaud, J. R., Wiggs, G. F. S. & Bailey, R. M.
Status: published in *Earth Surface Processes and Landforms*, *42,* 378–386 (2017)

Abstract
Wind erosion is a key component of land degradation in vulnerable dryland regions. Despite a wealth of studies investigating the impact of vegetation and windbreaks on windflow in controlled wind-tunnel and modelling environments, there is still a paucity of empirical field data for accurately parameterising the effect of vegetation in wind and sediment transport models. The aim of this study is to present a general parameterisation of wind flow recovery in the lee of typical dryland vegetation elements (grass clumps and shrubs), based on their height (h) and optical porosity (θ_i). Spatial variations in mean wind velocity around 8 isolated vegetation elements in Namibia (3 grass clumps and 5 shrubs) were recorded at 0.30 m height, using a combination of sonic and cup anemometry sampled at a temporal frequency of 10 s. Wind flow recovery in the lee of the elements was parameterised in an exponential form, $(u_{ref} - u_0).(1 - e^{-b\frac{x}{h}}) + u_0$. The best-fit parameters derived from the field data were $u_0 = u_{ref}(0.0146\theta - 0.4076)$ and $b = 0.0105\theta + 0.1627$. By comparing this parameterisation to existing models, it is shown that wind recovery curves derived from two-dimensional wind fence experiments may not be suitable analogues for describing airflow around more complex, three-dimensional forms. Field-derived parameterisations such as the one presented here are a crucial step for connecting plant-scale windflow behaviour to dryland bedform development at landscape scales.

This chapter addresses **Objective 1** (to quantify extremes I erosivity by measuring wind structures upwind and downwind of various plant types of different sizes and porosities). **Methods**: sonic anemometers, cup anemometers, optical porosity.

This chapter is a modified version of the paper by Mayaud et al. (2017b). The Introduction section of the paper has been shortened, to avoid repetition of material provided in Chapter 2 of this thesis.

7. A field-based parameterisation of wind flow recovery in the lee of dryland plants

7.1. Introduction

Wind erosion is a major abiotic driver in drylands that can have important consequences for landscape evolution, biogeochemical cycling, regional climate, land degradation and public health (Griffin et al., 2001; Reynolds et al., 2001; Wiggs et al., 2003; Goudie & Middleton, 2006; Li et al., 2007, 2013; Ravi et al., 2011). The extreme nature of drylands means that semi-arid vegetation is often patchy and sparsely distributed (Bailey, 2011; Getzin et al., 2014), providing drag on the overlying airflow and thus significantly complicating aeolian dynamics at the surface (Ash & Wasson, 1983; Wolfe & Nickling, 1993; Wiggs et al., 1994, 1995; King et al, 2005). Given the potential impacts of increased sediment mobility at the landscape scale (Thomas et al., 2005; Wang et al., 2009; Stewart et al., 2014) following dramatic shifts in vegetation structure (Li et al., 2008; Sankey et al., 2012), it is crucial to better constrain the behaviour of windflow around dryland plants.

It has been well documented that sparse dryland vegetation modulates the erodibility of the surface and the erosivity of the wind through three primary mechanisms (Wolfe & Nickling, 1993): directly sheltering a portion of the erodible surface (e.g. Al-Awadhi & Willetts, 1999; Leenders et al., 2007), trapping saltating particles (e.g. Gillies et al., 2000, 2014; Davidson-Arnott et al., 2012) and acting as a form of roughness that results in the growth of a boundary layer downwind (Greeley & Iversen, 1985; Wasson & Naninga, 1986; Gillies et al., 2002; Gillette et al., 2006). Using wind tunnel experiments, Judd et al. (1996) built upon this concept by identifying six distinct zones of airflow behaviour around single porous roughness elements, including a low-velocity (recirculation) zone in the immediate lee and a turbulent mixing zone growing downward from a thin layer at the top of the obstacle. It has been shown that

these downwind protective wakes extend to approximately 7–10 h, where h is the height of the element (Leenders et al., 2007; Youssef et al., 2012; Gillies et al., 2014; Wu et al., 2015; Mayaud et al., 2016b). Judd et al.'s (1996) model for single roughness elements has been subsequently supported by wind tunnel data (e.g. Sutton & McKenna-Neuman, 2008; Youssef et al., 2012; Suter-Burri et al., 2013; Lee et al., 2014; Wu et al., 2015) and a handful of field experiments (Leenders et al., 2007; Gillies et al., 2014; Mayaud et al., 2016b).

Several studies (e.g. Raupach, 1992; Hagen, 1996; Okin, 2008; Leenders et al., 2011; Dupont et al., 2014) have sought to analytically or numerically model the recovery of wind flow in the lee of vegetation elements. Such models rely on empirical data to properly parameterise their recovery curves, which are usually based on scaled-down wind tunnel experiments or measurements taken around sand fences and windbreaks. Windbreak studies (e.g. Perera, 1981; Grant & Nickling, 1998; Wu et al., 2015) have been particularly useful for determining relationships between height, width, porosity and species type of elements. For instance, Taylor (1988) found that drag coefficients decreased exponentially as the porosity of a two-dimensional barrier increased, whilst others (e.g. Wang & Takle, 1996; Kim & Lee, 2002; Lee et al., 2002; Cornelis & Gabriels, 2005) have shown that elements with intermediate porosity strike a compromise between shear stress reduction and the downwind distance for which it is effective. Although findings from windbreak studies are of some relevance to plants (Grant & Nickling, 1998), the two-dimensional nature of a fence is much simpler than the three-dimensional problem posed by plants. It is therefore necessary to provide robust, field-based parameterisations of wind flow recovery in the wakes of full-scale vegetation elements.

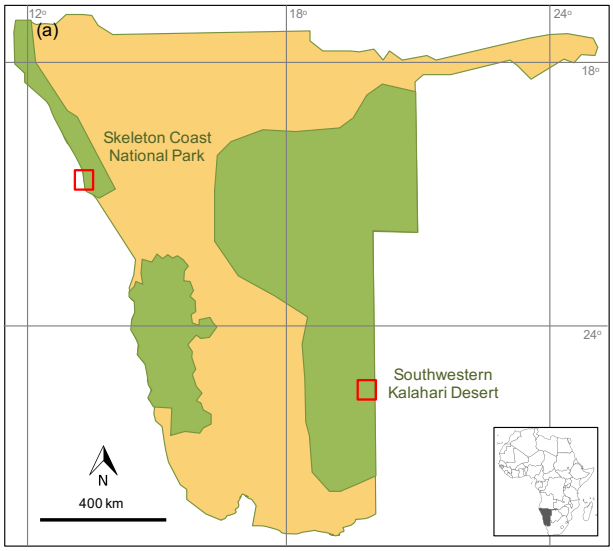
The aim of this study is to present a new parameterisation of flow recovery in the lee of porous, three-dimensional vegetation elements using a field dataset of eight

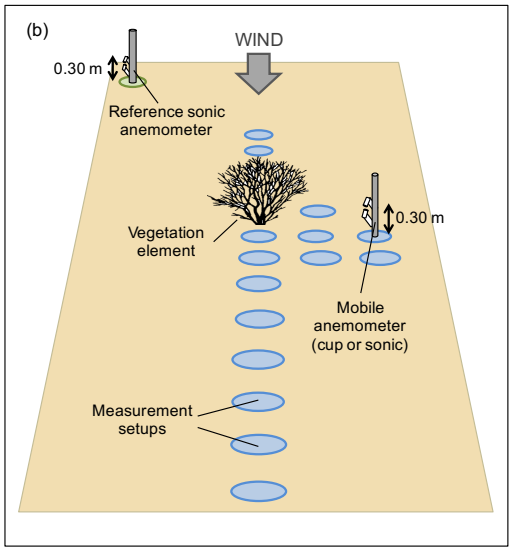
different isolated plants. By linking the rate of recovery and minimum velocities measured in the lee to the porosity of the elements, we contribute to a wider goal in the literature of improving the way windflow can be treated in large-scale models of dryland landscape evolution.

7.2. Methods

7.2.1. Field site

The field study was carried out in two locations in Namibia (see Figure 7.1a). Three grass experiments (denoted using the prefix '*Gr*') and two shrub experiments (denoted using the prefix '*Sh*') were conducted in the southwest Kalahari Desert, ~4 km north of the Auob River (25°29'15" S, 19°40'35" E), and three shrub experiments were conducted in the Skeleton Coast National Park, ~5 km inland from the coast along the Huab River valley (20°52'06" S, 13°29'24" E). The Kalahari Desert site was in a farmer's field on raised, flat terrain populated mainly by *Stipagrostis amabilis* grasses, *Rhigozum trichotomum* shrubs and *Acacia erioloba* trees. A wide strip of grazed land meant that the vegetation pattern did not change for > 500 m. The Skeleton Coast site consisted of small, irregularly spaced live and dead *Zygophyllum stapfii* shrubs, distributed on a large, flat gravel plain. Both sites were characterised by isolated roughness flow (Wolfe & Nickling, 1993). The eight vegetation elements in this study were chosen to be representative of their surrounding populations in terms of height, width and porosity (see Mayaud et al., 2016b for frequency distributions of vegetation types at the Kalahari site). The characteristics of the study elements are summarised in the table in Figure 7.1c.





(c)

Exp.	Species	Date	Field site	Height (m)	Reynolds number (Re)	Canopy width (m)		Optical porosity (%)	*U* during experiment (m s^{-1})			
						E-W	N-S		Min.	Max.	Mean	Std. Dev.
$Gr_{cup}1$	*Stipagrostis amabilis*	19/08/14	Kalahari	0.60	4.4×10^5	0.90	0.90	46	1.06	3.55	2.79	0.53
$Gr_{cup}2$	*Stipagrostis amabilis*	14/09/14	Kalahari	0.50	9.1×10^5	0.90	0.85	50	2.67	4.90	3.98	0.57
$Gr_{sonic}1$	*Stipagrostis amabilis*	27/09/14	Kalahari	0.75	8.8×10^5	1.30	1.10	53	1.72	4.83	3.02	0.72
$Sh_{cup}1$	*Rhigozum trichotomum*	19/08/14	Kalahari	0.60	5.0×10^5	0.95	0.75	69	1.21	5.21	3.29	0.88
$Sh_{cup}2$	*Zygophyllum stapfii*	05/09/14	Skeleton Coast	0.65	2.6×10^6	1.90	1.50	63	5.93	7.26	6.58	0.35
$Sh_{cup}3$	*Zygophyllum stapfii*	05/09/14	Skeleton Coast	0.55	2.0×10^6	1.50	1.40	71	5.25	7.89	6.89	0.52
$Sh_{cup}4$	*Zygophyllum stapfii*	06/09/14	Skeleton Coast	0.65	2.2×10^6	1.10	1.20	38	5.00	7.54	6.27	0.54
$Sh_{sonic}1$	*Rhigozum trichotomum*	30/09/14	Kalahari	1.30	7.9×10^5	1.80	1.60	69	0.89	4.22	2.64	0.73

Figure 7.1 (a) Locations of the two field sites in Namibia. (b) Example of the experiment setups designed to cover zones of interest around vegetation elements. (c) Description of the eight vegetation elements in this study, as well as experimental wind statistics measured at the reference anemometer at 0.30 m height.

The optical porosity (θ_i) of the study elements was determined using a digital photogrammetry method adapted from Kenney (1987). Digital photographs (Nikon D3100 DSLR camera with a resolution of 14.2 Megapixels) of part of the canopy were taken at approximately 0.40 m from the elements in the principal wind direction, thus accounting for the plant structures that the wind interacts with directly. The photographs were enlarged to fill the image dimensions, converted to greyscale images, and the perimeter of the plant was defined using a polygon that was inputted into the code manually. A variety of threshold values for black (plant branches) and white (open area) pixels were calculated, and the best fit to actual element shape was visually determined (as described by Gillies et al., 2000; Leenders et al., 2007).

The percentage of white pixels was taken as the mean optical porosity of the element canopy.

7.2.2. Experimental setup

Two types of experiments were conducted in this study: (i) 6 cup anemometer experiments (2 grass clumps and 4 shrubs); (ii) 2 sonic anemometer experiments (1 grass clump and 1 shrub). The cup anemometers collected horizontal wind velocity data at a sampling frequency of 10 s, whilst the sonic anemometers collected three-dimensional wind velocity data (u, horizontal; v, spanwise; and w, vertical) at a sampling frequency of 10 Hz, which was sub-sampled to 10 s. The sonic anemometer experiments were part of a related set of experiments (see Mayaud et al., 2016b) designed to provide three-dimensional, high frequency turbulent windflow measurements and these turbulence data are not reported here. The subscripts '*cup'* and '*sonic'* are employed to distinguish between the anemometer types used for each experiment. Except for a difference in the type and number of anemometers deployed, the format for both experiment types was the same.

For both experiment types, relevant anemometers (cup anemometers: *Vector Instruments A-100 R;* sonic anemometers: *Campbell CSAT-3*) were deployed around each study element to collect wind velocity data in a number of different 'setups' (see Figure 7.1b) designed to cover as many of the important zones of disturbed wind flow as possible (Judd et al., 1996). For the cup anemometer experiments, eight different 'mobile' anemometers fixed to thin steel masts were deployed simultaneously during each setup. For the sonic anemometer experiments, one mobile anemometer was deployed during each setup, with the anemometer arms aligned parallel with the prevailing wind direction and level in the horizontal plane. All mobile anemometers were mounted at 0.30 m height, which corresponds to a balance between capturing

wind characteristics that occur close to the surface, whilst minimising the interference of saltating sand with the sonic measurement path (Weaver & Wiggs, 2011). For both experiment types, an extra sonic anemometer was mounted at 0.30 m height and placed at a fixed location 20 h upwind and 15 h to the side of the experimental plots in a non-distorted environment (i.e. with a significant fetch over a flat, bare surface). This provided a mean upwind reference wind velocity ($\overline{U}$) for each setup against which mobile anemometry data could be normalised, as well as wind direction data. Normalisation is indicated using the '*norm*' subscript.

The mobile anemometer(s) were moved within a grid formation upwind, downwind and to the sides of each element (as shown by black dots in the Figure 7.2 plots), oriented in the direction of the wind. Each grid was divided into a number of measurement setups, during which the mobile anemometer(s) and reference anemometer simultaneously recorded wind velocity. To ensure sufficient data were acquired for subsequent analysis, each setup was run for a minimum of 20 minutes. The alignment of the experimental plot relative to the wind was altered after every instrumental setup to reflect any minor wind directional changes, and any misaligned data were removed in subsequent analysis (see Data analysis section). Throughout this study, annotation for measurement locations is given as h_d (downwind distance) and h_L (lateral distance) in terms of the height of the element. Wind flow was measured from -2 h_d (i.e. upwind) to 15–20 h_d depending on the element, and up to 3 h_L. Lateral wind flow was only measured on one side of each element, as wind dynamics were considered to be effectively symmetrical about the centreline of the wake (Leenders et al., 2007; Mayaud et al., 2016b).

Prior to the experiments, all eight cup anemometers were calibrated in the field by comparing their velocity readings to those obtained from one of the sonic anemometers at the Kalahari site. The cup anemometers and the sonic anemometer

were left to record wind velocity data simultaneously at 0.30 m height, at 10-second intervals, over a total period of 66 hours. There was a very strong (R^2 = 0.98; RMSE = 0.20) correlation between the full cup and sonic anemometer data. If only low wind velocities (< 3 m s^{-1}, as measured by the sonic anemometer) are considered, the correlation is still very strong (R^2 = 0.96; RMSE = 0.25). This suggests a lack of a significant 'hysteresis effect' (e.g. Kaganov & Yaglom, 1976; Knott & Warren, 1981; Weaver, 2008), whereby cup anemometers exhibit a nonlinear response to changes in wind velocity due to the inertia of the instrument.

7.2.3. Data analysis

The eight experiments were conducted on separate windy days in August and September 2014 (Figure 7.1c), at similar times of day and temperatures. Mean approach wind velocities as measured by the reference anemometer during each measurement setup ranged from 2.79 m s^{-1} ($Gr_{cup}1$) to 6.89 m s^{-1} ($Sh_{cup}3$). These velocities were representative of the general conditions measured at the respective field sites over a period of 2–4 weeks. Reynolds numbers (Re) were calculated using the element height and minimum upstream velocity for each experiment (Gillies et al., 2010), and ranged from 4.4 x 10^5 ($Gr_{cup}1$) to 2.6 x 10^6 ($Sh_{cup}2$) (see table in Figure 7.1c). These exceed the value of 2–3 x 10^4 above which negligible Re dependency is commonly assumed (Lim et al., 2007). No sediment transport was observed during the course of any of the experiments.

In order to ensure that the airflow detected at each measurement location had interacted as much as possible with the study element, the datasets were filtered to exclude oncoming wind directions > 5^o from the mean wind direction through the course of the experiment (Mayaud et al., 2016b). After this filtering process, the mean number of consecutive minutes of data per measurement setup ranged from

6.6 minutes ($Sh_{sonic}1$) to 23.0 minutes ($Sh_{cup}4$). These lengths satisfy van Boxel et al.'s (2004) recommendation that sampling periods for the wind velocity conditions and measurement height (0.30 m) reported here should ideally exceed ~4 minutes, in order to capture the full range of turbulent eddies in the boundary layer.

The sonic anemometer data (reference, and mobile, anemometers where appropriate) were post-processed to correct for any minor errors in aligning the anemometer heads into the mean approach wind flow. The streamwise frame of reference was rotated in accordance with the local streamline angle using yaw rotation (see Walker, 2005; Weaver & Wiggs, 2011), which effectively corrects the average spanwise velocity to zero ($\bar{V}$ = 0). Since the purpose of this study is to characterise the behaviour of wind flow horizontal to the surface, rather than along the plane of the streamlines, pitch rotation was omitted here. The application of roll rotation remains disputed practice for three-dimensional flow over non-uniform terrain (Kaimal & Finnigan, 1994; Lee & Baas, 2012), so this was also omitted from the correction procedure.

7.3. Results and Discussion

7.3.1. Wind velocity data

Figure 7.2 displays the spatial patterns of mean normalised wind velocity (Φ) around the eight study elements at 0.30 m height. Normalised wind velocities at each measurement location were interpolated using a triangulation-based natural neighbour algorithm, with a grid spacing of 0.1 m. This algorithm was chosen because it produced robust spatial features that were present using several other commonly used interpolation algorithms. Since wind velocity was quantified only on one side of each element in the field, the measured velocities were plotted

symmetrically over the centreline of the elements to provide better visualisation of recovery patterns.

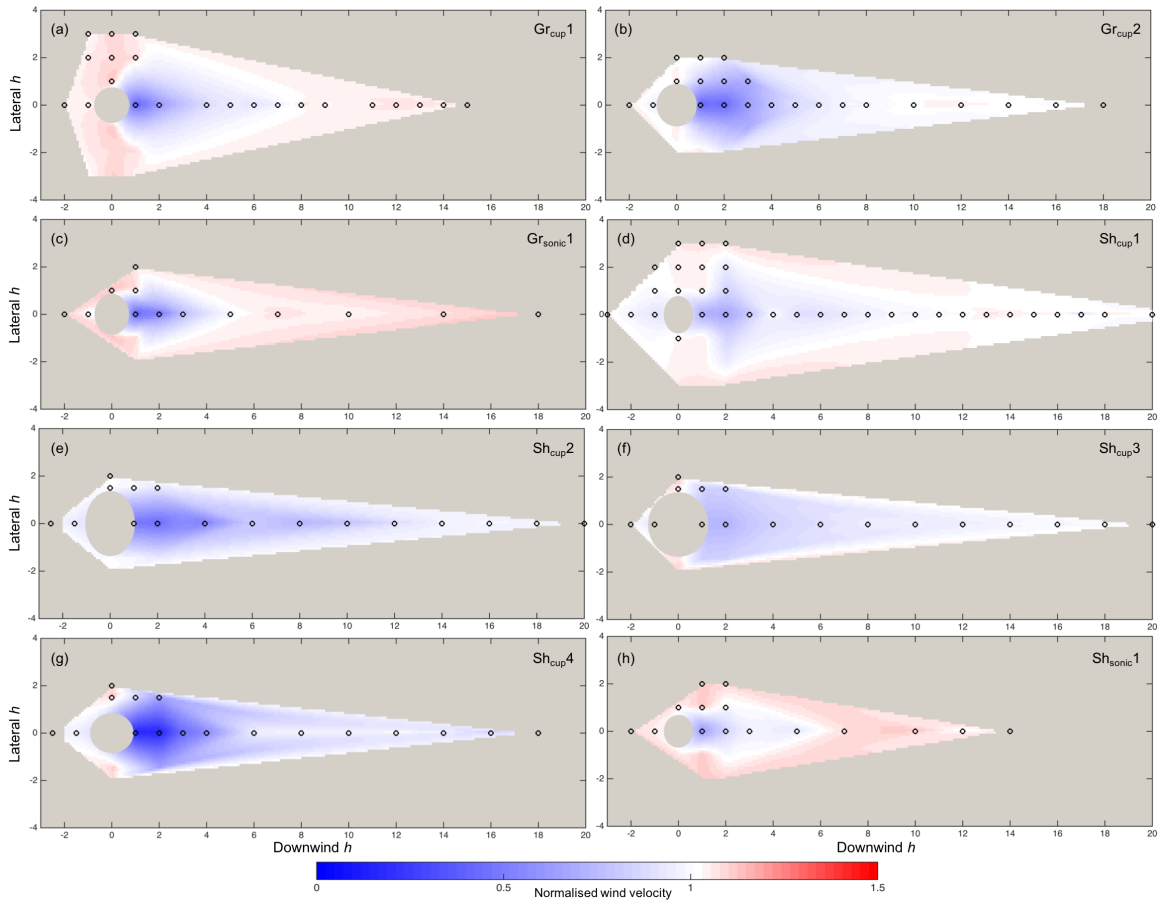
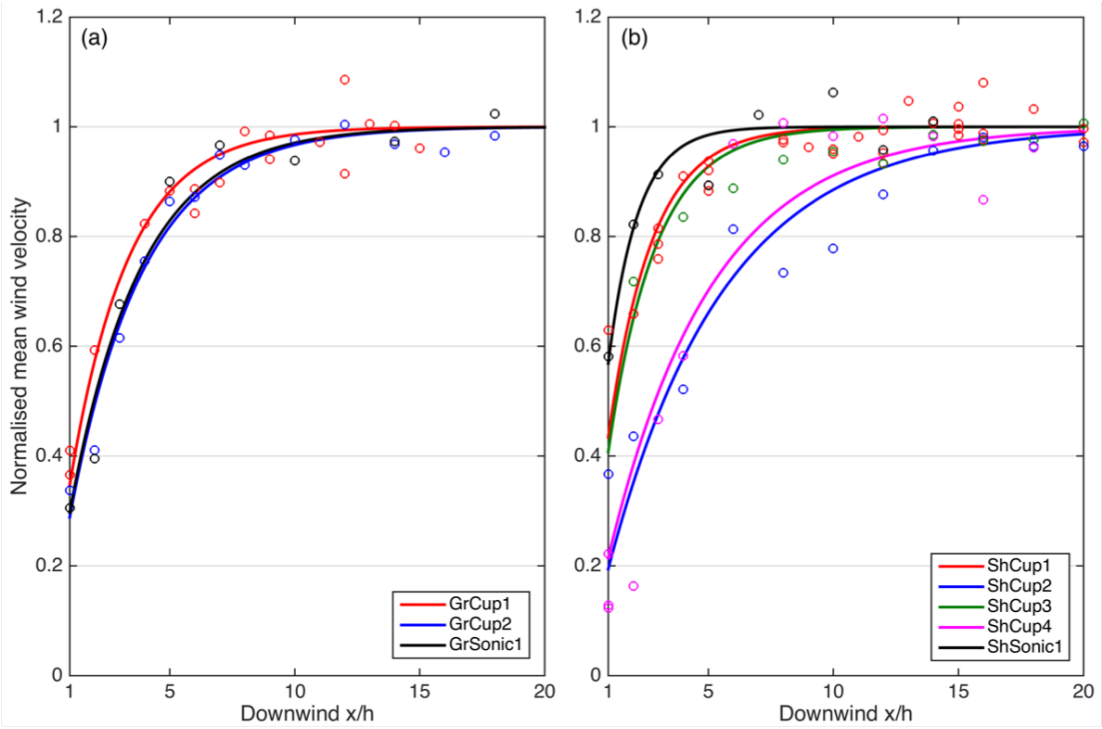


Figure 7.2 Spatial patterns of normalised mean wind velocity (Φ) at 0.30 m height for the eight study elements. Data were interpolated using a triangulation-based natural neighbour algorithm, with a grid spacing of 0.1 m. Location of grass and shrub elements are shown by grey ellipses, and black circles represent anemometer locations. Lateral wind velocity data are mirrored across the centrelines of the element wakes. The sampling designs were different for each experiment due to a changing availability of anemometers (and whether they were cup or sonic anemometers), and to differing lengths of time afforded to experiments by the wind conditions.

The contour plots (Figure 7.2) show clear regions of reduced wind velocity compared to upwind values (Φ < 1.0) in the wakes all the elements. The extent of the distinct low-velocity zones ranged from 5 h_d (Gr$_{sonic}$1) to 12 h_d (Sh$_{cup}$2), and the intensity of the slowdown varied across elements. The grasses tended to produce a more intense slowdown than the shrubs, due to their lower porosity in general (Figure 7.1c), which supports previous findings that low-porosity elements induce the

greatest slowdown (Hagen & Skidmore, 1971; Perera, 1981; Mayaud et al., 2016b). However, the element with the most visibly intense leeside reduction in wind velocity was $Sh_{cup}4$, which also had the lowest porosity (38%). Downwind of the low-velocity zones of $Gr_{cup}1$, $Gr_{sonic}1$ and $Sh_{sonic}1$, there was some evidence of slight wind velocity increases, likely due to the reattachment of the turbulent mixing zone (Judd et al., 1996). There was a reduction in wind velocity directly upwind and some flow acceleration to the sides of some elements, although the magnitude of these changes was much lower than the wind velocity changes observed along the wake centrelines.

Figure 7.3 displays the recovery of normalised mean wind velocity (Φ) at 0.30 m height along the centreline of the eight element wakes. The data for both grasses and shrubs was fitted using a saturating exponential function of the form $1 - e^{-bx}$, as the recovery of windflow downwind of an obstruction is generally described as an exponential curve (Bradley & Mulhearn, 1983 Vigiak et al., 2003; Leenders et al., 2007; Gillies et al., 2014; Wu et al., 2015, Mayaud et al., 2016b). There were very good fits between modelled and observed values (see table in Figure 7.3), with high R^2 and low sum of square error (SSE) and root-mean-square-error (RMSE) values. Wind velocity recovered to equilibrium flow at approximately the same distance (9–11 h_d) for the three grass elements (Figure 7.3a), whereas the recoveries in the shrub cases displayed a much wider spread. This reflects the larger variety in optical porosity among the shrubs, with the shrub with the lowest porosity ($Sh_{cup}4$, which was heavily leafed) showing a much slower recovery to equilibrium flow than the other elements, except $Sh_{cup}2$. $Sh_{cup}2$ was leafless and had a relatively high porosity, but most of its woody material was concentrated at its base. This structure is similar to grasses, which may have induced more bluff-body behaviour compared to other shrubs.



Exp.	Normalised min. wind velocity	Function	*b* coefficient	Goodness of fit		
				SSE	R^2	RMSE
$Gr_{cup}1$	0.37	$1 - e^{-bx}$	0.427	0.03	0.95	0.05
$Gr_{cup}2$	0.34	$1 - e^{-bx}$	0.341	0.02	0.97	0.04
$Gr_{sonic}1$	0.31	$1 - e^{-bx}$	0.353	0.02	0.96	0.06
$Sh_{cup}1$	0.63	$1 - e^{-bx}$	0.571	0.07	0.78	0.05
$Sh_{cup}2$	0.37	$1 - e^{-bx}$	0.216	0.07	0.86	0.08
$Sh_{cup}3$	0.72	$1 - e^{-bx}$	0.525	0.02	0.69	0.05
$Sh_{cup}4$	0.12	$1 - e^{-bx}$	0.242	0.15	0.91	0.11
$Sh_{sonic}1$	0.58	$1 - e^{-bx}$	0.842	0.02	0.91	0.05

Figure 7.3 Normalised mean wind velocity (Φ) along the centreline of the study element wakes at 0.30 m height. Table displays function form, coefficients and goodness-of-fit statistics for the general fitting model.

Some of the vegetation elements in this study, particularly the grasses, were pliable. Pliable plant stems can in some instances alter their form to become more streamlined in high winds, leading to less effective momentum extraction (Gillies et al., 2000) and a decreased sheltering effect (Walter et al., 2012b). Pliability is difficult to control for and quantify in the field, and further work is required to ascertain its impact on flow recovery and sediment transport in field contexts.

7.3.2. Parameterisation of wind velocity recovery

The recovery of surface wind velocity along the centreline of a porous element's wake (u_{surf}) can be formulated in relation to a reference flow that is undisturbed by plants (u_{ref}). Given the exponential nature of wind flow recovery, we parameterise the zone of reduced wind velocity in the wake of the grasses and shrubs as:

$$u_{surf} = (u_{ref} - u_0).(1 - e^{-b\frac{x}{h}}) + u_0 \quad (7.1)$$

where u_0 is the minimum wind velocity in the direct lee (in this study, 1 h_d) of the element, $\frac{x}{h}$ is the downwind distance from the nearest element in terms of element height, and b is a fitted coefficient that represents the recovery rate of the parameterised curve. The experimental data displayed in Figure 7.2 and Figure 7.3 are useful for deriving physically realistic values for u_0 and b, which can themselves be considered a function of element porosity (θ_i), since porosity determines the ratio between airflow that passes through the element's pores and airflow that diverges over the barrier (Leenders et al., 2011). Figure 7.4 shows the best-fit relationships between θ and the b (Figure 7.4a) and u_0 (Figure 7.4b) parameters for the eight study elements. The coefficient of determination in the case of b was moderately strong (R^2 = 0.41), and much stronger in the case of u_0 (R^2 = 0.83). This difference in correlation strengths is likely due to the better experiment constraint on single-point measurements at 1 h_d (on which u_0 is based), in comparison to an aggregation of multiple measurements along the centreline (on which b is based).

The equations shown in Figure 7.4a and Figure 7.4b are substituted as the coefficient values in Equation 7.1, such that:

$$u_0 = u_{ref}(0.0146\theta - 0.4076) \tag{7.2}$$

$$b = 0.0105\theta_i + 0.1627 \tag{7.3}$$

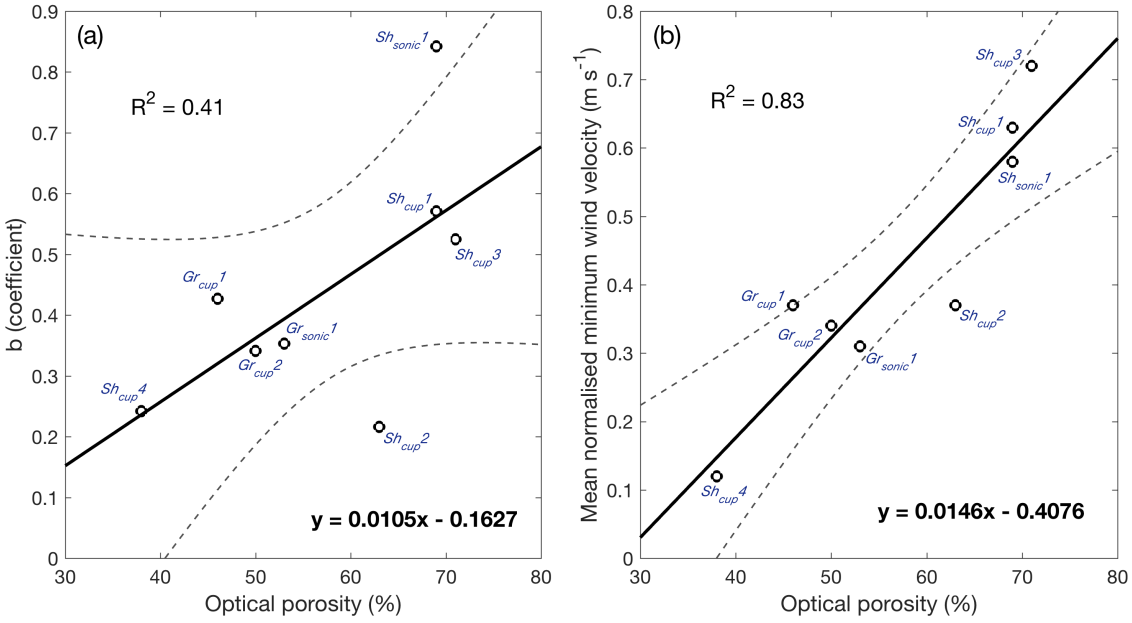


Figure 7.4 (a) Relationship between element optical porosity (θ_i) and *b* coefficient (i.e. recovery rate) in the exponential wind velocity recovery parameterisation; (b) Relationship between element optical porosity and the minimum mean normalised wind velocity (Φ) measured in the immediate lee of the elements. Data points represent the eight experiments, and are labelled accordingly. Linear fit lines with 95% confidence bounds (dotted lines), R^2 correlation coefficients and line equations are displayed.

7.3.3. Comparisons to existing models

The recovery parameterisation presented in this study is compared to three other published parameterisations: (i) Hagen's (1996) friction velocity reduction factor behind a windbreak (referred to as HA); (ii) Leender et al.'s (2011) adaptation of Hagen's (1996) function for a single shrub (referred to as LE); (iii) Okin's (2008; corrected in Li et al., 2013) parameterisation of reduced shear stress downwind of a plant, fitted to Bradley & Mulhearn's (1983) empirical data downwind of a wind fence

(referred to as OK). Although the HA and OK functions were developed to describe friction velocity/shear stress, these parameters are linearly related to wind velocity for a given surface roughness such that recovery rates should be comparable. For the purposes of comparison, an obstacle porosity of 50% was assumed for all parameterisations.

Figure 7.5 displays the recovery curve derived from our model alongside the curves for the three existing models. Our model compares relatively well to the LE model, particularly at distances greater than 5 h_d. In the immediate lee (1–3 h_d), wind velocity recovers more rapidly in our function than the LE model, but both reach near-equilibrium around the same downwind distance (~8 h_d). The LE model assumes a decrease in Φ between 0 h_d and 1 h_d, which could not be verified here as wind was not measured closer than 1 h_d during our experiments. However, the location of the minimum wind velocity is likely also located in this zone in the case of our grasses and shrubs. The recovery rates of the HA and OK models are significantly slower than our parameterised rate, with Φ reaching near-equilibrium around 21 h_d and 18 h_d, respectively.

The implication of these results, as previously noted by several studies (e.g. Gillies et al., 2014; Lee et al., 2014; Mayaud et al., 2016b), is that three-dimensional porous forms such as grasses and shrubs may not be suitably parameterised using data from two-dimensional wind fences. Whilst airflow cannot move around an infinitely wide fence, isolated elements divert wind flow around their sides, which leads to faster-moving lateral flow mixing with slower-moving wake flow via counter-rotating vortices (Sutton & McKenna-Neuman, 2008). This results in a more rapid recovery in wind velocity in the case of single elements. It follows that the relative width of an element could to a certain extent affect recovery in its wake. Basal to frontal area ratios in this study ranged from 1.23 ($Sh_{sonic}1$) to 2.54 ($Sh_{cup}3$), and elements with the

lowest ratios ($Gr_{cup}1$, $Gr_{cup}3$ and $Sh_{sonic}1$) experienced higher lateral velocity increases than the other elements (see Figure 7.2). However, in our experiments a significant proportion of airflow likely passed through the study elements as bleed flow, thus minimising the overall impact of element width on flow recovery.

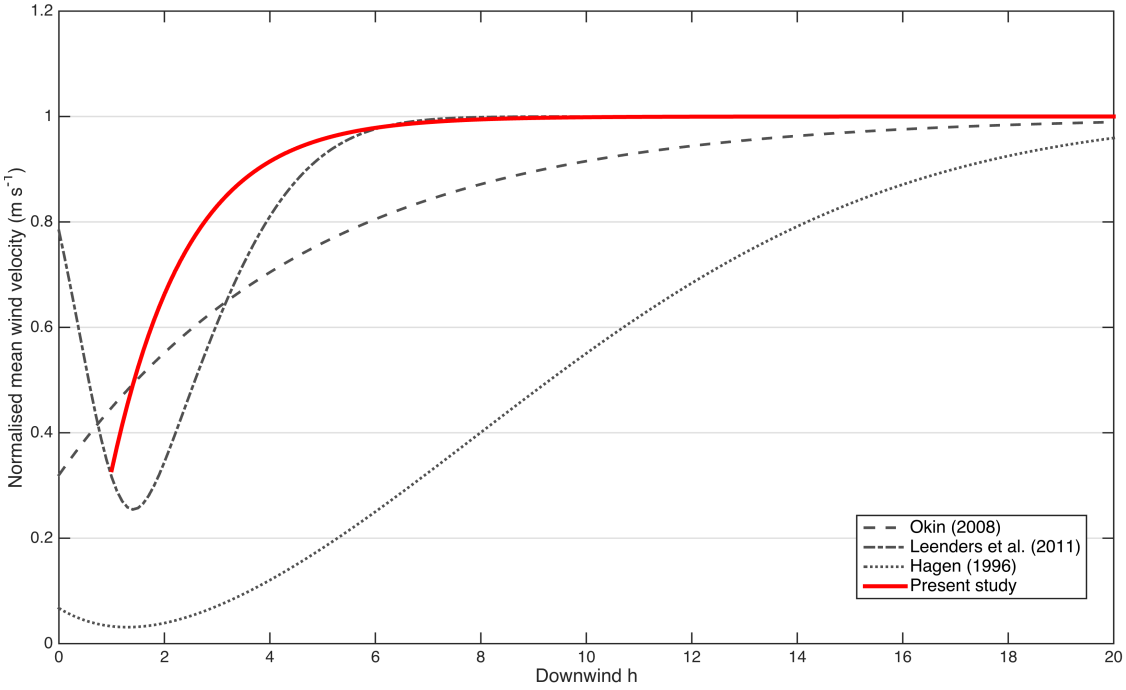


Figure 7.5 Parameterised wind velocity recovery along the wake centreline of an element with an optical porosity (θ_i) of 50%. The models of Okin (2008) and Leenders et al. (2011) for porous shrubs, and of Hagen (1996) for a porous windbreak, are shown for comparison.

The lowest element porosity recorded in this field study was 38%, so the impact of particularly dense elements on flow was not characterised. Wind flow recovery in the wake of a sufficiently large vegetation patch can effectively be considered to act as if it has a porosity of 0%, due to the cumulative effect of closely spaced plants forcing skimming flow to develop above the canopy and zero flow to occur at the base of the canopy (e.g. Frank & Ruck, 2008; Burri et al., 2011; Youssef et al., 2012; Mayaud et al., 2016c). Wind recovery in the wake of patches has been shown to be slightly longer than in the wake of individual elements (Mayaud et al., 2016c), so elements with very low porosities may result in slight changes to the u_0 and b parameters.

Since the wind in this study was not measured closer than 1 h_d, the specific flow dynamics between 0 h_d and 1 h_d are not accounted for in the current parameterisation of our model. Nevertheless, we do not expect this to significantly alter the parameter relations presented in this study, which are based on the much larger downwind wake zone extending to 15–20 h_d.

7.4. Conclusion

In this study, we present a new generalised parameterisation for the recovery of wind velocity along the centreline of porous vegetation wakes. Spatial variations in surface wind velocity downwind of 3 grass clumps and 5 shrubs were measured at a sampling frequency of 10 s, and normalised to upwind reference velocities. Normalised wind velocity data were fitted using an exponential function, from which a rate parameter (b) could be determined for each element. Best-fit linear functions were derived relating the b parameter and the minimum wind velocity recorded in the lee (u_0) to the optical porosity (θ_i) of each element, since porosity determines the ratio between airflow passing through pores and airflow diverging over and around the element.

A parameterisation for wind flow recovery in the lee of the elements was derived in an exponential form, $u_{surf} = (u_{ref} - u_0).(1 - e^{-b\frac{x}{h}}) + u_0$. The best-fit parameters derived from the field data were $u_0 = u_{ref}(0.0146\theta_i - 0.4076)$ and $b = 0.0105\theta_i + 0.1627$. This parameterisation was compared to three existing models (Hagen, 1996; Okin, 2008; Leenders et al., 2011), assuming an element porosity of 50%. Whilst our model compared relatively well with that of Leenders et al. (2011), which was parameterised using wind flow data around a real shrub, the models of Hagen (1996) and Okin (2008), which were parameterised using wind fence data, assume a slower

downwind recovery of wind velocity. This suggests that two-dimensional wind fence experiments may not be suitable analogues for describing airflow around complex, three-dimensional forms. There is therefore an imperative to collect more field-based data on windflow behaviour around a variety of dryland plant types.

The recent progress in image-based techniques (e.g. Karl et al., 2011) and high-resolution remote sensing using airborne (Jupp et al., 2008) and ground-based (Sankey et al., 2013) LiDAR, means that a variety of plant characteristics – notably height (McGlynn & Okin, 2006) and porosity (Omasa et al., 2007) – can be quantified more easily and extensively than ever before. These advances could help to establish potential wind velocity patterns over large areas, and thus better constrain landscape evolution models that seek to robustly link local-scale processes to bedform development at larger scales.

Summary: Paper 3

Paper 3 presented a large dataset of wind flow around three grass clumps and five shrubs. These data were used to derive a new generalised parameterisation for the recovery of wind velocity along the centreline of porous vegetation wakes, based on element height (h) and optical porosity (θ_i). Recovery was parameterised in an exponential form: $(u_{ref} - u_0).(1 - e^{-b\frac{x}{h}}) + u_0$.

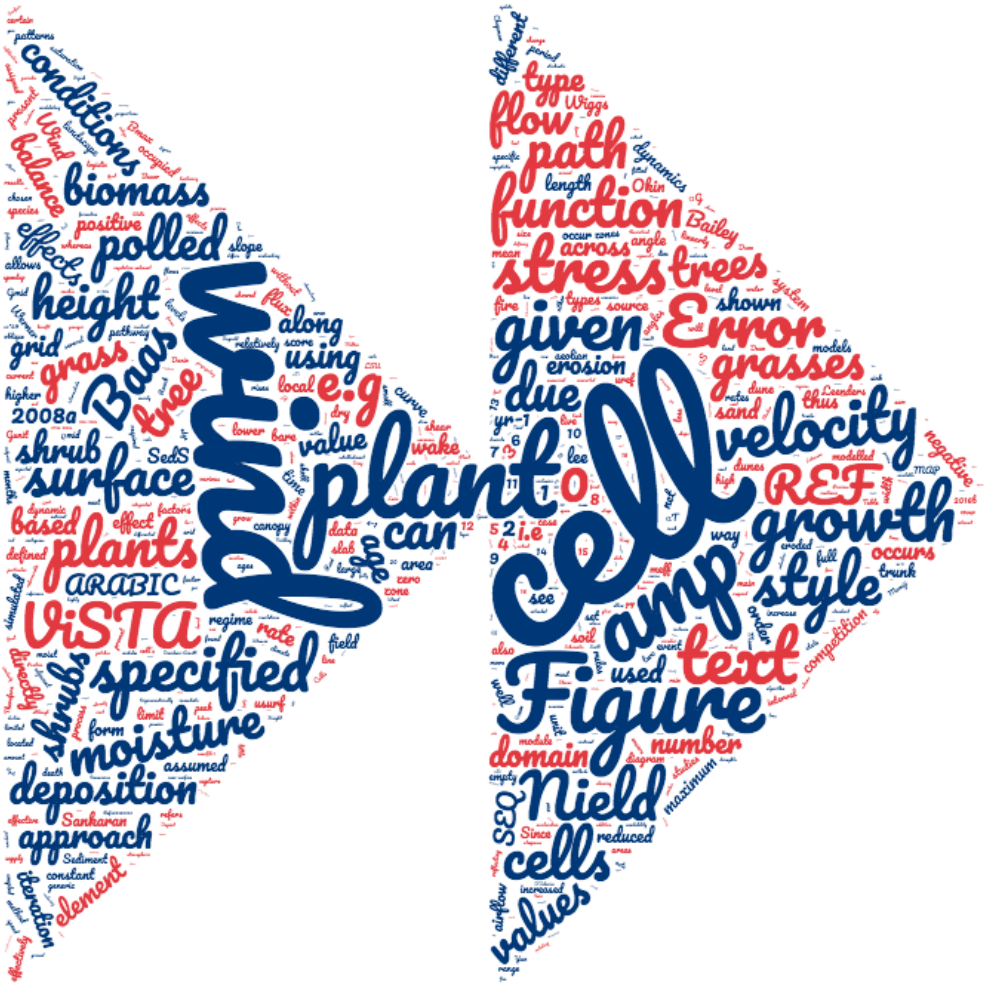
Comparison of this model with existing recovery models based on wind fence data (Hagen, 1996; Okin, 2008) suggests that two-dimensional fences are not suitable analogues for three-dimensional porous forms. Whilst airflow cannot move around an infinitely wide fence, isolated elements divert wind flow around their sides, resulting in a more rapid velocity recovery in the case of single elements.

Wind flow data from Papers 1, 2 and 3 can now be used to better parameterise flow recovery in the new Vegetation and Sediment TrAnsport model (ViSTA), which is described, verified and validated in the following chapter.

SECTION THREE

MODELLING EXPERIMENTS

CHAPTER EIGHT



A coupled vegetation/sediment-transport model for dryland environments: Model description

Paper 4 (part 1): Mayaud, J. R., Bailey, R. M. & Wiggs, G. F. S
Status: published as 'A coupled vegetation/sediment-transport model for dryland environments', *Journal of Geophysical Research: Earth Surface, 122* (2017)

Abstract
Dryland regions are characterised by patchy vegetation, erodible surfaces and erosive aeolian processes. Understanding how these constituent factors interact and shape landscape evolution is critical for managing potential environmental and anthropogenic impacts in drylands. However, modelling wind erosion on partially vegetated surfaces is a complex problem that has remained challenging for researchers. We present the new, coupled cellular automaton Vegetation and Sediment TrAnsport model (ViSTA), which is designed to address fundamental questions about the development of arid and semi-arid landscapes in a spatially explicit way. The technical aspects of the ViSTA model are described, including a new method for directly imposing oblique wind and transport directions onto a cell-based domain.

Note: The full ViSTA model code is available on GitHub, an open-source repository, at: *https://github.com/jeromemayaud/ViSTA*

This chapter addresses **Objective 3** (couple a spatial vegetation patterning model to a wind erosion model, and simulate potential levels of aeolian transport in locations with different distributions, scales and geometries of vegetated patches). **Methods**: cellular automaton modelling.

This chapter is a modified version of the paper by Mayaud et al. (2017a). The Introduction section of the paper has been shortened, to avoid repetition of material provided in Chapter 2 of this thesis. The Methods section and Supplementary Information of the paper have been combined, to provide a comprehensive overview of the formulation of the model.

8. Model description

8.1. Introduction

Aeolian landscapes in dryland regions are dominated by the interactions between ecological processes and sediment transport processes (Baas & Nield, 2007). Wind regime and sediment supply are known to largely control the formation of bare-sand dunes (e.g. Wasson & Hyde, 1983; Werner, 1995), but the dynamic interactions between vegetation and sediment movement, which form part of a wider, multi-scaled interplay of biophysical and anthropogenic factors, are less well understood (Schlesinger et al., 1990; Breshears et al., 2003; D'Odorico et al., 2007; Nield & Baas, 2008a; Ravi et al., 2010). Predictive modelling of ecogeomorphic dynamics is crucial for improving our understanding and management of potential dryland landscape responses to both environmental and anthropogenic influences. Applications include mitigation of land degradation (Barbier et al., 2006; D'Odorico et al., 2013), climate change impact assessments (Thomas et al., 2005; Seager et al., 2007; Wang et al., 2009; Bogle et al., 2015) and investigating the effects of changes in land use (Levin & Ben-Dor, 2004; Middleton & Sternberg, 2013) in drylands.

Modelling approaches are increasingly used to understand self-organised vegetation patchiness in drylands, and the transitions from vegetated to low-productivity (bare-soil) states (Scheffer et al., 2001; Bel et al., 2012; Bailey, 2011). However, relatively little is known about the effects of vegetation patch distribution, geometry and scale on the entrainment and transport of aeolian sediment at the meso-scale (10^1–10^3 m) and macro-scale (> 10^3 m) (Okin & Gillette, 2001; Sankey et al., 2012). Cellular automaton (CA) models, a class of numerical models consisting of a regular, discrete grid of cells operated on by predefined rules, allow distributed dynamics to be represented in a versatile way. This lends itself well to analysing ecogeomorphic systems (Baas, 2007). Importantly, CAs can be employed to capture full landscape-

scale dynamics using only fundamental processes, without the need for intricate grain-scale processes of sediment transport. Existing ecogeomorphic CA models (e.g. DECAL by Baas & Nield, 2007; later extended by Yan & Baas, 2017) already incorporate feedbacks between sedimentation balance and vegetation growth. However, the biotic component in DECAL in its original form only incorporated as a generic, unitless 'vegetation effectiveness', which acts as a proxy for the aerodynamic effect of plants on sediment transport. Plant-plant interactions are therefore not explicitly modelled, and the effects of vegetation form and porosity on local-scale wind flow are not considered.

In this paper, the new Vegetation and Sediment TrAnsport model (ViSTA) is presented. ViSTA couples a CA vegetation distribution model with a CA sediment transport model, encoding feedbacks among vegetation growth, wind flow dynamics and sediment flux. The evolution of landscapes with different distributions, scales and geometries of vegetated patches can therefore be simulated.

8.2. Model setup

The ViSTA model consists of two coupled models that interact with each other over various timescales (Figure 8.1a): (i) a vegetation model that simulates vegetation growth and decline in response to environmental stresses resulting from climate and land use changes, and (ii) a sediment transport model (composed of two modules) that moves sediment across the model domain in response to spatially varying wind speeds. The coupled scheme is formulated such that the distribution of vegetation (Module 1; Figure 8.1b) alters local wind flow characteristics (Module 2a; Figure 8.1c), thus impacting sediment flux patterns over the surface (Module 2b; Figure 8.1d), which in turn affects vegetation growth through ecological feedbacks. The ViSTA model also incorporates several sub-modules that can be activated to

simulate herbivore/grazing, fire and precipitation events. These events have a primary impact on the state of the vegetation in Module 1, although precipitation can also affect sediment transport directly by changing soil moisture levels. Since the focus of the work presented here is the aeolian component of dryland geomorphology, we do not explicitly model the movement of water across the landscape, nor the associated fluvial sediment transport. However, the benefits of a modular approach mean that fluvial processes can be incorporated into future versions of the ViSTA model.

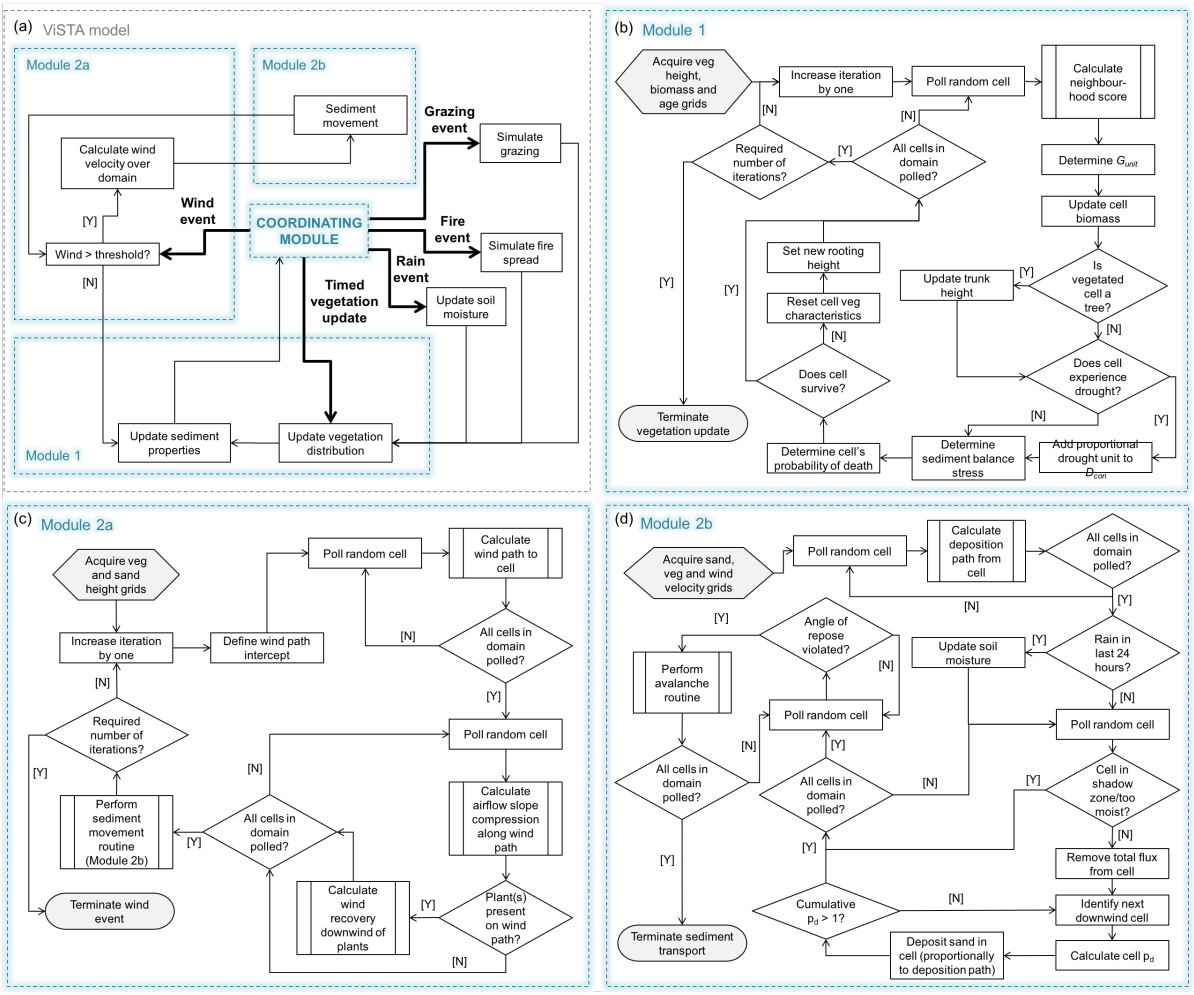


Figure 8.1 (a) Flow diagram summarising the main module interactions within the ViSTA model; (b) flow diagram for process flows in Module 1 (responsible for vegetation distribution); (c) flow diagram for process flows in Module 2a (responsible for wind dynamics); (b) flow diagram for process flows in Module 2b (responsible for sediment transport).

All modules in the ViSTA model rely on local neighbourhood operations to produce dynamic responses from basic rules centred on each discrete part of the grid. All grid cells hold a variety of attributes (including sand depth, soil moisture and nutrient levels, and vegetation characteristics such as plant type, height and porosity) that are altered by applying transition rules during each timestep. The state of all cells at the end of that timestep becomes the initial state of all cells at the beginning of the next timestep. Cells interact with adjacent cells based on their local von Neumann neighbourhood. Since sediment moves regularly across the ViSTA model domain, a wrap-around torus grid (i.e. periodic boundaries) is used to preserve sediment within a closed system. As such, there are no external sediment sources apart from the initial supply to the domain, and sediment is internally 'recycled' between adjacent landscape surfaces (although there is the possibility within ViSTA to specify non-periodic boundaries, in order to explore sediment supply effects (e.g. Eastwood et al., 2011)). While dryland landscapes will gain and lose sediment externally to the system, this is significant only over long (> 100 yr) timescales (Bailey & Thomas, 2014). Running the model on a large enough domain ($\geq 10^2$ m) ensures that model size effects are not propagated through the system in any meaningful way.

The model is implemented in the Python® programming language (Python 3.5.0 64bits, Qt 4.8.7, PyQt4 (API v2) 4.11.4 on Darwin; Spyder® development environment), using code written by the authors. The model code is available upon request from the authors.

8.3. Vegetation growth (Module 1)

The vegetation module consists of an adapted version of Bailey's (2011) CA model for simulating semi-arid vegetation. In brief, a neighbourhood is defined in the model that is used to calculate local plant-interaction effects, employing a similar approach

to Thiery et al. (1995). Grid cells accommodate plant biomass that is representative of three vegetation types: grasses, shrubs and trees. Cells are either occupied (alive) or unoccupied (dead and therefore bare), and plant type and age are also recorded. A cell only accommodates a single plant type at any given time, so the spatial resolution of the module should ideally be of the same order of magnitude as real plants (i.e. 10^{-1}–10^{1} m). Seven factors govern a given cell's probability of survival: (i) neighbourhood effects; (ii) response of vegetated cells to precipitation; (iii) cell biomass; (iv) cell age; (v) sediment balance (i.e. plant response to sediment erosion/deposition); (vi) grazing; and (vii) fire.

8.3.1. Biomass dependencies

Bailey (2011) originally formulated the dependence of generic plants on generic environmental stress and neighbourhood effects as a function of cell age. However, since vegetation growth effectively depends on photosynthetic gains being higher than losses due to respiration, age-dependent growth does not account for situations where plants have not experienced fully optimal growing conditions throughout their lives and thus do not have a biomass that is in proportion with their age (Danin, 1996). To correct for this ecological process, the majority of dependencies in Module 1 of the ViSTA model are formulated as a function of arbitrary growth units, such that individuals move along a predetermined nonlinear 'growth pathway' to provide equivalent changes in biomass (e.g. Yan & Baas, 2017). If a plant experiences optimal conditions (i.e. sufficient precipitation-derived moisture) at every module iteration, it will grow by the same number of growth units as the period of time (in months) represented by that iteration. If a plant experiences sub-optimal moisture conditions, it will grow by a fraction of a full growth unit that reflects the available moisture. If precipitation conditions are particularly poor, plants can lose growth units

and move back down their growth pathways. In other words, precipitation history determines the rate at which a plant travels along its growth pathway. This scheme means that plants can live for long periods, but accrue relatively little biomass if conditions are harsh.

In the ViSTA model, the biomass of a plant (B) determines the strength of competition/facilitation that it exerts on its neighbours, as well as its sensitivity to competition/facilitation from surrounding plants. Given the size-/age-dependent amplification of facilitation effects that has been noted in previous studies (e.g. Barbier et al., 2008), the modelled facilitation strength in this model grows monotonically with plant biomass, from zero to a maximum at full biomass maturity (B_{max}), and remains constant thereafter. Smaller plants are expected to exert less competitive pressure for soil moisture and nutrients to an adjacent area, due to less extensive root systems (Barbier et al., 2008). Modelled competition rises monotonically with biomass until B_{max}, and then reduces as biomass increases past B_{max}, reflecting reduced plant function at greater ages (Roach, 2009). Empirical studies (e.g. Pugnaire et al., 1996; Callaway, 1997) have shown that younger plants benefit proportionately more from facilitation than older plants, so smaller plants in the model benefit more from facilitation than larger plants. Cells are at their most resilient and sensitivity to competition reaches a minimum when plants reach B_{max}; beyond this, sensitivity to competition rises again, reflecting the aging of the plant (Roach et al., 2009).

8.3.2. Neighbourhood interactions and precipitation stress

The neighbourhood interactions in Module 1 are based on the original approach of Bailey (2011), with an additional formulation linking them to environmental

precipitation levels. The neighbourhood of a given cell is defined by five concentric shells in an extended-Moore neighbourhood, and each shell is assigned a coefficient (c_i), with positive values representing net facilitative effects at close distance (shells 1 and 2), negative values representing net competitive effects (shells 4 and 5), and zero being neutral (shell 3). The balance of total facilitative and competitive coefficients (the sum of positive and negative $\boldsymbol{c_i}$ values, +3 and -1.5 respectively), as well as the size of the neighbourhood, were chosen by Bailey (2011) to provide the greatest pattern diversity and the best qualitative agreement with observed semi-arid vegetation patterns. Increasing the total facilitative weighting (sum of positive $\boldsymbol{c_i}$ values) or reducing the total competitive weighting (sum of negative $\boldsymbol{c_i}$ values) was found to gradually extinguish emergent labyrinth-type patterns. Conversely, reducing the facilitation or increasing the competition weightings results in persistent and unrealistically angular patterning over a wide range of population densities (Bailey, 2011). Therefore, the same coefficient values and neighbourhood sizing as Bailey (2011) are employed here to describe the interactions of both shrubs and trees. Since grasses tend to have a smaller radial root reach (Carpenter et al., 1986; Abella et al., 2009) and produce weaker Turing-type patterns than shrubs, the balance of total competitive coefficients for grasses is set at $\boldsymbol{c_i}$ = -0.3.

The biomass-dependent contributions from all the occupied cells in a cell's neighbourhood are summed and combined with stress from incoming precipitation, (ρ, mm), to give a total neighbourhood score, T. The T score yields the net effect of all competitive and facilitative contributions, and thus accounts directly for the soil moisture that each plant can capture relative to its neighbours, without explicitly resolving the mechanism of water uptake. T is calculated for each cell, in each time-step, as:

$$T = \sum_{i=1}^{2}\left(\sum_{j=1}^{i\times 8}\left(a_{i,j}c_i k_{f(i,j)}\right)\right)s_f + \sum_{i=3}^{5}\left(\sum_{j=1}^{i\times 8}\left(a_{i,j}c_i k_{c(i,j)}\right)\right)s_c + \rho$$

(8.1)

where $\boldsymbol{a_{i,j}}$ is the value of the $\boldsymbol{j}^{\text{th}}$ cell in the $\boldsymbol{i}^{\text{th}}$ shell ($\boldsymbol{a}$ = 1 for an occupied (live) cell and $\boldsymbol{a}$ = 0 for an unoccupied cell); $\boldsymbol{c_i}$ is the competition/facilitation coefficient of shell $\boldsymbol{i}$ ($\boldsymbol{i}$ = 1…5); $\boldsymbol{k_c}$ is the competition strength (< 0); $\boldsymbol{k_f}$ is the facilitation strength (> 0); $\boldsymbol{s_c}$ is the sensitivity to competition (≥ 0); $\boldsymbol{s_f}$ is the sensitivity to facilitation (> 0); and $\boldsymbol{\rho}$ is the precipitation stress imposed globally on the system (see Equation 8.7). In the case of $\boldsymbol{k_c}$, $\boldsymbol{k_f}$, $\boldsymbol{s_c}$ and $\boldsymbol{s_f}$, whose values depend on plant type, the form of the normal distribution is used in the definition of the biomass-dependence. The function $\boldsymbol{N(B)}$ is introduced, followed by other definitions:

$$\boldsymbol{N(B) = \frac{1}{w\sqrt{2\pi}}e^{-\frac{(B-p_i)^2}{2w_i^2}}}$$

(8.2)

$$k_c(B) = \begin{cases} 60N(B), & (grass) \\ 240N(B), & (shrub) \\ 380N(B), & (tree) \end{cases}$$

(8.3)

$$k_f(\gamma) = \begin{cases} 60N(\gamma), & (grass) \\ 240N(\gamma), & (shrub) \\ 3800N(\gamma), & (tree) \end{cases}$$

$$\gamma = \begin{cases} B, & B \le B_{max} \\ B_{max}, & B > B_{max} \end{cases}$$

(8.4)

$$s_c(B) = \begin{cases} 1 - 54N(B), & (grass) \\ 1 - 216N(B), & (shrub) \\ 1 - 342N(B), & (tree) \end{cases}$$

(8.5)

$$s_f(B) = \begin{cases} 1 + 2e^{-0.2083B}, & (grass) \\ 1 + 2e^{-0.0416B}, & (shrub) \\ 1 + 2e^{-0.02604B}, & (tree) \end{cases}$$

(8.6)

where p_i and w_i are the peak position and width parameter respectively in B, and differ according to plant type (grasses: p_i = 60, w_i = 24; shrubs: p_i = 300, w_i = 96; trees: p_i = 480, w_i = 152). These p_i and w_i values are based on typical life expectancies for plants in the Kalahari (Danin, 1996). Figure 8.2a displays the relevant functions for the case of shrubs (the function shapes remain the same for the grass and tree cases, but differ in their ages of peak maturity).

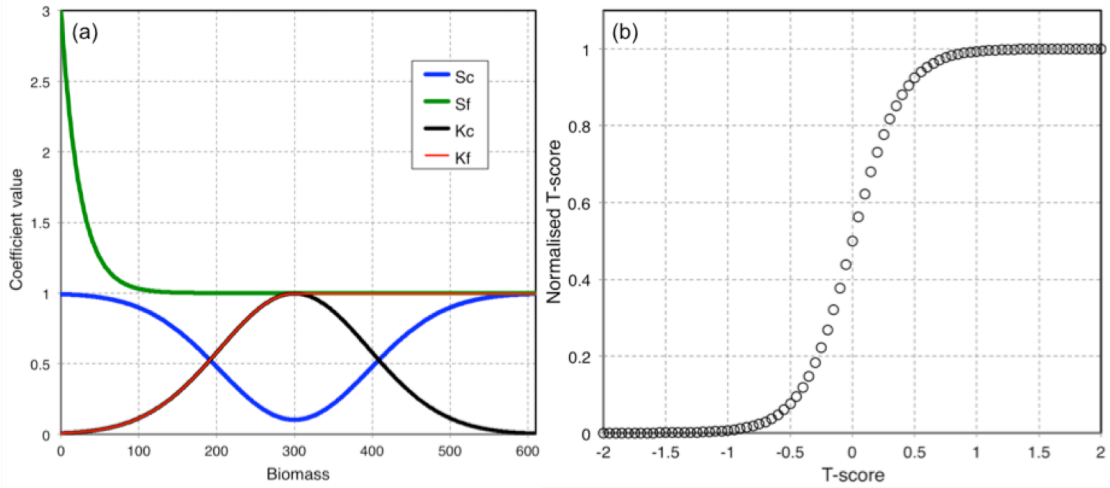


Figure 8.2 (a) Coefficient values for strength of competitive/facilitative effects depending on plant biomass (s_c is sensitivity to competition, s_f is sensitivity to facilitation, k_c is competition strength, k_f is facilitation strength); (b) Relationship between the T score and T normalised score ($\tilde{T}$).

The precipitation stress (ρ) imposed on each plant in the system is defined as:

$$\rho = m.\left(\frac{\rho_i - \rho_{mid}}{\rho_{mid}}\right)$$

(8.7)

where ρ_i is the precipitation during the given interval, ρ_{mid} represents the precipitation level that has neither an added beneficial nor detrimental effect on a plant, and m is a scaling parameter that extends ($m < 1$) or restricts ($m > 1$) the precipitation range across which patterning occurs. In order to reflect the fact that dry conditions favour the development of grass systems, whilst moist conditions promote the establishment of tree systems (Sankaran et al., 2005; Baudena et al., 2010; Lehmann et al., 2011; Staver et al., 2011), different precipitation stress relationships are assumed for grasses, shrubs and trees. For grasses, ρ_{mid} = 180 mm yr^{-1} and m = 1; for shrubs, ρ_{mid} = 200 mm yr^{-1} and m = 1; and for trees, ρ_{mid} = 500 mm yr^{-1} and m = 0.8. These values were chosen based on the data of Sankaran et al. (2005) for savannas in southern Africa, which shows a breakpoint in maximum tree cover at 650 ± 134 mm yr^{-1} and a very low occurrence of trees below 100 mm yr^{-1}. In this way, ρ acts as a more physically realistic version of Bailey's (2011) original global environmental stress parameter (α). Note that ρ and ρ_i are given as annual equivalents, even if Module 1 is run at finer (e.g. monthly) temporal resolutions, in order to facilitate comparisons of simulations at various temporal resolutions.

The T score is normalised to the range 0–1 (asymptotic at very high and very low values of ρ), giving $\tilde{T}$:

$$\tilde{T} = \frac{1}{1 + e^{-5T}}$$

(8.8)

Normalising in this way allows the proportional plant growth at each iteration to be determined. Figure 8.2b displays the function in graphical form.

8.3.3. Plant growth

Lag responses between precipitation decreases and assumed vegetation dieback must be integrated into any vegetation-sediment transport model (Knight et al., 2004). In reality, vegetation takes time to respond to changes in climate parameters, even in dryland systems that are frequently cited as having a 'pulse activity response' regime (Wand, 1999). For instance, Milton & Dean (2000) found that a 12-month period of reduced precipitation was required for Kalahari plant mortality. In order to build a precipitation response lag into the vegetation model (which was absent in Bailey's (2011) model), the value of $\tilde{T}$ is used to determine the proportion of a theoretical growth unit by which all plants can grow over a given iteration. A monthly growth gain unit (G_{unit}) increases monotonically from -0.05 (at $\tilde{T}$ = 0) to +1 (at $\tilde{T}$ = 1):

$$G_{unit} = \frac{1.05}{1 + e^{-k_1(\tilde{T} - \tilde{T}_{mid})}} - 0.05 \tag{8.9}$$

where the k_1 parameter determines the steepness of the curve (k_1 = 15 in the present model) and $\tilde{T}_{mid}$ is the value of the sigmoid's midpoint ($\tilde{T}_{mid}$ = 0.4 in the present model). Negative values of G_{unit} effectively represent a period of highly unfavourable conditions for a given plant, which results in slight biomass loss (see Equation 8.10) and thus affects a plant's competitive/facilitative interactions in the next iteration. Figure 8.3a displays the function for G_{unit} in graphical form.

The cumulative growth (G_{cum}) of a plant, which is used to determine the actual biomass (B) this represents along its growth pathway, is calculated as:

$$G_{cum} = \sum_{i=1}^{iter} G_{unit}$$

(8.10)

If the vegetated cell dies, its cumulated growth returns to zero. The growth pathway is formulated as a logistic curve (cf. Erickson, 1976):

$$B = \frac{B_{max}}{1 + e^{-k_2(G_{cum} - G_{mid})}}$$

(8.11)

where B_{max} is the maximum biomass a plant can achieve over its lifetime (equivalent to full age maturity in months), G_{mid} is the value of the sigmoid's midpoint, and the k_2 parameter determines the steepness of the curve (grasses: G_{mid} = 25; k_2 = 0.14; shrubs: G_{mid} = 130; k_2 = 0.025; trees: G_{mid} = 210; k_2 = 0.016). In this way, biomass change is most rapid when a plant is at an intermediate stage of development, and slowest during seedling growth and when approaching full maturity. Figure 8.3b displays the function for B in graphical form.

A plant's biomass B is converted into an equivalent vegetation height (h):

$$h = h_{max}\left(\frac{B}{B_{max}}\right)$$

(8.12)

where h_{max} is the maximum height (m) to which a plant can grow. The resultant value of h for each grid cell is exported to Modules 2a and 2b to determine wind speed patterns and sediment transport rates across the model domain.

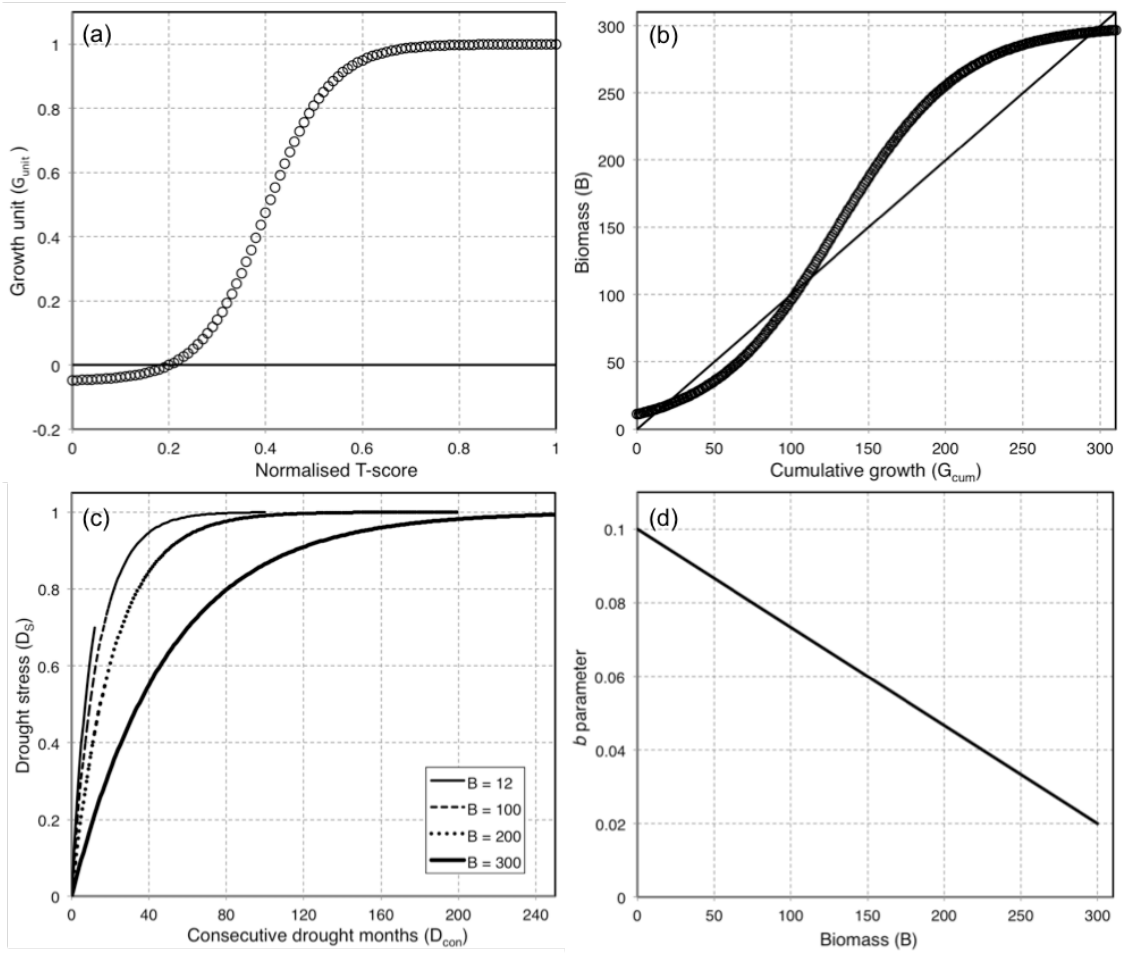


Figure 8.3 Schematic representations of functions for: (a) the relationship between normalised neighbourhood score ($\tilde{T}$) and monthly growth unit (G_{unit}) for a given cell; (b) the relationship between cumulative growth (G_{cum}) for a given cell and the actual biomass (B) this represents; (c) the impact of consecutive droughts (D_{con}) on the drought stress (D_S), with curves shown for four different biomass values for grasses; (d) the linear relationship between biomass and the b parameter determining saturation rate in panel (c), again for grasses.

When $\tilde{T}$ < 0.5 (Equation 8.8), a given plant experiences a period of generally unfavourable conditions, which for the purposes of this model is termed a 'plant drought'. The severity of a plant drought is proportional to the number of consecutive

(unbroken) months where $\tilde{T}$ is lower than 0.5, and is a function of plant type and the magnitude of $\tilde{T}$. The consecutive number of plant droughts (D_{con}) is given by:

$$D_{con} = \begin{cases} \sum \frac{0.5 - \tilde{T}}{0.5}, & \tilde{T} < 0.5 \\ 0, & \tilde{T} \geq 0.5 \end{cases}$$

(8.13)

The stress that a plant experiences due to drought (D_S) is an exponential function of D_{con}:

$$D_S = 1 - e^{-b_s . D_{con}}$$

(8.14)

where b_s controls the saturation rate of the exponential. D_S then contributes to the plant's probability of dying. Since larger plants are generally able to draw on more reserves than smaller plants in times of increased environmental stress (Becerra et al., 2013), the b_s parameter is dependent on plant biomass:

$$b_s = \begin{cases} -0.0002\dot{6}B + 0.1, & (grass) \\ \frac{-0.0002\dot{6}B + 0.1}{2}, & (shrub) \\ \frac{-0.0002\dot{6}B + 0.1}{5}, & (tree) \end{cases}$$

(8.15)

The dependence of the b_s parameter (and thus exponential saturation rate of D_S) on plant type reflects the differential resilience of grasses, shrubs and trees to drought (annual grasses generally being most vulnerable and trees being most resilient; Baudena et al., 2010). Figure 8.3c,d displays the functions for determining drought stress in graphical form.

8.3.4. Probability of death from stress

The probability that a given cell dies at each iteration of Module 1 is determined as a compound probability of five stresses, which themselves depend on plant type: (i) stress due to drought, D_S; (ii) stress due to age, Z_S; (iii) stress due to sediment balance, Sed_S; (iv) stress due to grazing, G_S; and (v) stress due to fire, F_S. Together, these stresses contribute to a total stress (T_S) for each grid cell.

If an age-related stress component is omitted, under low-stress conditions individual cells continue to age and the probability of death is unrealistically small. The age-dependent stress is greater than zero for very young individuals (due to relatively high mortality rates in younger plants; e.g. Lauenroth & Adler, 2008), drops to zero for mature individuals and then rises to an asymptotic value (*M*), reflecting increased mortality of relatively old plants as overall plant function deteriorates (e.g. Roach et al., 2009). The different ages to which grasses, shrubs and trees typically live is accounted for by changing the age of peak maturity, as well as the rate at which the age stress rises asymptotically to *M*. Stress due to age (Z_S) is given as:

$$Z_S(z) = \begin{cases} \begin{cases} \frac{0.2 - 12N(z)}{5}, & z \leq 60 \\ \frac{1 - 120N(z)}{5}, & z > 60 \end{cases} & (grass) \\ \begin{cases} \frac{0.2 - 48N(z)}{5}, & z \leq 300 \\ \frac{1 - 240N(z)}{5}, & z > 300 \end{cases} & (shrub) \\ \begin{cases} \frac{0.2 - 76N(z)}{5}, & z \leq 480 \\ \frac{1 - 480N(z)}{5}, & z > 480 \end{cases} & (tree) \end{cases} \quad (8.16)$$

where z = cell age and $z \geq 1$ for occupied cells. Figure 8.4a displays the Z_S function.

Semi-arid vegetation responds physiologically to sediment balance (Brown, 1997; Dech & Maun, 2005; Levin et al., 2008), and this can be represented in numerical models as elementary growth functions (e.g. Nield & Baas, 2008a,b). Although often derived from qualitative descriptions, growth functions based on sediment balance are an important inclusion in coupled vegetation-sediment movement models because they capture the differences in tolerance to burial and erosion between vegetation types. Moreover, such functions implicitly define differential colonization of geomorphological niche areas, without the explicit inclusion of interspecies interactions between vegetation types (Nield & Baas, 2008a).

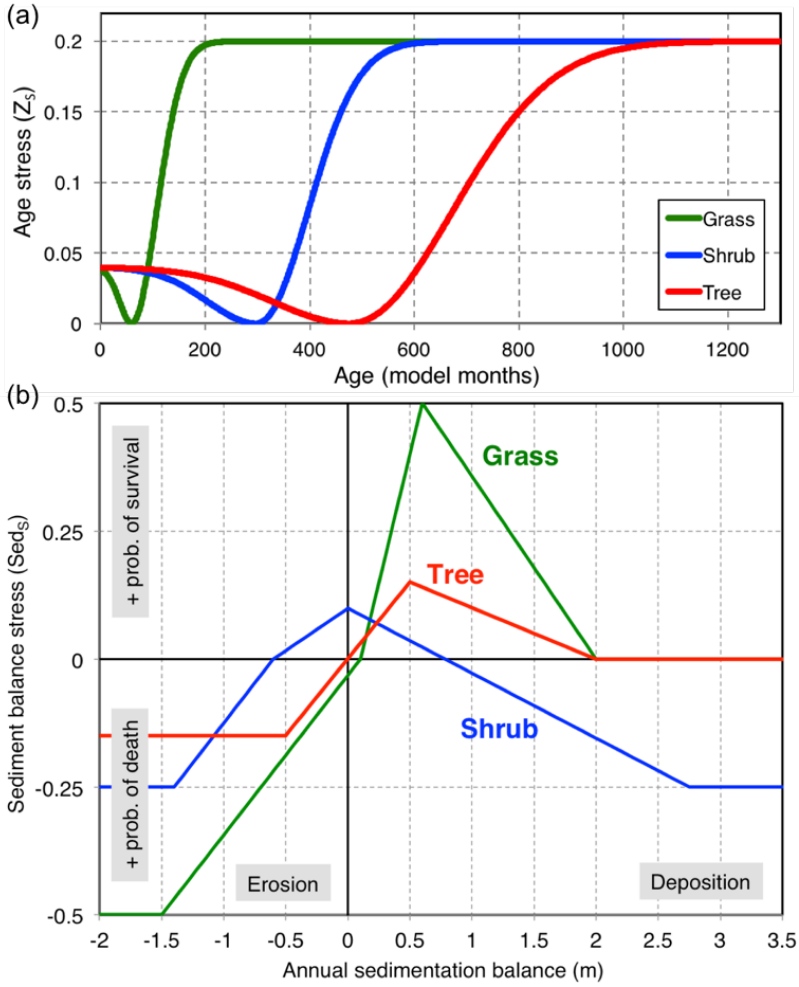


Figure 8.4 (a) Functions for stress due to plant age (Z_S), for grasses, shrubs and trees; (b) functions for stress due to sedimentation balance (Sed_S), representing the annual response to burial and/or erosion conditions for the different vegetation types (adapted from Nield & Baas, 2008a, p.731).

The sediment-balance stress (Sed_S) is calculated as a function of sedimentation balance (annual equivalent, in m) for each vegetated grid cell. The specific ranges of Sed_S are based in part on the elementary growth functions for generic grass and shrub species presented by Nield & Baas (2008a), which were derived from a combination of qualitative vegetation behaviour described in the literature and trial and error (Figure 8.4b). Pioneer dune grass species similar to *Stipagrostis amabalis* or marram grass (*Ammophila*) require fresh sediment input to stimulate and maintain growth (van der Putten et al., 1993; Danin, 1996; Moore, 1996), so peak positive Sed_S (i.e. reduced probability of death) occurs where there is net deposition on a cell. Neutral or negative balances lead to negative Sed_S (i.e. increased probability of death) due to the impact of parasites and soil pathogens (Maun, 1998). Invasive woody shrub species such as *Rhigozum trichotomum* can tolerate small changes in sedimentation balance (Dech & Maun, 2006), but prefer less active landscapes than grasses, so Sed_S rapidly declines when significant erosion or deposition occurs. There is relatively little literature on the impact of sedimentation balance on tree growth in drylands, but evidence suggests that some sediment accumulation can be beneficial to tree development (e.g. Zhang et al., 2010). When sedimentation balance is negative, trees are expected to behave similarly to woody shrub species, with a slightly more muted response due to the generally higher resilience of dryland trees compared to shrubs and grasses (Wagner et al., 2013).

The stress due to grazing (G_S) is calculated as a function of the stocking rate on the landscape, typically given as large stock units (LSU - i.e. livestock and wild ungulates with a body weight > 35 kg) per unit area (Dean & Macdonald, 1994). In the southern Kalahari and western Botswana rangelands (mean annual rainfall 150–200 mm yr^{-1}), stocking rates have been shown to typically range between 0.015–0.06 LSU ha^{-1} (Blaum et al., 2009; Burgess, 2009). Since livestock only graze on grasses, G_S is

always set to 0 for both shrubs and trees. For cells colonised by grasses, G_S is given as:

$$G_S = \begin{cases} n\Omega, & \Omega \leq 0.06 \\ 0.90, & \Omega > 0.06 \end{cases}$$

(8.17)

where Ω is the stocking rate (LSU ha^{-1}) and n is the slope factor (n = 15 in the present model).

The stress that a plant experiences due to fire (F_S) is constant for grasses of all ages, due to the high propensity for grassy material to burn, whereas it is calculated as an exponential function of cell age (z) in the case of shrubs and trees:

$$F_S = \begin{cases} 0.9, & (grass) \\ 0.4\left(e^{-lz}\right) + 0.5, & (shrub) \\ 0.6\left(e^{-lz}\right) + 0.3, & (tree) \end{cases}$$

(8.18)

where l controls the saturation rate of the exponential (l = 0.01 in the present model). In this way, trees of are more likely to survive a fire than shrubs of the same age.

The total stress (T_S) experienced by a plant is determined as:

$$T_S = Sed_S - Z_S(z) - D_S - F_S - G_S$$

(8.19)

T_S serves as a critical value against which a uniformly distributed random value (β) is compared. At each timestep, β is recalculated for each cell. If $\beta \leq T_S$, a dead/empty cell becomes occupied ($a: 0 \rightarrow 1$) and occupied cells live on (a = 1), increasing their

age by the appropriate time unit; if $\beta > T_S$, a live cell dies ($a: 1 \rightarrow 0$) and an empty cell remains empty (a = 0).

8.3.5. Probability of recolonisation

The recolonisation of an empty cell by a particular vegetation type (grass, shrub or tree) can either be determined using static probabilities imposed at the start of the simulation (mainly employed for model testing), or using dynamic probabilities. For dynamic recolonisation scenarios, the proportion of each vegetation type occupying the domain at the end of a given iteration determines the probabilities that the vegetation types recolonise a bare cell at the next iteration. This effectively replicates the existence of a 'seed bank' in the model domain, whose composition is dependent on the relative abundance of each vegetation type. The ability of perennial grasses to rapidly colonise bare surfaces at the expense of other vegetation types (e.g. Carpenter et al., 1986; Bhattachan et al., 2014) is accounted for by artificially adapting the current relative proportion of each vegetation type in the seed bank:

$$p_{RG} = \frac{(P_G + \alpha_G)}{(1 + \alpha_G + \alpha_S + \alpha_T)} \tag{8.20}$$

$$p_{RS} = \frac{(P_S + \alpha_S)}{(1 + \alpha_G + \alpha_S + \alpha_T)} \tag{8.21}$$

$$p_{RT} = \frac{(P_T + \alpha_T)}{(1 + \alpha_G + \alpha_S + \alpha_T)} \tag{8.22}$$

where p_{RG}, p_{RT} and p_{RS} are the probabilities of recolonisation of an empty cell by a grass, tree or shrub, respectively; P_G, P_S and P_T are the current proportions of grass, shrub and tree cells (respectively) in the entire model domain; and α_G, α_S and α_T are multiplicative factors that act to increase or decrease the recolonisation probabilities of a grass, shrub or tree, respectively. α_G, α_S and α_T are formulated as a function of the precipitation regime, to reflect the fact that dry conditions favour the dominance of grass and shrub recolonisation, whereas highly moist conditions are more beneficial to the establishment of tree systems (Sankaran et al., 2005; Baudena et al., 2010; Lehmann et al., 2011).

Savannas (mixed tree-C_4 grass systems) effectively occupy an intermediate position in the grassland-forest continuum, which is thought to be at least partly dependent on rainfall (other controlling mechanisms include fire disturbance, nutrient availability and large mammal herbivory) (Scholes & Archer, 1997; Higgins et al., 2000; van Langevelde et al., 2003). The wealth of existing empirical data on savanna/grassland transitions can be used to parameterise the model's multiplicative factors for recolonisation (α_G, α_S and α_T). Using a large dataset of African sites, Sankaran et al. (2005) demonstrated that below a mean annual precipitation (MAP) threshold of 650 mm yr^{-1}, maximum woody (tree) cover in savannas is constrained by, and increases linearly with, MAP. Below a MAP of 650 mm, moisture availability constrains permit grasses to coexist with trees, whereas above the threshold, disturbances such as fire and herbivory are required for a grass/tree coexistence (Sankaran et al., 2005). Since there is a high degree of variability in rainfall-based recolonisation dependence across different vegetation types and species, a reasonable approximation is used:

$$\alpha_{Gi} = \begin{cases} 0.5 - \dfrac{\rho}{1200}, & \rho \leq \rho_{equal} \\ 0, & \rho > \rho_{equal} \end{cases}$$

(8.23)

$$\alpha_{Si} = \begin{cases} 0.1 - \dfrac{\rho}{3000}, & \rho \leq \rho_{equal} \\ -0.1, & \rho > \rho_{equal} \end{cases} \tag{8.24}$$

$$\alpha_{Ti} = \begin{cases} \dfrac{\rho}{2400} - 0.25, & \rho \leq 2.\rho_{equal} \\ 0.25, & \rho > 2.\rho_{equal} \end{cases} \tag{8.25}$$

where α_{Gi}, α_{Si} and α_{Ti} are initial multiplicative factors, and ρ_{equal} represents the precipitation level where neither grass nor tree recolonisation dominates. A ρ_{equal} value of 600 mm yr^{-1} is assumed in the model, based on the data of Sankaran et al. (2005) and Staver et al. (2011) showing that 50% tree cover occurs at MAP ≈ 600 mm yr^{-1} in southern Africa. In order to introduce stochasticity to the recolonisation mechanism, a Gaussian frequency distribution is approximated ($\mu = \alpha_{G,temp}$, $\alpha_{S,temp}$ or $\alpha_{T,temp}$, $\sigma = 0.1$), from which the final values for α_G, α_S and α_T are randomly chosen. The inclusion of a stochastic element allows a small number of trees to become established even in dry conditions, as is the case in many arid areas in southern Africa (Sankaran et al., 2005). In this way, both the precipitation regime and current occupation proportions determine the likelihood of a certain vegetation type recolonising an empty cell.

8.3.6. Update frequencies for Module 1

For Module 1, the temporal scale of plant-plant interactions can be adapted by changing the number of months represented by a single iteration of the module. Given the 'pulse-activity response' regime observed in many dryland systems (Wand, 1999), it is important to allow plants to respond sufficiently quickly to individual

rainfall and sediment movement events in the model. However, the temporal resolution of the model must also be coarse enough for realistic lags in vegetation growth (e.g. Milton & Dean, 2000; Knight et al., 2004) to be preserved. Therefore, following a variety of preliminary tests, we set the standard vegetation update frequency (i.e. the frequency at which Module 1 is run) at 3 months in the ViSTA model, which fully captures seasonal variability. This matches the updating interval used by Yan & Baas (2017) in their extended DECAL model.

8.4. Wind dynamics (Module 2a)

The relative levels of erodibility and erosivity broadly determine the movement of sediment across the model domain. Sediment flux in the ViSTA model is formulated as a function of horizontal wind velocity (u) as opposed to the more commonly employed wind shear velocity (u_*), because several aeolian studies (e.g. Sterk et al., 1998; Schönfeldt & von Löwis, 2003; Leenders et al., 2005; Wiggs & Weaver, 2012) have shown that sediment transport is better correlated with wind velocity fluctuations than time-averaged wind shear velocity.

8.4.1. Wind velocity

An unobstructed wind velocity (u_{ref}) is derived at each timestep, which represents the mean flow over a flat, sandy surface with no elements. The stochastic nature of airflow (e.g. Rice et al., 1999; Böhner et al., 2003; Klose & Shao, 2012) is introduced in the ViSTA model by approximating a Gaussian frequency distribution ($\mu = u_{ref}$, $\sigma = 0.1$), from which a wind velocity is randomly chosen for each cell in the domain.

This wind velocity is further adjusted depending on vegetation morphology and surface topography, as described below.

Zones of reduced wind velocity in the ViSTA model are formulated as rectangular ‘corridors’ of recovery, following the theoretical approach of Okin (2008) (Figure 4.6). In contrast, the widely used formulation of Raupach (1992) for the recovery of shear stress – which is directly related to wind speed – assumes a zone of zero stress in the lee of plants. All vegetation elements distributed on the surface are assumed to produce a downwind zone of affected wind velocity. Previous studies (e.g. Perera, 1981; Vigiak et al., 2003; Leenders et al., 2011; Gillies et al., 2014; Wu et al., 2015; Mayaud et al., 2016b) have shown that wake zone dynamics are primarily determined by the height, width, porosity and plant type of elements. Element height in the model is directly integrated into the formulation for recovery, and the impact of element width is implicitly accounted for in Okin’s (2008) corridor approach. Plant wakes are assumed to have the same constant width as the frontal width of the elements forming them. A limit is imposed on wake length, such that wind flowing through a given cell is considered unaffected once the cell is located beyond a certain downwind distance from the nearest element. The ratio between the flow passing through the element (‘bleed flow’) and the airflow that diverges over the element is determined by plant porosity, which thus controls the extent to which wind speed is reduced through the element canopy and the rate of recovery in its lee (Mayaud et al., 2016b).

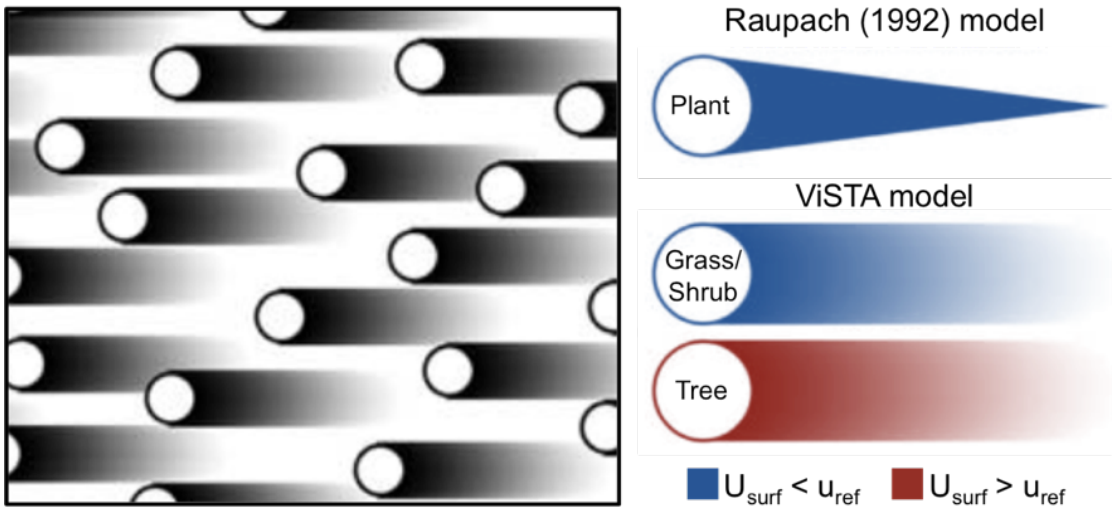


Figure 8.5 The distribution of reduced wind shear stress on the surface during wind erosion in the Raupach (1992) model, compared to the distribution of reduced wind velocity in the ViSTA model (based on the theory of Okin, 2008). The Raupach model assumes a triangular wake that experiences no shear stress at the surface (dark area). In the ViSTA model, wind velocity (u_{surf}) increases from the downwind edge of a grass shrub and eventually reaches the wind velocity for an equivalent un-vegetated surface (u_{ref}). In the immediate lee of trees, u_{surf} is higher than u_{ref} due to a 'bottom gap' effect. The landscape is formulated as a series of 'plant corridors' with wake zones sometimes interfering with others (adapted from Okin, 2008, p.5).

The type of vegetation (here grass, shrub, tree) determines whether an element acts to increase or decrease wind velocity in its wake. Grasses and shrubs are collectively defined as elements with growing points that are mainly located at ground level, while trees are distinguished as having a distinctive trunk below a canopy (Leenders et al., 2007). In the cases of grasses and shrubs, it has been shown in field and wind tunnel experiments (e.g. Bradley & Mulhearn, 1983; Vigiak et al., 2003; Leenders et al., 2007; Gillies et al., 2014; Wu et al., 2015, Mayaud et al., 2016b,c) that the surface wind velocity in the wake (u_{surf}) is lower than in the absence of plants (u_{ref}), and exponentially recovers with increasing downwind distance. Therefore, in the ViSTA model a zone of reduced wind velocity in the wake of grasses and shrubs is parameterised using an exponential curve:

$$u_{surf} = (u_{ref} - u_0).(1 - e^{-b\frac{x}{h}}) + u_0$$

(8.26)

where u_0 is the minimum wind velocity in the direct lee of the nearest upwind element, $\frac{x}{h}$ is the downwind distance from the nearest element in terms of element height, and b is a fitted coefficient. Physically realistic values for u_0 and b are derived using the field data of Mayaud et al. (2017b) (see Figure 7.3 and Figure 7.4), such that the recovery curve is determined by the height of the element (h) and its optical porosity (θ_i):

$$u_0 = u_{ref}(0.0146\theta_{cum} - 0.4076)$$

(8.27)

$$b = 0.0105\theta_{cum} + 0.1627$$

(8.28)

Wind recovery in the wake of patches has been shown to be slightly longer than in the wake of individual elements (Mayaud et al., 2016c). Rather than explicitly parameterising longer wind flow recovery once a skimming flow regime is arbitrarily assumed to occur, the cumulative impact of multiple adjoining elements on wind flow is allowed to emerge naturally by defining a cumulative porosity (θ_{cum}) for each patch (a 'patch' being defined as 2 or more contiguous plants along a given wind path):

$$\theta_{cum} = \theta_i.\theta_{i+1}.\theta_{i+2} \ldots \theta_n$$

(8.29)

where i is the first plant from a patch along the wind path, and n is the total number of contiguous plants downwind of the first plant. If the wind encounters a single plant, θ_{cum} simply equates to the porosity of that plant (θ_i).

In the case of the wake zone in the lee of trees, u_{surf} is higher than u_{ref} in the immediate lee due to a 'bottom gap' effect, which arises because of the compression of streamlines between the underside of the tree canopy and the ground (Gross, 1987; Kim & Lee, 2002; Dupont et al., 2014; Mayaud et al., 2016b). This zone of increased wind velocity is parameterised using a logistic curve:

$$u_{surf} = a\left(1 - \frac{1}{1 + e^{-2\left(\frac{x}{h}+c\right)}}\right) + 1 \quad (8.30)$$

where a and c are fitted coefficients. The tree trunk height dictates the extent to which airflow is compressed (i.e. coefficient a), while the height of the tree canopy determines the recovery distance back to the unobstructed wind velocity (i.e. coefficient c).

It is hypothesised that shorter trunks – and thus lower-lying canopies – should lead to higher compression than taller trunks. However, below a certain trunk size the wind becomes diverted away from the underside of the canopy, similarly to a shrub. Under these assumptions, the scaling coefficient a can be estimated for a given trunk height (h_t) by assuming normality around a mean using a Gaussian distribution:

$$a = \frac{D}{\sigma\sqrt{2\pi}} . e^{-\frac{(h_t-\mu_T)^2}{2\sigma^2}} \quad (8.31)$$

where μ_T is the trunk height at which maximum airflow compression occurs, σ is the standard deviation, and D is a constant.

If the maximum acceleration of airflow resulting from the bottom gap is assumed to be 40% of the unobstructed flow (i.e. a = 0.4), based on the field data of Mayaud et al. (2016b), and realistic values are substituted for μ_T (1.50 m) and σ (0.75 m), Equation 8.31 can be rearranged to give D = 0.75. In this study, the left-hand tail of Gaussian curve is curtailed, such that any tree element with a trunk height < 0.3 m is considered behave aerodynamically like a shrub and not a tree. Given the insufficient data on the relationship between canopy height and its relationship with coefficient c, the fit presented in Figure 7.3 (c = -4.20) is used as a constant. Substituting these relationships into the logistic curve gives the full parameterised recovery of wind flow downwind of a tree with a given trunk height:

$$u_{surf} = 0.4e^{-\frac{(h_t-\mu)^2}{1.13}}\left(1 - \frac{1}{1 + e^{-2\left(\frac{x}{h}-4.2\right)}}\right) + 1 \quad (8.32)$$

8.4.2. Airflow compression

Topographic steering and flow field compression are known to play an important role in the morphology of aeolian bedforms such as dunes at a variety of scales (Lancaster et al., 1996; Wiggs et al., 1996b; Walker & Nickling, 2002; Hesp et al., 2005; Baddock et al., 2011; Weaver & Wiggs, 2011; Bauer et al., 2012; Barrineau & Ellis, 2013; Chapman et al., 2012, 2013). The intrusion of topography into the atmospheric boundary layer initially results in flow retardation as a result of an adverse (increasing) pressure gradient, which is rapidly followed by a decline in pressure as the streamlines are compressed, and flow accelerates. Wind speedup is necessary to sustain the shape of the windward slope (Bagnold, 1941; Momiji &

Warren, 2000), and Momiji et al. (2000) showed that introducing the effect in a simple model of sand transport improves the realism of simulated dune forms.

In the field, wind flow has been shown to accelerate in a broadly linear manner over the stoss slope of dunes (e.g. Mulligan, 1988; Weaver & Wiggs, 2011). Consequently, airflow compression is simulated in the ViSTA model using an additive factor that scales linearly with the length of a given wind path along a slope. The slope-corrected wind velocity (u_{slope}) for a particular cell is dependent on the wind velocity of the upwind cell ($u_{surf[k-1]}$):

$$u_{slope} = u_{surf[k-1]} \cdot \gamma$$

$$\gamma = \begin{cases} (s_{h[k]} - s_{h[k-1]}) . \omega, & (s_{h[k]} - s_{h[k-1]}) \neq 0 \\ 1 & (s_{h[k]} - s_{h[k-1]}) = 0 \end{cases},$$

(8.33)

where $s_{h[k]}$ is the surface height of the polled cell, $s_{h[k-1]}$ is the surface height of the upwind cell, and ω is a change coefficient (set at 0.1 in the current model). Thus, when the height difference between a polled cell and its downwind cell is positive (i.e. rising slope), the additive factor (γ) is positive and wind speeds up (Figure 8.6). The reverse occurs on a negative slope. In order to prevent runaway wind velocities, the maximum amount of speedup is limited to 100% of the unobstructed wind velocity.

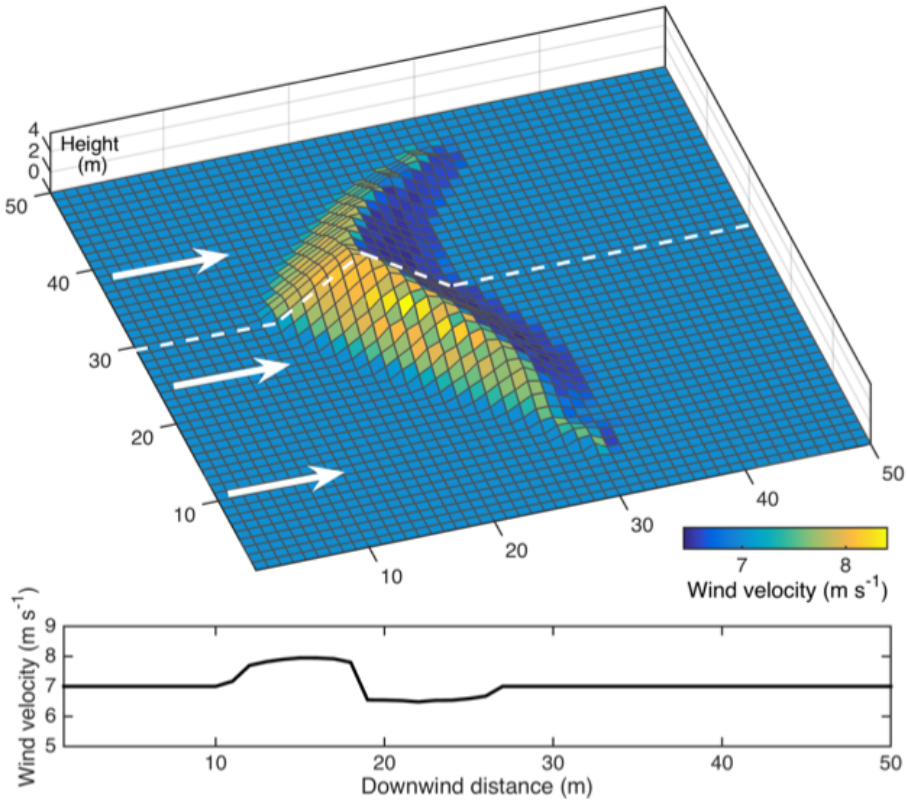


Figure 8.6 Example of wind speedup and slowdown as wind flow passes over a modelled barchanoid dune. Higher wind speeds occur along the stoss slope and lower wind speeds occur along the leeside slip face. White arrows show wind direction. Dotted white line shows wind velocity transect along the centre line of the dune. Wind velocity stochasticity was 'turned off' in the model, to ensure a homogenous approach flow for the purposes of this test.

8.4.3. Wind (transport) direction

Many field and modelling studies (e.g. Wasson & Hyde, 1983; Werner, 1995; Bishop et al., 2002; Lynch et al., 2009; Rubin & Hesp, 2009; Jackson et al., 2011; Bauer et al., 2012; Chapman et al., 2012; Gao et al., 2015b) have emphasised the importance of wind approach angles for the development of dunes, due to the alteration of near-surface wind velocity and turbulence, and thus sediment transport magnitudes and pathways. Simulating different transport directions is therefore vital in any realistic model of erosion at both the plant and dunefield scales (Nield & Baas, 2008a; Dupont et al., 2014). Broadly, two methods exist for simulating different directions in

cellular automata: (i) directly, which involves changing the direction slabs move across the grid, or (ii) passively, which involves the rotation of the resultant landforms in a fixed transport direction.

Previous implementations of these methods have suffered from several limitations. Werner (1995) directly modelled oblique transport by defining slab displacement with longitudinal and transverse components, but this is limited to a small number of discretised oblique directions and is restricted by the overall length of the displacement vector (Nield & Baas, 2008a). Another direct approach is to assign individual slab transport events to either a longitudinal or transverse direction according to the probabilities defined by obliqueness degree. However, test simulations using Nield & Baas's (2008a) DECAL model showed that this method produces dunes that are elongated perpendicular to the wind and exhibit unequal horns, which differs from the morphology that develops under a transport regime that is parallel to the grid.

In contrast, passive wind direction simulations involve rotating the grid and resampling the morphology, choosing the rotation point to maximise the area retained and using a large model space to ensure the exclusion of some morphology is minimised (e.g. Bishop et al., 2002). For instance, Nield & Baas (2008a) investigated a passive approach whereby the model grid was tessellated, and a triangulated irregular network was used to resample the central area of the extrapolated morphology. However, the need for artificial insertion or exclusion of slabs after rotation to maintain volume continuity using this method, and the destruction of the periodic nature of the boundaries, can be problematic (Bishop et al., 2002; Nield & Baas, 2008a). Narteau et al. (2006) presented a solution to the sediment conservation problem by rotating only a circular section of the grid, but this

does not prevent edge effects propagating from where the circular area intersects with the surrounding square model grid to the central region of the model space.

Here, we propose a new method for directly imposing continuous wind and transport directions onto any cell-based domain, based on an algorithm developed by R. M. Bailey (unpublished). Accurately determining the path of the wind and transported sand across the simulated surface requires the individual path to each cell in the domain to be calculated (Figure 8.7a). In effect, this parameterises the wind as a series of linear transport 'corridors' rather than a unified 'front' of airflow. First, the intercept (i) of the wind path with the edge of the domain from the target cell is determined trigonometrically:

$$i = r_t - c_t . \tan\theta \tag{8.34}$$

where r_t is the row number of the target cell, c_t is the column number of the target cell and θ is the wind angle for the given timestep. Then, the length of the wind/transport path that crosses each polled cell on its way to the target cell is calculated (Figure 8.7a). The path distance through a given polled cell can then be trigonometrically determined by identifying sets of local intercepts ($x_1{}^*$, $x_2{}^*$, $y_1{}^*$, $y_2{}^*$) around the polled cell, such that:

$$x_1 = c_p - 1; \quad x_2 = c_p; \quad y_1 = r_p - 1; \quad y_2 = r_p;$$

$$x_1{}^* = \frac{y_1 - i}{\tan\theta}; \quad x_2{}^* = \frac{y_2 - i}{\tan\theta}; \quad y_1{}^* = m . x_1 + i; \quad y_2{}^* = m . x_2 + i \tag{8.35}$$

where r_p is the row number of the polled cell and c_p is the column number of the polled cell. The location of these reference points relative to each other provides a spatial definition of whether the polled cell is located along the wind path to the target cell. If it is located along the wind path, the length of the individual (hypotenuse) path crossing through the polled cell can be calculated relative to the centreline of the target cell (Figure 8.7b). Table 8.1 summarises the calculations for determining the hypotenuse using the local intercepts for each possible wind path scenario. Determining the specific distance of the wind path crossing each cell allows wind speedup/slowdown to be accurately simulated given the vegetation properties of each cell. It also allows for transport to be probabilistically deposited along realistic 'deposition pathways' downwind of each flux-emitting cell.

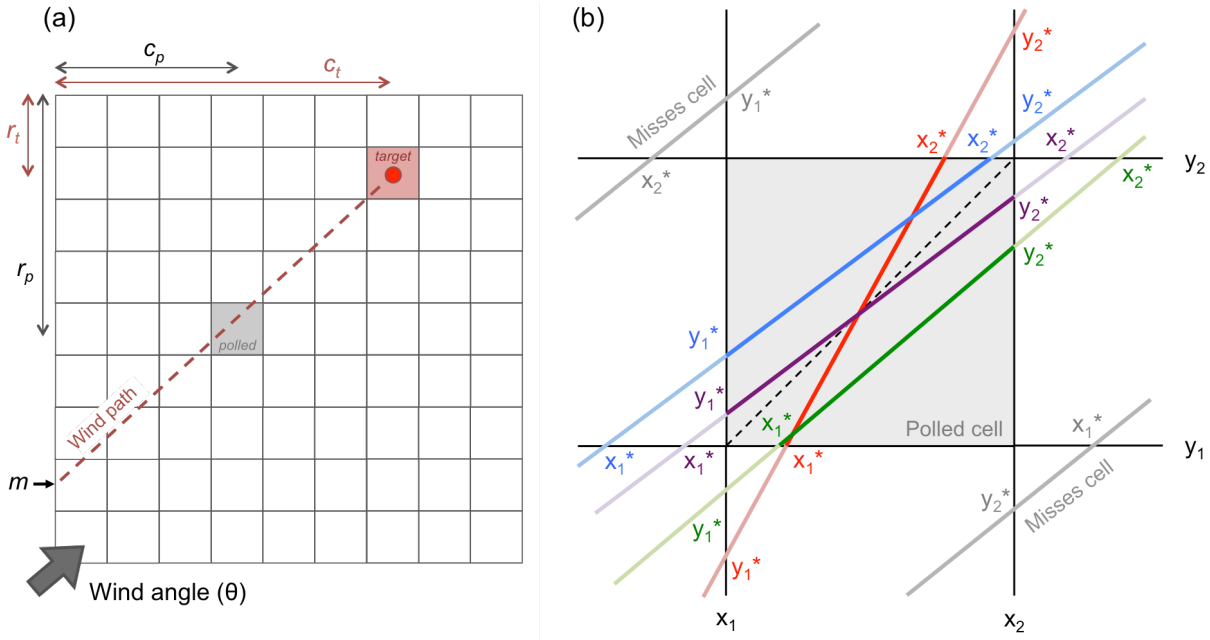


Figure 8.7 (a) Schematic diagram showing how the wind path (dotted red line) to a given target cell (in red) is determined in the model, and the various lengths required to calculate the wind path through any given polled cell (in grey); (b) Different wind approach scenarios for calculating length of wind's path through each polled cell, when the wind angle is oblique and gradient is positive. The reference points used for calculating path lengths differ depending on the gradient of the wind path, and the wind angle relative to the diagonal centreline (shown as dotted line) of the polled cell (see main text).

	Conditions	Wind path calculation
Positive gradient	$x_1^* < x_1$ and $x_2^* \leq x_1$	Misses cell
	$x_1^* \geq x_2$ and $x_2^* > x_2$	Misses cell
	$x_1^* \geq x_1$ and $x_2^* \geq x_2$	$\sqrt{(x_2 - x_1^*)^2 + (y_2^* - y_1)^2}$
	$x_2^* \leq x_2$ and $x_1^* \leq x_1$	$\sqrt{(x_2^* - x_1)^2 + (y_2 - y_1^*)^2}$
	$x_1^* > x_1$ and $x_2^* < x_2$	$\sqrt{(x_1^* - x_1)^2 + (y_2 - y_1)^2}$
	$y_1^* > y_1$ and $y_2^* < y_2$	$\sqrt{(x_2 - x_1)^2 + (y_2^* - y_1^*)^2}$
Negative gradient	$x_1^* \leq x_1$ and $x_2^* \leq x_1$	Misses cell
	$x_1^* > x_1$ and $x_2^* \geq x_2$	Misses cell
	$x_1^* \leq x_2$ and $x_2^* \leq x_1$	$\sqrt{(x_1^* - x_1)^2 + (y_1^* - y_1)^2}$
	$x_1^* \geq x_2$ and $x_2^* \geq x_1$	$\sqrt{(x_2 - x_2^*)^2 + (y_2 - y_2^*)^2}$
	$x_1^* < x_2$ and $x_2^* > x_1$	$\sqrt{(x_1^* - x_2^*)^2 + (y_2 - y_1)^2}$
	$y_1^* < y_2$ and $y_2^* > y_1$	$\sqrt{(x_2 - x_1)^2 + (y_1^* - y_2^*)^2}$

Table 8.1 Calculations of wind path through each polled cell, depending on the gradient of the wind trajectory (positive gradient refers to approach angles of 90°–180° and 270°–360°, negative gradient refers to approach angles of 0–90° and 180°–270°) and the local intercept conditions (see main text).

8.5. Sediment movement (Module 2b)

8.5.1. Erosion, transport and deposition

Sediment transport dynamics are introduced into the ViSTA model using a transport model based on Werner's (1995) algorithm for simulating dune formation in arid environments. Volumes of sediment are transported across the model domain based on probabilities of erosion (p_e) and deposition (p_d) and the wind velocities derived in Module 2a. Each cell is polled once per iteration ('polling without replacement', Baas & Nield (2007)), which contrasts the original approach of Werner (1995), whereby some cells are polled multiple times whilst others are not polled at all.

During all iterations of Module 2B, a function is applied to determine how much sediment is eroded from each cell. The total amount of sediment eroded from a given

cell is calculated deterministically as a function of the cell's wind velocity, using the semi-empirical flux relationship of Dong et al. (2003):

$$Q = a_D \left(1 - \frac{u_t}{u}\right)^2 \left(\frac{\rho_{air}}{g}\right) u^3 \quad (8.36)$$

where Q is the predicted mass flux for the given time interval (kg m^{-1} s^{-1}), u is the mean horizontal wind velocity over the given time interval (m s^{-1}), u_t is the horizontal velocity threshold for sediment entrainment (m s^{-1}), ρ_{air} is the density of air (1.25 kg m^{-3}), g is acceleration due to gravity (9.81 m s^{-2}), and a_D is an empirically fitted constant. Dong et al.'s (2003) model has been shown to perform well over a variety of averaging intervals using field-based wind velocity data (Leenders et al., 2011; Mayaud et al., 2016a).

The simulated flux is converted into an equivalent volumetric flux (m^2 s^{-1}), which can be specified directly in the model. For the experimental runs presented here, we assume a bulk density for sand of 2000 kg m^{-3} (Bailey & Thomas, 2014). In turn, the height of the sediment 'slab' moving from any given cell can be derived from the volumetric flux. The p_e value of a polled cell determines the proportion of the sediment slab that is eroded from it; p_e varies from 0 to 1 depending on the moisture level of the sediment in the cell and its location relative to shadow zones. The final slab height is removed from the polled cell and distributed downwind along a deposition pathway specifically calculated for each source cell.

Transport and deposition in the model occur stochastically, with each cell being characterised by a different p_d value. Destination cells already populated with sediment are assigned a p_d value of 0.7, whilst bare destination cells are assigned a lower p_d value of 0.4, to replicate the increased saltation distances on hard rock

through more efficient rebound (Bagnold, 1941; Bishop et al., 2002; Nield & Baas, 2008a,b). If a cell is vegetated, the p_d value increases proportionally to plant porosity, to replicate the more effective trapping of saltating grains by denser plants (Wolfe & Nickling, 1993; Okin et al., 2006; Suter-Burri et al., 2013). The probability of deposition in the presence of vegetation, p_{dV}, is given by:

$$p_{dV} = \begin{cases} (1 - p_d).\left(\frac{100 - \theta_i}{100}\right), & h > \varepsilon \\ p_d \quad , & h \leq \varepsilon \end{cases} \tag{8.37}$$

where θ_i is the porosity of the plant, h is the height of the plant, and ε is a height limit below which a plant has no impact on the probability of deposition. Surface moisture (e.g. after a precipitation event) also affects sediment transport dynamically by modulating the p_e and p_d values via a feedback function (see section 8.5.2).

The total volume eroded from a source cell is divided according to the p_d of each downwind cell (until a set limit of downwind cells is reached), as well as the length of the wind path traversing each downwind cell. A cumulative p_d is thus derived for the deposition path downwind of the source cell, and the proportional volume of eroded sediment is allocated to the relevant 'sink' cells. Once cumulative p_d = 1, no more deposition can take place downwind. The transport length of the moving sand volume is limited to a certain number of sink cells downwind of its source cell, to ensure that sand cannot 'jump across' intervening features such as vegetation. If the transport limit is exceeded and cumulative p_d < 1, the total remaining sediment is deposited onto the last cell of the limit. This approach differs to previous algorithms (e.g. Bishop et al., 2002; Baas & Nield, 2007; Nield & Baas, 2008a,b), where a slab is repeatedly moved downwind until it exceeds the probability of deposition, and is then deposited in its entirety. The Baas & Nield method effectively implies that all

sediment from one source area will travel together and be deposited in the same sink area, whereas the present model allows for more realistic deposition gradation downwind of a source.

8.5.2. Surface moisture

The influence of surface moisture on aeolian sediment transport is accounted for by modulating the values of p_e and p_d values as a function of 'effective surface moisture' (m_{eff}). In dryland areas, near-surface moisture – which is the most relevant to sediment transport – primarily occurs due to precipitation. The uppermost layers of sediment dry out quickly after a precipitation event, due to important evaporation and infiltration processes controlled by both atmospheric conditions (e.g. wind, relative humidity, air temperature, solar radiation) and soil conditions (e.g. grain size, soil texture, hydraulic conductivity and water table levels) (Wilson et al., 1994; Qiu et al. 1998; Ravi et al., 2006; Song et al., 2014; Okin, 2016). Chapman (1976) observed that the moisture content of the upper 10 cm of bare sand dunes decreased after rain, from ~10% to <1% after 18 hours. Similar rates have been reported for arid areas by Noy-Meir (1973) and Zhang et al. (2013). Gravimetric moisture thresholds for entrainment of between 4 and 10% have been identified in the field (Namikas & Sherman, 1995; Wiggs et al., 2004b), so it is assumed in the ViSTA model that moisture only affects the erosion and deposition properties of the surface within 24 hours of the last precipitation event (cf. Ravi et al., 2006; Okin, 2016). If a wind event occurs beyond this limit, the drying front is considered to have moved deep enough for the surface to be dry again.

Within the 24-hour period after a rain event, m_{eff} varies between 0 and 1, where 0 is dry (p_e = 1) and 1 represents a surface moisture threshold that prevents sediment

entrainment (p_e = 0) (e.g. Nield, 2011). Following the approximate evaporation rates reported by Zhang et al. (2013), effective surface moisture decreases linearly from 1 to 0 over 24 hours:

$$m_{eff} = \frac{(24 - t_r)}{24} \tag{8.38}$$

where t_r is the time since rain (in hours).

Sediment entrainment has been shown to decrease linearly with increasing surface moisture (Hotta et al., 1984), so p_e decreases from 1 to 0 at the same rate but inversely to m_{eff}. The impact of moisture on deposition is modelled as a step function, whereby moderately moist cells are assigned lower p_d values due to an elastic rebound effect resulting from a relative increase in surface hardness (McKenna-Neuman & Scott, 1998; Wiggs et al., 2004a,b; Nield, 2011). At high m_{eff}, complete deposition occurs (p_d = 1).

Grain entrainment is dynamically sensitive to the moisture status of the top layer of sediment, because entrainment thresholds decrease as a surface dries, revealing moist grains below that increase thresholds once again (McKenna Neuman & Scott, 1998; Davidson-Arnott & Bauer, 2009; Nield & Wiggs, 2011; Davidson-Arnott et al., 2012). The dynamic sensitivity of the transport system to surface moisture is incorporated via a feedback function in the ViSTA model. The function allows m_{eff} to be updated based on a sedimentation balance after a specific number of iterations, such that cells with net deposition become drier and cells with neutral or net erosion become moister (Nield, 2011). This reflects capillary action on neutral surfaces and burial-induced drying of depositional surfaces, without directly accounting for infiltration and evaporation effects. The shape and relative intercept locations of

Nield's (2011) feedback function are employed in the ViSTA model (Figure 8.8). Whilst the examples shown here and in the supporting material in Appendix 1 are based on an hourly timestep, the required resolution can be easily adapted to suit the scale of investigation, such as the second- and minute-scale feedbacks that operate in the formation of sand strips (Nield, 2011).

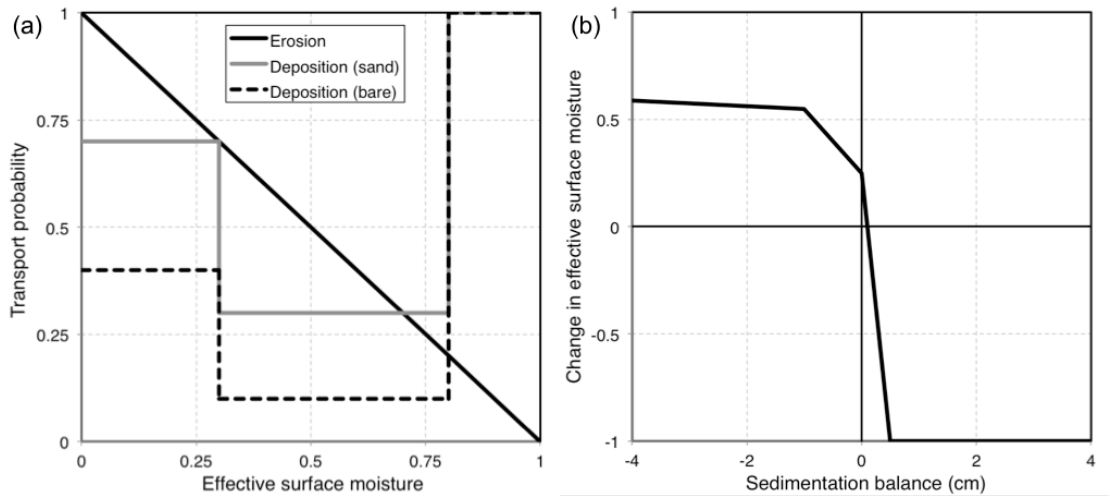


Figure 8.8 (a) Transport functions indicating link between effective surface moisture and erosion and deposition probabilities; (b) Feedback function employed to update surface moisture in response to sedimentation (adapted from Nield, 2011, p.916).

8.5.3. Additional rules

Besides the basic transport process described above, additional rules govern the movement of sediment in the system during polling. Shadow zones are applied in the downwind lee of topography at an angle of 15^{o} to the horizontal surface (Nield & Baas, 2008a,b), such that no erosion (p_e = 0) and complete deposition (p_d = 1) occur in these regions (Figure 8.9a). Nield & Baas (2008a) showed that recognisable dune forms only develop if shadow zones were included in their erosion model.

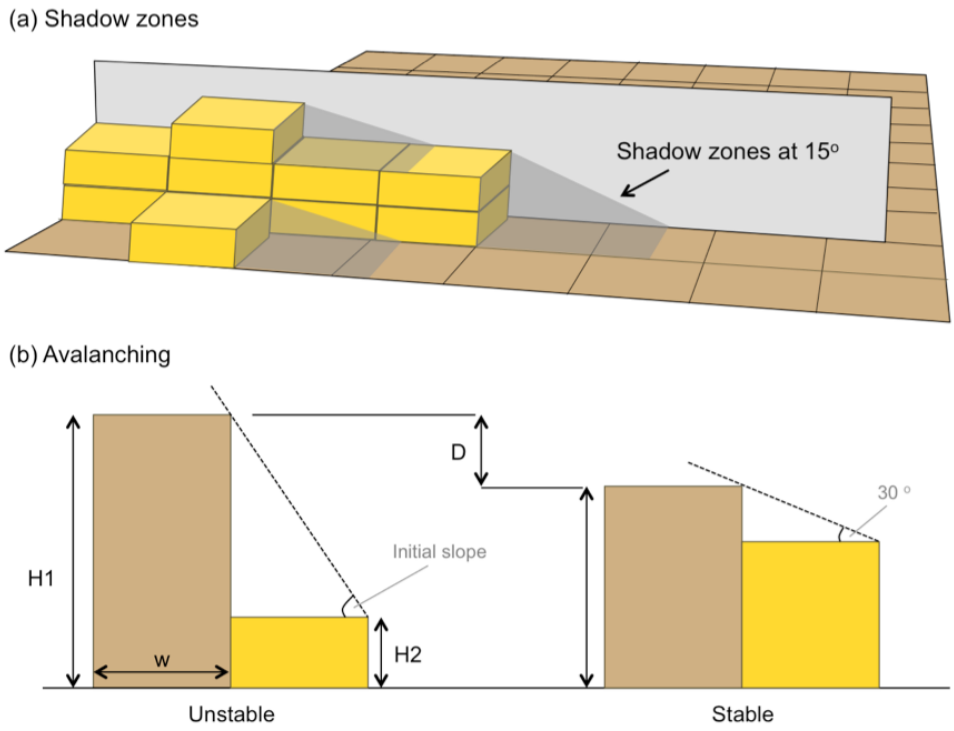


Figure 8.9 (a) Shadow zones at 15 degrees in the lee of topography, where no erosion and complete deposition occur in the ViSTA model (adapted from Elder, acc. 04/06/2014); (b) Avalanching occurs on unstable slopes above a threshold angle of 30°. When the difference in height between two neighbouring cells exceeds the threshold condition, part of the sand in the higher cell slides down to the lower one to maintain stability. The amount of sand displaced, D = (H1 – (H2 + tan(30°)*w))/2 (adapted from de Castro, 1995, p.209).

In addition, avalanching occurs in the direction of steepest descent to enforce an angle of repose, induced by gravity (cf. Werner, 1995; Momiji et al., 2000; Bishop et al., 2002; Baas & Nield, 2007) (Figure 8.9b). This angle changes according to the vegetation occupation of the cell (30° for bare sand, 40° for a vegetated cell; cf. Nield & Baas, 2008a, 2008b). In nature, the resultant slip face has a straight cross section, but is a complicated surface as a consequence of multi-scalar avalanches (Bak, 1996). In the present model, once sediment has been transported and deposited and all cells have been polled, each cell is polled again to determine whether sediment must avalanche to neighbouring cells in its von Neumann neighbourhood. At this stage the cells are polled randomly, to prevent artefacts propagating across the domain as a result of a specific avalanching order.

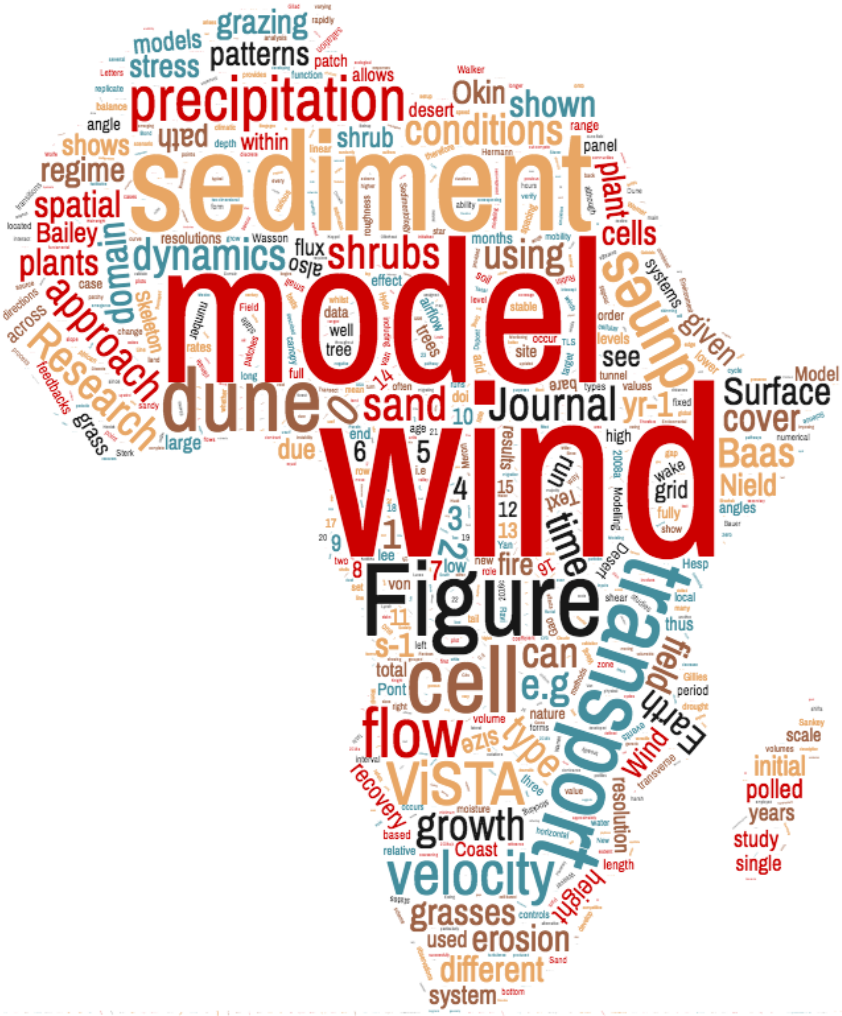
Summary: Paper 4 (part 1)

Paper 4 (part 1) presented the new cellular automaton Vegetation and Sediment TrAnsport (ViSTA) model. The novelty of the ViSTA model lies in its spatial explicit formulation of feedbacks among vegetation growth, wind flow dynamics and sediment flux. This allows surface erosion to be simulated in different vegetation contexts, and for the whole ecogeomorphic system to evolve over time. Where appropriate, wind flow-vegetation interactions in ViSTA are empirically parameterised using field data from Papers 1, 2 and 3.

ViSTA also provides a new method for directly imposing continuous wind and transport directions onto the model domain, which is convenient for implementing Okin's (2008) 'gap/corridor' concept for partially vegetated desert surfaces.

The behaviour of the model must now be verified (to check that no bugs exist in the code and that the model code is properly written), and then validated (to ensure that it is producing realistic and reliable dryland landscapes).

CHAPTER NINE



A coupled vegetation/sediment-transport model for dryland environments: Model verification and validation

Paper 4 (part 2): Mayaud, J. R., Bailey, R. M. & Wiggs, G. F. S
Status: published as 'A coupled vegetation/sediment-transport model for dryland environments', *Journal of Geophysical Research: Earth Surface, 122* (2017)

Abstract
Verification tests for the ViSTA model are reported, including stable state solutions, the impact of drought and fire stress, wake flow dynamics, temporal scaling issues and the impact of feedbacks between sediment movement and vegetation growth on landscape morphology. The model is then used to simulate an equilibrium nebkha dunefield, and the resultant bedforms are shown to have very similar size and spacing characteristics to nebkhas observed in the Skeleton Coast, Namibia. The ViSTA model is shown to be a versatile geomorphological tool that could be used to predict threshold-related transitions in a range of dryland ecogeomorphic systems.

This chapter addresses **Objective 4** (test model performance using: (i) theoretical relationships between sediment supply and wind direction variability to explore dune formation; (ii) high-resolution topography data of erosion/deposition zones in the wakes of plants). **Methods**: cellular automaton modelling; grain size analysis; terrestrial laser scanning (TLS); unmanned aerial vehicle (UAV).

This chapter is a modified version of the paper by Mayaud et al. (2017a). Only the verification and validation tests from the paper are presented here.

9. Model verification and validation

9.1. Introduction

The aim of developing ViSTA is to predict transitions from vegetated, geomorphically inactive landscapes to more active unvegetated landscapes in globally significant dryland ecogeomorphic systems. Before this can be reliably undertaken, ViSTA's performance must be verified (i.e. check the model code is properly written), and then validated (i.e. check realistic dryland landscapes and processes emerge in the model). Selected experiments are presented here, and additional verification tests are provided in Appendix 1. Note that unless stated, the following experiments are based on model runs with a single plant type (shrub). The wind flow and sediment transport (Modules 2a and 2b) were switched 'off' for the experiments on stable solutions (section 9.2) and the impact of stresses (section 9.3).

9.2. Stable solutions

When forcing conditions are constant (ρ = constant), the vegetation distribution module (Module 1), populated with a single vegetation type, equilibrates over time to a stable solution, where no periodic oscillations occur in the population density (p) (Figure 9.1). In all cases, sensitivity to precipitation (ρ) is relatively low above the highest levels shown, with spatial coverage remaining homogeneous and dense (p > 0.9). As ρ decreases to 0, lower density stable populations are observed, and spatial patterning spontaneously emerges. For shrubs (Figure 9.1, middle row), the patterning follows the predictable sequence of gap → labyrinth → isolated patch → isolated spot → bare, as derived in other spatial models (e.g. von Hardenberg et al., 2001; Rietkerk et al., 2004; Bailey, 2011). In the grass case (Figure 9.1, top row), as ρ decreases to 0, some spatial patterning emerges at lower stable populations,

although the classic patterning sequence is weaker than in the shrub case, owing to the weaker competition amongst grasses at large radial distances. Trees (Figure 9.1, bottom row), which have similar facilitative/competitive characteristics to shrubs, display the standard patterning sequence from gap to bare surface, although the sequence emerges at higher ρ, since tree colonisation is low in harsh precipitation regimes. The vegetation system in all cases displays distinct hysteresis (Bailey, 2011), whereby the semi-arid system moves along different degradation and recovery curves depending on the initial population density (Figure 9.S1). The stable solutions for shrubs show good visual agreement with shrub occurrence observed in satellite imagery along a dryland rainfall transect in Niger (Bailey, 2011; see Figure 9.S2). Quantitative spatial metric analysis shows that the model produces emergent vegetation patterns with realistic patch dimensions and distributions (see Text 9.S1, Figure 9.S3).

It should be noted that the exact point at which different patterns (i.e. gap, labyrinth, spot) arise for each plant type can be shifted by altering the parameters of the G_{unit}, specifically the steepness parameter (k_1) and the sigmoid midpoint ($\tilde{T}_{mid}$) (see section 8.3.3). This allows vegetation dynamics to be adapted to suit the conditions and patterning observed in different dryland regions. The vegetation cover changes displayed in Figure 9.1 should only be taken as indicative of a certain parameter set, which can be changed to be most appropriate for any given environment.

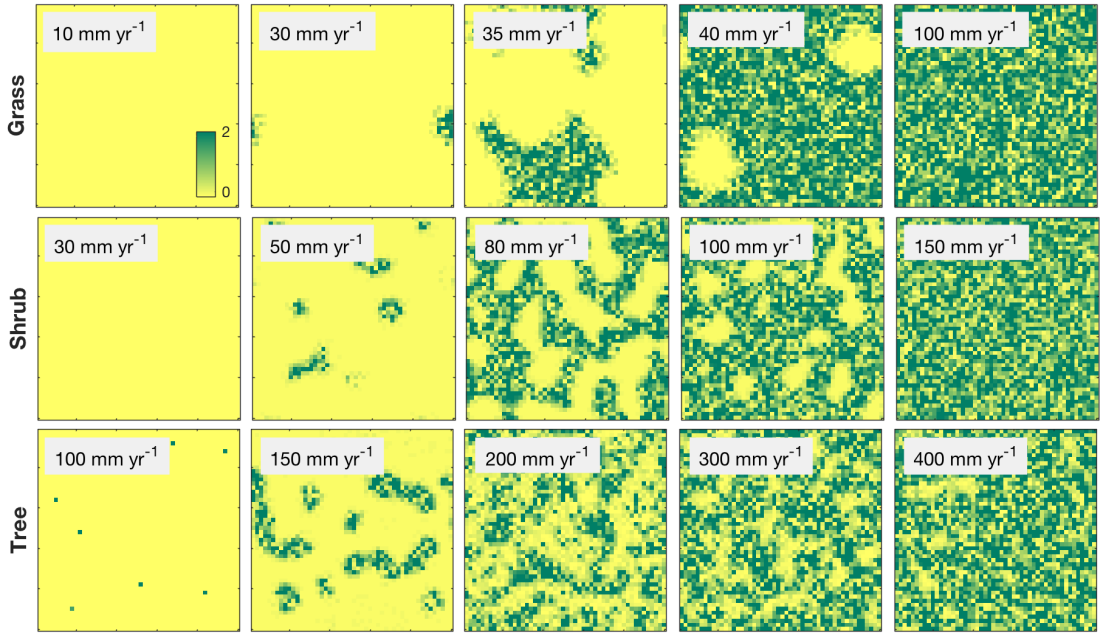


Figure 9.1 Emergence of spatial vegetation patterning at different precipitation stress levels (ρ, shown in grey boxes), for all three vegetation types. Stable patterns are shown as 50 m x 50 m grids, with yellow representing bare ground and darker green shades representing plants with greater height, to the level of full biomass maturity. Model in each case was run at a resolution of 6 months, with an initial condition of full cover (p_0 = 1).

9.3. Impact of stresses

In order to verify the combined impact of age stress (Z_S) and drought stress (D_S) – which both vary between vegetation types – the module was run with different initial vegetation proportions and in different precipitation scenarios (Figure 9.2). In these runs, precipitation was distributed evenly throughout the year. In a harsh precipitation regime (80 mm yr^{-1}), domains initialised with a majority of either grasses or shrubs (Figure 9.2a,b) equilibrate within ~50 years to an approximately equal distribution of grasses and shrubs. This occurs because grasses colonise bare cells more efficiently than shrubs, and achieve peak facilitation/completion capabilities quicker, but shrubs on average tend to survive longer due to a lengthier life cycle and an ability to better withstand accumulated drought. When the model is initiated with a majority of trees (Figure 9.2c), the trees die off due to their low resilience to

conditions of low precipitation, and the bare cells are rapidly colonised by grasses, before the shrub population begins to accumulate.

Shrubs benefit most from an intermediate precipitation level (400 mm yr^{-1}), as can be observed from the encroachment of shrubs in grass-dominated domain (Figure 9.2d), and the maintenance of shrub dominance over time (Figure 9.2e). This is due to the smaller difference in recolonisation abilities of shrubs and grasses at this precipitation level, which allows communities of shrubs to become established and rapidly out-compete grasses for nutrients and water (Puigdefabregas, 2005; Stewart et al., 2014). When trees initially dominate (Figure 9.2f), grasses out-compete shrubs for the remaining available space, and a stable tree-grass coexistence emerges (with a higher grass proportion at slightly lower precipitation levels). This last example effectively represents a 'climatically determined savanna' (Bond et al., 2003), whereby grasses persist in conditions where tree cover is restricted by water limitation (Sankaran et al., 2005).

At a high precipitation level (1000 mm yr^{-1}), trees eventually dominate in the equilibrium state, regardless of the initial vegetation type proportions. In these conditions, water availability is sufficient to allow trees to approach canopy closure such that grasses and shrubs are effectively excluded. Several studies (e.g. Sankaran et al., 2005; Lehmann et al., 2011; Staver et al., 2011) have shown that such 'disturbance-driven savannas' require disturbances external to the system to maintain a diversity of vegetation types.

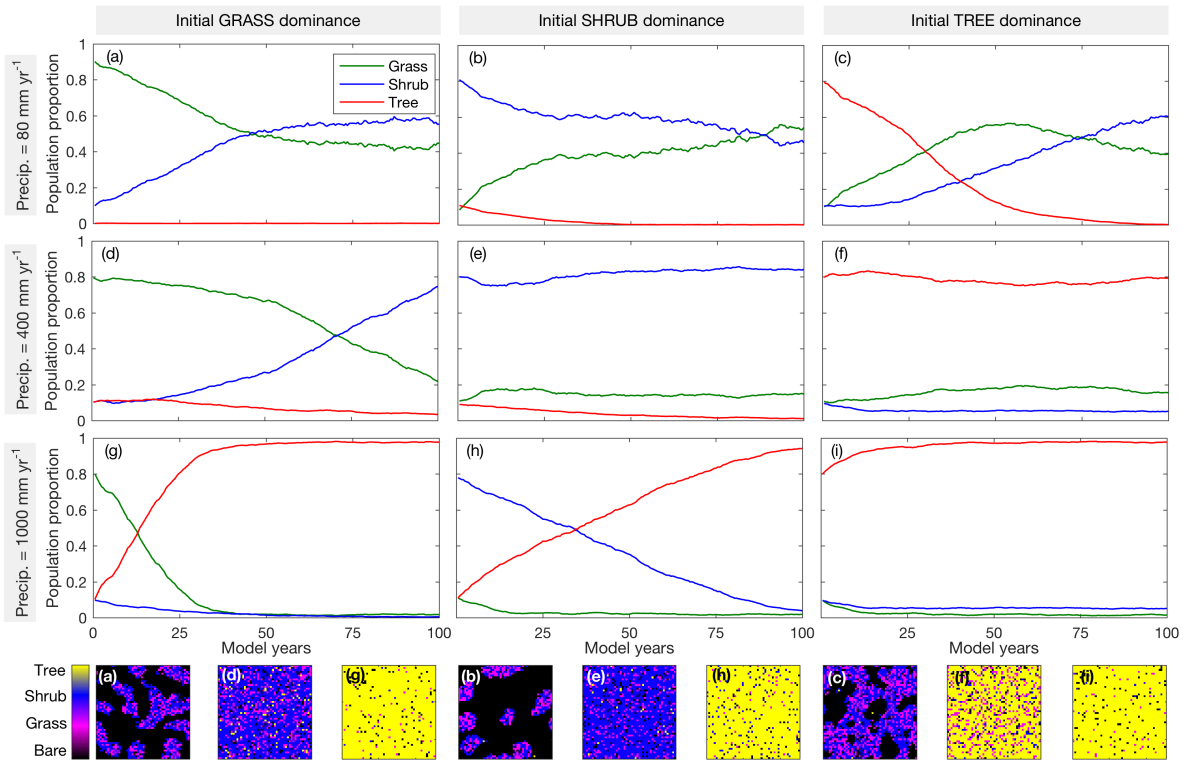


Figure 9.2 Change in vegetation type (grass, shrub and tree) proportions under low (ρ = 80 mm yr^{-1}), medium (ρ = 400 mm yr^{-1}) and high (ρ = 1000 mm yr^{-1}) precipitation regimes. Domain was initiated with a dominant vegetation type (80% proportion) and a low proportional cover of the two other vegetation types (10% each). Model was run for 200 iterations (1 iteration = 6 months of vegetation growth) over a grid of 50 m x 50 m and initial cover of 90% (p_0 = 0.9). Panels below show the corresponding final vegetation type distributions (see colour scale; black represents empty cells) at the end of each model run, with relevant panel indicated in top left corner.

A range of human disturbances – namely agriculture, grazing and fire – is a common feature of many drylands, and these can force the system to rapidly shift to an alternative stable state. Such disturbances often reduce vegetation cover, disturb soil structure and crusting, and create large patches of bare ground (Hagen, 1991; Belnap, 1995; Nash et al., 2004; Barbier et al., 2006; Miller et al., 2012). In turn, this affects surface roughness, cover and patch size distribution, which have important implications for the sediment transport rates and patterns (Okin & Gillette, 2001; Gillette & Pitchford, 2004; Bergametti & Gillette, 2010; von Hardenberg et al., 2010; Sankey et al., 2012; Stewart et al., 2014).

The impact of disturbance on vegetation growth can be investigated in the ViSTA model by changing the fire stress (F_S) and grazing stress (G_S) imposed on the domain. The dynamic equilibria reached for ρ = 80 mm yr^{-1} (as shown in Figure 9.2) are used to initialise the model and, with the same precipitation regimes, cyclical fire and grazing stresses imposed. Figure 9.3 shows the impact on vegetation type and cover of changing the frequency with which fires occur, in different precipitation regimes. In a harsh regime (ρ = 80 mm yr^{-1}), frequent fire occurrence leads to a relative increase in grass populations and decrease in shrub populations, as grasses burn more readily but also recolonise bare cells preferentially in these conditions.

A bistable region exists at intermediate (ρ = 150–400 mm yr^{-1}) precipitation levels, where the fire frequency determines whether the vegetation system becomes grass- or shrub-dominated. A short (5-year) fire cycle in these conditions allows short-lived grasses to continually populate the surface, whereas longer (20–40-year) cycles cannot prevent the establishment of large shrub colonies that increasingly out-compete grasses. This form of shrub encroachment has been shown to persist in nature through amplifying feedbacks linked to the fire regime (Anderies et al., 2002; Li et al., 2008; Sankey et al., 2012).

At high (ρ = 1000 mm yr^{-1}) precipitation levels, water availability allows canopy closure to eventually occur and ‘deterministic forest’ to develop (Staver et al., 2011), regardless of fire regime. However, the fire cycle does determine how rapidly the grass population declines relative to the tree population, such that more frequent fire events enables grasses to keep colonising bare surface over a longer period. This supports the ‘disturbance-driven savanna’ hypothesis (e.g. Sankaran et al., 2005), whereby fire and grazing buffer against the formation of closed-canopy forests, thus maintaining both trees and grasses in a mixed system (Bond et al., 2003).

Figure 9.4 shows the impact on vegetation type and cover of changing the frequency with which grazing occurs, at different stocking rates (with a constant precipitation regime, ρ = 150 mm yr^{-1}). This precipitation regime represents conditions in the southern Kalahari Desert, a semi-arid region that is heavily used by humans for agriculture and grazing (Thomas et al., 2005). For the grazing experiments, the stocking rates varied between 0.015 and 0.06 LSU ha^{-1}, as these are typical for Kalahari rangelands (Blaum et al., 2009; Burgess, 2009), and cycling ranges from constant grazing to one grazing period ever 20 years. When grazing occurs constantly, grass populations rapidly decline within a few decades and spot patterning emerges, which may eventually lead to vegetation collapse (Rietkerk et al., 1997; HilleRisLambers et al., 2001). As the time between grazing events increases, grass patches have more time to become established as they recolonise grazed surfaces, leading to a greater proportion of overall grass population (e.g. 30% cover for a grazing cycle of 20 years). Predictably, increasing the stocking rate results in more rapid declines in grass populations, as well as more dramatic responses in grass/shrub proportions following individual grazing events. Greater stocking rates also result in more dramatic population density oscillations, particularly in the early stages of grassland readjustment to shrubland.

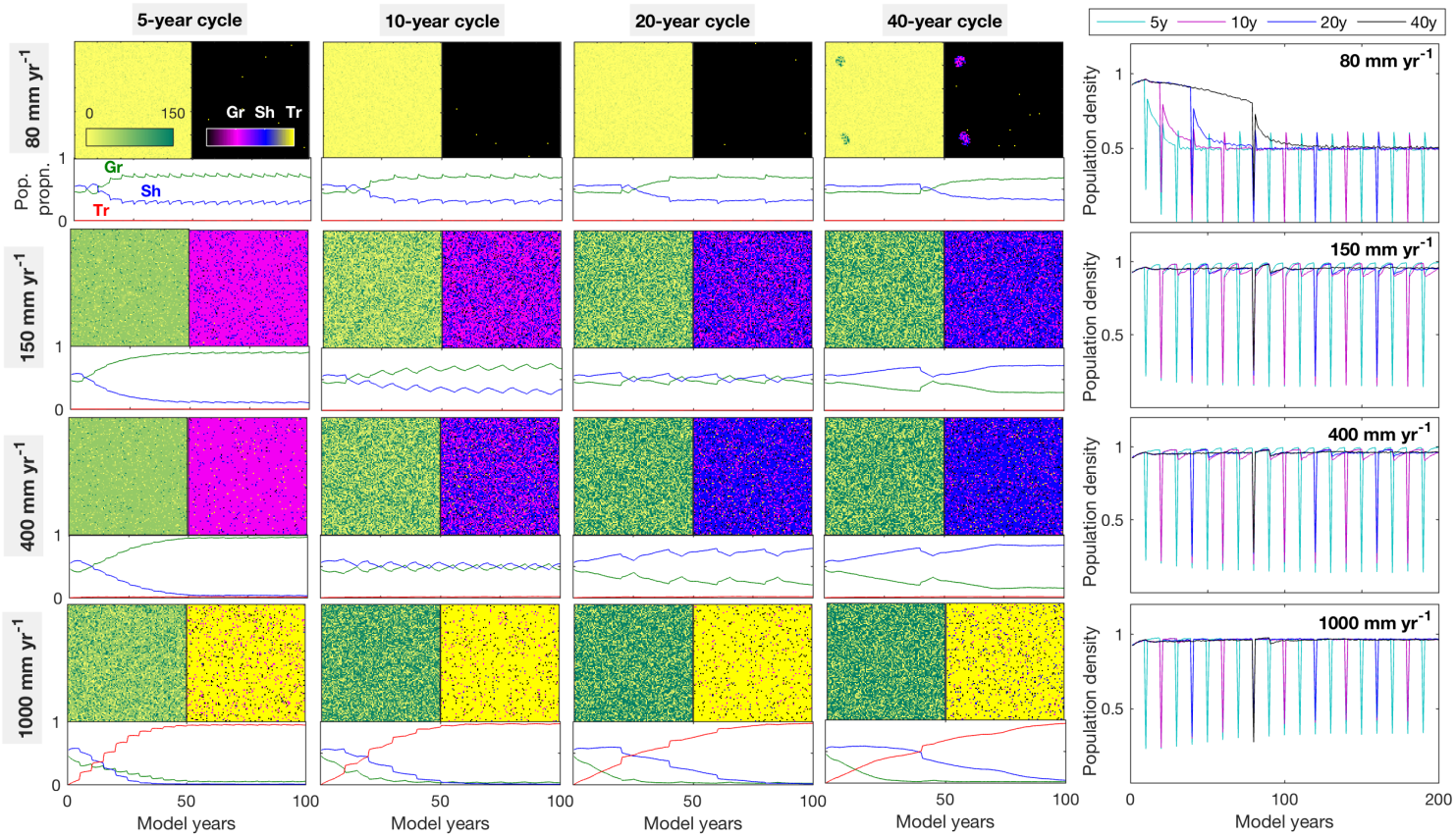


Figure 9.3 Change in vegetation type (grass, shrub and tree) proportions and population density under different fire regimes (5-, 10-, 20- and 40-year repeat cycles), for different precipitation regimes (ρ = 80, 150, 400 and 1000 mm yr^{-1}). For each scenario, left-hand panel shows spatial population age distribution, right-hand panel shows spatial vegetation type distribution, and line plot shows change in vegetation type proportions over time. Line plots at the end of each row display changes in population density over time, grouped according to precipitation regime. Domain was initiated with an approximately equal coverage of grasses and shrubs. Model was run for 200 iterations (1 iteration = 6 months of vegetation growth) over a grid of 50 m x 50 m and initial cover of 90% (p_0 = 0.9).

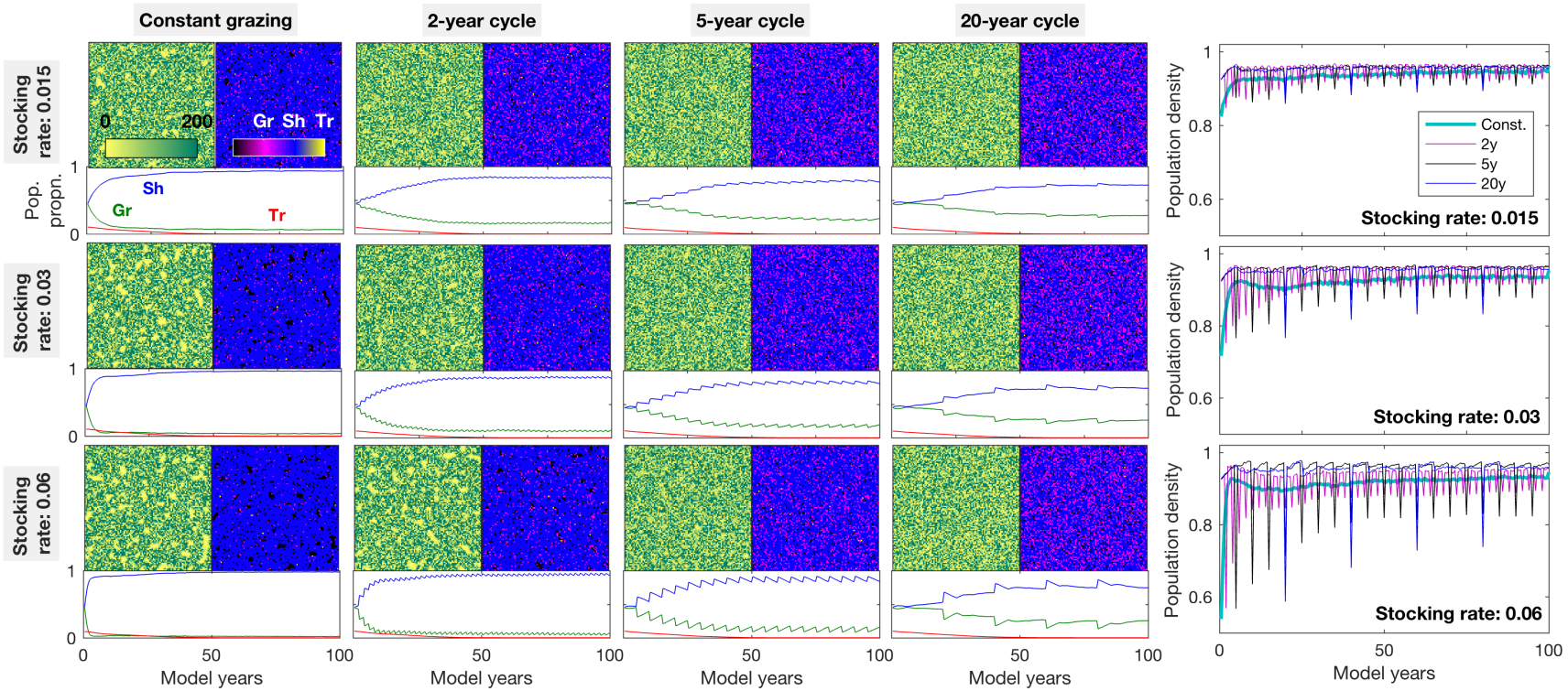


Figure 9.4 Change in vegetation type (grass, shrub and tree) proportions and population density under different grazing regimes (constant, 2-, 5- and 20-year repeat cycles), for different stocking rates (0.015, 0.03 and 0.06 LSU ha^{-1}). The precipitation regime was kept constant, at ρ = 150 mm yr^{-1}. For each scenario, left-hand panel shows spatial population age distribution, right-hand panel shows spatial vegetation type distribution, and line plot shows change in vegetation type proportions over time. Line plots at the end of each row display changes in population density over time, grouped according to stocking rate. Domain was initiated with an approximately equal coverage of grasses and shrubs. Model was run for 200 iterations (1 iteration = 6 months of vegetation growth) over a grid of 50 m x 50 m and initial cover of 90% (p_0 = 0.9).

9.4. Wake flow dynamics

In dryland landscapes composed of patchy vegetation, the wakes developing downwind of individual vegetation elements often interact with those of their neighbours (Wolfe & Nickling, 1993; Okin, 2008). It is essential to verify that these interactions are correctly formulated in the model. The modelled effect of patch configuration and size on wind flow recovery is shown in Figure 9.5. In cases where vegetation elements are relatively isolated from one another (e.g. Transects A and B), wind flow recovers fully between elements, such that the approach wind velocity for each element is the same. Once wake interference flow occurs (Transects C and D), wind flow recovers almost fully, although it should be noted that at lower element porosities, the recovery would not be complete in these configurations. Transect E is an extreme example of wake interference flow, whilst Transect F is an example of skimming flow, because a sufficient number of contiguous plants form a patch within which wind velocity is reduced to zero. At the point of recovery, the cumulative porosity of the plants along Transect F results in a much lower minimum leeward wind velocity (u_0) than along the other transects. Consequently, the recovery of wind flow in the lee of the long patch is longer than in the lee of individual elements, reflecting wind tunnel (Burri et al., 2011; Youssef et al., 2012) and field-based (Mayaud et al., 2016c) observations that the lack of lateral airflow moving around patches results in extended recovery lengths.

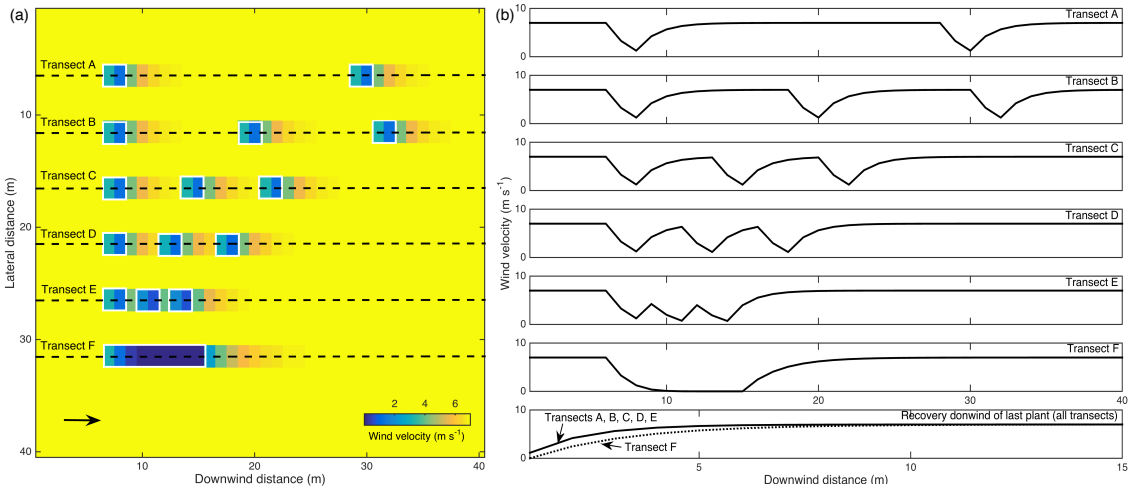


Figure 9.5 (a) Recovery of wind flow downwind of individual plants at differing distances apart. All individual plants are 1.0 m in height and have a porosity of 60%. Locations of individual plants are shown as white outlines; Transect F represents a patch of four continuous plants where skimming flow is assumed to develop. Black arrow shows approach wind angle; (b) Wind velocity transects across each vegetation patch (shown as dotted black lines in panel (a)). Bottom plot in panel (b) shows wind recovery downwind of the last plant of each transect, for comparison purposes. Stochasticity was removed from the wind velocity algorithm for these runs.

9.5. Temporal and spatial scaling

Unlike scale-less sediment-transport CA models, the inclusion of vegetation in the ViSTA model requires us to consider the spatial and temporal scales at which the landscape is simulated. Whilst several geomorphic features such as bare-sand dunes, river networks and coastlines can be considered fractal-like (and thus scale-less) in nature (Tarboton et al., 1988), vegetation imposes a characteristic physical scale on aeolian dune morphology. This arises because of the fundamental relationship between photosynthetic potential and size-range (Nield & Baas, 2008a). Here we present tests focused on temporal and spatial scaling in Module 2 (i.e. wind and sediment transport characteristics). Verification testing of scaling in Module 1 (vegetation growth) is given in Appendix 1 (Text 9.S2).

The temporal resolution of the ViSTA model can be adapted by changing the number of minutes of above-threshold wind velocities represented by each iteration of Modules 2a and 2b. Figure 9.6 shows bedform morphology resulting from increasing

the time of above-threshold wind per iteration (which effectively coarsens the temporal resolution of the model, since the total model runtime stays the same). Iteration durations of 60–300 minutes tend to produce relatively similar nebkha landscapes and sediment transport profiles. At iteration durations of 5000–10000 minutes, sediment transport rates are much lower (Figure 9.6, bottom left panel) than at iteration durations of 60–1000 minutes, due to fine-scale sediment interactions not being represented as time blocks get too large. This results in essential nebkha-forming mechanisms being bypassed, as the full range of geomorphic processes are not fully represented by the longest iteration resolutions. The clear step-change in sediment transport rates and bedform definition between intervals of 1000 and 5000 minutes suggests that erosion and deposition processes can be feasibly treated at relatively coarse temporal resolutions until ~1000 minutes, allowing transport mechanisms to be resolved in a computationally efficient manner.

The spatial scale of the ViSTA model can be altered by modifying the representative size of a cell (Figure 9.7). Dryland mesquite-type shrubs are typically on the order of 10^0–10^1 m in diameter (Okin et al., 2001), and simulations using this vegetation type produce nebkha dunes of 2–10 m diameter with a grid resolution of 1 m (Nield & Baas, 2008a). Reducing the cell size to below the resolution of single shrubs produces more closely packed nebkha forms. A breakdown in bedform development occurs at a resolution of 0.4 m, because vegetation elements effectively exceed their physical restraints by existing closer together, thus leading to the formation of connected sand patches around unrealistically small vegetation bunches. As the cell size increases to 2 m, nebkhas of a similar size to the 1 m resolution develop, but at a coarser resolution. At cell sizes of 5 m and 10 m, nebkhas exist as isolated, single sediment-covered cells, and lose their recognisable forms. Across the model domains, total transported sediment during the first ~50 iterations tended to be greatest at high (0.4–1.0 m) resolutions (Figure 9.S16, bottom panel). This likely

results from many individual small cells being eroded more readily than equivalent single large cells, since shadow zones are more finely resolved at the highest resolutions. However, by the end of the model runs, the total transported sediment was broadly similar across all resolutions, suggesting that an equilibrium transport rate was reached across all spatial resolutions.

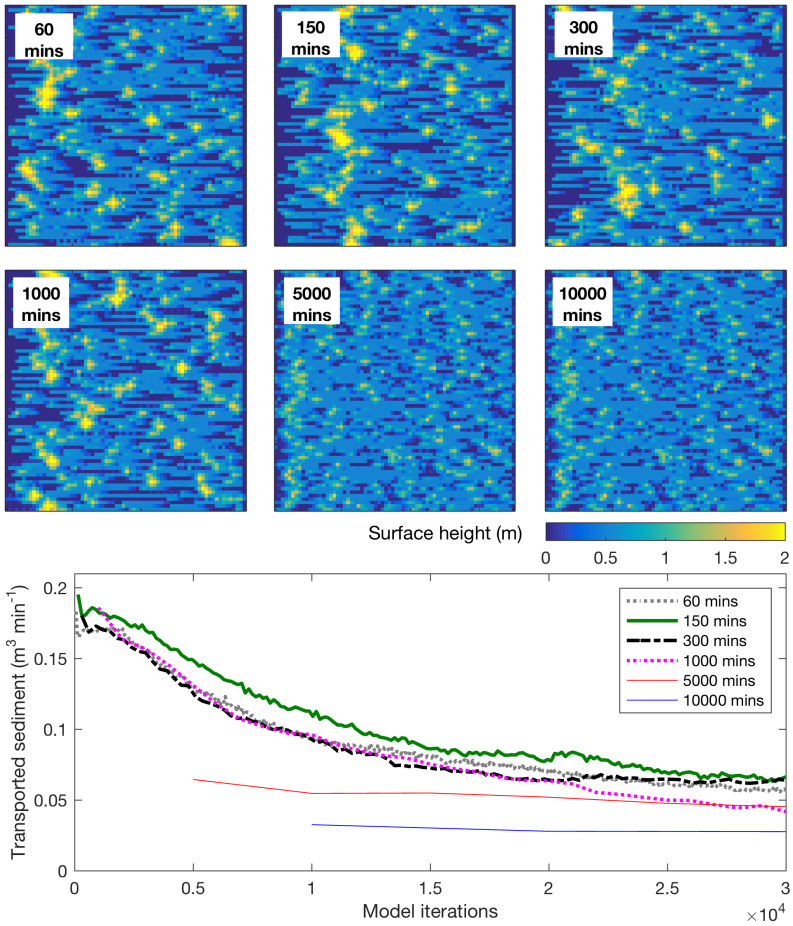


Figure 9.6 Simulated morphology under varying iteration resolutions (wind event resolution ranging from 60 to 1,000 minutes), with a fixed vegetation cover of 20% and an initial sediment depth of 0.5 m. Model was run over a grid of 70 m x 70 m for the model equivalent of 30,000 minutes (each iteration represents constant wind at 7 m s^{-1} threshold wind velocity = 5 m s^{-1}). Bottom right panel shows integral of total transported sediment for all resolutions. All vegetation elements had a fixed porosity of 30%. Transport direction from left to right.

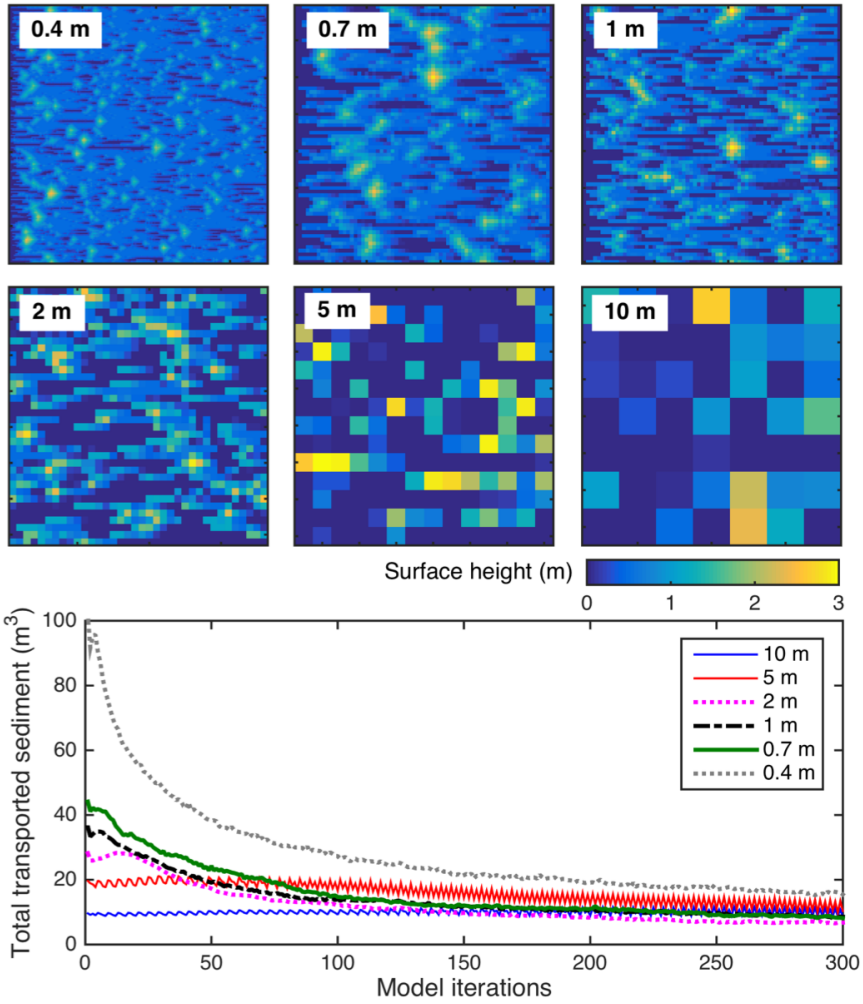


Figure 9.7 Simulated morphology evolving from different spatial grid resolutions (cell sizes from 0.4 m to 10.0 m), with a fixed vegetation cover of 20% and an initial sediment depth of 0.5 m. Model was run over a grid of 70 m x 70 m for 300 iterations (1 iteration = 200 hours of constant wind at 7 m s^{-1}; threshold wind velocity = 5 m s^{-1}). All vegetation elements had a fixed porosity of 30%. Transport direction from left to right.

9.6. Dune simulation

Dunes in arid sand seas are primarily classified according to sediment availability and wind directional variability (Wasson & Hyde, 1983; Pye & Tsoar, 1990). The reductionist framework of Wasson & Hyde (1983) has proven a useful method for characterising and predicting dunefield evolution at the landscape scale. Thanks to its reliance on two simple parameters, Wasson & Hyde's (1983) seminal phase diagram provides a simple way of testing the basic dynamics of sand transport

models. Therefore, the sediment movement module (Module 2) was forced with a range of wind approach angles and initial sediment volumes, based on the relative magnitudes of Wasson & Hyde's (1983) diagram.

Figure 9.8 shows that when wind is unidirectional and sediment availability is low, moving sand slabs coalesce to produce elongated barchanoid structures that propagate at different velocities according to their geometry and volume (Hersen et al., 2004). Smaller, faster-moving structures merge with larger ones and then decelerate, leading to the emergence of a crescentic barchan dunefield. A dynamic equilibrium in dune size-distribution is eventually reached, owing to the periodic boundary conditions and the small size of the system, which results in dunes propagating into their own shadows (Narteau et al., 2006). As the amount of sand increases in a unidirectional wind regime, the barchan dunes evolve into transverse ridges, which extend perpendicular to the wind direction (Courrech du Pont, 2015). Dune-dune interactions, amalgamations and the formation of secondary bedforms result in nonlinear pattern coarsening (Rubin & Hunter, 1982; Ewing & Kocurek, 2010; Kocurek et al., 2010; Gao et al., 2015a), with the average size and wavelength of the transverse dunes increasing during the simulation.

In moderately variable wind directions (in our case, a bimodal regime composed of an obtuse divergence angle between the primary and secondary winds), linear dunes are observed. These long, relatively straight, parallel ridges simultaneously display extension in the resultant wind direction and lateral migration (Tsoar, 1983; Rubin & Hunter, 1987). When a multidirectional wind regime is imposed onto a deep sand bed, a star dune dunefield forms. Star dunes exhibit a hierarchy of dune forms, limited at the lower end by the elementary dune length scale (Elbelrhiti et al., 2005; Zhang et al., 2012) and at the upper end by the convective boundary layer thickness (Andreotti et al., 2009). In the ViSTA model, when a discrete conical pile of sand is

exposed to a multidirectional regime (Zhang et al., 2012), a star dune always forms with a symmetry with respect to the imposed wind directions.

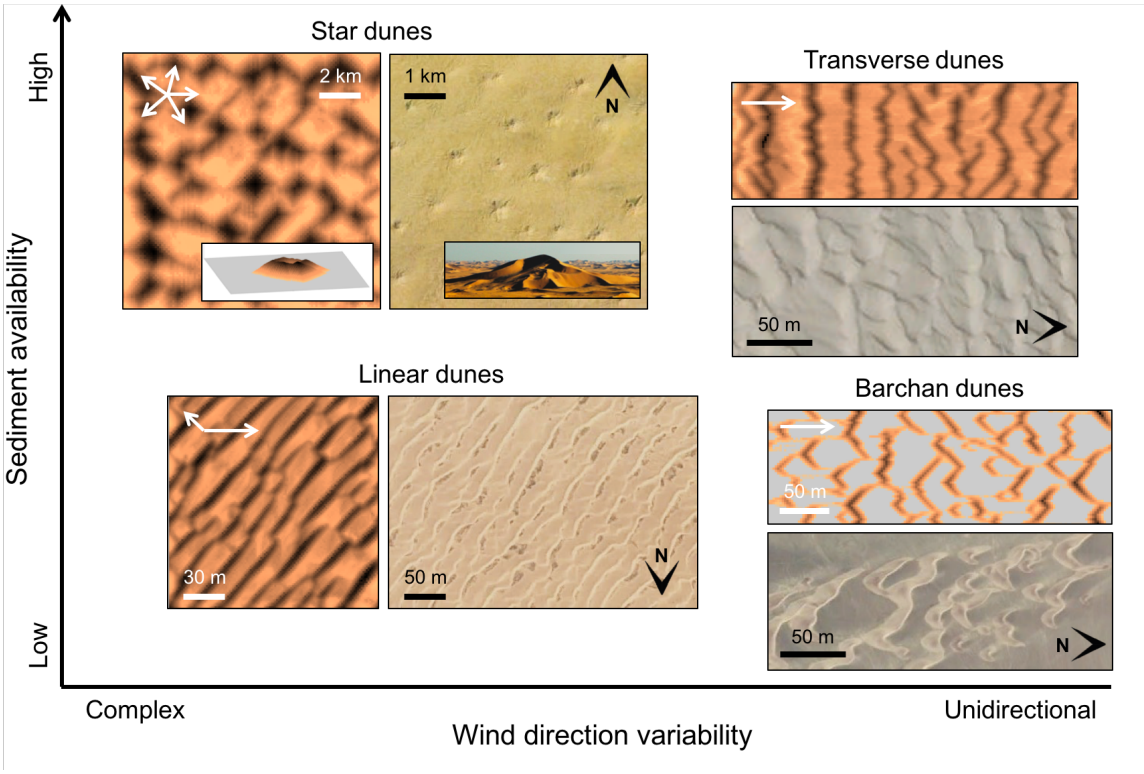


Figure 9.8 Simulated dune morphologies in different wind direction variability and sediment availability regimes, based on the dune classification scheme of Wasson & Hyde (1983). In each case, model was run without vegetation and with an initial uniform sediment depth (3 m for barchan; 20 m for transverse; 10 m for linear; 20 m for star), for 400 iterations (1 iteration = 300 hours of constant wind at 7 m s^{-1}; threshold wind velocity = 5 m s^{-1}). The sediment depths were based on relative differences in depth of Wasson & Hyde's (1983) original diagram, combined with extensive preliminary testing to identify which conditions best produced the relevant bedforms. Wind approach angles and relative frequencies are shown by white arrows in each plot. Example satellite images (Google Earth) are also presented alongside each simulated dunefield (barchan dunes: Namibia, -20.33° N, 13.33° E; transverse dunes: Morocco, 28.04° N, -12.25° E; oblique linear dunes: China, 38.66° N, 107.69° E; star dunes: Algeria, 31.23° N, 07.65° E (inset shows a star dune from the Grand Erg Oriental, Algeria; adapted from Zhang et al., 2012, p.464)).

An emerging body of numerical and experimental work (e.g. Courrech du Pont et al., 2014; Gao et al., 2015b; Lucas et al., 2015) suggests that sediment availability not only controls dune type, but also the dune orientation, due to a variation in the dune growth mechanism. Two modes for dune orientation, the 'fingering' and 'bed instability' modes, have been identified by Courrech du Pont et al. (2014). In addition to the tests described above, we examined the ability of the ViSTA model to replicate

the emergence of these two modes in bimodal wind regimes, following the approach of Gao et al. (2015b). The experimental conditions are described in detail in Text 9.S3. In conditions of high sand availability, the bed instability mechanism systematically led to the establishment of dunes aligned in one principal direction, which grew in height through pattern coarsening (Figure 9.S17a). When the sand source came from a single location, straight 'finger dunes' developed over a range of divergence angles, elongating with a constant orientation (Figure 9.S17b,c). Text 9.S3 provides detailed analysis of the experimental results. The diversity of patterns produced in these experiments supports the notion that sediment availability controls both dune type and orientation (Courrech du Pont et al., 2014; Gao et al., 2015b; Lucas et al., 2015).

9.7. Coupled model behaviour

In order to verify the feedbacks between vegetation growth and sediment movement, the fully coupled ViSTA model was run with a v-shaped precipitation regime in different wind strength scenarios. In the model runs, precipitation decreased linearly from 800 mm yr^{-1} to 0 mm yr^{-1} over the first half of a 240-year simulation, before increasing linearly back to 800 mm yr^{-1}. The domain was exposed to either low (0 m s^{-1}), moderate (7 m s^{-1}) or high (12 m s^{-1}) wind strengths.

Figure 9.9 displays the model results over the simulation period. As the precipitation decreased, vegetation cover decreased, allowing sediment movement to gradually increase. In the strongest wind regime, the high levels of erosion and deposition resulted in a more rapid and more dramatic decrease in cover, allowing even more transport to occur, and a single, large, migrating bedform to evolve. Compared to the low and moderate wind regimes, the conditions of the high-wind regime were more

conducive to grass growth at near-zero precipitation. As the precipitation started to increase again, the various wind regimes resulted in very different vegetation cover and dominant vegetation type. In low-wind conditions, shrubs rapidly colonised the patchy surface, resulting in a near-homogenous and densely populated shrubland. This arises because shrubs grow more optimally than grasses and trees in the model when the sediment balance is zero. In the moderate wind regime, the intermediate levels of erosion and deposition allow a mix of grasses, shrubs and trees to survive, with individual patches of shrubs emerging in the landscape, as is often seen in southern African drylands for example (Bhattachan et al., 2014). In the high-wind scenario, the migrating bedform creates an environment whereby shrubs populate the interdune area, where sediment balance is near zero, whilst low-lying grasses tend to dominate on the dune crest. Although this is an extreme case with a single dune, such a spatially distinct shrub-grass distribution is commonly observed in many semi-stable dune systems such as the Kalahari (Bhattachan et al., 2014).

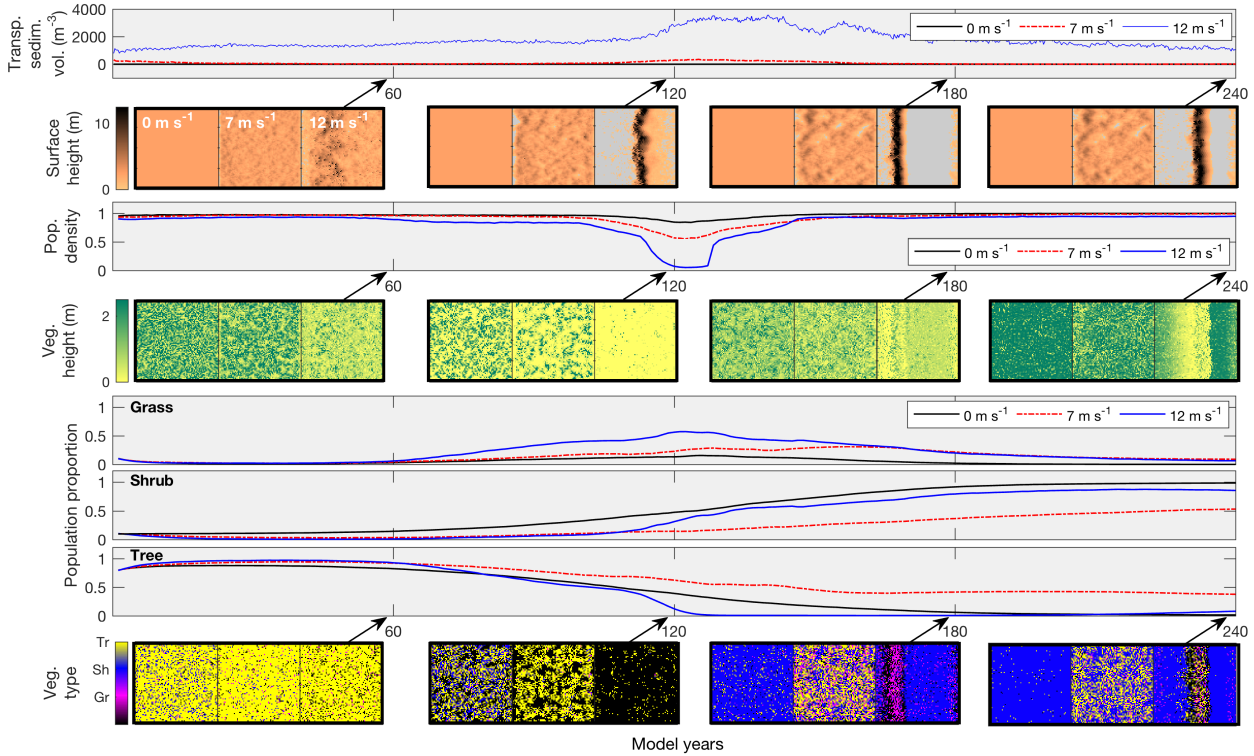


Figure 9.9 Simulated morphology, vegetation height and vegetation type in the fully coupled model, in a v-shaped precipitation regime and for different wind scenarios. In each case, model was run over a 100 m x 100 m grid with an initial vegetation cover of 90% (with initial grass, shrub and tree proportions derived from equilibrium conditions observed in Figure 9.2) and an initial uniform sediment depth of 2.0 m, for a model equivalent of 240 years. Rainfall decreased linearly from 800 mm yr^{-1} to 0 mm yr^{-1} over the first 120 years of the simulation, before increasing linearly back from 0 mm yr^{-1} to 800 mm yr^{-1} over the following 120 years. Wind regimes were characterised as no wind (0 m s^{-1}), moderate wind (7 m s^{-1}) and high wind (12 m s^{-1}). Vegetation module was updated every 3 months (5 model iterations), with each iteration corresponding to 300 hours of constant wind at the appropriate velocity (threshold wind velocity = 5 m s^{-1}). Transport direction from left to right. Line plots show (in order from top to bottom): total volumes of transported sediment within the model domain over time; vegetation population density over time; and the population proportions of grasses, shrubs and trees in the domain over time. Panels show (in order): surface height; vegetation height; and distribution of vegetation types, at specific points in time (60, 120, 180 and 240 model years). Panels are grouped to show the difference between wind regimes at each chosen point in time (low wind on the left, moderate wind in the middle, high wind on the right).

9.8. Summary of model verification

The verification experiments presented here and in Appendix 1 demonstrate the ability of the ViSTA model to accurately replicate a variety of ecogeomorphic features of dryland environments, including: the formation of a standard sequence of vegetation patterns in response to stress, which is hysteretic in nature; dominance of specific vegetation types in different precipitation regimes, replicating field-based and remote sensing observations of savannah/grass transitions; dynamic response of the vegetation system to fire and grazing regimes; realistic wind flow recovery in the wake of various vegetation patch configurations; the formation of standard dune forms in response to changing wind variability and sediment supply; and the impact of feedbacks between sediment movement and plant growth on landscape morphology and dominant vegetation systems.

In order to balance computational efficiency with simulation accuracy and physical length scaling, we define a standard set of vegetation and sediment update parameters for the ViSTA model, which can of course be adapted depending on the needs of the numerical experiment. Wind iteration resolutions are set at 300 minutes, the spatial model resolution is set at 1 m, and a minimum grid size of 100 x 100 cells is employed to minimise model size effects and prevent the development of large, self-affecting bedforms. Other standard parameters (e.g. avalanching, erosion/deposition probabilities) are provided in Text 9.S2.

We now provide results from an experiment designed to validate the output of the ViSTA model. This involves driving the model with a known precipitation regime and wind data collected in the field, and comparing the resultant bedforms with empirical field measurements.

9.9. Simulating the evolution of a nebkha dunefield

Nebkha dunefields are useful testing grounds for sediment transport models, as they are characterised by relatively simple vegetation and flow conditions (see Nield & Baas, 2008a). Here, data on vegetation, dune size and wind flow from a real nebkha dunefield in the Skeleton Coast National Park, Namibia, are used to validate equilibrium simulations produced by the fully coupled ViSTA model.

9.9.1. Field experiment setup

The field site was situated in the southern half of the Skeleton Coast National Park, Namibia, ~5km inland from the coast along the ephemeral Huab River valley (20°52'06" S, 13°29'24" E; see Mayaud et al. (2017b)). In this area, relatively small nebkhas (*Zygophyllum stapfii* shrubs) were distributed on a large, flat gravel plain with a fetch of > 2km, with fluvial deposits upwind supplying most of the sediment. The average grain size of the sandy substrate forming the dunes was 277 μm. Aerial photography of the field site was undertaken using an unmanned aerial vehicle (UAV), to characterise typical nebkha dune spacing (Figure 9.10a). Terrestrial laser scanning (TLS) was also performed *in situ* to analyse the characteristics of three specific nebkhas (N1, N2 and N3), which were chosen to reflect the range of shrub porosity and size observed at the study site. Nebkhas N1 and N2 were located ~30 m from one another, and N3 was located ~400 m away on the same gravel plain. The characteristics of the study nebkhas are summarised in Table 9.1. For all three nebkhas, a full scan was performed of the shrub and its associated sandy tail (Figure 9.10b), and another scan was performed after the removal of its tail with the use of a spade (Figure 9.10c). This allowed the optical and volumetric porosities of the shrubs, as well as the surface and thus total volume of sand in their leeside wakes (Figure 9.10d), to be accurately calculated.

Name	Height (m)	Width (m)	Porosity (%)	Tail volume (m^3)
N1	0.70	1.90	63	1.22
N2	0.50	1.50	71	0.26
N3	0.65	1.15	38	0.40

Table 9.1 Characteristics of the study nebkhas that were analysed using the *Leica P20 Scanstation* TLS for the purposes of model validation. Volumetric porosity values, which were compared to values derived from the standard optical porosity technique, are shown.

Wind velocity at the experimental site was measured for a total period of 10 days in early September 2014 (sampling frequency: 10 s; averaging interval: 60 s), using a two-dimensional sonic anemometer (1.5 m height) located ~1 km away from the study nebkhas, on the same gravel plain. Wind flow was broadly bidirectional over the study period (peaks at 160^o and 320^o), and wind velocities ranged from 2–12 m s^{-1}, showing a strong diurnal pattern with large peaks in the middle of the day, similar to the velocities measured at a nearby site by Mayaud et al. (2016a). The wind flow data are provided for reference in Figure 9.S18.

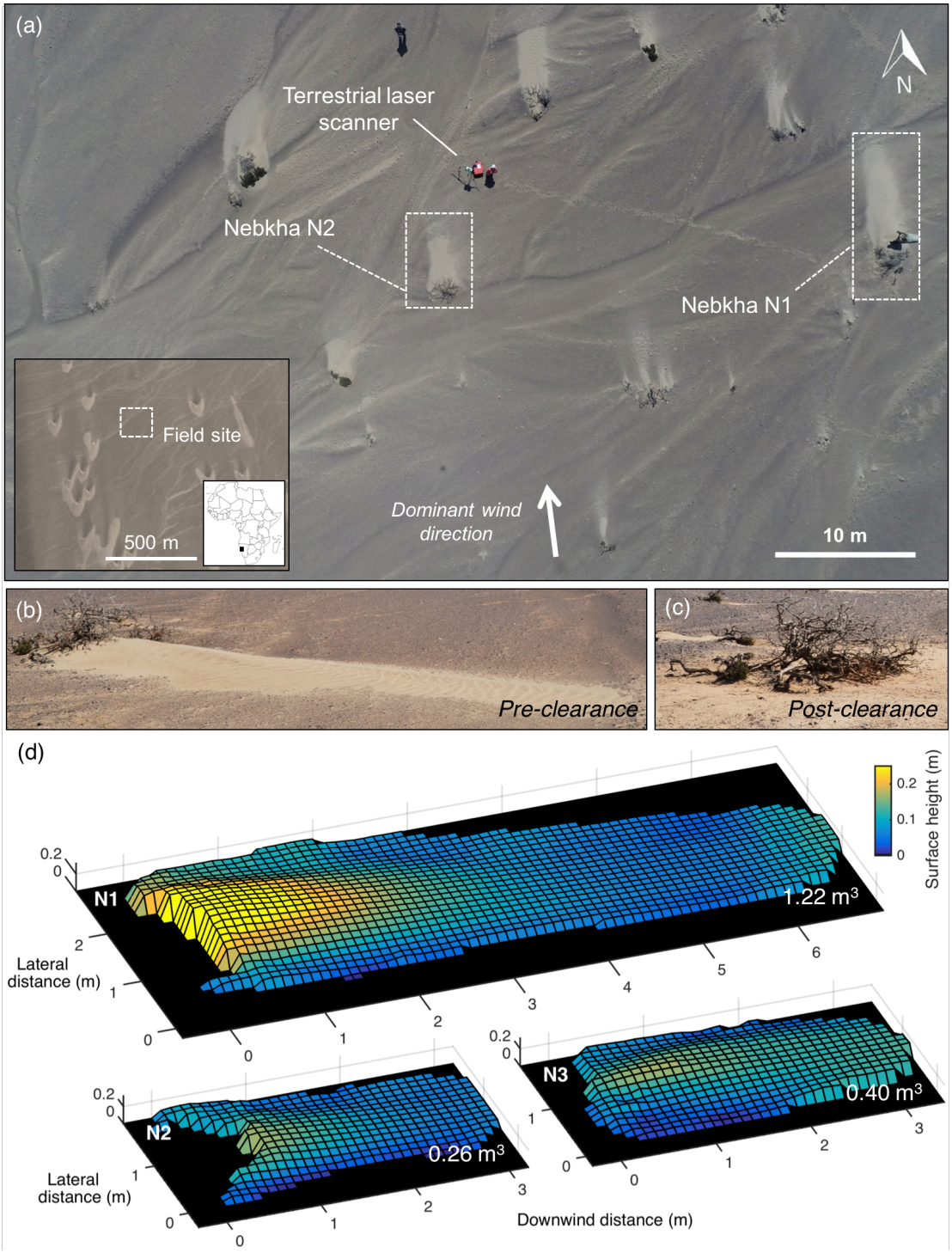


Figure 9.10 (a) Aerial photograph of the study site in the Skeleton Coast National Park, showing typical nebkha dune size, structure and spacing. Darker structures show ephemeral river flow channels. Two of the nebkhas (N1 and N2) characterised using the terrestrial laser scanner (TLS) are also highlighted. Inset shows context of field site; (b) Nebkha N1 before its sandy tail was cleared; (c) Nebkha N1 after its tail was cleared; (d) TLS-derived sandy tail surfaces of the three study nebkhas, at an interpolation resolution of 0.1 m. Total tail volumes are also shown.

9.9.2. Model setup

We ran ViSTA in an equilibrium (as opposed to transient) modelling exercise, to determine whether the model could equilibrate to resemble the present-day landscape when forced with contemporary climatic conditions. The domain was initialised with 90% vegetation cover, to verify the model's ability to cope with vegetation conditions that are unrealistically high for the Huab valley in current environmental conditions. The vegetation module was updated every 3 months, and the coupled model was run for a total period of 25 model years, at the end of which dynamic equilibria in plant population and sediment transport could be observed. The shrubs in the model domain were randomly initialised with porosities between 35–70%, to reflect the range of porosities of the three shrubs that were characterised using the TLS. A fixed annual precipitation of 60 mm yr^{-1} was imposed throughout the run, reflecting the hyper-arid nature of the Skeleton Coast (Lancaster, 1985), which receives occasional advective fog precipitation as cool moist oceanic air moves onshore (Viles, 2005).

The threshold wind velocity at the field site was calculated to be 5.10 m s^{-1}, following the method of Ravi et al. (2012). Wind velocities at the field site commonly exceeded this threshold during the experimental period, so for the model run, twenty above-threshold (7 m s^{-1}) wind events, each lasting 200 hours, were imposed on the domain each model year. This corresponds to Lancaster's (1985) observations that winds along the Skeleton Coast transport sand >40% of the time during the windy season.

The approach angle in natural wind flow is rarely exactly constant, with variations of a few degrees often observed even in supposedly unidirectional winds (as was the case at the Skeleton Coast site). Some multi-directionality in the wind regime is thought to be important for nebkha dunefield development, owing to its impact on the distribution of wind stress around dunes as the lee-side wakes around each plant

constantly change (Gillies et al., 2014). Since the ViSTA model can explicitly vary the wind direction by fractions of a degree from one time interval to the next, variations of up to ±5^{o} from the principal wind approach angle were chosen randomly from the same distribution of wind approach angles measured at the field site (during periods of roughly unidirectional wind flow), and used to drive the Skeleton Coast simulation.

9.9.3. Simulation results

Figure 9.11 shows the surface morphology and vegetation cover as the simulation progresses through time. After five years of model time, the decline of vegetation and emergence of labyrinth-type patterning due to precipitation stress allows increasing sediment transport to occur. Oscillations in the transported volume curve arise due to minor changes in wind direction, which to a certain extent re-work nascent bedforms from one interval to the next. Sediment avalanching begins to occur at around four model years, as accumulations of sediment around vegetation strips exceed critical angles.

The combination of precipitation stress and sediment balance changes lead to the development of isolated vegetation patches by 10 model years, at which point the landscape begins to stabilise (as can be seen from the equilibration of the transport and avalanching curves, as well as spatial bedform and vegetation patterns). From this point, existing nebkha dunes continue to grow and starve other parts of the landscape of available sediment, and provide ideal locations for further vegetation growth on the nebkhas themselves. The nebkha dunes are anchored bedforms but do shown some dynamism, with some migrating up to 5 m downwind in the final 10 years of the simulation (similar to nebkha migration rates of up to 1.5 m yr^{-1} reported by Necsoiu et al. (2009)).

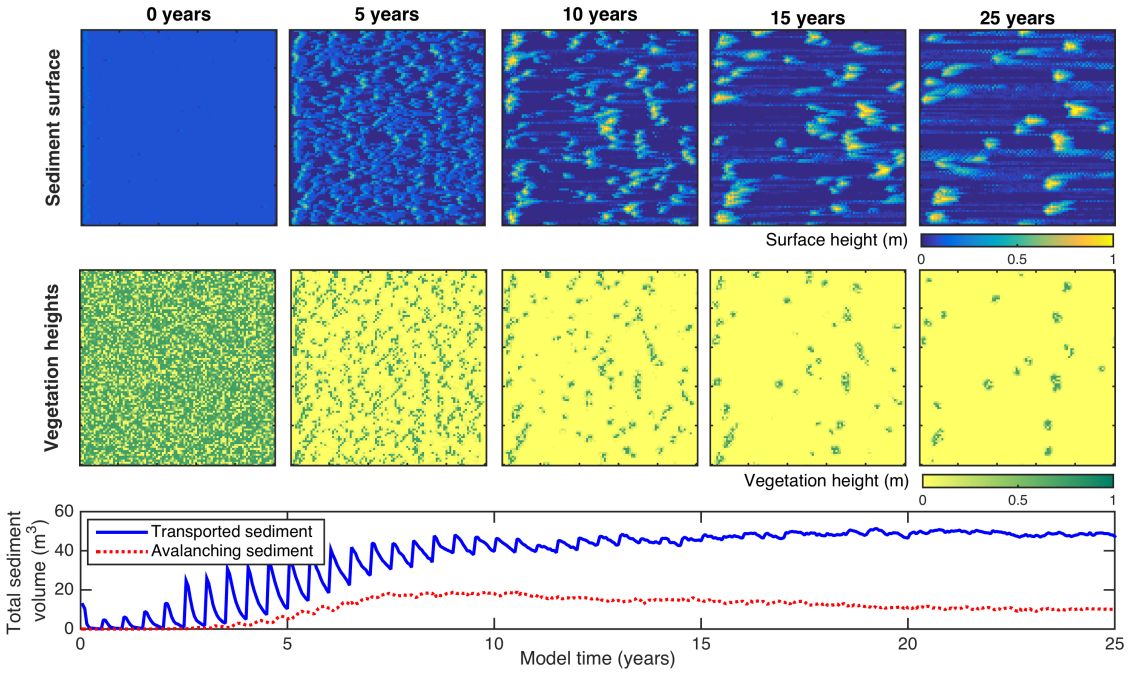


Figure 9.11 Simulated morphology and vegetation cover in conditions similar to those observed in the Skeleton Coast National Park, Namibia. Model was run over a 100 m x 100 m grid with an initial vegetation cover of 90% and an initial uniform sediment depth of 0.2 m, for a model equivalent of 25 years with a fixed annual rainfall equivalent of 90 mm yr^{-1}. Vegetation module was updated every 3 months (5 model iterations), with each iteration corresponding to 200 hours of constant wind at 7 m s^{-1} (threshold wind velocity = 5 m s^{-1}). Transport direction from left to right. Line plots show total volumes of avalanching and transported sediment within the model domain over time.

Three-dimensional representations of the modelled landscape are shown in Figure 9.12. The fully vegetated domain (Figure 9.12a), which is an unrealistic condition in the Huab valley, evolves to a landscape of fully developed nebkha dunes (Figure 9.12b) that is qualitatively very similar to that observed in the Skeleton Coast (Figure 9.10a,b). In quantitative terms, analysis of all the individual nebkhas in the model domain at the end of the simulation reveals that dune spacing ranged from 5–~40 m (Figure 9.12c), which is on the order of spacing observed in Figure 9.10a and in the field. Final vegetation spot heights in the model ranged from 0.3–1.0 m, which corresponds well to shrub heights in the field (N.B. the maximum height a vegetated cell can grow to is predetermined in the model setup). Sandy tails from 3 m to 8 m in length were observed in the final modelled landscape, with volumes ranging from

0.20–2.30 m^3, which is similar to the three nebkha volumes determined using TLS data (0.26–1.22 m^3).

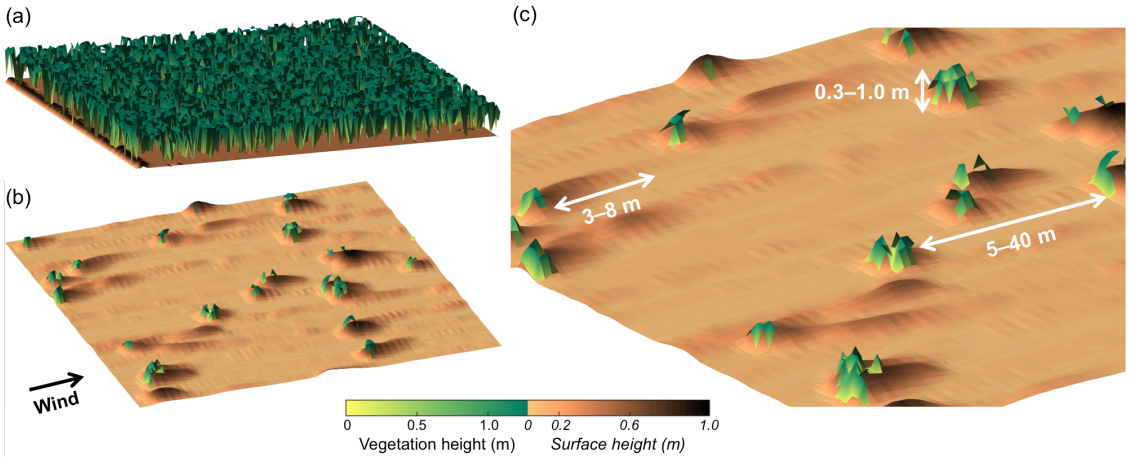


Figure 9.12 Three-dimensional representation of combined vegetation and surface morphology for the Skeleton Coast simulation, at: (a) 0 years; (b) 25 years. Average nebkha dune spacing, height and tail dimensions at the end of the simulation period are shown in panel (c). Black arrow shows average wind direction. Model was run over a 100 x 100 m grid. Simulation details are given in caption of Figure 9.11. Figures partly created using the algorithm of *Zekollari* (2016).

9.10. Conclusions

- A vegetation distribution model and a sediment transport model are coupled, allowing the ecogeomorphic evolution of dryland landscapes to be simulated in a spatially explicit way.
- The model requires only a few data inputs (precipitation, wind velocity and direction) to simulate landscape dynamics.
- A novel method is introduced in this paper for directly imposing oblique wind and transport directions onto a cell-based domain. This allows modelled landscapes to be simply and accurately exposed to natural wind velocity variations.
- The ViSTA model successfully simulates an equilibrium nebkha dunefield in the Skeleton Coast, producing realistic dune size and spacing characteristics.

The ViSTA model is now ripe for further testing and validation. For instance, we envisage applying it to further investigate nascent theories on possible ‘modes’ for dune orientation (Courrech du Pont et al., 2014), to recreate episodes of dune activation on semi-vegetated farmland, and to replicate meso-scale wind flow behaviour based on long-term field data.

The coupled ViSTA model represents a versatile geomorphological tool which, if parameterised correctly, can be applied to simulate a variety of dryland environments. In turn, the simplicity of the model inputs should allow for extensive investigation of future climatic and anthropogenic disturbances to dryland regions. Identifying the proximity of populated dryland systems to ecogeomorphic thresholds is directly relevant to land management policies.

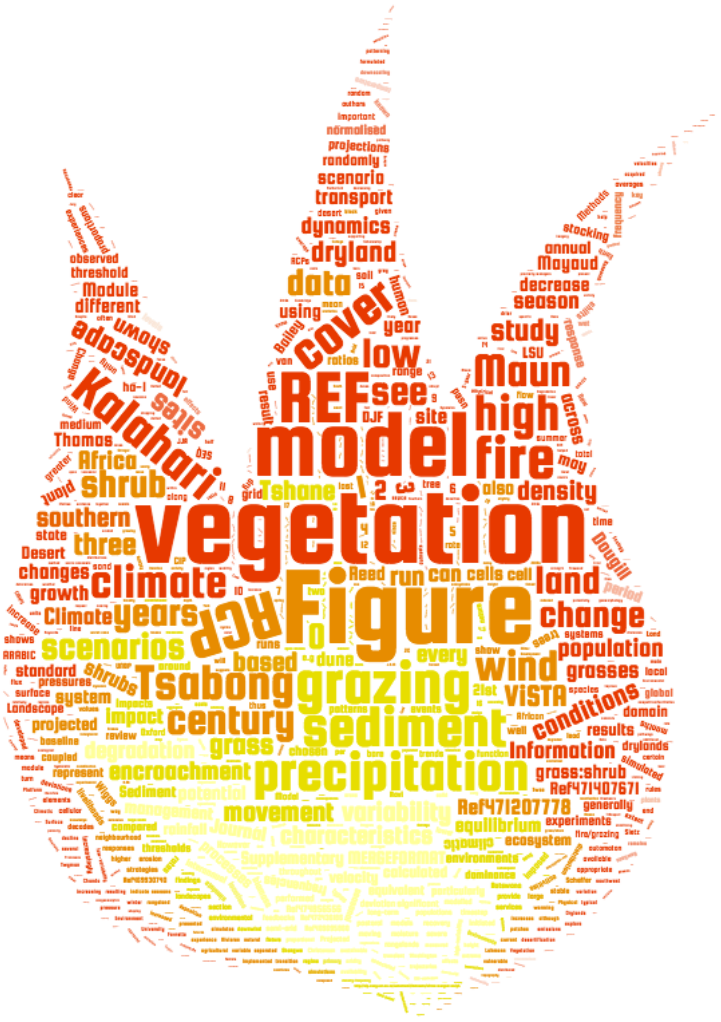
Summary: Paper 4 (part 2)

Paper 4 presented verification and validation tests for the ViSTA model. Hysteretic vegetation growth was shown to emerge in ViSTA, and resultant patterning compares well with satellite imagery of relevant dryland areas. The dominance of different vegetation types in certain climatic contexts can also be replicated, including in complex cases of human disturbance such as fire and grazing. Verification testing showed that realistic wind flow behaviour develops across a partially vegetated domain, without directly formulating wake interference or skimming flow in the model. Important links between plant photosynthetic potential and the fundamental length scales of bedforms was shown to impact the temporal and spatial resolution at which the model should be run.

Landscapes simulated by ViSTA compared well with theoretical dune forms (e.g. Wasson & Hyde's (1983) phase diagram) and emerging theories surrounding different 'modes' of dune orientation. Model output was also compared to detailed field data of a nebkha dunefield in the Skeleton Coast, demonstrating that ViSTA produces realistic dune spacing, height and tail volumes. This is important, because it implies that the processes within the model can reliably replicate basic emergent behaviour observed in nature.

Following these verification and validation tests, the ViSTA model can be used as a robust geomorphological tool for predicting landscape responses to a variety of human and environmental stresses. Paper 5 explores the potential evolution of Kalahari dunefields over the coming century.

CHAPTER TEN


vegetation
model
Figure
REF
Kalahari
Tsabong
grazing
sediment
precipitation
century
climate
RCP
fire
high
cover
data
dryland
dynamics
transport
scenario
projections
normalised
randomly
Maun
study
low
see
site
Tshane
shrub
Africa
southern
three
changes
growth
Climate
years
scenarios
based
dune
every
wind
land
change
population
grasses
conditions
VISTA
results
Information
grass:shrub
Ref471407671
Ref471207778
generally
experiments
ecosystem
equilibrium
variability
movement
encroachment
degradation
gross
Impact
projected
system
standard
pressures
surface
Landscape
Shrubs
Sediment
potential
characteristics
Supplementary
MENSEPARM
environments
dominance
calculated
velocity
Reed
run
can
cells
cell
also
density
across
summer
LSU
season
decrease
annual
Mayoud
methods
stocking
frequency
observed
threshold
Module
different
using
year
human
Desert
state
time
domain
drylands
Simulated
global
local
species
African
well
Oxford
review
baseline
coupled
represent
Wilcox
Thomas
medium
greater
DJF
JJA
SON
MAM
Period
Doughill
shows
ARABIC
increase
Landscape

Modelled responses of the Kalahari Desert to 21st century climate and land use change

Paper 5: Mayaud, J. R., Bailey, R. M. & Wiggs, G. F. S.
Status: published in *Nature Scientific Reports* (2017)

Abstract
Drylands are home to over 2 billion people globally, many of whom use the land for agricultural and pastoral activities. These vulnerable livelihoods could be disrupted if desert dunefields become more active in response to climate and land use change. Despite increasing knowledge about the role that wind, moisture availability and vegetation cover play in shaping dryland landscapes, relatively little is known about how drylands might respond to climatic and population pressures over the 21st century. Here we use a newly developed numerical model, which fully couples vegetation and sediment-transport dynamics, to simulate potential landscape evolution at three locations in the Kalahari Desert, under two future emissions scenarios: stabilising (RCP 4.5) and high (RCP 8.5). Our simulations suggest that whilst our study sites will experience some climatically-induced landscape change, the impacts of climate change alone on vegetation cover and sediment mobility may be relatively small. However, human activity could strongly exacerbate certain landscape trajectories. Fire frequency has a primary impact on vegetation cover, and, together with grazing pressure, plays a significant role in modulating shrub encroachment and ensuing land degradation processes. Appropriate land management strategies must be implemented across the Kalahari Desert to avoid severe environmental and socio-economic consequences over the coming decades.

This chapter addresses **Objective 5** (force the coupled model with potential scenarios of future climate and land-use change). **Methods**: cellular automaton modelling.

This chapter is a modified version of the paper by Mayaud et al. (2017, *Scientific Reports*). The Introduction section of the paper has been shortened, to avoid repetition of material provided in Chapter 2 of this thesis. The Methods section and parts of the Supplementary Information of the paper have been combined, and partly shortened to avoid repetition of material provided in Chapter 8 of this thesis.

10. Modelled responses of the Kalahari Desert to 21st century climate and land use change

10.1. Drylands as non-equilibrium environments

Dryland environments are extreme in their nature, typified by non-equilibrium conditions in climate, vegetation and geomorphology (Sietz et al., 2011; Viles, 2011; Lohmann et al., 2012). The interactions among these system components often result in shifts in the composition and patterning of dryland ecosystems, which can be detrimental to dryland ecosystems because they cause rapid and widespread loss of bioproductivity and biodiversity (Scheffer et al., 2001; van Nes & Scheffer, 2007). Whilst large-scale vegetation shifts are known to result from variations in external (climatic and CO_2) forcing (Ravi et al., 2010), the potential impacts of 21st century climatic change on dryland vegetation cover and composition remain unclear (UNDP, 2011).

Large, abrupt shifts can also be triggered or exacerbated by a range of human disturbances, such as agriculture, grazing and fire (HilleRisLambers et al., 2001; Barbier et al., 2006; Breshears et al., 2009; Huang et al., 2010; Levin et al., 2012; Miller et al., 2012). The potential existence of vastly different vegetation covers in the same climatic context has important implications for sediment movement and subsequent desertification processes (Okin et al., 2006; Li et al., 2013). In turn, these shifts can affect a broad range of dryland ecosystem services, from economic resources to recreation, firewood and food (Scheffer et al., 2009; Favretto et al., 2017), which help to sustain a large majority of dryland livelihoods. There is particular concern about how land degradation, particularly through bush encroachment and associated losses of grass species (van Auken, 2000; Thomas & Twyman, 2004; Gilad et al., 2007; Reed et al., 2007; Dougill et al., 2016), may intersect with increasing rural poverty levels (Chanda et al., 2003).

Ultimately, the combination of pressures from climate change and human activities could lead to large-scale reactivation of dune fields and desert encroachment in many of the world's most vulnerable regions (Thomas et al., 2005; Wang et al., 2009). However, the interactions of fire, grazing and factors affecting ecogeomorphic tipping points are not well understood (Sietz et al., 2011; Lohmann et al., 2012; Reed et al., 2015). It is therefore vitally important to model dryland systems in a holistic way, by emphasising the complex coupling between vegetation and sediment transport dynamics.

Here, we explore the potential impacts of climate change and human land management (fire and grazing) on landscape processes in the Kalahari Desert in southern Africa. For this we use a coupled cellular automaton, the Vegetation and Sediment TrAnsport model (ViSTA) (Mayaud et al., 2017a). ViSTA explicitly simulates known feedbacks between vegetation growth, wind flow dynamics and sediment flux over a surface (see section 10.2). Analysable outputs from the model include vegetation cover, proportions of different vegetation types (grasses, shrubs and trees) and sediment transport levels, which help to indicate land degradation processes. Mayaud et al. (2017a) provide an extensive set of verification tests for ViSTA, with empirical data supporting the model formulations as far as possible.

10.2. Methods

10.2.1. Study location

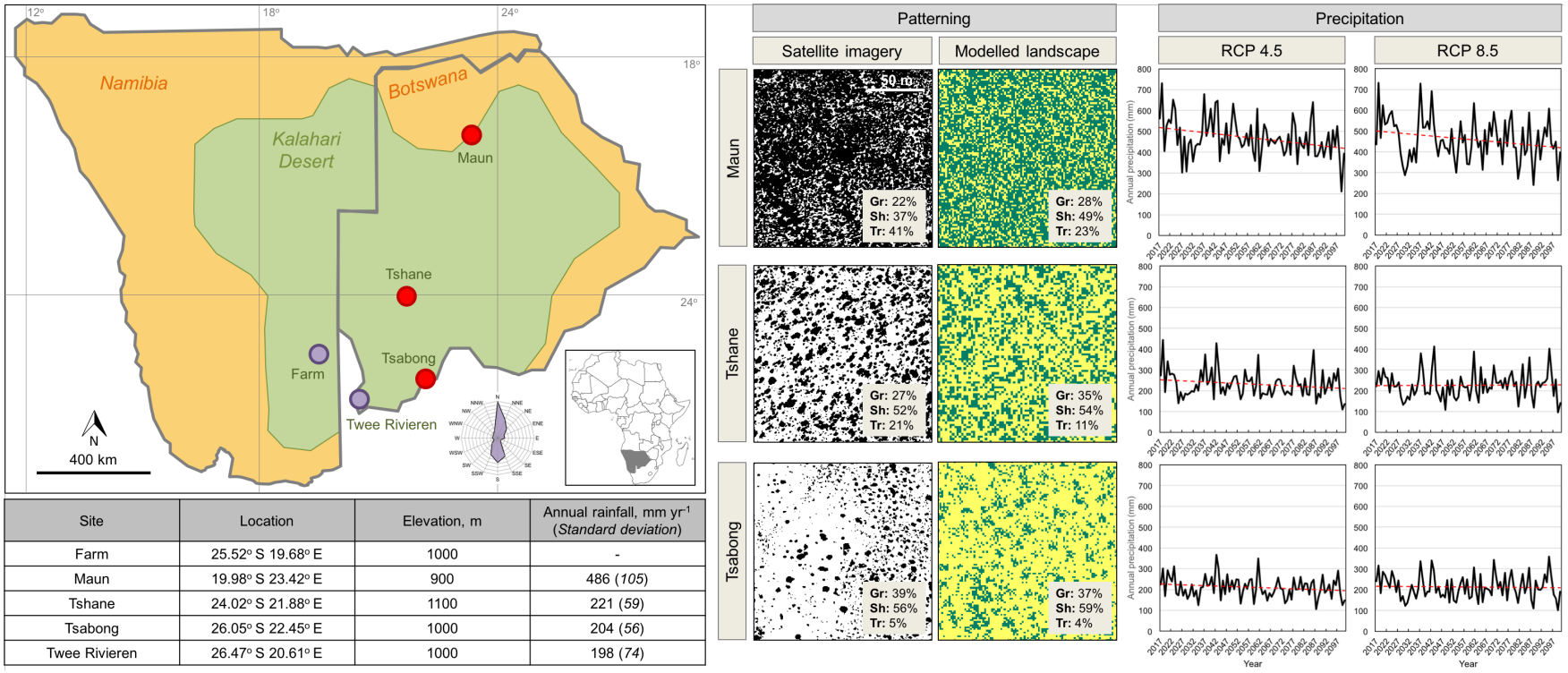
For our modelling experiments, we chose three sites along a North-South rainfall gradient across the Kalahari (Maun, Tshane and Tsabong; see Figure 10.1), to provide a variety of current environments and projected climatic changes. These locations were chosen because of the availability of downscaled open-source data

for their regions (see section 10.2.3). The degree of aeolian activity tends to decrease towards the northern end of the rainfall gradient, such that the silt/clay sediments around Maun do not form into large dunes. Dunes, some of them partly mobile, are present at Tshane and Tsabong (Bhattachan et al., 2014).

Although the southern African dune system is largely inactive today, it developed over the course of multiple episodes of aridity since the last interglacial period (Stokes et al., 1997; Thomas & Burrough, 2013), and is likely to experience enhanced dune activity in the coming decades (Thomas et al., 2005). We used two of the IPCC's (2013) main emissions scenarios ('representative concentration pathways', RCPs) to derive projected climate changes at our study sites: RCP 4.5, representing stabilisation of greenhouse gas (GHG) emissions (to 580 ppm CO_2-equivalent by 2100), and RCP 8.5, a high GHG emission scenario (to 1230 ppm CO_2-equivalent by 2100).

10.2.2. ViSTA model

The Vegetation and Sediment TrAnsport model (ViSTA) is a coupled cellular automaton (CA) model designed to simulate the evolution of semi-vegetated dryland landscapes. The model consists of two coupled modules that interact with each other over various timescales: (i) a vegetation model (adapted from Bailey, 2011) that simulates vegetation growth in response to environmental stresses resulting from climate and land use changes, and (ii) a sediment transport model that moves sediment across the model domain according to spatially varying wind velocities. The coupled scheme is formulated such that the distribution of vegetation (Module 1) alters local wind flow characteristics (Module 2a), thus impacting sediment flux patterns over the surface (Module 2b), which in turn affects vegetation growth (Module 1) through ecological feedbacks.



Site	Location	Elevation, m	Annual rainfall, mm yr^{-1} (*Standard deviation*)
Farm	25.52° S 19.68° E	1000	-
Maun	19.98° S 23.42° E	900	486 (*105*)
Tshane	24.02° S 21.88° E	1100	221 (*59*)
Tsabong	26.05° S 22.45° E	1000	204 (*56*)
Twee Rivieren	26.47° S 20.61° E	1000	198 (*74*)

Figure 10.1 Map: Locations of experimental sites (main analysis sites shown as red dots, additional sites shown as purple dots). Green shaded area shows the extent of the Kalahari Desert in Botswana and Namibia. Wind rose shows aggregated mean monthly wind directions over the period Jan 1994–Dec 2013 at Twee Rivieren. Modelled vegetation states for the three study sites (for 2000, RCP 4.5) are compared to satellite imagery (Google Earth, v.5.1; converted to black (vegetation present) and white (bare surface) using a visually determined threshold). Proportions of vegetation types, both modelled and measured along vegetation transects near each site, are shown in inset grey boxes. Maun (19.99° S, 23.69° E) is located on the edge of the Okavango Delta, with a dominant grass/shrub system and some dense tree cover. Tshane (24.13° S, 22.04° E), in the middle of the Kalahari Desert, is characterised by lower cover of mixed grasses and shrubs, with occasional trees. Tsabong (26.04° S, 22.21° E) in southern Botswana also has low vegetation cover, mainly composed of grasses and shrubs with isolated trees. Graphs show projected changes in annual precipitation over the period 2017–2100, for Maun, Tshane and Tsabong, under the RCP 4.5 and RCP 8.5 scenarios. Dotted red lines show linear best fit trends. Table shows mean observed annual rainfall over the period Jan 1984–Dec 2013 (standard deviations in brackets show interannual variability).

Like all models to a certain extent, ViSTA relies on various parameterisations for describing processes that occur within it. Modelled relationships between soil moisture and vegetation growth are currently based on arbitrary growth units linked to observed relationships between precipitation and vegetation state dominance (see Supplementary Information). These parameterisations could be improved using existing datasets on dryland soil moisture distribution (D'Odorico et al., 2007), supplemented by local- to regional-scale moisture patterns derived from remote sensing and land-surface modelling (Escorihuela & Quintana-Sequi, 2016). Growth functions linking sediment balance with vegetation growth are currently derived from a combination of qualitative vegetation behaviour described in the literature and trial and error (Baas & Nield, 2007). More empirical, field-based data are needed to improve these sediment balance parameterisations.

In terms of the climatic forcing, the vegetation module in ViSTA is currently formulated to work with precipitation only, and therefore temperature is not considered. Thomas et al. (2005), who also modelled the impact of future climatic change on Kalahari dunefields, employed an effective precipitation parameter instead of solely precipitation, thus integrating the impact of temperature on potential evapotranspiration from the surface. Potential evapotranspiration is somewhat difficult to determine accurately from limited climatic inputs, but ViSTA would benefit in future from including the impacts of temperature on vegetation growth dynamics.

In its current form, ViSTA simulates human management impacts in simplified probabilistic (e.g. fire) or spatially averaged (e.g. grazing) ways. Future development of ViSTA will involve more sophisticated coupling between the human system and landscape dynamics, for instance using cellular automata of fire front spread (e.g. Karafyllidis & Thanailakis, 1997) and agent-based modelling of animal foraging and avoidance behaviour (e.g. Marion et al., 2008).

10.2.3. Climate projections

Climate data were acquired from the open-source Climate Information Platform (CIP, 2016). CIP provides future climate projections (until 2100) based on several models from the fifth Coupled Model Intercomparison Project (CMIP5) for RCP 4.5 and RCP 8.5. The projections are downscaled locally to specific weather station locations through the statistical downscaling method of Hewitson & Crane (2006). This method uses modelled circulation fields to generate projections, by associating appropriate weather states based on observations, thus obviating the need for bias correction. A subset of three models was chosen from the CIP ensembles, based on Dieppois et al.'s (2015) ranking of CMIP5 model performance over southern Africa: CNRM-CM5, MIROC5 and MRI-CGCM3 (see Text 10.S1). For each of the three study sites, precipitation and temperature data were averaged across the three models at a monthly timestep. Additionally, observed climate datasets for each study site were acquired from the Botswana Department of Meteorology, to verify the modelled historical climate data and to indicate the reliability of future model projections (Figure 10.S2).

Wind was imposed in Module 2a using wind velocity distributions derived from a 20-year dataset measured at Twee Rivieren in the southwest Kalahari. Hourly wind velocity data were acquired for Twee Rivieren in the southwest Kalahari, based on the availability of long-term wind data available from the Botswana Meteorological Service. Wind velocity data at 08:00 (morning), 14:00 (afternoon) and 20:00 (evening) were selected for each day between 1st January 1994 and 31st December 2013. These times were chosen to account for diurnal wind variations. Days with missing data points were removed, and the resulting data were grouped by season (MAM, JJA, SON and DJF). The distribution of the data in each season was assessed using MATLAB's built-in 'wblplot' function, which graphically assesses whether the data could come from a Weibull distribution (Figure 10.S3). For each

month grouping, the maximum likelihood estimates of the 2-parameter Weibull distribution were calculated using MATLAB's built-in 'wblfit' function. These are summarised in Table 10.S1. Weibull distributions of wind velocity were generated using the parameters for each month grouping, and samples were drawn randomly from the appropriate distribution at each model iteration. The velocity threshold for entrainment was set at 5.1 m s^{-1}, based on realistic potential thresholds measured in the Kalahari (Knight et al., 2004).

10.2.4. Model experiments

For our chosen key years (2030, 2060 and 2090) and the baseline year (2000), we used mean projected precipitation data from the two decades around each year to improve reliability (e.g. data for 2020–2040 were used to represent the aggregate 'year' 2030). The sporadic nature of wind events in natural desert environments was simulated by randomly selecting wind velocities from Weibull distributions for each season, based on long-term wind data collected at Twee Rivieren in the southern Kalahari (see section 10.2.3). Wind directions were randomly selected from a probability density function based on the direction data presented in Figure 10.1.

For the equilibrium experiments, the model was run for each site, at the chosen years and for both RCPs, for the equivalent of 200 model years over a grid of 150 x 150 cells. Low variability (standard deviation, σ = 30 mm annual equivalent) and high variability (σ = 160 mm annual equivalent) precipitation conditions were simulated based on the variability range in observed historical data. The vegetation module was run every 3 model months, with 20 wind events between each vegetation module update. The domain was randomly initiated with 90% vegetation cover and random sediment depth. Landscape characteristics were calculated as means over

the last 10 years of each run, and normalised to those of the baseline year (2000), for RCP 4.5.

For the transient run experiments, the model was initialised with the equilibrium vegetation conditions observed for the year 1960 for each respective site, and forced with 140-year precipitation trajectories from the CIP datasets (i.e. 1960–2100). At each site and for both RCPs, 10 model runs were performed and the resulting landscape characteristics aggregated to indicate the average response. Variability was introduced by randomly sampling from a normal distribution around the projected precipitation trajectory for each run, with a standard deviation (σ) calculated from 5-year moving averages of the standard deviation for each season. The same grid and module update parameters were used as for the equilibrium experiments.

For the fire and grazing experiments, the model was run in the same way as for the transient run experiments, forced with precipitation trajectories from 1960–2100. Runs were performed for Maun and Tsabong only under RCP 4.5, to capture a range of dynamics in the Kalahari under a stabilising climate. At both sites, three stocking rates (given as large stock units (LSU) per hectare (ha)) were imposed to simulate different grazing pressures typical of Kalahari rangelands (Blaum et al., 2009; Burgess, 2009): 0.001 LSU ha^{-1} (low grazing), 0.01 LSU ha^{-1} (medium) and 0.06 LSU ha^{-1} (high). Three fire frequencies were also imposed: once every 10 years (low), once every 5 years (medium) and once every 2 years (high). 3 model runs were performed for each scenario, and the resulting aggregate landscape characteristics were calculated as means over the 10 years around each chosen date (e.g. 2025–2035 for 2030).

The model state parameters for all experiments presented in this study are summarised in Table 10.1.

Experiment (related figure)	N° of repeats	RCP	Modelled years	Veg. update interval	Wind freq.	Grid length (m)	Cell size (m)
Equilibrium runs (Fig. 10.3, Fig. 10.S7)	Equilibrium (200 yrs)	4.5, 8.5	2000, 2030, 2060, 2090	3 months	20 events / 3 months	150	1
Transient runs (Fig. 10.4)	10 per site/RCP	4.5, 8.5	1960 – 2100	3 months	20 events / 3 months	150	1
Fire/grazing runs (Fig. 10.5, Fig. 10.6)	3 per site/RCP	4.5	1960– 2100	3 months	20 events / 3 months	150	1
Rainfall variability runs (Fig. 10.S5, Fig 10.S6, Fig. 10.S7)	Single (250 yrs)	-	-	3 months	-	100	1

Table 10.1 Summary of model state parameters for the experiments presented in this study.

10.3. Kalahari futures

The current climate of southern Africa is characterised by marked interannual and interdecadal variability (Mason & Jury, 1997), due to influence from both tropical and mid-latitude climate systems (James & Washington, 2012). Against this significant interannual variability, precipitation is projected to decrease at all three sites over the 21st century, in both the RCP 4.5 and RCP 8.5 scenarios (see graphs in Figure 10.1). In this study, we focus on precipitation as the key driving factor for vegetation change in the ViSTA model, but there are also clear upward trends in temperature at all sites, even if their magnitude differs between RCP scenarios (see Text 10.S1 and Figure 10.S1). The rising temperatures may affect potential evapotranspiration at the

surface across the century, and thus vegetation growth dynamics may differ slightly from the predicted landscape changes presented in this study.

Projected seasonal changes in precipitation are shown in Figure 10.2. At Maun, there is a clear signal of increasingly dry winters (JJA), which are thought to result from poleward-shifting storm tracks (Christensen et al., 2007; Shongwe et al., 2009). However, drier winters may have limited societal impact because this is already a very dry season (Shongwe et al., 2009; Thornton et al., 2011). At Tshane and Tsabong, increased winter (JJA) aridity in the first half of the century does not appear to contribute to subsequently drier spring periods (SON), as has been previously hypothesized (Christensen et al., 2007; Cook & Vizy, 2012).



Figure 10.2 (a, c, e, g, i, k) Projected changes in precipitation, separated by season, over the period 2017–2100 at each study site. Dotted lines show linear best fit trends; (b, d, f, h, j, l) mean total precipitation in each season, for the chosen years (2030, 2060, 2090) and baseline year (2000). Error bars show standard deviations.

For each study site, the ViSTA model was run to equilibrium with the projected conditions in three key years (2030, 2060 and 2090) and a 'baseline' year (2000) (Figure 10.2b,d,f,h,j,l), using a low-variability and high-variability scenario (see section 10.2). Figure 10.3 displays certain landscape statistics at equilibrium separated by wet season (DJF) and dry season (JJA), normalised to annual statistics for the baseline year. We use the term 'population density' to refer to the overall number of plant-covered cells relative to the total grid size. The modelled equilibrium vegetation patterning states compare well with satellite imagery and vegetation transects at each study site (see Figure 10.1). The model replicates the high vegetation cover at Maun, with numerous trees amongst grass/shrub savanna. The model also simulates generally patchier cover at Tshane and Tsabong, with lower tree proportions and higher shrub and grass proportions than at Maun.

At Maun and Tsabong, vegetation population densities stay roughly stable throughout the 21st century, with few changes between RCPs, key years or variability scenarios (Figure 10.3a,b,e,f). At Tshane, vegetation population density increases by up to 30% around 2030 and 2060 (Figure 10.3c,d), particularly under RCP 8.5, due to an increase in spring (SON) and summer (DJF) rainfall (Figure 10.2h). In terms of grass:shrub ratios, high variability scenarios generally tend to result in reduced shrub encroachment (Figure 10.3g–l), because more variable rainfall favours the establishment of pioneer grass species. RCP scenarios also influence grass:shrub ratios. For instance, in the latter half of the century Tshane experiences greater shrub encroachment under RCP 4.5 compared with RCP 8.5. This occurs because drier summers (DJF) under RCP 8.5 allow grasses to compete more favourably with shrubs, as shown by changes in average plant ages (Figure 10.S8), and by the fact that grass:shrub ratios increase as DJF rainfall is ramped up (Text 10.S4 and Figure 10.S10a). At Maun, proportional tree cover generally increases during both wet and dry seasons as the century progresses, particularly in low-variability scenarios

(Figure 10.3m,n). At Tshane and Tsabong, proportional tree cover may decrease slightly over the century, remaining higher in low-variability scenarios than in high-variability scenarios, particularly under RCP 8.5 (Figure 10.3p,r).

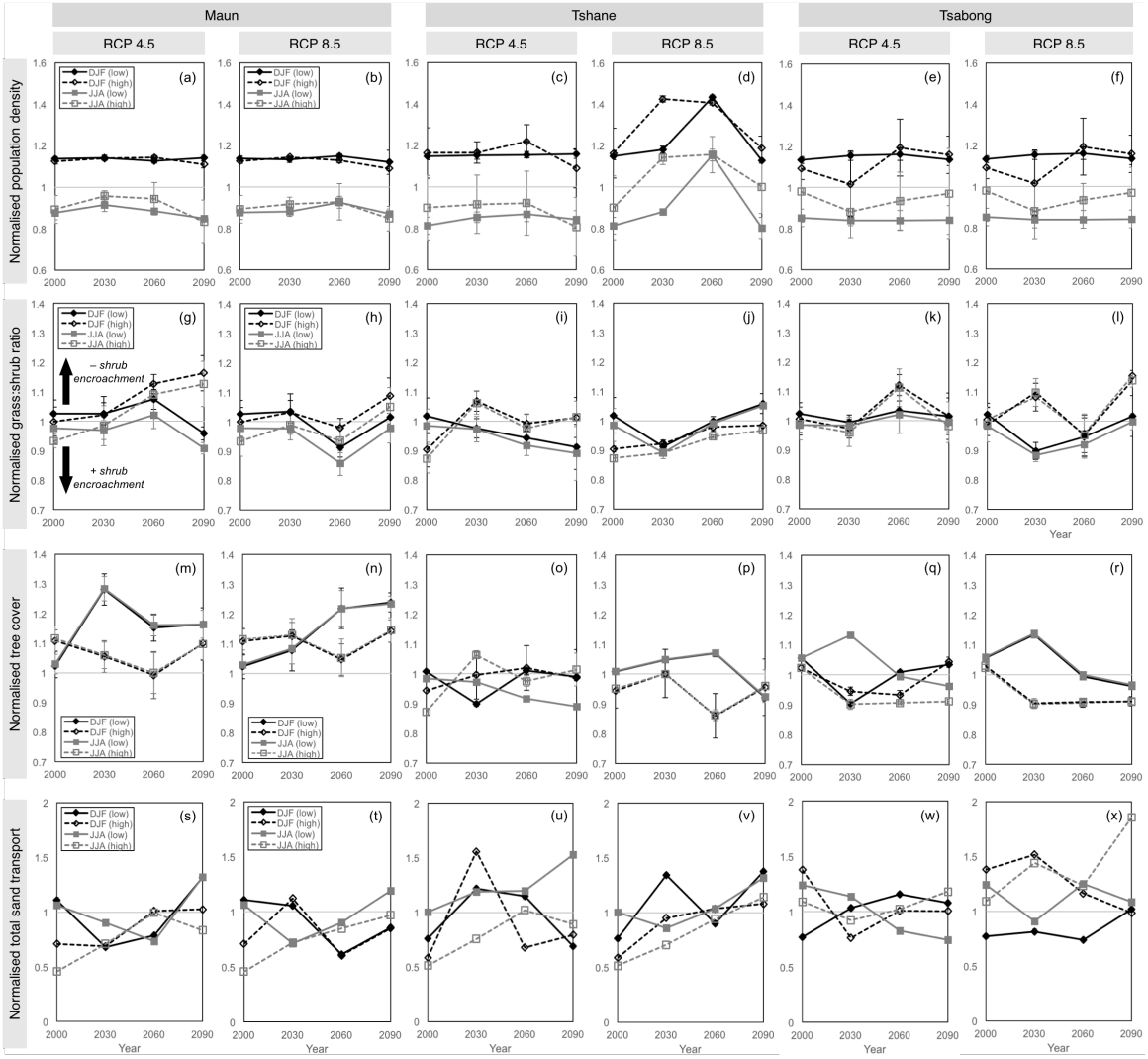


Figure 10.3 Equilibrium landscape characteristics at the three study sites for the three chosen years (2030, 2060 and 2090), separated by wet summer season (DJF) and dry winter season (JJA), and normalised to the annual average for the baseline year (2000, RCP 4.5). Results are shown for RCP 4.5 and RCP 8.5 scenarios, in low variability (standard deviation, σ = 30 mm annual equivalent) and high variability (σ = 160 mm annual equivalent) precipitation conditions. Landscape characteristics: (a–f) normalised population density; (g–l) normalised grass:shrub ratio, where values above unity represent decreased shrub encroachment; (m–r) normalised tree cover; (s–x) normalised total sediment transport across the domain. Model was run to equilibrium for the equivalent of 200 model years, with 20 wind events every 3 months, over a grid of 150 x 150 cells. The domain was randomly initiated with 90% vegetation cover and random sediment depth. Landscape characteristics were calculated as means over the last 10 years of each run. Error bars show coefficients of variation where appropriate.

The vegetation dynamics result in different sediment movement conditions at each site. In the ViSTA model, the strength of the feedbacks between sediment movement and vegetation growth can be modified to suit the parameterisation needed for different plant types and environments (Text 10.S4 and Figure 10.S9). Maun experiences a general increase in sediment movement in both seasons throughout the century (Figure 10.3s,t), although sediment movement tends to decrease in the wet season (DJF) under RCP 8.5. Tshane also experiences increased sediment movement throughout the century (Figure 10.3u,v), particularly under RCP 8.5, despite an increase in general vegetation cover. This is attributed to greater shrub encroachment during this period, since porous shrubs tend to provide less extensive sheltering effects than the bluff bodies of grasses (Mayaud et al., 2016b). An additional experiment (Text 10.S4 and Figure 10.S10b) demonstrates that a landscape populated with low-porosity elements experiences lower sediment transport rates than one populated with high-porosity elements. Sediment movement patterns are less clear at Tsabong (Figure 10.3w,x), although there is the potential for much greater transport during winter in a high-variability scenario under RCP 8.5.

Transient experimental runs were also performed (see section 10.2), because dryland landscape responses are path-dependent and can be hysteretic in nature (Bailey, 2011; Mayaud et al., 2017a). Figure 10.4 displays landscape characteristics as they change continuously through the century. At Maun, vegetation population density generally declines as the century progresses under both RCPs (Figure 10.4a), with simultaneous trends of increasing sediment movement (Figure 10.4d) and decreasing shrub dominance (Figure 10.4g). In the early 2030s, a drop in population density, accompanied by a spike in the grass:shrub ratio, can be linked to a significant drop in summer (DJF) precipitation (Figure 10.2a). At Tshane and Tsabong, population density remains lower and more variable than at Maun (Figure 10.4b,c), with no discernible directional trend. Population density at Tshane and

Tsabong shows greater variability because of the system's proximity to collapse at these locations, owing to generally low precipitation levels. This leads to higher grass proportions than at Maun (Figure 10.4h,i), with Tsabong experiencing outright grass dominance in the early 2030s as a result of the summer precipitation decline. This may reduce sediment movement and be more amenable to livestock grazing, but could also promote greater fire propagation (Miller et al., 2012; Stewart et al., 2014). Sediment movement at Tshane remains broadly stable throughout the century (Figure 10.4e), whilst at Tsabong sediment movement tends to be highest in the first half of the century (Figure 10.4f).

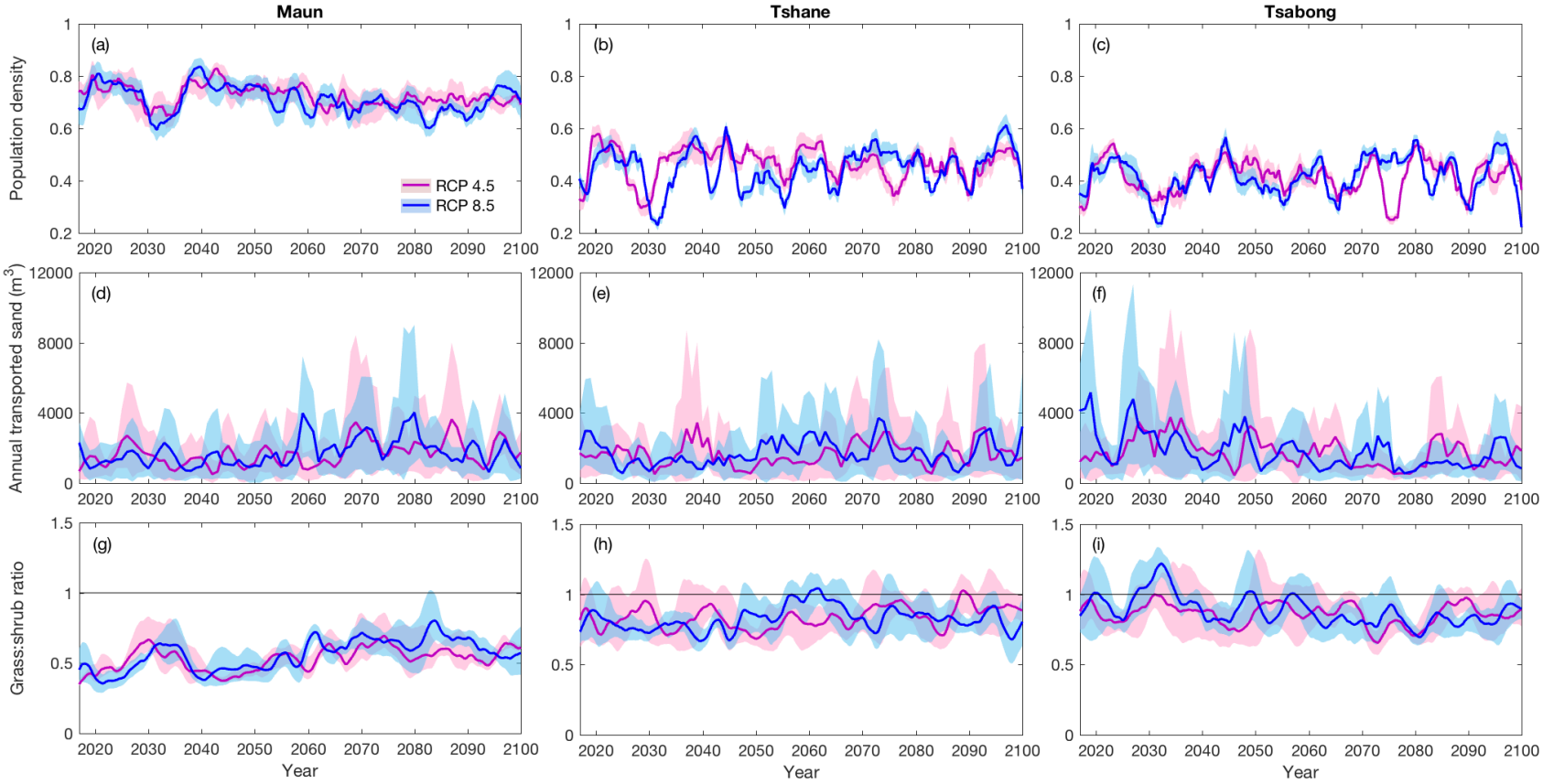


Figure 10.4 Landscape characteristics during the transient model runs, from 2017 to 2100, at the three study sites. Results are shown for RCP 4.5 (pink) and RCP 8.5 (blue) scenarios. Landscape characteristics: (a,b,c) population density; (d,e,f) total annual sand transport across the domain; (g,h,i) grass:shrub ratio, where values above unity represent grass dominance, and values below unity represent shrub dominance. Model was run 10 times per site and RCP from the year 1960, using projected precipitation data with random variation based on 5-year moving averages of seasonal standard deviations. 20 wind events occurred every 3 months, over a grid of 150 x 150 cells. The domain was randomly initiated with vegetation cover and species proportions observed at the end of an equilibrium run for 1960. Landscape characteristics are shown as three-year moving averages (solid coloured lines). Shaded area shows the range of model output across the 10 model runs for each site and RCP.

10.4. The impact of fire and grazing

To explore the added impact of human management on the Kalahari Desert system, grazing and periodic fires were imposed in the ViSTA model. Low, medium and high grazing was simulated (based on typical animal stocking rates for Kalahari rangelands), in combination with low, medium and high fire frequencies (see section 10.2). Simulations for Maun and Tsabong were performed, as these represent the climatic extremes of our sites, under RCP 4.5 only. To focus our results on the relevant scale of a human lifetime, we present results for 2030 and 2060 in Figure 10.5.

At both Maun and Tsabong, the biggest impact on vegetation population density is fire frequency, with density decreasing by up to 48% at high fire frequencies compared to low frequencies (Figure 10.5). Grazing pressure has a secondary impact, with up to 43% decrease in density between low stocking rate and high stocking rate. In the worst-case scenarios, population density may decrease to 8% at Tsabong. This could lead to important dune reactivation, as evidence shows that sand transport increases dramatically below a threshold of 12–15% vegetation cover (Wiggs et al., 1995; Lancaster & Baas, 1998; Davidson-Arnott et al., 2012).

Both fire frequency and stocking rate have a notable impact on grass:shrub ratios at the two sites (Figure 10.5). Ratios decrease (i.e. shrubs increasingly dominate) by up to 68% at low fire frequencies compared to high frequencies, and ratios decrease by up to 77% at high grazing pressures compared to low grazing pressures. Frequent fire occurrence leads to a relative increase in short-lived grass populations because grasses preferentially recolonise bare areas (Bond et al., 2003; Sankaran et al., 2005). Longer fire cycles allow shrubs to more readily establish and increasingly out-compete grasses. The establishment of shrub communities is also enabled by the generally higher precipitation levels at Maun. At Tsabong, the harsher precipitation

conditions ensure that grasses dominate the system when grazing is low and/or fires are frequent. In the worst-case scenarios, grass:shrub ratios could decline to 0.21 at Maun and 0.34 at Tsabong, representing severe shrub encroachment. Such a shrub-dominated state would persist through amplifying feedbacks linked to the fire regime (Anderies et al., 2002; Li et al., 2008; Sankey et al., 2012). This could result in a substantial increase in bare soil fractions and subsequent enhancement of soil erosion rates in barren patches (Schlesinger et al., 1990; Huenneke et al., 2002; Ravi et al., 2012).

These findings corroborate oral history evidence of vegetation and dune dynamics in the southwest Kalahari (see Text 10.S2). Over the last thirty years, the region has experienced increased agricultural intensification and fence construction, which has led to greater grazing pressures and severe shrub encroachment in some areas (Chanda et al., 2003; Thomas & Twyman, 2004; Dougill et al., 2016). Shrub encroachment can be combatted using 'debushing' herbicides (Figure 10.S4), but this remains expensive to deliver over large areas (Reed & Dougill, 2010). Much heavily grazed farmland in the southwest Kalahari now consists of bare, intermittently active dune crests (Hesse et al., 2015), which have migrated noticeably within a human lifetime (Rutherford & Powrie, 2009; Dougill et al., 2016).

It is difficult to define optimal vegetation and soil conditions for agriculture and pastoral livelihoods (Reed & Dougill, 2010). For instance, shrub encroachment is often cited as having negative impacts on pastoral activities (e.g. van Rooyen, 1998; UNDP, 2011), yet over the short-term land managers perceive certain shrub species to be important windbreak and forage resources (Thomas & Twyman, 2004; Reed et al., 2007). Furthermore, the extent to which shrub-encroached land can be considered 'degraded' depends heavily on shrub traits (Eldridge et al., 2011). At Tshane and Tsabong, decreased shrub encroachment under some scenarios (Figure

10.3j–l) could ameliorate conditions for cattle, and the associated decrease in sediment movement (e.g. Figure 10.4j) may help to improve soil fertility (Belnap et al., 2009). However, a decrease in proportional tree cover (Figure 10.3p–r) at these locations could negatively affect other ecosystem services such as firewood provision and cultural usages (Reed et al., 2015; Favretto et al., 2017).

Despite a wealth of empirical research in this field, few quantitative thresholds for dryland degradation have been proposed. This reflects the fact that equilibrium conditions rarely exist in drylands (Sietz et al., 2011), rendering fixed thresholds meaningless over certain timescales, and that dryland inhabitants regularly change their coping strategies in response to climatic and resource stress (Reed et al., 2007). Nevertheless, it can be helpful to determine amount of time a dryland vegetation system spends below specific threshold population densities. Figure 10.6 categorises the seasonal frequency of different grass and shrub covers during the 21st century at Maun and Tsabong, according to the fire/grazing regime. For example, at Maun (Figure 10.6a), a low fire, high grazing scenario results in grass cover dropping below an arbitrary 20% threshold for 98% of the century. In a high fire, high grazing scenario, grass cover drops below the 20% threshold only 4% of the time. At Tsabong (Figure 10.6b), a low fire, low grazing scenario is most favourable for high grass cover (grass drops below the 20% threshold 51% of the time, compared with 78–97% of the time in the other three regimes shown). At both Maun (Figure 10.6c) and Tsabong (Figure 10.6d), a high fire, low grazing scenario results in shrub populations dropping below the 20% threshold most often, at 57% and 95% of the time respectively. In this way, categorising the time spent in sub-threshold conditions allows land managers to better understand the potential medium- to long-term effects of their strategies.

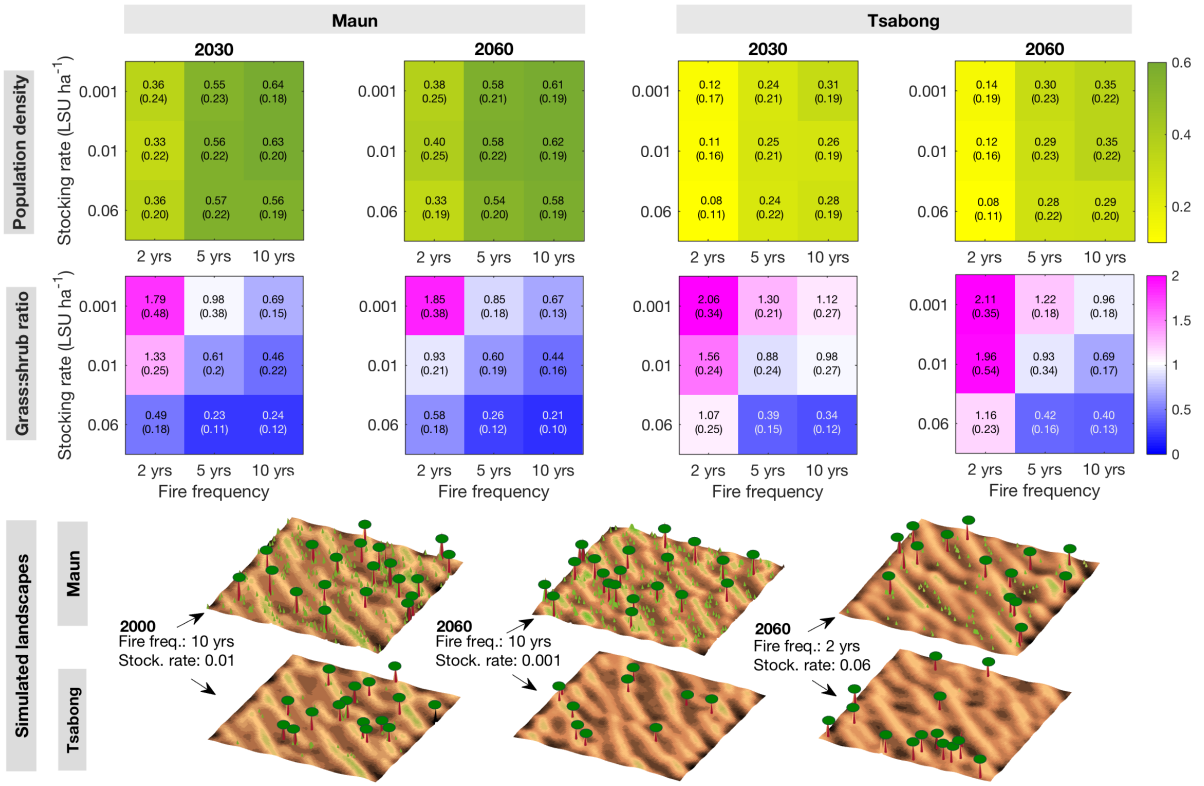


Figure 10.5 Matrices of population density and grass:shrub ratios at Maun and Tsabong under RCP 4.5, for 2030 and 2060, with three different fire frequencies (low: once every 10 years, medium: once every 5 years, high: once every 2 years) combined with three different grazing pressures (low stocking rate: 0.001 LSU ha^{-1}, medium: 0.01 LSU ha^{-1}, high: 0.06 LSU ha^{-1}) imposed on the landscape (see section 10.2). Values are given in each matrix square (standard deviation in brackets), with colour scaling. Three-dimensional examples of simulated landscapes in 2000 and 2060 are displayed for comparison purposes (trees shown as trunks with distinct crowns, shrubs/grasses shown as green patches). Values above grass:shrub unity represent grass dominance, and values below unity represent shrub dominance. Model was run 3 times per fire/grazing scenario at both sites from the year 1960, using projected precipitation data with random variation based on 5-year moving averages of seasonal standard deviations. 20 wind events occurred every 3 months, over a grid of 150 x 150 cells. The domain was randomly initiated with vegetation cover and species proportions observed at the end of an equilibrium run for 1960. Landscape characteristics in the matrices were calculated as means over the 10 years around both chosen dates.

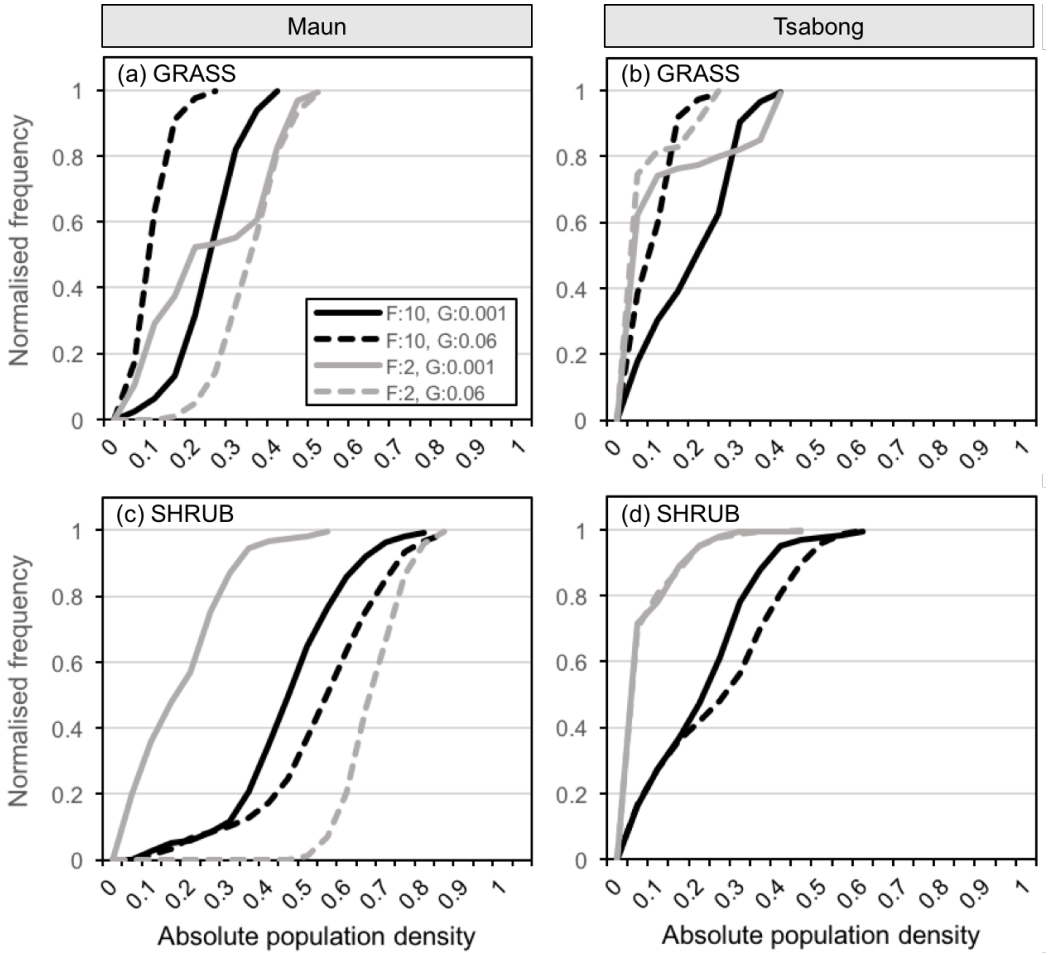


Figure 10.6 Cumulative frequency curves of absolute population density of grasses and shrubs at Maun and Tsabong, over the period of 2017–2100, for different fire/grazing scenarios. Data are from the same model runs presented in Figure 10.5. Curve data represents averaged density-frequency data (every 3 months) from the 3 model runs for each fire/grazing scenario. Four management scenarios are presented: low fire and low grazing (fire: every 10 years, grazing: 0.001 LSU ha^{-1}; solid black line), low fire and high grazing (f: 10, g: 0.06; dotted black line), high fire and low grazing (f: 2, g: 0.001; solid grey line), and high fire and high grazing (f: 2, g: 0.06; dotted grey line).

10.5. Conclusions

Thomas et al. (2005) demonstrated, at the relatively coarse dunefield scale, that the Kalahari Desert could experience significant reactivations as a result of 21st century climate change. The ViSTA model represents an evolution in the reduced complexity approach adopted by Thomas et al. (2005) by explicitly including known feedbacks between vegetation growth, wind flow and sediment transport. Crucially, our cellular automaton method allows ecogeomorphic processes to be simulated at appropriately

fine spatial and temporal scales. However, in its present form, the ViSTA model does not incorporate temperature effects on vegetation growth (e.g. through changes to potential evapotranspiration), so it reduces the complexity of the climate system in this respect.

Findings from this study suggest that the impact of precipitation changes alone on the landscape may not be as drastic as predicted by Thomas et al. (2005). At Maun, vegetation cover could decrease slightly throughout the century because of declining summer precipitation, which may in turn lead to enhanced sediment transport and land degradation (Geist & Lambin, 2004; Ravi et al., 2010). A late onset and decline in the main rainfall season (DJF), which has been observed in most of southern Africa over recent decades (New et al., 2006; Kniveton et al. 2009), will have potentially severe implications for maize growing in this region (Tadross et al. 2005). At Tshane and Tsabong, the existing proximity of the desert system to ecogeomorphic thresholds results in some interannual variability in landscape response to climatic change, but no clear long-term trends. These findings are independent of the RCP used. The difference in our model's output compared to the results of Thomas et al. (2005) may in part arise from ViSTA not accounting for temperature impact. Indeed, rising temperatures throughout the 21st century (Figure 10.1; Figure 10.S1) will likely increase surface evaporation and thus the amount of moisture available for plant growth. This could result in reduced vegetation population densities, and potentially increased sediment movement.

However, the inclusion of fire and grazing dynamics in our simulations results in vastly differing potential landscape responses through the 21st century. Fire frequency has a primary impact on vegetation cover, and together with grazing pressure dictates the proportion of grasses and shrubs in the vegetation system. Reduced fire intensity clearly results in more established shrub populations at the

expense of grass populations. This in turn affects sediment mobility, potentially enhancing land degradation processes in barren soil patches. Our study therefore suggests that human activities could shape a range of Kalahari landscapes, above and beyond climate change impacts. To protect agricultural and pastoral livelihoods, which generally benefit from high grass cover, it will be necessary to carefully balance fire cycles (both anthropogenic and natural) with animal stocking rates. This is usefully predicted by comparing the potential state of the vegetation system at different thresholds, using density-frequency plots based on several fire/grazing scenarios. If appropriate land management strategies are not implemented in vulnerable dryland regions, the socio-economic and environmental consequences could be significant.

Summary: Paper 5

Paper 5 sets out potential future trajectories for three sites in the Kalahari Desert over the 21st century. The ViSTA model was forced with climate model output under two future emissions scenarios (stabilising (RCP 4.5) and high (RCP 8.5)), as well as a range of fire and grazing regimes.

Experimental results suggest that the impacts of climate change alone may be relatively minor at all three sites, with no clear long-term trends under either RCP. However, the variability of future precipitation could impact the landscape response, with highly variable rainfall conditions leading to much more rapid vegetation decline and greater shrub encroachment than low-variability conditions. Given the difficulties in predicting the full range of future rainfall variability, vegetation decline and subsequent dune reactivation could be more dramatic than the modelling results presented here. Moreover, not including temperature forcing may have impacted model output, since rising potential evapotranspiration is likely to reduce the amount of surface moisture available for vegetation growth.

Human disturbance, however, was shown to strongly impact landscape trajectories. Fire and grazing demonstrably affect vegetation cover and composition, by modulating the colonisation of bare surfaces by certain plant types. Indeed, agricultural intensification and fence construction has led to greater grazing pressures and severe shrub encroachment in some areas of the Kalahari. Much farmland now consists of bare, intermittently active dune crests. Human activity could continue to exacerbate this process of dune reactivation.

Nonlinearity and lack of equilibria in dryland landscapes means it is difficult to confidently define land degradation thresholds, and therefore optimal levels of agricultural and pastoral activity. However, ViSTA model output can be usefully categorised to reveal the seasonal frequency of grass and shrub cover in different fire/grazing scenarios. This allows a quantification of the amount of time the vegetation system spends below specific threshold population densities, and potential aeolian activity that may occur at different thresholds. ViSTA is a robust predictive model that could be used alongside local knowledges and practices to inform land management strategies, and thus help to avoid the severe environmental and socio-economic consequences of land degradation.

SECTION FOUR

CHAPTER ELEVEN

Conclusions

11. CONCLUSIONS

The overall aim of this thesis was to measure, model and evaluate the interactions between wind flow, spatial vegetation patterning and sediment flux in dryland landscapes. A series of field experiments were conducted in Namibia to provide data on turbulent wind flow around different dryland plants and patches (Chapters 5–7). These data then formed the basis for parameterisations that could be used in developing the fully coupled Vegetation and Sediment Transport model (ViSTA) (Chapter 8). Finally, ViSTA was used for predictive modelling of ecogeomorphic systems in the Kalahari (Chapter 9).

The three key questions designed to address the main aim (section 1.2) are presented below, and the findings relating to each question and associated objective are discussed. Wider issues are raised, and potential avenues for future research are outlined.

11.1. Summary of findings

11.1.1. Key Question 1: How does turbulent airflow vary around single vegetation elements in a dryland, and how is this affected by the type, size and porosity of plants?

This key question was addressed by measuring wind structures (velocity and turbulence statistics) upwind, downwind and to the sides of various plant types: shrubs, grasses and trees (**Objective 1**). Plants of different heights and porosities were studied in three desert locations in Namibia.

The first paper (Chapter 5) focused on evaluating turbulence around three individual plants. It showed that dryland grass, shrub and tree elements impact turbulent wind

flow in differing ways. Despite similar recovery distances for the grass and shrub, the bluff nature of the grass induced more intense wind slowdown in the lee than the shrub (Figure 5.2, Figure 5.3). The greater proportion of bleed flow in the shrub case meant that it disrupted flow less intensely, but over a greater distance, than the grass clump. There was some evidence for the formation of a recirculation in the lee of the grass, and for a more intense vertical exchange of turbulent eddies along its wake compared to the shrub (Figure 5.6, Figure 5.7). This supports previous findings (Skidmore & Hagen, 1970; Perera, 1981) that low-porosity elements induce turbulence in their lee but allow flow to recover to upstream conditions sooner than more porous elements.

Coherent flow structures were analysed to segregate the stress budget of disrupted flow around the study elements. The relative changes in flow structures is important to quantify, because of the role they are understood to play in driving sediment transport (Finnigan, 1979; van Boxel et al., 2004; Wiggs & Weaver, 2012). The flow exuberance (EX_{FL}), which expresses the ratio of negative to positive contributions to Reynolds stress generation, has previously been used to quantify a turbulent 'bursting process' that may determine sediment transport (e.g. Shaw et al., 1983; Chapman et al., 2012). For the first time, this study introduced a combined measure of the horizontal strength and occurrence of exuberance, the flow exuberance magnitude (EX_{MAG}). The overall 'positivity' of the flow (i.e. the relative domination of outward interaction (Q1) and sweep (Q4) events), which may be better correlated with aeolian sand transport, was similarly characterised using the flow positivity magnitude (PO_{MAG}). Chapter 5 presented a novel approach for combining information from the EX_{MAG} and PO_{MAG} parameters (Figure 5.8), which allows plant-scale turbulent structures, such as recirculation zones and vortical structures, to be identified.

It remains difficult to make conclusive statements about the impact of turbulent structures on likely erosion/deposition zones around vegetation elements, particularly in field settings. Spatial analysis of a shelter parameter (ψ), which emphasises the salient features of horizontal turbulent flow, suggested that sediment transport potential was lower in the protective wake of the grass clump than in that of the shrub (Figure 5.9). The tree produced a different wake structure to both the grass and shrub, because its elevated canopy produced a 'bottom gap' effect, whereby streamline compression under the tree crown results in wind speeding up. The bottom gap effect led to decreased sheltering beneath the crown and in the immediate lee, but the frontal impact of the crown subsequently resulted in a far more extensive sheltering effect compared to the grass and shrub.

The third paper (Chapter 7) presented a bigger dataset of wind flow around eight individual plants (3 grass clumps and 5 shrubs). These data were used to derive a new generalised parameterisation for the recovery of wind velocity along the centreline of porous vegetation wakes, based on element height (h) and optical porosity (θ_i). In this parameterisation, height controls the scaling of the recovery, and porosity determines the ratio between airflow passing through pores and airflow diverging over and around each element (Figure 7.3). Recovery was parameterised in an exponential form, $(u_{ref} - u_0).(1 - e^{-b\frac{x}{h}}) + u_0$, with the best-fit parameters $u_0 = u_{ref}(0.0146\theta_i - 0.4076)$ and $b = 0.0105\theta_i + 0.1627$ (Figure 7.4).

Comparison of this model with existing recovery models based on wind fence data (Hagen, 1996; Okin, 2008) suggests that wind flow around three-dimensional porous forms such as grasses and shrubs may not be suitably parameterised using two-dimensional analogues (Figure 7.5). This supports the conclusions of several field (e.g. Gillies et al., 2014) and wind tunnel (e.g. Lee et al., 2014) studies. Whilst airflow cannot move around an infinitely wide fence, isolated elements divert wind flow

around their sides, which leads to faster-moving lateral flow mixing with slower-moving wake flow via counter-rotating vortices (Sutton & McKenna-Neuman, 2008). This results in a more rapid recovery in wind velocity in the case of single elements. It follows that the relative width of an element could to a certain extent affect recovery in its wake, as has been demonstrated through numerical modelling by Hesp & Smyth (2017).

The effects of plant type and porosity on wind flow have yet to be fully explored in the literature, so these two studies represent a valuable addition to our understanding of flow dynamics on vegetated desert surfaces. The new high-frequency data presented in Paper 1 and Paper 3 were used to empirically parameterise wind flow recovery in the coupled Vegetation and Sediment TrAnsport model (ViSTA).

11.1.2. Key Question 2: How do different vegetation patterns affect windflow, and therefore sediment movement, across a semi-arid landscape?

In a field context, this key question was addressed by measuring wind structures in the wake of a vegetation patch (**Objective 2**). The second paper (Chapter 6) was designed to provide data on windflow in the lee of an extensive vegetation patch experiencing skimming flow, as opposed to the isolated roughness or wake-interference flow (Wolfe & Nickling, 1993). Skimming flow, which tends to occur when vegetation cover exceeds 40%, results from increased drag acting to displace the aerodynamic roughness (z_0) upwards, extracting momentum from the surface and increasing wind shear stress above the canopy.

The recovery length downwind of the patch (~12 h_d) was shown to be longer compared with isolated elements of equivalent height reported in other studies (7–9 h_d; Leenders et al., 2007; Gillies et al., 2014; Wu et al., 2015; Chapter 5). This

supports results from modelling studies of forest patches (e.g. Liu et al., 1996; Frank & Ruck, 2008) and observations downwind of wide wind fences (e.g. Bradley & Mulhearn, 1983; Hagen, 1996; Grant & Nickling, 1998). The difference in recovery length is attributed to a lack of flow moving laterally around a patch, in contrast to isolated vegetation elements where faster-moving airflow mixes with slower-moving airflow in the wake via counter-rotating vortices (Sutton & McKenna-Neuman, 2008).

Chapter 6 also demonstrated the use of turbulence statistics for identifying flow recovery in the lee of the patch. The use of Reynolds shear stress (τ_r) measurements at multiple heights was a useful tool for characterising airflow structure across the patch/bare surface transition (Figure 6.4). The downwind convergence of shear stress and quadrant values (Figure 6.5), combined with the decline in aerodynamic roughness length downwind of the patch, implied that a new internal boundary layer (formed in response to the smoother bare surface) was progressively equilibrating. The dataset presented in Chapter 6 represents the first field-based assessment of turbulent wind flow in the wake of a real vegetation patch. It therefore provides additional data for deriving more accurate parameterisations of flow recovery in vegetated contexts.

Findings on wind flow behaviour from Chapters 5, 6 and 7 were integrated into the new Vegetation and Sediment TrAnsport model (ViSTA) (Chapter 8). ViSTA, a cellular automaton model, consists of sediment transport model coupled with an adapted version of Bailey's (2011) vegetation distribution model. ViSTA is designed to overcome the challenges of previous wind erosion models, by accounting for the heterogeneous nature of dryland ecogeomorphic processes whilst allowing simulations over large areas and long timescales. ViSTA explicitly formulates feedbacks among vegetation growth, wind flow dynamics and sediment flux, thus allowing potential levels of aeolian transport to be simulated in locations with different

distributions, scales and geometries of vegetated patches (**Objective 3**). In the vegetation growth module (Module 1), most dependencies are formulated as a function of growth units that respond directly to precipitation conditions. This represents the balance between photosynthetic gains and respiration losses more realistically than Bailey's (2011) original model, which was based on generic environmental stress and cell age. Where appropriate, wind flow-vegetation interactions in ViSTA are empirically parameterised using field data presented in Chapters 5, 6 and 7.

As well as representing a novel approach for holistically simulating ecogeomorphic interactions in drylands, ViSTA provides a new method for directly imposing continuous wind and transport directions onto the model domain. In this approach, wind is parameterised as a series of linear transport 'corridors' leading to every cell, rather than a unified front of airflow. This allows wind dynamics to be accurately simulated given the vegetation and topographical properties along the path of the wind, and fits Okin's (2008) conception of vegetated desert surfaces as a collection of gaps between roughness elements. It also avoids issues associated with methods that directly alter the slab movement direction (e.g. elongation perpendicular to the wind and unequal horn formation; Nield & Baas, 2008) and methods that passively rotate and resample the grid (e.g. destruction of periodic nature of boundaries and the need for artificial insertion/exclusion of slabs; Narteau et al., 2006). ViSTA's new trigonometric approach to imposing continuous wind directions could theoretically be applied to parameterised flows on any cell-based domain.

Basic responses in vegetation growth were shown to emerge in ViSTA. Different spatial vegetation patterns develop depending on the precipitation regime, and these patterning states compare well with satellite imagery of relevant dryland areas (Figure 9.S2, Figure 9.S3). Moreover, the model displays distinct hysteresis, whereby

vegetation cover degrades or recovers different depending on the initial population density (Figure 9.S1). Hysteresis has been shown to be a central feature of a variety of ecogeomorphic processes in drylands. The model also replicates the dominance of different vegetation types in different precipitation regimes (e.g. grassland, shrubland and forest), as well as a 'climatically determined savanna', where trees and grasses coexist in a stable ecosystem when water limitation restricts tree growth (Figure 8.5). Human disturbance was shown to impact these modelled stable states. Cyclical fire occurrence reinforces the grass-dominated state in low-precipitation conditions, whilst a bistable region (grass domination vs shrub domination) exists at intermediate precipitation levels (Figure 8.6). Grazing levels can severely affect the recovery time of grass populations, such that spot patterning and eventual population collapse may occur if grazing is maintained above a critical threshold (Figure 8.7). In highly moist conditions, model results support the 'disturbance-driven savanna' hypothesis (Sankaran et al., 2005), whereby fire and grazing buffer against the formation of closed-canopy forests.

ViSTA's ability to replicate interactions between vegetation, windflow and sediment transport was also verified in Chapter 8. In the model, the impact of vegetation on windflow is parameterised at the level of individual vegetated cells, such that there is no explicit formulation for wake interference or skimming flow. However, Figure 8.8 and Figure 9.S10 show how wind recovery in the wake of a patch is slower than in the case of individual elements, because a lower minimum leeward wind velocity emerges from a certain number of contiguous plants. This reflects observations from wind tunnel studies (Burri et al., 2011; Youssef et al., 2012) and field data (Chapters 5, 6 and 7) that reduced lateral airflow moving around patches results in extended recovery lengths.

The morphology of modelled landscapes was shown to be dependent upon temporal and spatial scaling within ViSTA. High temporal resolutions are computationally inefficient, but if the temporal resolution is too low, essential dune-forming mechanisms are bypasses and geomorphic processes cannot be fully represented (Figure 8.9). Similarly, running the model at coarser spatial resolutions than the size range of plants leads to unrecognisable dune forms (Figure 8.10) and a loss of granularity in vegetation patterning (Figure 9.S16). This arises due to the fundamental link between photosynthetic potential and size-range, resulting in vegetation imposing a physical length scale in the model domain (Nield & Baas, 2008a). The spatial and temporal dependency of ViSTA and other models like it (e.g. DECAL; see Nield & Baas, 2008a, and Yan & Baas, 2017) suggests that parameterised relationships built into the model should be based on empirical data wherever possible. This is especially difficult to achieve with regards to feedbacks between sediment movement and plant growth, as they are poorly constrained owing to a paucity of field data.

Simulated landscapes were compared against theoretical dune patterns and empirical data collected in the field (**Objective 4**). Basic aeolian dynamics were tested by varying the sediment availability and wind variability across the domain (**Objective 4.i**). In conditions of unidirectional wind and low sediment availability, barchan dunes emerged in the model (Figure 8.11). As sediment availability increased, the barchans linked up into a series of transverse dunes. In a bimodal wind regime, linear dunes extended in the resultant wind direction and migrated laterally. In a multidirectional wind regime with high sediment availability, star dunes formed with a symmetry with respect to the imposed wind directions. A phase diagram of dune morphologies was thus created, echoing the dune classification scheme of Wasson & Hyde (1983). Whilst characterising dunes in the reductionist framework proposed by Wasson & Hyde (1983) is contentious, it is a useful way of

verifying the essential pattern-forming mechanisms that emerge from sand transport models (Courrech du Pont, 2015).

ViSTA's performance was also tested by comparing its output to 'modes' of dune orientation identified in recent numerical and experimental studies (e.g. Courrech du Pont et al., 2014; Gao et al., 2015b; Lucas et al., 2015). In conditions of high sediment availability, a 'bed instability' mechanism led to dunes aligning in one principal direction and then growing through pattern coarsening (Figure 9.S17). When bedforms developed from a localised sand source exposed to bimodal winds, straight 'finger' dunes elongated from the source in a constant orientation, with stable heights and widths along most of their length. The emergent dunes closely resemble linear dunes the extend from topographic obstacles in the Sahara (Lucas et al., 2015). These findings corroborate the mode theory of Courrech du Pont et al. (2014), which states that sediment availability controls both dune type and dune orientation. There is great potential to explore these modes further using a model such as ViSTA, for instance by considering how their mechanisms are affected by the presence of vegetation.

A lack of relevant empirical data means that feedbacks between vegetation growth and sediment transport were difficult to parameterise in ViSTA. Nevertheless, realistic ecogeomorphic patterns emerged from several simulations presented at the end of Chapter 8. A verification exercise based on full model coupling (Figure 8.12) demonstrated that in low-wind conditions, shrubs rapidly colonise new bare surfaces at the expense of grasses, because shrubs grow preferentially when the sediment balance is close to zero. As wind speeds increase, intermediate levels of erosion and deposition allow a mix of vegetation types to survive in patchy formations, and eventually distinct zones of grasses emerge on dune crests, whilst shrubs populate the interdunes. This patterning is often observed in intermittently active dunefields

(Bhattachan et al., 2014), and to the author's knowledge has not been explicitly demonstrated using existing numerical dune evolution models. An equilibrium nebkha dunefield in the Skeleton Coast, Namibia, was also successfully simulated. ViSTA was driven with a precipitation regime typical of the region and with wind data collected in the field, and the resultant bedforms were compared with empirical field measurements from aerial imagery and terrestrial laser scanning (TLS) (**Objective 4.ii**). Analysis of the nebkhas in the final model domain showed the emergence of realistic dune spacing, and nebkha height and tail volumes compared well to TLS data (Figure 8.13).

11.1.3. Key Question 3: What is the likely response of a dryland landscape to future climate and land use change, and can we predict threshold-related transitions from stability to accelerating aeolian activity?

The ViSTA model was forced with potential scenarios of future climate and land-use change, to understand the likely response of dryland landscapes in the Kalahari Desert to such pressures (**Objective 5**). The simple inputs needed for the ViSTA model (precipitation and wind velocity) can be easily acquired from climate modelling datasets via open-source platforms such as the Climate Information Platform (CIP, 2016). In its current form, ViSTA does not use temperature as a forcing factor for the vegetation system, which limits its ability to represent potential decreases in effective precipitation that result from greater evapotranspiration levels at the surface.

In the fifth paper (Chapter 9), three locations (Maun, Tshane and Tsabong) were analysed under two future emissions scenarios (stabilising (RCP 4.5) and high (RCP 8.5)). A range of fire and grazing regimes was subsequently imposed. Results from both equilibrium (Figure 9.3) and transient (Figure 9.4) experiments suggest that the

effects of precipitation changes alone may be relatively small. At Maun, vegetation cover could decrease slightly throughout the century because of declining summer precipitation, which may in turn lead to enhanced sediment transport. At Tshane and Tsabong, the current proximity of the desert system to ecogeomorphic thresholds resulted in occasionally significant landscape responses to climate variability, but no long-term trends were evident under either RCP. Under conditions of high precipitation variability, dramatic population declines combined with rapid repopulation of bare patches lead to distinct vegetation patterning emerging earlier (by up to 60 years in these simulations) than in low-variability conditions (Figure 10.S4, Figure 10.S5). High variability can also drive the system towards a more shrub-encroached state, depending on average precipitation levels. The magnitude of stress fluctuations thus impacts post-perturbation recovery in semi-arid systems. It is difficult to confidently predict both mean precipitation change and its variability over decadal to centennial timescales. The ViSTA model was driven using high and low variability scenarios, but these may not encapsulate the full range of future variability. Landscape responses could therefore be more dramatic than suggested by the equilibrium and transient experiments that were driven by precipitation changes alone. The results presented here contrast slightly with the results of Thomas et al. (2005), who demonstrated that parts of the Kalahari Desert could reactivate in response to 21st century climate change. Some of the observed differences may be partly due to Thomas et al.'s (2005) inclusion of temperature in their model formulation, as well as different climatic inputs from different generations of global climate models (GCMs).

However, human disturbances (grazing and fire) were shown to strongly impact landscape trajectories over the coming century (Figure 9.5). Both fire and grazing impact vegetation cover and composition, particularly through modulating shrub encroachment and related land degradation processes. For instance, reduced fire

intensity leads to the progressive establishment of shrubs at the expense of grass populations, which in turn has an impact on sediment mobility. Evidence from oral history and long-term studies shows that over the last few decades, the Kalahari Desert has experienced increased agricultural intensification and fence construction for wildfire control. This has led to greater grazing pressures and severe shrub encroachment in some areas, and much farmland now consists of bare, intermittently active dune crests. The experiments presented in Chapter 9 suggest that human activity will continue to shape a range of Kalahari landscapes, above and beyond climate change impacts.

Understanding the relationships between climate, human disturbances and ecogeomorphic tipping points in drylands has remained an ongoing challenge for researchers. In terms of land management, the nonlinearities and disequilibria that characterise dryland environments render it difficult to define optimal vegetation and soil conditions for agricultural and pastoral livelihoods. Shrub encroachment, for example, can present advantages and disadvantages for land users depending on the timescale in question. By categorising the seasonal frequency of grass and shrub cover in different fire/grazing scenarios (Figure 9.6), it was possible to determine the amount of time the vegetation system spends below specific threshold population densities. At Maun, for instance, a low-fire, high-grazing scenario led to grass cover dropping below an arbitrary 20% threshold over 24 times more often than in a high fire, high grazing scenario. This allows for specific vegetation threshold-related transitions to be predicted in a variety of contexts. ViSTA can be used to provide an indication of changes in aeolian activity that may result from such transitions.

Dryland inhabitants will continue to regularly adapt their coping strategies in response to environmental changes. However, results presented in Chapter 9, which focus on the Kalahari Desert but are likely applicable to other drylands, suggest that

fire and grazing rates will have to be carefully balanced against the backdrop of 21st century climate change. Using robust predictive models such as ViSTA, in conjunction with local knowledges and practices, could help to avoid severe environmental and socio-economic consequences of land degradation over the coming decades.

11.1.4. Overall conclusions

The challenge of linking empirical and modelling approaches merits acknowledgement. This thesis set out to develop and test a model that fully coupled the key processes driving the evolution of drylands. As noted by Penny et al. (2013, p.15):

"Despite the advances in understanding vegetation patterns in the past ten years, theoretical models still require the use of effective parameters to describe feedbacks, soil-plant-water interactions and the resulting landscape fluxes."

Considering this, the ViSTA model was well parameterised using a new, high-resolution, field-based dataset of wind flow dynamics around plants. The mechanistic links between wind flow and sediment movement in ViSTA were also based on well-developed concepts in the literature, and the parameters for the sand transport model were derived empirically from robust field datasets. Since relatively few data are available to reliably constrain the feedbacks between sediment movement and vegetation growth, upscaling existing local, mechanistic theories of plant ecology to a geomorphologically relevant scale remains an outstanding challenge.

Nevertheless, the ViSTA model has been shown to convincingly reproduce a variety of ecogeomorphic processes, vegetation patterns and dune forms. By including known feedbacks between vegetation growth, wind flow and sediment transport, and

allowing these to evolve in an explicitly spatial model domain, ViSTA represents a move away from reduced complexity modelling. However, the simplicity of ViSTA's required inputs, coupled with the relatively high computational efficiency of the cellular automaton approach, also allows in-depth exploration of a variety of potential future drylands scenarios.

11.2. Future research

Whilst it is clearly beneficial to conduct wind flow studies in field situations to account for natural processes and variability, it is not possible to control for vegetation parameters (height, width, porosity, pliability) and flow parameters (speed, turbulence, intermittency) to the same degree as in wind tunnels. Wind tunnel experiments have proved valuable for understanding the impacts of a wide variety of parameters on flow behaviour, and should be extended to address some of the knowledge gaps highlighted here. No wind tunnel study to the author's knowledge has systematically investigated the impact of porosity and/or pliability of three-dimensional, live plants on wind flow. Porosity and pliability are relatively difficult to control for in live plants when attempting to keep height and width parameters constant. Some wind tunnel studies have begun to investigate porosity variability in high detail using porous mesh cubes and cylinders (e.g. Gillies et al., 2016), although these remain crude approximations to live plants. Other studies have begun to account for plant pliability, for instance through measuring the temporally-averaged frontal area of flexible plants in wind tunnels (e.g. Walter et al., 2012a).

Findings presented in this thesis suggest that two-dimensional wind fences do not approximate well to three-dimensional live plants. However, only a handful of studies have examined airflow dynamics in the wake of single rows of three-dimensional

plants (e.g. Wu et al., 2015). These could display different behaviours to traditional wind fences, especially with regards to flow turbulence. Linked to this issue, the impact of roughness element width on wind flow recovery remains under-studied, perhaps because it intuitively does not have as great an impact on drag as element height or porosity. Recent numerical modelling of nebkhas (Hesp & Smyth, 2017) has revealed that nebkha width strongly controls wind flow recovery, so wind tunnel and field studies investigating element width would help to better parameterise wind flow in vegetated contexts. In general, there remains a need to collect more windflow data around a variety of dryland plant types in the field. Plant characteristics (e.g. height, width and porosity) could be quantified over relatively large scales thanks to the recent progress in image-based techniques (e.g. Karl et al., 2011) and high-resolution remote sensing (Omasa et al., 2007; Jupp et al., 2008; Sankey et al., 2013). This could help to more extensively and rapidly establish parameterised relationships between plants and windflow recovery in their lee.

An explicit link also needs to be made between the impact of vegetation on wind flow, and the subsequent impact on sediment transport processes. Some wind tunnel studies (e.g. Burri et al., 2011; Suter-Burri et al., 2013) have used creative methods, such as coloured sand, for tracking erosion and deposition around roughness elements, but detailed exploration of flow field behaviour and the evolution of bedforms around plants is still required. The feedbacks between flow disruption and shadow dune formation in the lee of nebkhas has been modelled using computational fluid dynamics (CFD) by Hesp & Smyth (2017). In wind tunnels, high-resolution terrestrial laser scanning could be used to detect mm-scale changes in height around partially vegetated erodible surfaces (Nield et al., 2013), thus helping to identify erosional and depositional regions to a high level of accuracy. Identifying relationships between the shelter parameter, which emphasises the salient features of horizontal turbulent flow in the lee of plants (Chapter 5), and sediment transport

potential, would increase the accuracy of parameterisations employed in models such as ViSTA.

Continuing to develop, refine and test the ViSTA model could be a lifetime's work. However, there are key next steps to be taken to improve its performance. Code optimisation would allow for simulations to be run over larger domains, thus minimising the impact of model size effects. Whilst all the simulations presented in this thesis have relied on periodic domain boundaries (i.e. sediment is recycled internally), it would be interesting to explore the effects of sediment supply on landscape morphology though setting non-periodic boundaries. In certain dryland systems, (e.g. fluvial-aeolian systems), sediment sources may vary spatially and temporally, especially over longer (> 100 yr) timescales. ViSTA's computational efficiency allows for such long-term simulations to be performed – for instance, a 100-year fully-coupled simulation on a grid of 100 x 100 m takes a couple of hours on a moderately powerful laptop computer. However, a dual approach could be adopted for simultaneously increasing both the scale and resolution of model simulations. ViSTA could initially be run at a coarse resolution (e.g. cell width of 100 m) to classify landscape cells in terms of relevant metrics such as population density. Then, the model could be run at a higher resolution to evaluate the evolution of each coarse cell type, and the changes summed to provide the overall landscape effect. Alternatively, ViSTA could be run using large-scale computation facilities to simulate high-resolution cells simultaneously on individual computers (ensuring correct mass and wind transfers), and orchestrate the results into a full-landscape model.

Like all models to a certain extent, ViSTA relies on various parameterisations for describing processes that occur within it. In the model's current form, soil moisture dynamics are treated in a heavily parameterised way. To account for cases where sub-optimal moisture conditions affect the biomass a plant can accrue, most

dependencies in Module 1 are formulated as a function of arbitrary 'growth units'. The growth units are directly tied to precipitation levels, but since precipitation is given as an average across the entire model domain, soil moisture dynamics are not resolved at the plant level. However, biomass-dependent neighbourhood interactions are modelled at the scale of individual plants, which is why realistic vegetation patterning can emerge in response to generalised precipitation stress. Nevertheless, the accuracy of plant-plant competition/facilitation processes could be improved by coupling ViSTA with a more sophisticated dynamic hydrological model (e.g. DryMOD, Tarnavsky et al., 2013). The relationships between soil moisture and vegetation growth could be usefully parameterised using existing datasets on dryland soil moisture distribution (e.g. D'Odorico et al., 2007), supplemented by local- to regional-scale moisture patterns derived from remote sensing and land-surface modelling (e.g. Escorihuela & Quintana-Segui, 2016). Similarly, feedbacks between sediment balance and vegetation growth are based on the elementary growth functions of Nield & Baas (2008a), which were derived from a combination of qualitative vegetation behaviour described in the literature and trial and error. More empirical data are needed to improve these sediment balance parameterisations.

The ViSTA model can simulate the impact of human management (e.g. grazing and fire) on vegetation growth and therefore sediment movement, but currently only in basic terms. For instance, the stress plants experience due to fire is imposed probabilistically on all cells in the domain, without considering the spatial spreading of fire. Similarly, grazing stress is imposed on all plants in the domain based on the average stocking rate, rather than accounting for animal movement across the landscape. A more sophisticated treatment of both fire and grazing dynamics would help to improve ViSTA's accuracy. Module 1 could in future be coupled with a cellular automaton model of fire front spread (e.g. Karafyllidis & Thanailakis, 1997; Yassemi et al., 2008), as well as a simple agent-based model of foraging and avoidance

behaviour in grazing animals (e.g. Marion et al., 2008). Explicitly linking the spread of fire to physiological changes in soil properties may also allow realistic amplifying feedbacks to emerge, for instance those leading to a persistence in shrub-dominated states (e.g. Anderies et al., 2002; Li et al., 2008; Sankey et al., 2012).

A personal interest would be to continue exploring the 'dune mode' theory that has developed from recent experimental and numerical modelling work (e.g. Courrech du Pont et al., 2014; Gao et al., 2015b; Lucas et al., 2015). In Chapter 8, it was demonstrated using ViSTA that sediment availability does indeed control both dune type and dune orientation, due to a variation in the underlying dune growth mechanism. The next step would be to study the role of vegetation in initiating, maintaining or destroying the bed instability and fingering modes in different contexts. The ViSTA model could be used to further investigate the links between the shape and orientation of dunes and local climatic conditions, both on Earth and other planetary surfaces such as Mars and Titan (e.g. Fernandez-Cascales et al., 2015).

REFERENCES

Abella, S. R., Engel, E. C., Lund, C. L. & Spencer, J. E. (2009). Early post-fire plant establishment on a Mojave Desert burn. *Madrono, 56*(3), 137–148. doi:10.3120/0024-9637-56.3.137

Aguiar, M. R. & Sala, O. E. (2009). Patch structure, dynamics and implications for the functioning of arid ecosystems. *Trends in Ecology & Evolution, 14*, 273–277.

Al-Awadhi, J. M. & Willetts, B. B. (1999). Sand transport and deposition within arrays of non-erodible cylindrical elements. *Earth Surface Processes and Landforms, 24,* 423–435.

Anderies, J. M., Janssen, M. A. & Walker, H. (2002). Grazing, management, resilience and the dynamics of fire-driven rangeland system. *Ecosystems, 5*, 23–44.

Andreotti, B., Fourrière, A., Ould-Kaddour, F., Murray, B. & Claudin, P. (2009). Size of giant dunes limited by the depth of the atmospheric boundary layer. *Nature, 457,* 1120–1123.

Ariza, C. & Tielbörger, K. (2012). Biomass explains the intensity of facilitative – not competitive – interactions: three intraspecific tests with annuals. *Web Ecology*, *12*(1), 49–55.

Armas, C. & Pugnaire, F. I. (2005). Plant interactions govern population dynamics in a semi-arid plant community. *Journal of Ecology, 93,* 978–989.

Ash, J. E. & Wasson, R. H. (1983). Vegetation and sand mobility in the Australian desert dunefield. *Zeitschrift für Geomorphologie [Suppl.], 45,* 7–25.

Baas, A. C. W. (2002). Chaos, fractals and self-organization in coastal geomorphology: simulating dune landscapes in vegetated environments. *Geomorphology*, *48*(1-3), 309–328.

Baas, A. C. (2004). Evaluation of saltation flux impact responders (Safires) for measuring instantaneous aeolian sand transport intensity. *Geomorphology*, *59*(1-4), 99–118.

Baas, A. C. W. (2007). Complex systems in aeolian geomorphology. *Geomorphology*, *91*(3-4), 311–331.

Baas, A. C. W. & Nield, J. M. (2007). Modelling vegetated dune landscapes. *Geophysical Research Letters*, *34*, L06405.

Baas, A. C. W. & Sherman, D. J. (2005a). Formation and behaviour of aeolian streamers. *Journal of Geophysical Research*, *110*, F03011.

Baas, A. C. W. & Sherman, D. J. (2005b). Spatiotemporal variability of aeolian sand transport in a coastal dune environment. *Journal of Coastal Research, 22*, 1198–1205.

Baddock, M. C., Livingstone, I. & Wiggs, G. F. S. (2007). The geomorphological significance of airflow patterns in transverse dune interdunes. *Geomorphology, 87,* 322-336.

Baddock, M. C. & Wiggs, G. F. S. & Livingstone, I. (2011). A field study of mean and turbulent flow characteristics upwind, over and downwind of barchan dunes. *Earth Surface Processes and Landforms*, *36*(11), 1435–1448. doi:10.1002/esp.2161

Bagnold, R. A. (1941) *The Physics of Blown Sand and Desert Dunes*, Methuen, London.

Bailey, R. M. (2011). Spatial and temporal signatures of fragility and threshold proximity in modelled semi-arid vegetation. *Proceedings of the Royal Society B*, *278*, 1064–71.

Bailey, R. M. & Thomas, D. S. G. (2014). A quantitative approach to understanding dated dune stratigraphies. *Earth Surface Processes and Landforms, 39*(5), 614–631. doi:10.1002/esp.3471

Bak, P. (1996). *How Nature Works,* Springer, New York.

Barbier, N., Couteron, P., Lefever, R., Deblauwe, V. & Lejeune, O. (2008). Spatial decoupling of facilitation and competition at the origin of gapped vegetation patterns. *Ecology, 89*(6), 1521– 1531.

Barbier, N., Couteron, P., Lejoly, J., Deblauwe, V. & Lejeune, O. (2006). Self-organized vegetation patterning as a fingerprint of climate and human impact on semi-arid ecosystems. *Journal of Ecology, 94*(3), 537–547.

Barrineau, C. P. & Ellis, J. T. (2013). Sediment transport and wind flow around hummocks. *Aeolian Research*, *8*, 19–27. doi:10.1016/j.aeolia.2012.10.002

Baudena, M., D'Andrea, F. & Provenzale, A. (2010). An idealized model for tree-grass coexistence in savannas: the role of life stage structure and fire disturbances. *Journal of Ecology, 98,* 74–80. doi: 10.1111/j.1365-2745.2009.01588.x

Bauer, B. O., Davidson-Arnott, R. G. D., Walker, I. J., Hesp, P. A. & Ollerhead, J. (2012). Wind direction and complex sediment transport response across a beach-dune system. *Earth Surface Processes and Landforms*, *37*(15), 1661–1677.

Bauer, B. G. & Namikas, S. L. (1998). Design and field test of a continuously weighing, tipping-bucket assembly for aeolian sand traps. *Earth Surface Processes and Landforms, 23,* 1171–1183.

Bauer, B. O., Yi, J., Namikas, S. L. & Sherman, D. J. (1998). Event detection and conditional averaging in unsteady aeolian systems. *Journal of Arid Environments, 39,* 345–375.

Becerra, P. I., Cruz, G., Rios, S. & Castelli, G. (2013). Importance of irrigation and plant size in the establishment success of different native species in a degraded ecosystem of central Chile. *Bosque, 34*(1), 103–111.

Beisner, B. E., Haydon, D. T. & Cuddington, K. (2003). Alternative stable states in ecology. *Frontiers in Ecology and the Environment, 1*, 376–382.

Bel, G., Hagberg, A. & Meron, E. (2012). Gradual regime shifts in spatially extended ecosystems. *Theoretical Ecology*, *5*(4), 591–604.

Belcher, S., Jerram, N. & Hunt, J. (2003). Adjustment of a turbulent boundary layer to a “canopy” of roughness elements. *Journal of Fluid Mechanics*, *488*(-1), 369–398. doi:10.1017/S0022112003005019

Belnap, J. (1995). Surface disturbances: Their role in accelerating desertification. *Environmental Monitoring Assessment, 37*, 39–57.

Belnap, J., Reynolds, R. L., Reheis, M. C., Phillips, S. L., Urban, F. E. & Goldstein, H. L. (2009). Sediment losses and gains across a gradient of livestock grazing and plant invasion in a cool, semi-arid grassland, Colorado Plateau, USA. *Aeolian Research*, *1*(1–2), 27–43. doi:10.1016/j.aeolia.2009.03.001

Bergametti, G. & Gillette, D. A. (2010). Aeolian sediment fluxes measured over various plant/soil complexes in the Chihuahuan desert. *Journal of Geophysical Research, 155*, F03044.

Best, J. L. & Kostaschuk, R. A. (2002). An experimental study of turbulent flow over a low-angle dune. *Journal of Geophysical Research, 107*(C9), 3135. doi:10.1029/2000JC000294.

Bhattachan, A., D’Odorico, P., Dintwe, K., Okin, G. S. & Collins, S. L. (2014). Resilience and recovery potential of duneland vegetation in the southern Kalahari. *Ecosphere*, *5*(January), 1–14. doi:10.1890/ES13-00268.1

Biggs, R., Carpenter, S. R. & Brock, W.A. (2009). Turning back from the brink: detecting an impending regime shift in time to avert it. *Proceedings of the National Academy of Sciences of the United States of America, 106*, 826–883.

Bishop, S. R., Momiji, H., Carretero-Gonzalez, R. & Warren, A. (2002). Modelling desert dune fields based on discrete dynamics. *Discrete Dynamics in Nature and Society, 7*, 7–17.

Blaum, N., Tietjen, B. & Rossmanith, E. (2009). Impact of livestock husbandry on small- and medium-sized carnivores in Kalahari savannah rangelands. *The Journal of Wildlife Management, 73*(1): 60–67.

Bogle, R., Redsteer, M. H. & Vogel, J. (2015). Field measurement and analysis of climatic factors affecting dune mobility near Grand Falls on the Navajo Nation, southwestern United States. *Geomorphology, 228,* 41–51. doi: 10.1016/j.geomorph.2014.08.023

Böhner, J., Schäfer, W., Conrad, O., Gross, J. & Ringeler, A. (2003). The WEELS model: Methods, results and limitations. *Catena*, *52*(3-4), 289–308. doi:10.1016/S0341-8162(03)00019-5

Bond, W. J., Midgley, G. F. & Woodward, F. I. (2003). What controls South African vegetation – climate or fire? *South African Journal of Botany, 69,* 79–91.

Borgogno, F., D'Odorico, P., Laio, F. & Ridolfi, L. (2009). Mathematical models of vegetation pattern formation in ecohydrology. *Reviews of Geophysics, 47*, RG1005.

Bradley, E. F. & Mulhearn, P. J. (1983). Development of velocity and shear-stress distributions in the wake of a porous shelter fence. *Journal of Wind Engineering and Industrial Aerodynamics, 15*(1-3), 145–156.

Breshears, D. D., Whicker, J. J., Johansen, M. P. & Pinder, J. E. (2003). Wind and water erosion and transport in semi-arid shrubland, grassland and forest ecosystems: Quantifying dominance of horizontal wind-driven transport. *Earth Surface Processes and Landforms, 28,* 1189–1209. doi:10.1002/esp.1034

Breshears, D. D., Whicker, J. J., Zou, C. B., Field, J. P. & Allen, C. D. (2009). A conceptual framework for dryland aeolian sediment transport along the grassland–forest continuum: effects of woody plant canopy cover and disturbance. *Geomorphology, 105*, 28–38.

Brooker, R. W., Maestre, F. T., Callaway, R. M., Lortie, C. L. et al. (2008). Facilitation in plant communities: the past, the present, and the future. *Journal of Ecology, 96*, 18–34.

Brown, J. F. (1997). Effects of experimental burial on survival, growth, and resource allocation of three species of dune plants. *Journal of Ecology, 85*, 151–158.

Buckle, C. (1996). *Weather and Climate in Africa.* Longman, Harlow.

Buffin-Bélanger, T. & Roy, A. G. (1998). Effects of a pebble cluster on the turbulent structure of a depth-limited flow in a gravel-bed river. *Geomorphology, 32*, 417–435.

Bullard, J. E., Thomas, D. S. G., Livingstone, I. & Wiggs, G. F. S. (1997). Dunefield activity and interactions with climatic variability in the Southwest Kalahari Desert. *Earth Surface Processes and Landforms*, *22*, 165–174.

Burgess, J. (2009). Botswana. *Food and Agricultural Organisation (FAO) Country Pasture/Forage Resources Profiles*, 1–46.

Burke, J. & Knobloch, E. (2006). Localized states in the generalized Swift-Hohenberg equation. *Physical Reviews, E, 73*, 056211.

Burri, K., Gromke, C., Lehning, M. & Graf, F. (2011). Aeolian sediment transport over vegetation canopies: a wind tunnel study with live plants. *Aeolian Research, 3,* 205–213.

Butterfield, G. R. (1991). Grain transport rates in steady and unsteady turbulent airflows. *Acta Mechanica (Suppl.)*, *1*, 97–122.

Butterfield, G. R. (1993). Sand transport response to fluctuating wind velocity. In: Clifford, N. J., French, J. R. & Hardisty, J. (eds). *Turbulence: Perspectives on Sediment Transport*, Wiley, Chichester, 305–334.

Callaway, R. M. & Walker, L. R. (1997). Competition and facilitation: a synthetic approach to interactions in plant communities. *Ecology, 78*(7), 1958–1965.

Campbell Scientific User Guide (2012). Campbell Scientific Instruments, Loughborough.

Carpenter, D. E., Barbour, M. G. & Bahre, C. J. (1986). Old field succession in Mojave Desert scrub. *Madrono, 33,* 111–122.

Carpenter, S. R. & Brock, W. A. (2006). Rising variance: a leading indicator of ecological transition. *Ecological Letters, 9,* 308–315.

Caylor, K., Scanlon, T. & Rodriguez-Iturbe, I. (2004). Feasible optimality of vegetation patterns in river basins. *Geophysical Research Letters, 31*(13), L13502.

Chanda, R., Totolo, O., Moleele, N. M., Setshogo, M. & Mosweu, S. (2003). Prospects for subsistence livelihood and environmental sustainability along the Kalahari Transect: the case of Matsheng in Botswana's Kalahari rangelands. *Journal of Arid Environments, 54*, 425–445.

Chapman, V. J. (1976). *Coastal Vegetation*. Pergamon, Oxford, UK.

Chapman, C. A., Walker, I. J., Hesp, P. A., Bauer, B. O., Davidson-Arnott, R. G. D. (2012). Turbulent Reynolds stress and quadrant event activity in wind flow over a coastal foredune. *Geomorphology*, *151-152,* 1–12.

Chapman, C., Walker, I. J., Hesp, P. A., Bauer, B. O., Davidson-Arnott, R. G. D., Ollerhead, J. (2013). Reynolds stress and sand transport over a foredune. *Earth Surface Processes and Landforms*, *38*(14), 1735–1747.

Christensen, J. H., Hewitson, B., Busuioc, A. et al. (2007). Regional Climate Projections. In: Solomon, S., Qin, D., Manning, M. et al. (eds). *Climate Change 2007: The Physical Science Basis. Contribution of Working Group I to the Fourth Assessment Report of the Intergovernmental Panel on Climate Change*, Cambridge University Press, Cambridge and New York, 847–940.

Clifford, N. J. & French, J. R. (1993). Monitoring and modelling turbulent flows: historical and contemporary perspectives. In: Clifford, N. J., French, J. R. & Hardisty J. (eds). *Turbulence: Perspectives on Flow and Sediment Transport,* John Wiley & Sons, New York, 1–34.

Climate Information Platform (CIP) [*accessed November 2016*]. *Merged CMIP 5 datasets, http://cip.csag.uct.ac.za/webclient2/datasets/africa-merged-cmip5/*

Cook, K. H. & Vizy, E. K. (2012). Impact of climate change on mid-twenty-first century growing seasons in Africa. *Climate Dynamics, 39*(12), 2937–2955.

Cornelis, W. M. & Gabriels, D. (2005). Optimal windbreak design for wind-erosion control. *Journal of Arid Environments*, *61*(2), 315–332.

Courrech du Pont, S. (2015). Dune morphodynamics. *Comptes Rendus Physique*, *16*(1), 118–138. doi:10.1016/j.crhy.2015.02.002

Courrech du Pont, S., Narteau, C. & Gao, X. (2014). Two modes for dune orientation. *Geology*, *42*(9), 743–746. doi:10.1130/G35657.1

Crawley, D. M., Nickling, W. G. (2003). Drag partition for regularly-arrayed rough surfaces. *Boundary Layer Meteorology, 107,* 445–468.

Dakos, V., Kéfi, S., Rietkerk, M., van Nes, E. & Scheffer, M. (2011). Slowing down in spatially patterned ecosystems at the brink of collapse. *American Naturalist, 177*(5), E153–66.

Dakos, V., Scheffer, M., van Nes, E. H., Brovkin, V., Petoukhov, V. & Held, H. (2008). Slowing down as an early warning signal for abrupt climate change. *Proceedings of the Natural Academy of Science USA, 105*(38), 14,308–14,312.

Dakos, V., van Nes, E. H., Donangelo, R., Fort, H. & Scheffer, M. (2010). Spatial correlation as leading indicator of catastrophic shifts. *Theoretical Ecology, 3,* 163–174.

Danin, A. (1996). *Plants of Desert Dunes,* Springer Verlag, Berlin.

Davidson-Arnott, R. G. D. & Bauer, B. O. (2009). Aeolian sediment transport on a beach: Thresholds, intermittency, and high frequency variability. *Geomorphology*, *105*(1-2), 117–126. doi:10.1016/j.geomorph.2008.02.018

Davidson-Arnott, R. G. D., Bauer, B. O., Walker, I. J., Hesp, P. A., Ollerhead, J. & Chapman, C. (2012). High-frequency sediment transport responses on a vegetated foredune. *Earth Surface Processes and Landforms*, *37*(11), 1227–1241.

Dean, W. R. J. & Macdonald, I. A. W. (1994). Historical changes in stocking rates of domestic livestock as a measure of semi-arid and arid rangeland degradation in the Cape Province, South Africa. *Journal of Arid Environments, 26*, 281-298.

Dech, J. P. & Maun, M. A. (2005). Zonation of vegetation along a burial gradient on the leeward slopes of Lake Huron sand dunes. *Canadian Journal of Botany, 83*, 227–236.

Dech, J. P. & Maun, M. A. (2006). Adventitious root production and plastic resource allocation to biomass determine burial tolerance in woody plants from central Canadian coastal dunes. *Annals of Botany, 98,* 1095–1105.

Dieppois, B., Rouault, M. & New, M. (2015). The impact of ENSO on Southern African rainfall in CMIP5 ocean atmosphere coupled climate models. *Climate Dynamics*, *45*(9-10), 2425–2442. doi:10.1007/s00382-015-2480-x

D'Odorico, P., Bhattachan, A., Davis, K. F., Ravi, S. & Runyan, C. W. (2013). Global desertification: Drivers and feedbacks. *Advances in Water Resources, 51,* 326–344. doi: 10.1016/j.advwatres.2012.01.013

D'Odorico, P., Caylor, K., Okin, G. S. & Scanlon, T. M. (2007). On soil moisture–vegetation feedbacks and their possible effects on the dynamics of dryland ecosystems. *Journal of Geophysical Research, 112*, G04010.

D'Odorico, P., Laio, F. & Ridolfi, L. (2006a). Patterns as indicators of productivity enhancement by facilitation and competition in dryland vegetation. *Journal of Geophysical Research, 111*, G03010.

D'Odorico, P., Laio, F. & Ridolfi, L. (2006b). A probabilistic analysis of fire-induced tree-grass coexistence in savannas. *American Naturalist, 167*(3), E79–E87.

Doerr, S. H., Shakesby, R. A. & Walsh, R. P. D. (2000). Soil water repellency: its causes, characteristics and hydro-geomorphological significance. *Earth-Science Reviews, 51*(1–4), 33–65.

Dong, Z., Liu, X., Wang, H. & Wang, X. (2003). Aeolian sand transport: a wind tunnel model. *Sedimentary Geology, 161,* 71–83.

Dougill, A. J., Akanyang, L., Perkins, J. S. et al. (2016). Land use, rangeland degradation and ecological changes in the southern Kalahari, Botswana. *African Journal of Ecology, 54*(1), 59–67. doi:10.1111/aje.12265

Dunkerley, D. L. (1997). Banded vegetation: development under uniform rainfall from a simple cellular automaton model. *Plant Ecology, 129*, 103–111.

Dupont, S., Bergametti, G., Marticorena, B. & Simoëns, S. (2013). Modeling saltation intermittency. *Journal of Geophysical Research: Atmosphere, 118,* 1–20, doi:10.1002/jgrd.50528.

Dupont, S., Bergametti, G. & Simoëns, S. (2014). Modeling aeolian erosion in presence of vegetation. *Journal of Geophysical Research: Earth Surface*, *119*(2), 168–187. doi:10.1002/2013JF002875

Durán, O. & Hermann, H. J. (2006). Vegetation against dune mobility. *Physical Review Letters, 97,* 188001. doi:10.1103/PhysRevLett.97.188001

Eastwood, E., Nield, J., Baas, A. & Kocurek, G. (2011). Modelling controls on aeolian dune-field pattern evolution. *Sedimentology*, *58*(6), 1391–1406. doi:10.1111/j.1365-3091.2010.01216

Elbelrhiti, H., Claudin, P. & Andreotti, B. (2005). Field evidence for surface-wave-induced instability of sand dunes. *Nature, 437,* 720–723.

Elder, J. Dune Field Simulator, *http://web.ncf.ca/aa456/sand/dunefieldMorphology/index.html* [website accessed 04/06/2014]

Eldridge, D. J., Bowker, M. A., Maestre, F. T., Roger, E., Reynolds, J. F. & Whitford, W. G. (2011). Impacts of shrub encroachment on ecosystem structure and functioning: towards a global synthesis. *Ecological Letters, 14*(7), 709–722. doi: 10.1111/j.1461-0248.2011.01630.x

Endalew, A. M., Hertog, M., Gebrehiwot, M. G., Baelmans, M., Ramon, H., Nicolaï, B. M., & Verboven, P. (2009). Modelling airflow within model plant canopies using an integrated approach. *Computers and Electronics in Agriculture*, *66*(1), 9–24. doi:10.1016/j.compag.2008.11.002

Erickson, R. O. (1976). Modeling of plant growth. *Annual Review of Plant Physiology, 27,* 407–434.

Escorihuela, M. J. & Quintana-Segui, P. (2016). Comparison of remote sensing and simulated soil moisture datasets in Mediterranean landscapes. *Remote Sensing of the Environment, 180,* 99–114.

Ewing, R. C. & Kocurek, G. A. (2010). Aeolian dune interactions and dune-field pattern formation: White Sand Dune Field, New Mexico. *Sedimentology, 57,* 1199–1219. doi:10.1111/j.1365-3091.2009.01143.x

Favretto, N., Luedeling, E., Stringer, L. C. & Dougill, A. J. (2017). Valuing ecosystem services in semi-arid rangelands through stochastic simulation. *Land Degradation and Development, 28,* 65–73. doi:10.1002/ldr.2590

Fenton, L. K., Michaels, T. I. & Beyer, R. A. (2014). Inverse maximum gross bedform-normal transport 1: How to determine a dune- constructing wind regime using only imagery. *Icarus, 230*, 5–14.

Fernandez-Cascales, L., Lucas, A., Rodriquez, S. et al. (2015). Two modes for dune orientation on Mars. *Fourth International Planetary Dunes Workshop,* Boise, Idaho, 19–22 May.

Field, J. P., Breshears, D. D., Whicker, J. J. & Zou, C. B. (2012). Sediment capture by vegetation patches: Implications for desertification and increased resource redistribution. *Journal of Geophysical Research*, *117*(G1), G01033.

Finnigan, J. J. (1979). Turbulence in waving wheat: 1. Mean statistics and honami. *Boundary Layer Meteorology, 16,* 181–211.

Frank, A., Kocurek G. 1996. Airflow up the stoss slope of sand dunes: limitations of current understanding. *Geomorphology,* 17: 47–54.

Frank, C. & Ruck, B. (2008). Numerical study of the airflow over forest clearings. *Forestry*, *81*(3), 259–277. doi:10.1093/forestry/cpn031

Fryrear, D. W. (1986). A field dust sampler. *Journal of Soil and Water Conservation, 41,* 117–120.

Gao, X., Narteau, C. & Rozier, O. (2015a). Development and steady states of transverse dunes: A numerical analysis of dune pattern coarsening and giant dunes. *Journal of Geophysical Research F: Earth Surface*, *120*(10), 2200–2219. doi:10.1002/2015JF003549

Gao, X., Narteau, C., Rozier, O. & Courrech du Pont, S. (2015b). Phase diagrams of dune shape and orientation depending on sand availability. *Scientific Reports*, *5*, 14677. doi:10.1038/srep14677

Gandemer, J. (1979). Wind shelters. *Journal of Wind Engineering and Industrial Aerodynamics*, *4*, 371-389.

Gash, J. H. C. (1986). Observations of turbulence downwind of a forest-heath interface. *Boundary Layer Meteorology, 36,* 227–237.

Geist, H. J. & Lambin, E. F. (2004). Dynamic causal patterns of desertification. *Bioscience, 54*(9), 817–829.

Getzin, S., Wiegand, K., Wiegand, T., Yizhaq, H., von Hardenberg, J. & Meron, E. (2014). Adopting a spatially explicit perspective to study the mysterious fairy circles of Namibia. *Ecography*, DOI: 10.1111/ecog.00911

Gherardi, L. A. & Sala, O. E. (2015). Enhanced precipitation variability reduces grass- and increases shrub-productivity. *Proceedings of the National Academy of Sciences, 112*(41), 12735–12740. 10.1073/pnas.1506433112

Gilad, E., von Hardenberg, J., Provenzale, A., Shachak, M. & Meron, E. (2007). A mathematical model for plants as ecosystem engineers. *Journal of Theoretical Biology, 244,* 680–691.

Gillette, D. A., Herrick, J. E. & Herbert, G. A. (2006). Wind characteristics of Mesquite Streets in the northern Chihuahuan Desert, New Mexico, USA. *Environmental Fluid Mechanics*, *6*(3), 241–275.

Gillette, D. A. & Pitchford, A. M. (2004). Sand flux in the northern Chihuahuan desert, New Mexico, USA, and the influence of mesquite-dominated landscapes *Journal of Geophysical Research, 109,* F04003.

Gillette, D. A., Stockton, P. A. (1989). The effects of non-erodible particles on wind erosion of erodible surfaces. *Journal of Geophysical Research*, *94*(D10), 12885–12893.

Gillies J. A., Lancaster, N., Nickling, W. G. & Crawley, D. (2000). Field determination of drag forces and shear stress partitioning effects for a desert shrub (*Sarcobatus vermiculatus*, Greasewood). *Journal of Geophysical Research: Atmosphere*, 105(D20): 24871–24880.

Gillies, J. A., Nickling, W. G. & King, J. (2002). Drag coefficient and plant form-response to wind velocity in three plant species: Burning bush (Euonymus alatus), Colorado blue spruce (Picea pungens glauca.), and fountain grass (Pennisetum setaceum). *Journal of Geophysical Research, 107*(D24), 4760.

Gillies, J. A., Nickling, W. G. & King, J. (2006). Aeolian sediment transport through large patches of roughness in the atmospheric inertial sublayer. *Journal of Geophysical Research*, *111*(F2), F02006.

Gillies, J. A., Nickling, W. G. & King, J. (2007). Shear stress partitioning in large patches of roughness in the atmospheric inertial sublayer. *Boundary-Layer Meteorology*, *122*, 367–396.

Gillies, J. A., Nickling, W. G., King, J. & Lancaster, N. (2010). Modeling aeolian sediment transport thresholds on physically rough Martian surfaces: A shear stress partitioning approach. *Geomorphology*, *121*(1-2), 15–21. doi:10.1016/j.geomorph.2009.02.016

Gillies, J. A., Nickling, W. G., Nickolich, G. & Etyemezian, V. (2017). A wind tunnel study of the aerodynamic and sand trapping properties of porous mesh 3-dimensional roughness elements. *Aeolian Research, 25,* 23–35. doi: 10.1016/j.aeolia.2017.02.001

Gillies, J. A., Nield, J. M. & Nickling, W. G. (2014). Wind velocity and sediment transport recovery in the lee of a vegetated and denuded nebkha within a nebkha dune field. *Aeolian Research*, *12*, 135–141.

Goossens, D., Offer, Z. & London, G. (2000). Wind tunnel and field calibration of five Aeolian sand traps. *Geomorphology, 35*, 233–252.

Goudie, A. S. (2002). *Great Warm Deserts of the World,* Cambridge University Press, Cambridge.

Goudie, A. S. & Middleton, N. J. (2006). *Desert Dust in the Global System,* Springer, Berlin.

Gowda, K., Riecke, H. & Silber, M. (2014). Transitions between patterned states in vegetation models for semi-arid ecosystems. *Physical Reviews E,* 1–9.

Grant, P. F. & Nickling, W. G. (1998). Direct field measurement of wind drag on vegetation for application to windbreak design and modeling. *Land Degradation and Development, 9*, 57–66.

Greeley, R. & Iversen, J. D. (1985). *Wind as a Geomorphological Process,* Cambridge University Press, Cambridge.

Griffin, D. W., Garrison, V. H., Herman, J. R. & Shinn, E. A. (2001). African desert dust in the Caribbean atmosphere: microbiology and public health. *Aerobiologia, 17,* 203–213.

Gross, G. (1987). A numerical study of the air flow within and around a single tree. *Boundary-Layer Meteorology*, *40*, 311–327.

Guttal, V. & Jayaprakash, C. (2008). Changing skewness: an early warning signal of regime shifts in ecosystems. *Ecological Letters, 11,* 450–460.

Guttal, V. & Jayaprakash, C. (2009). Spatial variance and spatial skewness: leading indicators of regime shifts in spatial ecological systems. *Theoretical Ecology, 2,* 3–12.

Hagen L. J. (1991). A wind erosion prediction system to meet user needs. *Journal of Soil Water Conservation*, *46*, 106–111.

Hagen, L. J. (1996). *WEPS: Wind Erosion Prediction System, Technical Documentation*. Wind Erosion Research Unit, Manhattan, USA

Hagen, L. J. & Skidmore, E. L. (1971). Turbulent velocity fluctuations and vertical flow as affected by windbreak porosity. *Transactions of the American Society of Agricultural Engineers, 14,* 634–637.

Havstad, K. M. & James, D. (2010). Prescribed burning to affect a state transition in a shrub-encroached desert grassland. *Journal of Arid Environments, 74*, 1324–1328.

Held, I. M., Delworth, T. M., Lu, J., Findell, K. L., Knutson, T. R. (2005). Simulation of Sahel Drought in the 20th and 21st centuries. *Proceedings of the National Academy of Sciences of the United States of America, 102*(50), 17,891–17,896.

Hennessy, J. T., Gibbens, R. P., Tromble, J. M. & Cardenas, M. (1985). Mesquite (Prosopis glandulosa Torr.) dunes and interdunes in southern New Mexico: A study of soil properties and soil water relations. *Journal of Arid Environments, 9*(1), 27–38.

Hennessy, J. T., Kies, B., Gibbens, R. P. & Tromble, J. M. (1986). Soil sorting by forty-five years of wind erosion on a southern New Mexico Range. *Soil Science Society of America Journal, 50*, 391–394.

Hermann, H. J., Duran, O., Parteli, E. J. R. & Schatz, V. (2008). Vegetation and induration as sand dunes stabilizators. *Journal of Coastal Research, 24,* 1357–1368. doi: 10.2112/08A-0011.1

Hersen, P., Anderson, K. H., Elbelrhiti, H., Andreotti, B., Claudin, P. & Douady, S. (2004). Corridors of barchans dunes: stability and size selection, *Geomorphology, 22*, 193–204.

Hesp, P. (2002). Foredunes and blowouts: Initiation, geomorphology and dynamics. *Geomorphology, 48,* 245–268.

Hesp, P. A., Davidson-Arnott, R., Walker, I. J. & Ollerhead, J. (2005). Flow dynamics over a fore dune at Prince Edward Island, Canada. *Geomorphology, 65*: 71–84.

Hesp, P. A. & Smyth, T. A. G. (2017). Nebkha flow dynamics and shadown dune formation. *Geomorphology*. doi:10.1016/j.geomorph.2016.12.026

Hesse, P., Lancaster, N. & Telfer, M. (2015). Digital mapping of the extent of global dune systems. *EGU General Assembly, Vienna, Austria, 12-17 April*

Hewitson, B. C. & Crane, R. G. (2006). Consensus between GCM climate change projections with empirical downscaling: precipitation downscaling over South Africa. *International Journal of Climatology*, *26*, 1315–1337.

Higgins, S. I., Bond, W. J. & Trollope, W. S. W. (2000). Fire, resprouting and variability: a recipe for grass–tree coexistence in savanna. *Journal of Ecology, 88,* 213–229.

HilleRisLambers, R., Rietkerk, M., Van den Bosch, F., Prins, H. & de Kroon, H. (2001). Vegetation pattern formation in semi-arid grazing systems. *Ecology, 82*, 50–61.

Holling, C. S. (1973). Resilience and stability of ecological systems. *Annual Review of Ecology and Systematics, 4*, 1–23.

Hotta, S., Kubota, S., Katori, S. & Horikawa, K. (1984). Sand transport by wind on a wet sand surface. *American Society of Civil Engineers, 19th Coastal Engineering Conference Proceedings, 2*, 1265–1281.

Huang, J., Minnis, P., Yan, H. Yi, Y., Chen, B., Zhang, L. & Ayers, J. (2010). Dust aerosol effect on semi-arid climate over Northwest China detected from A-Train satellite measurements. *Atmospheric Chemistry and Physics, 10*, 6863–6872.

Huenneke, L. F., Anderson, J. P., Remmenga, M. & Schlesinger, W. H. (2002). Desertification alters patterns of aboveground net primary production in Chihuahuan ecosystems. *Global Change Biology, 8*(3), 247–264.

Hugenholtz, C. H. & Wolfe, S. A. (2005). Recent stabilization of active sand dunes on the Canadian prairies and relation to recent climate variations. *Geomorphology, 68*, 131–147.

IPCC, Intergovernmental Panel on Climate Change. (2013). Summary for Policymakers. In: Stocker, T. F., Qin, D., Plattner, G.K., Tignor, M., Allen, S. K. et al. (eds.), *Climate Change 2013: The Physical Science Basis. Contribution of Working Group I to the Fifth Assessment Report of the Intergovernmental Panel on Climate Change,* Cambridge University Press, Cambridge, UK, and New York, NY, USA.

Jackson, D. W. T., Beyers, J. H. M., Lynch, K., Cooper, J. A. G., Baas, A. C. W. & Delgado-Fernandez, I. (2011). Investigation of three-dimensional wind flow behaviour over coastal dune morphology under offshore winds using computation fluid dynamics (CFD) and ultrasonic anemometry. *Earth Surface Processes and Landforms, 36*, 1113–1124.

Jackson, P. S. (1981). On the displacement height in the logarithmic profile. *Journal of Fluid Mechanics, 111,* 15–25.

Jackson, P. S. & Hunt, J. C. R. (1975). Turbulent windflow over a low hill. *Quarterly Journal of the Royal Meteorological Society, 101*, 929–955.

James, R. & Washington, R. (2012). Changes in African temperature and precipitation associated with degrees of global warming. *Climatic Change, 117*(4)*,* 859–872. doi:10.1007/s10584-012-0581-7

Judd, M. J., Raupach, M. R., Finnigan, J. J. (1996). A wind tunnel study of turbulent flow around single and multiple windbreaks. Part I: velocity fields. *Boundary Layer Meteorology,* 80: 127–165.

Jupp, D. L. B., Culvenor, D. S., Lovell, J. L., Newnham, G. J., Strahler, A. H. & Woodcock, C. E. (2008). Estimating forest LAI profiles and structural parameters using a ground-based laser called 'Echidna'. *Tree Physiology*, *29,* 171–181.

Kaganov, E. I. & Yaglom, A. M. (1976). Errors in wind speed measurements by rotation anemometers. *Boundary-Layer Meteorology, 10***,** 1–11.

Kaimal, J. C. & Finnigan, J. (1994). *Atmospheric Boundary Layer Flows: Their Structure and Measurement,* Oxford University Press, New York.

Karafyllidis, I. & Thanailakis, A. (1997). A model for predicting forest fire spreading using cellular automata. *Ecological Modelling, 99*(1), 87–97. doi:10.1016/S0304-3800(96)01942-4

Karl, J. W., Duniway, M. C. & Schrader, T. S. (2011). A technique for estimating rangeland canopy-gap size distributions from high-resolution digital imagery. *Rangeland Ecology Management, 65*(2), 196–207.

Kéfi, S., Rietkerk, M., Alados, C. L., Pueyo, Y., Papanastasis, V. P., Elaich, A., & de Ruiter, P. C. (2007a). Spatial vegetation patterns and imminent desertification in Mediterranean arid ecosystems. *Nature*, *449*(7159), 213–7.

Kéfi, S., Rietkerk, M., Roy, M., Franc, A., de Ruiter, P. C. & Pascual, M. (2011). Robust scaling in ecosystems and the meltdown of patch size distributions before extinction. *Ecology Letters*, *14*(1), 29–35.

Kéfi, S., Rietkerk, M., van Baalen, M., & Loreau, M. (2007b). Local facilitation, bistability and transitions in arid ecosystems. *Theoretical Population Biology*, *71*(3), 367–79.

Kenney, W. A. (1987). A method for estimating windbreak porosity using digitized photographic silhouettes. *Agricultural and Forest Meteorology, 39*, 91–94.

Kim, H. B. & Lee, S-J. (2002). The structure of turbulent shear flow around a two-dimensional porous fence having a bottom gap. *Journal of Fluids and Structures*, *16*(3), 317–329.

Kinast, S., Meron, E., Yizhaq, H. & Ashkenazy, Y. (2013). Biogenic crust dynamics on sand dunes. *Physical Review E*, *87*(2), 1–5.

King, J., Nickling, W. G. & Gillies, J. A. (2005). Representation of vegetation and other non-erodible elements in aeolian shear stress partitioning models for predicting transport threshold. *Journal of Geophysical Research, 110*, F04015.

King, J., Nickling, W. G., & Gillies, J. A. (2008). Investigations of the law-of-the-wall over sparse roughness elements. *Journal of Geophysical Research*, *113*(F2), F02S07.

King, J., Nickling, W. G. & Gillies, J. A. (2006) Aeolian shear stress ratio measurements within mesquite-dominated landscapes of the Chihuahuan Desert, New Mexico, USA. *Geomorphology*, *82*(3–4), 229–244.

Klose, M. & Shao, Y. (2012). Stochastic parameterization of dust emission and application to convective atmospheric conditions. *Atmospheric Chemistry and Physics*, *12*(16), 7309–7320.

Knight, M., Thomas, D. S. G. & Wiggs, G. F. S. (2004). Challenges of calculating dunefield mobility over the 21st century. *Geomorphology*, *59*(1-4), 197–213.

Kniveton, D. R., Layberry, R., Williams, C. J. R., et al. (2009). Trends in the start of the wet season over Africa. *International Journal of Climatology, 1225,* 1216–1225. doi:10.1002/joc

Knott, P. & Warren, A. (1981). Aeolian Processes. In: Goudie AS. (ed) *Geomorphological Techniques,* Allen & Unwin, London.

Kocurek, G. & Ewing, R. (2005). Aeolian dune field self-organization-implications for the formation of simple versus complex dune-field patterns. *Geomorphology, 72*, 94–105.

Kocurek, C., Ewing, R. & Mohrig, D. (2010). How do bedforms arise? New views on the role of bedform interactions within a set of boundary conditions. *Earth Surface Processes and Landforms, 35*(1), 51–63.

Krapf, C. E., Stollhofen, H. & Stansitreet, I. G. (2003). Constrasting styles of ephemeral river systems and their interaction with dunes of the Skeleton Coast erg (Namibia). *Quaternary International, 104,* 41-52.

Lancaster, N. (1985). Variations in wind velocity and sand transport on the windward flanks of desert sand dunes. *Sedimentology, 32*, 581–593.

Lancaster, N. (1988). Development of linear dunes in the southwestern Kalahari, southern Africa. *Journal of Arid Environments, 14*, 233-244.

Lancaster, N. (1989). The dynamics of star dunes: an example from the Gran Desierto, Mexico. *Sedimentology, 36*, 273–289.

Lancaster, N. & Baas, A. (1998). Influence of vegetation cover on sand transport by wind: field studies at Owens Lake, California. *Earth Surface Processes and Landforms, 23*, 69–82.

Lancaster, N., Nickling, W. G., McKenna Neuman, C. K. & Wyatt, V. E. (1996). Sediment flux and airflow on the stoss slope of a barchans dune. *Geomorphology, 17,* 55–62.

Lancaster, N., Nickling, W. G. & Gillies, J. A. (2010). Sand transport by wind on complex surfaces: Field studies in the McMurdo Dry Valleys, Antarctica. *Journal of Geophysical Research*, *115*(F3), F03027.

Langford, R. P. (2000). Nabkha (coppice dune) fields of south-central New Mexico, U.S.A. *Journal of Arid Environments, 46*, 25– 41.

Lapointe, M. F. (1992). Burst-like sediment suspension events in a sand bed river. *Earth Surface Processes and Landforms, 17*, 253–270.

Lauenroth, W. K. & Adler, P. B. (2008). Demography of perennial grassland plants: survival, life expectancy and life span. *Journal of Ecology, 96*, 1023–1032.

Lawrence, D., D'Odorico, P., Diekmann, L., DeLonge, M., Das, R. & Eaton, J. (2007). Ecological feedbacks following deforestation create the potential for a catastrophic ecosystem shift in tropical dry forest. *Proceedings of the National Academy of Sciences, 104*, 20696–20701.

Le, H., Moin, P. & Kim J. (1997). Direct numerical simulation of turbulent flow over a backward-facing step. *Journal of Fluid Mechanics, 330,* 349–374.

Lee, Z. S., & Baas, A. C. W. (2012). Streamline correction for the analysis of boundary layer turbulence. *Geomorphology*, *171-172*, 69–82. doi:10.1016/j.geomorph.2012.05.005

Lee, Z. S. & Baas, A. C. W. (2016). Variable and conflicting shear stress estimates inside a boundary layer with sediment transport. *Earth Surface Processes and Landforms*, *41*(4), 435–445. doi:10.1002/esp.3829

Lee, J-P., Lee, E-J. & Lee, S-J. (2014). Shelter effect of a fir tree with different porosities. *Journal of Mechanical Science and Technology*, *28*(2), 565–572. doi:10.1007/s12206-013-1123-6

Lee, S-J., Park, K. C. & Park, C. W. (2002). Wind tunnel observations about the shelter effect of porous fences on the sand particle movements. *Atmospheric Environment, 36*, 1453–1463.

Lee, B. E. & Soliman, B. F. (1977). An investigation of the forces on three-dimensional bluff bodies in rough wall turbulent boundary layer. *Journal of Fluids, 99*(3), 503–509.

Leenders, J. K., Sterk, G. & van Boxel, J. H. (2011). Modelling wind-blown sediment transport around single vegetation elements. *Earth Surface Processes and Landforms*, *36*(9), 1218–1229. doi:10.1002/esp.2147

Leenders, J. K., van Boxel, J. H. & Sterk, G. (2005). Wind forces and related saltation transport. *Geomorphology*, *71*, 357–372.

Leenders, J. K., van Boxel, J. H. & Sterk, G. (2007). The effect of single vegetation elements on wind velocity and sediment transport in the Sahelian zone of Burkina Faso. *Earth Surface Processes and Landforms*, *32*(10), 1454–1474. doi:10.1002/esp

Lefever, R. & Lejeune, O. (1997). On the origin of tiger bush. *Bulletin of Mathematical Biology, 59*(2), 263–294.

Lehmann, C. E. R., Archibald, S. A., Hoffmann, W. A. & Bond, W. J. (2011). Deciphering the distribution of the savanna biome. *New Phytologist*, *191*(1), 197–209. doi:10.1111/j.1469-8137.2011.03689.x

Lejeune, O., Couteron, P. & Lefever, R. (1999). Short range co-operativity competing with long range inhibition explains vegetation patterns. *Acta Oecologia, 20*(3), 171–183.

Lenton, T. M. (2013). What early warning systems are there for environmental shocks? *Environmental Science & Policy*, *27*, S60–S75.

Levin, N. & Ben-Dor, E. (2004). Monitoring sand stabilization along the coastal dunes of Ashdod-Nizanim, Israel, 1945–1999. *Journal of Arid Environments, 58*, 335–355.

Levin, N., Kidron, G. J. & Ben-Dor, E. (2008). A field quantification of the adaptations of costal dune plants to erosion and deposition of sand. *Sedimentology, 55*, 751–772. doi:10.1111/j.1365-3091.2007.00920.x

Levin, N., Levental, S. & Morag, H. (2012). The effect of wildfires on vegetation cover and dune activity in Australia's desert dunes: A multi-sensor analysis. *International Journal of Wildland Fire*, *21*(4), 459–475.

Leys, J. F. & McTainsh, G. (1994). Soil loss and nutrient decline by wind erosion—cause for concern. *Australian Journal of Soil and Water Conservation, 7*, 30–35.

Li, J., Okin, G. S., Alvarez, L. & Epstein, H. (2007). Quantitative effects of vegetation cover on wind erosion and soil nutrient loss in a desert grassland of southern New Mexico, USA. *Biogeochemistry, 85*,317–332.

Li, J., Okin, G. S., Alvarez, L. & Epstein, H. (2008). Effects of wind erosion on the spatial heterogeneity of soil nutrients in two desert grassland communities. *Biogeochemistry, 88*, 73–88.

Li, J., Gilhooly, W. P., Okin, G. S. & Blackwell, J. (2017). Abiotic processes are insufficient for fertile island development: A ten-year artificial shrub experiment in a desert grassland. *Geophysical Research Letters.* doi:10.1002/2016GL072068

Li, J., Okin, G. S., Herrick, J. E., Belnap, J., Miller, M. E., Vest, K. & Draut, A. E. (2013). Evaluation of a new model of aeolian transport in the presence of vegetation. *Journal of Geophysical Research: Earth Surface*, *118*(1), 288–306.

Lim, H. C., Castro, I. P. & Hoxey, R. P. (2007). Bluff bodies in deep turbulent boundary layers: Reynolds-number issues. *Journal of Fluid Mechanics, 571*, 97–118.

Liu, J., Chen, J. M., Black, T. A. & Novak, M. D. (1996). E-ε modelling of turbulent air flow downwind of a model forest edge. *Boundary Layer Meteorology, 77*, 21–44.

Liu, S., Wul, H., Lytton, R. L. & Sharpe, P. J. (1990). Aerodynamic sheltering effects of vegetative arrays on wind erosion : a numerical approach. *Journal of Environmental Management*, *30*, 281–294.

Livingstone, I. & Warren, A. (1996). *Aeolian Geomorphology: An Introduction*. Longman, London.

Lohmann, D., Tietjen, B., Blaum, N., Joubert, D. F. & Jeltsch, F. (2012). Shifting thresholds and changing degradation patterns: climate change effects on the simulated long-term response of a semi-arid savanna to grazing. *Journal of Applied Ecology, 49,* 814–823.

Loreau, M., Naeem, S., Inchausti, P., Bengtsson, J., Grime, J., Hector, A., Hooper, D., Huston, M., Raffaelli, D. B. S., Tilman, D. & Wardle, D. (2001). Biodiversity and ecosystem functioning: current knowledge and future challenges. *Science, 294*, 804–808.

Lu, S. S. & Willmarth, W. W. (1973). Measurements of the structure of Reynolds' stress in a turbulent boundary layer. *Journal of Fluid Mechanics, 60*, 481–511.

Lucas, A., Narteau, C., Rodriguez, S., Rozier, O., Callot, Y., Garcia, A. & Courrech du Pont, S. (2015). Sediment flux from the morphodynamics of elongating linear dunes. *Geology*, *43*(11), 1027–1030. doi:10.1130/G37101.1

Ludwig, J. A., Wilcox, B. P., Breshears, D. D., Tongway, D. J. & Imeson, A. C. (2005). Vegetation patches and runoff-erosion as interacting ecohydrological processes in semiarid landscapes. *Ecology, 86*(2), 288–297.

Lyles, L., Schrandt, R. L. & Schmeidler, N. F. (1974). How aerodynamic roughness elements control sand movement. *Transactions of the ASAE, 17*, 134-139.

Lynch, K., Jackson, D. W. T. & Cooper, J. A. G. (2009). Foredune accretion under offshore winds. *Geomorphology, 105*, 139–146.

MacKinnon, D. J., Clow, G. D., Tigges, R. K., Reynolds, R. L. & Chavez, J. P. S. (2004). Comparison of aerodynamically and model-derived roughness lengths (Zo) over diverse surfaces, central Mojave Desert, California, USA. *Geomorphology, 63,* 103–113.

Marion, G., Smith, L. A., Swain, D. L., Davidson, R. S. & Hutchings, M. R. (2008). Agent-based modelling of foraging behaviour: the impact of spatial heterogeneity on disease risks from faeces in grazing systems. *Journal of Agricultural Science, 146*(5), 507–520.

Marshall, J. K. (1971). Drag measurements in roughness arrays of varying densities and distribution. *Agricultural Meteorology, 8*, 269–292.

Martens, S. N., Breshears, D. D., Meyer, C. W. & Barnes, F. J. (1997). Scales of above-ground and below-ground competition in a semi-arid woodland detected from spatial pattern. *Journal of Vegetation Science, 8*, 655–664.

Marticorena, B. & Bergametti, G. (1995). Modeling the atmospheric dust cycle: 1. Design of a soil-derived dust emission scheme. *Journal of Geophysical Research*, *100*(D8), 16415.

Maruyama, T. (2008). Large eddy simulation of turbulent flow around a windbreak. *Journal of Wind Engineering and Industrial Aerodynamics*, *96*(10-11), 1998–2006.

Mason, S. & Jury, M. (1997). Climatic variability and change over southern Africa: a reflection on underlying processes. *Progress in Physical Geography, 21*(1), 23–50.

Maun, M. A. (1998). Adaptations of plants to burial in coastal sand dunes. *Canadian Journal of Botany, 76,* 713–738.

Mayaud, J. R., Bailey, R. M. & Wiggs, G. F. S. (2017a). A coupled vegetation/sediment-transport model for dryland environments. *Journal of Geophysical Research: Earth Surface, 122,* doi:10.1002/2016JF004096

Mayaud, J. R., Wiggs, G. F. S. & Bailey, R. M. (2017b). A field-based parameterization of wind flow recovery in the lee of dryland plants. *Earth Surface Processes and Landforms.* doi: 10.1002/esp.4082

Mayaud, J. R., Bailey, R. M. & Wiggs, G. F. S. (2016a). Modelling aeolian sand transport using a dynamic mass balancing approach. *Geomorphology, 280,* 1-8–121. doi:10.1016/j.geomorph.2016.12.006

Mayaud, J. R., Wiggs, G. F. S. & Bailey, R. M. (2016b). Characterizing turbulent wind flow around dryland vegetation. *Earth Surface Processes and Landforms, 41*(10), 1421–1436. doi: 10.1002/esp.3934

Mayaud, J. R., Wiggs, G. F. S. & Bailey, R. M. (2016c). Dynamics of skimming flow in the wake of a vegetation patch. *Aeolian Research, 22,* 141–151. doi: 10.1016/j.aeolia.2016.08.001

McGarigal, K., Cushman, S. A. & Ene, E. (2012). FRAGSTATS v4: Spatial Pattern Analysis Program for Categorical and Continuous Maps. Computer software program

produced by the authors: [http://www.umass.edu/landeco/research/fragstats/fragstats.html]

McGlynn, I. O. & Okin, G. S. (2006). Characterization of shrub distribution using high spatial resolution remote sensing: ecosystem implication for a former Chihuahuan Desert Grassland. *Remote Sensing Environment, 101(*4), 554–566.

McKenna-Neuman, C. & Bédard, O. (2015). A wind tunnel study of flow structure adjustment on deformable sand beds containing a surface-mounted obstacle. *Journal of Geophysical Research: Earth Surface, 120*(9), 1824–1840.

McKenna-Neuman, C., Lancaster, N. & Nickling, W. (2000). The effect of unsteady winds on sediment transport on the stoss slope of a transverse dune, Silver Peak, NV, USA. *Sedimentology, 47,* 211-226.

McKenna-Neuman, C. & Scott, M. M. (1998). A wind tunnel study of the influence of pore water on aeolian sediment transport. *Journal of Arid Environments, 39,* 403–419.

McMenamin, R., Cassidy, R. & McCloskey, J. (2002). Self-organised criticality at the onset of aeolian sediment transport. Journal of Coastal Research SI 36, 498–505.

Mendez, M. J., Funk, R., & Buschiazzo, D. E. (2011). Field wind erosion measurements with Big Spring Number Eight (BSNE) and Modified Wilson and Cook (MWAC) samplers. *Geomorphology*, *129*(1-2), 43–48. doi:10.1016/j.geomorph.2011.01.011

Meron, E., Gilad, E., von Hardenberg, J., Shachak, M. & Zarmi, Y. (2004). Vegetation patterns along a rainfall gradient. *Chaos, Solitons & Fractals*, *19*(2), 367–376.

Middleton, N. (2011). The human impact. In: Thomas, D. S. G. (ed). *Arid Zone Geomorphology: Process, Form and Change in Drylands,* Third Edition, John Wiley & Sons Ltd, 571-582.

Middleton, N. J. & Sternberg, T. (2013). Climate hazards in drylands: A review. *Earth-Science Reviews, 126,* 48–57. doi: 10.1016/j.geomorph.2014.08.023

Millennium Ecosystem Assessment (MEA), (2005a). Ecosystems and Human Wellbeing: Desertification Synthesis. *Technical Report of the Millennium Ecosystem Assessment*, World Resources Institute, Washington, D. C.

Millennium Ecosystem Assessment (MEA), (2005b). Ecosystems and Human Wellbeing: Biodiversity Synthesis. *Technical Report of the Millennium Ecosystem Assessment,* World Resources Institute, Washington, D. C.

Miller, M. E., Bowker, M. A., Reynolds, R. L. & Goldstein, H. L. (2012). Post-fire land treatments and wind erosion – Lessons from the Milford Flat Fire, UT, USA. *Aeolian Research*, *7*, 29–44. doi:10.1016/j.aeolia.2012.04.001

Milton, S. J. & Dean, W. R. J. (2000). Disturbance, drought and dynamics of desert dune grassland, South Africa. *Plant Ecology, 150*, 37–51.

Minvielle, F., Marticorena, B., Gillette, D. A., Lawson, R. E., Thompson, R. & Bergametti, G. (2003). Relationship between the Aerodynamic Roughness Length and the Roughness Density in Cases of Low Roughness Density. *Environmental Fluid Mechanics*, *3*, 249–267.

Molina-Aiz, F. D., Valera, D. L., Álvarez, A. J. & Madueño, A. (2006). A wind tunnel study of airflow through horticultural crops: determination of the drag coefficient. *Biosystems Engineering, 93* (4), 447–457.

Momiji, H., Carretero-Gonzalez, R., Bishop, S. R. & Warren, A. (2000). Simulation of the effect of wind speedup in the formation of transverse dune fields. *Earth Surface Processes and Landforms, 25*, 905–918.

Momiji, H. & Warren, A. (2000). Relations of sand trapping efficiency and migration speed of transverse dunes to wind velocity. *Earth Surface Processes and Landforms, 25,* 1069–1084.

Moore, A. E. & Dingle, R. V. (1998). Evidence for fluvial sediment transport of Kalahari sands in central Botswana. *South African Journal of Geology, 101,* 143–154.

Moore, P. D. (1996). Mystery of moribund marram. *Nature, 380,* 285–286.

Moore, A. E. & Dingle, R. V. (1998). Evidence for fluvial sediment transport of Kalahari sands in central Botswana. *South African Journal of Geology*, *101*, 143–154.

Mulligan, K. R. (1988). Velocity profiles measured on the windward slope of a transverse dune. *Earth Surface Processes and Landforms, 13,* 573–582.

Munson, S. M., Belnap, J. & Okin, G. S. (2011). Responses of wind erosion to climate-induced vegetation changes on the Colorado Plateau. *Proceedings of the National Academy of Sciences, 108*, 3854–3859.

Musick, H. B. & Gillette, D. A. (1990). Field evaluation of relationships between a vegetation structural parameter and sheltering against wind erosion. *Land Degradation and Rehabilitation*, *2*, 87–94.

Musick, H. B., Trujillo, S. M. & Truman, C. R. (1996). Wind-tunnel modelling of the influence of vegetation structure on saltation threshold. *Earth Surface Processes and Landforms*, *21*(7), 589–605.

Namikas, S. L. (2003). Field measurement and numerical modelling of aeolian mass flux distributions on a sandy beach. *Sedimentology*, *50*(2), 303–326.

Namikas, S. L., Bauer, B. O. & Sherman, D. J. (2003). Influence of averaging interval on shear velocity estimates for aeolian transport modelling. *Geomorphology, 53*(3–4), 235–246.

Namikas, S. L. & Sherman, D. J. (1995). A review of the effects of surface moisture content on aeolian sand transport. In: Tchakerian, V. P. (ed.), *Desert Aeolian Processes*, Chapman & Hall: New York, p. 269–293.

Narteau, C., Lajeunesse, E., Métivier, F. & Rozier, O. (2006). Modelling of dune patterns by short range interactions. *River, Coastal and Estuarine Morphodynamics*, 1035–1046.

Nash, M. S., Jackson, E. & Whitford, W. G. (2004). Effects of intense, short-duration grazing on microtopography in a Chihuahuan Desert grassland. *Journal of Arid Environments, 56*, 383–393.

Naylor, L. A., Viles, H. A. & Carter, N. E. A. (2002). Biogeomorphology revisited: looking towards the future. *Geomorphology, 47*, 3–14.

Necsoiu, M., Leprince, S., Hooper, D. M., Dinwiddie, C. L., McGinnis, R. N. & Walter, G. R. (2009). Monitoring migration rates of an active subarctic dune field using optical imagery. *Remote Sensing of Environment, 113,* 2442–2447.

New, M., Hewitson, B., Stephenson, D. B. et al. (2006). Evidence of trends in daily climate extremes over southern and west Africa. *Journal of Geophysical Research D: Atmospheres, 111*(14). doi:10.1029/2005JD006289

Nickling, W. & McKenna-Neuman, C. (1997). Wind tunnel evaluation of a wedge-shaped aeolian sediment trap. *Geomorphology, 18,* 333-345.

Nield, J. M. (2011). Surface moisture−induced feedback in aeolian environments. *Geology*, *39*(10), 915–918. doi:10.1130/G32151.1

Nield, J. M. & Baas, A. C. W. (2008a). Investigating parabolic and nebkha dune formation using a cellular automaton modelling approach. *Earth Surface Processes and Landforms*, *33*, 724–740. doi:10.1002/esp

Nield, J. M. & Baas, A. C. W. (2008b). The influence of different environmental and climatic conditions on vegetated aeolian dune landscape development and response. *Global and Planetary Change*, *64*(1-2), 76–92. doi:10.1016/j.gloplacha.2008.10.002

Nield, J. M., King, J., Wiggs, G. F. S., Leyland, J., Bryant, R. G., Chiverrell, R. C., … Washington, R. (2013). Estimating aerodynamic roughness over complex surface terrain. *Journal of Geophysical Research: Atmospheres*, *118*(23), 12,948–12,961. doi:10.1002/2013JD020632

Nield, J. M. & Wiggs, G. F. S. (2011). The application of terrestrial laser scanning to aeolian saltation cloud measurement and its response to changing surface moisture. *Earth Surface Processes and Landforms*, *36*(2), 273–278.

Noy-Meir, I. (1973). Desert ecosystems: Environment and producers. *Annual Review of Ecological Systems, 4,* 25–51.

Okin, G. S. (2008). A new model of wind erosion in the presence of vegetation. *Journal of Geophysical Research*, *113*(F2), F02S10.

Okin, G. (2016). Should precipitation influence dust emission in global dust models? *Geophysical Research Abstracts, Vol. 18,* EGU2016-17947.

Okin, G. S., D'Odorico, P. & Archer, S. R. (2009a). Impacts of feedbacks on Chihuahuan Desert grasslands: transience and metastability driven by grass recruitment. *Journal of Geophysical Research, 114*, G01004.

Okin, G. S. & Gillette, D. A. (2001). Distribution of vegetation in wind-dominated landscapes: Implications for wind erosion modeling and landscape processes. *Journal of Geophysical Research, 106*, 9673–9683.

Okin, G. S., Gillette, D. A. & Herrick, J. E. (2006). Multi-scale controls on and consequences of aeolian processes in landscape change in arid and semi-arid environments. *Journal of Arid Environments*, *65*(2), 253–275.

Okin, G. S., Murray, B. & Schlesinger W. H. (2001). Degradation of sandy arid shrubland environments: observations, process modeling, and management implications. *Journal of Arid Environments, 47*, 123–144.

Okin, G. S., Parsons, A. J., Wainwright, J., Herrick, J. E., Bestelmeyer, B. T., Peters, D. C. & Fredrickson, E. L. (2009b). Do changes in connectivity explain desertification? *Bioscience, 59*(3), 237–244.

Olivier, J. (1995). Spatial distribution of fog in the Namib. *Journal of Arid Environments, 29,* 129-138.

Omasa, K., Hosoi, F. & Konishi, A. (2007). 3D lidar imaging for detecting and understanding plant responses and canopy structure. *Journal of Experimental Botany, 58*(4), 881–898. doi:10.1093/jxb/erl142

Parteli, E. J., Duran, O., Bourke, M., Tsoar, H., Pöschel, T. & Herrmann, H. (2014). Origins of barchan dune asymmetry: insights from numerical simulations. *Aeolian Research, 12,* 121–133.

Penny, G. G., Daniels, K. E. & Thompson, S. E. (2013). Local properties of patterned vegetation : quantifying endogenous and exogenous effects. *Philosophical Transactions. Series A, Mathematical, Physical, and Engineering Sciences*, *371*, 1–18.

Perera, M. D. (1981). Shelter behind two-dimensional solid and porous fences. *Journal of Wind Engineering and Industrial Aerodynamic, 8,* 93–104.

Peters, D. P. C., Bestelmeyer, B. T., Herrick, J. E., Monger, H. C., Fredrickson, E. & Havstad, K. M. (2006). Disentangling complex landscapes: New insights to forecasting arid and semiarid system dynamics. *BioScience, 56*, 491–501.

Phillips, J. D. (1999). *Earth Surface Systems: Complexity, Order and Scale*, Blackwell, Oxford.

Pugnaire, F. I., Haase, P., Puigdefabregas, J., Cueto, M., Clark, S. C. & Incoll, L. D. (1996). Facilitation and succession under the canopy of a leguminous shrub, Retama sphaerocarpa, in a semiarid environment in southeast Spain. *Oikos, 76*, 455–464.

Puigdefabregas, J. (2005). The role of vegetation patterns in structuring runoff and sediment fluxes in drylands. *Earth Surface Processes and Landforms, 30*(2), 133–147.

Pye, K. & Tsoar, H. (1990). *Aeolian Sand and Sand Dunes*, Unwin Hyman, London.

Qiu, G. Y., Yano, T. & Momiji, K. (1998). An improved methodology to measure evaporation from bare soil based on comparison of surface temperature with a dry soil surface. *Journal of Hydrology, 210*(1–4), 93–105. doi:10.1016/S0022-1694(98)00174-7

Raupach, M. R. (1992). Drag and drag partition on rough surfaces. *Boundary-Layer Meteorology*, *60*(4), 375–395.

Raupach, M. R., Gillette, D. A. & Leys, J. F. (1993). The effect of roughness elements on wind erosion threshold. *Journal of Geophysical Research*, *98*(D2), 3023–3029.

Raupach, M. R. & Lu, H. (2004). Representation of land-surface processes in aeolian transport models. *Environmental Modelling and Software, 19*, 93–112.

Raupach, M. R., Woods, N., Dorr, G., Leys, J. F. & Cleugh. H. A. (2001). The entrapment of particles by windbreaks. *Atmospheric Environment, 35*, 3373–3383.

Ravi, S., Baddock, M. C., Zobeck, T. M. & Hartman, J. (2012). Field evidence for differences in post-fire aeolian transport related to vegetation type in semi-arid grasslands. *Aeolian Research*, *7*, 3–10.

Ravi, S., Breshears, D. D., Huxman, T. E. & D'Odorico, P. (2010). Land degradation in drylands: Interactions among hydrologic–aeolian erosion and vegetation dynamics. *Geomorphology*, *116*(3-4), 236–245.

Ravi, S., D'Odorico, P., Breshears, D. D., Field, J. P., Goudie, A. S. et al. (2011). Aeolian processes and the biosphere. *Review of Geophysics*, *RG3001*, 1–45.

Ravi, S., D'Odorico, P., Wang, L., & Collins, S.L. (2008). Form and function of grass ring patterns in arid grasslands: the role of abiotic controls. *Oecologia, 158*, 545–555.

Ravi, S., D'Odorico, P., Wang, L., White, C. S., Okin, G. S., Macko, S. A. & Collins, S. L. (2009a). Post-fire resource redistribution in desert grasslands: A possible negative feedback on land degradation. *Ecosystems, 12*, 44–444.

Ravi, S., D'Odorico, P., Zobeck, T. M. & Over, T. M. (2009b). The effect of fire-induced soil hydrophobicity on wind erosion in a semiarid grassland: experimental observations and theoretical framework. *Geomorphology, 105*, 80–86.

Ravi, S., Zobeck, T. M., Over, T. M., Okin, G. S. & D'Odorico, P. (2006). On the effect of moisture bonding forces in air-dry soils on threshold friction velocity of wind erosion. *Sedimentology, 53,* 597–609.

Reed, M. S. & Dougill, A. J. (2010). Linking degradation assessment to sustainable land management: a decision support system for Kalahari pastoralists. *Journal of Arid Environments, 74,* 149–155.

Reed, M. S., Dougill, A. J. & Taylor, M. J. (2007). Integrating local and scientific knowledge for adaptation to land degradation: Kalahari rangeland management options. *Land Degradation and Development, 18*, 249–268.

Reed, M. S., Stringer, L. C., Dougill, A. J., Perkins, J. S., Atlhopheng, J. R., Mulale, K. & Favretoo, N. (2015). Reorienting land degradation towards sustainable land management: Linking sustainable livelihoods with ecosystem services in rangeland systems. *Journal of Environmental Management, 151,* 472–485.

Reffet, E., Courrech du Pont, S., Hersen, P. & Douady, S. (2010). Formation and stability of transverse and longitudinal sand dunes. *Geology, 38,* 491–494.

Reynolds, R., Belnap, J., Reheis, M., Lamothe, P. & Luiszer, F. (2001). Aeolian dust in Colorado Plateau soils: nutrient inputs and recent change in source. *Proceedings of the National Academy of Sciences U.S.A., 98,* 7123–7127.

Rice, M. A., McEwan, I. K. & Mullins, C. E. (1999). A conceptual model of wind erosion of soil surfaces by saltating particles. *Earth Surface Processes and Landforms*, *24*, 383-392.

Ridolfi, L., Laio, F. & D'Odorico, P. (2008). Fertility island formation and evolution in dryland ecosystems. *Ecological Society, 13*(1), 5.

Rietkerk, M., Boerlijst, M., van Langevelde, F., HilleRisLambers, R., van de Koppel, J., Kumar, L., Prins, H. & De Roos, A. (2002). Self-organization of vegetation in arid ecosystems. *Amereican Nature, 160,* 524–530.

Rietkerk, M., Dekker, S. C., de Ruiter, P. C. & van de Koppel, J. (2004). Self-organized patchiness and catastrophic shifts in ecosystems. *Science*, *305*(5692), 1926–9.

Rietkerk, M., van den Bosch, F. & van de Koppel, J. (1997). Site-specific properties and irreversible vegetation changes in semi-arid grazing systems. *Oikos, 80*, 241-252.

Roach, D. A., Ridley, C. E. & Dudycha, J. L. (2009). Longitudinal analysis of Plantago: Age-by-environment interactions reveal aging. *Ecology, 90*(6), 1427–1433.

Rohani, P., Lewis, T. J., Grunbaum, D. & Ruxton, G. D. (1997). Spatial self-organization in ecology: Pretty patterns or robust reality? *Trends in Ecology & Evolution, 12*(2), 70–74.

Roy, A. G., Biron, P. M., Buffin-Bélanger, T. & Levasseur, M. (1999). Combined visual and quantitative techniques in the study of natural turbulent flows. *Water Resource Research, 35*, 871–877. doi:10.1029/1998WR900079

Roy, A. G., Biron, P. & De Serres, B. (1996). On the necessity of applying a rotation to instantaneous velocity measurements in river flows. *Earth Surface Processes and Land- forms, 21*, 817–827.

Rubin, D. M. & Hesp, P. A. (2009). Multiple origins of linear dunes on Earth and Titan. *Nature Geoscience, 2,* 653–658. doi:10.1038/ngeo610

Rubin, D. M. & Hunter, R. E. (1982). Bedform climbing in theory and nature. *Sedimentology, 29,* 121–138.

Rubin, D. M. & Hunter, R. E. (1987). Bedform alignment in directionally varying flows. *Science, 237*, 276–278.

Ruck, V. B. & Schmitt, F. (1986). Das Strömungsfeld der Einzelbaumuströmung. Abschätzung von Depositionswahrscheinlichkeiten für Feinsttröpfchen. *Forstwissenschaftliches Centralblatt, 105,* 178–196.

Rutherford, M. C. & Powrie, L. W. (2009). Severely degraded dunes of the southern Kalahari: local extinction, persistence and natural re-establishment of plants. *African Journal of Ecology, 48,* 930–938.

Sankaran, M., Hanan, N. P., Scholes, R. J., Ratnam, J., Augustine, D. J., Cade, B. S. et al. (2005). Determinants of woody cover in African savannas. *Nature*, *438*(7069), 846–849. doi:10.1038/nature04070

Sankey, J. B., Law, D. J., Breshears, D. D., Munson, S. M. & Webb, R. H. (2013). Employing lidar to detail vegetation canopy architecture for prediction of aeolian transport. *Geophysical Research Letters*, *40*(9), 1724–1728. doi:10.1002/grl.50356

Sankey, J. B., Ravi, S., Wallace, C. S. A., Webb, R. H. & Huxman, T. E. (2012). Quantifying soil surface change in degraded drylands: Shrub encroachment and effects of fire and vegetation removal in a desert grassland. *Journal of Geophysical Research: Biogeosciences*, *117*(G2), 1-11.

Scheffer, M., Bascompte, J., Brock, W. A., Brovkin, V., Carpenter, S. R., Dakos, V., Held, H., van Nes, E. H., Rietkerk, M. & Sugihara, G. (2009). Early-warning signals for critical transitions. *Nature, 461*, 387–393.

Scheffer, M. & Carpenter, S. R. (2003). Catastrophic regime shifts in ecosystems: linking theory to observation. *Trends in Ecology and Evolution, 18*(12), 648–656.

Scheffer, M., Carpenter, S. R., Lenton, T. M., Bascompte, J., Brock, W., Dakos, V., et al. (2012). Anticipating critical transitions. *Science*, *338*(6105), 344–348.

Scheffer, M., Carpenter, S. R., Poley, J. A., Folke, C. & Walter, B. (2001). Catastrophic shifts in ecosystems. *Nature, 413*, 591–596.

Schlesinger, W. H., Raikes, J. A., Hartley, A. E. & Cross, A. F. (1996). On the spatial pattern of soil nutrients in desert ecosystems. *Ecology, 77*, 364–374.

Schlesinger, W. H., Reynolds, J. F., Cunningham, G. L., Huenneke, L. F., Jarrell, W. M., Virginia, R. A. & Whitford, W. G. (1990). Biological feedbacks in global desertification. *Science, 247*(4946), 1043–1048.

Schlesinger, W. H., Ward, T. J. & Anderson, J. (2000). Nutrient losses in runoff from grassland and shrubland habitats in southern New Mexico: II. Field plots. *Biogeochemistry, 49*, 69–86.

Schlichting, H. (1936). Experimentelle untersuchungen zum Rauhigkeitsproblem, *Ine-Arch, 7*, 1–34.

Schlichting, H. (1955). *Boundary Layer Theory*, Pergamon Press, New York.

Scholes, R. J. & Archer, S. R. (1997). Tree-grass interactions in savannas. *Annual Review of Ecological Systems*, *28*, 517–544.

Schönfeldt, H. J. & von Löwis, S. (2003). Turbulence-driven saltation in the atmospheric surface layer. *Meteorologische Zeitschrift*, *12*(5), 257–268.

Schröttle, J. & Dörnbrack, A. (2012). Turbulence structure in a diabatically heated forest canopy composed of fractal Pythagoras trees. *Theoretical and Computational Fluid Dynamics*, *27*(3-4), 337–359. doi:10.1007/s00162-012-0284-8

Schwämmle, V. & Herrmann, H. J. (2005). A model for barchan dunes including lateral shear stress. *The European Physical Journal E, 16*, 57–65.

Seager, R., Ting, M., Held, M.I., Kushnir, Y., Lu, J., Vecchi, G., Huang, H.-P., Harnik, N., Leetmaa, A., Lau, N.-C., et al. (2007). Model projections of an imminent transition to a more arid climate in southwestern North America. *Science, 316*, 1181–1184.

Shao, Y., McTainsh, G. H., Leys, J. F. & Raupach, M. R. (1993). Efficiencies of sediment samplers for wind erosion measurement. *Australian Journal of Soil Research, 31*, 519–532.

Shaw, R. H., Tavangar, T. & Ward, D. P. (1983). Structure of the Reynolds stress in the canopy layer. *Journal of Climate and Applied Meteorology, 22,* 1922–1931.

Sheffer, E., von Hardenberg, J., Yizhaq, H., Shachak, M. & Meron, E. (2012). Emerged or imposed: a theory on the role of physical templates and self-organisation for vegetation patchiness. *Ecology letters*, *16*(2), 127–39.

Sheffer, E., Yizhaq, H., Gilad, E., Shachak, M. & Meron, E. (2007). Why do plants in resource-deprived environments form rings? *Ecological Complexity*, *4*(4), 192–200.

Sheffer, E., Yizhaq, H., Shachak, M. & Meron, E. (2011). Mechanisms of vegetation-ring formation in water-limited systems. *Journal of Theoretical Biology*, *273*(1), 138–46.

Shen, S. & Leclerc, M. Y. (1997). Modelling the turbulence structure in the canopy layer. *Agricultural Forest Meteorolgy, 87*, 3–25.

Sherman, D. J., Li, B., Farrell, E. J., Ellis, J. T., Cox, W. D., Maia, L. P., & Sousa, P. H. G. O. (2011). Measuring Aeolian Saltation: A Comparison of Sensors. *Journal of Coastal Research*, *59*(10059), 280–290. doi:10.2112/SI59-030.1

Sherratt, J. A. (2015). Using wavelength and slope to infer the historical origin of semiarid vegetation bands. *Proceedings of the National Academy of Sciences*, *112*(14), 4202–4207. doi:10.1073/pnas.1420171112

Shongwe, M. E., van Oldenborgh, G. J., van, d. H., et al. (2009). Projected changes in mean and extreme precipitation in Africa under global warming. Part I: Southern Africa. *Journal of Climate, 22*(13), 3819–3837.

Sietz, D., Ludeke, M. K. B. & Walther, C. (2011). Categorisation of typical vulnerability patterns in global drylands. *Global Environmental Change, 21,* 431–440.

Smith, C. R. (1996). Coherent flow structures in smooth-wall turbulent boundary layers: facts, mechanisms and speculation. In: Ashworth, P. J., Bennett, S. J., Best J. L. & McLelland, S. J. (eds). *Coherent Flow Structures in Open Channels,* John Wiley & Sons, New York, 1–39.

Song, W-K., Cui, Y-J., Tang, A. M., Ding, W-Q. & Tran, T. D. (2014). Experimental study on water evaporation from sand using environmental chamber. *Canadian Geotechnical Journal, 51,* 115–128. doi:10.1139/cgj-2013-0155

Staver, A. C., Archibald, S. & Levin, S. A. (2011). The global extent and determinants of savanna and forest as alternative biome states. *Science*, *334*(6053), 230–232. doi:10.1126/science.1210465

Sterk, G. (2000). Flattened residue effects on wind speed and sediment transport. *Soil Science Society of America Journal*, *64,* 852–858.

Sterk, G., Jacobs, A. F. G. & van Boxel, J. H. (1998). The effect of turbulent flow structures on saltation sand transport in the atmospheric boundary layer. *Earth Surface Processes and Landforms*, *23*(10), 877–887.

Stewart, J., Parsons, A. J., Wainwright, J., Okin, G. S., Bestelmeyer, B., Fredrickson E. L. & Schlesinger, W. H. (2014). Modelling emergent patterns of dynamic desert ecosystems. *Ecological Monographs*, *84*(3), 373–410.

Stockton, P. H., & Gillette, D. A. (1990). Field measurement of the sheltering effect of vegetation on erodible land surfaces. *Land Degradation and Rehabilitation*, *2*(September), 77–85.

Stokes, S., Thomas, D. S. G. & Washington, R. (1997). Multiple episodes of aridity in southern Africa since the last interglacial period. *Nature, 388*, 154–158.

Stout, J.E. (2004). A method for establishing the critical threshold for aeolian transport. *Earth Surface Processes and Landforms, 29*(10), 1195-1207.

Stull, R. B. (1988). *An Introduction to Boundary Layer Meteorology,* Kluwer Academic, The Netherlands.

Su, H-B., Shaw, R. H., Paw, K. T., Moeng, C. H. & Sullivan, P. P. (1998). Turbulent statistics of neutrally stratified flow within and above a sparse forest from large-eddy simulation and field observations. *Boundary Layer Meteorology, 88,* 363–397.

Suding, K. N. & Hobbs, R. J. (2009). Threshold models in restoration and conservation: a developing framework. *Trends in Ecology and Evolution, 24*, 271–279.

Suter-Burri, K., Gromke, C., Leonard, K. C. & Graf, F. (2013). Spatial patterns of aeolian sediment deposition in vegetation canopies: Observations from wind tunnel experiments using colored sand. *Aeolian Research*, *8,* 65–73. doi:10.1016/j.aeolia.2012.11.002

Sutton, S. L. F. & McKenna-Neuman, C. (2008). Sediment entrainment to the lee of roughness elements: Effects of vortical structures. *Journal of Geophysical Research, 113*, F02S09.

Tadross, M. A., Hewitson, B. C. & Usman, M. T. (2005). The interannual variability of the onset of the maize growing season over South Africa and Zimbabwe. *Journal of Climate,* 3356–3372. doi:10.1175/JCLI3423.1

Tarboton, D. G., Bras, R. L. & Rodriguez-Iturbe I. (1988). The fractal nature of river networks. *Water Resources Research 24,* 1317–1322.

Tarnavsky, E., Mulligan, M., Ouessar, M., Faye, A. & Black, E. (2013). Dynamic hydrological modeling in drylands with TRMM based rainfall. *Remote Sensing, 5*, 6691–6716. doi:10.3390/rs5126691

Taylor, P. A. (1988). Turbulent wakes in the boundary layer. In: Steffen, W. L. & Denmead, O. T. (eds). *Flow and Transport in the Natural Environment: Advances and Applications*, Springer-Verlag, Berlin, 270–292.

Taylor, R. G., Todd, M. C., Kongola, L., et al. (2012). Evidence of the dependence of groundwater resources on extreme rainfall in East Africa. *Nature Climate Change, 2*(11), 1–5. doi:10.1038/nclimate1731

Tegen, I., Harrison, S. P., Kohfeld, K., Prentice, C., Coe, M. & Heimann, M. (2002). Impact of vegetation and preferential source areas on global dust aerosol: Results from a model study. *Journal of Geophysical Research*, *107*(D21), 4576.

Thiery, J. M., D'Herbes, J. M. & Valentin, C. (1995). A model simulating the genesis of banded vegetation patterns in Niger. *Journal of Ecology, 83,* 497–507.

Thomas, D. S. G. (1997). Science and the desertification debate. *Journal of Arid Environments, 37*, 599–608.

Thomas, D. S. G. (2011). Aeolian landscapes and bedforms. In: Thomas, D. S. G. (ed). *Arid Zone Geomorphology: Process, Form and Change in Drylands*, Third Edition, John Wiley & Sons Ltd, 427-454.

Thomas, D. S. G. & Burrough, S. L. (2013). Luminescence-based dune chronologies in southern Africa: Analysis and interpretation of dune database records across the subcontinent. *Quaternary International, 410*, 30–45. doi:10.1016/j.quaint.2013.09.008

Thomas, D. S. G., Knight, M. & Wiggs, G. F. S. (2005). Remobilization of southern African desert dune systems by twenty-first century global warming. *Nature*, *435*(7046), 1218–21.

Thomas, D. S. G. & Leason, H. C. (2005). Dunefield activity response to climate variability in the southwest Kalahari. *Geomorphology, 64*(1–2), 117–132. doi:10.1016/j.geomorph.2004.06.004

Thomas, D. S. G. & Shaw, P. A. (1991). *The Kalahari Environment*. Cambridge University Press, Cambridge.

Thomas, D. S. G. & Twyman, C. (2004). Good or bad rangeland? Hybrid knowledge, science, and local understandings of vegetation dynamics in the Kalahari. *Land Degradation and Development*, *15*(3), 215–223. doi:10.1002/ldr.610

Thompson, S., Katul, G. & McMahon, S. M. (2008). Role of biomass spread in vegetation pattern formation within arid ecosystems. *Water Resources Research*, *44*(10), E10421.

Thornton, P. K., Jones, P. G., Ericksen, P. J., et al. (2011). Agriculture and food systems in sub-Saharan Africa in a 4°C+ world. *Philosophical Transactions, Series A, Mathematical, Physical, and Engineering Sciences, 369*(1934), 117–136. doi:10.1098/rsta.2010.0246

Tischmacher, M. & Ruck, B. (2013). Interaction of gusts and forest edges - An experimental wind-tunnel study. *Forestry*, *86*(5), 523–532. doi:10.1093/forestry/cpt029

Tobler, W. R. (1979). Cellular Geography. In: Gale, S. & Olsson, G. (eds.) *Philosophy in Geography*, D. Reidel, Dordrecht, The Netherlands, 279–386.

Tschinkel, W. R. (2012). The life cycle and life span of Namibian fairy circles. *PloS One*, *7*(6), e38056. doi:10.1371/journal.pone.0038056

Tsoar, H. (1983). Dynamic processes acting on a longitudinal (seif) sand dune. *Sedimentology, 30*(4), 567–578.

Turnbull, L., Wainwright, J. & Brazier, R. E. (2008). A conceptual framework for understanding semi-arid land degradation: ecohydrological interactions across multiple-space and time scales. *Ecohydrology, 1*(1), 23–34.

Turnbull, L., Wainwright, J. & Brazier, R. E. (2010). Changes in hydrology and erosion over a transition from grassland to shrubland. *Hydrological Processes, 24*, 393–414.

Turnbull, L., Wilcox, B., & Belnap, J. (2012). Understanding the role of ecohydrological feedbacks in ecosystem state change in drylands. *Ecohydrology*, *183*, 174–183.

Turpin, C., Badr, T. & Harion, J.-L. (2010). Numerical modeling of aeolian erosion over rough surfaces. *Earth Surface Processes and Landforms, 35*, 1418-1429.

Tyson, P. D. (1986). *Climatic Change and Variability in Southern Africa.* Oxford University Press, Cape Town.

Tyson, P. D. & Seely, M. K. (1980). Local winds over the central Namib Desert. *South African Geographical Journal, 62*, 136-150.

Udo, K. & Takewaka, S. (2007). Experimental study of blown sand in a vegetated area. *Journal of Coastal Research, 23*(5), 1175–1182.

UNDP (2011). *The Forgotten Billion: MDG Achievement in Drylands.* UNDP, New York, NY

UNEP (1998). *World Atlas of Desertification*, Second Edition, Edward Arnold, Sevenoaks.

Valentin, C., d'Herbès, J-M. & Poesen, J. (1999). Soil and water components of banded vegetation patterns. *Catena, 37*, 1–24.

van Auken, O. W. (2000). Shrub invasions of North American semiarid grasslands. *Annual Review of Ecology and Systematics, 31*, 197–215.

van Boxel, J., Sterk, G. & Arens, S. (2004). Sonic anemometers in aeolian sediment transport research. *Geomorphology*, *59*(1-4), 131–147.

van der Putten, W. H., van Dijk, C. & Peters, B. A. M. (1993). Plant-specific soil-borne diseases contribute to succession in foredune vegetation. *Nature, 362,* 53–56.

van der Stelt, S., Doelman, A., Hek, G. & Rademacher, D. M. (2012). Rise and fall of periodic patterns for a generalized Klausmeier–Gray–Scott model. *Journal of Nonlinear Science, 23,* 39.

van Gardingen, P. & Grace, J. (1991). Plants and wind. *Advances in Botanical Research, 18,* 189–253.

van Langevelde, F. et al. (2003). Effects of fire and herbivory on the stability of savanna ecosystems. *Ecology, 84*, 337–350.

van Nes E. H. & Scheffer, M. (2007). Slow recovery from perturbations as a generic indicator of a nearby catastrophic shift. *American Naturalist, 169*, 738–747.

van Pelt, R. S., Peters, P. & Visser, S. (2009). Laboratory wind tunnel testing of three commonly used saltation impact sensors. *Aeolian Research, 1*(1–2), 55-62. doi:10.1016/ j.aeolia.2009.05.001

van Rooyen, N., Bezuidenhout, H. & de Kock, E. (2001). *Flowering plants of the Kalahari dunes*, Ekotrust.

Veron, S. R., Paruelo, J. M. & Oesterheld, M. (2006). Assessing desertification. *Journal of Arid Environments, 66*(4), 751–763.

Vigiak, O., Sterk, G., Warren, A. & Hagen, L. J. (2003). Spatial modeling of wind speed around windbreaks. *Catena*, *52*(3-4), 273–288. doi:10.1016/S0341-8162(03)00018-3

Viles, H. A. (2005). Microclimate and weathering in the central Namib Desert, Namibia. *Geomorphology, 67,* 47-59.

Viles, H. A. (2011). Weathering systems. In: Thomas, D. S. G. (ed). *Arid Zone Geomorphology: Process, Form and Change in Drylands,* Third Edition, John Wiley & Sons Ltd, 85-101.

von Hardenberg, J., Kletter, A. Y., Yizhaq, H., Nathan, J. & Meron, E. (2010). Periodic versus scale-free patterns in dryland vegetation. *Proceedings. Biological sciences / The Royal Society*, *277*(1688), 1771–1776.

von Hardenberg, J., Meron, E., Shachak, M. & Zarmi, Y. (2001). Diversity of vegetation patterns and desertification. *Physical Review Letters, 89*(198101).

Wagner, B., de Leeuw, J., Njenga, M., Iiyama, M. & Jamnadass, R. (2013). *Towards Greater Resilience in the Drylands: Trees Are the Key*. Nairobi, Kenya.

Wainwright, J. (2009). Desert Ecogeomorphology. In: Parsons, A. J. & Abrahams, A. D. (eds.), *Geomorphology of Desert Environments*, Second Edition, Springer, Berlin, 21–66.

Walker, I. J. (2005). Physical and logistical considerations of using ultrasonic anemometry in aeolian sediment transport research. *Geomorphology*, *68*, 57–76.

Walker, B., Holling, C. S., Carpenter, S. R. & Kinzig, A. (2004). Resilience, adaptability and transformability in social-ecological systems. *Ecology and Society 9. Article 5.*

Walker, I. J. & Nickling, W. G. (2002). Dynamics of secondary airflow and sediment transport over and in the lee of transverse dunes. *Progress in Physical Geography*, *26*(1), 47–75.

Walker, I. J. & Nickling, W. G. (2003). Simulation and measurement of surface shear stress over isolated and closely spaced transverse dunes in a wind tunnel. *Earth Surface Processes and Landforms, 28*, 1111–1124.

Walter, B., Gromke, C., Leonard, K., Clifton, A. & Lehning, M. (2012a). Spatially resolved skin friction velocity measurements using Irwin sensors: A calibration and accuracy analysis. *Journal of Wind Engineering and Industrial Aerodynamics*, *104-106*, 314–321. http://doi.org/10.1016/j.jweia.2012.02.018

Walter, B., Gromke, C., Leonard, K. C., Manes, C. & Lehning, M. (2012b). Spatio-temporal surface shear-stress variability in live plant canopies and cube arrays. *Boundary-Layer Meteorology, 143*(2), 337–356.

Wand, S. J. E. (1999). A preliminary study of the responsiveness to seasonal atmospheric and rainfall patterns of wash woodland species in the arid Richtersveld. *Plant Ecology, 142,* 149–160.

Wang, H. & Takle, E. S. (1996). Momentum budget and shelter mechanism of bounda-layer flow near a shelterbelt*. Boundary-Layer Meteorology, 82*, 417–435.

Wang, X., Yang, Y., Dong, Z. & Zhang, C. (2009). Responses of dune activity and desertification in China to global warming in the twenty-first century. *Global and Planetary Change*, *67*, 167-185.

Wasson, R. J. & Hyde, R. (1983). Factors determining desert dune type*. Nature, 304*, 337–339.

Wasson, R. J. & Nanninga, P. M. (1986). Estimating wind transport of sand on vegetated surfaces. *Earth Surface Processes and Landforms*, *11*, 505-514.

Weaver, C. M. (2008). Turbulent flow and sand dune dynamics: identifying controls on aeolian sediment transport. *Unpublished PhD thesis, University of Oxford.*

Weaver, C. M. & Wiggs, G. F. S. (2011). Field measurements of mean and turbulent airflow over a barchan sand dune. *Geomorphology*, *128*(1-2), 32–41.

Weber, R. O. (1999). Remarks on the definition and estimation of friction velocity. *Boundary-Layer Meteorology, 2,* 197–209.

Wengle, H., Huppertz, A., Bärwolff, G., & Janke, G. (2001). Manipulated transitional backward-facing step flow: an experimental and direct numerical simulation investigation. *European Journal of Mechanics, B/Fluids*, *20*(1), 25–46. doi:10.1016/S0997-7546(00)01105-5

Werner, B. T. (1995). Eolian dunes: computer simulations and attractor interpretation. *Geology, 23*, 1107–1110.

Wiggs, G. F. S., Atherton, R. A. & Baird, A. J. (2004a). Thresholds of aeolian sand transport: establishing suitable values. *Sedimentology, 51*, 95-108.

Wiggs, G. F. S., Baird, A. J. & Atherton, R. A. (2004b). The dynamic effects of moisture on the entrainment and transport of sand by wind. *Geomorphology*, *59*(1–4), 13–30.

Wiggs, G. F. S., Livingstone, I., Thomas, D. S. G. & Bullard, J. E. (1994). Effect of vegetation removal on airflow patterns and dune dynamics in the southwest Kalahari Desert. *Land Degradation and Rehabilitation*, *5,* 13–24.

Wiggs, G. F. S., Livingstone, I., Thomas, D. S. G. & Bullard, J. E. (1996a). Airflow and roughness characteristics over partially vegetated linear dunes in the southwest Kalahari Desert. *Earth Surface Processes and Landforms, 21*, 19–34.

Wiggs, G. F. S., Livingstone, I., Warren, A. (1996b). The role of streamline curvature in sand dune dynamics: Evidence from field and wind tunnel measurements. *Geomorphology, 17*(1–3), 29–46. doi:10.1016/ 0169-555X(95)00093-K

Wiggs, G. F. S., O'Hara, S. L., Wegerdt, J., Van Der Meer, J., Small, I. & Hubbard, R. (2003). The dynamics and characteristics of aeolian dust in dryland Central Asia: possible impacts on human exposure and respiratory health in the Aral Sea basin. *The Geographical Journal*, *169*(2), 142–157.

Wiggs, G. F. S., Thomas, D. S. G., Bullard, J. E. & Livingstone, I. (1995). Dune mobility and vegetation cover in the southwest Kalahari Desert. *Earth Surface Processes and Landforms*, *20*(6), 515–529.

Wiggs, G. F. S. & Weaver, C. M. (2012). Turbulent flow structures and aeolian sediment transport over a barchan sand dune. *Geophysical Research Letters, 39(*5), 1–7.

Wilczak, J. M., Oncley, S. P. & Stage, S. A. (2001). Sonic anemometer tilt correction algorithms. *Boundary-Layer Meteorology, 99*, 127–150.

Wilson, G. W., Fredlund, D. G. & Barbour, S. L. (1994). Coupled soil-atmosphere modelling for soil evaporation. *Canadian Geotechnical Journal, 31*(2), 151–161. doi:10.1139/t94-021

Wilson, J. D. & Yee, E. (2003). Calculation of winds disturbed by an array of fences. *Agricultural and Forest Meteorology*, *115*(1-2), 31–50.

Wolfe, S. A. & Nickling, W. G. (1993). The protective role of sparse vegetation in wind erosion. *Progress in Physical Geography, 17*, 50–68.

Wu, X., Zou, X., Zhou, N., Zhang, C. & Shi, S. (2015). Deceleration efficiencies of shrub windbreaks in a wind tunnel. *Aeolian Research*, 1*6,* 11–23. doi:10.1016/j.aeolia.2014.10.004

Wuyts, K., Verheyen, K., De Schrijver, A., Cornelis, W.M. & Gabriels, D. (2008). The impact of forest edge structure on longitudinal patterns of deposition, wind speed, and turbulence. *Atmospheric Environment, 42* (37), 8651–8660.

Yan, N. & Baas, A. C. W. (2015). Parabolic dunes and their transformations under environmental and climatic changes: Towards a conceptual framework for understanding and prediction. *Global and Planetary Change, 124,* 123–148. doi: 10.1016/j.gloplacha.2014.11.010

Yan, N. & Baas, A. C. W. (2017). Environmental controls, morphodynamic processes, and ecogeomorphic interactions of barchan to parabolic dune transformations. *Geomorphology, 278,* 209–237. doi: 10.1016/j.geomorph.2016.10.033

Yassemi, S., Dragicevic, S. & Schmidt, M. (2008). Design and implementation of an integrated GIS-based cellular automata model to characterize forest fire behaviour. *Ecological Modelling, 210,* 71–84.

Youssef, F., Visser, S. M., Karssenberg, D., Erpul, G., Cornelis, W. M., Gabriels, D & Poortinga, A. (2012). The effect of vegetation patterns on wind-blown mass transport at the regional scale: A wind tunnel experiment. *Geomorphology*, *159-160*, 178–188. doi:10.1016/j.geomorph.2012.03.023

Yue, W., Meneveau, C., Parlange, M. B., Zhu, W., van Hout, R. & Katz, J. (2007). A comparative quadrant analysis of turbulence in a plant canopy. *Water Resources Research*, *43*(5), 2–15. doi:10.1029/2006WR005583

Zekollari, H. (2016). A MATLAB function for 3-D and 4-D topographical visualization in geosciences. *Poster, European Geophysical Union Annual Conference, Vienna, Austria.*

Zhang, D., Narteau, C. & Rozier, O. (2010). Morphodynamics of barchan and transverse dunes using a cellular automaton model. *Journal of Geophysical Research: Earth Surface*, *115*(3), 1–16. doi:10.1029/2009JF001620

Zhang, D., Narteau, C., Rozier, O. & Courrech du Pont, S. (2012). Morphology and dynamics of star dunes from numerical modelling, *Nature Geoscience, 5,* 463–467. doi:10.1038 /ngeo1503

Zhang, J. G, Xu, X. W, Lei, J. Q, Li, S. Y, Hill, R. L.& Zhao, Y. (2013). The effects of soil salt crusts on soil evaporation and chemical changes in different ages of Taklimakan Desert Shelterbelts. *Journal of Plant Science and Soil Nutrition*, *13*(4), 1019–1028.

Zobeck, T. M., Sterk, G., Funk, R., Rajot, J. L., Stout, J.E. & Van Pelt, R. S. (2003). Measurement and data analysis methods for field-scale wind erosion studies and model validation. *Earth Surface Processes and Landforms, 28*, 1163–1188.

APPENDICES

Appendix 1: Supplementary Information (Paper 4)

Text 9.S1. Model verification: Vegetation patterning

Stable solutions

Under constant forcing conditions (ρ = constant), minor fluctuations that arise due to the probabilistic nature of the model result in a continuous slow adjustment of spatial patterning of shrubs, although the pattern type is always preserved (Figure 9.S1). There is good qualitative agreement between the simulated patterns and satellite imagery of vegetation patterning observed along a rainfall transect in Niger (Figure 9.S2). However, bistability is observed over a range of ρ ($30 \leq \rho \leq 190$ mm yr^{-1}), referred to as the 'bistable region'. Within the bistable region, the initial population (p_0) determines the patterning that is observed for any given ρ (Figure 9.S1). The transition to bistability is an important aspect of system behaviour to consider, since it provides information about the potential for population collapse to a lower state (Rietkerk et al., 2004; Kéfi et al., 2007). A difference in the present model compared to that of Bailey (2011) is that the stable population curve starting from $p_0 = 0$ (red squares) does not reconnect with the upper limb starting from $p_0 = 1$ (blue squares) until non-patterned full cover is achieved at $\rho \approx 190$ mm yr^{-1}. Instead of forming labyrinth-style patterns at intermediate precipitation levels, the growth of vegetation from an initially bare surface is relatively homogeneous. This results from the important control that drought stress plays on smaller, younger plants, which reduces the relative impact of neighbourhood interactions on their survival probability.

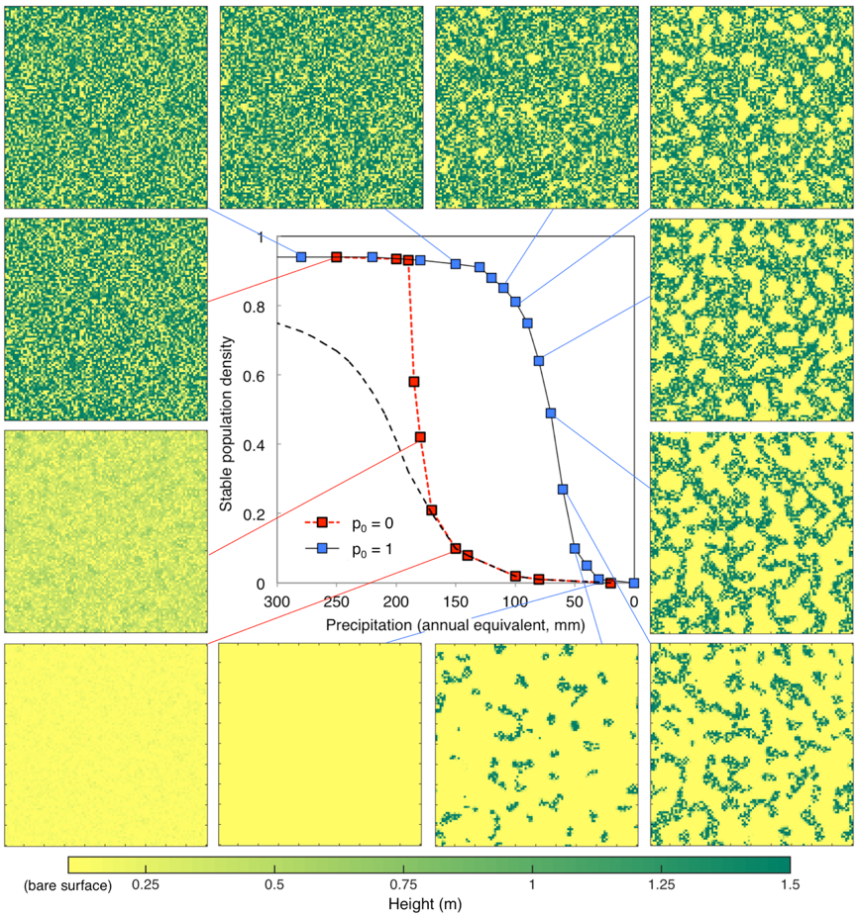


Figure 9.S1. Emergence of spatial vegetation patterning at different precipitation stress levels ($\boldsymbol{\rho}$), for shrubs. Central figure shows stable population density ($\boldsymbol{p_{eq}}$) at different $\boldsymbol{\rho_S}$ values, for two initial conditions: full cover ($\boldsymbol{p_0}$ = 1, blue squares) and bare surface ($\boldsymbol{p_0}$ = 0, red squares). Solid black line represents progressive vegetation degradation, whilst dashed red line represents recovery. Dashed black line shows $\boldsymbol{p_{eq}}$ for the case where all neighbourhood scores are neglected (i.e. the survival curve for lone cells). Stable patterns are shown for reference (100 x 100 cells), with yellow representing bare ground and darker green shades representing plants with greater height, to the level of full height/biomass maturity. Model was run at a resolution of 12 months (i.e. each iteration corresponds to 1 year of growth).

The modelled and observed landscapes in Figure 9.S2 can be quantitatively compared by analysing their patch metrics using FRAGSTATS (McGarigal et al., 2012), a spatial pattern analysis program designed for quantifying landscape structure. For this, the aerial photographs and the modelled landscapes were transformed into binary images (0 for unoccupied, 1 for occupied). White-balance thresholds for the photos were manually determined, whereas the minimum plant

age (i.e. 12 months) was used as a threshold for the model output. For all landscapes, FRAGSTATS analyses were run assuming the 4-neighbour rule, and several spatial statistical tests were performed (see definitions in Figure 9.S3).

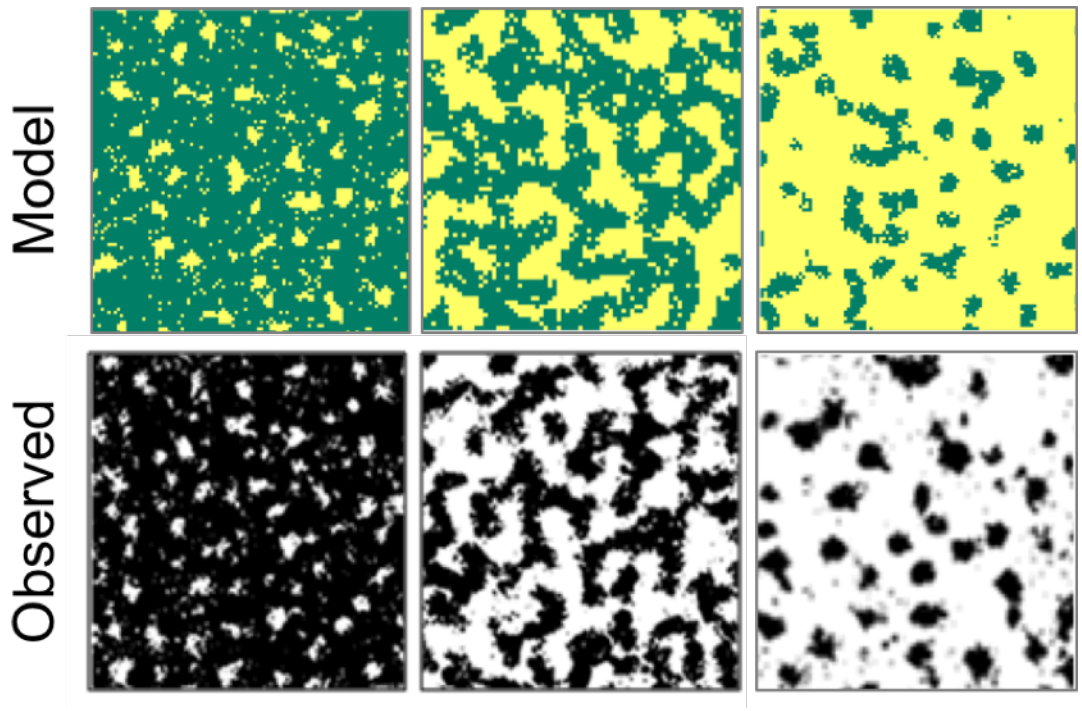
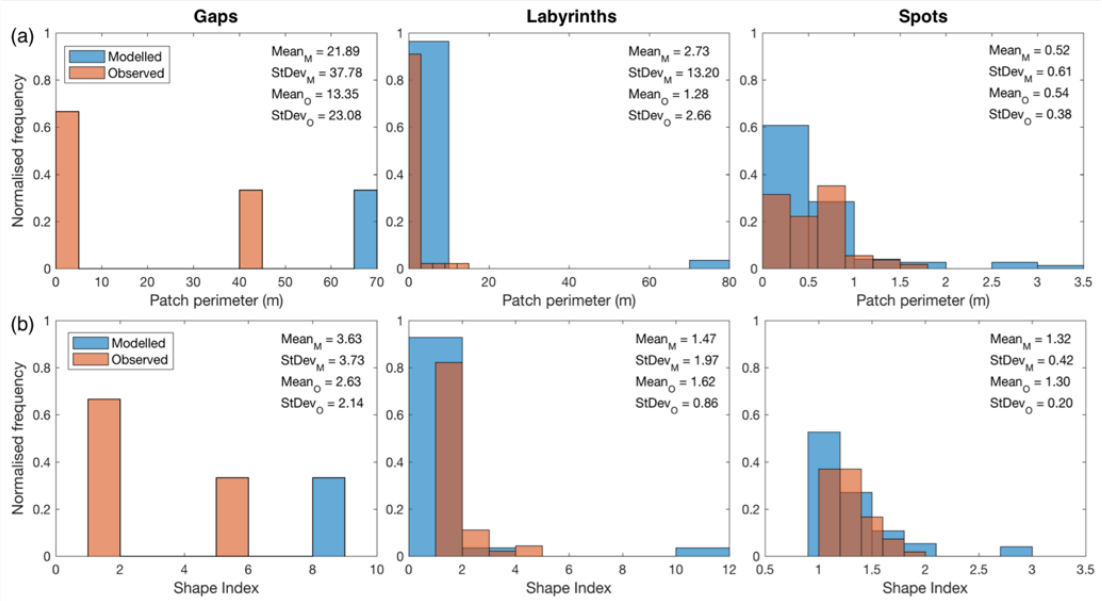


Figure 9.S2. Comparison of selected modelled vegetation patterning states and satellite imagery of semi-arid vegetation in Niger, captured by Bailey (2011) from Google Earth (v.5.1). Black colouring represents inferred vegetation and white colouring infers bare sediment. From left to right, satellite image locations are: 12°44'02" N, 3°05'40" E; 13°06'08" N, 2°13'19" E; 13°11'52" N, 2°00'15" E.

The number of patches, a simple measure of fragmentation extent, predictably increased from the 'gap' state to the 'spot' state, and was similar across modelled and observed landscapes, with the largest discrepancy in the 'labyrinth' state. Conversely, the Largest Patch Index (LPI) decreased from the gap state to the spot state, reflecting the increasing fragmentation of the vegetation. The mean Shape Index (SI), which provides a measure of the average complexity of patch shapes compared to standard (square) shapes of the same size, decreased from the gap state to the spot state in both the modelled and observed cases, implying that plant

patches become more homogenous in shape as the landscape fragments. The Aggregation Index (AI) again supports the notion that the degree of aggregation, or 'contagion' in ecological terms, decreases as the rainfall stress increases. The degree of aggregation was substantially higher in all three observed landscapes compared to the modelled landscapes. This difference may arise because AI is calculated based on cell adjacencies, and the binary threshold for the photographs likely resulted in very small gaps within patches to be counted as vegetated, whereas bare and vegetated cells can be distinguished perfectly in the model.



	Number of Patches (NP)		Largest Patch Index (LSI) (%)		Aggregation Index (AI) (%)	
	Modelled	Observed	Modelled	Observed	Modelled	Observed
Gaps	3	3	84.6	88.8	91.3	99.4
Labyrinths	28	45	46.6	21.8	85.1	98.4
Spots	74	63	1.84	1.41	74.6	96.4

Definitions of spatial statistics

- Perimeter: Perimeter (m) of the patch, including any internal holes in the patch.
- Shape Index: Patch perimeter (m) divided by the minimum perimeter possible for a maximally compact patch (i.e. a square).
- Largest Patch Index: Area of the largest patch (m^2), as a proportion of the total landscape area.
- Aggregation Index: Degree to which occupied cells are clumped into a single compact patch.

Figure 9.S3. (a) Normalised frequency distributions of patch perimeter lengths for all patches identified using FRAGSTATS from the modelled and observed landscapes in Figure 9.S2, divided according to patterning type. Mean and standard deviations for the distributions are also shown; (b) Normalised frequency distributions of the Shape Index (see definitions) for all patches identified using FRAGSTATS from the modelled and observed landscapes, divided according to patterning type. Table shows other FRAGSTAT-derived indices (see definitions) for the modelled and observed landscapes shown in Figure 9.S2.

Neighbourhood interactions

Verifying spatial neighbourhood interactions that are integrated into Module 1 is important, because these determine the balance of facilitation and competition that individual plants are subjected to, and thus affect the development of patterning. Figure 9.S4 displays the distribution of $\tilde{T}$ across a model domain that has been initialised with single isolated spots or gaps of various sizes. When an isolated spot is small (e.g. 6 x 6 cells), the 5-shell interaction zones for each individual plant in the spot combine to produce a zone of higher competition around its immediate edge. As the spot size increases, 'hotspots' of even more intense competition begin to appear in zones where opposing facilitation from corner cells is not as strong. Values of $\tilde{T}$ within the spot itself remain constantly high due to inter-plant facilitation, and as expected this does not change despite any change in spot size. In the gap case, a small gap results in a very low value of $\tilde{T}$ in its centre, which shifts to the outer corners of the gap as the gap size increases, due to the influence of a higher number

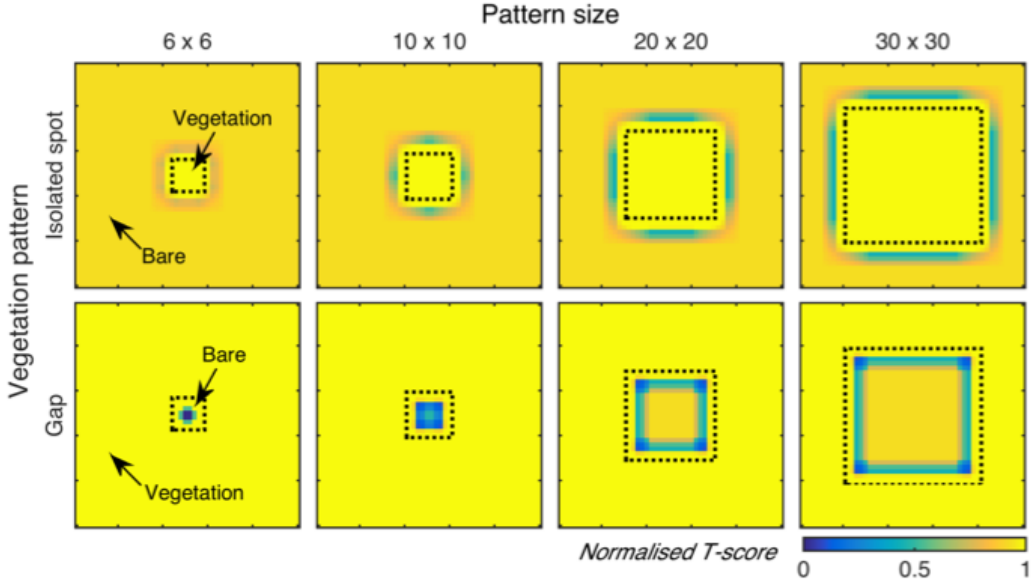


Figure 9.S4. Neighbourhood interactions (i.e. normalised T-score) for isolated spots and gaps of differing sizes, in grid cell units. A spot represents a patch of vegetation on an otherwise bare surface, whereas a gap represents a patch of bare ground amongst an otherwise vegetated surface (as shown by labelled arrows). The edge of the spot/gap in each panel is shown as a dotted black line. Model was run on a 50 x 50 grid, and precipitation was set at a constant $\boldsymbol{\rho}$ = 300 mm yr^{-1}.

of competing cells having an effect from the vegetated zone. As gap size increases, the value of $\tilde{T}$ remains constant at the centre of the gap, because there is no longer any competition from vegetated cells at the edge of the gap.

The influence of biomass on neighbourhood interactions is illustrated in Figure 9.S5. By initialising the model with an isolated spot of uniform biomass (or height), and then varying the incoming precipitation, it is possible to isolate the different mechanisms that contribute to the value of $\tilde{T}$ (i.e. plant-plant interactions and precipitation stress, ρ). When the biomass of each plant in the patch is low (12), there is no discernible neighbourhood impact from the patch itself; the stress from precipitation dictates the $\tilde{T}$ value across the entire domain. As the biomass of the

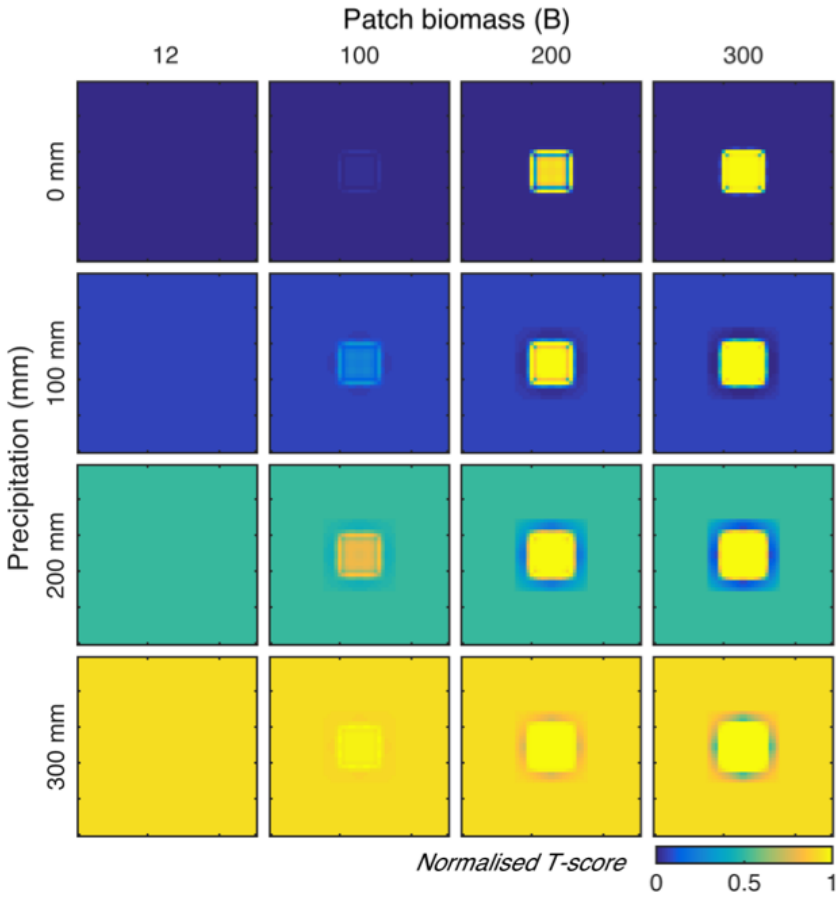


Figure 9.S5. Influence of plant biomass (linearly related to height) on neighbourhood interactions (i.e. normalised T-score), at different precipitation levels. Model was initialised with a 10 x 10 patch of vegetation at the centre of a 50 x 50 grid, with varying uniform plant biomass within the patch ($\boldsymbol{B}$ = 12–300, with 300 representing B_{max} in the model).

plants in the patch increases, the impact of the patch on its members (large net facilitation) and on the cells immediately adjoining the patch (large net competition) becomes more evident. The starkest difference between cells adjoining the patch and those within it occur when patch biomass is highest (300) and at intermediate precipitation levels (100–200 mm yr^{-1}).

Figure 9.S6 displays population decline curves when dead vegetation cells are not permitted to regrow in the model, for different initial uniform ages. A grid initialised with old plants (500 months) experiences dramatic population decline, as all plants experience senescence. At intermediate ages (200–300 months), the plants experience lowest probability of death, resulting in an initially quasi-stable population for the first ~10 years, before surviving plants begin to senesce again. When the grid is initialised with very young (<100 months) plants, an initial population decline is observed, as younger plants have a higher probability of death than plants of intermediate ages. However, as the surviving plants continue to mature and thus become most resilient, death rates decline and population stabilised around 20–30 years into the runs. By ~50 years, most plants in all runs have died due to the natural limits on their survival.

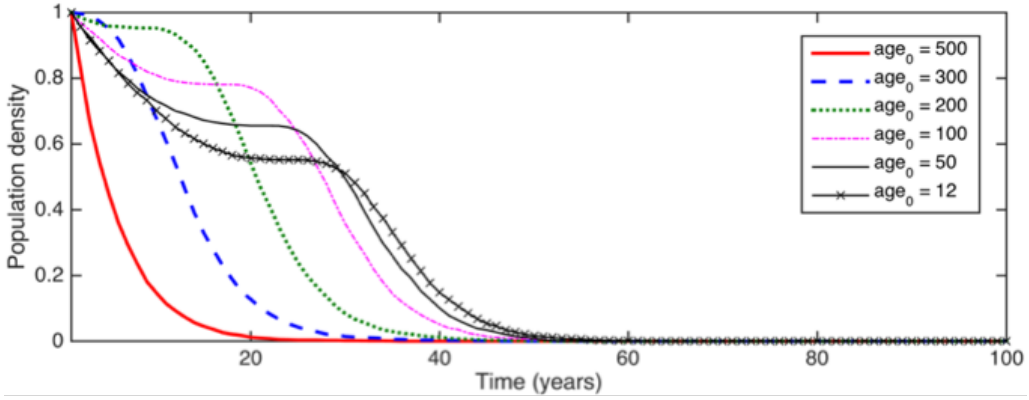


Figure 9.S6. Impact of initial uniform vegetation age (age_0, in months) on population decline trajectories, when dead cells are not permitted to regrow in the model. Model was run on a 100 x 100 m grid with a constant precipitation, ρ = 300 mm yr^{-1}, and initialised with an initial population density p_0 = 1.

Impact of stresses

In order to verify the effect of sediment balance stress (Sed_S) on plant mortality and thus vegetation patterning, the coupled model was initialised with three scenarios: no sand, a 2 m-deep patch of sand in the centre of the domain, and a uniform sand depth of 2 m (Figure 9.S7). Wind was permitted to transport sediment if it was present. When the domain was initialised with no sand (top row), isolated spots formed randomly, since there was no variability in sediment stress across the surface. In the patch case, vegetation was maintained along the downwind edge of the sand accumulation, as small positive changes in sediment balance promote grass growth. Upwind of the patch, where sand tends to be winnowed away, the negative sediment balance led to a higher plant mortality rate. In the run with uniform vegetation height of 2 m, the build-up of sand at the upwind edge of the domain (resulting from the relatively small size of the grid) was much greater than on bedforms further downwind, which led to lower vegetation growth on the crest of the large dune. Plant growth was lowest in zones of net erosion (such as interdunes), due to higher mortality rates linked to nutrient and water loss.

Text 9.S2. Model verification: Wind/transport dynamics

Shadow zones

A flow separation zone is included in the ViSTA model by eliminating all transport in the lee of topography, where the angle between the surface and the point of highest elevation along the wind path is greater than a given angle (the 'shadow zone'). Figure 9.S8 shows the effect of varying the maximum angle at which shadowing occurs on morphology. At low angles (1^o and 5^o), large ridges tend to develop across

the domain, with little transport in the large lee leading to the formation of low-topography, 'washed out' forms. At higher angles (45° and 90°), the resultant landscape is composed of a series of closely spaced, spiky ridges controlled solely by the angle of repose and values of p_d. In previous CA models (e.g. Werner, 1995; Momiji et al., 2000; Baas & Nield, 2007), shadow zones have been assumed to occur on slopes greater than 15°, and the simulations in Figure 9.S8 show that a 15° angle produces realistic dune forms in the context of the ViSTA model.

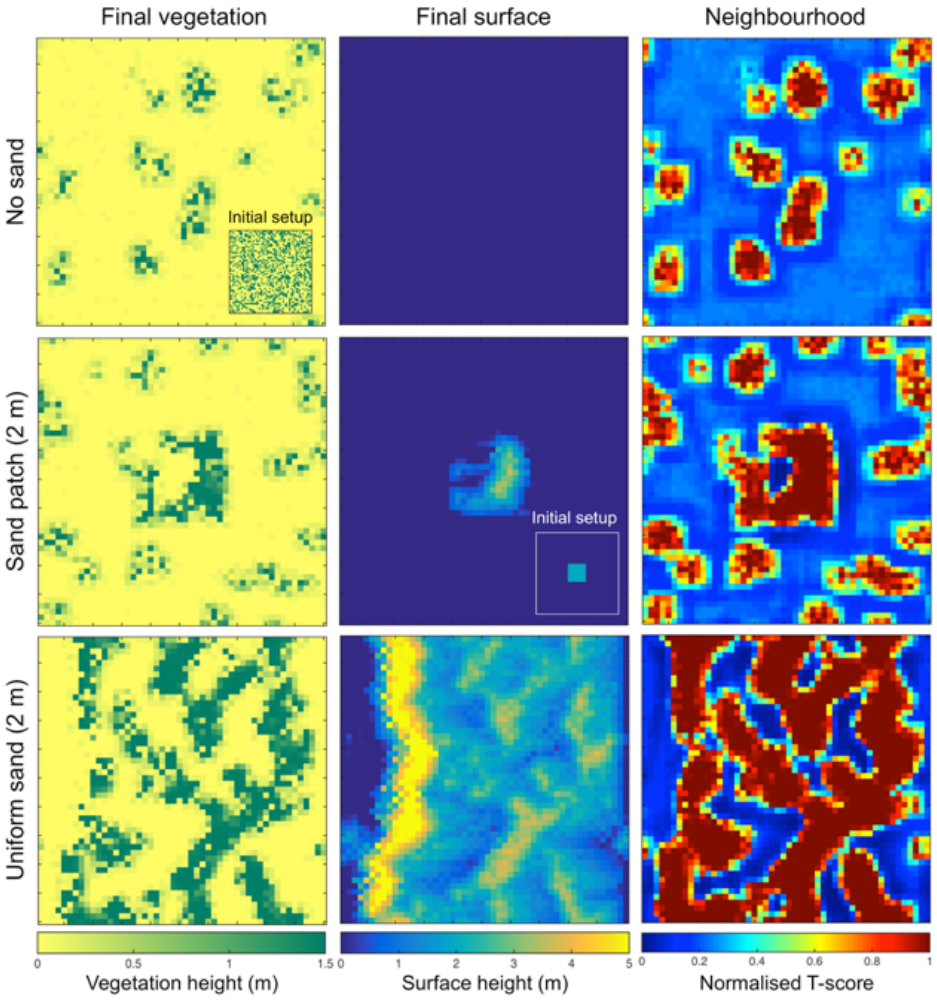


Figure 9.S7 Effect of sediment balance stress (Sed_S) on vegetation growth, as illustrated by initialising the model with different sand surface configurations. Panels show final vegetation heights and sand surface at the end of each model run. Model was run for 100 iterations (1 iteration = 12 months of vegetation growth and 3000 minutes of wind at 7 m s^{-1}, with threshold wind velocity = 6 m s^{-1}) over a grid of 50 x 50 m, with constant precipitation (ρ = 150 mm yr^{-1}) and random initial vegetation cover of 50% (p_0 = 0.5) (as shown in inset). Top row presents results from a run initialised with no sand, middle row with a 10 x 10 m patch of sand of 2 m depth (as shown in inset), and bottom row with a uniform sand depth of 2 m.

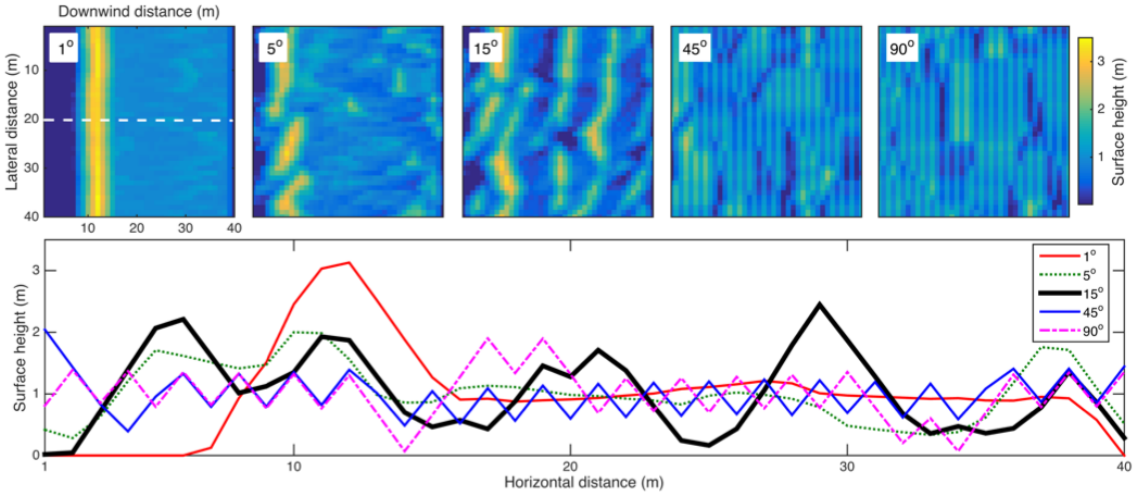


Figure 9.S8 Simulated morphology developing from different maximum angles at which shadowing (i.e. the elimination of transport) occurs; transport direction is from left to right. An angle of 90° effectively represents the absence of shadow zones. Top sequence displays the end-point of each model run after 300 iterations (1 iteration = 3 hours of constant wind at 7 m s^{-1}; threshold wind velocity = 6 m s^{-1}), over a grid of 40 x 40 m at a uniform initial depth of 1 m. Line plots represent transects along the centreline of each model grid (as shown using the dotted white line in top left panel).

Wind direction and recovery

In order to test the possibilities of varying wind direction and recovery within the ViSTA model, the model was run with single vegetation elements with differing characteristics. Figure 9.S9 displays the model's ability to vary the approach angle of the wind to a high degree of precision, with a plant inserted in its path to demonstrate the direction of flow recovery. This allows great versatility for modelling a multi-directional wind regime at both the local and regional scale.

The porosity of individual plants can be altered to simulate the impact of a heterogeneously populated landscape. Figure 9.S10 shows the impact of altering the porosity of vegetated cells on the recovery of wind velocity downwind of an individual vegetation patch. At low porosities (0–20%), the minimum mean wind velocity in the body of the plant and in its immediate lee (u_0) was lower than at greater porosities, as formulated in Equation 8.27. Wind flow recovery was also slower at lower

porosities, resulting in more extensive wakes. At 0% porosity, the wake of disturbed flow extended almost 25 h_d, whereas at 80% it only extended 2–3 h_d. 100% porosity effectively represents the absence of a plant, which explains the completely undisturbed flow in this panel.

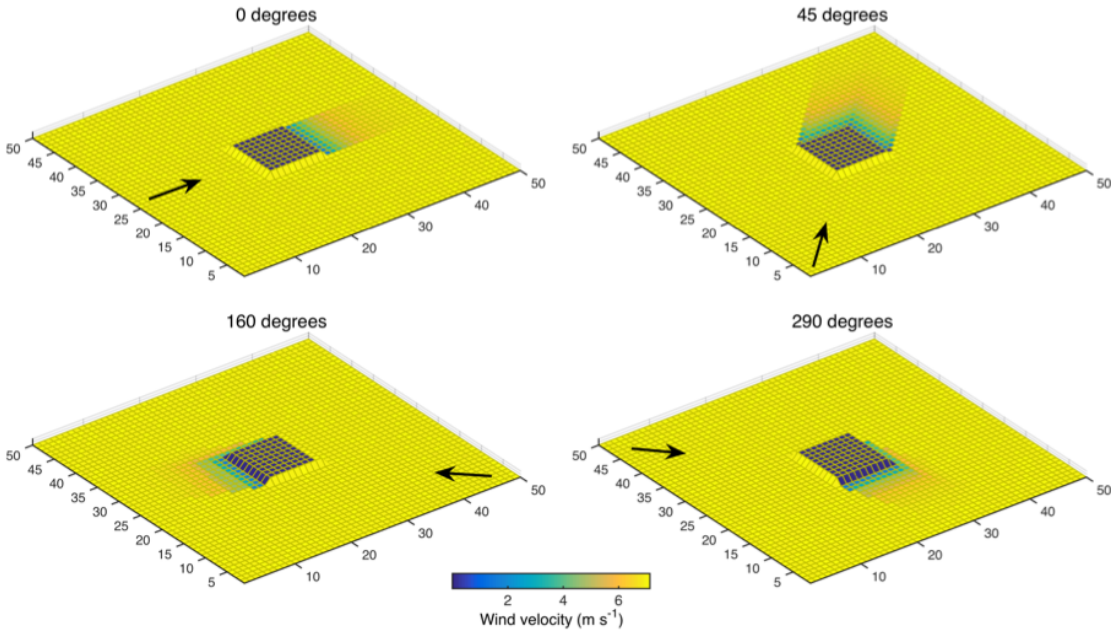


Figure 9.S9 Examples of wind direction variation across the model domain. A static plant (10% porosity) of 2.0 m height was placed in the wind path to highlight the changing direction of the wind recovery shadow in its lee. Black arrows show approach wind angle. Stochasticity was removed from the wind velocity algorithm for these runs.

Figure 9.S11 shows the interaction of two plant wakes, with a smaller patch (20% porosity) located in the wake of a larger patch (40% porosity). The upwind element reduces wind speed through its plant body, which then partially recovers to approximately two thirds of the unobstructed wind velocity, before flow interacts with the downwind element and declines to zero velocity through the patch (Figure 9.S11c). Finally, the flow velocity recovers exponentially, as expected for an unobstructed wake zone.

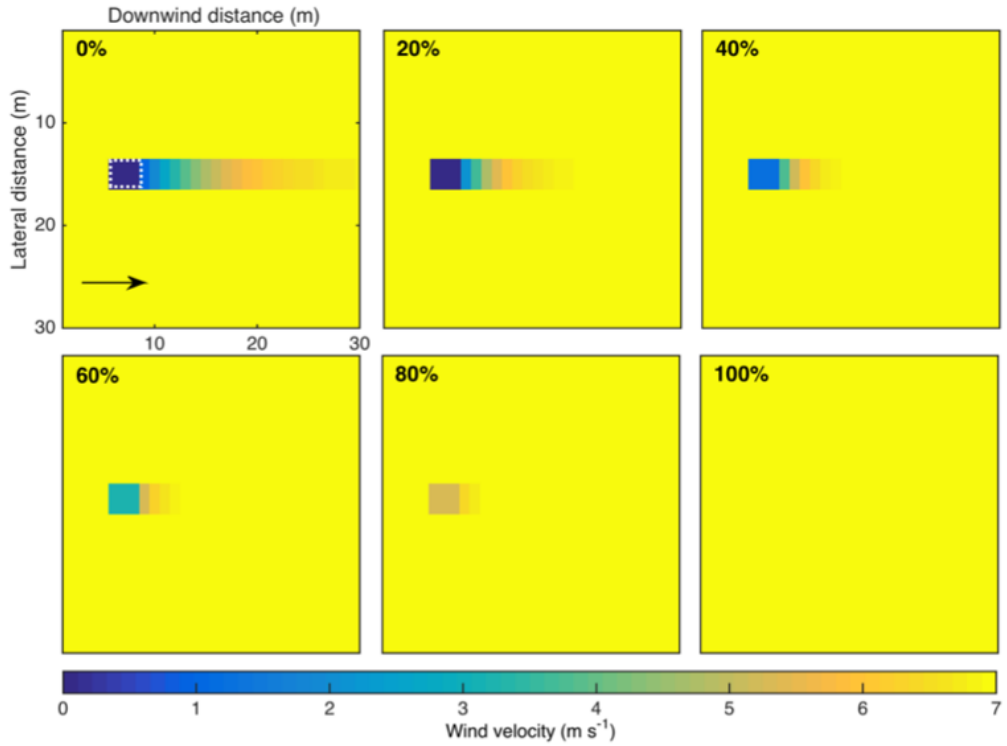


Figure 9.S10 The effect of vegetation porosity on the recovery of wind velocity downwind of a vegetation patch of 1.0 m height. Black arrow shows approach wind angle and the location of the vegetation patch is shown by the dotted white square in the top left panel. Stochasticity was removed from the wind velocity algorithm for these runs.

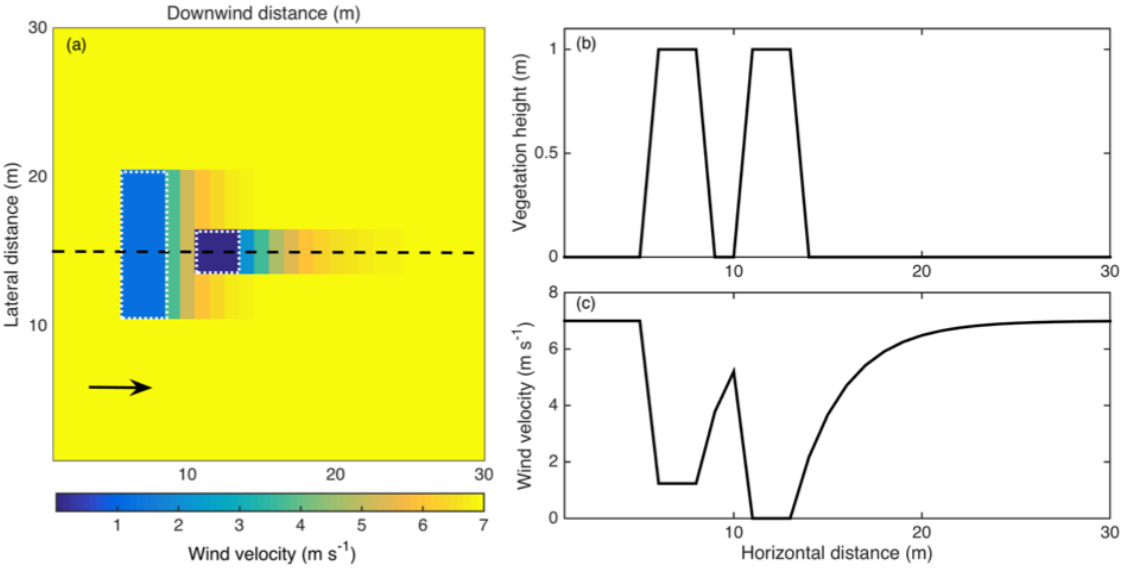


Figure 9.S11 (a) Wake interactions between vegetation patches. A smaller vegetation patch (20% porosity, 1.0 m height) was placed in the wake of a wider vegetation patch (40% porosity, 1.0 m height). Black arrow shows approach wind angle and the locations of the vegetation patches are shown as dotted white rectangles; (b) vegetation height and (c) wind velocity transects taken along the centreline of the model grid (shown as dotted black line in panel (a)). Stochasticity was removed from the wind velocity algorithm for these runs.

Figure 9.S12 displays wind flow recovery transects in the lee of trees of different crown/trunk configurations. The maximum speedup in the lee of Tree 1 is lower than in the lee of Tree 2 and 3, because its lower-lying canopy diverts wind away from the underside of the canopy, thus reducing the 'bottom gap' effect. Trees 2 and 3 experience the same speedup magnitude due to their similarly sized trunks, but the larger canopy in the case of Tree 2 results in a slower recovery back to the upwind wind velocity.

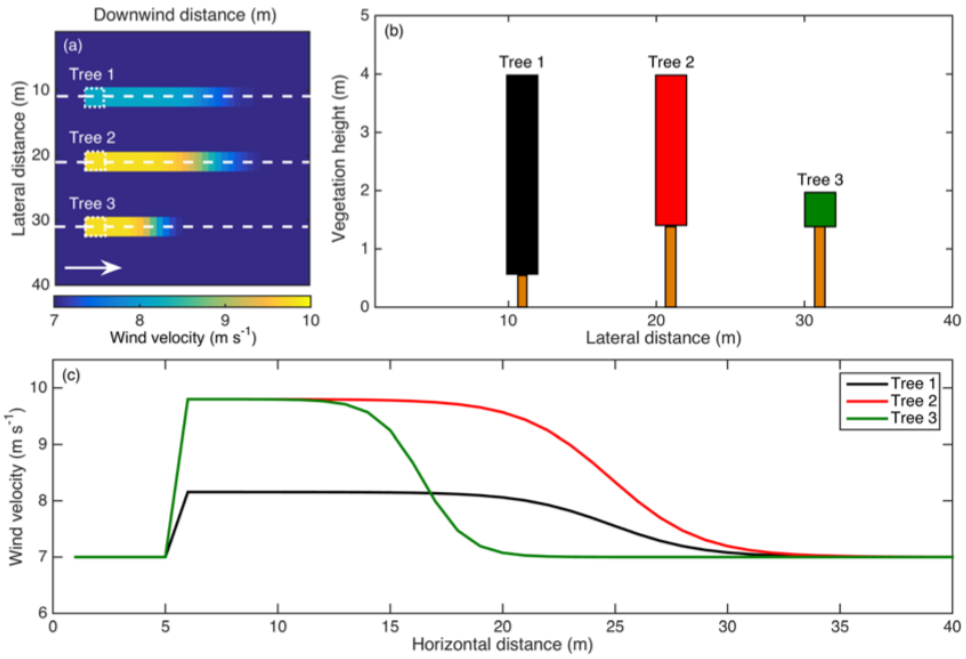


Figure 9.S12 (a) Wind recovery downwind of three trees with different characteristics: Tree 1 (trunk height: 0.5 m, crown height: 3.5 m), Tree 2 (trunk height: 1.5 m, crown height: 2.5 m), Tree 3 (trunk height: 1.5 m, crown height: 0.5 m). White arrow shows approach wind angle and the locations of the tree crowns are shown as dotted white rectangles; (b) frontal view of trunk and crown heights of the trees; (c) wind velocity transects taken along the centreline of the model grid (shown as dashed white lines in panel (a)). Stochasticity was removed from the wind velocity algorithm for this run.

Probability of deposition

Previous sediment transport models (e.g. Bishop et al., 2002; Baas & Nield, 2007; Nield & Baas, 2008a,b) have formulated the deposition process in such a way that the entire eroded sediment volume from one source cell is deposited into a single,

probabilistically derived sink cell. In contrast, the eroded sediment volume from each source cell in the ViSTA model is distributed proportionally along a cumulative probabilistic deposition path. This avoids situations where eroded sediment travels across the entire grid in a single iteration (as was theoretically possible in previous models), and thus prevents sediment from arbitrarily bypassing pattern formation mechanisms. However, the proportion of sediment being deposited along each deposition path in the ViSTA model is affected by: (i) the the p_d values for bare and sand surfaces (which are set in the model at 0.4 and 0.7 respectively, based on extensive preliminary testing and the models of Bishop et al. (2002) and Nield & Baas (2008a,b); and (ii) the maximum number of cells that moving sand is permitted to travel downwind from its source cell.

Since the deposition of sand slabs in the ViSTA model occurs proportionally along deposition paths, individual slabs are prevented from travelling unrealistically large distances across the domain (which is theoretically possible in previous CA models of sand transport). This prevents upper-stage planar bed behaviour from occurring, as noted by Nield & Baas (2008a) in their model for very low p_d values. However, it is important to balance the computational efficiency of setting a low maximum potential travel distance with the physical reality of how far a saltation cloud can travel over a given time interval. Figure 9.S13 displays the impact of changing the maximum potential travel distance of a sand slab on surface development. Low potential travel distances (1 or 2 cells, Figure 9.S13a,b) result in slower bedform evolution, and over longer time periods this restricts the ability for system dynamics to develop. As the maximum potential travel distance increases, the resultant bedform has virtually the same dimensions from 4 to 20 cells (Figure 9.S13h). Therefore, the maximum potential travel distance of a slab can be set at 4 cells in this setup to reduce computational expense.

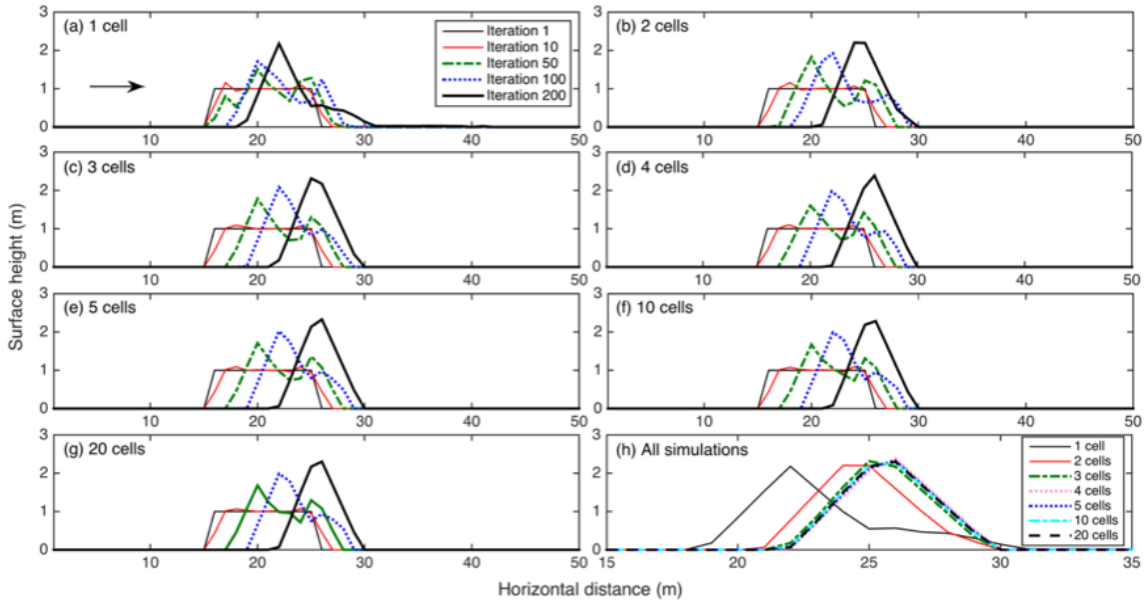


Figure 9.S13 (a–g) The impact on surface evolution of changing the maximum number of cells a sand slab can travel downwind of its source cell. Surface height plots represent transect along the centreline of a model grid of 50 m x 50 m with a 1 m-high rectangular block of sediment across the domain. Model was run for 200 iterations (1 iteration = 3 hours of constant wind at 7 m s^{-1}; threshold wind velocity = 6 m s^{-1}). Transport from left to right (as shown by the arrow in panel (a)); (h) Comparison of final surface morphology after 200 model iterations, for all runs (note that x axis is shortened to allow for closer examination of bedform details).

Moisture effects

Moisture has been shown to play an important role in initiating the development of transient sand strips and protodunes at event-based timescales (Nield, 2011). After rainfall, the top few mm (termed the 'active layer' for aeolian transport) of sandy soils tends to dry completely within half a day (Ravi et al., 2006; Okin, 2016). Furthermore, Okin's (2016) reanalysis of global dust models suggests that the probability of an above-threshold wind event occurring during the period after a rain event where the surface is wet is small (< 2%). Therefore, over short (< 24 hour) timescales, the ViSTA model incorporates a surface moisture feedback similar to that of Nield (2011), which does not affect sediment transport over timescales longer than a day. The feedback is therefore irrelevant to model runs run at coarse (daily or greater) resolutions. Figure 9.S14 displays final surface heights 24 hours after a rain event,

given different timescales over which the feedback cycle was permitted to operate, and different resolutions represented by each feedback cycle. When the feedback cycle was short (i.e. surface moisture was re-evaluated every model iteration), increasing the resolution of each cycle from 1 to 6 hours resulted in increasingly large patches of mobile, dry sediment. However, once the resolution increased to 12 or 24 hours, the time available for the feedback function to supply erodible sediment was reduced, leading to a largely non-mobile surface. For longer feedback cycles (i.e. surface moisture re-evaluated every 5–10 model iterations), more sediment transport could occur between surface moisture updates. This disrupts the sedimentation function relationship, leading to increased volumes of eroded/deposited sediment in the landscape compared to the short feedback cycle (particularly at the 12–24 hour resolutions), and forcing large changes in surface moisture.

It should be noted that the update resolution can easily be changed in the model setup, to reflect the scale of investigation required, and that the resolutions used to create Figure 9.S14 are merely given as an example. For instance, the formation of mm-scale sand strips require update resolutions on the scale of seconds/minutes (Nield, 2011).

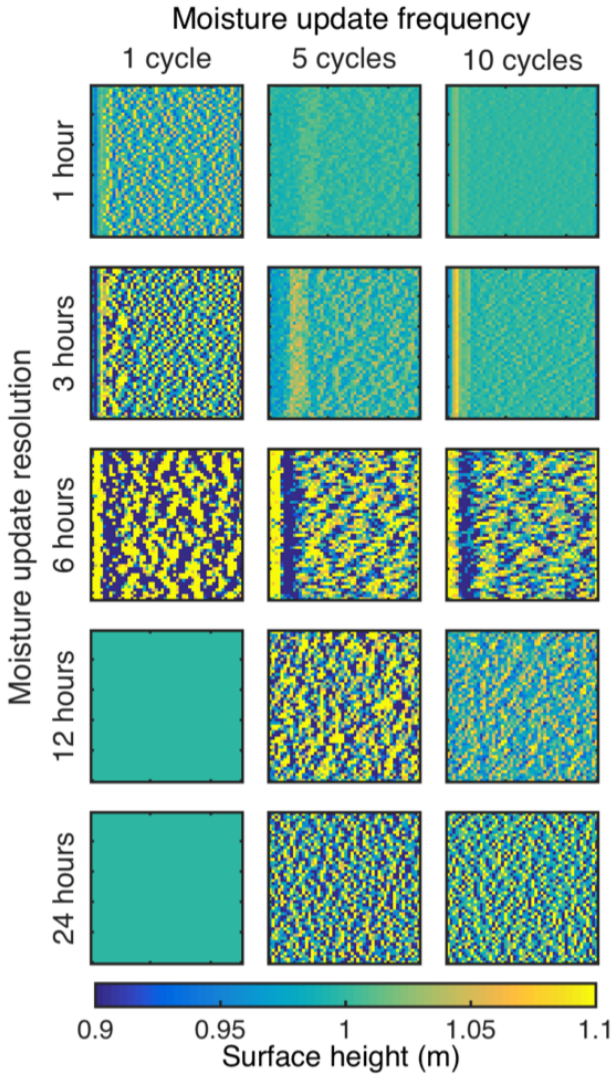


Figure 9.S14 Simulated surface height 24 hours after a rain event, with different moisture feedback update frequencies (i.e. every 1, 5 or 10 iterations of the sediment transport module) and different update resolutions (e.g. '1 hour' indicates the condition where each moisture update represents 1 hour of real time in the model). Model was run over a grid of 50 m x 50 m at a uniform initial depth of 1.0 m with no vegetation, and with constant wind velocity of 10 m s^{-1} (threshold wind velocity = 5 m s^{-1}). Transport direction from left to right.

Sediment supply

In bare-sand and vegetated dune systems with unidirectional winds, an increase in sediment supply is known to influence the morphology of resultant dunes (Wasson & Hyde, 1983; Langford, 2000; Bishop et al., 2002; Nield & Baas, 2008a). The sediment supply can be controlled by altering both the initial sediment volume within

the system (since it is a closed system with no external sediment sources), as well as the initial vegetation distribution (Nield & Baas, 2008a). Figure 9.S15a illustrates dune patterning evolution as the initial sediment base (i.e. supply) is increased, with the same initial vegetation distribution (20% cover). Low sediment supply results in the formation of isolated patches of sand or barchanoid dunes, whereas a more connected dune system tends to form in conditions of higher sediment supply. When the sediment base is 3.0 m deep, the volume of available of sand precludes the formation of recognisable dune forms over 300 iterations due to the lack of difference in deposition probabilities across the model domain. A larger model grid size would likely improve the sensitivity of the model to different deposition probabilities.

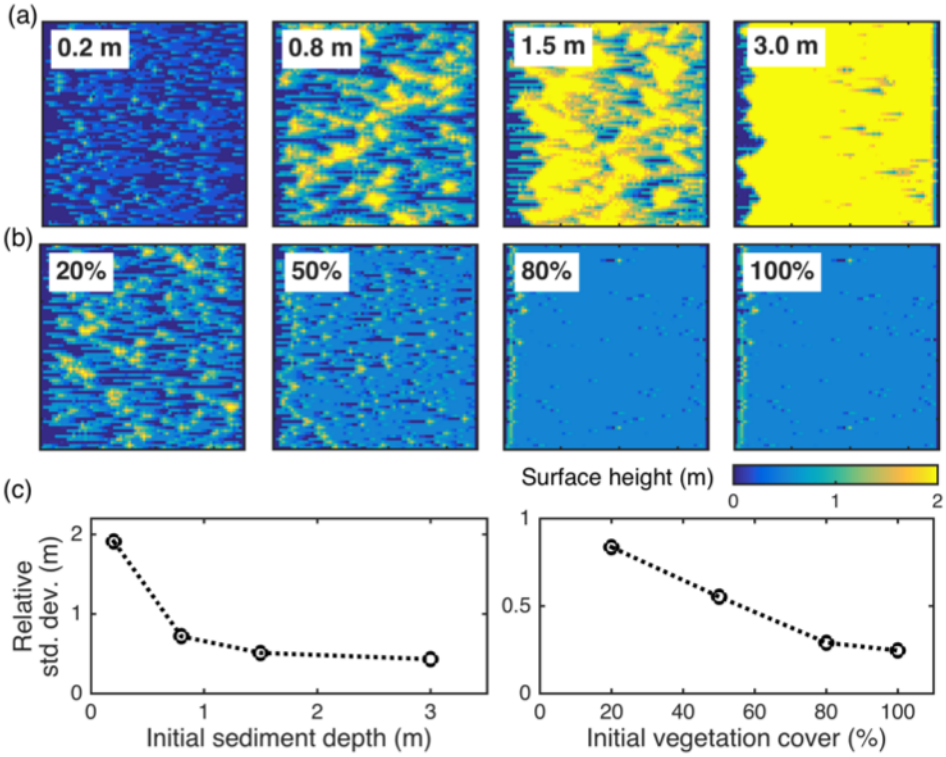


Figure 9.S15 (a) Simulated morphology evolving from varying the sediment depth from 0.2 m to 3.0 m, with a fixed vegetation cover of 20%; (b) Simulated morphology evolving from varying vegetation cover from 20% to 100%, with a fixed sediment depth of 0.5 m. Model was run over a grid of 100 m x 100 m for 300 iterations (1 iteration = 300 hours of constant wind at 7 m s^{-1}; threshold wind velocity = 5 m s^{-1}). All vegetation elements had a fixed porosity of 30%. Transport direction from left to right; (c) Relative standard deviation of the surface heights for each resultant morphology shown in (a) and (b), according to initial sediment depth or initial vegetation cover.

Figure 9.S15b shows how increasing initial vegetation cover decreases the effective supply of sediment to the system, which in turn results in little or no bedform development. In contrast, at relatively low cover, individual plants trap mobile sediment to produce a nebkha-type landscape, as supported by field observations of vegetated dune fields (e.g. Hugenholtz & Wolfe, 2005; Okin et al., 2006). The relative standard deviations of the surface heights for the resultant morphologies (Figure 9.S15c) indicates that landscape heterogeneity decreases as initial sediment depth or vegetation cover are increased.

Spatial scaling

The spatial scale of the ViSTA model can be altered by modifying the representative size of a cell. For the vegetation module (Module 1), changing the cell size alters the typical length scale of emergent vegetation patterns (Figure 9.S16). For small cell sizes (0.4–0.7 m), individual vegetation spots coexist closely (in absolute terms) to their neighbours, such that spots and inter-canopy gaps are 10^{-1}–10^{0} m in size. At intermediate spatial resolutions (1–2 m), emergent spots of vegetation are 10^{0}–10^{1} m in size, which is on the order of those commonly observed in drylands (e.g. Rietkerk et al., 2004). At the largest cell sizes (5–10 m), very large, single spots emerge, akin to vegetation patches up to 10^{2} m in diameter. At this scale, the granularity of patterning is lost. These fundamental variations in length scales of arise because plant-plant interactions in the model are formulated using a fixed five-shell neighbourhood, which does not change according to the cell size. Intermediate cell sizes of ~1 m appear to best represent amalgamations of individual plants.

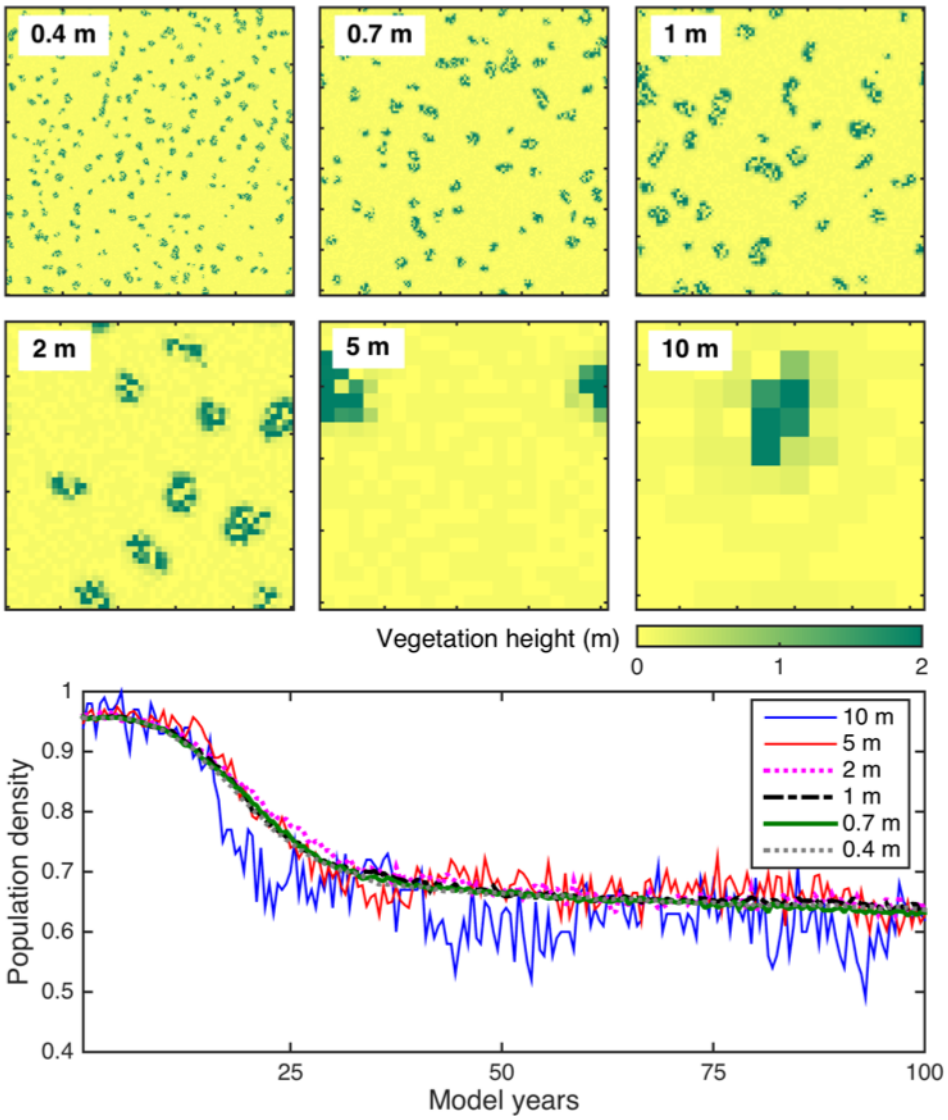


Figure 9.S16 Simulated patterning for different spatial grid resolutions of the vegetation module (Module 1). Model was run with cell sizes ranging from 0.4 m to 10.0 m, with a fixed annual rainfall of 90 mm yr^{-1} and an initial vegetation cover of 90%. Model was run over a grid of 100 m x 100 m for the equivalent of 100 years, with each model iteration representing 6 months of growth time. Line plot shows plant population density within the model domain over time.

Text 9.S3. 'Fingering' and 'bed instability' modes

When considering a bidirectional flow regime, Rubin & Hunter (1987) introduced the gross bedform-normal transport rule (GBNR), based on observations that bedforms select the orientation for which the sum of the normal-to-crest components of the two transport vectors is maximised. Together with the dune-type classification of Pye &

Tsoar (1990) and others, the GBNR rule suggests that a given wind regime should be associated with a specific dune shape and a single orientation (Kocurek & Ewing, 2005; Fenton et al., 2014). However, field observations (Courrech du Pont et al., 2014) and numerical modelling experiments (Gao et al., 2015b; Lucas et al., 2015) have challenged this concept. Courrech du Pont et al. (2014) demonstrated that sediment availability not only controls dune type, but also the underlying dune growth mechanism and the subsequent dune orientation. Courrech du Pont et al. (2014) proposed two modes for dune orientation: (i) the 'bed instability' mode, whereby dunes on an erodible sand bed grow in height and migrate selecting an orientation that maximises the normal-to-crest components of transport (cf. Rubin & Hunter, 1987); and (ii) the 'fingering' mode, whereby dunes grow by extending away from a localised sediment source in the direction of the resultant sand flux at the crest.

In support of the existence of these modes, Gao et al. (2015b) numerically modelled the development of bedforms in bidirectional wind regimes for an erodible sand bed (bed instability mode), as well as for a localized sand source on a non-erodible surface (fingering mode). By plotting the parameter space for resulting bedforms, Gao et al. (2015b) demonstrated that only linear dunes developed over an erodible bed in a bimodal regime, with the divergence angle and the transport ratio between the two winds controlling dune orientation and dynamics. However, when dunes developed from a localised source of sediment, either finger linear dunes or barchans emerged, depending on the wind regime.

Following the approach of Gao et al. (2015b), two types of experiments were conducted using Module 2 of the ViSTA model, in order to verify the emergence of the two hypothesised modes for dune formation. The first set of experiments reflected conditions of high sand availability: a flat sand bed with a thickness larger than the flow depth to ensure that bedforms never reached the non-erodible ground

at the bottom of the domain, and periodic boundary conditions. The second set of experiments, reflecting low sediment availability, were run with a rectangular (5 x 5 m) source of sediment of 0.5 m height, located upstream of a non-erodible surface with open boundary conditions (i.e. allowing sediment to be lost from the edges of the domain). The diameter and height of the source were determined through trial and error, as simulation results are relatively sensitive to source dimensions (Narteau, pers. comm, 2016). The source dimensions were kept constant at the start of all model iterations, in order to replace any cells that had been transported away. This meant the input flux was not fixed, but rather adapted to experimental conditions (cf. Gao et al., 2015b). For the two conditions of sediment availability, the wind transport capacity was kept constant, but the direction and the duration of the secondary winds varied across simulations. The bidirectional wind regimes reported here are characterised by the divergence angle θ_D (the difference in angle between the primary and secondary winds), and the transport ratio N:

$$N = \frac{\Delta T_N}{\Delta T_1} \tag{9.S1}$$

where ΔT_N is the time spent in the primary wind over a period of wind reorientation and ΔT_1 is the time spent in the secondary wind (i.e. $N \geq 1$). The initial conditions and parameters of the bidirectional regimes for all the simulations are shown in Table 9.S1.

Figure 9.S17a displays steady-state dunefield morphology in the parameter space $\{\theta_D, N\}$ of bidirectional wind regimes in different sediment availability conditions. When bedforms grow from a flat surface with an unrestricted sediment supply, the bed instability mechanism systematically leads to the establishment of dunes aligned

in one principal direction, which then grow in height through pattern coarsening. For θ_D < 90°, the primary and secondary winds blow from the same side of the dune and thus create linear transverse dunes with gentle upstream slopes (cf. Zhang et al., 2010; Gao et al., 2015b). For θ_D > 90°, winds blowing from alternative sides of the dunes means that the slip constantly switches from one side to another. This results in less distinct dunefield wavelengths with steeper slopes. As noted by Gao et al. (2015b), the alignments and features that develop in the bed instability mode are in agreement with the GBNR.

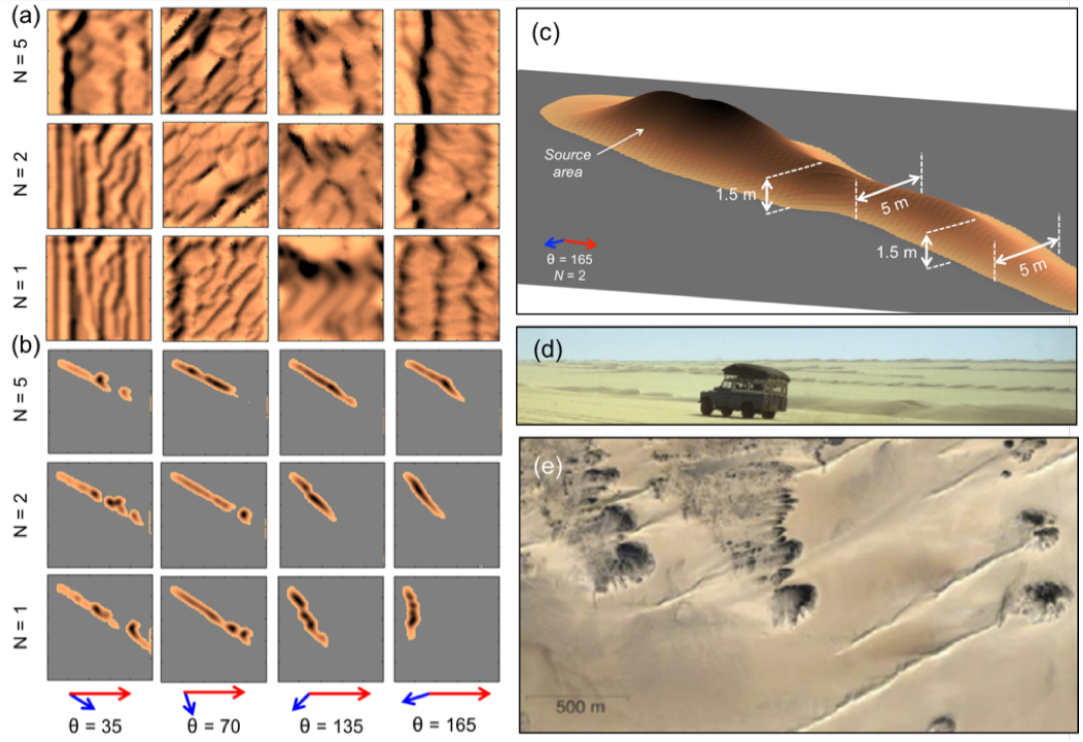


Figure 9.S17 Simulated dune morphologies in the parameter space $\{\theta_D, N\}$ of bidirectional wind regimes for two conditions of sediment availability: (a) a flat bed with no restriction in sediment availability; and (b) a localised sand source (5 x 5 x 0.5 m) on a non-erodible surface. Red and blue arrows show the sand flux vectors of the primary and secondary winds, respectively. In all cases, the model was run over a 100 x 100 m grid with no vegetation, over the number of iterations specified in Table S2 (1 iteration = 300 hours of constant wind at 7 m s^{-1}; threshold wind velocity = 5 m s^{-1}); (c) oblique view of a finger dune resulting from a bimodal wind regime (θ_D = 165°; N = 2), showing constant height and width downwind of the source area; (d, e) Elongating dunes in the Erg of Fachi-Bilma, Niger (16°52'00" N, 13°20'00" E), growing from the lee slope of residual hills, with well-defined width and height extending over tens of kilometres (adapted from Lucas et al., 2015, p.1028).

When bedforms develop from a localised sand source (Figure 9.S17b), relatively straight finger dunes develop over a range of divergence angles for certain transport ratios (e.g. 135 < θ_D < 165 for N = 2), which elongate with a constant orientation. These fingers, whose shape are spatially and temporally stable despite permanent sediment flux parallel to the crest on both sides of the dune (Gao et al., 2015b), extend downwind but do not grow in height and width except at the source location (Figure 9.S17c). The finger dunes, with their constant heights and widths at their tips, and their theoretical ability to extend indefinitely, closely resemble linear dunes extending from topographic obstacles in the Erg of Fachi-Bilma in Niger (Figure 9.S17d,e). The bimodal wind regime in this east-cental Saharan region, which is composed of a dominant northeasterly wind and a weaker southeasterly wind separated by a divergence angle of 75° (Lucas et al., 2015), results in elongated forms that are aligned with the resultant sand flux over considerable distances (> 10 km).

Sand availability	θ_D (°)	N	ΔT_N	ΔT_1
Erodible sand bed	≤ 90	1	100	100
Erodible sand bed	> 90	1	300	300
Erodible sand bed	≤ 90	2	200	100
Erodible sand bed	> 90	2	400	200
Erodible sand bed	≤ 90	5	400	80
Erodible sand bed	> 90	5	500	100
Localised sand source	0–180	1	300	300
Localised sand source	0–180	2	300	150
Localised sand source	0–180	5	300	60

Table 9.S1. Initial conditions and parameters of the bidirectional wind regime in the numerical simulations on modes of dune formation. θ_D is the divergence angle between the primary (ΔT_N) and secondary (ΔT_1) winds; N is the transport ratio between the two winds. Parameters based on those of Gao et al. (2015b).

Outside a specific $\{\theta_D, N\}$ range, unstable finger-like structures extending away from the sand source eventually break up into small barchans (cf. Reffet et al., 2010; Gao et al., 2015b). The asymmetric barchans observed at high divergence angles by Gao

et al. (2015b) and Parteli et al. (2014) are not present in the morphologies presented in Figure 9.S17, probably because simulation results are sensitive to source conditions, and the spatial resolution at which the model was run was not as high as in the mentioned studies. In any case, dune orientation in the fingering mode is always more parallel than perpendicular to the dominant wind direction, contrary to dunes developing in the bed instability mode.

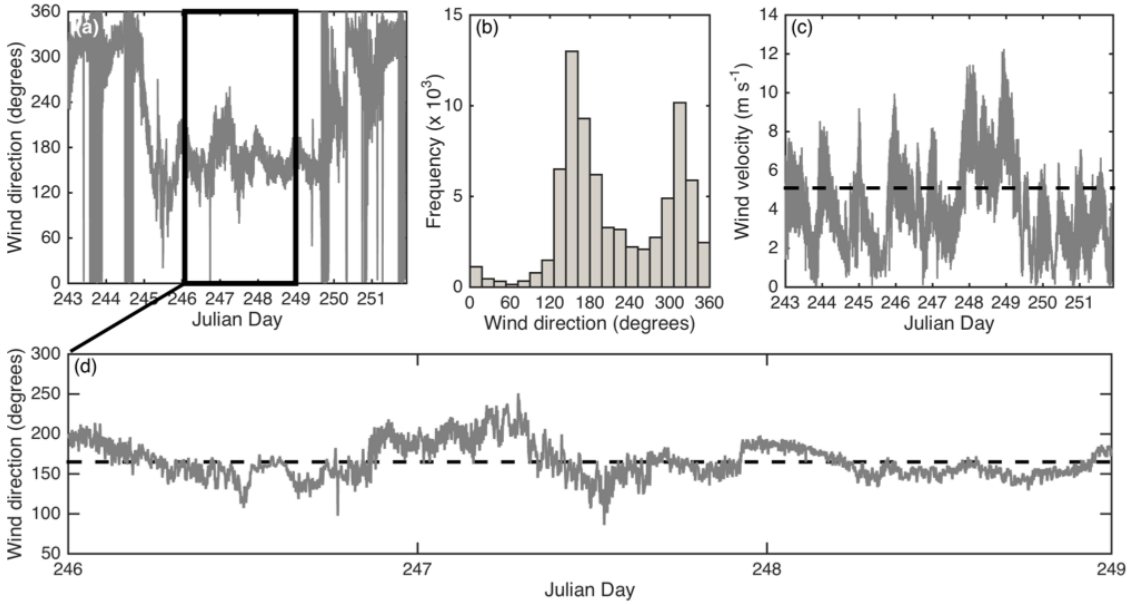


Figure 9.S18 Wind flow data from a 10-day period in September recorded in the Huab Valley, Skeleton Coast, Namibia: (a) Wind direction data over the full period (10-second average); (b) Frequency distribution of wind direction over the full period; (c) Wind velocity over the full period (10-second average), with the calculated entrainment threshold shown as a dotted black line; (d) Detailed wind direction data (1-minute average) over a selected four-day period, with average wind direction for that period shown as a dotted black line.

Appendix 2: Supplementary Information (Paper 5)

Text 10.S1. Climate data

Future climate projections

Projections of changes in the climate system in the IPCC framework are made using a hierarchy of climate models (IPCC, 2013). A set of scenarios, termed 'representative concentration pathways' (RCPs), are identified by their approximate total radiative forcing in the year 2100 relative to 1750 (IPCC, 2013). Commonly used scenarios in environmental modelling studies are RCP 4.5, representing stabilisation of greenhouse gas (GHG) emissions, and RCP 8.5, a high GHG emission scenario. Therefore, the RCP 4.5 and RCP 8.5 scenarios were chosen for this study.

There is much debate in the literature concerning how best to combine information from different models, which models to include, and the statistics that should be presented (Frame et al., 2007; Knutti, 2010; McSweeney & Jones, 2013). However, it is generally held that using a range of model projections instead of relying on any single model improves the robustness of analysis (Thornton et al., 2011; James & Washington, 2012; Whetton et al., 2012). In this study, a subset of three models was chosen from the CIP ensembles, based on Dieppois et al.'s (2015) ranking of CMIP5 model performance over southern Africa: CNRM-CM5, MIROC5 and MRI-CGCM3. For each of the three study sites, precipitation and temperature data were averaged across the three models at a monthly timestep.

Figure 10.S1 displays projected changes in annual precipitation over the period 2017–2100, for all three sites under RCP 4.5 and RCP 8.5.

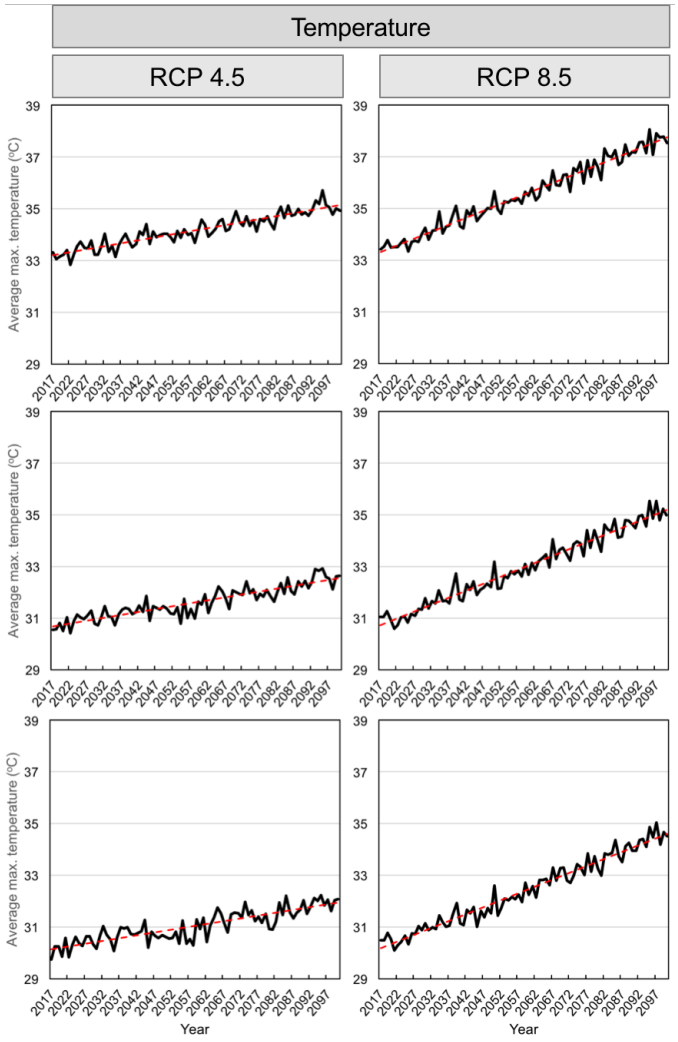


Figure 10.S1 Projected changes in average maximum daily temperature over the period 2017–2100, for Maun, Tshane and Tsabong, under the RCP 4.5 and RCP 8.5 scenarios. Dotted red lines show linear best fit trends.

Verifying climate projections

Observed climate data can be used to verify modelled historical climate, which in turn can inform the reliability of model projections into the future. Figure 10.S2 displays modelled and observed precipitation and temperature data (on a monthly timescale) for Maun, Tshane and Tsabong over historical periods for which observed data were available from the Botswana Department of Meteorological Services. Whilst temperature patterns at the three locations were relatively well back-cast (Figure

10.S2d,e,f), with strong coefficients of determination between observed and modelled data (R^2 = 0.70–0.84; Figure 10.S2h,j,l), the variability in precipitation data was not so well simulated (Figure 10.S2a,b,c), with weak coefficients of determination between observed and modelled data (R^2 = 0.11–0.20; Figure 10.S2g,i,k). The relatively poor representation of past precipitation is a common issue in climate modelling due to large uncertainties in the underlying forcing factors (Raisanen, 2007). The ability of the chosen models to faithfully replicate past temperature changes provides some indication of reliable model performance. The uncertainty in precipitation changes is accounted for in our experimental runs by imposing random precipitation variability, based on the variability characterising the two decades around each chosen year (i.e. 2020–2040, 2050–2070 and 2080–2100).

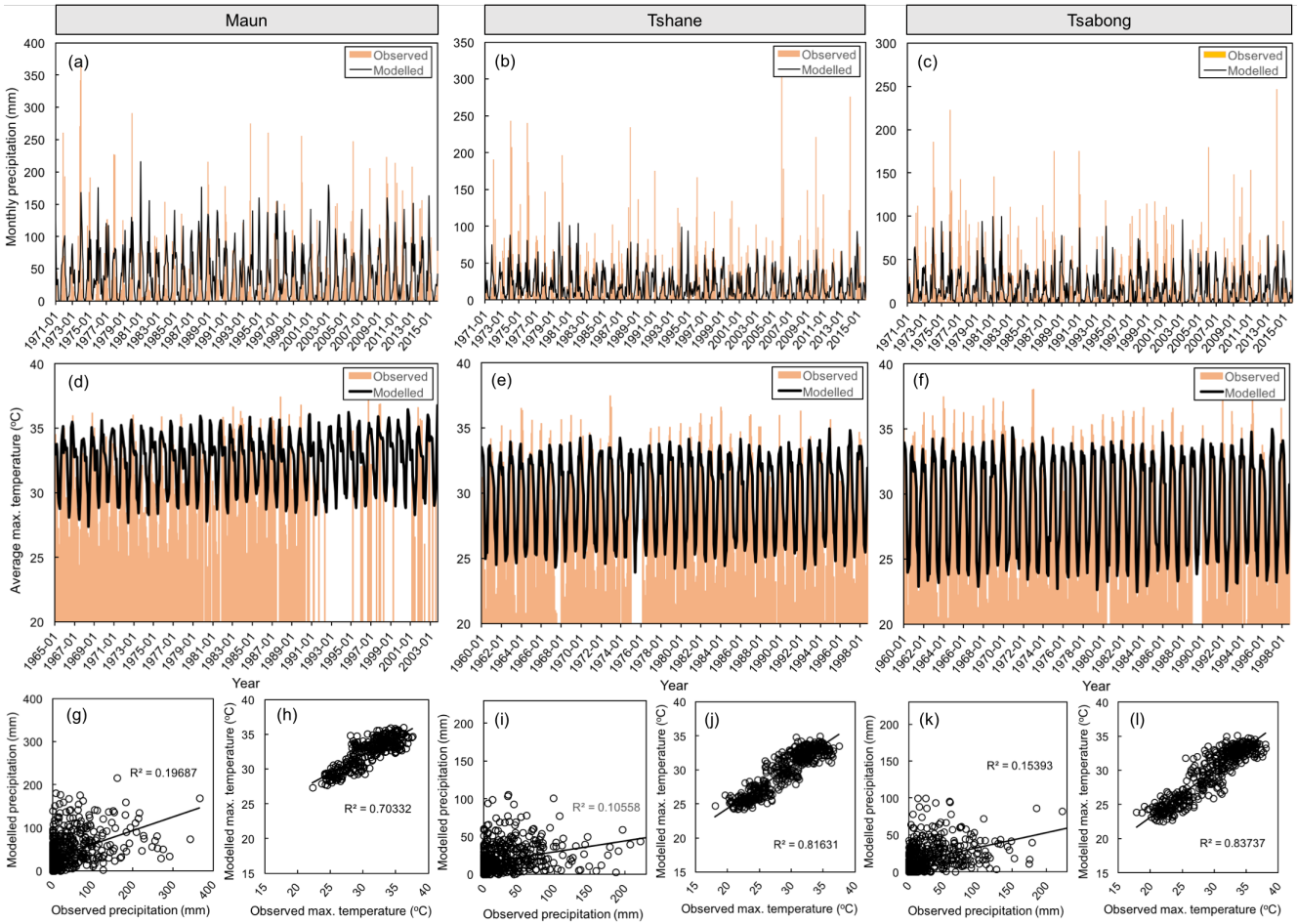


Figure 10.S2 Modelled and observed total monthly precipitation for (a) Maun, (b) Tshane, and (c) Tsabong, over periods for which observed data were available (missing data are shown as gaps). Modelled and observed average maximum daily temperature for (d) Maun, (e) Tshane, and (f) Tsabong. Observed vs modelled temperature and precipitation for (g, h) Maun, (i,j) Tshane, (k, l) Tsabong, and (g, h) Tshane. R^2 coefficients of determination and lines of best fit are shown.

Wind forcing

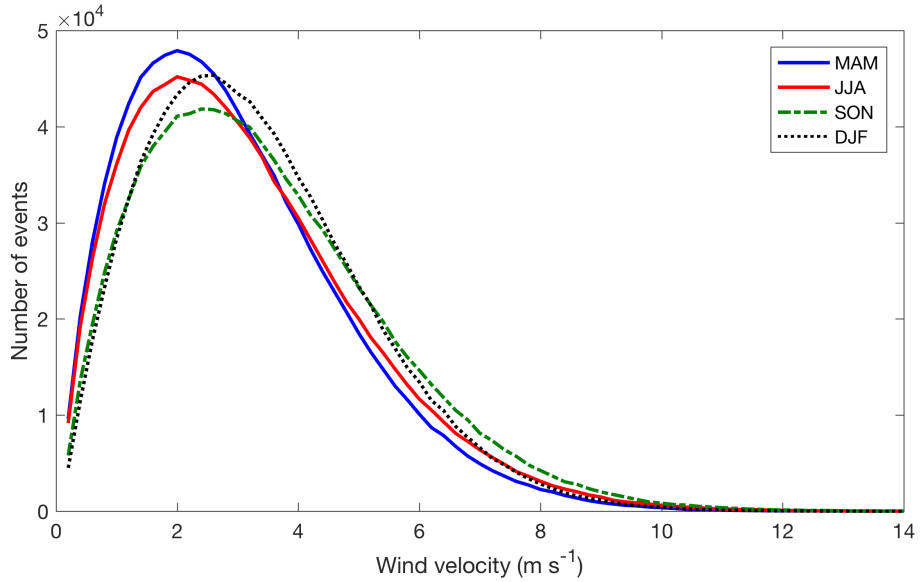


Figure 10.S3 Weibull distributions of wind velocities recorded at Twee Rivieren at 08:00, 14:00 and 20:00 over the period 1994–2013, grouped by season.

Months	Number of usable data points	Weibull shape parameter (β)	Weibull scale parameter (η)
MAM	5378	1.67	3.24
JJA	5232	1.65	3.42
SON	5183	1.75	3.78
DJF	5188	1.87	3.64

Table 10.S1 Number of usable data points (over the period 1994–2013), and maximum likelihood estimates of the 2-parameter Weibull distribution, for each month grouping.

Text 10.S2. Oral history of shrub encroachment

In addition to climate model datasets, oral history data were collected on a farm located in the southwest Kalahari Desert, just north of the Auob River. The farm extends across approximately 13,000 h.a. of vegetated linear dunes, with a variety of dryland grasses, shrubs and trees. The sole current farmer of the property was

interviewed informally over a period of several weeks in the period August–October 2014 and in September 2016.

In the 1980s, the farmer recalls a landscape much more populated by grasses than shrubs. Whilst wild game moved through in large numbers, placing pressure on the vegetation system, their manure and urine helped to fertilise the land and contributed to rapid grass recolonisation. The lack of human management of wildfires (which are mainly caused by lightning in this region) also helped to maintain low shrub populations. From the 1990s onwards, the region experienced increased agricultural intensification and fence construction, which led to greater grazing pressures and severe shrub encroachment in some areas. Whereas most dunes were covered with grasses ~40 years ago, according to the farmer, much of the heavily grazed farmland now consists of bare, intermittently active dune crests. The region's strong northeasterly winds result in a relatively slow southwesterly migration of the most denuded dunes.

In an attempt to reverse shrub encroachment on his land, the farmer started using herbicide that targets shrubs only (known as 'de-bushing'; Reed et al., 2015), and allows grasses to dominate the system within 2–3 years. On this particular farm, the application of herbicide in late 2009 resulted in the widespread replacement of *Rhigozum trichotomum* woody shrubs (Figure 10.S4a) with perennial grasses such as *Stipagrostis amabilis* and *Stipagrostis uniplumis* (Figure 10.S4b,c).

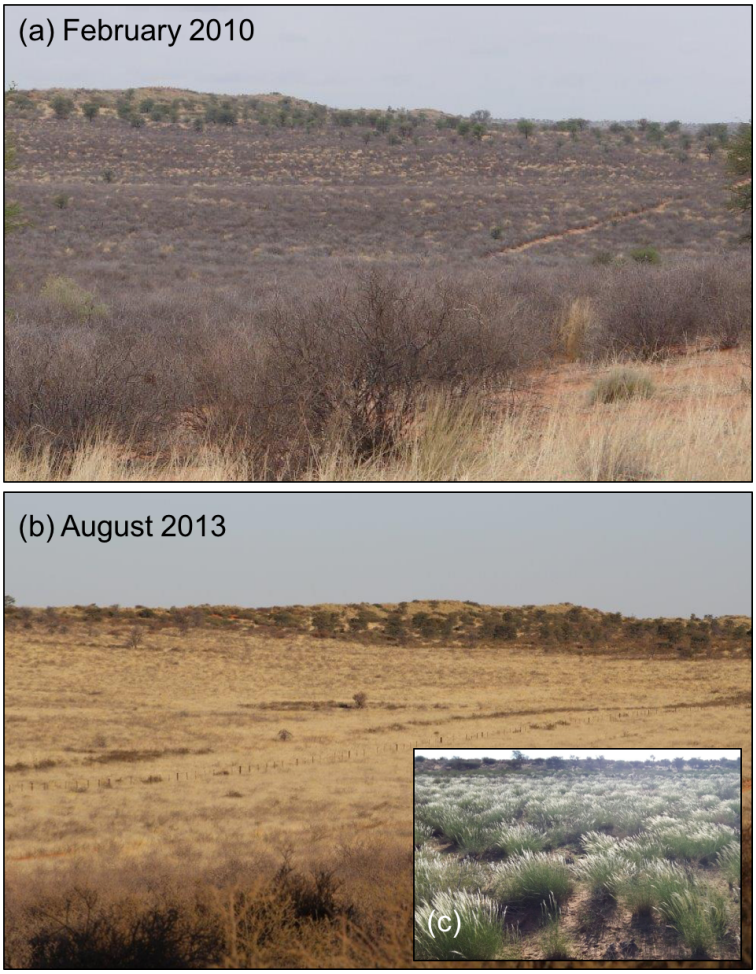


Figure 10.S4 The replacement of woody shrubs by perennial grasses following herbicide application ('de-bushing'): (a) shrub-dominated system in early 2010, a few months after application; (b) grass-dominated system a few years later; (c) close-up of *Stipagrostis amabilis* grasses that emerged after de-bushing. Photos: P. Möller (25.50^{o} S, 19.73^{o} E).

Text 10.S3 Impact of precipitation variability

Bailey (2011) showed that conditions of fluctuating generic stress can result in readjustments of vegetation patterns over time, and that the magnitude of stress variability can impact post-perturbation recovery in semi-arid systems. It is therefore important to investigate the impact of precipitation variability on landscape response within the fully-coupled ViSTA model. Variability was imposed by randomly sampling precipitation from a normal distribution around a series of idealized precipitation

scenarios: no trend (Figure 10.S5), v-shaped trend (Figure 10.S5), decreasing trend (Figure 10.S6), and increasing trend (Figure 10.S7). For each scenario, no variability, low variability (standard deviation, σ = 50 mm annual equivalent) and high variability (σ = 100 mm annual equivalent) conditions were imposed, based on realistic variabilities observed in historical data at our study sites.

In the no-trend scenario (Figure 10.S5), a lack of variability resulted in a baseline 'equilibrium' state of high, non-patterned vegetation cover, with stable proportions of grass, shrubs and trees. The addition of variability led to pattern formation, with more dramatic population declines at high variability, and grass:shrub ratios that fluctuated significantly. In the v-shaped trend scenario (Figure 10.S5), distinct labyrinthine patterns emerged as vegetation cover declined in response to decreasing precipitation. Variability in the precipitation signal resulted in a less rapid, predictable decline than the no-variability case, because occasional peaks in precipitation helped to rapidly repopulate existing vegetation patches. In the decreasing trend scenario (Figure 10.S6), greater variability led to an earlier decline in population density, as well as an earlier appearance of patterning (by up to ~60 years). At low average precipitation levels, occasional peaks result in grasses and shrubs to grow rapidly (occasionally to cover of 60–90%), but these die off quickly in subsequent low-precipitation years. Conversely, in the increasing trend scenario (Figure 10.S7), the presence of variability allowed grasses to establish quickly in response to vegetation peaks and, eventually, to form viable patches earlier than in the no-variability case. An intermediate level of variability provided the best conditions for vegetation regrowth, possibly because high variability leads to occasional precipitation lows that drive the vegetation system back down its recovery trajectory. Greater fluctuations in grass:shrub ratios in the high variability case suggest that the system may be closer to flipping to a shrub-encroached landscape.

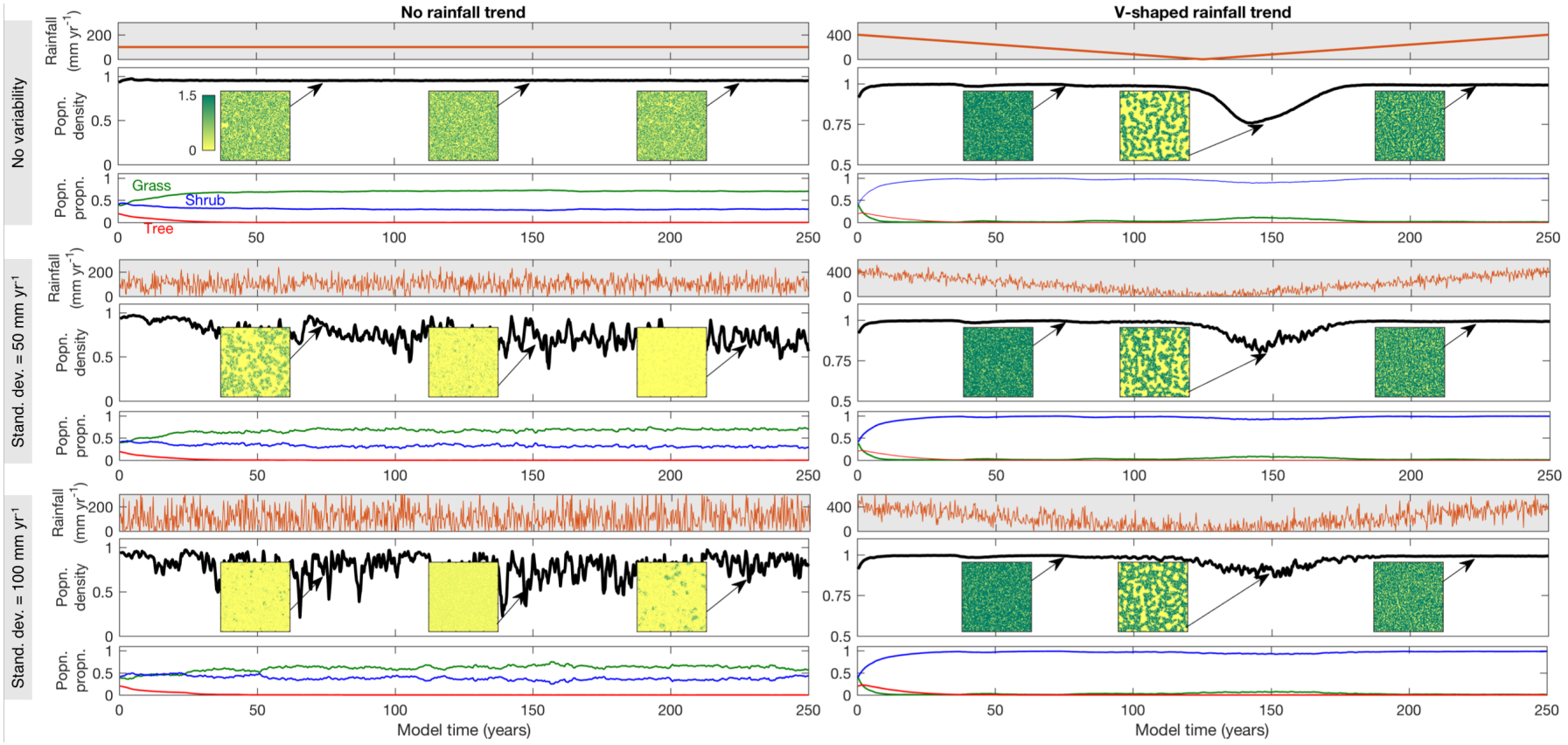


Figure 10.S5 Effect of rainfall variability on population density and proportions of vegetation types, for two rainfall scenarios: (1) no trend in rainfall (constantly 100 mm yr^{-1}), and (2) v-shaped rainfall (decreasing from 400 mm yr^{-1} to 0 mm yr^{-1} before increasing back to 400 mm yr^{-1}). For both scenarios, three rainfall variability cases were imposed: (1) no variability, (2) normally-distributed variability with a standard deviation of 50 mm yr^{-1} (annual equivalent), and (3) normally-distributed variability with a standard deviation of 100 mm yr^{-1}. For all cases, model was run for 250 years, with vegetation updated every 3 months (the rainfall in the grey panels is given as an annual rainfall equivalent for each 3-month iteration). At the start of each run, the model was initiated with approximate equilibrium proportions of grasses, shrubs and trees (as derived by Mayaud et al., 2017a). Inset panels show spatial distributions of vegetation heights across the domain at 75, 150 and 225 model years.

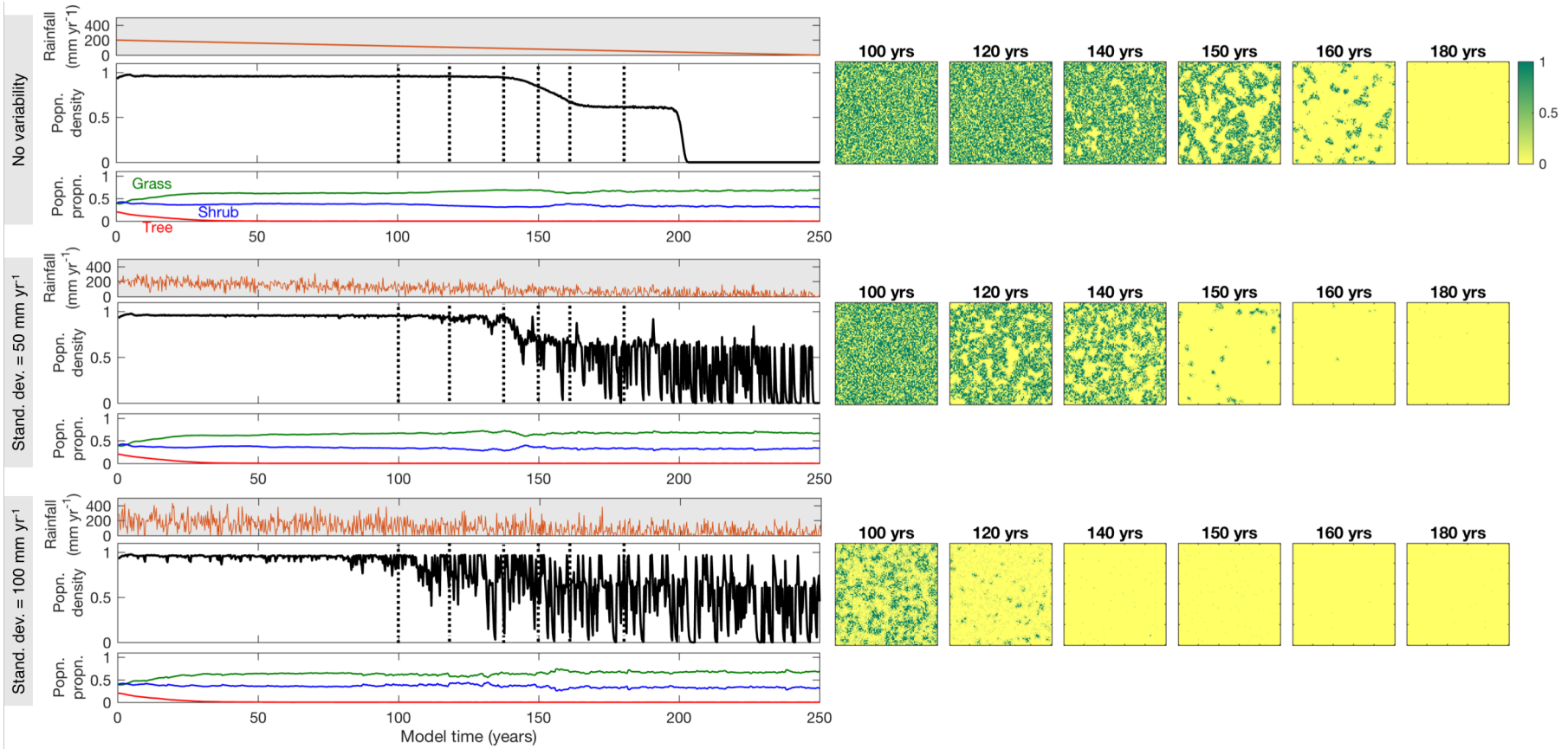


Figure 10.S6 Effect of rainfall variability on population density and proportions of vegetation types, for a scenario of decreasing rainfall (from 200 mm yr^{-1} to 0 mm yr^{-1}. Three rainfall variability cases were imposed: (1) no variability, (2) normally-distributed variability with a standard deviation of 50 mm yr^{-1} (annual equivalent) and (3) normally-distributed variability with a standard deviation of 100 mm yr^{-1}. For all cases, model was run for 250 years, with vegetation updated every 3 months (the rainfall in the grey panels is given as an annual rainfall equivalent for each 3-month iteration). At the start of each run, the model was initiated with approximate equilibrium proportions of grasses, shrubs and trees (as derived by Mayaud et al., 2017a). Panels show spatial distributions of vegetation heights at selected years spanning the observed collapse in population density (marked as dotted lines on population density graphs).

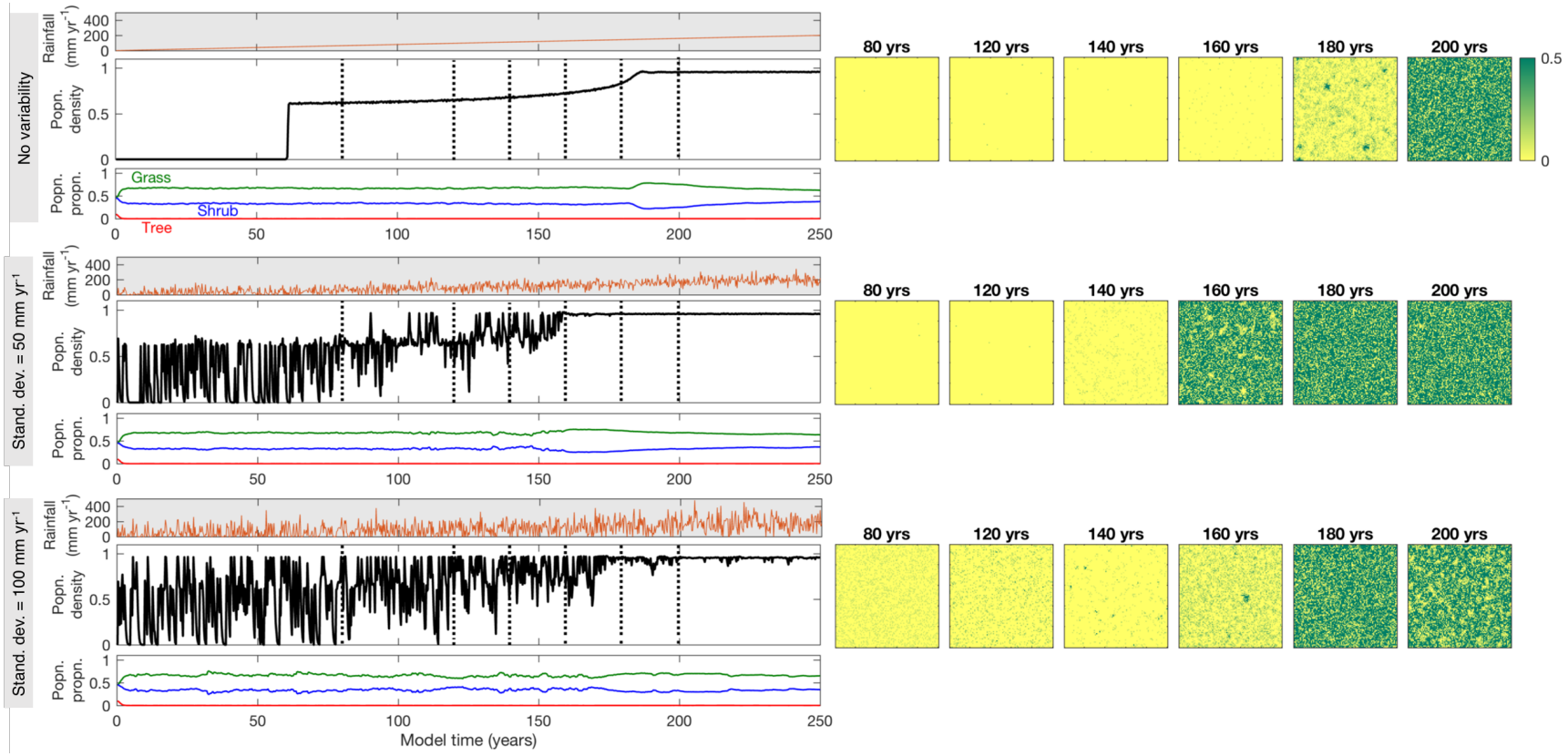


Figure 10.S7 Effect of rainfall variability on population density and proportions of vegetation types, for a scenario of increasing rainfall (from 0 mm yr^{-1} to 200 mm yr^{-1}. Three rainfall variability cases were imposed: (1) no variability, (2) normally-distributed variability with a standard deviation of 50 mm yr^{-1}, and (3) normally-distributed variability with a standard deviation of 100 mm yr^{-1}. For all cases, model was run for 250 years, with vegetation updated every 3 months (the rainfall in the grey panels is given as an annual rainfall equivalent for each 3-month iteration). At the start of each run, the model was initiated with approximate equilibrium proportions of grasses, shrubs and trees (as derived by Mayaud et al., 2017a). Panels show spatial distributions of vegetation heights at selected years spanning the observed collapse in population density (marked as dotted lines on population density graphs).

Text 10.S4 Equilibrium conditions

In addition to the equilibrium landscape characteristics presented in the main manuscript, Figure 10.S8 displays normalised plant ages at the chosen years across all three sites. At Maun, for both variability scenarios and both RCPs, grasses and shrubs on average live increasingly longer until 2060, then experience a decline in age at 2090. Trees tend to live longer as the century progresses. At Tshane, in most cases grasses and shrubs tend to live longer throughout the century than in 2000, particularly in the RCP 8.5 scenario. Average ages for trees do not tend to vary as strongly. At Tsabong, a clear decreasing trend in average ages for grasses and shrubs is evident for RCP 8.5, but for RCP 4.5 high variability leads to an increase in average ages in 2090. Trees do not experience a significant change in average age.

The strength of the feedbacks between sediment movement and vegetation growth can be modified depending on the plant types and environments. Figure 10.S9 shows the effect of varying the 'sediment importance factor' in the ViSTA model. This multiplicative factor changes the weighting of the sediment stress (Sed_S) in the formulation for the total stress (T_S). The sediment importance factor is at least greater than zero (i.e. the movement of sediment must have at least some impact on vegetation growth), but its upper bound is poorly constrained by a lack of appropriate experimental data. The sediment importance factor affects the population density (Figure 10.S9a), average sediment transport (Figure 10.S9b) and grass:shrub ratios (Figure 10.S9c) at equilibrium. These landscape characteristics do not change linearly with the value of the factor, demonstrating the potential existence of several equilibria that depend on sediment feedback strength.

Figure 10.S10 shows results from two additional equilibrium experiments. Summer (DJF) rainfall was varied between 80–120 mm yr^{-1} to verify the impact on grass:shrub

ratio and population density in equilibrium state (Figure 10.S10a). As summer rainfall increases, population density increases whilst grass:shrub ratios decline (i.e. greater shrub encroachment). This occurs because of more favourable conditions for shrub establishment over grasses. The effect of varying fixed shrub porosities on total sediment transport is shown in Figure 10.S10b. Although there is significant seasonal variability in transported sediment due to seasonal vegetation cover, sediment transport is greater when the model is populated with high-porosity (90%) shrubs compared with low-porosity (10%) shrubs. A landscape composed of intermediately porous shrubs (50%) experiences the lowest sediment transport rates, reflecting findings that intermediately porous elements strike a compromise between the strength of their sheltering effect and the downwind distance over which it is effective (Musick et al., 1996; Lee et al., 2002; Mayaud et al., 2016b).

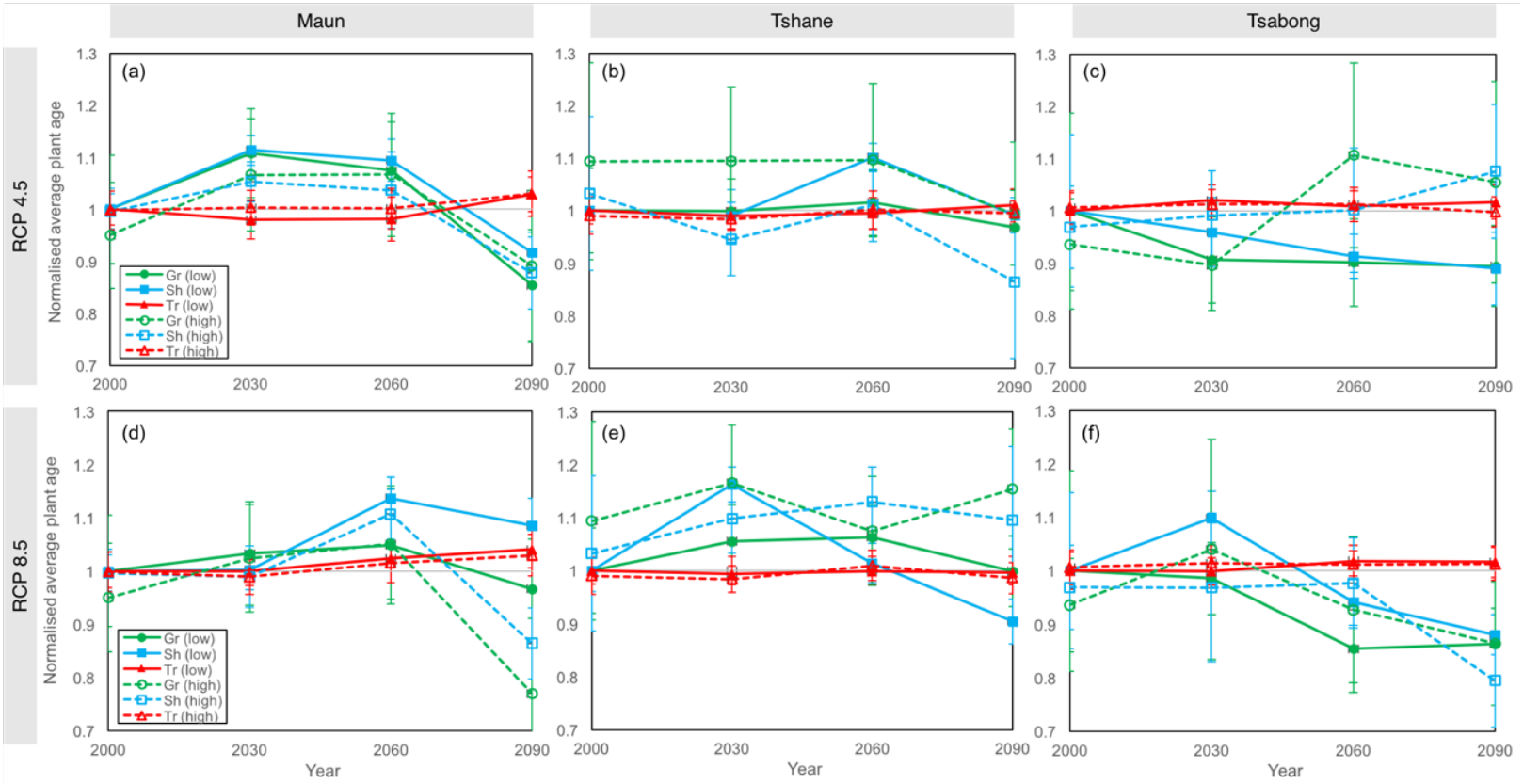


Figure 10.S8 Equilibrium normalised annual average plant age for grasses (Gr), shrubs (Sh) and trees (Tr) at the three chosen years (2030, 2060 and 2090), normalised to the baseline year (2000, RCP 4.5), at the three study sites. Results are shown for RCP 4.5 and RCP 8.5 scenarios, in low variability (standard deviation, σ = 30 mm annual equivalent) and high variability (σ = 160 mm annual equivalent) precipitation conditions. Model was run to equilibrium for the equivalent of 200 model years, with 20 wind events every 3 months, over a grid of 150 x 150 cells. The domain was randomly initiated with 90% vegetation cover and random sediment depth. Average ages were calculated as means over the last 10 years of each run. Error bars show coefficients of variation (thus partly representing seasonal variations).

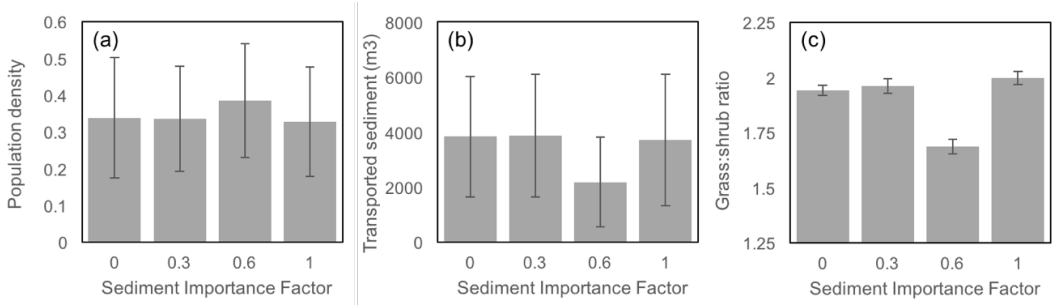


Figure 10.S9 Effect of varying the sediment importance factor on: (a) average population density; (b) average transported sediment; (c) grass:shrub ratio, where values above unity represent grass dominance. Model was run to equilibrium for the equivalent of 100 model years, with precipitation conditions for year 2030 (RCP 4.5) at Tsabong, over a grid of 150 x 150 cells. 10 wind events of constant wind velocity (7 m s^{-1}; threshold for entrainment = 5 m s^{-1}) occurred every 3 months. The domain was randomly initiated with 90% vegetation cover and random sediment depth. Average statistics were calculated as means over the last 10 years of each run. Error bars show standard deviations (thus partly representing seasonal variations).

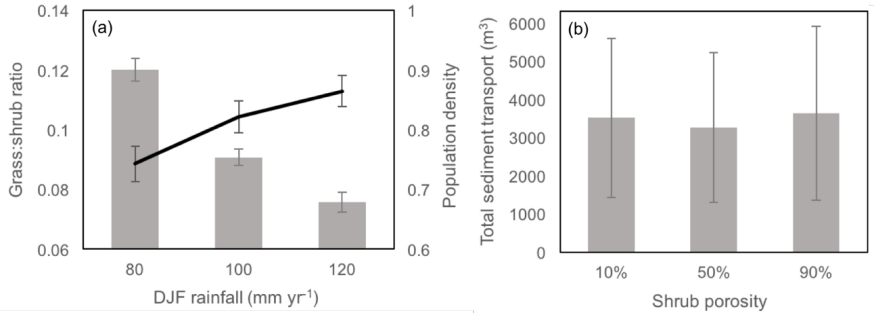


Figure 10.S10 (a) Impact of varying summer (DJF) rainfall on grass:shrub ratios (grey bars) and population density (black line). Model was run to equilibrium for the equivalent of 100 model years, over a grid of 150 x 150 cells, with MAM, JJA and SON precipitation conditions for year 2030 (RCP 4.5) at Tsabong, and DJF rainfall was varied between 80 mm yr^{-1} and 120 mm yr^{-1}. The domain was randomly initiated with 90% vegetation cover and no sediment transport was simulated; (b) Impact of varying fixed shrub porosity on total sediment transport across the domain. Model was run to equilibrium for the equivalent of 100 model years, with precipitation conditions for year 2030 (RCP 4.5) at Tsabong, over a grid of 150 x 150 cells. 10 wind events of constant wind velocity (7 m s^{-1}; threshold for entrainment = 5 m s^{-1}) occurred every 3 months. The domain was randomly initiated with 90% vegetation cover and random sediment depth. In both figures, error bars show standard deviations (thus partly representing seasonal variations), and average statistics were calculated as means over the last 10 years of each run.